

X-RAYS FROM PLANETARY NEBULAE:  
UNVEILING WIND COLLISIONS AND BINARITY

by

Rodolfo Montez Jr.

A dissertation proposal submitted in partial fulfillment of the  
requirements for the degree of Ph.D. in Astrophysical  
Sciences and Technology, in the College of Science,  
Rochester Institute of Technology

November 19, 2010

Approved by \_\_\_\_\_  
Dr. Andy Robinson Date  
Director, Astrophysical Sciences and Technology



ASTROPHYSICAL SCIENCES AND TECHNOLOGY  
COLLEGE OF SCIENCE  
ROCHESTER INSTITUTE OF TECHNOLOGY  
ROCHESTER, NEW YORK

CERTIFICATE OF APPROVAL

**Ph.D. DEGREE DISSERTATION**

The Ph.D. Degree Dissertation of Rodolfo Montez Jr. has  
been examined and approved by the dissertation committee  
as satisfactory for the dissertation requirement for the  
Ph.D. degree in Astrophysical Sciences and Technology

---

Dr. Joel H. Kastner, Dissertation Advisor

---

Dr. Carl Salvaggio, Committee Chair

---

Dr. Don Figer

---

Dr. Andrew Robinson

---

Dr. Jennifer Sokoloski

---

Date





DISSERTATION RELEASE PERMISSION  
ROCHESTER INSTITUTE OF TECHNOLOGY  
CHESTER F. CARLSON CENTER FOR IMAGING SCIENCE

Title of Dissertation:

**X-RAYS FROM PLANETARY NEBULAE:  
UNVEILING WIND COLLISIONS AND BINARITY**

I, Rodolfo Montez Jr., hereby grant permission to Wallace Memorial Library of R.I.T. to reproduce my thesis in whole or in part. Any reproduction will not be for commercial use or profit.

Signature \_\_\_\_\_ Date \_\_\_\_\_



# X-RAYS FROM PLANETARY NEBULAE: UNVEILING WIND COLLISIONS AND BINARITY

by

Rodolfo Montez Jr.

## Abstract

Planetary nebulae (PNe), the ionized, ejected envelopes of low- to inter-mediate-mass stars, are thought to be shaped by a nascent fast wind from the spent core (a future white dwarf) that collides with and sweeps up previously ejected material (red and asymptotic branch giant winds). This collision can generate an X-ray emitting “hot bubble” that fills the swept-up cavity. Circumstellar material in a dense torus or disk, likely due to an interacting binary in the PN nucleus, is widely believed to collimate the winds that shape non-spherical PNe. Hence, PNe offer excellent opportunities to study astrophysical shocks and binary interactions. In my thesis, I address these topics via a comprehensive analysis of new and archival (pointed and serendipitous) X-ray observations performed by Chandra and XMM-Newton X-ray satellite observatories. This analysis yields new information on the X-ray characteristics (detections and non-detections) of over 50 PNe ( $\sim 40\%$  of which were detected). Based on spatial/spectral analysis of a dozen diffuse X-ray emitting PNe, I confirm that hot bubble temperatures are generally much lower than predicted by simple shock models given measured central star fast wind velocities. Comparison of the X-ray emission and central star properties of the sample PNe with the predictions of heat conduction models indicates that some hot bubbles are regulated by heat conduction, while others appear to require alternative temperature-regulating mechanisms. From new detections of point-like hard X-ray emission from the binary star nuclei of LoTr5, DS1, and HFG1, I demonstrate that the X-ray emission most likely arises from rejuvenated coronae around the spun-up companions in these systems. These results place constraints on putative spun-up binary companions within other PNe in which point-like central sources have gone undetected by XMM and/or Chandra. I conclude with suggestions as to the most promising directions for future X-ray observations of PNe.



## Acknowledgements

I would like to acknowledge the following: the support and guidance provided by my thesis advisor Joel H. Kastner; encouragement, discussions, and advice from my collaborators Orsola De Marco, Jeno Sokoloski, You Hua Chu, Bruce Balick, and Noam Soker; the helpful input from my thesis committee members Don Figer, Andrew Robinson, Carl Salvaggio, and Jeno Sokoloski; tireless academic assistance provided by Sue Chan (RIT) and Barbara Warren (UR); the computational assistance provided by Jim Bodie and other CIS system administrators; the support and companionship from Heather R. Jacobson, Julie M. Lijoi (née Langú), Elizabeth Groves, Justin Comparetta, and Jesse Chvojka; the discussions with my officemates over the years: Young Sam Yu, Dave Principe, and Christine Trombley; the entire staff at Java Wally's for supplying me with freshly roasted, single-estate coffees from Africa and Indonesia and putting up with my coffee snobbery; and last, but definitely not least, my family for their love and support.

A special acknowledgement—with its own paragraph—must be made to Shauna Walczak for bringing large poster-board cut-outs of a 'D' and a white picket fence and alternatively holding them up in the air as I defended my thesis.



*Dedicated to the memory of Bernadette.*





# Contents

<b>1</b>	<b>Introduction to PNe</b>	<b>1</b>
1.1	Planetary Nebulae . . . . .	1
1.2	Evolution of Low- to Intermediate-Mass Stars . . . . .	4
1.3	Stellar Winds and Planetary Nebulae . . . . .	7
1.4	Towards a New Paradigm . . . . .	9
1.5	Unveiling Binarity and Wind Collisions . . . . .	10
<b>2</b>	<b>X-rays from PNe</b>	<b>13</b>
2.1	An Overview of X-ray Emission . . . . .	13
2.2	Point-like X-ray Emission from PNe . . . . .	15
2.2.1	Hot Photospheres of Central Stars . . . . .	15
2.2.2	Coronal and Accretion-Related Emission . . . . .	17
2.3	Extended X-ray Emission from PNe . . . . .	18
2.3.1	Hot Bubbles from Colliding Stellar Winds . . . . .	18
2.3.2	Shocks from Collimated Flows or Jets . . . . .	25
2.4	Emerging Trends and New Questions . . . . .	27
<b>3</b>	<b>X-ray Data and Analysis</b>	<b>31</b>
3.1	Satellite X-ray Observatories . . . . .	31
3.1.1	XMM Observations and Data . . . . .	32
3.1.2	CXO Observations and Data . . . . .	33
3.2	Mission-Specific Data Preparation and Analysis Software . . . . .	34
3.2.1	XMM Scientific Analysis System . . . . .	34
3.2.2	CXO CIAO Software . . . . .	34
3.3	Case Study: X-ray Observations of the Eskimo Nebula . . . . .	35
3.3.1	Locating Observations . . . . .	35
3.3.2	Preliminary Data Preparation . . . . .	36
3.3.3	Creating Energy Filtered X-ray Images . . . . .	37
3.3.4	Source and Background X-ray Spectra . . . . .	40

3.4	Off-axis Sources . . . . .	46
3.5	Non-detections and Upper Limit Determinations . . . . .	47
3.5.1	Determining the Upper Limit Count Rate . . . . .	47
3.5.2	Calculating the Upper Limit Flux for Undetected Sources . . . . .	48
3.6	Chapter Summary . . . . .	49
<b>4</b>	<b>X-rays from WR-Type PNe</b>	<b>53</b>
4.1	Wolf-Rayet Central Stars in PNe . . . . .	53
4.2	Data and Analysis . . . . .	56
4.2.1	NGC 40 . . . . .	57
4.2.2	Hen 2-99 . . . . .	61
4.2.3	NGC 5315 . . . . .	64
4.3	Discussion . . . . .	67
4.4	Chapter Summary . . . . .	71
<b>5</b>	<b>X-rays from the Bipolar PN Hb 5</b>	<b>73</b>
5.1	Bipolar PNe and the Shaping and Evolution of PNe . . . . .	73
5.2	Data and Analysis . . . . .	76
5.2.1	Spatial Analysis . . . . .	77
5.2.2	Spectral Analysis . . . . .	78
5.3	Discussion . . . . .	79
5.4	Chapter Summary . . . . .	85
<b>6</b>	<b>X-rays from Binary PNe</b>	<b>87</b>
6.1	Binary Central Stars in Planetary Nebulae . . . . .	87
6.2	Target CSPNe . . . . .	90
6.2.1	HFG 1 and DS 1 . . . . .	91
6.2.2	LoTr 5 . . . . .	92
6.3	Data and Analysis . . . . .	94
6.3.1	Observations . . . . .	94
6.3.2	Spectral Analysis . . . . .	96
6.3.3	Timing Analysis . . . . .	105
6.4	Discussion . . . . .	107
6.4.1	X-ray Emission from the WD . . . . .	107
6.4.2	X-rays from Colliding Wind Shocks . . . . .	110
6.4.3	X-rays from Accretion-related Processes . . . . .	112
6.4.4	X-rays from Internal O-star Wind Shocks . . . . .	115
6.4.5	X-rays from Coronal Activity Associated with the CSPNe Com- panions . . . . .	115

6.5	Chapter Summary . . . . .	120
<b>7</b>	<b>XMM Serendipitous Survey of PNe</b>	<b>123</b>
7.1	Serendipitous Survey . . . . .	123
7.1.1	Search Method and Observation Filtering . . . . .	124
7.1.2	Data Preparation and Analysis . . . . .	125
7.2	Detections . . . . .	127
7.2.1	Hubble 5 . . . . .	127
7.2.2	LoTr 5 . . . . .	128
7.2.3	NGC 6543 . . . . .	128
7.2.4	Symbiotic System: H 1-36 . . . . .	133
7.2.5	Symbiotic System: V2416 Sgr (PN M 3-18) . . . . .	135
7.3	Non-Detections . . . . .	139
7.3.1	Determining the $3\text{-}\sigma$ Count Rate . . . . .	140
7.3.2	Selection of Characteristic $T_X$ for Hot Bubbles and Coronae . . . . .	142
7.3.3	Intervening Absorption of X-rays . . . . .	143
7.3.4	Distances of the Sample PNe . . . . .	143
7.3.5	Results of Upper Limit X-ray Properties Calculations . . . . .	144
7.4	Evolution of X-ray Emitting Hot Bubbles . . . . .	144
7.4.1	Central Star Temperatures . . . . .	145
7.4.2	Constraining the Evolution of X-ray Emitting Hot Bubbles . . . . .	146
7.5	Constraining the Existence of Spun-up Companions . . . . .	147
<b>8</b>	<b>Summary and Conclusions</b>	<b>153</b>
8.1	Unveiling Binarity . . . . .	153
8.2	Unveiling Wind Collisions . . . . .	155
8.3	New Questions and Future Directions . . . . .	156
	<b>Bibliography</b>	<b>158</b>
<b>A</b>	<b>Tables and Data for the XMMSSPNe</b>	<b>173</b>
A.1	Survey Sample Tables and Data . . . . .	173
A.2	Non-Detections . . . . .	181



# List of Figures

1.1	False color images of planetary nebulae from the Hubble Space Telescope. . . . .	3
1.2	A Hertzsprung-Russell (HR) diagram depicting the evolution of a low-to intermediate-mass star. . . . .	5
1.3	A schematic of ISW and GISW theories of the formation and evolution of PNe. . . . .	12
2.1	Hot bubble X-ray emission detected from BD+30 3639 by the Chandra X-ray Observatory. . . . .	22
2.2	Model Predictions of X-ray Emission from Hot Bubbles in PNe . . .	24
2.3	Model Predictions of X-ray Emission from Hot Bubbles in PNe . . .	25
2.4	The asymmetrical X-ray emission detected from NGC 7027 by the Chandra X-ray Observatory. . . . .	27
3.1	Images of the X-ray emission observed from the Eskimo Nebula. . .	38
3.2	Smoothed X-ray contours of the Eskimo Nebula. . . . .	40
3.3	Soft and Hard energy band images of the X-ray emission observed from the Eskimo Nebula. . . . .	41
3.4	CXO X-ray Spectrum of the Eskimo Nebula. . . . .	43
3.5	XMM X-ray Spectrum of the Eskimo Nebula. . . . .	44
3.6	Model Predictions of X-ray Emission from Hot Bubbles in PNe . . .	45
3.7	Model Predictions of X-ray Emission from Hot Bubbles in PNe . . .	46
4.1	Images of the PN NGC 40. . . . .	58
4.2	Discovery Spectrum of X-ray Emission from the PN NGC 40. . . . .	59
4.3	Image of the X-ray and Optical Emission from the PN NGC 40. . .	60
4.4	CXO X-ray Spectrum of the PN NGC 40. . . . .	62
4.5	Images of PN Hen 2-99. . . . .	63
4.6	Discovery of X-ray emission from the PN NGC 5315 . . . . .	65

4.7	Image of the PN NGC 5315 with Smoothed Contours of the X-ray Emission . . . . .	66
4.8	CXO X-ray Spectrum of the PN NGC 5315. . . . .	67
5.1	XMM Imaging of the Bipolar PN Hb 5 Field. . . . .	80
5.2	XMM Imaging of the Bipolar PN Hb 5 Field. . . . .	81
5.3	XMM Imaging of the Bipolar PN Hb 5 Field. . . . .	82
5.4	XMM EPIC X-ray Spectra of the Bipolar PN Hb 5. . . . .	83
6.1	CXO X-ray Spectrum of Binary PN HFG 1. . . . .	99
6.2	CXO X-ray Spectrum of Binary PN DS 1. . . . .	100
6.3	XMM X-ray Spectrum of Binary PN LoTr 5. . . . .	102
6.4	CXO X-ray Spectrum of Binary PN LoTr 5. . . . .	103
6.5	Unfolded X-ray Spectra of Binary PN LoTr 5. . . . .	104
6.6	X-ray Light Curves of Binary PNe HFG 1 and DS 1. . . . .	108
6.7	X-ray Light Curves of Binary PN LoTr 5. . . . .	109
7.1	Distributions of Survey Observations . . . . .	126
7.2	Serendipitous XMM pn Observation of NGC 6543. . . . .	130
7.3	Serendipitous XMM MOS1 and MOS2 Observations of NGC 6543 . . . . .	131
7.4	X-ray Spectra from the Serendipitous XMM Observation of NGC 6543. . . . .	132
7.5	Serendipitous XMM Observation of the Symbiotic System H 1-36. . . . .	134
7.6	X-ray Spectrum of the Serendipitous XMM Observation of the Symbiotic System H 1-36. . . . .	136
7.7	Serendipitous XMM pn Observation of the Symbiotic System V2416 Sgr. . . . .	137
7.8	Serendipitous XMM MOS1 and MOS2 Observations of the Symbiotic System V2416 Sgr. . . . .	138
7.9	X-ray Spectra from the Serendipitous XMM Observation of the Symbiotic System V2416 Sgr. . . . .	140
7.10	Model Predictions of Hot Bubble X-ray Luminosity . . . . .	141
7.11	Model Predictions of Hot Bubble X-ray Luminosity . . . . .	147
7.12	Upper Limits on Putative Spun-up Main Sequence Companions . . . . .	149
7.13	Upper Limits on Putative Spun-up Giant Companions . . . . .	150
A.1	XMM EMOS1 observation (ObsID 0206590101) of PN Bl 3-10 . . . . .	183
A.2	XMM EMOS2 observation (ObsID 0206590101) of PN Bl 3-10 . . . . .	184
A.3	XMM EPN observation (ObsID 0206590101) of PN Bl 3-10 . . . . .	185
A.4	XMM EMOS1 observation (ObsID 0206590201) of PN Bl 3-10 . . . . .	187
A.5	XMM EMOS2 observation (ObsID 0206590201) of PN Bl 3-10 . . . . .	188

A.6	XMM EPN observation (ObsID 0206590201) of PN Bl 3-10 . . . . .	189
A.7	XMM EMOS1 observation (ObsID 0402280101) of PN Bl 3-10 . . . .	191
A.8	XMM EMOS2 observation (ObsID 0402280101) of PN Bl 3-10 . . . .	192
A.9	XMM EPN observation (ObsID 0402280101) of PN Bl 3-10 . . . . .	193
A.10	XMM EMOS2 observation (ObsID 0203040201) of PN Bl 3-13 . . . .	195
A.11	XMM EPN observation (ObsID 0203040201) of PN Bl 3-13 . . . . .	196
A.12	XMM EMOS1 observation (ObsID 0302570101) of PN Bl 3-13 . . . .	198
A.13	XMM EMOS2 observation (ObsID 0302570101) of PN Bl 3-13 . . . .	199
A.14	XMM EPN observation (ObsID 0302570101) of PN Bl 3-13 . . . . .	200
A.15	XMM EMOS1 observation (ObsID 0150220101) of PN H 1-13 . . . .	202
A.16	XMM EMOS2 observation (ObsID 0150220101) of PN H 1-13 . . . .	203
A.17	XMM EMOS1 observation (ObsID 0203750101) of PN H 1-43 . . . .	205
A.18	XMM EMOS2 observation (ObsID 0203750101) of PN H 1-43 . . . .	206
A.19	XMM EPN observation (ObsID 0203750101) of PN H 1-43 . . . . .	207
A.20	XMM EPN observation (ObsID 0500540101) of PN H 1-43 . . . . .	209
A.21	XMM EPN observation (ObsID 0032940101) of PN H 1-43 . . . . .	211
A.22	XMM EMOS1 observation (ObsID 0157960101) of PN H 1-54 . . . .	213
A.23	XMM EMOS2 observation (ObsID 0157960101) of PN H 1-54 . . . .	214
A.24	XMM EMOS1 observation (ObsID 0205800201) of PN H 1-54 . . . .	216
A.25	XMM EMOS2 observation (ObsID 0205800201) of PN H 1-54 . . . .	217
A.26	XMM EPN observation (ObsID 0205800201) of PN H 1-54 . . . . .	218
A.27	XMM EMOS2 observation (ObsID 0403110601) of PN H 1-58 . . . .	220
A.28	XMM EPN observation (ObsID 0403110601) of PN H 1-58 . . . . .	221
A.29	XMM EMOS1 observation (ObsID 0152420101) of PN H 2-37 . . . .	223
A.30	XMM EMOS2 observation (ObsID 0152420101) of PN H 2-37 . . . .	224
A.31	XMM EPN observation (ObsID 0152420101) of PN H 2-37 . . . . .	225
A.32	XMM EMOS1 observation (ObsID 0124710401) of PN H 4-1 . . . . .	227
A.33	XMM EMOS2 observation (ObsID 0124710401) of PN H 4-1 . . . .	228
A.34	XMM EPN observation (ObsID 0124710401) of PN H 4-1 . . . . .	229
A.35	XMM EMOS1 observation (ObsID 0007422401) of Hen 2-102 . . . .	231
A.36	XMM EMOS2 observation (ObsID 0007422401) of Hen 2-102 . . . .	232
A.37	XMM EPN observation (ObsID 0007422401) of Hen 2-102 . . . . .	233
A.38	XMM EPN observation (ObsID 0110950501) of PN K 1-16 . . . . .	235
A.39	XMM EMOS1 observation (ObsID 0212481201) of PN K 3-57 . . . .	237
A.40	XMM EMOS2 observation (ObsID 0212481201) of PN K 3-57 . . . .	238
A.41	XMM EMOS1 observation (ObsID 0153752201) of PN K 3-92 . . . .	240
A.42	XMM EMOS2 observation (ObsID 0153752201) of PN K 3-92 . . . .	241
A.43	XMM EMOS1 observation (ObsID 0153751701) of PN K 3-92 . . . .	243

A.44	XMM EMOS2 observation (ObsID 0153751701) of PN K 3-92 . . .	244
A.45	XMM EMOS1 observation (ObsID 0153751701u) of PN K 3-92 . . .	246
A.46	XMM EMOS2 observation (ObsID 0153751701u) of PN K 3-92 . . .	247
A.47	XMM EMOS2 observation (ObsID 0306700501) of PN M 1-28 . . .	249
A.48	XMM EPN observation (ObsID 0306700501) of PN M 1-28 . . . . .	250
A.49	XMM EMOS1 observation (ObsID 0202790101) of PN M 1-29 . . .	252
A.50	XMM EMOS2 observation (ObsID 0202790101) of PN M 1-29 . . .	253
A.51	XMM EMOS1 observation (ObsID 0154750301) of PN M 1-29 . . .	255
A.52	XMM EMOS2 observation (ObsID 0154750301) of PN M 1-29 . . .	256
A.53	XMM EMOS1 observation (ObsID 0152420101) of PN M 1-37 . . .	258
A.54	XMM EMOS2 observation (ObsID 0152420101) of PN M 1-37 . . .	259
A.55	XMM EPN observation (ObsID 0152420101) of PN M 1-37 . . . . .	260
A.56	XMM EMOS1 observation (ObsID 0206590201) of PN M 2-19 . . .	262
A.57	XMM EMOS1 observation (ObsID 0402280101) of PN M 2-19 . . .	264
A.58	XMM EMOS1 observation (ObsID 0206590101) of PN M 2-19 . . .	266
A.59	XMM EMOS2 observation (ObsID 0206590101) of PN M 2-19 . . .	267
A.60	XMM EPN observation (ObsID 0206590101) of PN M 2-19 . . . . .	268
A.61	XMM EMOS1 observation (ObsID 0206590101) of PN M 2-19 . . .	269
A.62	XMM EMOS2 observation (ObsID 0206590101) of PN M 2-19 . . .	270
A.63	XMM EPN observation (ObsID 0206590101) of PN M 2-19 . . . . .	271
A.64	XMM EMOS1 observation (ObsID 0206590101) of PN M 2-19 . . .	272
A.65	XMM EMOS2 observation (ObsID 0206590101) of PN M 2-19 . . .	273
A.66	XMM EPN observation (ObsID 0206590101) of PN M 2-19 . . . . .	274
A.67	XMM EMOS1 observation (ObsID 0301880401) of PN M 2-45 . . .	276
A.68	XMM EMOS2 observation (ObsID 0301880401) of PN M 2-45 . . .	277
A.69	XMM EPN observation (ObsID 0301880401) of PN M 2-45 . . . . .	278
A.70	XMM EMOS1 observation (ObsID 0085581101) of PN M 3-17 . . .	280
A.71	XMM EMOS2 observation (ObsID 0085581101) of PN M 3-17 . . .	281
A.72	XMM EMOS1 observation (ObsID 0085581001) of PN M 3-17 . . .	283
A.73	XMM EMOS2 observation (ObsID 0085581001) of PN M 3-17 . . .	284
A.74	XMM EPN observation (ObsID 0085581001) of PN M 3-17 . . . . .	285
A.75	XMM EMOS1 observation (ObsID 0085580201) of PN M 3-17 . . .	287
A.76	XMM EMOS2 observation (ObsID 0085580201) of PN M 3-17 . . .	288
A.77	XMM EPN observation (ObsID 0085580201) of PN M 3-17 . . . . .	289
A.78	XMM EMOS1 observation (ObsID 0050940201) of PN M 3-19 . . .	291
A.79	XMM EMOS1 observation (ObsID 0135741601) of PN M 3-28 . . .	293
A.80	XMM EMOS2 observation (ObsID 0135741601) of PN M 3-28 . . .	294
A.81	XMM EPN observation (ObsID 0135741601) of PN M 3-28 . . . . .	295



A.82	XMM EMOS1 observation (ObsID 0135744401) of PN M 3-28 . . .	297
A.83	XMM EMOS2 observation (ObsID 0135744401) of PN M 3-28 . . .	298
A.84	XMM EPN observation (ObsID 0135744401) of PN M 3-28 . . . . .	299
A.85	XMM EMOS1 observation (ObsID 0154750301) of PN M 3-44 . . .	301
A.86	XMM EMOS2 observation (ObsID 0154750301) of PN M 3-44 . . .	302
A.87	XMM EMOS1 observation (ObsID 0085580201) of PN M 3-46 . . .	304
A.88	XMM EMOS2 observation (ObsID 0085580201) of PN M 3-46 . . .	305
A.89	XMM EMOS1 observation (ObsID 0085581001) of PN M 3-46 . . .	307
A.90	XMM EMOS2 observation (ObsID 0085581001) of PN M 3-46 . . .	308
A.91	XMM EMOS1 observation (ObsID 0085581101) of PN M 3-46 . . .	310
A.92	XMM EMOS2 observation (ObsID 0085581101) of PN M 3-46 . . .	311
A.93	XMM EMOS1 observation (ObsID 0050940201) of PN M 3-47 . . .	313
A.94	XMM EMOS2 observation (ObsID 0050940201) of PN M 3-47 . . .	314
A.95	XMM EPN observation (ObsID 0050940201) of PN M 3-47 . . . . .	315
A.96	XMM EMOS1 observation (ObsID 0122700401) of PN M 3-55 . . .	317
A.97	XMM EMOS2 observation (ObsID 0122700401) of PN M 3-55 . . .	318
A.98	XMM EPN observation (ObsID 0122700401) of PN M 3-55 . . . . .	319
A.99	XMM EMOS1 observation (ObsID 0201200101) of PN PBOZ 10 . .	321
A.100	XMM EMOS2 observation (ObsID 0201200101) of PN PBOZ 10 . .	322
A.101	XMM EPN observation (ObsID 0201200101) of PN PBOZ 10 . . .	323
A.102	XMM EMOS1 observation (ObsID 0050940101) of PN SHWI 5 . .	325
A.103	XMM EMOS2 observation (ObsID 0050940101) of PN SHWI 5 . .	326
A.104	XMM EPN observation (ObsID 0050940101) of PN SHWI 5 . . . . .	327
A.105	XMM EMOS1 observation (ObsID 0203040101) of PN SHWI 5 . .	329
A.106	XMM EMOS2 observation (ObsID 0203040101) of PN SHWI 5 . .	330
A.107	XMM EPN observation (ObsID 0203040101) of PN SHWI 5 . . . . .	331
A.108	XMM EMOS1 observation (ObsID 0007421401) of PN SUWT 2 . .	333
A.109	XMM EMOS2 observation (ObsID 0007421401) of PN SUWT 2 . .	334
A.110	XMM EPN observation (ObsID 0007421401) of PN SUWT 2 . . . . .	335
A.111	XMM EMOS1 observation (ObsID 0007422301) of PN SUWT 2 . .	337
A.112	XMM EMOS2 observation (ObsID 0007422301) of PN SUWT 2 . .	338
A.113	XMM EPN observation (ObsID 0007422301) of PN SUWT 2 . . . . .	339
A.114	XMM EMOS1 observation (ObsID 0112971801) of Terz N 2022 . . .	341
A.115	XMM EMOS2 observation (ObsID 0112971801) of Terz N 2022 . . .	342
A.116	XMM EPN observation (ObsID 0112971801) of Terz N 2022 . . . . .	343
A.117	XMM EPN observation (ObsID 0112970901) of Terz N 2022 . . . . .	345
A.118	XMM EMOS1 observation (ObsID 0306700501) of PN Th 4-3 . . .	347
A.119	XMM EMOS2 observation (ObsID 0306700501) of PN Th 4-3 . . .	348

A.120 XMM EMOS1 observation (ObsID 0204270101) of PN VBE 2	. . .	350
A.121 XMM EMOS2 observation (ObsID 0204270101) of PN VBE 2	. . .	351
A.122 XMM EMOS1 observation (ObsID 0204270101) of PN VBE 3	. . .	353
A.123 XMM EMOS2 observation (ObsID 0204270101) of PN VBE 3	. . .	354
A.124 XMM EMOS1 observation (ObsID 0083280101) of PN Vd 1-8	. . .	356
A.125 XMM EMOS2 observation (ObsID 0083280101) of PN Vd 1-8	. . .	357
A.126 XMM EMOS1 observation (ObsID 0083280201) of PN Vd 1-8	. . .	359
A.127 XMM EMOS2 observation (ObsID 0083280201) of PN Vd 1-8	. . .	360
A.128 XMM EMOS1 observation (ObsID 0083280301) of PN Vd 1-8	. . .	362
A.129 XMM EMOS2 observation (ObsID 0083280301) of PN Vd 1-8	. . .	363
A.130 XMM EMOS1 observation (ObsID 0083280401) of PN Vd 1-8	. . .	365
A.131 XMM EMOS2 observation (ObsID 0083280401) of PN Vd 1-8	. . .	366

# List of Tables

2.1	CXO and XMM X-ray Observations of PNe . . . . .	23
3.1	Frequently Used SAS Tasks for XMM Data Analysis . . . . .	50
3.2	Frequently Used CIAO Tasks for CXO Data Analysis . . . . .	51
3.3	Frequently Used XSPEC X-ray Spectral Models . . . . .	51
3.4	X-ray Emission Processes and Characteristics . . . . .	52
6.1	Properties of Observed Binary PNe . . . . .	91
6.2	X-ray Observations of Binary PNe . . . . .	95
6.3	Spectral Fitting of the X-ray Emission from Binary CSPNe . . . . .	119
7.1	XMMSSPNe Upper Limits . . . . .	151
7.2	XMMSSPNe Upper Limits (Unknown Distances) . . . . .	152
A.1	XMM Serendipitous PNe: Observations . . . . .	173
A.2	Serendipitous Symbiotic Systems . . . . .	177
A.3	Removed Objects and Observations . . . . .	178
A.4	XMM Serendipitous PNe: Basic Data . . . . .	179
A.5	Summary of the Analysis for the XMM EPIC observation (ObsID 0206590101) of PN Bl 3-10. . . . .	182
A.6	Summary of the Analysis for the XMM EPIC observation (ObsID 0206590201) of PN Bl 3-10. . . . .	186
A.7	Summary of the Analysis for the XMM EPIC observation (ObsID 0402280101) of PN Bl 3-10. . . . .	190
A.8	Summary of the Analysis for the XMM EPIC observation (ObsID 0203040201) of PN Bl 3-13. . . . .	194
A.9	Summary of the Analysis for the XMM EPIC observation (ObsID 0302570101) of PN Bl 3-13. . . . .	197
A.10	Summary of the Analysis for the XMM EPIC observation (ObsID 0150220101) of PN H 1-13. . . . .	201

A.11 Summary of the Analysis for the XMM EPIC observation (ObsID 0203750101) of PN H 1-43. . . . .	204
A.12 Summary of the Analysis for the XMM EPIC observation (ObsID 0500540101) of PN H 1-43. . . . .	208
A.13 Summary of the Analysis for the XMM EPIC observation (ObsID 0032940101) of PN H 1-43. . . . .	210
A.14 Summary of the Analysis for the XMM EPIC observation (ObsID 0157960101) of PN H 1-54. . . . .	212
A.15 Summary of the Analysis for the XMM EPIC observation (ObsID 0205800201) of PN H 1-54. . . . .	215
A.16 Summary of the Analysis for the XMM EPIC observation (ObsID 0403110601) of PN H 1-58. . . . .	219
A.17 Summary of the Analysis for the XMM EPIC observation (ObsID 0152420101) of PN H 2-37. . . . .	222
A.18 Summary of the Analysis for the XMM EPIC observation (ObsID 0124710401) of PN H 4-1. . . . .	226
A.19 Summary of the Analysis for the XMM EPIC observation (ObsID 0007422401) of Hen 2-102. . . . .	230
A.20 Summary of the Analysis for the XMM EPIC observation (ObsID 0110950501) of PN K 1-16. . . . .	234
A.21 Summary of the Analysis for the XMM EPIC observation (ObsID 0212481201) of PN K 3-57. . . . .	236
A.22 Summary of the Analysis for the XMM EPIC observation (ObsID 0153752201) of PN K 3-92. . . . .	239
A.23 Summary of the Analysis for the XMM EPIC observation (ObsID 0153751701) of PN K 3-92. . . . .	242
A.24 Summary of the Analysis for the XMM EPIC observation (ObsID 0153751701u) of PN K 3-92. . . . .	245
A.25 Summary of the Analysis for the XMM EPIC observation (ObsID 0306700501) of PN M 1-28. . . . .	248
A.26 Summary of the Analysis for the XMM EPIC observation (ObsID 0202790101) of PN M 1-29. . . . .	251
A.27 Summary of the Analysis for the XMM EPIC observation (ObsID 0154750301) of PN M 1-29. . . . .	254
A.28 Summary of the Analysis for the XMM EPIC observation (ObsID 0152420101) of PN M 1-37. . . . .	257
A.29 Summary of the Analysis for the XMM EPIC observation (ObsID 0206590201) of PN M 2-19. . . . .	261

A.30 Summary of the Analysis for the XMM EPIC observation (ObsID 0402280101) of PN M 2-19. . . . .	263
A.31 Summary of the Analysis for the XMM EPIC observation (ObsID 0206590101) of PN M 2-19. . . . .	265
A.32 Summary of the Analysis for the XMM EPIC observation (ObsID 0301880401) of PN M 2-45. . . . .	275
A.33 Summary of the Analysis for the XMM EPIC observation (ObsID 0085581101) of PN M 3-17. . . . .	279
A.34 Summary of the Analysis for the XMM EPIC observation (ObsID 0085581001) of PN M 3-17. . . . .	282
A.35 Summary of the Analysis for the XMM EPIC observation (ObsID 0085580201) of PN M 3-17. . . . .	286
A.36 Summary of the Analysis for the XMM EPIC observation (ObsID 0050940201) of PN M 3-19. . . . .	290
A.37 Summary of the Analysis for the XMM EPIC observation (ObsID 0135741601) of PN M 3-28. . . . .	292
A.38 Summary of the Analysis for the XMM EPIC observation (ObsID 0135744401) of PN M 3-28. . . . .	296
A.39 Summary of the Analysis for the XMM EPIC observation (ObsID 0154750301) of PN M 3-44. . . . .	300
A.40 Summary of the Analysis for the XMM EPIC observation (ObsID 0085580201) of PN M 3-46. . . . .	303
A.41 Summary of the Analysis for the XMM EPIC observation (ObsID 0085581001) of PN M 3-46. . . . .	306
A.42 Summary of the Analysis for the XMM EPIC observation (ObsID 0085581101) of PN M 3-46. . . . .	309
A.43 Summary of the Analysis for the XMM EPIC observation (ObsID 0050940201) of PN M 3-47. . . . .	312
A.44 Summary of the Analysis for the XMM EPIC observation (ObsID 0122700401) of PN M 3-55. . . . .	316
A.45 Summary of the Analysis for the XMM EPIC observation (ObsID 0201200101) of PN PBOZ 10. . . . .	320
A.46 Summary of the Analysis for the XMM EPIC observation (ObsID 0050940101) of PN SHWI 5. . . . .	324
A.47 Summary of the Analysis for the XMM EPIC observation (ObsID 0203040101) of PN SHWI 5. . . . .	328
A.48 Summary of the Analysis for the XMM EPIC observation (ObsID 0007421401) of PN SUWT 2. . . . .	332

A.49 Summary of the Analysis for the XMM EPIC observation (ObsID 0007422301) of PN SUWT 2. . . . .	336
A.50 Summary of the Analysis for the XMM EPIC observation (ObsID 0112971801) of Terz N 2022. . . . .	340
A.51 Summary of the Analysis for the XMM EPIC observation (ObsID 0112970901) of Terz N 2022. . . . .	344
A.52 Summary of the Analysis for the XMM EPIC observation (ObsID 0306700501) of PN Th 4-3. . . . .	346
A.53 Summary of the Analysis for the XMM EPIC observation (ObsID 0204270101) of PN VBE 2. . . . .	349
A.54 Summary of the Analysis for the XMM EPIC observation (ObsID 0204270101) of PN VBE 3. . . . .	352
A.55 Summary of the Analysis for the XMM EPIC observation (ObsID 0083280101) of PN Vd 1-8. . . . .	355
A.56 Summary of the Analysis for the XMM EPIC observation (ObsID 0083280201) of PN Vd 1-8. . . . .	358
A.57 Summary of the Analysis for the XMM EPIC observation (ObsID 0083280301) of PN Vd 1-8. . . . .	361
A.58 Summary of the Analysis for the XMM EPIC observation (ObsID 0083280401) of PN Vd 1-8. . . . .	364

# Chapter 1

## Introduction to Planetary Nebulae

### 1.1 Planetary Nebulae

A planetary nebula<sup>1</sup> is a glowing shell of material ejected and illuminated by a dying star. The widely-held mechanism responsible for the formation of planetary nebulae (PNe) stems from the interacting stellar winds (ISW) theory posed by Kwok et al. (1978). Stars lose mass throughout their life through a stellar wind; the sun is no different, ejecting a steady solar wind of charged particles which can interact with the Earth's magnetic fields to create the aurora borealis. For much of a star's life, this mass loss rate is very low ( $< 10^{-7} M_{\odot} \text{ yr}^{-1}$ ) and the stellar wind is slow ( $\sim 10 -$

---

<sup>1</sup>The name planetary nebula is a misnomer introduced by William Herschel in the late 1700s. The misnomer arises from the disk-like and greenish appearance of planetary nebulae in small telescopes, which share characteristics with the planet, Uranus, which Herschel had recently discovered. Typically, a planetary nebula has nothing to do with planets. However, the material in the planetary nebula provides the fuel and the impetus for the subsequent generation of stars, their planets, and potential life forms on those planets.

$30 \text{ km s}^{-1}$ . But during the star’s death, the mass loss rate rises up to  $10^{-4} M_{\odot} \text{ yr}^{-1}$ , filling the circumstellar environment with enriched stellar material. A faster stellar wind emerges from the star, it catches up to the previously ejected, slower, stellar wind. The winds interact in a collision which sweeps material into a dense shell that becomes the PN. The collision also creates a region of high temperature shocked gas called the “hot bubble”. The core of the dying star is hot and as this mass loss occurs, its apparent temperature rises, when the apparent temperature reaches 30 kK, the swept-up shell of material becomes ionized by the strong ultra-violet (UV) flux from the exposed core. Now the planetary nebula is born. The PN continues to expand ( $\sim 25 \text{ km s}^{-1}$ ) from the momentum transferred during collision between the slow and fast stellar winds or from the high pressure force exerted by the hot bubble. A PN will continue to shine until its star cools or the material dissipates below observational detectability.

From the vibrant imagery of PNe captured by the Hubble Space Telescope (HST)—a sample of which are provided in Figure 1.1—we find a vast array of morphologies with strong deviations from spherical symmetry. The morphological attributes of PNe range from narrow-waisted, bipolar nebula to the multi-shelled, elliptical nebula, which show evidence for high velocity outflows along the semi-major axis of the nebula. These observed morphologies cannot be explained by the simple ISW theory. Frank et al. (1993) used hydrodynamical simulations to show that the variety of morphologies could be described if we assume that a collimating obstruction exists around the central star of the PN. This new assumption provides the framework for the generalized interacting stellar wind (GISW) theory. The success of the GISW



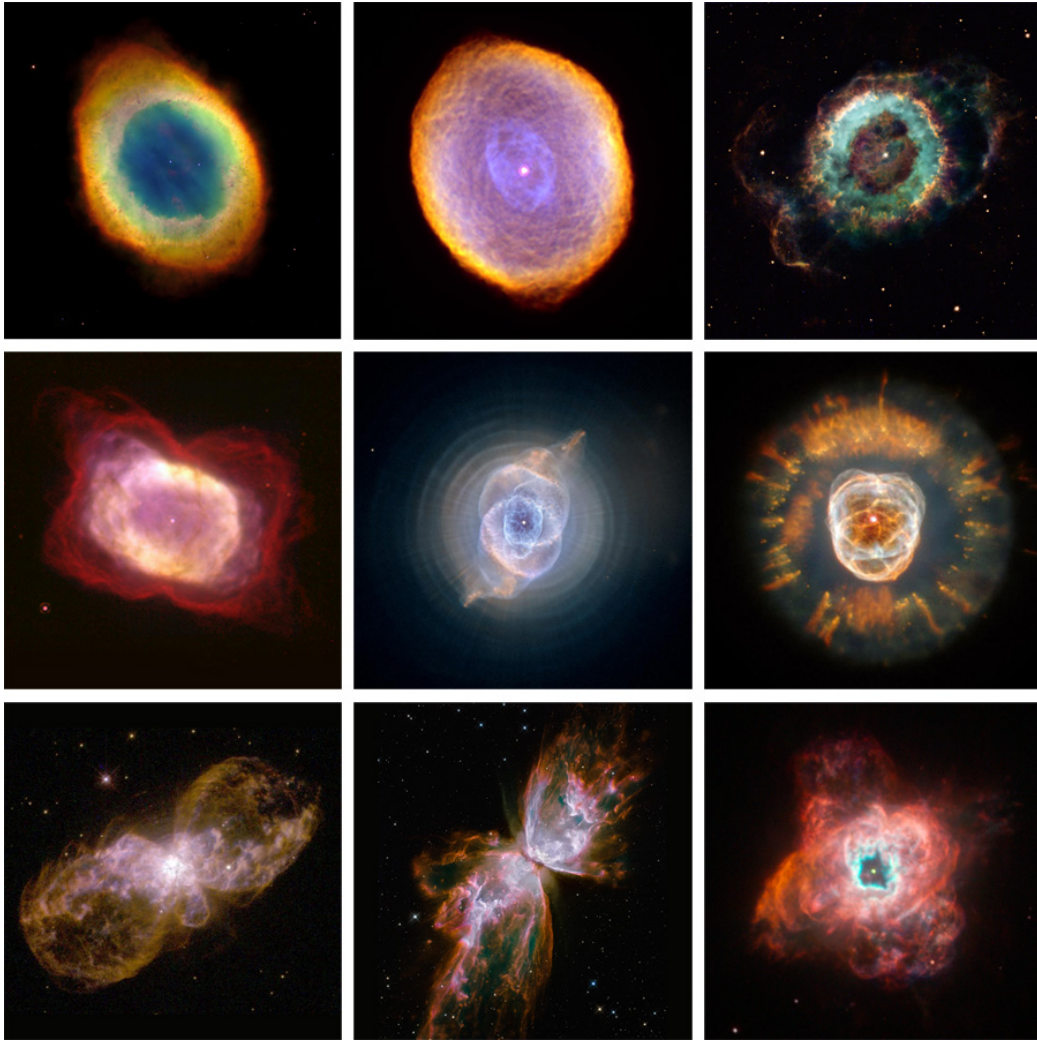


Figure 1.1 False color images of planetary nebulae from the Hubble Space Telescope. A variety of morphological properties are found among planetary nebulae. Top row, left to right: M 57 (Ring Nebula; NASA and The Hubble Heritage Team), IC 418 (Spirograph Nebula; R. Sahai and A. R. Hajian), NGC 6369 (Little Ghost Nebula; NASA and The Hubble Heritage Team). Middle row, left to right: NGC 7027 (J. Westphal and W. Latter), NGC 6543 (Cat's Eye Nebula; J.P. Harrington and K.J. Borkowski), NGC 2392 (Eskimo Nebula). Bottom row, left to right: Hubble 5 (B. Balick, V. Icke, G. Mellema), NGC 6302 (Bug or Butterfly Nebula; NASA, ESA, and the Hubble SM4 ERO Team), NGC 5315 (NASA and The Hubble Heritage Team).

theory is tempered by observational results that do not completely fit within the theoretical framework describing the origin and evolution of PNe (see, for example, the review by Balick & Frank 2002). First and foremost, the source of a collimating obstruction is unknown. Results gained from observations of asymmetric PNe have provide new challenges to our understanding of the PNe phenomenon and are the focus of a series of a conferences called Asymmetrical Planetary Nebulae (APN) I (Harpaz & Soker 1995) to V (2010, in press). Since APN IV (2007), a growing number of PNe researchers have supported the hypothesis that the origin, formation, and evolution of PNe is closely, perhaps exclusively, linked to the death of a star in binary system (see De Marco 2009). In this thesis, I will address the prevailing and emerging paradigms with X-ray observations of PNe. Before delving further into the subject of X-ray emission from PNe, a brief overview of the the paradigms on the origin of PNe is in order<sup>2</sup>.

## 1.2 Evolution of Low- to Intermediate-Mass Stars

Not all dying stars will form a PN; stars between one and eight solar masses (low- to intermediate-mass stars) typically evolve to form PNe, stars above the mass range have more exotic end states, such as supernovae, while those below this mass range do not initiate the changes in their stellar structure necessary to form a PN. To help visualize the evolution of a low- to intermediate-mass star, we consider the Hertzsprung-Russell (HR) diagram in Figure 1.2, which plots the luminosity of a star

---

<sup>2</sup>The book *The origin and evolution of planetary nebulae* (Kwok 2000) provides the basis for this overview and is a highly recommended text on the subject of PNe.

versus its effective temperature. By convention, the temperature is plotted in reverse, high to low.

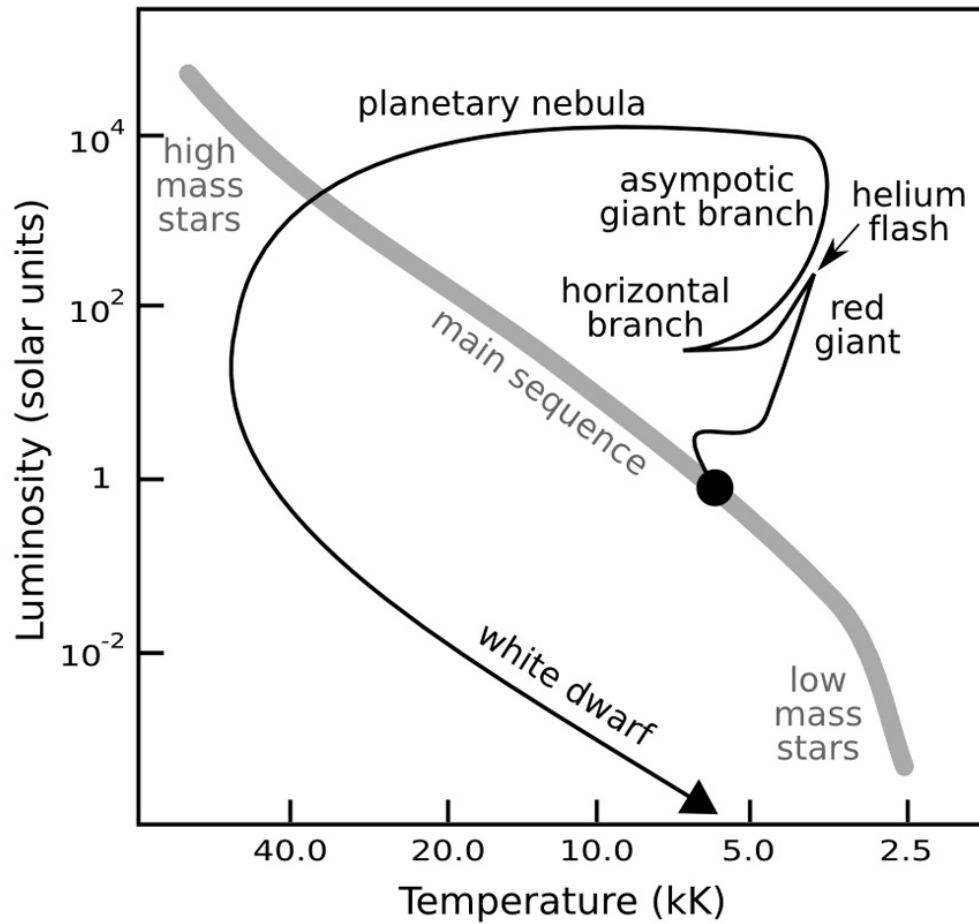


Figure 1.2 A Hertzsprung-Russell (HR) diagram depicting the evolution of a low- to intermediate-mass star. The stars path is shown by the solid line, with key positions in the HR diagram labeled accordingly. The evolution is described in the text. The main sequence of star's of all masses is the shown by the grey line.

For most of the lifetime of a star, it resides along a locus of points called the main sequence. Higher mass stars populate the upper left of the HR diagram, towards

the hot and bright end of the main sequence, while lower mass stars fill in towards the lower right of the HR diagram, decreasing in luminosity and temperature with decreasing mass. While on the main sequence, a star is steadily burning hydrogen in its core via fusion, or nuclear burning, which steadily builds up helium ash in the core. During this period of steady hydrogen burning, the star exists in a state of hydrostatic equilibrium, where the outward pressure of the radiation field emerging from the core balances the inward gravitational contraction from the mass of the star.

Once most of the hydrogen in the core is exhausted, the helium ash, too cool to burn, cannot provide a strong enough radiation field to counteract gravity. A gravitational contraction begins and the helium in the core is compacted while any remaining hydrogen is squeezed into a thin shell around the compacted helium core. Above this hydrogen layer is a hot plasma of hydrogen, helium, and heavier elements called the stellar envelope. As the shell of hydrogen heats up, fusion ignites, which drives away the stellar envelope, creating a large, puffy star called a Red Giant. Meanwhile, the hydrogen burning shell continues to deposit additional helium ash on to the core, enhancing the gravitational contraction which heats the core to the point where helium fusion ignites, in what is called a helium flash. The helium flash raises the star's luminosity sharply before the helium burning in the core settles into steady state on the horizontal branch of the HR diagram.

Core helium burning ultimately leaves a degenerate core of carbon and oxygen surrounded by shells undergoing hydrogen and helium burning. At this point, the star is said to be on the Asymptotic Giant Branch (AGB) of the HR diagram. The events that transpire during the AGB are the most important with respect to the

physical parameters of the subsequent PN.

## 1.3 Stellar Winds and Planetary Nebulae

During the AGB phase, the hydrogen shell is heated by gravitational contraction, which triggers steady hydrogen burning in the shell, while the helium shell below grows and undergoes periodic helium burning, also called thermal pulses or helium shell flashes. As the layers furthest from the core cool, the material condenses into dust grains which are efficiently driven away by radiation pressure due to the tremendous luminosity generated by the hydrogen and helium burning shells. Gas couples to the dust grains and is dragged along with the dust away from the core. This dust-driven expansion process is referred to as the slow AGB wind. Through this slow AGB wind the star can lose 40 to 80% of its initial mass. The helium shell flashes also bring the ashes of previous episodes of nuclear burning into the outer layers (also called dredge-up) which enhances the chemistry of the slow AGB wind with heavier elements like nitrogen, neon, and oxygen. In addition to these slow-neutron-capture elements, the building block of life, carbon, is dredged up from the deepest layer of the helium shell. This enhanced slow AGB wind escapes from the gravitation of the core and enters the interstellar medium (ISM), providing an enriched fuel for the subsequent generation of stars, planets, and potential life forms.

The star leaves the AGB phase when the copious mass loss ceases. During the post-AGB phase, the star's effective temperature steadily increases as the core contracts further. Any emerging stellar wind must be faster than the escape velocity of the

core, which has increased due to the contraction. The emerging stellar wind is called the fast wind; it surges away from the core at velocities from 500 to 3000 km/s. This fast wind is on a collision course with the denser, slower moving AGB wind. The collision between the fast stellar wind and the slow AGB wind creates shocks and plows the AGB wind material into a dense shell. When the effective temperature of the central star reaches 30 kK or higher, the dense, swept-up shell of AGB material is excited by the energetic UV photons from the star and the formation of the PN is complete. This theory of the formation of PNe by two colliding winds is called the Interacting Stellar Wind (ISW) theory.

While shining brightly, PNe appear in an assortment of shapes and sizes (recall Figure 1.1). While the observed morphologies can be broadly classified as round, elliptical, and bipolar, the ISW theory described above can only account for spherically symmetric PNe. Therefore, it became necessary to expand the ISW theory from a one-dimensional, spherically symmetric calculation to two-dimensional hydrodynamical simulations. The expanded theory is called the generalized interacting stellar wind theory (GISW) and assumes that the circumstellar environment is disk-like, or a dense equatorial torus, which collimates the emerging stellar wind by focusing it towards the less dense poles. Under GISW, the range of observed morphologies in PNe could be successfully attributed to the evolution of the hydrodynamical interaction between the fast wind of the central star and a collimated flow focused by the dense equatorial torus.

## 1.4 Towards a New Paradigm

Despite the initial success of GISW, high resolution images obtained by the Hubble Space Telescope (HST) revealed details from PNe that simply could not be explained by hydrodynamical interactions. The HST observations reveal narrow low-ionization structures with younger kinematical ages compared to the dominate morphology of the PN, suggesting that multiple events with drastically evolving morphological properties might shape a PN throughout its relatively short lifetime. The faint halos revealed around PNe (the remnants of prior mass loss episodes) appear as nested spherical shells, in contrast to the present day asymmetrical PNe, suggesting the drastic evolution of the mass loss and structure of emerging stellar winds.

GISW theory also presumed the existence of dense equatorial material which gives rise to collimated flows responsible for the observed PNe morphologies. This presents a new question on the nature and origin of this dense equatorial material. One attractive potential solution posits that interactions between two stars in a binary system provide this dense equatorial material. Hydrodynamical modeling of the equatorial mass loss by an interacting binary star system (Mastrodemos & Morris 1998, 1999) demonstrates that binary interactions can provide the dense equatorial material, however much fewer than half of PNe are known to harbor binary systems. Finding binary companions near the bright dying star illuminating the PN is a difficult task, but in recent years, new searches for binary companions in the nuclei of PNe have been performed, and the detection of binary systems in PNe is steadily growing. As a result, a new paradigm called the Binary Hypothesis is developing that suggests PNe are

purely a binary phenomenon. The new paradigm posits that binary systems account for the enhanced and episodic mass loss during the AGB phase and the dense equatorial material and collimated flows assumed by the GISW theory. Although still in development, the Binary Hypothesis has spurred the scientific community interested in the origin and evolution of PNe.

## 1.5 Unveiling Binarity and Wind Collisions

In this thesis, I will show how X-ray observations of PNe inform our understanding of PNe, pose new questions, and introduce new avenues that utilize PNe to explore new physics. Chapter 2 provides a brief overview of astronomical X-ray observations, the historical X-ray observations of PNe, the source of X-ray emission from PNe, and emerging trends and new questions raised by recent X-ray observations of PNe. Chapter 3 presents a thorough review of the analysis of X-ray observations and compiles the results of many targeted X-ray observations, some for the first time. The results and questions presented in Chapters 2 and 3 are addressed in the remaining chapters. Chapter 4 presents the analysis of X-ray emission from PNe with hydrogen-poor, Wolf-Rayet-type central stars, which have higher X-ray luminosities than their hydrogen-rich counterparts, suggesting a distinct physical process for the thermal regulation of the PNe. Chapter 5 presents the serendipitous detection of a bipolar PN and discusses the role of X-ray emitting mechanisms on the shaping of PNe. Chapter 6 presents the discovery of hard X-ray emission from PNe with binary star systems, and argues that this hard X-ray emission likely arises from spun-up



companions. Chapter 7 presents the results of an extensive search for serendipitously observed PNe in the ever-growing XMM X-ray data archive. Finally, in Chapter 8, I conclude with a discussion of the questions posed by the X-ray observations of PNe (Chapter 2) and the new avenues X-ray observations of PNe provide.

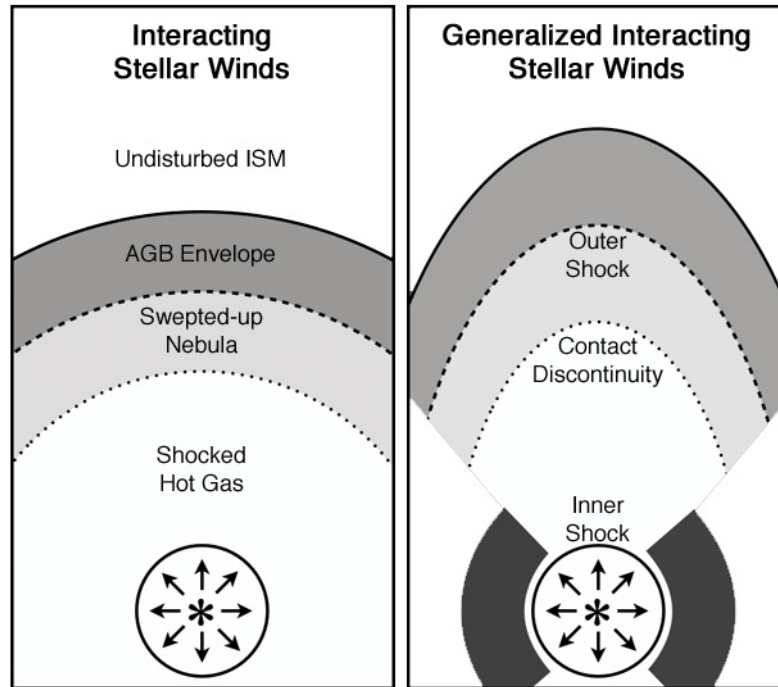


Figure 1.3 A schematic of ISW (left) and GISW (right) theories of the formation and evolution of PNe. A fast wind launched by the central star (indicated by the asterisk), collides with the previously ejected AGB wind (envelope), sweeping material into the nebular shell and setting up distinct regions separated by shock boundaries. On the left panel, the these distinct regions are labeled, on the right panel, their boundaries are labeled. By assuming a dense circumstellar torus around the central star the hydrodynamical simulations can predict the range of morphological properties observed from PNe.

## Chapter 2

# X-ray Emission from Planetary Nebulae

### 2.1 An Overview of X-ray Emission

Photons with wavelengths between 0.01 nm and 10 nm are called X-rays. However, convention describes X-ray photons by their energy in kilo-electron Volts, or keV. The energy of an X-ray photon is determined from the wavelength,  $\lambda$ , by the simple formula  $E = hc/\lambda \approx 1.24(\text{keV nm})/\lambda(\text{nm})$ . In this convention, X-ray photons have energies in the range of 0.12 to 120 keV. Below 0.12 keV reside the Ultraviolet photons, like those responsible for ionizing the PN, and above 120 keV are highly energy gamma-rays not observed from PNe.

X-ray emission is characterized by the temperature,  $T_X$ , and density,  $n_e$ , of the X-

ray emitting material. The nature of X-ray emission at low temperatures ( $< 500$  kK) and high temperatures ( $> 50$  MK) is relatively straightforward. Low temperature X-ray emission arises from the tail of blackbody emission spectrum of a hot stellar photosphere, while highest temperature X-ray emission, not observed from PNe, arises from strongly-shocked plasma due to accretion onto a very compact core, such as a black hole or neutron star. In the remaining temperature range,  $500 \text{ kK} < T_X < 50 \text{ MK}$ , the interpretation of the X-ray emission requires a careful consideration of all available information.

The density of the X-ray emitting material is a useful diagnostic for determining the nature of such X-ray emission, however, the density can only be directly determined from high-resolution grating X-ray spectra. High-resolution grating X-ray spectra are difficult to obtain from PNe due to the low rate of photons arriving at the telescope. Low-resolution X-ray spectra obtained from imaging-spectrometers can determine the distance-dependent emission measure,  $EM = \int n_e n_p dV \sim n_e^2 V$ , of the X-ray emitting material. By assuming an emitting volume, the density can be estimated from the emission measure.

In PNe, point-like X-ray emission from a high density gas in a small volume tends to have a larger emission measure than extended X-ray emission from a lower density gas in a large volume. A division of the potential types of X-ray emission from PNe are small, unresolved, point-like X-ray sources and larger, diffuse, extended X-ray sources; in some instances, both types of X-ray emission can be present (for an example see the Chandra X-ray Observatory images of the Eskimo Nebula (NGC 2392) presented in Chapter 3).

## 2.2 Point-like X-ray Emission from PNe

### 2.2.1 Hot Photospheres of Central Stars

The photosphere of hot central stars radiate similar to a blackbody characterized by the effective temperature of the photosphere,  $T_{eff}$ . Typical effective temperatures for the evolved CSPNe range from 30 kK, that required to ionize the nebulae, up to 400 kK, in the hottest central stars with highly excited emission lines observed in the nebulae. For  $T_{eff} \geq 100$  kK, a blackbody spectrum contributes soft X-ray photons up to 0.4 keV.

This soft blackbody X-ray emission was first detected from PNe with the *Einstein Observatory* and reported by Tarafdar & Apparao (1988). X-ray observations on *Einstein*'s imaging proportional counter (IPC) were sensitive to photon energies in the range of 0.2 to 3.5 keV. Only five of the 19 PNe observed were detected by the *Einstein Observatory*. The X-ray emission detected from these five PNe (NGC 246, NGC 1360, NGC 6853, NGC 7293, and A 33) is attributed to blackbody emission from their hot ( $> 10^5$  K) central stars. The five detected PNe are the closest PNe of those observed by *Einstein Observatory* and have the lowest extinction values, which led Tarafdar & Apparao (1988) to conclude that the non-detections were due to a combination of soft X-ray absorption by the interstellar medium (ISM) and the limiting sensitivity of the detector. Four of the PNe not detected by *Einstein* were later detected by the more sensitive *EXOSAT* X-ray observatory. These four additional PNe were discovered in the *EXOSAT* data archive and reported by Apparao & Tarafdar (1989). The

observations performed on the low-energy experiment (LE) of *EXOSAT* were sensitive to photon energies in the range of 0.05 to 2.0 keV. Eight of the twelve PNe observed by *EXOSAT* were found to emit detectable X-rays, four of which (NGC 4361, NGC 1535, NGC 3587, and A 36) were previously unknown X-ray sources. The X-ray emission in all sources discovered by the *Einstein* and *EXOSAT* observatories is attributed to blackbody emission from the hot central stars in these PNe.

The launch of the ROSAT observatory, sensitive to photon energies in the range of 0.1 to 2.0 keV, provided improved spatial resolution and, for the first time, robust spectral information. The ROSAT observations of PNe revealed that two of the prior detections of X-ray emission from PNe were, in fact, due to X-ray emitting background stars near the PNe and not the PNe themselves [NGC 1535 (Chu et al. 1998) and A 33 (Conway & Chu 1997)]. Guerrero et al. (2000) collected and analyzed targeted and serendipitous ROSAT observations of 63 PNe. Of the 63 observed PNe, 20-25% emit detectable X-ray emission the 0.1 to 2.0 keV energy band. The X-ray emitting PNe detected by ROSAT fall into three categories (Guerrero et al. 2000): (1) soft sources with emission between 0.1 and 0.4 keV and no emission above 0.5 keV, (2) hard sources with significant emission above 0.5 keV, and (3) composite sources with emission similar to the soft sources but with appreciable emission above 0.5 keV. The soft X-ray emitting sources are unanimously attributed to blackbody emission from the hot central star, while the harder X-ray emitting sources indicate a hot thermal plasma, perhaps arising from shocks in the nebula or from coronal emission near the central star.

### 2.2.2 Coronal and Accretion-Related Emission

Coronal X-ray emission from the hot central stars in PNe are not expected since the layers on the WD are too hot to support the magnetic fields that fuel coronal activity. However, binary companions to the central stars in PNe which are still on the main sequence or in a giant phase can still power the magnetic fields. In fact, main sequence companions in close binary systems are expected spin faster due to the transfer of angular momentum during a common envelope stage as the primary evolves through the AGB phase. Coronal X-ray luminosity is strongly correlated with rotation for late-type main sequence stars (see review by Güdel & Nazé 2009). This correlation is believed to arise, as in our sun, from dynamo-generated magnetic fields in a differentially rotating late-type star's convective zone. For such stars, X-ray luminosity linearly increases with increasing rotation until saturation is reached at a relative X-ray luminosity  $\log L_X/L_{\text{bol}} \sim -3$ .

Accretion-related processes on the central star can also create X-ray emission. Hot accretion disks in accreting systems can reach X-ray emitting temperatures, but for the lower mass and larger sizes of the pre-WD found in the nuclei of PNe, any potential accretion disk would not reach temperatures high enough to emit X-rays (Frank et al. 2002). If a binary system in the central star of a PN is undergoing mass transfer from Roche lobe overflow, the material falling onto the compact component of the system can reach velocities up to the free fall velocity and form shocks from a few tens of MK to a few hundred MK (Frank et al. 2002).

Both coronal and accretion-related X-ray emission produce high density, high

temperature X-ray emission confined to a small volume near the central star. These sources of hard X-ray emission are found in a few PNe. Trying to decipher the physical process responsible for hard X-ray emission detected from the nuclei of PNe is the subject of Chapter 6.

## 2.3 Extended X-ray Emission from PNe

### 2.3.1 Hot Bubbles from Colliding Stellar Winds

Chapter 1 introduced the theory of Interacting Stellar Winds (ISW), where a nascent fast stellar wind catches up to and collides with an older, slower, and more dense AGB wind, and the generalization of that theory (GISW) to two- and three-dimensional hydrodynamical simulations with a variety of shape-altering mechanisms. In addition to forming the dense shell that constitutes the planetary nebulae, the collision between the fast stellar wind and AGB wind gives rise to a super-heated, shocked gas, called the hot bubble. This hot bubble fills the cavity of the PN and is expected to emit X-rays.

With a few assumptions, the characteristics of the X-ray emission are readily estimated by the physics describing a strong shock. From the Rankine-Hugoniot jump conditions, which describe the behavior of conserved quantities across a strong shock, the velocity,  $v$ , and density,  $\rho$ , jump conditions for a monoatomic gas approach the limits  $v_1/v_0 \rightarrow 1/4$  and  $\rho_1/\rho_0 \rightarrow 4$ , respectively, where the subscripts denote the upstream, pre-shock medium (0) and the downstream, post-shock medium (1).



Applying the conservation of mass, the conservation of momentum, and the Rankine-Hugoniot jump conditions gives in a simple expression for the pressure of the post-shock gas,  $P_s = \frac{3}{4}\rho_0 v^2$ , and assuming an ideal gas,  $P = \frac{\rho k T}{\mu m}$ , where  $\mu$  is the mean atomic weight and  $m$  is the mass of hydrogen, allows for the elimination the density and gives the following simple estimate of the temperature in the post-shock region (the hot bubble),  $T_s = \frac{3}{16} \frac{\mu m}{k} v^2$ . For winds greater than a few hundred kilometers per second, the shocked gas temperature can reach X-ray emitting temperatures ( $T_s > 1$  MK).

Volk & Kwok (1985) modeled the evolution of PNe using a numerical solution in the energy and momentum conserving case of the ISW theory. From these numerical solutions, the evolution of the X-ray emission from the shocked hot bubble was calculated for a range of empirical mass loss rates and central star masses and under the assumption of radiative cooling via bremsstrahlung radiation. The solutions suggested that the temperature of the hot bubble was approximately independent of time and depended only on the velocity of the fast wind,  $v$ , via,  $T_s \approx \frac{\mu m v^2}{9k}$ , again where  $\mu$  is the mean atomic weight and  $m$  is the mass of hydrogen. For typical fast wind velocities, 1000-2000 km s<sup>-1</sup>, the hot bubble temperatures are expected to range from 10<sup>7</sup> to 10<sup>8</sup> K. Calculations of the X-ray flux in the 0.2 to 4.0 keV range from such a hot plasma would drop exponentially from  $\sim 10^{-12}$  erg cm<sup>-2</sup> s<sup>-1</sup> shortly after the formation of the hot bubble to below 10<sup>-15</sup> erg cm<sup>-2</sup> s<sup>-1</sup> within 10<sup>4</sup> years after the formation of the hot bubble. These calculations explained the lack of detections of such hot gas by the *Einstein X-ray Observatory*, which had a sensitivity limit of 10<sup>-13</sup> erg cm<sup>-2</sup> s<sup>-1</sup>.

Zhekov & Perinotto (1996) revisited the evolution of PNe and the X-ray emission with analytical similarity solutions which used the evolutionary tracks of a  $0.61M_{\odot}$  central star (Blocker & Schonberner 1993) and the predictions from radiation driven-wind theory (Pauldrach et al. 1988) as inputs. The solutions also considered the thermal conductivity, or heat conduction, between the hot bubble material and the cool material in the nebular shell and showed that the thermal conductivity could cool the shocked gas significantly and immediately to temperatures between  $10^5$  K and  $10^6$  K, which would radiate primarily through strong X-ray emission lines from 0.3 to 1.0 keV as opposed to the bremsstrahlung-dominated, continuous X-ray emission spectrum expected for a hot gas above  $10^7$  K. These results suggested that, in a few instances, the softer,  $10^6$  K, X-ray emission from PNe observed by ROSAT could be due to X-ray emission from the hot bubble. However, the large ROSAT PSF (FWHM  $\sim 8 - 15''$ ) could not quite resolve the X-ray emission detected from PNe, making it difficult to determine its precise nature.

In 1999, the launch of the Chandra X-ray Observatory (CXO) ushered in a new era of unprecedented spatial and spectral resolution and sensitivity for X-ray observatories (CXO is discussed further in Chapter 3). High spatial resolution CXO observations of PNe definitively revealed extended X-ray emission from the hot bubble, a cornerstone prediction of the interacting stellar winds theory, for the first time. CXO observations by Kastner et al. (2000) of the PN BD+30 3639 revealed extended X-ray emission confined within the sharply defined nebular cavity seen in HST images (see Figure 2.1). The X-ray emission detected from BD+30 3639 is consistent with an optically-thin thermal plasma at  $2.5 \times 10^6$  K with chemical enhancements of

C and Ne, indicative of dredged-up material from below the surface of the star and liberated into the circumstellar environment by mass loss via the stellar wind (Yu et al. 2009; Kastner et al. 2000). Extended X-ray emission from the hot bubble was also suspected from ROSAT observations of NGC 6543 (Kreysing et al. 1992) and again CXO observations showed the X-ray emission was confined to the inner elliptical bubble visible in HST images of NGC 6543 (Chu et al. 2001). The XMM-Newton X-ray Observatory (XMM), also launched in 1999, has spatial resolution only slightly better than ROSAT but has a much higher sensitivity and spectral resolving power than ROSAT (XMM is discussed further in Chapter 3). XMM observations found evidence for extended X-ray emission from the PNe NGC 7009 (Guerrero et al. 2002), NGC 2392 (Guerrero et al. 2005), and NGC 7026 (Gruendl et al. 2006). These PNe and their X-ray emitting properties are listed in Table 2.1.

These new discoveries of extended X-ray emission from hot bubbles in PNe show a marked difference between the simple estimates for the temperature of a hot bubble. They are all cooler, in many cases by an order of magnitude, than their fast winds would suggest (Soker & Kastner 2003). These concerns led Steffen et al. (2008) to revisit the evolution of the X-ray emission from PNe, using a similar treatment as Zhekov & Perinotto (1996). However, instead of using analytical similarity solutions, Steffen et al. (2008) perform numerical 1D hydrodynamical calculations of the evolution of the hot bubble and its X-ray emitting properties. These calculations consider the evolutionary properties of the central star (mass loss, fast wind speed, temperature, mass) and a new treatment of the thermal conductivity, or heat conduction, at the shock-nebula interface. The authors find that the X-ray luminosities predicted

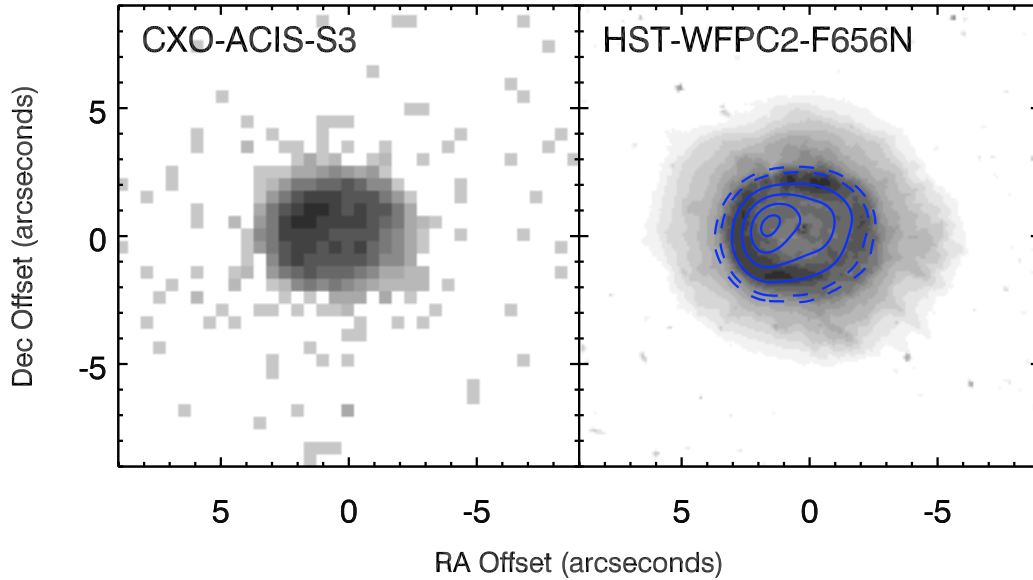


Figure 2.1 Hot bubble X-ray emission detected from BD+30 3639 by the Chandra X-ray Observatory. Left: the X-ray emission observed by CXO. Right: contours of the smoothed X-ray emission overlaid upon the optical image from the HST. The X-ray emission appears is nested within the sharply defined nebular rim seen the the optical image from HST.

from their calculations agree with the observed X-ray luminosities and are lower than those found by Zhekov & Perinotto (1996). Furthermore, their calculations suggest that the solutions found by Zhekov & Perinotto (1996) overestimate the effects of thermal conductivity, but the new results still argue that thermal conductivity plays an important role in defining the X-ray emitting characteristics of the hot bubble. Of particular importance are the hot bubble temperatures, which Steffen et al. (2008) show quickly reach  $\sim 10^6$  K at which point thermal conductivity becomes very effective and regulates the temperature of the hot bubble to a roughly constant value

Table 2.1 CXO and XMM X-ray Observations of PNe

Object	Type <sup>a</sup>	Observatory	$T_X$ ( $10^6$ K)	$\log L_X^b$ ( $\text{erg s}^{-1}$ )	Note <sup>c</sup>	$T_{eff}^d$ (kK)
BD+30 3639	PN	CXO	2.60	32.4150	D	45.70
IC 418	PN	CXO	2.30	29.8325	D	44.50
PN MZ 3	SY?	CXO	3.00	31.4771	C	106.90
NGC 2392	PN	XMM	1.50	32.1303	D	67.60
NGC 3242	PN	XMM	1.70	31.6848	D	89.90
NGC 6543	PN	CXO	1.70	32.0000	D (P)	63.00
NGC 6826	PN	CXO	2.00	30.5514	D (P)	56.10
NGC 7009	PN	XMM	1.80	31.3424	D	87.80
NGC 7026	PN	XMM	1.10	32.6532	C	82.60
NGC 7027	PN	CXO	7.90	32.1139	C	200.00
PN PS 1	PN	XMM	7.40	32.0000	P	27.50
Hen 2-104	SY?	CXO	—	<30.4160	(P)	97.00
NGC 246	PN	CXO	—	<30.2283	(P)	88.60
NGC 4361	PN	CXO	—	<29.8595	(P)	93.20
NGC 7293	PN	CXO	—	<30.0322	(P)	108.50
PN M 1-16	PN	CXO	—	<30.3010	—	45.70
NGC 2346	PN	XMM	—	<31.6021	—	100.00

<sup>a</sup>Classification of object, PN for a planetary nebula, and SY? for a planetary nebula that might be a symbiotic system.

<sup>b</sup>For upper limit  $L_X$ , indicated by the leading <, the upper limit is calculated from the upper limit count rate determined from the observation and assuming an absorbed, thermal plasma model with  $T_X = 2.5 \times 10^6$  K with intervening absorption determined from the literature.

<sup>c</sup>Note on the type of X-ray emission described by  $T_X$  and  $L_X$  columns: D - diffuse source, C - collimated source, P - point source. P in parentheses indicates object also has a detected central point source, but only X-ray properties for diffuse emission are considered.

<sup>d</sup>Effective temperatures,  $T_{eff}$ , of the central star are the Zanstra temperatures given in Phillips (2003).

that depends on the wind power (hence mass) of the central star. These thermal conductivity-regulated hot bubble temperatures agree quite well with the observed X-ray temperatures (see Figures 2.2 and 2.3). The calculations also find that the

density of the hot bubble increases due to “evaporation” of nebular material into the hot bubble by the heat conduction and as a result the hot bubble densities rise and agree with those determined from X-ray observations.

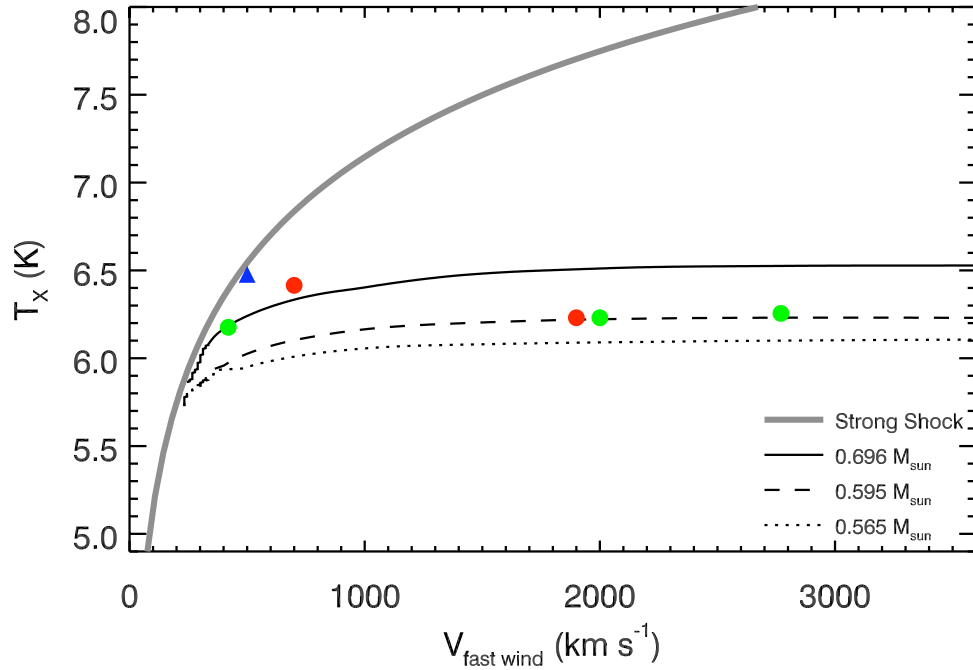


Figure 2.2 The model predictions from Steffen et al. (2008) of the evolution of the X-ray emission from colliding winds in a PNe with effective temperature of the central star with typical masses of  $0.696 M_{\odot}$  (solid line),  $0.595 M_{\odot}$  (dashed line), and  $0.565 M_{\odot}$  (dotted line). Over plotted are the detections of diffuse X-ray emission from the PNe listed in Table 2.1. Triangles indicate collimated X-ray sources and circles indicate hot bubble X-ray sources. The red symbols indicate objects with H-poor chemical compositions (e.g. the Wolf-Rayet-type central star of BD+30 3639, which are discussed further in Chapter 4), the green symbols indicate H-rich chemical compositions, and the blue symbol indicates the possible symbiotic system Mz 3.

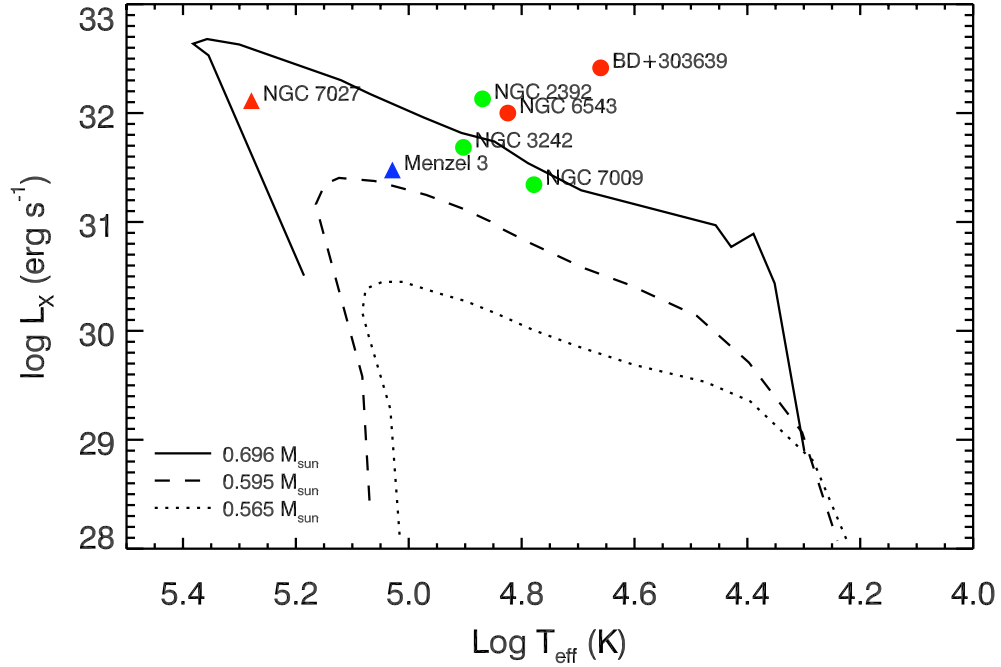


Figure 2.3 The model predictions from Steffen et al. (2008) of the evolution of the X-ray emission from colliding winds in a PNe with effective temperature of the central star with typical masses of  $0.696M_{\odot}$  (solid line),  $0.595M_{\odot}$  (dashed line), and  $0.565M_{\odot}$  (dotted line). Over plotted are the detections of diffuse X-ray emission from the PNe listed in Table 2.1. Triangles indicate collimated X-ray sources and circles indicate hot bubble X-ray sources. The red symbols indicate objects with H-poor chemical compositions (e.g. the Wolf-Rayet-type central star of BD+30 3639, which are discussed further in Chapter 4), the green symbols indicate H-rich chemical compositions, and the blue symbol indicates the possible symbiotic system Mz 3.

### 2.3.2 Shocks from Collimated Flows or Jets

CXO observations of the PN NGC 7027 show multiple lobed asymmetries in the X-ray emission in an otherwise elliptically-shaped PN (see Figure 2.4) and provide a

compelling example for some form of collimated flow in the PN (Kastner et al. 2001). Similarly, CXO observations of the bipolar PN Mz 3, reveal that the brightest X-ray emission is confined along the symmetry polar axis, near polar caps that seems to be breaking through the nebula (Kastner et al. 2003). Kastner et al. (2002) suggested that some of the asymmetry observed from the X-ray observations of the hot bubbles in PNe could be explained by variable extinction across the nebula, but stressed that other processes should be considered which can better explain the asymmetries, the low X-ray temperatures, and the low X-ray luminosities observed from PNe. The potential solutions were outlined by Soker & Kastner (2003) and include attributing the X-ray emission to (1) a slower post-AGB wind, rather than the extant fast wind, (2) jets, or collimated fast winds, driven by a main sequence companion at the end of the AGB phase, (3) thermal conductivity, as discussed in Zhekov & Perinotto (1996). Akashi et al. (2008) considered the case of a jet, or collimated fast wind, driven by a main sequence companion at the end of the AGB phase using numerical 2D hydrodynamical simulations. For a range of opening angles, Akashi et al. (2008) find that collimated a fast wind blown by a companion with velocities from 500 to 3000  $\text{km s}^{-1}$  can account for the observed X-ray properties of PNe. The morphology of the X-ray emission determined from emissivity maps of these simulations are consistent with that observed from NGC 7027. Although the models do not include thermal conductivity, the authors concluded that it is not needed for the case where a slower wind is responsible for the X-ray emission.



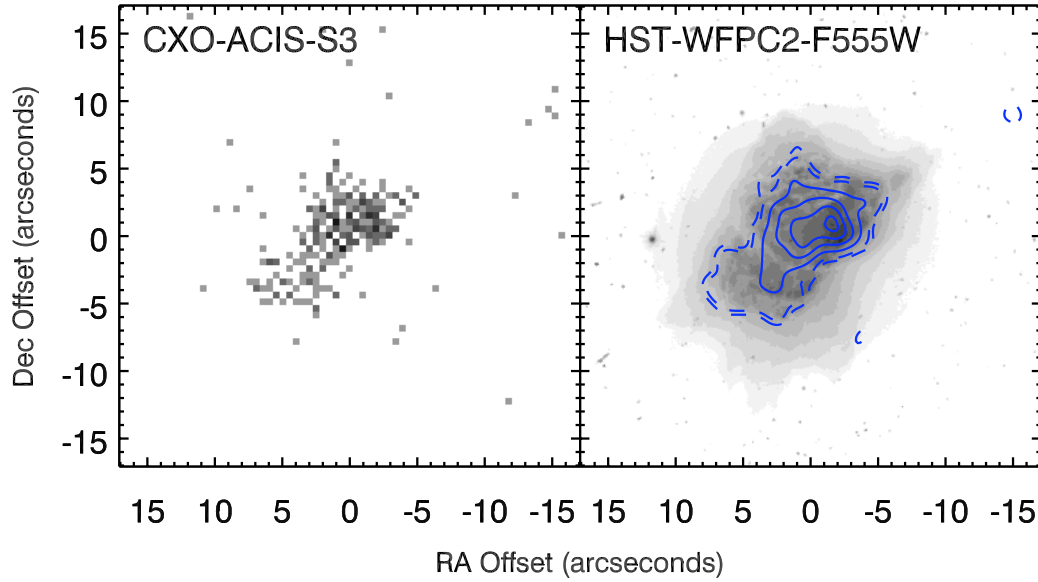


Figure 2.4 The asymmetrical X-ray emission detected from NGC 7027 by the Chandra X-ray Observatory. Left: the X-ray emission observed by CXO. Right: contours of the smoothed X-ray emission overlaid upon the optical image from the HST. The X-ray emission coincides with bright peaks and spokes that suggest collimated outflows breaking through the elliptical nebula.

## 2.4 Emerging Trends and New Questions

It is perhaps more likely that many of the processes previously described in this chapter occur simultaneously, in succession, or in some combination. These sequences and combinations could be responsible for the varied characteristics of the X-ray emission observed from PNe. In this thesis, I concentrate on sources of X-ray emission that can advance our understanding of the formation and evolution of PNe. These are the sources which reveal the hot bubble and shocked jets predicted by ISW and GISW

and evidence for an active companion in a mass-exchanging binary system. Prior X-ray observatories could not quite distinguish the nature of these X-ray sources in PNe. It was not until the launch of CXO and XMM that these X-ray sources could be adequately studied. The indisputable discovery by CXO of the hot bubble in BD+30 3639 and subsequent high-resolution X-ray spectral analysis (Yu et al. 2009) demonstrate the ability of X-ray observatories to expand our understanding of the formation and evolution of PNe and allow us to witness the enrichment of the interstellar medium with nucleosynthesis products that include the critical building blocks of life. The highly asymmetric X-ray emission detected from NGC 7027 challenges the notion that NGC 7027 is an elliptical PN and emphasizes the role of collimated flows in shaping PNe.

These X-ray observations also reveal short-comings in the (G)ISW theory, which predicts hot bubble gas temperatures up to  $10^7$  K. Instead, the X-ray observations, which show the gas in the range of  $\sim 1 - 3 \times 10^6$  K suggest hot bubble temperatures suppressed by heat conduction. Yet, as I will show, present models describing heat conduction do not accurately describe the X-ray properties of hydrogen-poor PNe. Does this suggest an additional mechanism is required to explain the well-regulated hot bubble gas temperature of hydrogen-poor PNe? Or perhaps there remains a poor understanding of the physics of heat conduction in hydrogen-poor environments, which would offer a new avenue for PNe to serve as pioneering astrophysical laboratories? Hard X-ray-emitting, point-like emission from the nuclei of PNe is a surprising discovery and, as I will argue, it suggests a history of binary interaction. Can we use such hard X-ray emission as a diagnostic of central star binarity in PNe? In the

remaining chapters, I will address these questions with a comprehensive survey of the X-ray emission from targeted and serendipitous observations of PNe.



# Chapter 3

## X-ray Observatories, Data, and Analysis

### 3.1 Satellite X-ray Observatories

Modern X-ray satellite observatories are built from a series of nested paraboloid and hyperboloid mirrors (Wolter Type I) which X-ray photons strike at grazing incidence angles to arrive at the focal plane. Coatings on these mirrors increase the reflectance of desirable photon energies. The product of the reflectance and geometrical area available to collect photons is called the effective area and quantifies the sensitivity of the telescope. The effective area at 1 keV has steadily increased over successive X-ray observatory missions (200 cm<sup>2</sup> for Einstein, 400 cm<sup>2</sup> for ROSAT, 800 cm<sup>2</sup> for CXO, and 4650 cm<sup>2</sup> for XMM). This thesis relies on observations performed by the X-ray

Multiple Mirror-Newton Observatory (XMM) and the Chandra X-ray Observatory (CXO). These X-ray satellite observatories, both launched in 1999 and still operating at the time of this thesis, provide X-ray imaging spectroscopy and X-ray grating spectroscopy.

The data obtained through X-ray imaging spectroscopy provide a wealth of information since every X-ray photon detected during an observation is tagged with spatial, spectral, and temporal information. This multifaceted data set is stored in an event list, or a table containing all the information for each individually detected photon or event. A suite of data products (images, spectra, and light curves) can be created by manipulating and filtering the event list. In this chapter the imaging spectrometers onboard XMM and CXO are described followed by the detailed creation and analysis of a sample of data products from the X-ray observations of the PN NGC 2392 (Eskimo Nebula).

### 3.1.1 XMM Observations and Data

The XMM observatory X-ray observations used in this thesis are performed by the European Photon Imaging Camera (EPIC). EPIC is comprised of three separate detectors each comprised of numerous X-ray CCD chips. Since the XMM observatory has three separate X-ray mirrors, a single EPIC detector resides at the focal plane of each of the three X-ray focusing mirrors, allowing for simultaneous observations of a target. In two mirrors, reflection gratings redirect half of the incident flux onto two reflection grating spectrometers (RGS1 and RGS2), while 44% of the incident

flux falls onto metal oxide semi-conductor X-ray CCD detectors (EPIC-MOS1 and EPIC-MOS2). The third mirror is unobstructed and 100% of the incident flux falls onto the pn X-ray CCD detector (EPIC-pn). All three mirrors have a field of view (FOV) of approximately  $30'$  in diameter with gaps in coverage due to chip boundaries. The EPIC X-ray CCD detectors are sensitive to X-ray photons with energies from 0.15 to 12 keV (MOS) and 0.15 to 15 keV (pn). The spectral resolution of the EPIC detectors at 1 keV is  $\sim 70$  eV (MOS) and  $\sim 80$  eV (pn). The nominal pixel size is  $1.1''$  (MOS) and  $4.1''$  (pn) and the inflight, on-axis point spread function (PSF) of the telescope-detector combinations have a FWHM  $\sim 5''$  (MOS) and  $\sim 12''$  (pn) with broad wings characterized by the Half Energy Width (HEW) of  $\sim 14''$  (MOS) and  $\sim 15''$ . Sources located away from the telescope axis are called off-axis sources and suffer from additional aberrations leading to larger and deformed PSFs.

### 3.1.2 CXO Observations and Data

The Chandra observatory X-ray observations used in this thesis were performed by the Advanced CCD for Imaging Spectroscopy (ACIS). ACIS is comprised of two main detectors arrays comprised of a total of 10 X-ray CCD chips. The imaging array (ACIS-I) has four  $8.3' \times 8.3'$  X-ray CCD chips arranged in a 2x2 grid and the grating spectroscopy array (ACIS-S) has six  $8.3' \times 8.3'$  X-ray CCD chips in a single row along the grating dispersion direction and are curved to accommodate the highly curved grating-dispersed focal plane. Unlike the XMM observatory, CXO only has one mirror and the desired chip is placed in the focal plane for each observation. When performing imaging spectroscopy with ACIS-S, the S3 chip is placed at the prime

focus. The ACIS-S3 chip is back-illuminated which is optimal for targets expected to produce lower energy photons, such as the hot bubbles of PNe. The S3 chip is sensitive to X-ray photons with energies from 0.3 to 10 keV. The spectral resolution of the S3 chip is  $\sim 100$  eV at 1 keV. The nominal pixel size is  $0.492''$  and the on-axis PSF of the telescope and detector has a FWHM  $\sim 0.5''$ . Since the ACIS-S array is designed for spectroscopy, the off-axis PSF degrades much more quickly than that in XMM.

## 3.2 Mission-Specific Data Preparation and Analysis Software

### 3.2.1 XMM Scientific Analysis System

The European Space Agency (ESA) provides the Scientific Analysis System (SAS) software package for the data preparation and analysis of data acquired by XMM. ESA provides continually updated calibration files (CCF), documentation for each SAS task, and data preparation and analysis threads. An ordered list of routinely performed tasks and their descriptions is given in Table 3.1.

### 3.2.2 CXO CIAO Software

The Chandra X-ray Center (CXC) provides the CIAO software package for data preparation and analysis of data acquired by CXO. The CXC provides continually



updated calibration database (CALDB), documentation for each CIAO task, and data preparation and analysis threads. An ordered list of routinely performed tasks and their descriptions is given in Table 3.2.

### 3.3 Case Study: X-ray Observations of the Eskimo Nebula

The data preparation and analysis is illustrated through CXO and XMM X-ray observations of NGC 2392, also known as the the Eskimo Nebula. The data preparation and analysis performed on the observations of the Eskimo Nebula are indicative of the data preparation and analysis used throughout this thesis. An exception applies to off-axis sources, which are covered in detail in the next section.

#### 3.3.1 Locating Observations

The High Energy Astrophysics Science Archive Research Center (HEASARC)<sup>1</sup>. provides tools to search the large and growing database of observations made by previous and current missions with particular detail for High Energy Astrophysics missions. The service is provided by the Astrophysics Science Division at NASA/Goddard Space Flight Center and the High Energy Astrophysics Division of the Smithsonian Astrophysical Observatory. In addition to providing information on observations, HEASARC directs the user to the archived data products, from raw observational

---

<sup>1</sup>HEASARC can be found online at <http://heasarc.gsfc.nasa.gov>

data files to scientific-grade, pipeline-processed, data files. A search for XMM and CXO observations of the Eskimo Nebula yields two observations, one by XMM (ObsID 0200240301) started on 2004-04-02 for 32.9 ks and one by CXO (ObsID 7421) started on 2007-09-13 for 58.2 ks. The raw observation data files (ODF) of the XMM observation and the primary and secondary data files of the CXO observation are downloaded.

### 3.3.2 Preliminary Data Preparation

For XMM observations, the raw observation data files (ODF) are reprocessed with SAS to create science-grade raw event lists for each detector based on the current calibration files (CCF) installed on the workstations used for analysis (Release Note XMM-CCF-REL-249, released in on 2009 May 07, for this thesis). High background periods are filtered out by analyzing the light curve of the entire event list for energies above 10 keV, where the background often dominates. By examining the light curve of these high energy photons, the time intervals with large and flaring count rates can be filtered from the event list. The remaining event list is then filtered for the highest quality event grades (events with the PATTERN keyword set to a value equal to or less than 12) and energies in the range of 0.2 to 12 keV for MOS observations and 0.2 to 15 keV for pn observations.

For CXO observations, the CXC routinely updates the calibration database and applies the latest calibration to all the data in the data archive. This periodic re-processing means that most of the science-grade event lists (Level 2 files) are ready

for prompt analysis. The calibration and processing levels are stored in the header files of the event lists and reviewed before continuing with analysis. A few of the raw observation data files (Level 1) are required for analysis. High background periods are typically not a problem on ACIS observations because observations do not occur while the observatory is near the earth's radiation belts. The level 2 event list are filtered for the higher quality event grades (GRADE keyword set to 0, 2, 3, 4, and 6) and energies in the range of 0.3 to 10 keV.

These temporally- and quality-filtered event lists are used to create the robust data products, such as images and spectra, which are used for scientific analysis. Once an image or spectrum is created, the additional information in the event list is lost. By applying a variety of filters when creating these data products, a rich suite of informative data products can be created.

### 3.3.3 Creating Energy Filtered X-ray Images

Filtering for photons in a particular energy range creates an endless variety of images of the X-ray emission. Photons in the broad energy range of 0.5 to 8.0 keV provide a good starting point with moderately low background noise. This broad energy range image is created for the XMM and CXO observations of the Eskimo Nebula with the CIAO *dmcopy* task filtering on the *PI* and *ENERGY* columns of the event list. Images of the X-ray emission detected from the Eskimo Nebula are depicted in Figure 3.1 with nominal pixel sizes of  $0.492''$  and  $5''$  for the CXO and XMM observations, respectively.

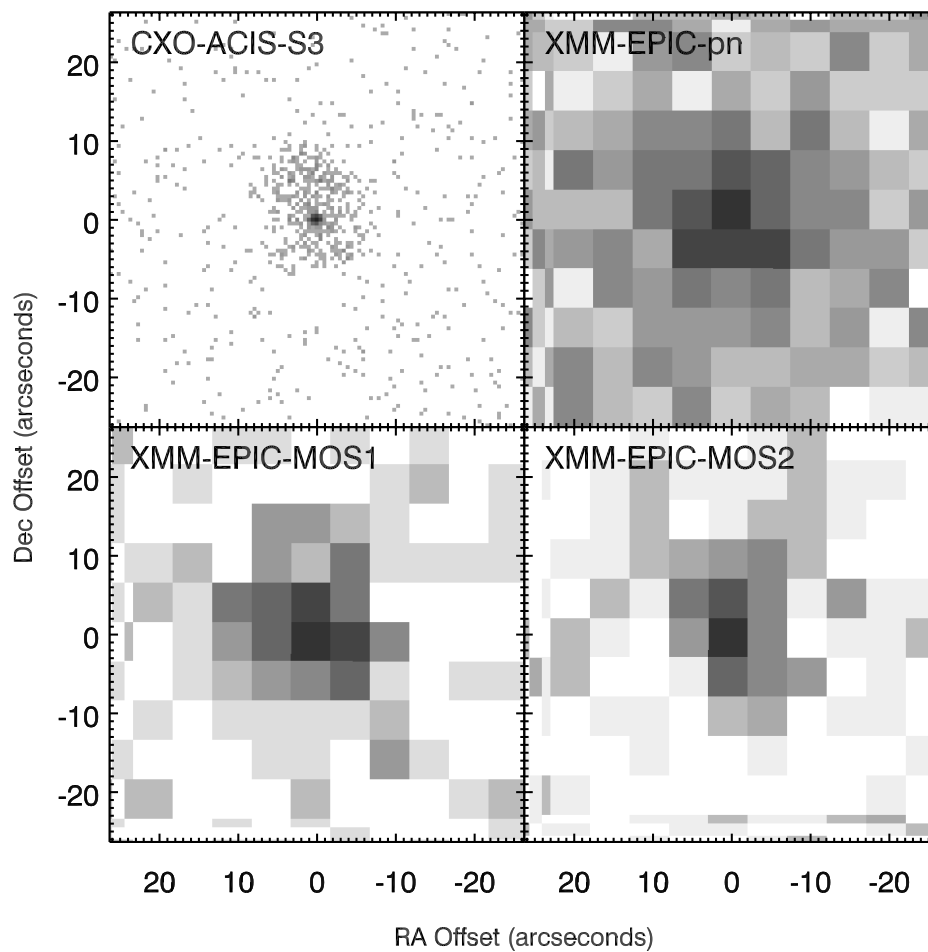


Figure 3.1 Broad energy band (0.3-8.0 keV) images of the X-ray emission observed from the Eskimo Nebula by CXO and XMM. The high-resolution CXO observation resolves the diffuse X-ray emission and a central point source. The lower-resolution image completely confuses these two sources of X-ray emission.

To aid the interpretation of the X-ray emission, contour overlays of the X-ray emission onto images in other wavelengths are desirable. When calculating the contours of the X-ray emission, it is convenient to smooth the X-ray image with a gaussian filter

with a FWHM similar to that of the instrumental PSF FWHM, then calculate the contours from this smoothed image. The XMM-EPIC PSF has a FWHM of  $\sim 6 - 12''$  with even broader wings that can spread up to  $15''$  across, hence the PSF is poorly sampled by the low count rate sources typically found in PNe. The CXO-ACIS PSF has FWHM of  $\sim 0.5''$  and is under sampled by the nominal  $0.492'' \times 0.492''$  pixels. In Figure 3.2, contours of the X-ray emission created from the smoothed X-ray image are overlaid upon the HST, narrow-band filter 502N, optical image of the Eskimo Nebula.

Evidently, the higher resolution provided by the CXO observation of the Eskimo Nebula reveals information loss in the lower resolution XMM observation. In the CXO image, the central star is resolved and easily distinguished from the diffuse X-ray emitting hot bubble, while in the XMM image, these two sources are confused as one large source. Indeed, the original presentation of the XMM observation by Guerrero et al. (2005) stresses the uncertain of the nature of the X-ray emission detected from the Eskimo and successfully argued for the higher-resolution CXO observations.

Data products from narrower energy ranges can provide useful diagnostics. For example, in Figure 3.3 several energy ranges are used to create images of the CXO X-ray observation of the Eskimo Nebula. These narrow energy band images show that the X-ray emission from the hot bubble is primarily producing X-ray photons with energies in the range of 0.5 to 1.0 keV, while the X-ray photons from the central star suggest a broader energy emitting source. The selection of these narrower energy bands is aided by examination of the X-ray spectrum from a source.

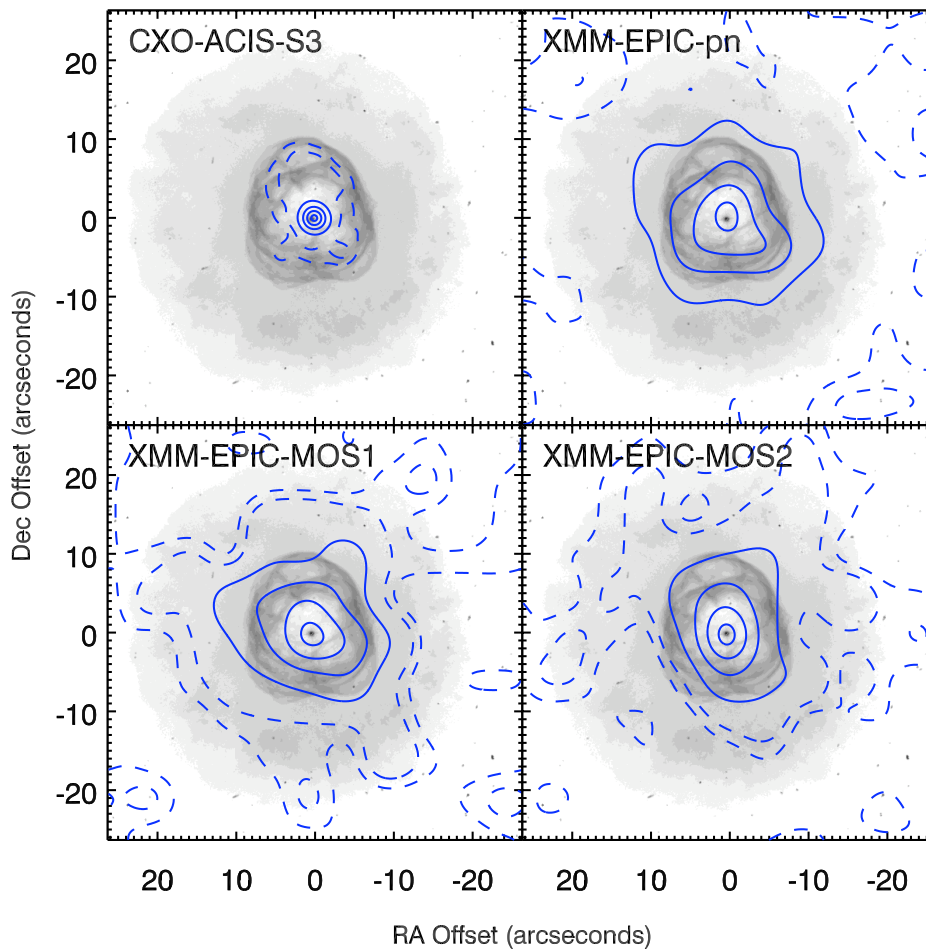


Figure 3.2 Contours of the smoothed X-ray emission observed from the Eskimo Nebula overlaid upon a narrow-band HST image of the nebula. X-ray observations are smoothed with a gaussian kernel with FWHM  $\sim 1''$  for the CXO observation and  $\sim 6''$  for the XMM observations.

### 3.3.4 Source and Background X-ray Spectra

To create a background-subtracted, X-ray spectrum, the events associated with the source and source-free background must be isolated from the rest of the observation.

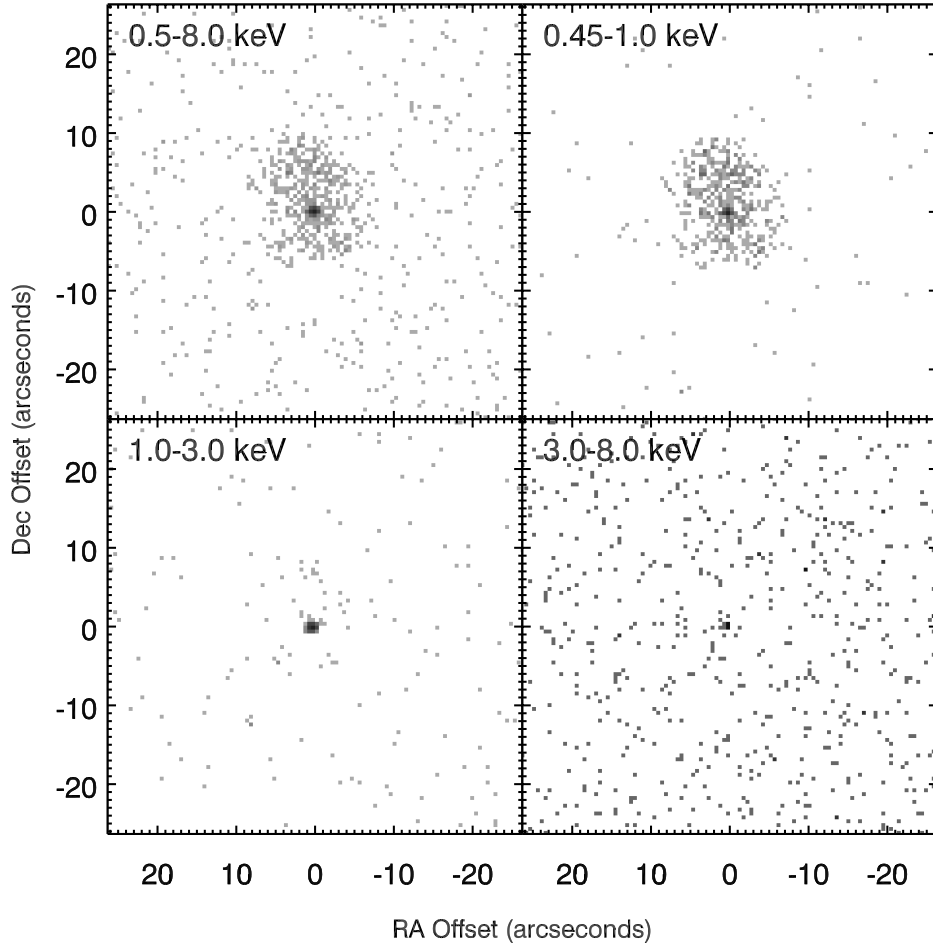


Figure 3.3 Soft and Hard energy band images of the X-ray emission observed from the Eskimo Nebula by CXO. The diffuse X-ray emission can be seen clearly in the 0.45-1.0 keV band, while the central point source extends from 0.45-3.0 keV.

This is achieved by defining regions of interest using the X-ray images created in the prior section. The background region is defined as close to the source region as possible without creating region overlap and with a large enough area to adequately

sample the background spectrum. The source region is defined by considering both the physical size of the PN and the encircled energy fraction (EEF). The encircled energy fraction is the fraction of a source that is encompassed by a region with a specified radius. The EEF depends on the median energy of the source, the position of the source on the FOV, and the detector itself. For on-axis sources, a 90% EEF is desirable, off-axis sources are considered in a later section. On ACIS-S3, for a source with median energy of 1.5 keV, the 90% EEF is reached with a region with a radius of  $1''$ , while on XMM-EPIC-pn, a similar source would reach the 90% EEF with a region with a radius of  $35''$ . The larger PSF of the XMM mirror assembly, compared to that of CXO, plays the most significant role in the discrepancy between the EEFs.

With a suitable source and background region defined, the event extractions are performed with CIAO for CXO observations and SAS for XMM observations. The resulting spectral files must be folded with the respective instrumental response. The instrumental response is comprised of two components, each stored in a file associated with the spectral file. The first component details the effective area for the extracted source and includes the probability that a photon of particular energy would be detected, this is called the ancillary response file (ARF). The second component is the mapping of the observed properties of the detected event to the physical properties of actual photon, this is called the response matrix file (RMF). Although the CXC and XMM center provide a library of RMF and ARF files, the best accounting of the instrumental response is achieved by creating unique RMF and ARF files for each source spectrum; this is the practice used in this thesis. Additionally, the channels of the spectra can be grouped to boost the signal-to-noise in each spectral bin. The



source and background spectral files and response files (RMF and ARF), are all necessary for spectral analysis.

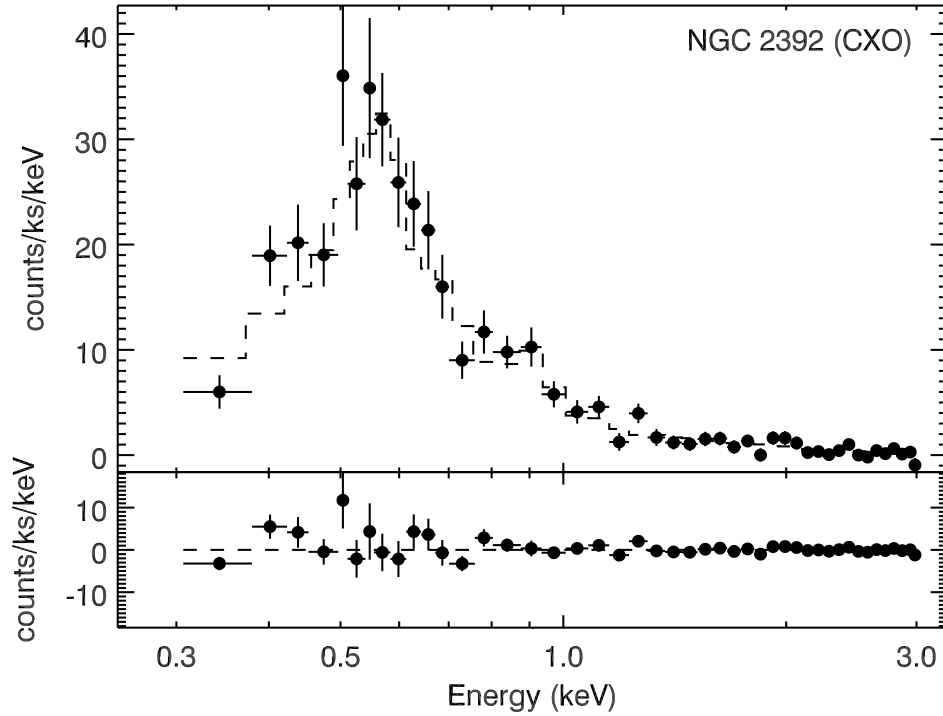


Figure 3.4 Top frame: Background-subtracted X-ray spectrum of Eskimo Nebula, with best-fit thermal plasma model overlaid (dashed line). Bottom frame: residuals of the fit.

The spectral analysis is performed in XSPEC, a interactive, X-ray spectral-fitting program (Arnaud 1996). XSPEC reads the source and background spectral files, along with the associated response files (RMF and ARF) and performs the background subtraction and response folding. There is a full suite of spectral models to choose from with varying degrees of complexity. The most appropriate models for the types of X-ray emission detected from PNe are blackbody, Bremsstrahlung, and

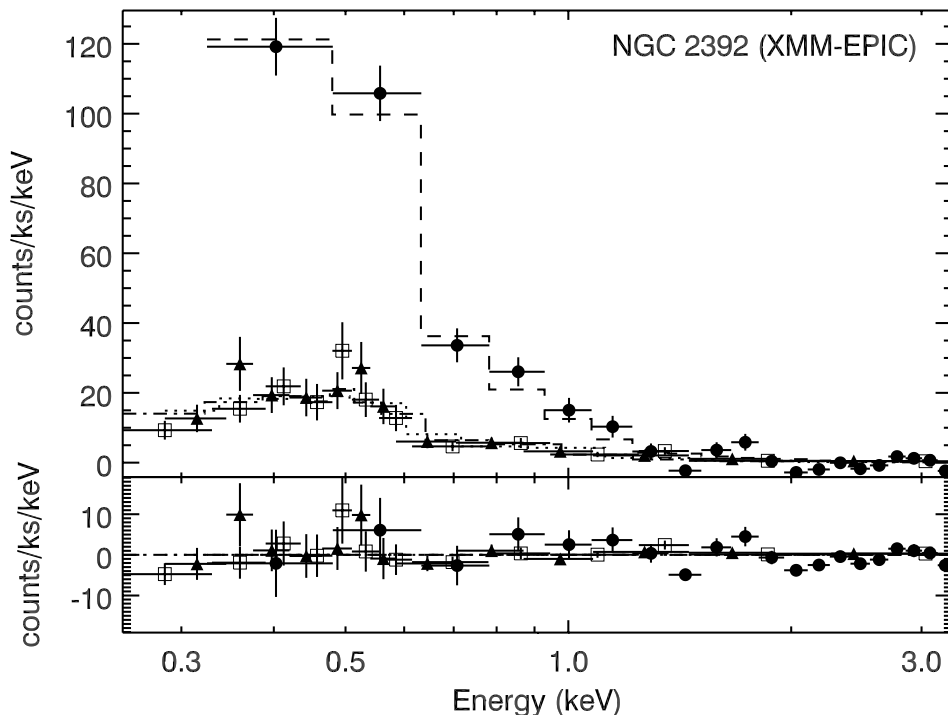


Figure 3.5 Top frame: Background-subtracted X-ray spectrum of Eskimo Nebula, with best-fit thermal plasma model overlaid (dashed line). Bottom frame: residuals of the fit. Individual EPIC spectra are as follows pn – filled circle, MOS1 – open squares, MOS2 – filled triangle.

optically-thin, thermal emission plasma models; brief descriptions of these models are provided in Table 3.3. In addition to the source emission, intervening absorption by the interstellar medium, which decreases the observed flux, is included in the spectral modeling. XSPEC determines the best-fit model parameters by calculating a fit statistic, typically the  $\chi^2$ , of the response-folded, background-subtracted source spectrum against the response-folded spectral model. Spectral fits to the CXO and XMM background subtracted spectra are shown in Figures 3.4 and 3.5. Additional

archival observations of PNe are reanalyzed for consistency and given in Table 2.1 and displayed in updated figures of the X-ray temperature (Figure 3.6) and X-ray luminosity (Figure 3.7).

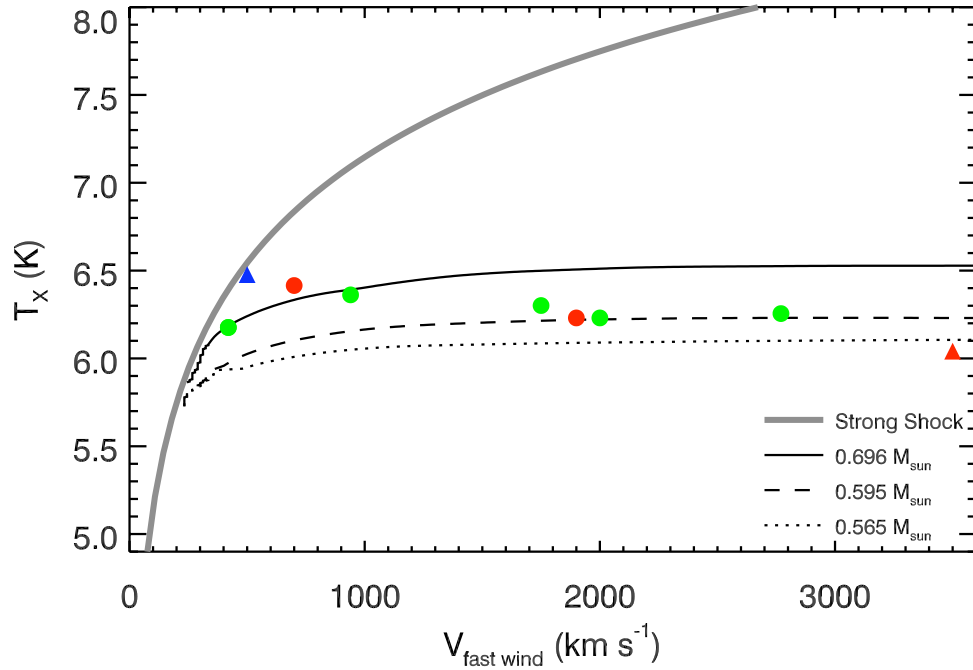


Figure 3.6 The model predictions from Steffen et al. (2008) of the evolution of the X-ray emission from colliding winds in a PNe with effective temperature of the central star. An update of Figure 2.2 introducing the results of a reanalysis of archived X-ray observations of hot bubbles using the methods described in this chapter.

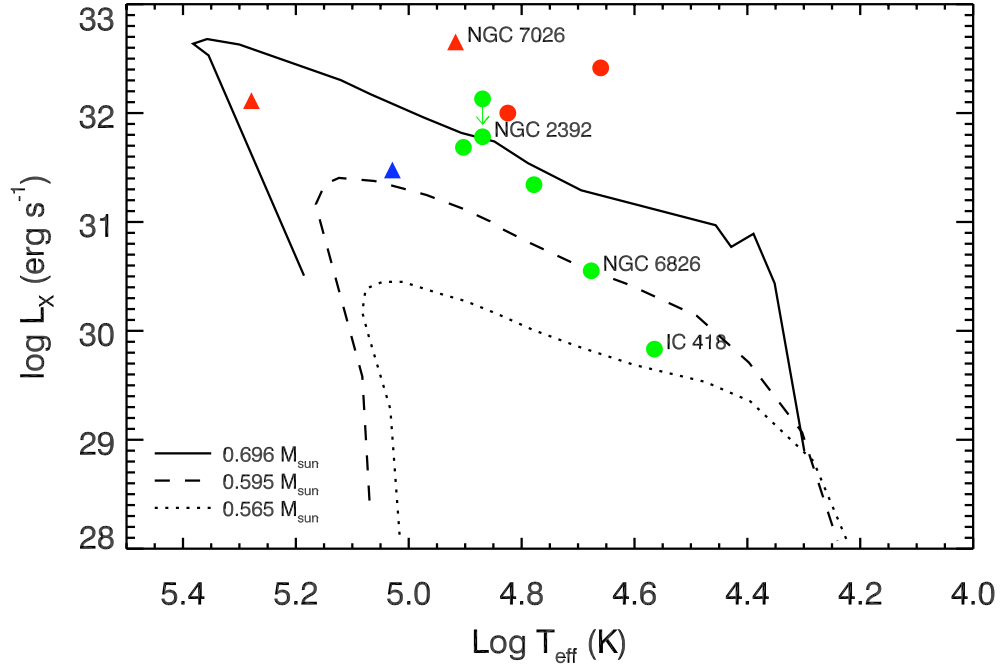


Figure 3.7 The model predictions from Steffen et al. (2008) of the evolution of the X-ray emission from colliding winds in a PNe with effective temperature of the central star. An update of Figure 2.3 introducing the results of a reanalysis of archived X-ray observations of hot bubbles using the methods described in this chapter. Note: the CXO observation of NGC 2392 (Eskimo Nebula), which resolves the diffuse emission from the point source emission, reduces the  $L_X$  for this hot bubble.

### 3.4 Off-axis Sources

Sources detected away from the on-axis prime focus suffer from vignetting and an increasing PSF on both the XMM and CXO observations. In all cases, the farther away a source lies from the aim-point, the more severe are these effects. To quantitatively account for these effects, the observatories have determined the encircled energy

fractions (EEF) for synthetic PSF at various off-axis sources. From an EEF, one can determine the appropriate radius for an extraction region for spectral extraction and also determine if a source is extended or simply distorted by the off-axis position. As for on-axis EEFs, the off-axis EEFs depend on the median energy of a source, in addition to the off-axis position. The spectral extractions for sources in this work are extracted to at least the 90% EEF for the median energy and off-axis angle of a given source. For the EPIC detectors, an extraction region of  $1'$  achieves the 90% EEF. The response files (RMF and ARF) improve the accuracy of the spectral information for off-axis sources by accounting for vignetting and applying EEF corrections at the off-axis positions.

## 3.5 Non-detections and Upper Limit Determinations

### 3.5.1 Determining the Upper Limit Count Rate

For undetected targets with adequate detector coverage<sup>2</sup>, the  $3\sigma$  upper limit count rate,  $CR_{3\sigma}$ , is determined from the  $3\sigma$  background count rate scaled to the source area. This upper limit count rate is a conservative source count rate upper limit for a given X-ray observation. A source with such a count rate should easily be detected by the X-ray observation. Since the CXO and XMM X-ray CCD observations are

---

<sup>2</sup>Adequate detector coverage is defined in this thesis as those targets that fall within the 90% EEF radius of the edge of a chip and result in at least 10 ks of exposure time of the filtered observation.

governed by Poisson statistics, the variance of the signal,  $\sigma$ , is given by  $\sqrt{N}$ , where  $N$  is the number of counts (photons) observed in the period,  $t_{exp}$ . If  $N_{bg}$  is the number of counts in a given energy range within a background region of area  $A_{bg}$ , then the  $3\sigma$  upper limit count rate, the  $3\sigma$  background count rate normalized to the area of the source region ( $A_{src}$ ), is given by

$$CR_{3\sigma} = 3\sqrt{N_{bg}} \left( \frac{A_{src}}{A_{bg}} \right) t_{exp}^{-1}. \quad (3.1)$$

By assuming a physical model for the undetected source, this  $3\sigma$  upper limit count rate can now be used to determine the upper limit X-ray flux.

### 3.5.2 Calculating the Upper Limit Flux for Undetected Sources

The upper limit X-ray flux intrinsic to the source is calculated by assuming an underlying emission process, i.e., an optically-thin thermal emission spectrum at an assumed temperature and absorbed by intervening medium between the observatory and the central star or nebula. The theoretically predicted and observed X-ray properties provide characteristic temperatures for the variety of emission processes, while extinction measurements for each PN provide values for the intervening absorption. Characteristic temperatures and energy ranges for a variety of these emission processes are provided in Table 3.4.

The calculation of the upper limit X-ray flux is performed with the Portable, Interactive Multi-Mission Simulator, or PIMMS<sup>3</sup>. PIMMS is designed as a proposal

---

<sup>3</sup>PIMMS is available online at <http://heasarc.gsfc.nasa.gov/docs/software/tools/pimms.html>

planning tool for many of the high energy satellite missions, but can be used to determine fluxes under certain assumptions. Equipped with a library of instrumental responses for many X-ray satellite observatories, PIMMS can convert an observed count rate in a specified energy range into the normalization of an instrumental response-folded model and intervening absorption. From the normalized model, both the observed flux, absorbed by the intervening medium, and unabsorbed flux, intrinsic to the source, can be calculated for a desired energy range.

## 3.6 Chapter Summary

This chapter covered the basic properties of the X-ray observations that are used to complete this thesis. I highlighted the unique nature of the X-ray observations, namely, the event lists data format, and the suite of data products one can create to aid the analysis and interpretation of the X-ray observations. With careful consideration at each step of preparation (images and spectra), I discussed how the noise, aberrations, and other sources of signal loss can be minimized and improve the scientific output gained from the analysis. Special attention was given to serendipitously observed off-axis sources, which require careful consideration to accurately account for off-axis aberrations and effects. Finally, I concluded with an upper limit treatment of non-detections. In closing, it must be noted that the recommended preparation and analysis of X-ray data is continuously updated and improved, hence the analysis presented here is only a current snapshot.

Table 3.1 Frequently Used SAS Tasks for XMM Data Analysis

Task	Description
<i>emchain,</i> <i>epchain</i>	Metatasks that perform pipeline processing to the Observation Data Files (ODF) of MOS and pn observations using the Current Calibration Files (CCF). Produces raw event lists of the observations.
<i>evselect</i>	The central task to perform filtering on any of the columns in event lists. Used extensively to create a variety of data products (e.g., images, spectra, and light curves) from event lists.
<i>tabgtigen</i>	Creates Good Time Intervals (GTI) using boolean expressions on the temporal information available in observations. The GTI files created by tabgtigen are used with evselect to remove periods of high background counts from an observation.
<i>backscale</i>	Calculates the areas of source and background regions used in spectral extraction. Area is geometric area minus chip gaps and bad pixels.
<i>rmfgen</i>	Creates the Redistribution Matrix File (RMF) that describes the instrumental response of an extracted spectral region as a function of energy and channel.
<i>arfgen</i>	Creates the Ancillary Response File (ARF) that describes the instrument effective area of an extracted spectral region as a function of energy.



Table 3.2 Frequently Used CIAO Tasks for CXO Data Analysis

Task	Description
<i>dmcoppy</i>	General task used mainly for filtering and image creation.
<i>dmextract</i>	Extracts region of interest from event lists. Used to create a variety of data products (e.g., spectra and light curves) from event lists. Typically called from metatasks <i>psextract</i> or <i>spextract</i> .
<i>mkacisrmf</i>	Creates the Redistribution Matrix File (RMF) that describes the instrumental response of an extracted spectral region as a function of energy and channel.
<i>mkarf</i>	Creates the Ancillary Response File (ARF) that describes the instrument effective area of an extracted spectral region as a function of energy.

Table 3.3 Frequently Used XSPEC X-ray Spectral Models

Model	Description
<i>bbbody</i>	Blackbody emission, parameterized by the temperature and the physical size of the emitting region.
<i>brems</i>	Thermal bremsstrahlung continuum emission spectrum; dominant form of emission for plasma temperatures above 100 MK.
<i>(v)mekal</i> , <i>(v)raymond</i>	Optically-thin thermal plasma, or a hot diffuse gas, typically a few MK, with strong atomic emission lines which can be varied by using the variable abundance version of the model.

Table 3.4 X-ray Emission Processes and Characteristics

Process	Energy Range (keV)	$T_X$ (MK)	Features
Hot WD	0.1-0.4	0.1-0.5	Blackbody
Hot Bubble	0.3-1.0	1-3	O & Ne lines
Coronal	0.4-2.0	2-40	O, Ne, & Mg lines
Accretion	1.0-5.0	5-100	6.4 keV Fe-line

# Chapter 4

## X-ray Imaging of PNe with Wolf-Rayet-type Central Stars<sup>1</sup>

### 4.1 Wolf-Rayet Central Stars in PNe

Planetary nebulae harboring relatively cool, WC-type Wolf-Rayet central stars (typically designated [WCL] objects; e.g., Leuenhagen et al. (1996)) represent important test cases for understanding the origin and nature of X-ray emission from PNe. The central stars of [WCL] PNe are characterized by their overall spectral resemblance to “bona-fide,” massive WR stars, but as a group they extend to both hotter and cooler effective temperatures (Górny & Tyłenda 2000). The luminosities determined for the

---

<sup>1</sup>Portions of this chapter have appeared in articles published in *The Astrophysical Journal*, Volume 635, Issue 1, pp. 381-385 (2005) co-authored by Joel H. Kastner, Orsola De Marco, and Noam Soker and in *The Astrophysical Journal*, Volume 672, Issue 2, pp.957-961 (2008) co-authored by Joel H. Kastner, Rodolfo Montez Jr, Orsola De Marco, and Bruce Balick. This version features updated results for NGC 40 gained by applying the latest calibration to the data sets discussed.

WC central stars of PNe, given reasonable distance estimates, confirm that these stars are much less luminous than the WC remnants of massive stars and establish beyond doubt their post-AGB nature.

Key properties of the [WCL]s indicate they should offer prime examples of strong wind-wind interactions in PNe. The [WCL] central stars exhibit extreme hydrogen deficiency, similar to that of their likely progeny, the PG 1159-type pulsating white dwarfs (Koesterke et al. 1998). By virtue of the high opacity characteristic of a C- and O-enriched, yet H-depleted gas mix (De Marco & Barlow 2001), the [WCL] central stars develop powerful winds characterized by mass loss rates  $\sim 10^{-6} M_{\odot} \text{ yr}^{-1}$  (Leuenhagen et al. 1996). The central star wind velocities of [WCL]s range from  $\sim 200$  to  $\sim 1000 \text{ km s}^{-1}$  and appear correlated with spectral type, wherein the coolest [WCL]s have the lowest wind speeds (Leuenhagen et al. 1996). These velocities are unusually large for such relatively cool central stars. The very large stellar wind momenta of [WC] PNe appear to result in systematically larger nebular expansion velocities among these objects, relative to PNe with H-rich central stars (Gorny & Stasińska 1995). Furthermore, as a group, the [WCL] PNe are characterized by dense, blobby structures and are rich in dust and molecular gas. These nebulae also tend to be relatively compact; most feature optically bright shells with radii  $< 3000 \text{ AU}$  (Górny & Tyłenda 2000) which, given typical late AGB expansion velocities ( $\sim 15\text{--}30 \text{ km s}^{-1}$ ), suggest they are quite young (dynamical ages  $< 1000 \text{ yr}$ ).

Taken together, the foregoing suggests that the H abundances of [WCL]s sharply declined just at the end of their AGB evolution (Herwig 2001). Hence, these stars have acquired large envelope opacities, resulting in strong winds — much stronger than

in normal, H-rich central stars of PNe. Furthermore, the strong winds have emerged very early in post-AGB evolution, before the remnant, ejected AGB envelope has had time to disperse into the interstellar medium. Thus, the [WCL] PNe should make ideal tests for the theory of production of X-rays via interacting wind shocks, as the very large wind momenta of [WCL] central stars and the large, lingering masses of AGB ejecta in [WCL] PNe should offer precisely the right conditions for production of hot, post-shock gas at high emission measure. Furthermore, the blobby and/or filamentary structure of [WCL] PNe should favor heat conduction and mixing of “hot bubble” and nebular gas (Soker & Kastner 2003).

Indeed, among the prototype [WCL] objects is BD +30°3639, the first well-established — and brightest — example of diffuse X-ray emission from a PN (Kreysing et al. 1992; Arnaud et al. 1996; Kastner et al. 2000, 2002; Soker & Kastner 2003). The central star within the second-brightest diffuse X-ray PN, NGC 6543, also has long been classified as Wolf-Rayet type (Swings 1940). Its wind speed and mass loss rate ( $1750 \text{ km s}^{-1}$  and  $\sim 10^{-7} M_{\odot} \text{ yr}^{-1}$ , respectively; Perinotto et al. (1989)) are quite large, explaining the star’s broad emission line spectrum. However, most of the key optical emission lines characteristic of the central stars of [WC] PNe (Crowther et al. 1998) are not present in the spectrum of the central star of NGC 6543 (De Marco, unpublished), and the star is not H deficient (Mendez et al. 1988). Therefore, a [WC] classification is precluded. Nevertheless, NGC 6543 may represent a transient stage in the evolution of [WC] PNe, as its central star may belong to a potentially related, “weak emission line” class (Acker et al. 1996; Peña et al. 2001).

Additional X-ray observations of [WC] PNe should further clarify the role of post-

AGB fast winds in generating diffuse X-ray emission within PNe. To this end, we used the *Chandra* X-ray Observatory (CXO) to search for X-ray emission from two well-studied [WC] PNe, NGC 40 (central star spectral type [WC8], fast wind speed  $v_f = 1000 \text{ km s}^{-1}$ ; Leuenhagen et al. (1996)) and Hen 2-99 ([WC9],  $v_f = 900 \text{ km s}^{-1}$ ). The low-resolution optical morphologies (e.g., Kaler et al. (1989)), central star spectral types, fast wind speeds, and (large) central star mass loss rates ( $\sim 3 \times 10^{-6} M_{\odot} \text{ yr}^{-1}$ ; Leuenhagen et al. (1996)) of these two PNe bear close resemblance to BD +30°3639 ([WC9],  $v_f = 700 \text{ km s}^{-1}$ , Leuenhagen et al. (1996); mass loss rate  $\sim 10^{-6} M_{\odot} \text{ yr}^{-1}$ , Soker & Kastner (2003)). Unlike BD +30°3639 and NGC 6543 — both of which have been the subject of intensive, multi-epoch observing campaigns by the *Hubble Space Telescope* (HST; Balick & Hajian (2004); Li et al. (2002)) — neither NGC 40 nor Hen 2-99 has been the subject of deep HST imaging. An additional [WC] PN, NGC 5315, was serendipitously discovered in the CXO observation of Hen 2-99. The surprising discovery was highlighted in the *Chandra Chronicles*<sup>2</sup>, a journal aimed at disseminating the discoveries made by CXO to the public.

## 4.2 Data and Analysis

The CXO observed Hen 2-99 and NGC 40, with the back-illuminated CCD S3 of the Advanced CCD Imaging Spectrometer (ACIS) as the focal plane instrument, on 2003 November 12 (ObsID 4480) and 2004 June 13 (ObsID 4481), respectively. Exposure times were 29 ks for Hen 2-99 and 20 ks for NGC 40. ACIS has a pixel size of  $0.49''$  and

---

<sup>2</sup>The electronic version of the *Chandra Chronicles* article by Joel H. Kastner is available at: <http://chandra.harvard.edu/chronicle/0307/ngc5315/index.html>

the field of view of ACIS-S3 is  $\sim 8' \times 8'$ . The CXO/ACIS combination is sensitive over the energy range 0.3–10 keV. The data were subject to standard processing by the Chandra X-ray Center pipeline software (CIAO, V. 2.3). We further applied energy-dependent sub-pixel event position corrections appropriate for back-illuminated CCD ACIS-S3 (Li et al. 2003).

### 4.2.1 NGC 40

In Figure 4.1 we present WIYN<sup>3</sup> optical (composite BVR) and 2MASS<sup>4</sup> near-infrared (J- and K-band) images of NGC 40 along with the narrow-band (0.3–1 keV) Chandra/ACIS X-ray image (raw and smoothed) of the same region. The morphology of the  $\sim 40''$  diameter nebula is similar in these three optical/near-infrared images: in each case NGC 40 appears as a limb-brightened shell, with a bright rim that is interrupted by fainter protrusions to the north-northeast and south-southwest. Deep optical images reveal jet-like features in the vicinity of each protrusion, although there is no kinematical evidence for collimated, fast outflows in NGC 40 (Meaburn et al. 1996).

The detection of soft X-rays from NGC 40 is apparent upon extraction of a

---

<sup>3</sup>The WIYN Observatory is owned and operated by the WIYN Consortium, which consists of the University of Wisconsin, Indiana University, Yale University, and the National Optical Astronomy Observatories (NOAO). NOAO is operated by the Association of Universities for Research in Astronomy (AURA), Inc. under cooperative agreement with the National Science Foundation. See <http://www.noao.edu/wiyn/wiynimages.html>

<sup>4</sup>This chapter makes use of data products from the Two Micron All Sky Survey, which is a joint project of the University of Massachusetts and the Infrared Processing and Analysis Center/California Institute of Technology, funded by the National Aeronautics and Space Administration and the National Science Foundation. (<http://www.ipac.caltech.edu/2mass/>)

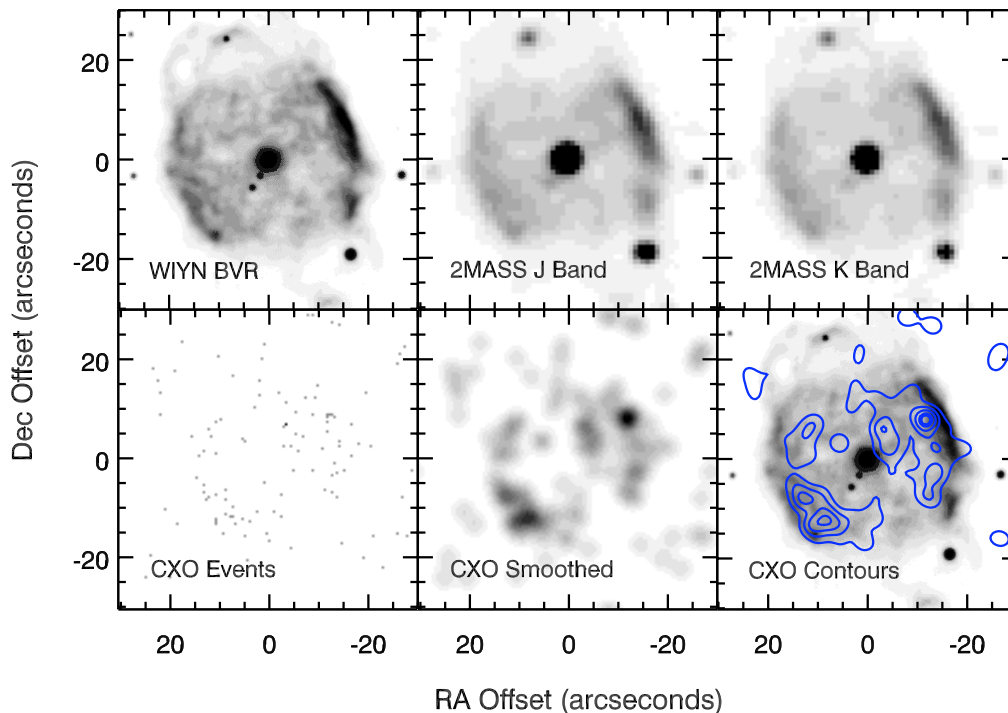


Figure 4.1 Optical, near-infrared, and X-ray images of NGC 40. *Top row, left to right:* WIYN BVR composite image (converted to greyscale) and 2MASS J- and K-band images. *Bottom row, left to right:* CXO X-ray and smoothed (see below) CXO X-ray images, and contours of the smoothed CXO X-ray image overlaid on the WIYN BVR composite greyscale image. The images are  $60'' \times 60''$  with N up and E to the left. The 2MASS images are displayed on a linear greyscale. The smoothed CXO X-ray images in this figure and in Figure 4.5 were obtained by convolving the original image with a PSF with FWHM  $\sim 4''$ . The contours of the CXO X-ray image in the lower right panel are at 20%, 40%, 60%, 80%, and 90% of the image maximum of  $1.6 \times 10^{-3}$  counts  $\text{ks}^{-1} \text{arcsec}^{-2}$  (0.3-1.0 keV).

spectrum from a region of the Chandra/ACIS image encompassing the optical/near-infrared nebula. This spectrum is displayed in Figure 4.2. An image extracted over the soft (0.3-1.0 keV) energy range spanned by the detected photons reveals that the



X-ray emission arises from an annular region that lies nested just within, and follows the overall surface brightness distribution of, the bright, partial rim seen in the optical and near-infrared (Figures 4.1, 4.3).

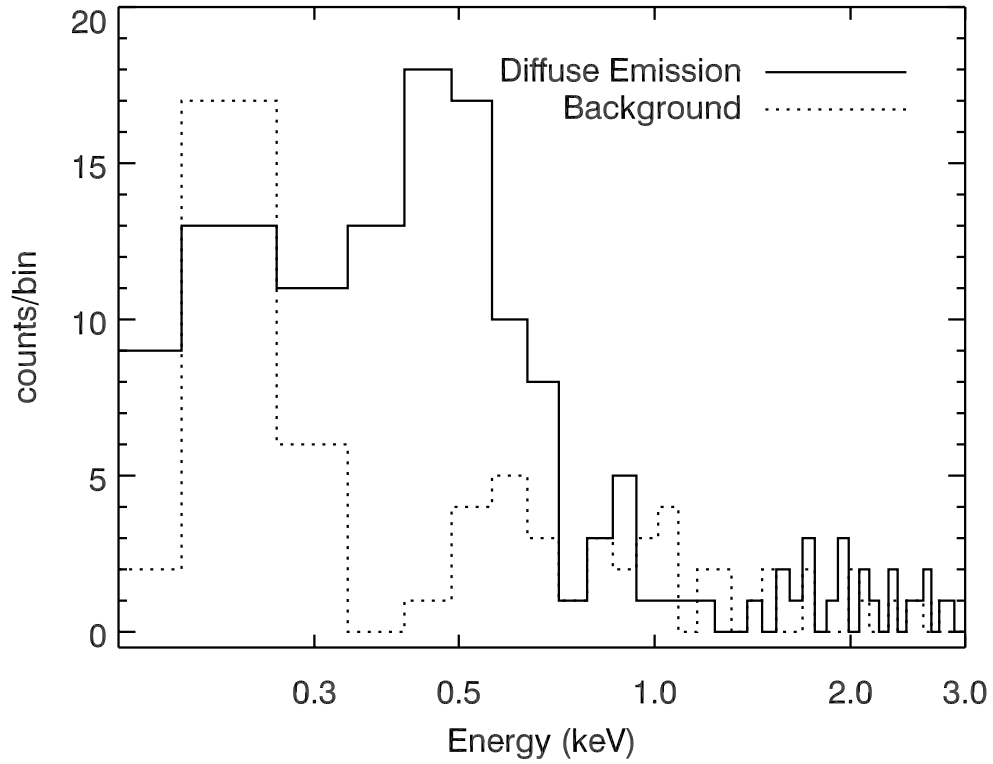


Figure 4.2 “Raw” (counts vs. energy) X-ray spectrum of NGC 40 (solid histogram), extracted from the region encompassed by the optical/near-IR nebula (the raw background spectrum is displayed as a dotted-line histogram).

Refining the spectral extraction region to an annulus with inner radius  $4''$  and outer radius of  $20''$  results in the background-subtracted spectrum displayed in Figure 4.4. The background-subtracted count rate of this diffuse emission was  $(2.8 \pm 0.9) \times 10^{-3}$

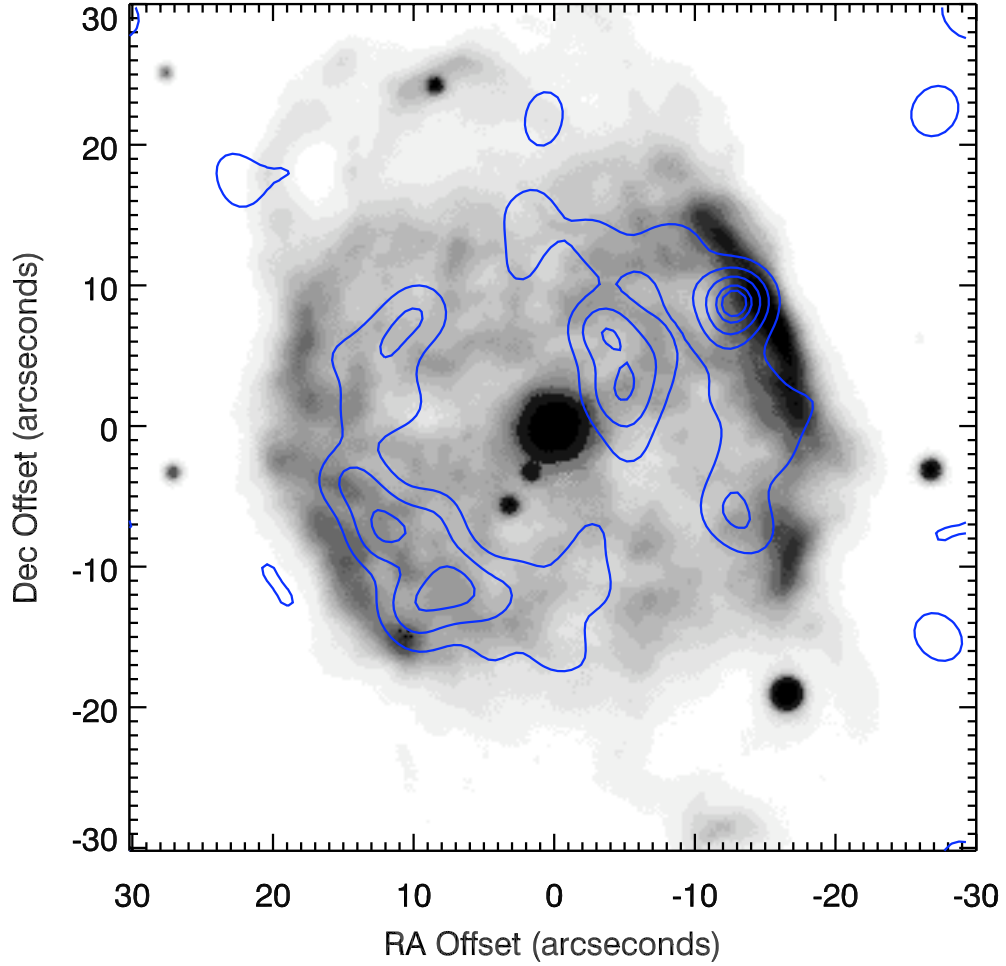


Figure 4.3 WIYN BVR greyscale composite image of NGC 40 with smoothed CXO X-ray contours overlaid.

counts  $\text{s}^{-1}$ , where the background region was defined as a circular region of radius  $\sim 40''$  lying  $\sim 135''$  SE of NGC 40. We used XSPEC (V. 12.2.0; Arnaud (1996)) to fit the spectrum with a Raymond-Smith thermal plasma emission model suffering

intervening absorption. Based on the inferred nebular color excess of  $E(B-V) = 0.38$  (Pottasch et al. 1977), we fixed the absorbing column at  $N_H = 2.2 \times 10^{21} \text{ cm}^{-2}$ . The best fit indicates a plasma temperature of  $T_X \sim 9.4 \times 10^6 \text{ K}$ , with an uncertainty of  $\sim 20\%$ . The model fit is marginally improved by the inclusion of a Gaussian component at an energy  $0.5 \pm 0.2 \text{ keV}$ , which is suggestive of the presence of excess O VII emission. The inclusion of this second component would imply a somewhat higher plasma temperature ( $T_X \sim 1.8 \times 10^6 \text{ K}$ ). The modeling indicates an unabsorbed X-ray flux  $\sim 1.7 \times 10^{-13} \text{ ergs cm}^{-2} \text{ s}^{-1}$  (the mean of the flux from plasma components obtained by fits with and without the 0.5 keV Gaussian component), corresponding to an intrinsic X-ray luminosity  $L_X \sim 2 \times 10^{31} (D/1.0\text{kpc})^2 \text{ erg s}^{-1}$  where  $D$  is the distance to NGC 40. The estimate  $D = 1.0 \text{ kpc}$  was determined by Leuenhagen et al. (1996).

#### 4.2.2 Hen 2-99

In Figure 4.5 we present Anglo-Australian Observatory Digitized Sky Survey<sup>5</sup> Short R-band and 2MASS J- and K-band images of Hen 2-99 along with the broad-band (0.3–10 keV) Chandra/ACIS X-ray image (raw and smoothed) of the same region. The object appears as a  $\sim 25''$  diameter nebula in the R-band image, while only the central star is detected in the near-infrared image. Point-like X-ray sources in the immediate vicinity of Hen 2-99 — including one source that lies  $\sim 6''$  from the central star and has no optical or near-infrared counterpart — have similar and relatively hard spectra, and are most likely background sources.

---

<sup>5</sup><http://archive.eso.org/dss/dss>

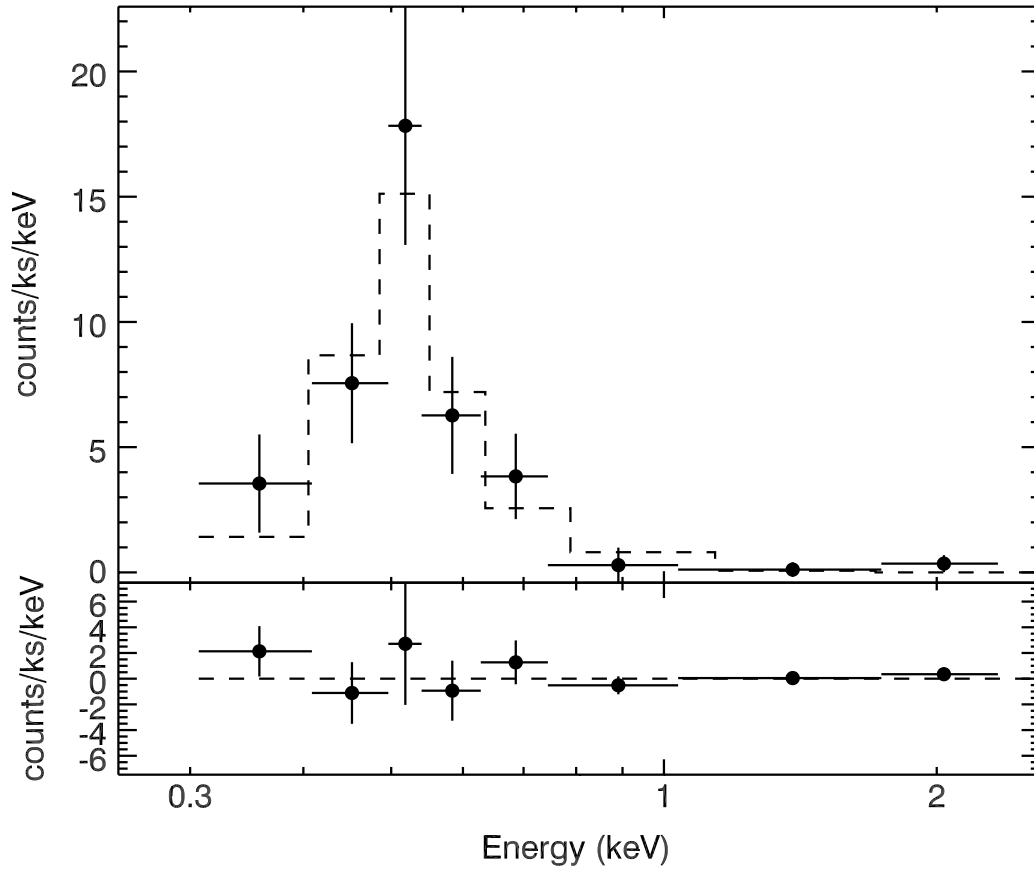


Figure 4.4 Top frame: Background-subtracted X-ray spectrum of NGC 40 (crosses), with best-fit thermal plasma model overlaid (dashed line; see text). Bottom frame: residuals of the fit.

We searched for diffuse emission from Hen 2-99 via the same approach used for NGC 40, i.e., we extracted a 0.3–10 keV spectrum from the region of the Chandra/ACIS image encompassing the R-band emission from Hen 2-99. The spectral extraction avoided the point source that lies closest to the position of the central star. Upon subtraction of background emission within a region defined by a cir-

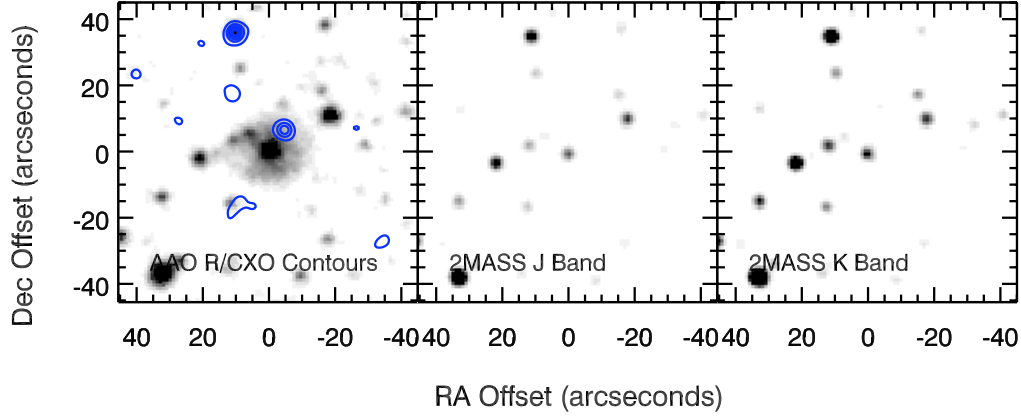


Figure 4.5 Optical, near-infrared, and X-ray images of the Hen 2-99 region. *Left:* AAO Short R-band image, with smoothed CXO X-ray image overlaid as a contour map. *Center:* 2MASS J-band image. *Right:* 2MASS K-band image. The images are  $90'' \times 90''$  with N up and E to the left. The AAO and 2MASS images are presented as linear greyscale. The contours in the left panel are at 20%, 40%, 60%, 80%, and 90% of the X-ray image maximum of  $0.14 \text{ counts ks}^{-1} \text{ arcsec}^{-2}$  (0.3-10.0 keV).

cle with radius  $\sim 10''$ , the resulting X-ray spectrum (not shown) reveals no source photons.

From the  $1\sigma$  uncertainty in the background count rate ( $2 \times 10^{-3} \text{ counts s}^{-1}$ ) we find a ( $3\sigma$ ) upper limit on the unabsorbed X-ray luminosity of  $L_X < 5 \times 10^{30} \times (D/2.5 \text{ kpc})^2 \text{ erg s}^{-1}$ . The estimate  $D = 2.5 \text{ kpc}$  was determined by Leuenhagen et al. (1996). For this upper limit, we (conservatively) assume an X-ray emission temperature at the upper end of the range determined thus far for the diffuse emission from PNe ( $T_x = 3 \times 10^6 \text{ K}$ ), and adopt  $N_H = 2.9 \times 10^{21} \text{ cm}^{-2}$  based on a color excess of  $E(B - V) = 0.5$  (Leuenhagen et al. 1996).

### 4.2.3 NGC 5315

The position of NGC 5315 lies just within the field of view of the ACIS-S detector array, on a CCD (the front-illuminated S4) that lies adjacent to the prime imaging CCD (the back-illuminated S3). Examination of the Chandra ACIS image reveals an X-ray source at the position of NGC 5315,  $12.5'$  off-axis (Figure 4.6). Due to the large off-axis angle and the fact that—when not used in conjunction with the high-energy transmission gratings—ACIS-S4 deviates significantly from the focal surface of the Chandra mirror assembly, the NGC 5315 X-ray source is subject to severe image aberrations (Figure 4.7). The Chandra point-spread function semimajor axis is  $10''$ - $20''$  at such off-axis angles, without accounting for the displacement of the S4 detector from the focal surface. Hence, apart from establishing that an X-ray source is coincident with the position of NGC 5315, no spatial information can be readily extracted from the ACIS-S4 image.

We extract source and background spectra, spectral responses, and light curves. The circular source extraction region radius was  $34''$ , which encompass the 95% encircled energy of a point source at the off-axis angle corresponding to the position of NGC 5315. Background was extracted from a  $\sim 2.5' \times 3.5'$  rectangular region adjacent to the NGC 5315 source. The resulting, background-subtracted spectrum displays prominent Ne ix emission at  $0.9$  keV and a blend of O vii and O viii emission lines at  $0.65$  keV (Figure 4.8). The background-subtracted count rate of the source is  $12.4 \pm 0.7$  ks $^{-1}$ . The light curve (not shown) reveals no significant variation in this count rate during the 28.7 ks exposure.

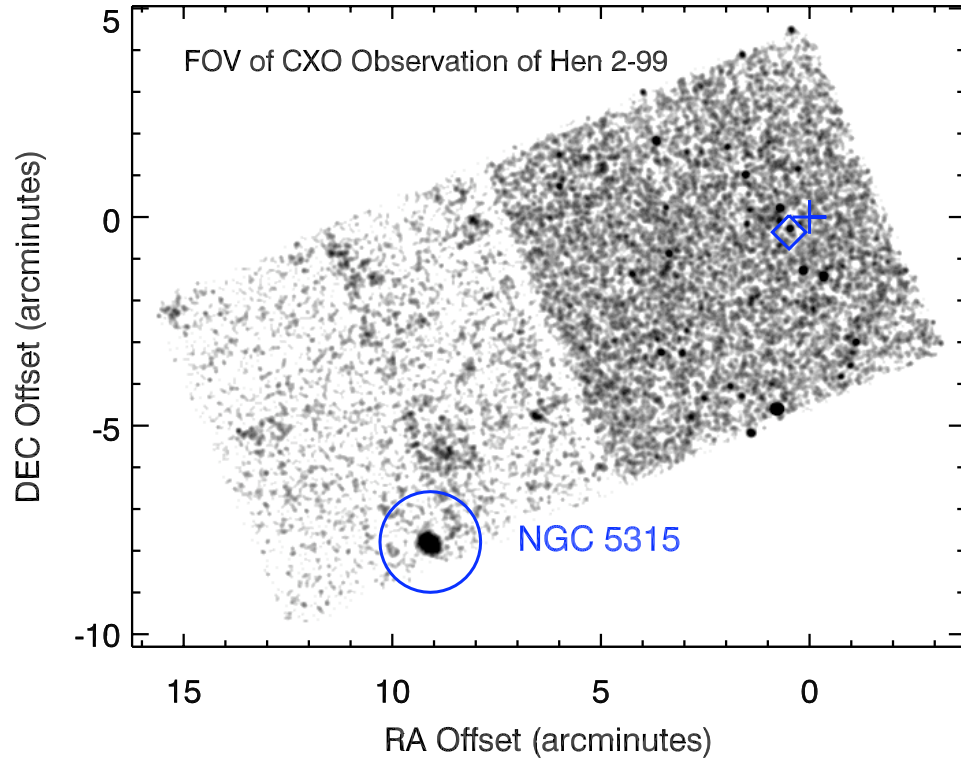


Figure 4.6 Field of view (FOV) of CXO observation of Hen 2-99 showing the aimpoint (cross), the position of Hen 2-99 (diamond) and the location of the X-ray emission associated with NGC 5315 (circle).

The background-subtracted spectrum was fit with an absorbed thermal plasma emission model with the absorbing column density set to  $\log N_H(\text{ cm}^{-2}) = 21.36$ , corresponding to the measured extinction toward NGC 5315 ( $A_V \approx 1.3$  Peimbert et al. 2004; Pottasch et al. 2002; Cahn et al. 1992). The best-fit temperature is  $T_X = 2.6 \times 10^6 \text{ K}$  ( $\pm 10\%$ ) and the inferred intrinsic X-ray luminosity is  $L_X \sim 2.6 \times 10^{32} \text{ erg s}^{-1}$  in the 0.3-2.0 keV energy range and assuming a distance of 2.5 kpc (Marcolino et al. 2007). The plasma model suggests Ne is enhanced and Fe is depleted; the best-fit

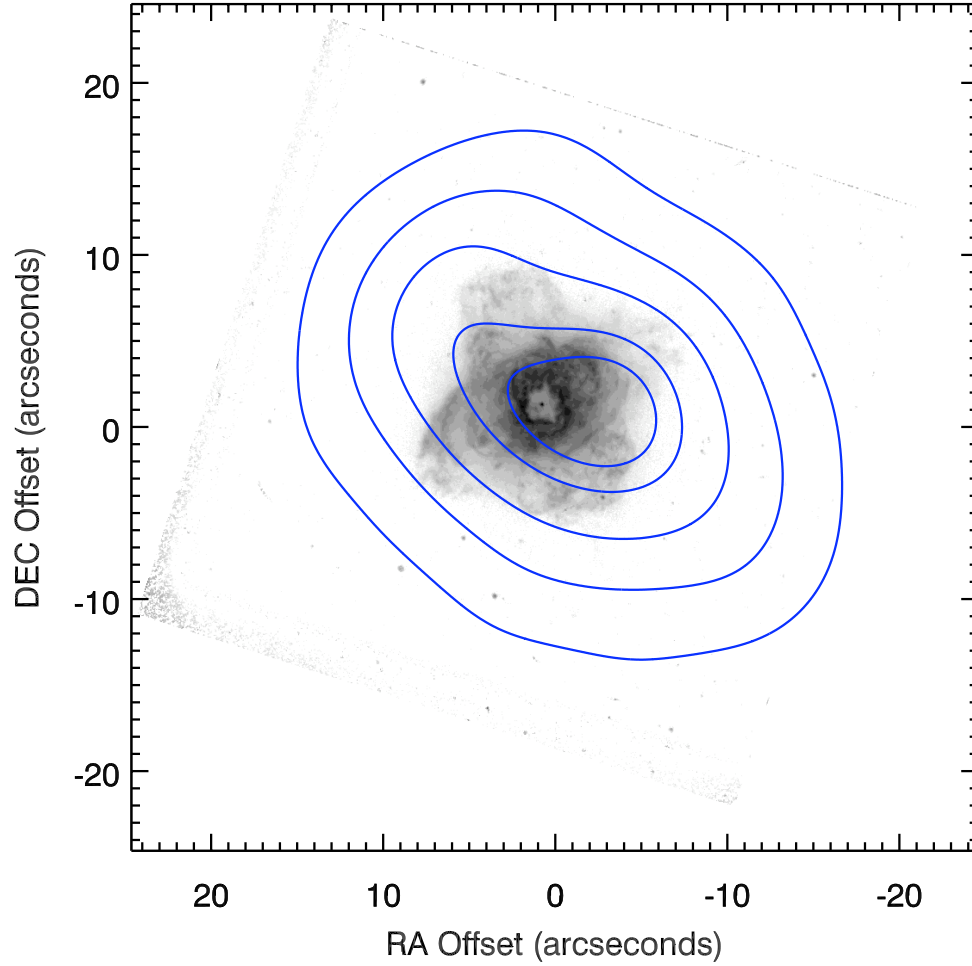


Figure 4.7 HST narrowband (F658N) image of the PN NGC 5315 with contour overlays of the X-ray emission smoothed with a gaussian filter.

VMEKAL model abundances are  $4.3 \pm 1.3$  and  $0.6 \pm 0.3$ , respectively, relative to solar (Anders & Grevesse 1989). The X-ray spectrum observed from NGC 5315 is depicted in Figure 4.8 with the best-fit model overlaid.



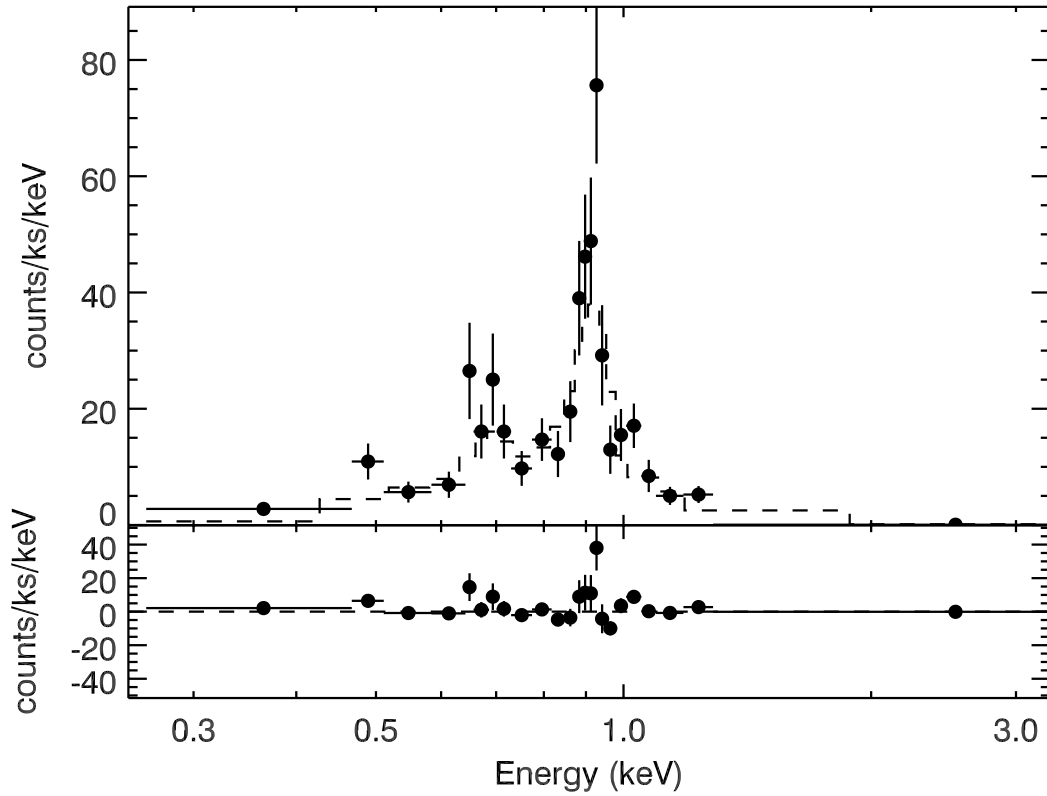


Figure 4.8 Top frame: Background-subtracted X-ray spectrum of NGC 5315 (crosses), with best-fit thermal plasma model overlaid (dashed line; see text). Bottom frame: residuals of the fit.

### 4.3 Discussion

The shell-like shape of the X-ray emitting region in NGC 40, and the correspondence of this region to the bright optical/near-IR rim in this nebula, indicates that the bright rim has been generated by the shocked fast wind from the central star. The lack of X-ray emission associated with the apparent “blowouts” (interruptions in the rim) that are aligned along an axis running NNE-SSW in NGC 40 further suggests that

this wind is more or less spherically symmetric, with a possible enhancement along the equatorial plane of the system rather than along the polar axis. We note that there is no kinematic evidence for the presence of collimated jets in NGC 40, despite the appearance of polar “blowouts” or jet-like features in this nebula (Meaburn et al. 1996; Martin et al. 2002).

The X-ray morphology of NGC 40 appears similar to (but is better resolved than) those of BD +30°3639 (Kastner et al. 2000) and NGC 7009 (Guerrero et al. 2002). The appearances of these structures are fully consistent with the generation of “hot bubbles” via wind-wind interactions (Akashi et al. 2006). These X-ray morphologies stand in sharp contrast to the radially directed X-ray structures within the young planetary nebulae NGC 7027 and Mz 3, however. These two PNe display X-ray evidence for the action of collimated jets (Kastner et al. 2001, 2002, 2003; Cox et al. 2002) and, in both cases, the X-ray emission appears intimately associated with the ongoing structural changes apparent in the optical/near-infrared nebulae. Thus it appears that two quite different processes — jets on the one hand, and quasi-spherical fast winds on the other — may be responsible for energetic shocks and, hence, high-temperature plasma in PNe (see also Guerrero et al. (2005) and Akashi et al. (2006)). It is clear, furthermore, that the different processes responsible for X-ray emission are closely tied to the different PN shapes that are seen in optical emission lines.

The radii of the bright rim and X-ray emitting shell in NGC 40 are  $\sim 10$  times larger than these same structures in BD +30°3639. In light of the similarity of the properties of the central stars of NGC 40 and BD +30°3639, the comparison between physical sizes and X-ray emission properties indicates that the former PN might best

be considered as an evolved version of the latter. This interpretation places constraints on [WC] PN evolutionary schemes wherein the central stars evolve from late to early [WC] spectral types (see Peña et al. (2001) and references therein). Specifically, given the subtle differences between the central star spectral types ([WC9] and [WC8], respectively) and wind properties of NGC 40 and BD +30°3639 (Leuenhagen et al. 1996), the contrast in their X-ray and optical/near-infrared properties indicates that [WCL] stars and their associated PNe may evolve between subclasses on timescales  $< 5000$  yr, i.e., a time period shorter than the approximate dynamical age of the hot bubble in NGC 40 (Akashi et al. 2006). We stress, however, that the notion that [WC] PN central stars evolve from late to early subtypes remains the subject of debate (Peña et al. 2001).

Due to the very poor off-axis Chandra ACIS-S image quality at the position of NGC 5315, it is not possible to ascertain from the ACIS image alone whether the X-rays trace a hot bubble within this PN, emanate from the PN nucleus, or are emitted by both the nebula and its central star(s). However, the background-subtracted spectrum (Figure 4.8), the luminosity, and the temporal behavior of the X-ray source associated with NGC 5315 appear quite definitive regarding the origin of the X-rays. The spectrum shows strong Ne ix line emission as well as a blend of O vii and O viii lines, with no evidence for Fe L-shell lines. Spectral modeling indicates that the emission arises in a  $\sim 2.5$  MK thermal plasma with enhanced Ne and depleted Fe. These results and the inferred source  $L_X$  are very similar to those obtained for the best-characterized diffuse X-ray emitting PN, BD +30 3639 (Kastner et al. 2000). Meanwhile, the Chandra ACIS light curve shows no evidence for variability, and the

absorption-corrected X-ray luminosity of NGC 5315 is at least an order of magnitude larger than that of any unresolved PN core region detected thus far (Guerrero et al. 2001; Kastner et al. 2003), further supporting the interpretation that the X-rays arise from an extended region within NGC 5315. Assuming the X-rays from NGC 5315 indeed arise from its compact ( $\sim 1''$  radius), sharply delineated central cavity (Figure 4.7), these results establish NGC 5315 as one of the most luminous “hot bubble” X-ray sources yet detected

The upper limit on X-ray luminosity that we obtain for Hen 2-99 ( $L_X < 5 \times 10^{30}$  ergs  $s^{-1}$ ; §2.2) constrains this nebula to be less X-ray luminous than all PNe thus far detected in X-rays (Soker & Kastner 2003; Kastner et al. 2003; Guerrero et al. 2005). The non-detection of Hen 2-99 by CXO therefore would suggest either that the fast wind from the central ([WC9]) star has yet to collide with the ionized ejecta seen in optical images, or that any diffuse X-ray emission emanating from shocks produced by its fast wind has now faded to a level less than that detected in NGC 40. The former interpretation would appear to be more consistent with the lack of a clearly defined inner rim in Hen 2-99 in near-infrared images (Figure 4.5), if the presence of such limb-brightened bubble structures in optical/near-infrared images of PNe is interpreted as evidence of wind-wind shocks. Additional X-ray observations of [WC] PNe with and without well-formed optical/near-infrared bubbles are required to test the hypothesis that the lack of detectable X-ray emission from Hen 2-99 indicates that this PN has yet to enter a phase of strong wind-wind shocks, despite the very large wind momentum of its central star.

## 4.4 Chapter Summary

Observations of the PNe NGC 40 and Hen 2-99 were acquired by CXO. In the observation of Hen 2-99, the PN NGC 5315 was serendipitously observed. These three PNe feature late-type Wolf-Rayet central stars that are presently driving fast ( $\sim 1000 \text{ km s}^{-1}$ ), massive winds into denser, slow-moving ( $\sim 10 \text{ km s}^{-1}$ ) material ejected during recently terminated asymptotic giant branch (AGB) evolutionary phases. Hence, these observations provide key tests of models of wind-wind interactions in PNe. NGC 40 features faint, diffuse X-ray emission distributed within a partial annulus that lies nested within a  $\sim 40''$  diameter ring of nebulosity observed in optical and near-infrared images. NGC 5315 is a strong source, but severely distorted due to the off-axis location in the observation. Hen 2-99 is undetected. The spectral fit of the X-ray emission from NGC 40 indicates an X-ray temperature of  $2 \times 10^6 \text{ K}$  and an X-ray luminosity of  $\sim 2 \times 10^{31} \text{ erg s}^{-1}$ . These results, combined with the ring-like morphology of the X-ray emission from NGC 40, suggest that its X-ray emission arises from a “hot bubble” that is highly evolved and is generated by a shocked, quasi-spherical fast wind from the central star, as opposed to AGB or post-AGB jet activity. Similarly, the spectral fit of the X-ray emission from NGC 5315 indicates an X-ray temperature of  $2.5 \times 10^6 \text{ K}$  and X-ray luminosity of  $2.6 \times 10^{32} \text{ erg s}^{-1}$  and suggests the X-ray emission is due to a “hot bubble” in the compact PN. In contrast, the lack of detectable X-ray emission from Hen 2-99 suggests that this PN has yet to enter a phase of strong wind-wind shocks.



# Chapter 5

## Serendipitous XMM-Newton Detection of X-ray Emission from the Bipolar PN Hb 5<sup>1</sup>

### 5.1 Bipolar PNe and the Shaping and Evolution of PNe

The shaping and evolution of planetary nebulae (PNe) has been an active field of study for a few decades and is continually spurred on by new observations that do not fit the existing theoretical models (Balick & Frank 2002, and references therein).

---

<sup>1</sup>This chapter originally appeared in the The Astrophysical Journal, Volume 694, Issue 2, pp. 1481-1484 (2009) and is coauthored by Joel H. Kastner, Bruce Balick, and Adam Frank.

Of particular note are the bipolar PNe, with their large lobes and narrow waists, many showing residual evidence of a spherical AGB wind in the form of nested rings centered on the PN central star (Corradi et al. 2004). The implied transition from seemingly spherical mass loss to profoundly bipolar outflow remains an unsolved mystery. Possible shaping and evolutionary mechanisms have been developed ranging from the interacting stellar winds model (Kwok et al. 1978), wherein a hot fast stellar wind shocks a slower moving AGB wind, to collimated flows (Soker 2004; Akashi et al. 2008) possibly launched and shaped by a magnetocentrifugal force fueled by an AGB dynamo (Blackman et al. 2001).

In all of these PN shaping models the presence of gas heated to X-ray emitting temperatures is predicted. The advent of high-spatial-resolution, X-ray observatories (Chandra and XMM-Newton) facilitated the discovery and scrutiny of this shock-heated gas (Guerrero et al. 2005; Kastner et al. 2008, and references therein) and the results were surprising. The observed X-ray temperatures of the shocked plasma have been much lower,  $1 - 3 \times 10^6$  K, than predicted,  $> 10^7$  K (Stute & Sahai 2006; Kastner et al. 2008), spawning a variety of potential solutions (see Soker & Kastner 2003, for a review). Akashi et al. (2006, 2007, 2008) and Steffen et al. (2008) have since produced more detailed models in an attempt to resolve the temperature discrepancy while adequately reproducing other observed quantities. Steffen et al. (2008) investigate the role played by thermal conduction in establishing the physical properties of the X-ray emitting gas, while Akashi et al. (2006, 2007) consider the possibility that the X-ray emitting gas arose from a slower, post-AGB wind ( $\sim 500$  km/s), and Akashi et al. (2008) present numerical simulations that suggest the observed X-ray properties



could be explained by jet-wind interaction. These newer models describing PN X-ray emission should, in turn, provide feedback to generalized models describing the origin of the flows shaping PNe, which, taken together, will provide a complete theoretical description of the shaping and evolution of PNe.

The identification of X-ray sources within bipolar PNe should provide unique constraints on this new generation of PN shaping and evolution models. However, thus far such detections have been few and far between (Gruendl et al. 2006; Kastner et al. 2001, 2003; Sahai et al. 2003). During an archival program to identify serendipitous X-ray sources associated with PNe, we established that the XMM-Newton Serendipitous Survey<sup>2</sup> includes an X-ray source, 2XMM J174756.2-295937, that is spatially coincident, within errors ( $\sim \pm 2''$ ), with PN Hubble 5 (Hb 5), a large, narrow-waist bipolar planetary nebula with a bright, compact, core (Pottasch & Surendiranath 2007). Quireza et al. (2007) classify Hb 5 as Peimbert Type I PN, i.e., a He- and N-rich PN descended from a relatively massive progenitor star. Hb 5 is a high-excitation PN and, in particular, is one of the few PNe showing the  $7.652 \mu\text{m}$  Ne VI line (Pottasch & Surendiranath 2007). A photodissociation region immediately surrounding the nebula may account for the presence of molecular hydrogen emission (Bernard-Salas & Tielens 2005; Pottasch & Surendiranath 2007). The distance to Hb 5 is highly uncertain. Rice et al. (2004) derive a distance of  $1.4 \text{ kpc} \pm 0.3 \text{ kpc}$  from 3D photoionization modeling, while Pottasch & Surendiranath (2007) argue for a much larger distance, ranging from 3 to 7 kpc. Corradi & Schwarz (1993) find a polar expansion velocity of  $\sim 250 \text{ km s}^{-1}$ , while Pismis et al. (2000) reported a faster,

---

<sup>2</sup>See Watson et al. (2009) for information on the XMM-Newton Serendipitous Survey catalog.

possibly collimated, wind of  $400 \text{ km s}^{-1}$  near the center of Hb 5.

## 5.2 Data and Analysis

Hb 5 lies within the field of an XMM-Newton observation of the pulsar PSR J1747-2958 and pulsar wind nebula (MOUSE NEBULA). This observation (ObsID 0152920101) was performed during XMM Revolution 607 on 2003 April 02. The European Photon Imaging Camera (EPIC) detector arrays pn, MOS1, and MOS2 were operated in Full-Frame Mode, with the thick filter, for total exposures of 45.1, 51.3, and 51.3 ks, respectively. We reprocessed the XMM-Newton Observation Data Files using the XMM-Newton Science Analysis Software (SAS) package version 7.1.0 with the calibration files available in Current Calibration File Release 241 (XMM-CCF-REL-241). We filtered out high background periods and bad events from all observations using standard filters for imaging mode observations. The resulting net exposure times are 44.1, 50.6, and 50.8 ks, in the pn, MOS1, and MOS2 arrays, respectively.

From the source and background regions used in the spectral extraction of the X-ray source at the position of Hb 5 (described in Section 2.3), we determined that the net count rates (source plus background) in the energy range 0.2-2.0 keV are  $1.9 \pm 0.4 \times 10^{-3} \text{ cts s}^{-1}$  in pn,  $8.0 \pm 1.8 \times 10^{-4} \text{ cts s}^{-1}$  in MOS1, and  $8.7 \pm 1.9 \times 10^{-4} \text{ cts s}^{-1}$  in MOS2. We merged the three observations using the SAS task *merge*. Using this merged event list, we generated a soft band image for the energy range 0.2-2.0 keV, binned to  $5''$  pixels (Figure 5.1).

### 5.2.1 Spatial Analysis

Figure 5.1 indicates that the X-ray emission at the position of Hb 5 is marginally resolved. Hb 5 is located  $\sim 7.8'$  off-axis in the XMM observation, and the coincident X-ray source displays peak emission around 1 keV. This off-axis angle and peak emission are within the range of application of the XMM/EPIC PSF model described in Ghizzardi (2002), i.e., a King profile whose core radius and slope depend on energy and off-axis angle. Specifically, we expect a PSF core radius of  $4.71''$  and slope of -1.44. This suggests that using a normalized Gaussian smoothing filter with a FWHM of  $7.5''$  will reduce the loss of information, while aiding our interpretation of the detected X-ray emission. In Figures 5.1-5.3, the smoothed X-ray image contours are overlaid onto the unsmoothed X-ray image (Figure 5.1), a 2MASS J-band image (Figure 5.2), and a HST WFPC2 F658N ( $H\alpha + [NII]$ ) narrowband image (Figure 5.3). The image registration was performed by the IDL Astro Library<sup>3</sup> task *hastrom*. A slight eastward shift ( $\sim 0.45''$ ) of the HST image was required to align the stars appearing in both the 2MASS J-band and chip 3 of the HST WFPC2 F658N fields. Figures 5.2 and 5.3 demonstrate that the peak of the X-ray emission coincides with the bright core regions of Hb 5 seen in the 2MASS and HST images, respectively. The apparent extension of the X-ray emission lies along the brightest features observed in the  $H\alpha + [NII]$  image.

---

<sup>3</sup><http://idlastro.gsfc.nasa.gov>

### 5.2.2 Spectral Analysis

The spatial region available for spectral extraction within the XMM image of the Hb 5 field is severely constrained by several unavoidable artifacts. Immediately surrounding the region of interest are chip gaps (in all three EPIC arrays), a bright nearby soft source, and a readout streak from the nearby soft source. Guided by the optical HST position of Hb 5 along with the evident soft X-ray emission, we selected an extraction region that optimized the signal in the spectrum while avoiding these artifacts. An annulus surrounding the source region and omitting nearby sources was used to estimate the background. We used the SAS tasks *rmfgen* and *arfgen* to generate source-specific response matrices and effective area curves; the latter accounts for off-axis vignetting ( $\sim 30\%$  loss at  $7.8'$ , Ehle et al. (2008)).

The resulting spectra from the three EPIC CCD detector arrays were simultaneously fit in XSPEC (version 12.3.1; Arnaud (1996)) with a variable abundance thermal plasma model, *vmekal* (Mewe et al. 1985, 1986; Kaastra 1992; Liedahl et al. 1995), and intervening absorption, *wabs* (Morrison & McCammon 1983). We used the extinction value  $C = 1.60$  at  $H\beta$  listed in Pottasch & Surendiranath (2007) to fix the column density at  $N_H = 6.0 \times 10^{21} \text{ cm}^{-2}$  and – noting the apparent presence of a strong spectral feature at  $\sim 1.0$  keV that is likely due to Ne IX and Ne X lines – left as free parameters the gas temperature and the abundance of Ne. We fixed all other abundances at their solar values (Anders & Grevesse 1989). Although fixing the abundance of Ne to its solar value results in a global fit that is acceptable, this fit is poor at the spectral feature near 1.0 keV. There is a modest improvement in the fit

when we allow the abundance of Ne to be a free parameter. This latter fit is presented in Figure 5.4. The temperature is found to lie in the range 2.4-3.7 MK (90% confidence range) and the Ne abundance factor lies in the range 1.8-6.9 (90% confidence range) relative to the solar abundance given by Anders & Grevesse (1989). The best model fit indicates an observed 0.2-2.0 keV flux of  $7.9 \times 10^{-15}$  ergs cm<sup>-2</sup> s<sup>-1</sup>, and an unabsorbed flux of  $1.2 \times 10^{-13}$  ergs cm<sup>-2</sup> s<sup>-1</sup>. We assume a distance of 3.2 kpc after Pottasch & Surendiranath (2007) and find  $L_X = 1.5 \times 10^{32} (D/(3.2 \text{ kpc}))^2$  ergs s<sup>-1</sup>.

### 5.3 Discussion

Hb 5 is the fourth bipolar PNe – after NGC 7026 (Gruendl et al. 2006), the transitional object NGC 7027 (Kastner et al. 2001), and the possibly symbiotic system Mz 3 (Kastner et al. 2003) – with suspected diffuse X-ray emission and only the second Type I PN known to display X-ray emission. The other Type I PN with evidence for shocked X-ray emission is the [WC] PN NGC 5315, which was also discovered serendipitously, far off-axis, by the Chandra X-ray Observatory (Kastner et al. 2008). Indeed, the X-ray emission regions detected in Hb 5 and NGC 5315 display similar characteristics, despite the fact that one is associated with a high excitation, bipolar PN and the other with a compact [WC] PN. Specifically, these two PNe have similar plasma temperatures (within errors) and similar X-ray luminosities (though the  $L_X$  values are very uncertain, due to distance uncertainties). In addition, both appear to show strong X-ray Ne lines. Pottasch & Surendiranath (2007) find an Ne abundance factor of 2.2 relative to solar in the infrared spectrum of Hb 5, similar to the (uncertain)

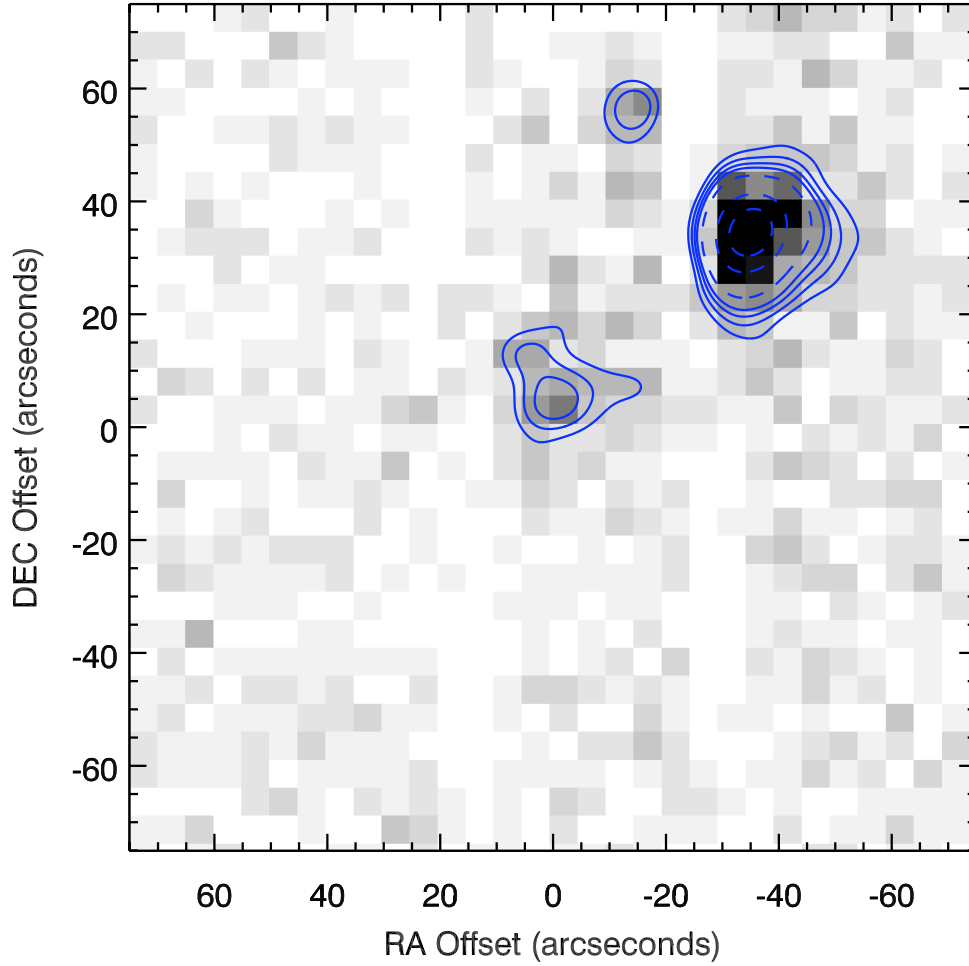


Figure 5.1 XMM Imaging of the Bipolar PN Hb 5 Field. Smoothed X-ray contours at 9, 11, 13, and 15 counts (solid contours) and at 20, 40, and 60 counts (dotted contours) are overlaid upon the unsmoothed XMM X-ray image.

overabundance tentatively determined from the X-ray spectrum.

The bipolar PNe detected thus far have closed bipolar lobes, while many of the

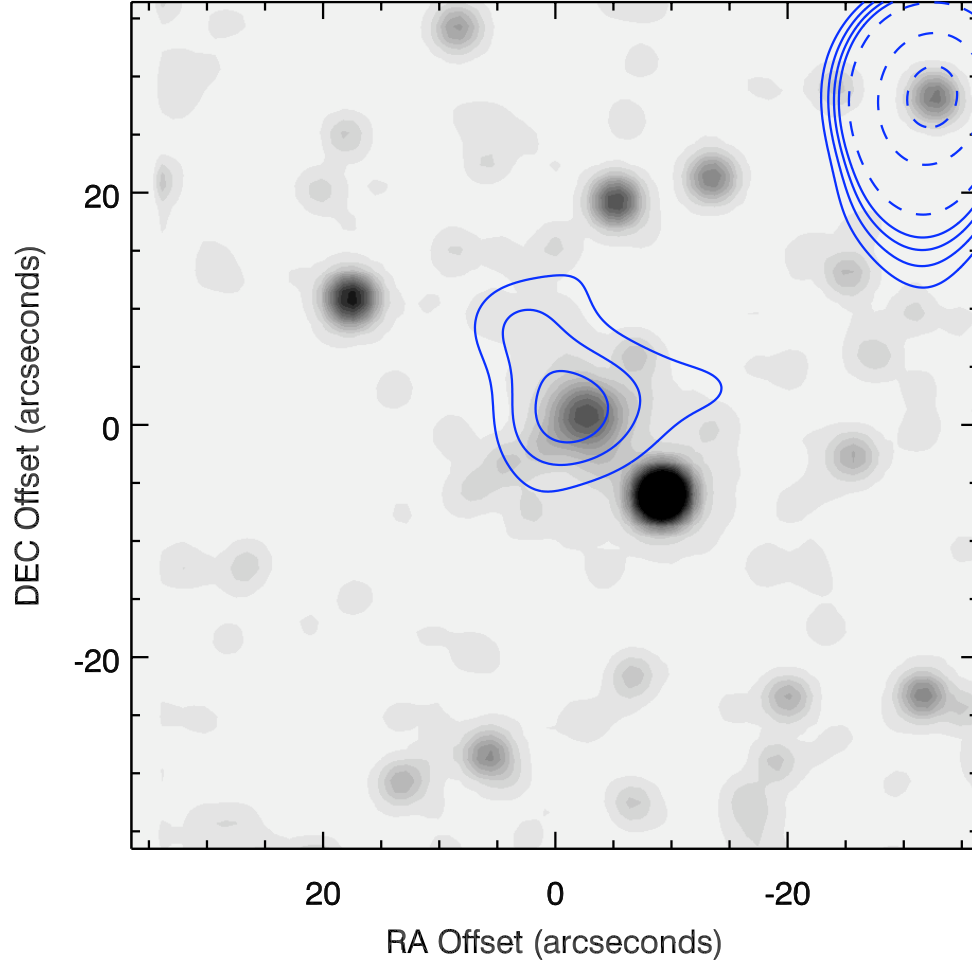


Figure 5.2 XMM Imaging of the Bipolar PN Hb 5 Field. Smoothed X-ray contours at 9, 11, 13, and 15 counts (solid contours) and at 20, 40, and 60 counts (dotted contours) are overlaid upon the 2MASS J-band image.

bipolar PNe observed but not detected have open bipolar lobes (Gruendl et al. 2006). The role of open and closed lobes is an important factor that may determine key

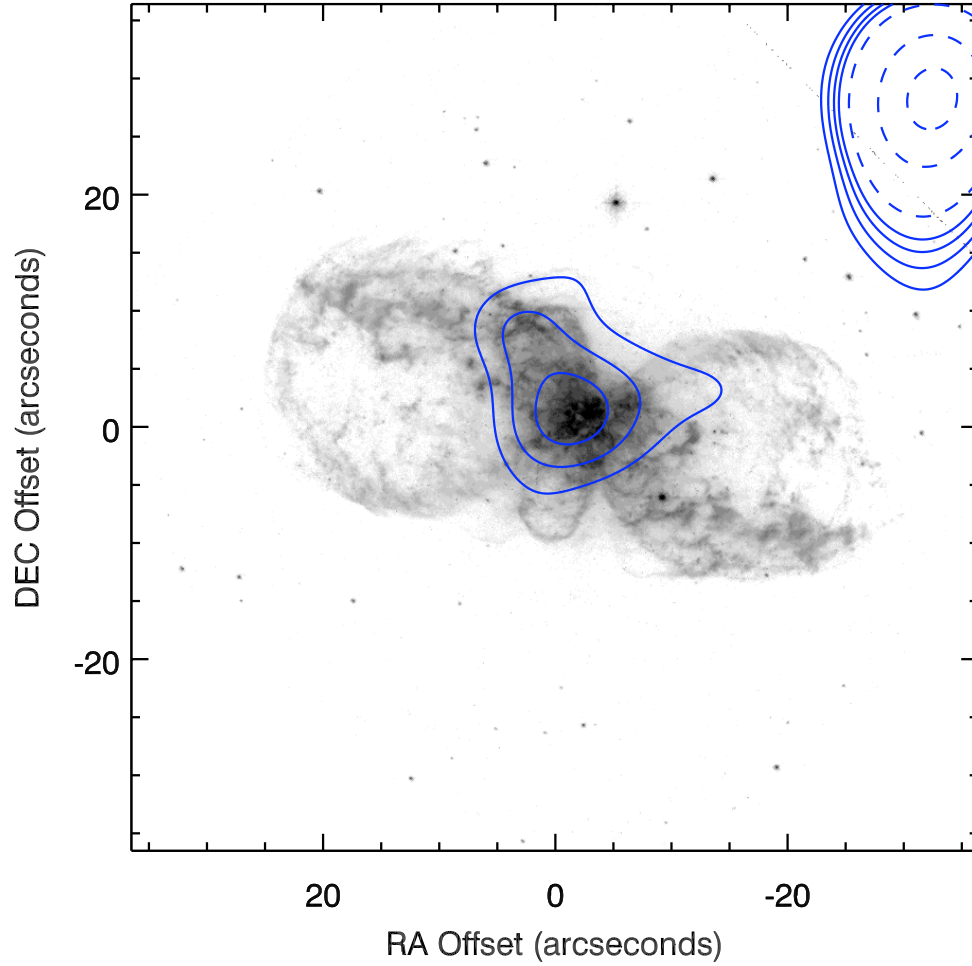


Figure 5.3 XMM Imaging of the Bipolar PN Hb 5 Field. Smoothed X-ray contours at 9, 11, 13, and 15 counts (solid contours) and at 20, 40, and 60 counts (dotted contours) are overlaid upon the HST F658N narrowband image ( $H\alpha + [NII]$ ).

characteristics regarding the presence or absence of hot gas due to wind shocks; open lobes allow the gas to expand and, thus, quickly cool, whereas closed lobes evidently



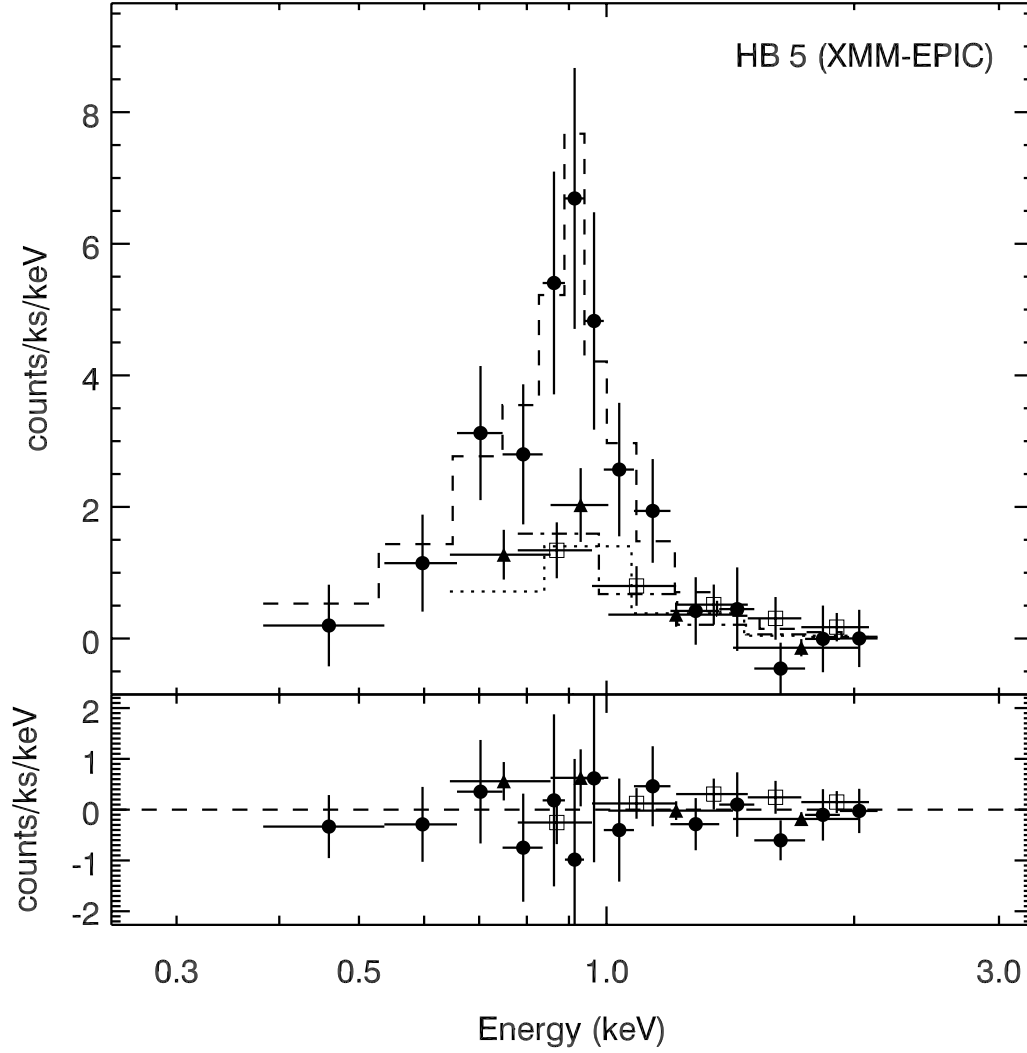


Figure 5.4 XMM EPIC X-ray Spectra of the Bipolar PN Hb 5. X-ray spectra of the Hb 5 source as obtained from the three EPIC CCD detector arrays (crosses, diamonds, and squares; pn: top panel; MOS: bottom panel) overlaid with the result of the best simultaneous fit to a model consisting of a thermal plasma (*vmekal*) and intervening absorption (*wabs*).

contain the gas, and cooling through heat conduction at the nebular-hot gas boundary may dominate (Steffen et al. 2008). In this regard, it appears significant that the extended X-ray emission in Hb 5 corresponds closely to the brighter regions seen in the HST image, suggesting the X-rays are coming from shocked material within the most tightly confined regions of the lobes.

Recent simulations of axisymmetric jets expanding into a spherical wind by Akashi et al. (2008) reproduced optical features seen in some bipolar PNe. This study focused on Mz 3 and M 1-92, but included simulations with generic PNe parameters. Some of these key optical features are also seen in Hb 5, i.e., an equatorial dense region and bright polar rim. The evidence of a fast, possibly collimated, wind reported by Pismis et al. (2000) suggests that the extended X-ray emission observed in Hb 5 can likely be traced to a collimated fast wind (Akashi et al. 2006, 2007). The point-symmetric features of the nebula and the extension in the X-ray emission support the possibility of an X-ray jet or shocks from such a collimated flow. The spatial coincidence with the central region of Hb 5 suggests that some X-rays may originate from the core and/or the central star itself. However, caution is warranted, given the small number of counts detected due to vignetting at the large off-axis angle of Hb 5 and the large background due to nearby bright sources convolved with the XMM PSF.

A deep, targeted X-ray observation of Hb 5 might bring our Ne abundance factor into agreement with the infrared-determined value and would decrease the uncertainties in Ne abundance by allowing us to fit the abundances of additional elements. Also, in the archival XMM-Newton observation of Hb 5, small but significant (termination) portions of the bipolar lobes lie in the detector chip gap and the readout

streak of the nearby source. Hence, a targeted Chandra X-ray Observatory X-ray observation of Hb 5 would provide the higher spatial resolution imagery that might enhance the role this PN plays in our understanding of the shaping and evolution of planetary nebulae.

## 5.4 Chapter Summary

Our spatial and spectral analysis of a moderately resolved, off-axis, low count XMM-Newton detection of X-ray emission at the location of the bipolar PN Hb 5 leads us to conclude that the emission originates with Hb 5. The X-ray emission is indicative of a thermal plasma at 2.4-3.7 MK with X-ray luminosity of  $1.5 \times 10^{32}$  erg s<sup>-1</sup>. Comparison with images of infrared and optical emission shows that the peak of the X-ray emission corresponds closely with the bright core of Hb 5 and the extension of the X-ray emission lies along bright extensions in the optical image. The X-ray temperature and luminosity, as compared to PNe known to exhibit shock-induced X-ray emission (Kastner et al. 2008), further suggest that the emission arises from shocks in the nebula, as opposed to the harder and less luminous X-ray emission associated with central stars (e.g. Mz 3; Kastner et al. (2003)). As only the fourth bipolar PNe with detected X-ray emission, Hb 5 may play an important role in the evolving study of the shaping and evolution of PNe. This PN therefore merits future targeted, deep, high spatial resolution X-ray observation.



# Chapter 6

## X-ray Emission from Binary Central Stars of PNe<sup>1</sup>

### 6.1 Binary Central Stars in Planetary Nebulae

Close binary systems have been found in  $17 \pm 5\%$  of the central stars of planetary nebulae (CSPNe) (Miszalski et al. 2009). These systems are typically comprised of a hot, compact white dwarf (WD) or pre-WD primary and a low mass, late-type, main sequence companion and, hence, are likely the products of common envelope interactions (Paczynski 1976; Iben & Livio 1993). In such systems, the primary star overfills its Roche lobe as it evolves onto the red giant branch (RGB) or asymptotic giant branch (AGB), engulfing the main sequence companion and forming a common

---

<sup>1</sup>A version of this chapter has been accepted for publication in the October 2010 issue of the *Astrophysical Journal*, it is coauthored by Orsola De Marco, Joel H. Kastner, and You-Hua Chu.

envelope (CE). Drag forces in the dense CE drain orbital energy from the binary, bringing the two stars closer together. The CE phase ends when either the companion spirals onto the primary's core; or the envelope is ejected. In the latter case, the residual is a close binary called a post-common envelope binary (PCEB). Although PCEBs in PNe are thought to derive from CE interactions that took place during the AGB phase of the primary or secondary, other post-CE binaries may have originated in CE interactions on the RGB (e.g., Schreiber & Gänsicke 2003).

The ejected CE can account for the morphological properties of some PNe. Bond & Livio (1990) argue that PNe with dense equatorial waists, often called butterfly PNe, form from a CE ejection immediately following the primary's early AGB phase, while elliptical PNe form from a CE ejection following a later AGB phase. Recent observational (Miszalski et al. 2009) and hydrodynamical (Ricker & Taam 2008) studies appear to bear out these assertions. Indeed, within the PNe community, there is momentum building behind the idea that the entire diverse population of PNe may be the result of binary interactions (De Marco 2009).

In most studies of PCEBs emphasis is placed on the evolution of the primary star into a mass accreting WD, i.e., a cataclysmic variable (CV). However, in this paper we are more interested in the evolution of the late-type, secondary companions. The rapid rotation in young, single stars generates magnetic fields strong enough to power bright X-ray coronae (Mathioudakis et al. 1995); however, as these stars age, their magnetic activity decays (see reviews in Güdel 2004; Güdel & Nazé 2009). Hence, the old, late-type, companions in PCEB are not expected to exhibit strong coronal activity unless their rotation rates have increased by accretion of angular momentum

during the CE phase (Jeffries & Stevens 1996; Soker & Kastner 2002). Although the degree to which the companion may undergo such accretion is uncertain (e.g., Hjellming & Taam 1991; Ricker & Taam 2008), there is compelling evidence from extreme UV and X-ray observations of PCEBs that such a process occurs. From EUV spectra, Sanz-Forcada et al. (2003) find evidence for strong coronae around the cool companions in close binaries, while abundance anomalies determined from high resolution X-ray spectra of the close binary V471 Tauri show that the K dwarf companion must have accreted the highly processed and enriched material liberated by the primary on its RGB ascent (Drake & Sarna 2003).

By analogy with main sequence stars, coronae around the cool companions in PCEBs should be characterized by thermal plasmas from a few MK to tens of MK and therefore should emit hard X-rays with energies  $\gtrsim 0.5$  keV. Soker & Kastner (2002) argue that for CSPNe, a plasma temperature above 10 MK and  $L_X > 5 \times 10^{29}$  ergs s<sup>-1</sup> would serve as compelling evidence for a "reborn" corona around a spun-up companion. There is little or no coronal contribution expected from the hot primary, since coronal activity from hot WDs or pre-WDs with effective temperatures  $>30$  or  $>60$  kK, respectively, is difficult to maintain when photospheric convection ceases (Bohm & Cassinelli 1971; Groth et al. 1985). Furthermore, if the CE is ejected, the magnetic field is ejected along with the CE (Nordhaus et al. 2007). Any remaining magnetic field will slow down the rotation of the remnant AGB core via magnetic braking (Blackman et al. 2001), resulting in decreased coronal activity. Indeed, O'Dwyer et al. (2003) discovered numerous sources of hard X-ray emission from WDs and argued that in all but two cases, this hard X-ray emission is a result of either accretion from

a companion onto the WD or coronal activity on the companion itself.

Thus, the potential exists to use X-ray observations as a tool for detecting otherwise unseen binary companions to CSPNe. As an initial test, we targeted two binary systems, HFG 1 and DS 1, with the Chandra X-ray Observatory (CXO), and analyzed archival data from the serendipitous observations by CXO and the XMM-Newton X-ray Observatory (XMM) of the binary CSPNe in LoTr 5. All three CSPNe were detected in these X-ray observations. In this chapter, we present analysis and interpretation of the X-ray emission from these three binary CSPNe. In Section 6.2, we summarize the properties of these binary systems; in Section 6.3 we describe the data and analyses; and in Section 6.4, we discuss the possible interpretations of the X-ray emission and their implications for models of binary interaction and PN shaping.

## 6.2 Target CSPNe

The binary systems we consider are the PCEBs in the PNe HFG 1 and DS 1, and the evolved binary in LoTr 5. Throughout the text, we will generally refer to both the central star and PN by the PN name. In each case, the primary, and presumed origin of the CE and PN, is a hot ( $T_{eff} > 60$  kK) O-type subdwarf (sdO) evolving towards a WD, while the secondaries are cool, late-type stars (see Table 6.1). These systems are the precursors to cataclysmic variables (CV), but do not exhibit characteristics of active accretion, and they feature strong reflection effects, i.e., irradiation of the secondary by the primary.



Table 6.1 Properties of Binary PNe: HFG 1, DS 1, and LoTr 5<sup>a</sup>

PN	$M_1, M_2$ ( $M_\odot$ )	$R_1, R_2$ ( $R_\odot$ )	$T_{\text{eff},1}, T_{\text{eff},2}$ ( $kK$ )	$L_{\text{bol},1}, L_{\text{bol},2}$ ( $L_\odot$ )	References
HFG 1	0.57,1.09	0.19,1.30	83,5.4	1500,1.3	1
HFG 1	0.63,0.41	...,1.15	...,5.3	...,0.9	2
DS 1	0.63,0.23	0.157,0.402	77,3.4	776,0.02	3
LoTr 5	0.6,1.1	0.05,8-12	185,5.3	2600,100	4,5,6

<sup>a</sup>The stellar properties of the primary and secondary components are labeled by the 1 and 2 subscripts, respectively.

<sup>b</sup>References: 1-Shimanski et al. 2004, 2-Exter et al. (2003) solution for  $K_p = 49 \text{ km s}^{-1}$  and  $i = 29^\circ$ , 3-Hilditch et al. (1996), 4-Feibelman & Kaler (1983), 5-Jasniewicz et al. (1996), 6-Graham et al. (2004)

### 6.2.1 HFG 1 and DS 1

Properties of the PCEB systems in the PNe HFG 1 (V664 Cas) and DS 1 (KV Vel, LSS 2018) have been summarized by De Marco et al. (2008) and are listed in Table 6.1. Here, we briefly highlight the key properties. The binary orbital periods are well-determined due to strong reflection effects (e.g. Exter et al. 2005; Hilditch et al. 1996). The binary period of V664 Cas (within HFG 1) is 14 hours (Grauer et al. 1987). Assuming a primary mass  $\sim 0.6M_\odot$ , Exter et al. (2005) determined a range of acceptable fits for the secondary mass ( $M_2 \sim 0.4 - 1.1M_\odot$ ). The spectral analysis by Shimanskii et al. (2004) suggests the chemical composition of the secondary in V664 Cas is near solar, but with some anomalies (overabundances of nitrogen, magnesium, and silicon) that are interpreted as enriched primary material accreted by the secondary during the CE phase. Distance estimates to HFG 1 by Exter et al. (2005) range from 0.31 to 0.95 kpc, which is consistent with the statistical determination

by Heckathorn et al. (1982) of 0.4 kpc and a distance of 0.6 kpc found from the PN surface brightness relation (Frew 2008). Here, we adopt a value of 0.6 kpc.

The binary period of KV Vel (within DS 1) is 8.5 hours (Drilling 1985). Hilditch et al. (1996) determine  $M_1 = 0.63M_\odot$  and  $M_2 = 0.23M_\odot$  for the components of KV Vel. Schonberner & Drilling (1984) used the color excess measured from KV Vel to estimate a distance range of 0.5 to 1.4 kpc. We adopt the distance of 0.7 kpc obtained via the PN surface brightness relation by Frew (2008).

The PNe HFG 1 and DS 1 are large and faint (Bond & Livio 1990). HFG 1 shows strong evidence of interacting with the interstellar medium (Heckathorn et al. 1982; Heckathorn & Fesen 1985) and Boumis et al. (2009) recently discovered a trail of shocked material behind the star as it plows through its local environment. The PN DS 1 suggests a late elliptical PN with blown out edges (Bond & Livio 1990), and Miszalski et al. (2009) point out the presence of low ionization structures that suggest an outflow along the E-W axis of the PN.

### 6.2.2 LoTr 5

The binary system in the PN LoTr 5 (IN Com, HD 112313) is comprised of an sdO primary and a rapidly rotating G5III-IV companion (Feibelman & Kaler 1983; Strassmeier et al. 1997). Jasiewicz et al. (1996) considered the similarities with rapidly rotating FK Comae stars (Bopp & Stencel 1981), arguing that FK Comae systems end the CE phase as a coalesced star, whereas LoTr 5 ended the CE phase as a close binary after ejecting its envelope. As the binary orbital period is unknown,

Jasniewicz et al. (1996) consider a few alternatives: a) a very short period of  $\sim 1$  day, b) a moderately short period of a few days, and c) a wide binary with a period of a few years. The radius of the giant star ( $\sim 12R_{\odot}$ ) rules out the close separation required for a very short period binary, but beyond this lower bound, there is little constraint on the binary orbital period. The observed photometric variation of 5.9 days is attributed to the rotation of the giant companion (see detailed discussion on the history of orbital solutions for LoTr 5 in Strassmeier et al. 1997). This interpretation is supported by the presence of Ca II H & K emission lines that are indicative of chromospheric activity due to rotation, and which imply a projected rotational velocity of  $v \sin i = 67 \text{ km s}^{-1}$  (Strassmeier et al. 1997).

Long slit spectra and narrow band images of the large ( $\sim 6'.5 \times 1'.7$ ), faint PN are modeled by Graham et al. (2004) as a bipolar nebula inclined  $17^{\circ}$  to the line of sight. If the nebula is formed from the ejection of a CE, then the orbital plane is likely to coincide with the bipolar axis (e.g. Bond & Livio 1990). Such a low binary inclination would then explain the inability to observe radial velocity variability from the binary system. However, Strassmeier et al. (1997) found that the inclination of the rapidly rotating giant is  $i \sim 45^{\circ}$ . If one takes the orbital inclination to be identical to that of the bipolar lobes, then this suggests that the binary and its components are not coplanar. This is considered in Jasniewicz et al. (1996) as evidence for a longer orbital period, since the components are not close enough to become synchronized via tidal interactions. Thevenin & Jasniewicz (1997) argue that the high projected equatorial velocity suggests LoTr 5 is a wide binary system, in which the rapid rotation inferred for the giant companion is due to accretion from the AGB wind and does not require

a CE phase.

Distance estimates to LoTr 5 are widely discrepant, ranging from 0.5 to 6.9 kpc (Graham et al. 2004); the closer distance is favored (e.g. Strassmeier et al. 1997). We adopt a distance of 0.5 kpc, after Frew (2008). The high galactic latitude ( $+88^{\circ}46'$ ) of this PN renders interstellar reddening negligible.

## 6.3 Data and Analysis

### 6.3.1 Observations

We acquired targeted observations of HFG 1 and DS 1 on the back-illuminated S3 chip of the ACIS detector array onboard CXO. A summary of the CXO observations of HFG 1 and DS 1 is presented in Table 6.2. In these two on-axis CXO observations we detect X-ray point sources centered on the positions of the central stars in HFG 1 and DS 1. There is no evidence for diffuse X-ray emission from either nebula (see also Section 6.4). These CXO observations were prepared and analyzed according to data analysis threads accompanying the Chandra X-ray Center CIAO software (version 4.1) (Fruscione et al. 2006). We find no high-background periods during the CXO observations of HFG 1 and DS 1.

Archival data of the serendipitous observations of LoTr 5 from both CXO and XMM were obtained through the High Energy Astrophysics Science Archive Research Center, a service of the Astrophysics Science Division at NASA's Goddard Space Flight Center and the High Energy Astrophysics Division of the Smithsonian

Table 6.2 X-ray Observations of Binary PNe: HFG 1, DS 1, and LoTr 5

Object	Date	ObsID	Chip	$t_{exp}$ (ks)	Net CR (cnt ks <sup>-1</sup> )
HFG 1	2008 Dec 11	9954	ACIS-S3	11.3	12.4
DS 1	2009 Jul 19	9953	ACIS-S3	23.8	2.30
LoTr 5	2002 Jun 06	12850201	EPIC pn	20.9	34.7
	...	...	EPIC MOS1	25.7	11.3
	...	...	EPIC MOS2	25.7	8.78
LoTr 5	2002 Dec 04	3212	ACIS-S4	27.7	26.1

Astrophysical Observatory. A summary of the XMM and CXO observations of LoTr 5 is presented in Table 6.2. LoTr 5 lies 7'3" off axis in the XMM observation (ObsID 0012850201; 2002 June 06) of the galaxy group NSCS J125606+255746 and is detected on all three European Photon Imaging Camera (EPIC) detector arrays (pn, MOS1, and MOS2). The XMM observations were operated in Full-Frame Mode with the thin filter. Data were reprocessed completely from the Observation Data Files using the XMM-Newton Science Analysis Software (SAS) package version 7.1.0 with the calibration files available in Current Calibration File Release 241 (XMM-CCF-REL-241). In the XMM observations of LoTr 5, the detected emission is consistent with a point source at the off-axis position of the CSPN. There is no evidence of diffuse X-ray emission associated with the nebula (see also Section 6.4). The Chandra observation (ObsID 3212; 2002 December 04) of the same galaxy group field was obtained six months after the XMM-Newton observation. In this CXO observation, LoTr 5 lies  $\sim 8'6''$  off axis in the CXO observation, just within the field of view of the Advanced CCD Imaging Spectrometer (ACIS) detector array, on a CCD (the front-illuminated S4) that lies adjacent to the prime imaging CCD used to target the

galaxy cluster (the back-illuminated S3). Since the ACIS-S chip array is optimally aligned for use with the curved focal plane Rowland circle for grating spectroscopy, the S4 image of LoTr 5 is very out of focus. Hence, it is difficult to ascertain the nature of the emission; however, its spectrum is useful. The CXO data obtained for LoTr 5 were prepared and analyzed according to data analysis threads accompanying the CIAO software. We filtered the XMM observations of LoTr 5 for high background periods and bad events using the standard filters for the imaging mode observations. No high background periods were found during the CXO observation of LoTr 5. A summary of the observations of LoTr 5 is presented in Table 6.2.

### 6.3.2 Spectral Analysis

The source and background spectra from the on-axis X-ray point sources in HFG 1 and DS 1 were extracted using the *psextract* task in CIAO. The source and background spectra from the off-axis, serendipitous XMM and CXO sources at the position of the central star of LoTr 5 were extracted from source regions determined by the 90% encircled energy radius for a point source at the appropriate source off-axis angles. For the XMM observations of LoTr 5 the 90% encircled energy radius is  $45''$  and for the CXO observation the 90% encircled energy radius is  $10''$ . For each source spectrum, we generated target- and observation-specific response matrix (RMF) and ancillary response (ARF) files. This extraction of the source and background spectra and responses accounts for the broadening and vignetting due to the off-axis angle of the serendipitous observations of LoTr 5.

All spectral fits were performed with XSPEC version 12.3.1x (Arnaud 1996). We use reduced  $\chi^2_\nu$  statistics to distinguish best fit models, where  $\nu$  represents the number of degrees of freedom. When multiple models give acceptable  $\chi^2_\nu$  values ( $\chi^2_\nu < 2$ ) we use goodness-of-fit tests (*goodness* in XSPEC), to determine the more appropriate model. This goodness-of-fit test performs Monte-Carlo simulations of the spectrum as drawn from the best-fit model, and calculates the  $\chi^2_\nu$  statistic for each simulation. A value of  $\sim 50\%$  is returned if the data is accurately described by the set of simulated spectra, while values closer to 100% suggest the data are not well described by the model. We performed 500 simulations per test. Due to the small number of counts detected for HFG 1 and DS 1, we used Churazov weighting (Churazov et al. 1996) on the unbinned spectra. Such weighting is preferred for sources with low count rates and many empty spectral channels. Weighting is assigned with respect to the average of the surrounding channels. The best-fit spectral parameters (and their 90% confidence levels) and the resulting inferred X-ray emission properties are presented in Table 6.3. We now discuss specific aspects of the spectral fitting for each source.

### **X-ray Spectrum of HFG 1**

We attempted to fit single-temperature-component (1-T) and two-temperature-component (2-T) optically thin thermal plasma (*mekal*) models to the X-ray spectrum of HFG 1. Attempts to determine the intervening absorption from the model fits failed to constrain the absorbing column density ( $N_H$ ), so we adopted an intervening absorption,  $N_H = 2.4 \times 10^{21} \text{ cm}^{-2}$ , corresponding to the value of  $E_{B-V} \sim 0.5$  mag estimated to the central star (Exter et al. 2005). The absorbed 1-T model can only fit the

data when the plasma abundance is allowed to vary. The best-fit 1-T model gives  $\chi_{511}^2 \sim 0.80$  and requires an abundance of 0.06 times solar (with solar values given by Anders & Grevesse 1989), with 90% confidence range of 0.02 to 0.14 solar. However, this abundance result is inconsistent with the conclusions drawn by Shimanskii et al. (2004) who found stellar abundances near or slightly above solar. The goodness-of-fit test yields 98% of the simulations with a better  $\chi_\nu^2$  value, suggesting the flexibility introduced by freeing the model abundance parameter simply allows the model to fit features that are due to noise. Adding a second thermal plasma component improves the overall appearance of the fit and produces a similar  $\chi_\nu^2$  value of  $\chi_{510}^2 \sim 0.79$ . The goodness-of-fit test yields 68% of the simulations with a better  $\chi_\nu^2$  value, however, indicating that the 2-T plasma model is a better description of the data than the 1-T, variable abundance model. The parameters of this best-fit 2-T model are presented in Table 6.3 and the model is overlaid on the source X-ray spectrum in Figure 6.1.

### X-ray Spectrum of DS 1

As in the case of HFG 1, the intervening absorption to DS 1 could not be constrained. We adopted  $N_H = 8.3 \times 10^{20} \text{ cm}^{-2}$  based on the value of  $E_{B-V} \sim 0.15$  mag estimated toward the central star (Schonberner & Drilling 1984). The best-fit 1-T model with solar abundances gives  $\chi_{512}^2 \sim 0.49$  for a hot component at  $T_X \sim 14.3$  MK, while the best-fit 2-T model gives  $\chi_{510}^2 \sim 0.49$  for a similar hot component at  $T_X \sim 14.5$  MK and a cooler component at  $T_X \sim 3$  MK. The best-fit 1-T and 2-T models are indistinguishable, based solely on their  $\chi_\nu^2$  values. The X-ray fluxes determined from the best-fit 1-T and 2-T models agree within their 90% confidence ranges. We find



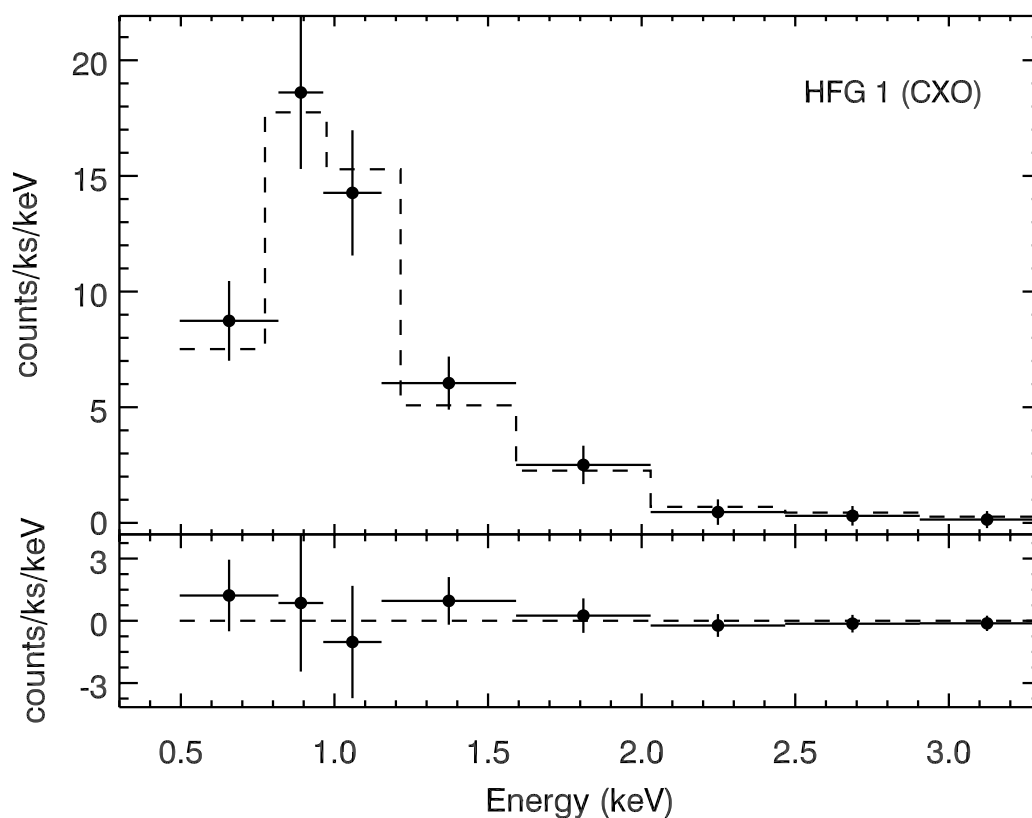


Figure 6.1 X-ray spectrum of HFG 1 observed by CXO overlaid with the best-fit model (top) and residuals of the spectral modeling (bottom). The best fit model (dashed line) requires two thermal plasma components at 6 MK and 21 MK, with intervening absorption of  $N_H \sim 2.4 \times 10^{21} \text{ cm}^{-2}$ .

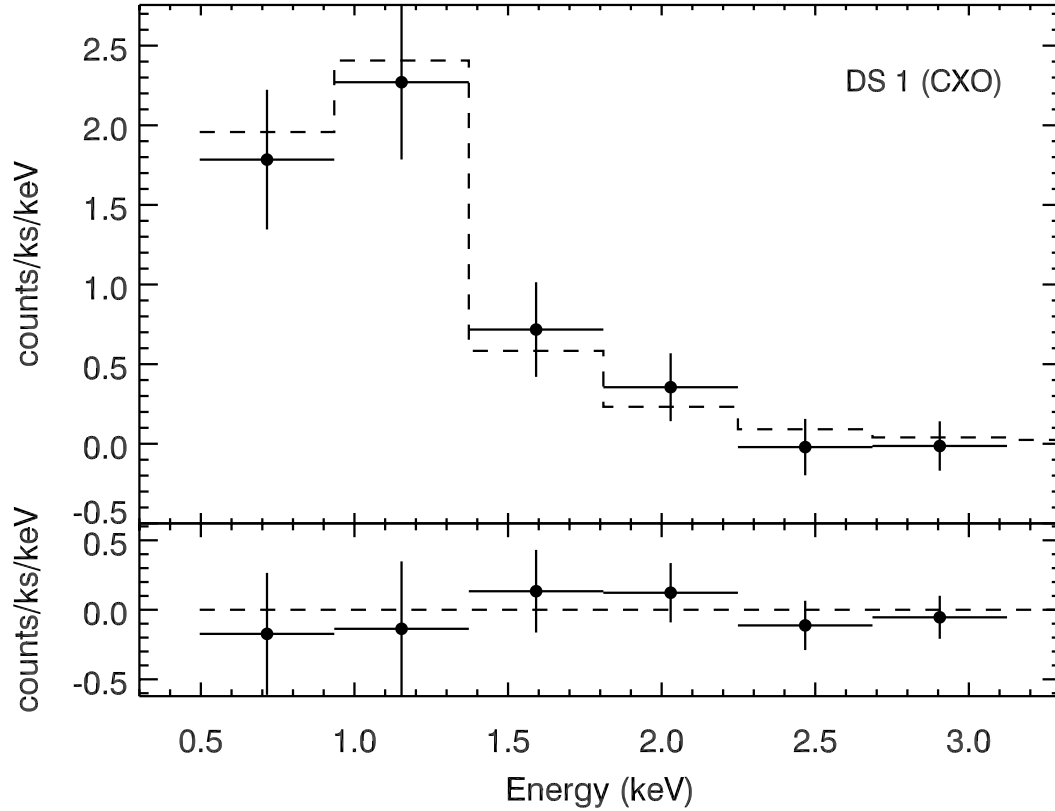


Figure 6.2 X-ray spectrum of DS 1 observed by CXO overlaid with the best-fit model (top) and residuals of the spectral modeling (bottom). The best fit model (dashed line) requires two thermal plasma components at 3 MK and 15 MK, with intervening absorption of  $N_H \sim 8 \times 10^{20} \text{ cm}^{-2}$ .

from visual inspection, however, that the 2-T model locally improves the fit at the soft end of the spectrum. Hence, we adopt the 2-T model as the best fit. Additionally, the goodness-of-fit tests for the two models shows a modest improvement, from 85% to 63%, when the second component is added. Adopting the 2-T model over the 1-T model does not effect the overall interpretation of the X-ray emission observed from the central star of DS 1. The parameters of the best-fit 2-T model are presented in Table 6.3, and the model is overlaid on the source X-ray spectrum in Figure 6.2.

### **X-ray Spectra of LoTr 5**

We attempted to fit single-temperature models with wide ranges of absorption and elemental abundances to the XMM and CXO spectra of LoTr 5, but all such fits resulted in  $\chi^2_{30} \sim 3-6$ . The best-fit models of the X-ray spectra are instead comprised of two, optically thin, thermal plasma components. Attempts to add foreground absorption to the model did not appreciably improve the fit and did not constrain the absorbing column density. This is consistent with the high galactic latitude and proximity of LoTr 5, which suggest there is negligible intervening absorption. The parameters of the best fits of the X-ray spectra using 2-T models are presented in Table 6.3 and overlaid on the source X-ray spectra in Figures 6.3 & 6.4. The difference between the apparent flux levels measured from the XMM and CXO observations is larger than the cross-calibration discrepancy between EPIC observations and CXO ACIS-S3 observations (Snowden 2002), however, there are no specific cross-calibration data comparing XMM EPIC observations and CXO ACIS-S4, where the X-ray emission from LoTr 5 is detected. To facilitate direct comparison, we present the unfolded

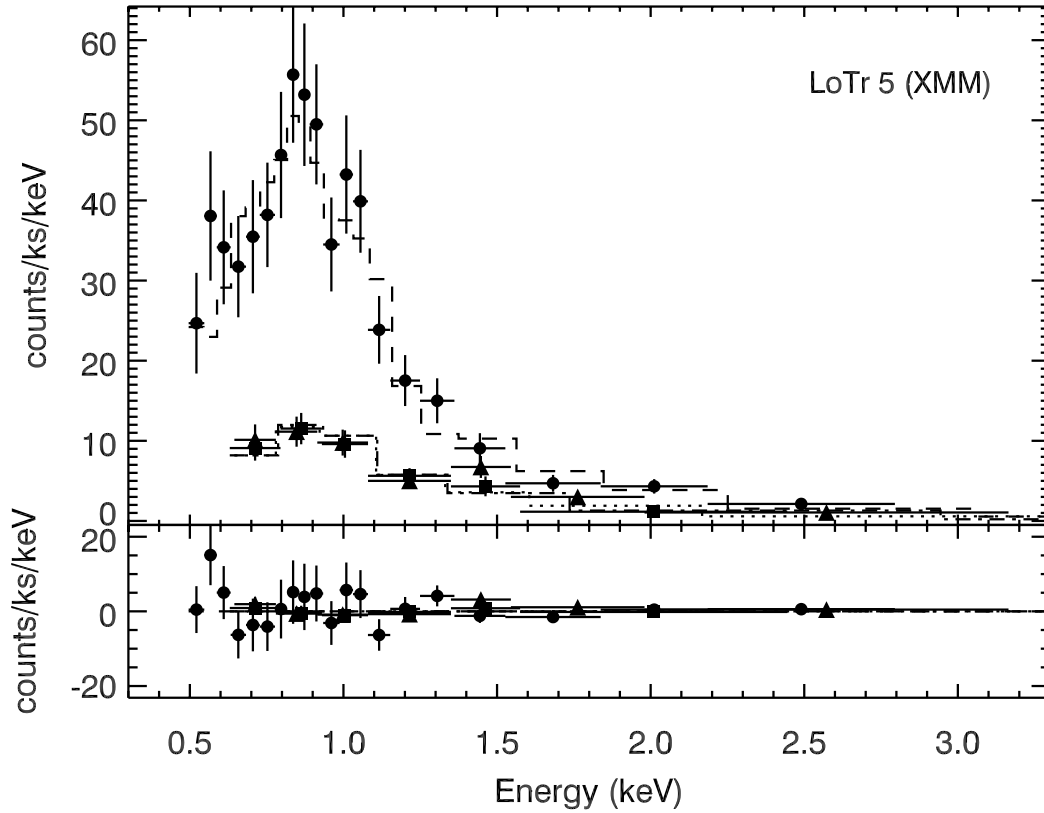


Figure 6.3 X-ray spectra of LoTr 5 observed by the three EPIC detectors (pn - circles, MOS1 - triangles, MOS2 - squares) overlaid with the best-fit model (top) and residuals of the simultaneous spectral modeling (bottom). The best fit model (broken lines) requires two thermal plasma components at 7.6 MK and 26 MK. No intervening absorption component is required, reflecting the small distance and high galactic latitude to LoTr 5.

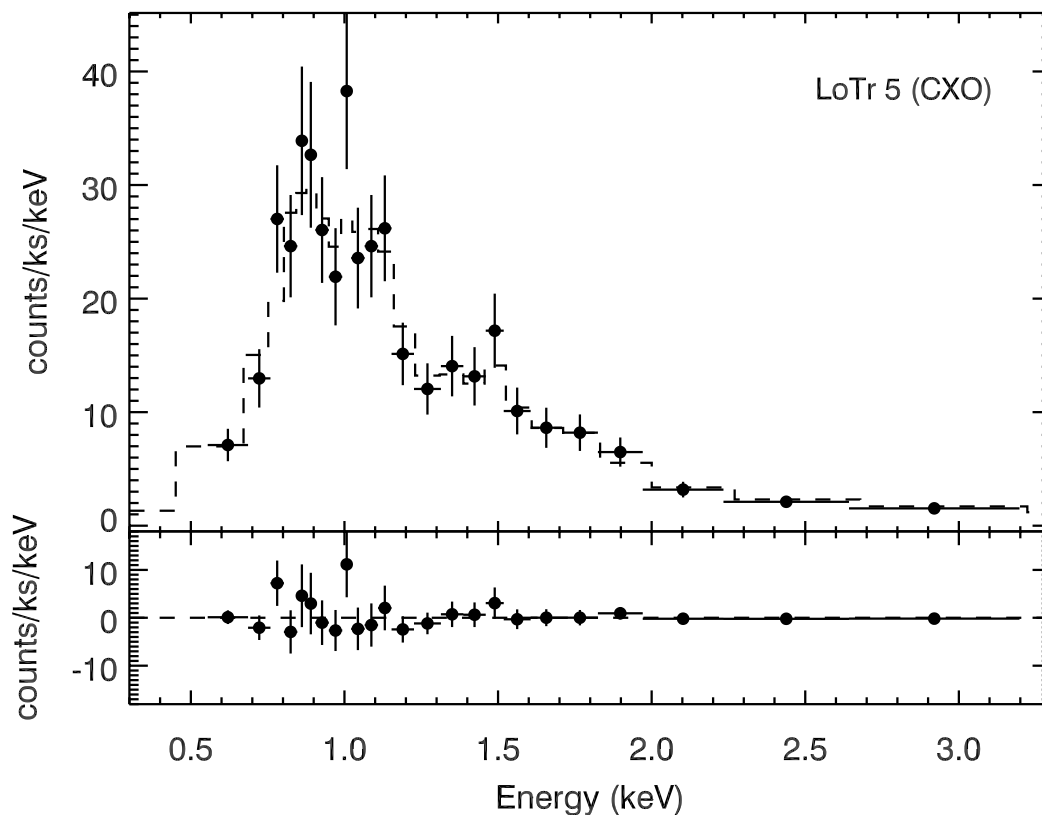


Figure 6.4 X-ray spectrum of LoTr 5 observed by CXO overlaid with the best-fit model (top) and residuals of the spectral modeling (bottom). The best fit model (dashed line) requires two thermal plasma components at 7.5 MK and 40 MK, with no intervening absorption.

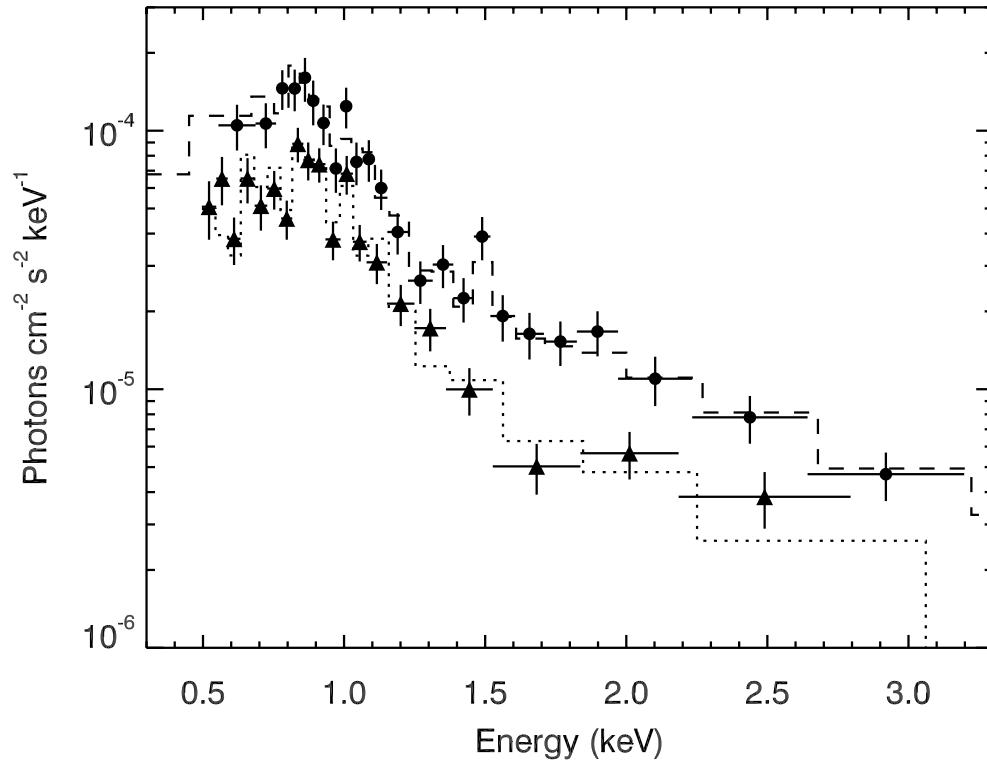


Figure 6.5 Unfolded X-ray spectra of LoTr 5 observed by XMM EPIC pn (squares) and CXO ACIS-S (circles) overlaid with the best-fit, two temperature plasma models (CXO - dashed line, XMM - dotted line). An increase in flux during the six month interval between the XMM and CXO observations is apparent across the energy range.

spectra from the CXO ACIS-S and XMM EPIC pn detectors together in Figure 6.5. In the absence of any significant cross-calibration discrepancies, it appears that in the six month interval between the XMM and CXO observations the brightness increased across the entire energy range, indicating that the two spectral components arise from a common physical process.

### 6.3.3 Timing Analysis

To test for variability, we performed Kuiper tests (Press et al. 1992) to assess whether the cumulative distribution of the barycenter-corrected source and background photon arrival times can be described by a Poisson process. These tests are independent of temporal bin size, but do not provide information on the period or amplitude of variability. Where the Kuiper test suggested deviation from a Poisson process, we constructed background-subtracted light curves with a variety of temporal bin widths. These background-subtracted light curves were extracted using the same source and background regions used for spectral extraction (using the *ltc1* option of the CIAO tool *dmextract*). The low source count rates and relatively short temporal windows do not permit us to effectively use Fourier period detection methods or create phase-binned spectra. Hence, we restricted our assessments of source variability to the Kuiper test, comparison with the background, and visual inspection of the light curves.

### **HFG 1 and DS 1**

The Kuiper test gives a 98% and 87% probability, respectively, that the photon arrival times of HFG 1 and DS 1 can be ascribed to a constant Poisson process. The minimum temporal bin widths to obtain a signal-to-noise ratio of 3 are 670 s and 3300 s for HFG 1 and DS 1, respectively. Below this signal-to-noise ratio the source count rate approaches the background rate and it becomes difficult to discern source variability from noise fluctuations. At these temporal bin widths, the rms noise is on par with that expected from a Poisson distribution. Improving the signal-to-noise ratios by widening the light curve bins to half the exposure times for HFG 1 and DS 1 confirms the Kuiper test result that HFG 1 produces a steady count rate, and suggests that DS 1 may exhibit variability (Figure 6.6).

### **LoTr 5**

For LoTr 5, Kuiper tests yield only 16% and 2% probabilities, respectively, that the X-ray sources detected in the XMM and CXO observations can be described by a constant Poisson process. In both observations, this deviation between the source and a simulated constant Poisson process is not present in the background. The minimum temporal bin width for a signal-to-noise ratio of 3 is 200 s and 320 s for the XMM and CXO observations, respectively. In the XMM observation, for temporal bin widths greater than 1000 s, the rms noise of the source is consistently 1.3 times that expected from a Poisson distribution. In the CXO observation, the rms noise of the source increases to 1.8 times that expected from a Poisson distribution. Since



there are too few counts to construct phase-binned spectra, we cannot make proper inter-observatory comparisons of fluxed light curves. The background-subtracted light curves are presented in Figure 6.7. These light curves and the results of the Kuiper tests suggest that the X-ray source in LoTr 5 is modestly variable.

## 6.4 Discussion

As noted in Section 6.1, we anticipate that the X-ray emission from the central stars of DS 1, HFG 1, and LoTr 5 is due to the presence of coronal activity associated with the late-type companions in these likely or candidate PCEBs. However, there are other mechanisms which may give rise to thermal plasma emission in the range of temperatures we observe. We consider these alternative interpretations before discussing the coronal interpretation.

### 6.4.1 X-ray Emission from the WD

White dwarfs can be sources of X-ray emission, if they have low opacities or high effective temperatures (e.g. Jordan et al. 1994; Marsh et al. 1997; Motch et al. 1993). However, WD photospheric emission is much softer than the X-ray emission detected from the three CSPNe considered in this paper. Theoretically, cool WDs with convective envelopes may generate magnetic fields and coronae and emit X-rays (Serber 1990; Thomas et al. 1995), however, no such emission has been detected from field WDs (Weisskopf et al. 2007) and the primaries in the three CSPNe considered here

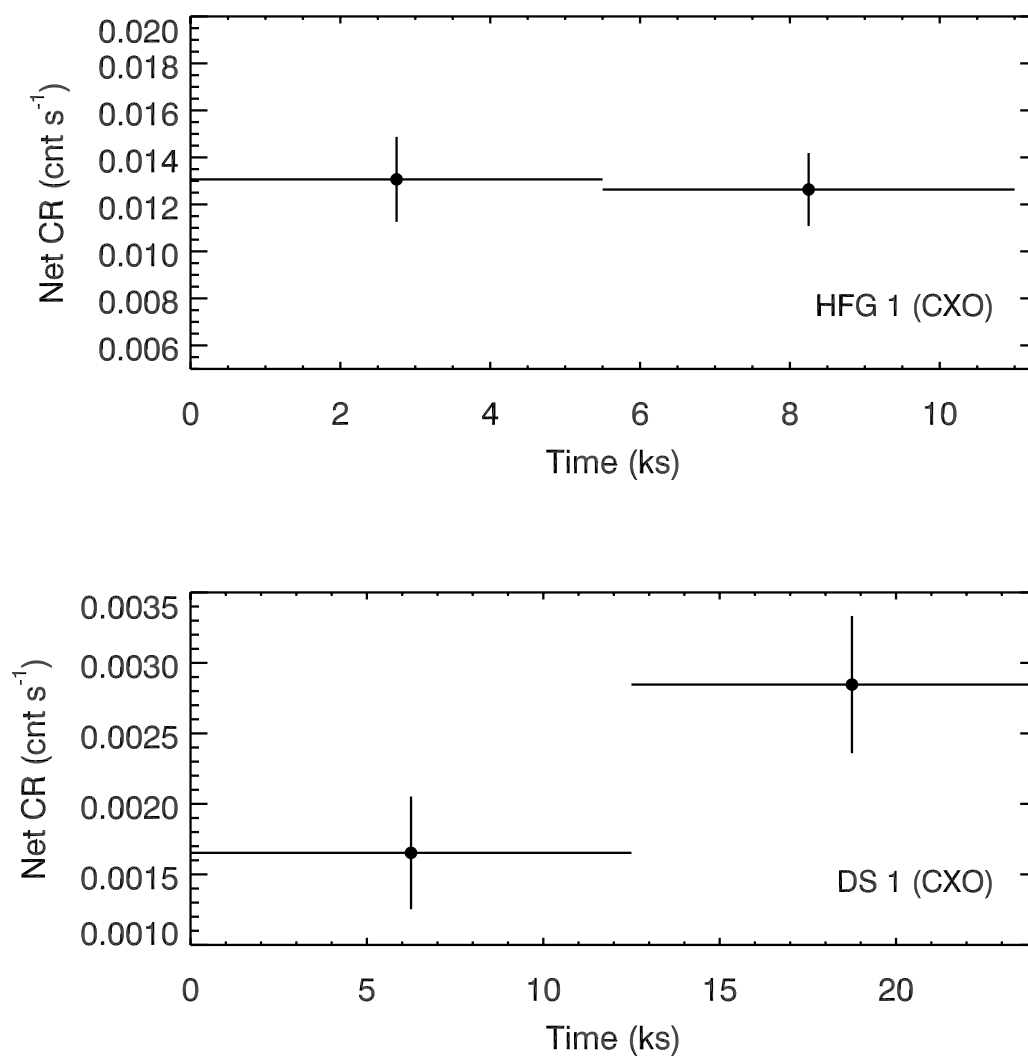


Figure 6.6 Background-subtracted X-ray light curves of HFG 1 (upper panel) and DS 1 (lower panel). The light curve of HFG 1 is consistent with a steady count rate, while DS 1 exhibits a marginally significant increase in the count rate during the second half of the observation.

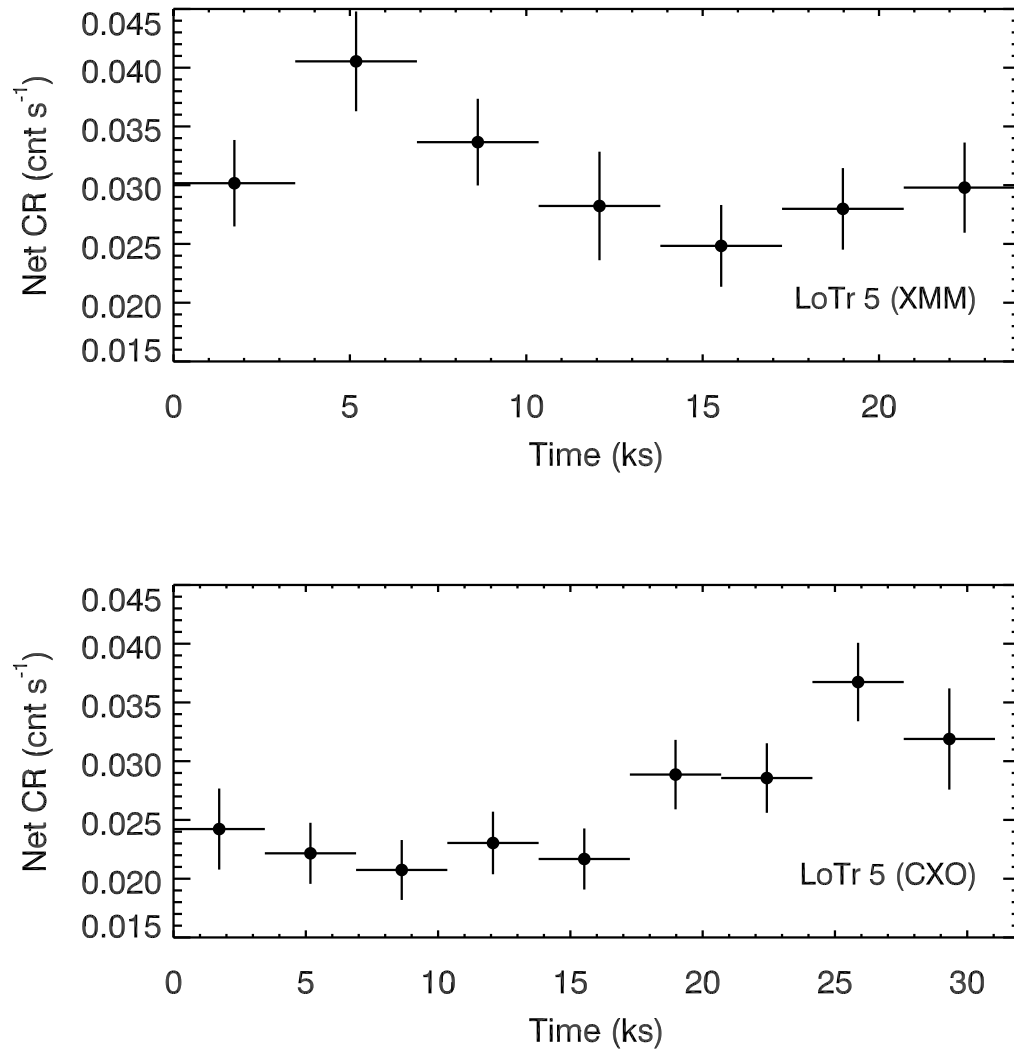


Figure 6.7 X-ray light curves of LoTr 5 from XMM EPIC pn (upper panel) and the CXO ACIS-S (lower panel) observations.

are too hot to sustain coronal activity. Hard X-ray emission from single WDs at  $T_X$  similar to those of the three CSPNe considered here is very rare; only two cases are known: KPD 0005+5106 and the central star of the Helix Nebula (O’Dwyer et al. 2003; Guerrero et al. 2001; Chu et al. 2004). It is possible, but statistically unlikely, that the X-ray emission detected from one or all of the three CSPNe considered here is of the same (unknown) origin.

### 6.4.2 X-rays from Colliding Wind Shocks

Shocks from colliding winds associated with these CSPNe may come in two forms: (1) a fast stellar wind colliding with a slower, previously ejected, stellar wind—as in the interacting stellar wind (ISW) theory that successfully explains the emissivity patterns of PNe (Kwok et al. 1978); and (2) collision of the two winds generated by the components of low-mass binary systems. Both types of energetic wind interactions can create X-ray emitting shocks with plasma temperatures in the range 1-8 MK and with X-ray luminosities from  $10^{31}$  to  $10^{33}$  erg s<sup>-1</sup> (e.g. Muerse et al. 1997; Kastner et al. 2008). A significant contrast between the two types of colliding winds is the scale at which each occurs. The ISW collisions form large hot bubbles that fill the PN cavity on the order of a few thousand AU (e.g. Kastner et al. 2000; Montez et al. 2005), while colliding-binary winds occur in a thin, conical interaction region with a vertex located at the stagnation point of the two winds, typically on the order of the binary separation (Muerse et al. 1995).

In the targeted, on-axis, CXO observations of HFG 1 and DS 1, and the off-axis

XMM observation of LoTr 5, there is no evidence for any extended X-ray emission. In the case of NGC 40, the X-ray emission is of such a low surface brightness that it was only revealed via blind spectral extraction from the expected emission region (Montez et al. 2005). We performed similar blind spectral extractions for the X-ray observations of the large PNe in LoTr 5, HFG 1, and DS 1 and found no evidence for diffuse, low surface brightness X-ray emission. Furthermore, the X-ray luminosities determined from the X-ray spectral fits to the point source emission in these three, large PNe (Table 6.3) are fainter than the faintest diffuse X-ray emitting plasma in PNe ( $\sim 10^{31}$  erg s $^{-1}$ ) and the plasma temperatures are hotter (see Kastner et al. 2008).

The emitting volumes of the unresolved X-ray emission can be explored through the emission measures determined from the X-ray spectral fits. The emission measure ( $EM = \int n_e n_H dV \sim n_e^2 V$ ) of large, diffuse, X-ray emitting plasmas in PNe suggest plasma densities of a few 100 cm $^{-3}$  (Steffen et al. 2008), whereas the emission measure from colliding binary winds suggest densities of  $1 - 5 \times 10^6$  cm $^{-3}$  (Muerse et al. 1995). For a typical emitting volume characteristic of colliding binary winds ( $\sim 10^{41}$  cm $^3$ ) the emission measure determined from the X-ray spectral fits (Table 6.3) suggest the density is  $\sim 10^6$  cm $^{-3}$ . This density is similar to that inferred for colliding binary winds in symbiotic stars (Muerse et al. 1997). However, the X-ray luminosities reported in Table 6.3 are one to two orders of magnitudes fainter than such systems. Additionally, in HFG 1 and DS 1, there is no evidence for a wind fast enough ( $> 500$  km s $^{-1}$ ) to account for colliding-binary wind shocks. Modigliani et al. (1993) reported a fast wind speed of 3300 km s $^{-1}$  from their analysis of the IUE high resolution UV

spectrum of LoTr 5 that potentially could explain the temperatures determined from the X-ray spectra of LoTr 5, although the evidence for such a fast wind is disputed (Guerrero; private communication).

### 6.4.3 X-rays from Accretion-related Processes

Although there is no evidence for accretion disks in prior studies of HFG 1 and DS 1, given that these systems are candidate pre-cataclysmic variables, we should consider whether the X-rays from the core of each PN could be due to a hot accretion disk or from accretion onto the compact sdO primary. From Frank et al. (2002), the maximum temperature for an accretion disk around a compact object (in this case, a white dwarf) is given by

$$T_{max} = 120kK \left[ \left( \frac{M}{0.6M_{\odot}} \right) \left( \frac{\dot{M}}{1 \times 10^{-7}M_{\odot} \text{ year}^{-1}} \right) \left( \frac{R}{0.01R_{\odot}} \right)^{-3} \right]^{1/4}. \quad (6.1)$$

Considering the primary star masses and radii listed in Table 6.1, the maximum disk temperature for these three binary systems would exist around the compact primary in LoTr 5. However, this temperature,  $T_{max} \sim 40$  kK, is much too cool to account for the detected X-ray emission, hence, the X-ray emission cannot arise from a hot accretion disk, but this does not preclude the existence of a disk, nor a disk as a source of accretion material.

If material is falling onto the compact object from Roche lobe overflow (RLO) from the companion, or from the inner region of an accretion disk. Such material can

reach velocities up to the free fall velocity,  $v_{ff} = (GM/R)^{1/2}$ , forming shocks in the boundary layer (BL) between the flow and compact object. From Frank et al. (2002), the temperature of the shocked material is given by

$$T_{ff} = 150MK \left( \frac{\mu}{0.6} \right) \left( \frac{M}{0.6M_{\odot}} \right) \left( \frac{R}{0.01R_{\odot}} \right)^{-1}. \quad (6.2)$$

The resulting implied temperature for the compact companion in LoTr 5 would be  $T_{ff} \sim 90$  MK. This is higher than the temperature determined from the X-ray spectral fits, though not high enough to confidently dismiss as the origin of the X-ray emission. Meanwhile, the implied temperature for the compact companions in HFG 1 and DS 1 is in the range  $T_{ff} \sim 8 - 10$  MK, which is consistent with the range we determine from the X-ray spectral fits.

Since an accretion disk and/or infalling material can imply the presence of RLO, we consider the possibility of RLO in the three binary CSPNe. We estimate the Roche lobe ( $R_L$ ) radius using the approximation given in Eggleton (1983),

$$\frac{R_L}{A} \approx \frac{0.49q^{2/3}}{0.6q^{2/3} + \ln(1 + q^{1/3})}, \quad (6.3)$$

where  $A$  is the orbital semi-major axis and  $q = M_1/M_2$ . We find that a few of the possible solutions given by Exter et al. (2005) for the binary system parameters in HFG 1 suggest that the main sequence companion can fill its Roche lobe, but the solution provided by Shimanskii et al. (2004) suggests it cannot (see Table 6.1). The binary system parameters determined by Hilditch et al. (1996) suggest that the main sequence companion in DS 1 is unable to fill its Roche lobe and, therefore, is not

capable of actively supplying material for accretion streams or accretion disks. The lack of support for RLO suggests that accretion is likely not the source of the observed X-ray emission from HFG 1 and DS 1.

For LoTr 5, if we assume synchronized orbital and rotational periods ( $P_{orb} = P_{rot}$ ), then the binary separation,  $A$ , is  $\sim 16R_{\odot}$  and the  $R_L \sim 7R_{\odot}$ . In this scenario, even at the lower limit on the giant's radius ( $\sim 7.8 R_{\odot}$  according to Strassmeier et al. 1997), the giant can lose mass to the sdO primary via RLO. If the orbital period of LoTr 5 is longer than 13 days, the giant is unlikely to be undergoing RLO. However, there is evidence of short-term variability (perhaps rapid flickering) in the optical (Strassmeier et al. 1997) and longer-timescale variability in the X-ray (Figure 6.7). Both forms of variability could be indicative of accretion on the sdO star, a la CV systems (Bruch 1992). A period of  $\sim 0.25$  days was reported by Kuczawska & Mikolajewski (1993) for LoTr 5. Strassmeier et al. (1997) searched for a similar periodicity but could not find one, leading them to suggest the period found by Kuczawska & Mikolajewski (1993) was an artifact or a time variable phenomenon. The origin of this putative 0.25 day period could be a hot spot on an accretion disk around the sdO, or, as Strassmeier et al. (1997) suggest, a reflection effect off an as-yet undiscovered third component in LoTr 5. The X-ray lightcurves in Figure 6.7 do not clearly support the periodicity proposed by Kuczawska & Mikolajewski (1993), but we cannot be certain from our data. Further observations are required to determine if such a periodicity can be found in the X-ray source in LoTr 5.



#### 6.4.4 X-rays from Internal O-star Wind Shocks

The shocked winds of O and B stars display  $\log L_X/L_{\text{bol}} \sim -7$  (Cassinelli et al. 1994, 1981). If we attribute the detected X-ray emission to the primary in HFG 1, then  $\log L_X/L_{\text{bol}} \sim -6.1 \pm 0.2$ , which is higher than that found in Cassinelli et al. (1994, 1981). For the primary in HFG 1, a shock velocity of  $\sim 1200 \text{ km s}^{-1}$  relative to the wind velocity is required to produce the measured 20 MK plasma. From the theory of radiative driven winds (Owocki et al. 1988), this would suggest the wind speed is at least twice the shock velocity, i.e.,  $> 2000 \text{ km s}^{-1}$ . As of yet, no such wind has been found in HFG 1; hence, it is unlikely that the X-ray emission arises from shocks in the wind from the primary. Alternatively, the observed value of  $L_X/L_{\text{bol}}$  could suggest a magnetically active primary, but as we have stated, such a scenario is difficult to reconcile in a star with such a high effective temperature. Similarly, attributing the X-ray emission from the point source in DS 1 to the primary leads to  $\log L_X/L_{\text{bol}} \sim -6.6 \pm 0.3$ , again suggesting a fast shock velocity ( $\sim 1000 \text{ km s}^{-1}$ ) or a high level of magnetic activity in a star that is unlikely to support active magnetic fields.

#### 6.4.5 X-rays from Coronal Activity Associated with the CSPNe Companions

Coronal X-ray luminosity is strongly correlated with rotation for late-type main sequence stars (see review by Güdel & Nazé 2009). This correlation is believed to arise, as in our sun, from dynamo-generated magnetic fields in a differentially rotating

late-type star's convective zone. For such stars, X-ray luminosity linearly increases with increasing rotation until saturation is reached at a relative X-ray luminosity  $\log L_X/L_{\text{bol}} \sim -3$ . The origin of this plateau in  $L_X/L_{\text{bol}}$  is unknown, but possible explanations include saturation of the dynamo or limits on the number and size of active areas imposed by the surface area of the star (e.g. Güdel & Nazé 2009). Dempsey et al. (1993a,b) studied the X-ray emission properties of a large sample of rapidly rotating companions in RS CVn systems, where tidal interactions amongst the companions helps maintain a more rapid rotation than that of single stars at a similar age. The X-ray spectra of the coronae of such stars are best described by 2-T thermal plasma models comprised of a cool component of a few MK and a hot component of tens of MK (Dempsey et al. 1993b). EUV spectra of the coronal emission from nearby active binary systems reveal a continuous emission measure distribution (EMD) that varies with temperature (Sanz-Forcada et al. 2003). The EMD is explained by Cargill & Klimchuk (2006) as indicative of a number of unresolved, stable, coronal loops, varying from solar-like loops with modest temperatures ( $\sim 2$  MK) and densities ( $\sim 10^9 \text{ cm}^{-3}$ ) to hotter loops ( $> 8$  MK) with higher densities ( $> 10^9 \text{ cm}^{-3}$ ).

If we attribute the detected X-ray emission to the main sequence companion in HFG 1, then the activity ratio,  $\log L_X/L_{\text{bol}} \sim -3.0 \pm 0.2$ , is at the saturation level. Assuming fully ionized coronal plasma,  $n_H = 0.85n_e$ , the emission measure, EM, determined from the X-ray spectral fit is related to the density of coronal plasma by  $n_e = (EM/0.85V)^{1/2}$ , where  $V$  is the emitting volume. The emitting volume can be approximated as a shell on the stellar surface by  $V = \frac{4\pi}{3}R_*^3[(L+1)^3 - 1]$ , where  $L$  is the characteristic coronal loop length in stellar radii,  $R_*$ . For inactive stars, densities

up to  $10^9 \text{ cm}^{-3}$  and loop lengths  $\sim 0.1R_*$  are typical, while active stars have higher densities, from  $10^{10}$  to  $10^{11} \text{ cm}^{-3}$  and up to  $10^{13} \text{ cm}^{-3}$  in extreme cases, with generally smaller loop lengths,  $L < 0.1R_*$  (Güdel 2004). If we take  $L = 0.1R_*$ , then the lower bound on the density of the hot X-ray gas in HFG 1 is  $\sim 10^{10} \text{ cm}^{-3}$ , consistent with a corona around the companion.

Applying similar considerations to the X-ray emission detected from DS 1, if we attribute the X-ray emission to the companion, the resulting value of  $\log L_X/L_{\text{bol}} \sim -2.0 \pm 0.3$  is significantly above saturation. However, the uncertainty in  $L_X/L_{\text{bol}}$  does not include the poorly constrained uncertainties in the temperature and radius of the companion, which can raise  $L_{\text{bol}}$  enough to bring  $L_X/L_{\text{bol}}$  down to the saturation level. Nevertheless, a value of  $L_X/L_{\text{bol}}$  as large as  $\sim -2.0$  would not be without precedent. Indeed, many studies find a large scatter in the  $L_X/L_{\text{bol}}$  ratio in the saturated region (e.g., the pre-main sequence sample studied by Stassun et al. 2004), with some stars reaching  $\log L_X/L_{\text{bol}} \sim -2.0$ . The possibility of X-ray flaring activity from DS 1 may also account for the high value of  $L_X/L_{\text{bol}}$ . Applying similar coronal assumptions to the X-ray emission detected from DS 1 results in a lower bound on the coronal density of  $\sim 10^{10} \text{ cm}^{-3}$ .

Although the variability of LoTr 5 (in light of the uncertainty in its orbital period) suggests that the X-ray emission detected from LoTr 5 might arise from accretion processes, there is corroborating evidence that supports the notion that the X-rays arise as a consequence of coronal emission from the giant companion. Good indicators of such coronal activity are the strong Ca II H & K, Mg II, and H $\alpha$  emission lines, which are more likely due to chromospheric activity associated with the giant com-

panion than any accretion-related associated with the sdO primary (Jasniewicz et al. 1996). Indeed, the ratio  $\log L_X/L_{\text{bol}} \sim -5$  and projected rotational velocity  $v \sin i \sim 67 \text{ km s}^{-1}$  (Strassmeier et al. 1997) of the giant companion in LoTr 5 are consistent with those of rapidly rotating, intermediate mass, G- and K-type giants with coronal activity, both in single systems (Gondoin 2005) and binary systems (Gondoin 2007). Such giants do not follow the empirical activity-rotation relation,  $L_X \sim 10^{27}(v \sin i)^2$ , found by Pallavicini et al. (1981) for main sequence late-type stars and do not appear to reach a saturation level (Gondoin 2007). Gondoin (2007) interpret the linear relation between the coronal radiative flux density and the average surface magnetic flux density as evidence for increasing magnetic surface flux in response to an increasing angular rotation velocity. The X-ray properties of LoTr 5 also agree with those by found by Dempsey et al. (1993a,b) for RS CVn systems. The available evidence indicates that the binary in LoTr 5 may be similar to such systems, as also suggested by Strassmeier et al. (1997).

Table 6.3 Spectral Fitting of the X-ray Emission from Binary CSPNe

PNe	$\chi^2$ (d.o.f. <sup>a</sup> )	$\log N_H$ (cm <sup>-2</sup> )	kT (keV)	$T_X$ (MK)	$\log \text{norm.}^b$ (cm <sup>-5</sup> )	$\log \text{EM}^b$ (cm <sup>-3</sup> )	$\log F_{X,\text{obs}}$ (erg cm <sup>-2</sup> s <sup>-1</sup> )	$\log F_{X,\text{unabs}}$ (erg cm <sup>-2</sup> s <sup>-1</sup> )	$\log L_X$ (erg s <sup>-1</sup> )
HFG1	0.79 (510)	21.4	0.5 <sup>+0.1</sup> <sub>-0.1</sub>	5.8	-4.5 <sup>+0.1</sup> <sub>-0.1</sub>	53.10	-13.57	-13.13	30.51
			1.8 <sup>+1.1</sup> <sub>-0.5</sub>	21.3	-4.5 <sup>+0.2</sup> <sub>-0.2</sub>	53.11	-13.56	-13.39	30.25
DS 1	0.49 (510)	20.9	0.3 <sup>+0.2</sup> <sub>-0.1</sub>	3.1	-5.7 <sup>+0.2</sup> <sub>-0.5</sub>	52.07	-14.65	-14.45	29.32
			1.2 <sup>+0.4</sup> <sub>-0.2</sub>	14.5	-5.3 <sup>+0.2</sup> <sub>-0.2</sub>	52.47	-14.14	-14.06	29.71
LoTr 5	1.34 (34)	0.00	0.65 <sup>+0.05</sup> <sub>-0.05</sub>	7.6	-4.93 <sup>+0.05</sup> <sub>-0.08</sub>	52.54	-13.54	-13.54	29.93
(XMM)			2.27 <sup>+0.51</sup> <sub>-0.35</sub>	26.3	-4.37 <sup>+0.06</sup> <sub>-0.05</sub>	53.11	-13.22	-13.22	30.25
LoTr 5	0.50 (23)	0.00	0.64 <sup>+0.07</sup> <sub>-0.07</sub>	7.5	-4.71 <sup>+0.10</sup> <sub>-0.09</sub>	52.77	-13.30	-13.30	30.18
(CXO)			3.49 <sup>+0.83</sup> <sub>-0.64</sub>	40.5	-3.93 <sup>+0.04</sup> <sub>-0.05</sub>	53.55	-12.74	-12.74	30.73

<sup>a</sup>When fitting the unbinned spectra of HFG 1 and DS 1, the empty bins are used as constraints, hence the inflated number of degrees of freedom (d.o.f.).

<sup>b</sup>Emission Measure (EM) is determined from the normalization value of the *mekal* model according to:

$$\text{EM} = \int n_e n_H dV = 1.2 \times 10^{58} \text{ cm}^{-3} \left[ \text{norm.} \times \left( \frac{D}{1 \text{ kpc}} \right)^2 \right] \quad (6.4)$$

## 6.5 Chapter Summary

The X-ray emission sources detected at the binary central stars of three PNe—two suspected post-common envelope binaries, HFG 1 and DS 1, and the binary LoTr 5, whose period is unknown—reveal properties consistent with coronae in late-type, spun up companions. For HFG 1 and DS 1, the measured ratio of X-ray to bolometric luminosity,  $L_X/L_{\text{bol}}$ , indicates that the main sequence companions are at or beyond the saturation level determined for rapidly rotating late-type stars. The X-ray light curves suggest a steady source in HFG 1 and a possibly flaring source in DS 1, which may account for the large relative X-ray luminosity measured for the latter central star, if the companion is the source. The value of  $L_X/L_{\text{bol}}$  inferred for the companion star in LoTr 5 is similar to that of rapidly-rotating giants and RS CVn systems. The X-ray temperatures and emission measures determined from the X-ray spectral fits are furthermore consistent with those found for active, late-type stars. Although, the X-ray temperatures would also be consistent with those expected from accretion onto the pre-WD, sdO, primary stars, the lack of evidence for Roche lobe overflow from the late-type stars in HFG 1 and DS 1 casts doubt on such an origin for the X-ray emission. Since the period of the binary in LoTr 5 is unknown, we cannot determine if the late-type giant secondary in LoTr 5 is capable of filling its Roche lobe, and Roche lobe overflow remains a possible source of accreting material in this case. However, there is compelling and corroborating evidence that the X-ray emission is due to coronal activity associated with the rapidly rotating giant. We conclude that the observed X-ray emission in each of these three binary CSPN systems is most likely due to coronal activity associated with the late-type companions. Although

it is clear that supporting observations are required to detect and characterize any putative companions more directly, these X-ray observations thereby demonstrate the potential utility of X-ray searches for faint companions in the central stars of PNe.





# Chapter 7

## XMM Serendipitous Survey of PNe

### 7.1 Serendipitous Survey

With a radius of  $\sim 15'$ , the wide field of view (FOV) of XMM EPIC observations provides an excellent source for serendipitous science. Although the sensitivity and quality of data gathered in regions of fields imaged far from the target of an observation suffer from vignetting and pronounced aberrations, proper and careful data analysis, as described in Chapter 3, can account for (though not correct) the defects in off-axis X-ray imaging and thereby provide quality science at no extra observing cost to the telescope. In this chapter, a search for X-ray emission from serendipitously observed PNe is performed using the data archive of XMM EPIC observations, sim-

ilar to the serendipitous source searches performed on the *Einstein*, *EXOSAT*, and *ROSAT* data archives discussed in Chapter 2.

### 7.1.1 Search Method and Observation Filtering

Potential serendipitous observations of PNe are discovered by cross-correlating the coordinates of PNe in the Strasbourg-ESO Catalogue of Galactic Planetary Nebulae (Acker et al. 1994) with the target coordinates of archived XMM observations. As the XMM data archive is continuously growing, the search is time-sensitive. For this thesis, the search was performed for all archived observations as of June 2007, using a search radius of  $15'$ . This initial search retrieves 80 object matches between the Acker et al. (1994) catalog and the archived XMM observations.

These 80 object matches include PNe targeted by XMM. Serendipitously observed PNe tend to have correlation offset angles greater than  $2'$ ; applying this filter removes the targeted PNe (NGC 40 [Optical Monitor only], NGC 2346, NGC 2392, NGC 3242, NGC 6543, NGC 7009, NGC 7026, NGC 7293, and K 3-35 [apparently coincident with nearby background X-ray emitting star]). Cross-correlating the remaining list of serendipitously observed PNe with an updated object classification acquired through the SIMBAD astronomical database<sup>1</sup> reveals a handful of objects that may not be PNe (classifications of possible PN, supernova remnants, and H II regions) and a few symbiotic binary systems. For the survey presented in this chapter, only bona-fide

---

<sup>1</sup>SIMBAD database, operated at CDS, Strasbourg, France, is available at: <http://simbad.u-strasbg.fr/simbad/>.

PNe and symbiotic systems<sup>2</sup> are included, leaving 49 PNe (Table A.1) and 2 symbiotic stars (Table A.2) in the potential serendipitous sample.

Not all of the matched observations in Tables A.1 and A.2 have adequate detector coverage<sup>3</sup> of the serendipitously observed PN. Each observation is inspected by eye and examined for gaps in the detector coverage of the FOV that may result in loss of target coverage and exposure time. The results of this examination are given in the fifth column of Table A.1. Twenty-one observations do not meet the adequate detector coverage criterion; this filtering eliminates 13 PNe from the list (PN HATR 8, Hen 2-81, Hen 2-96, Hen 2-207, PN K 1-16, PN M 2-20, PN M 2-21, PN M 3-28, PN Pe 1-11, Terz N 41, WRAY 16-146, WRAY 16-158, and WRAY 17-107). This resulting sample that comprises the XMM Serendipitous Survey of PNe (XMMSSPNe; as of June 2007) and features 36 PNe and 2 symbiotic systems. The distribution of various parameters of the observations of this sample are provided in Figure 7.1.

### 7.1.2 Data Preparation and Analysis

For every serendipitous observation in the XMMSSPNe, the basic Observation Data Files (ODF) of MOS and pn observations are reprocessed completely with the XMM-SAS meta-tasks *emchain* and *epchain*, respectively, and the current calibration files (CCF) are used for the data analysis (Release Note XMM-CCF-REL-249, released

---

<sup>2</sup>Symbiotic systems are evolved objects and have many physical characteristics in common with PNe. The classification and separation of PNe and symbiotic systems is an unresolved issue and an active area of debate (e.g., Kastner et al. 2003), hence the inclusion of potential detections of symbiotic systems in this survey is worthwhile to both the PNe field and the symbiotics field.

<sup>3</sup>We define adequate detector coverage as observations wherein the physical location of the PN is on an exposed portion of the CCD chips for at least 10 ks.

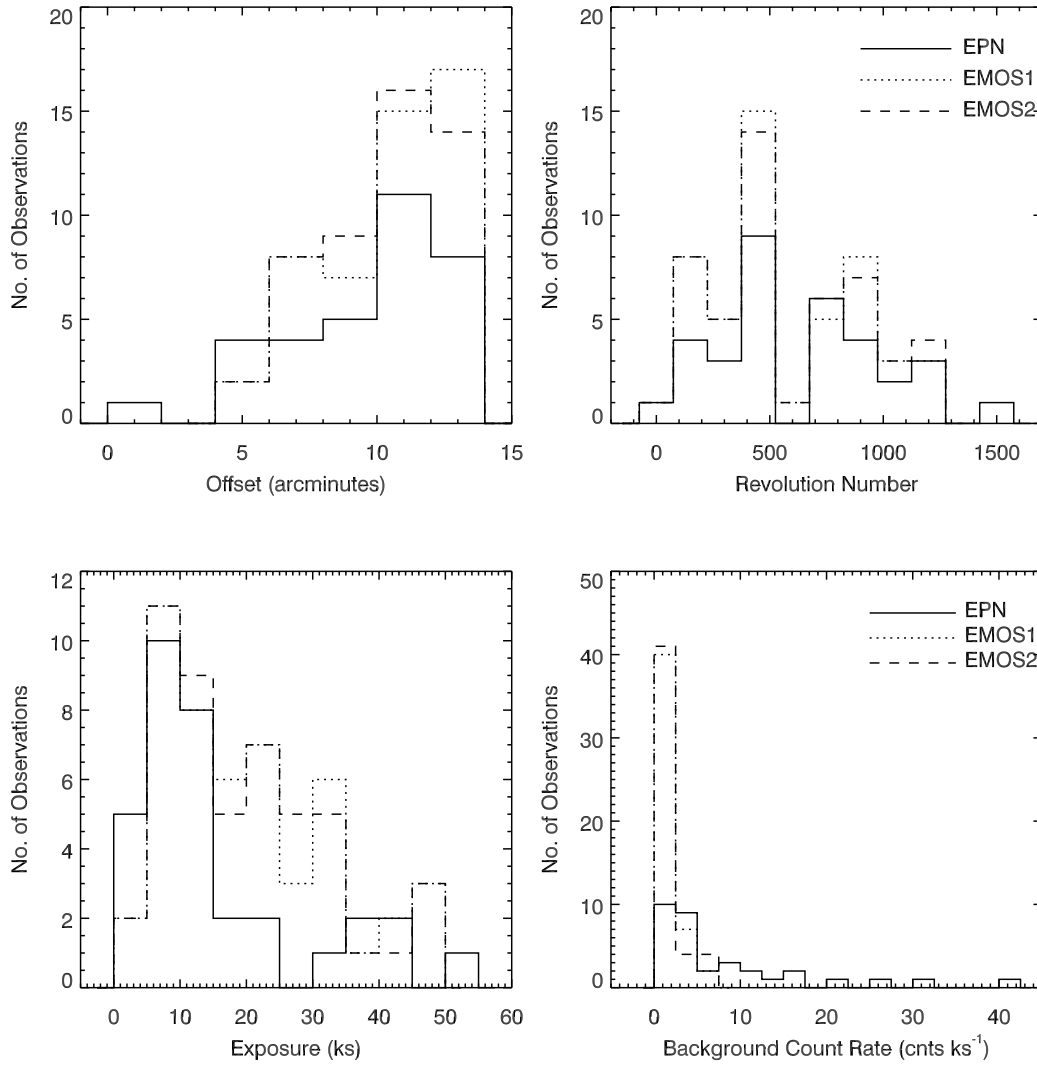


Figure 7.1 Distributions of Survey Observations (*top left*: off-axis offset angles in arcminutes, *top right*: revolution numbers, *bottom left*: exposure times in kiloseconds, *bottom right*: background count rates.)

on 2009 May 07). Details of the data preparation are described in Chapter 3 along with the handling of off-axis sources (common in serendipitous observations).

## 7.2 Detections

In this section, I present the discoveries of PN X-ray emission from the serendipitous observations of the XMMSSPNe sample. These sources are detected spatially and spectroscopically with count rates at least  $2\text{-}\sigma$  above the background count rate. I also describe the analysis and interpretation of the X-ray observations for each object. A few of the PN detections presented here were also observed and detected by CXO (e.g. LoTr 5 and NGC 6543).

### 7.2.1 Hubble 5

Hubble 5 (Hb 5) is Type I (He- and N-rich) bipolar planetary nebula. The Hb 5 X-ray source appears marginally resolved. While the small number of total counts ( $\sim 170$ ) and significant off-axis angle of the X-ray source ( $\sim 7.8'$ ) precludes a definitive spatial analysis, the morphology of the X-ray emission appears to trace the brightest features seen in optical images of Hb 5. The X-ray spectrum is indicative of a thermal plasma at a temperature between 2.4 and 3.7 MK and appears to display strong Neon emission. The inferred X-ray luminosity is  $L_X = 1.5 \times 10^{32} \text{ ergs s}^{-1}$ . These results, detailed in Chapter 5, suggest that the detected X-ray emission is dominated by shock-heated gas in the bipolar nebula, although a point-like component at the position of the central star cannot be ruled out. Chapter 5 also discusses the implications for and correspondence with current models of shock-heated gas in planetary nebulae.

### 7.2.2 LoTr 5

LoTr 5 is an old and evolved bipolar PN with a binary central star composed of a pre-WD sdO star and a rapidly rotating giant companion. LoTr 5 lies  $7.3'$  off axis in the XMM EPIC pn, MOS1, and MOS2 observations. The strong X-ray source coincident with the position of LoTr 5 is consistent with a point source at the off-axis position. The source spectrum is best fit by a model consisting of two thermal plasmas with temperatures of 8 and 26 MK. The value of  $L_X/L_{\text{bol}}$  inferred for the companion star in LoTr 5 is similar to that of rapidly-rotating giants and RS CVn systems. The X-ray temperature and emission measure determined from the X-ray spectral fit is furthermore consistent with those found for active, late-type stars. The details of the spectral fit and its interpretation, including a comparison with the CXO observation, is discussed in Chapter 6.

### 7.2.3 NGC 6543

NGC 6543, also known as the Cat's Eye Nebula, is a well-studied PN that exhibits a complex morphology consisting of spiral-like density enhancements, nested cavities, and multiple shell-like rings in its halo. The results of a 46 ks, targeted, CXO observation were reported in Chu et al. (2001). The CXO observation resolved the diffuse X-ray emission arising from the hot bubble in an inner cavity along the semi-major axis of the elongated PN, and the hard X-ray emitting point source at the position of the central star. Chu et al. (2001) report a plasma temperature much lower than predicted by a typical CSPN fast wind ( $\sim 1750 \text{ km s}^{-1}$ ), suggesting that efficient mixing

between the nebula and the shocked fast wind material has cooled the hot bubble gas. Such mixing should also have changed the hot bubble composition toward that of the nebular abundances; however, the X-ray emission cannot be fit with nebular abundances.

NGC 6543 lies  $\sim 9.0'$  off-axis within XMM observations (ObsIDs 0112310401 and 0112310801) of the galaxy NGC 6552. The longer observation, ObsID 0112310401, is severely effected by high background flares and hence was discarded. The shorter observation, ObsID 0112310801, was performed during XMM Revolution 523 on 18 October 2002. All three EPIC observations were obtained in full-frame imaging mode with the medium filter. After filtering for high background periods and applying the standard imaging mode event and grade filters, the resulting net exposure times are 5.2, 7.4, and 7.4 ks on pn, MOS1, and MOS2, respectively. The X-ray emission in the range of 0.3 to 3.0 keV and the smooth X-ray contours overlaid upon the HST ACS FR656N narrow-band image are presented In Figures 7.2-7.3 for each EPIC detector. The contours are created by smoothing the X-ray emission with a Gaussian filter with a FWHM of  $\sim 8''$ . Due to the image aberrations at the off-axis position of NGC 6543 and the short exposure time, the instrumental point spread functions are not well-sampled, leading to the strange morphological properties seen in the X-ray images.

The X-ray spectrum extracted from the position of NGC 6543 on the EPIC detectors is shown in Figure 7.4. The spectrum is fit in XSPEC with an optically-thin thermal plasma model (*mekal*) with intervening absorption (*wabs*). The best-fit model folded with the individual instrumental responses is plotted as a dashed histogram

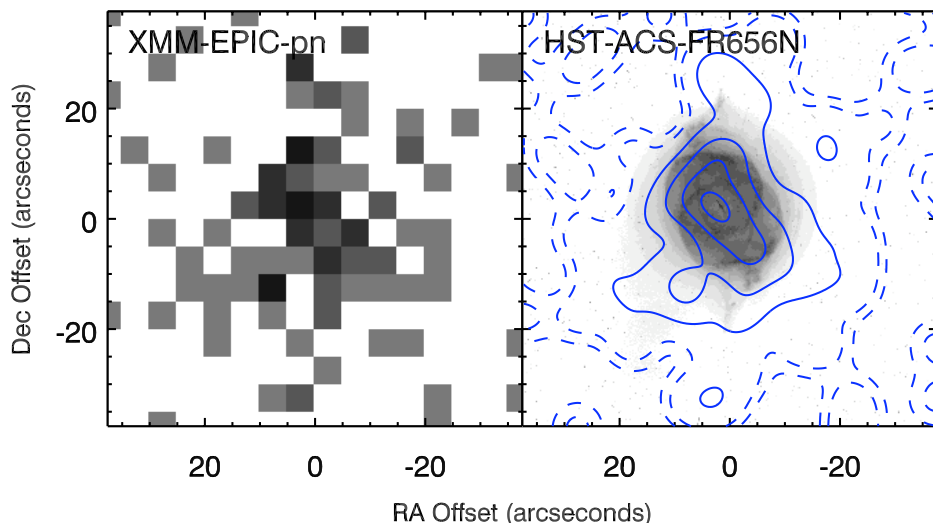


Figure 7.2 The X-ray emission detected from the serendipitous XMM pn observation of NGC 6543. Left: the X-ray emission from the EPIC pn detector filtered from 0.3 to 3.0 keV. Right: the contours of the X-ray emission smoothed by a Gaussian filter with a FWHM of  $\sim 8''$  overlaid upon the HST ACS FR656N narrow-band image.

in Figure 7.4. The best-fit temperature is  $10^6$  K with a 90% confidence range of  $0.9 - 1.4 \times 10^6$  K, while the best-fit column density is  $1.1 \times 10^{21} \text{ cm}^{-2}$  with a 90% confidence range of  $0.1 - 2 \times 10^{21} \text{ cm}^{-2}$ . The best-fit model gives an observed flux in the energy range of 0.3 to 3.0 keV of  $9.5 \times 10^{-14} \text{ ergs cm}^{-2} \text{ s}^{-1}$ , an unabsorbed flux of  $5.0 \times 10^{-13} \text{ ergs cm}^{-2} \text{ s}^{-1}$ , and an X-ray luminosity of  $6.0 \times 10^{31} (D/(1 \text{ kpc}))^2 \text{ ergs s}^{-1}$  assuming the distance of 1 kpc (Cahn et al. 1992). The best-fit column density agrees with the 99% confidence range given by Chu et al. (2001) for the CXO observation of NGC 6543, while the best-fit temperature from the XMM observation is cooler than and just outside the 99% confidence range determined from the CXO observation. The luminosity determined from the XMM observation is also lower than that deter-



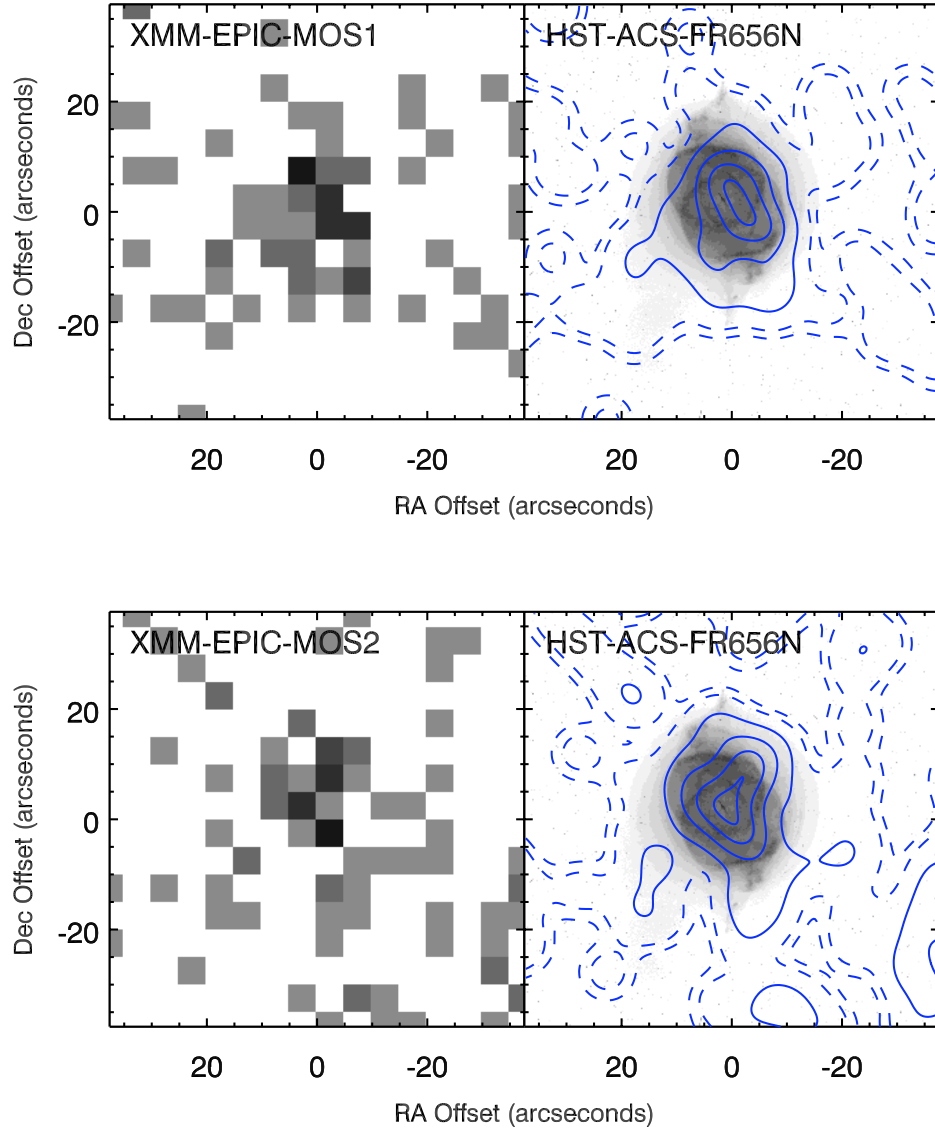


Figure 7.3 The X-ray emission detected from the serendipitous XMM MOS1 and MOS2 observations of NGC 6543. Left: the X-ray emission from the EPIC MOS1 (top) and MOS2 (bottom) detectors filtered from 0.3 to 3.0 keV. Right: the contours of the respective X-ray emission smoothed by a Gaussian filter with a FWHM of  $\sim 8''$  overlaid upon the HST ACS FR656N narrow-band image.

mined by the CXO observation. The very short net exposure after filtering out high background periods ( $\sim 7$  ks) of the XMM observation is the likely culprit responsible for the discrepancy between the CXO- and XMM-derived X-ray properties.

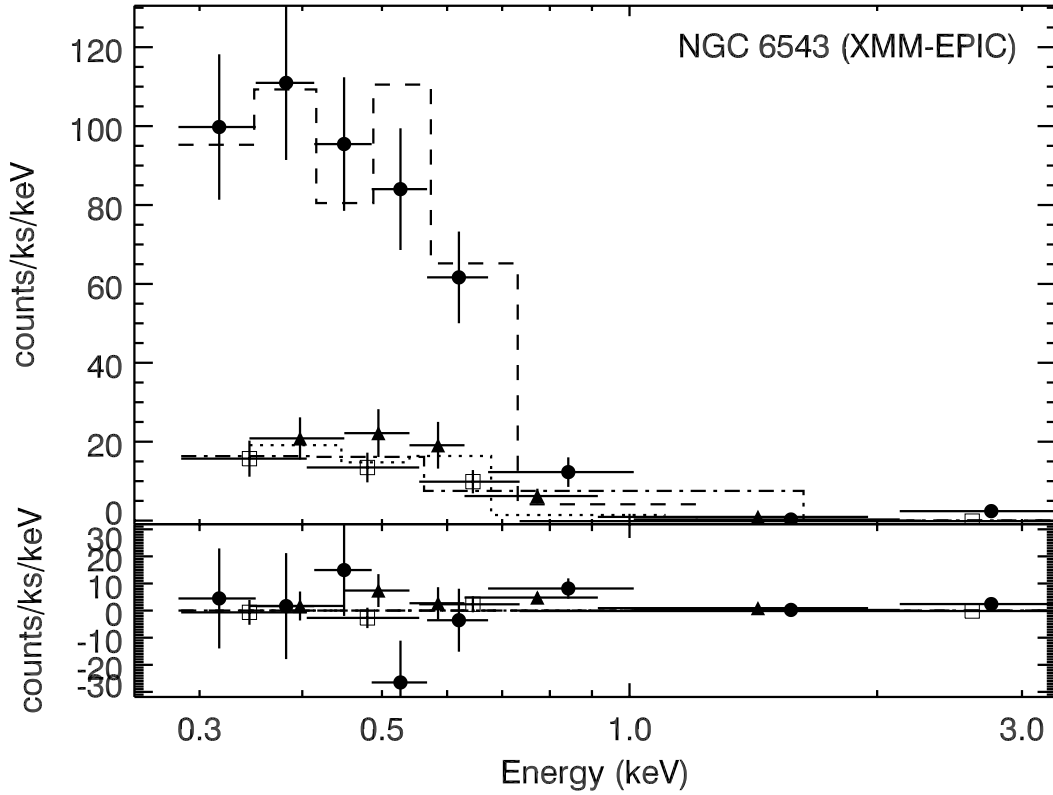


Figure 7.4 The X-ray spectra detected from the serendipitous XMM observation of NGC 6543. The best-fit optically-thin thermal plasma model with intervening absorption is over plotted (dashed histogram) on the X-ray spectrum extracted from the position of NGC 6543 on the three EPIC detectors (pn – filled circle, MOS1 – open squares, MOS2 – filled triangle).

### 7.2.4 Symbiotic System: H 1-36

H 1-36 is a D-type symbiotic system comprised of a hot primary, a Mira-type companion, and a high-excitation emission-line spectrum (Allen 1983; Belczyński et al. 2000)<sup>4</sup>. The orbital period is 450-500 days (Whitelock 1987). Angeloni et al. (2007) analyzed available data for H 1-36 across a broad range of the electromagnetic spectrum and found the data were consistent with a colliding-wind scenario (Girard & Willson 1987; Kenny & Taylor 2005). Angeloni et al. (2007) suggest that H 1-36 would make a promising X-ray target with the possible jet-like outflows and predict the presence of Bremsstrahlung emission at  $T_X \sim 3.6 \times 10^6$  K arising from a high velocity component,  $V_s \sim 500$  km s<sup>-1</sup>, detected in the infrared spectrum. The serendipitous observation described here is the first report of X-ray emission from H 1-36.

H 1-36 lies  $\sim 4.4'$  off-axis within an XMM observation of the Low-Mass X-ray Binaries (LMXBs) XB 1254-690 and 4U 1746-371. Although there are numerous XMM observations of these LMXBs, only one observation, ObsID 0139560101, has an active detector at the location of H 1-36. This observation was performed during XMM Revolution 509 on 19 September 2002. Only the EPIC MOS2 detector covers the position of H 1-36. The EPIC MOS2 observation was obtained in Full-Frame Mode with the medium filter, while the other EPIC detectors were operated in sub-array modes, limiting their coverage of the FOV. After filtering for high background periods and applying the standard imaging mode event and grade filters, the resulting

---

<sup>4</sup>Allen (1983) argues that the hot star is photo-ionizing the dust shell surrounding the M-star companion, hence H 1-36 does not pass the definition of a planetary nebula, which requires that the star that ionizes the nebula be the star that ejected the nebula (Soker 2006).

net exposure time is 36.5 ks. The X-ray emission in the range of 0.3 to 3.0 keV and the smooth X-ray contours overlaid upon a 2MASS J band image centered on H 1-36 are presented in Figure 7.5. The contours are created by smoothing the X-ray emission with a Gaussian filter with a FWHM of  $\sim 6''$ . The aberrations due to the off-axis position of H 1-36 can account for the extended appearance of the X-ray emission detected from H 1-36. The relatively weak source signal is superimposed on the elevated background from the extended PSF wings of the nearby LMXBs. This superposition limits the interpretation of the spatial features observed.

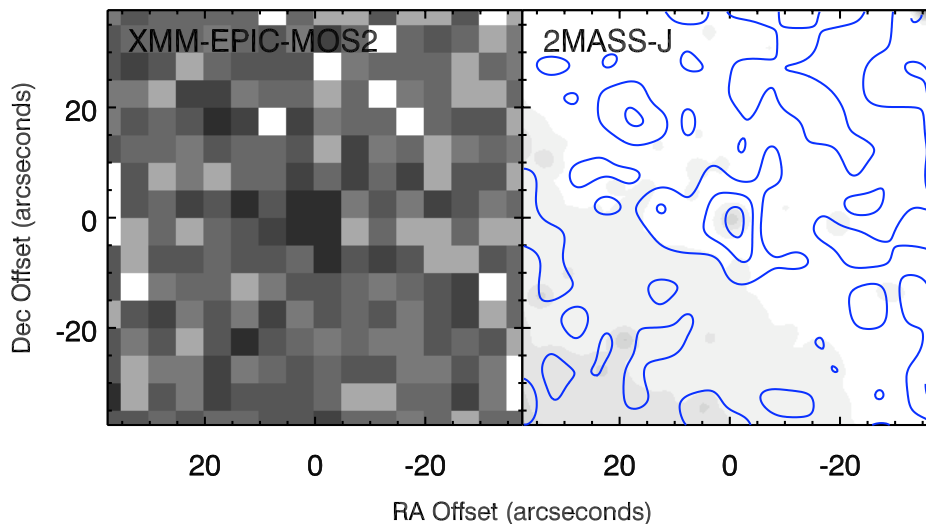


Figure 7.5 The X-ray emission detected from the serendipitous XMM observation of the symbiotic system H 1-36. Left: the X-ray emission from the EPIC MOS2 detector filtered from 0.3 to 3.0 keV. Right: the contours of the X-ray emission smoothed by a Gaussian filter with a FWHM of  $\sim 6''$  overlaid upon the 2MASS J band image.

The X-ray spectrum extracted from the position of H 1-36 on the EPIC MOS2 detector is shown in Figure 7.6. The faint source produces a weak and noisy spectrum,

yet it can be fit successfully, albeit with large uncertainties in the best-fit parameters. The spectrum is fit in XSPEC with a thermal bremsstrahlung model (*brems*) with intervening absorption (*wabs*). The intervening absorption is set to  $N_H = 2 \times 10^{21} \text{ cm}^{-2}$  after Luna & Costa (2005). The best-fit model is plotted as a dashed line in Figure 7.6. The best-fit temperature is  $4.6 \times 10^6 \text{ K}$  with a 90% confidence range of  $2.8 - 8.3 \times 10^6 \text{ K}$ . The best-fit model gives an observed flux in the energy range of 0.3 to 3.0 keV of  $1.2 \times 10^{-14} \text{ ergs cm}^{-2} \text{ s}^{-1}$ , an unabsorbed flux of  $3.1 \times 10^{-14} \text{ ergs cm}^{-2} \text{ s}^{-1}$ , and an X-ray luminosity of  $7.4 \times 10^{31} (D/(4.5 \text{ kpc}))^2 \text{ ergs s}^{-1}$ , where the distance of 4.5 kpc was reported by Allen (1983). The noisy spectrum and off-axis position restrict the conclusions that can be drawn from the X-ray emission, but the best-fit spectral parameters agree with the predictions made by Angeloni et al. (2007) based on the colliding-winds model for H 1-36.

### 7.2.5 Symbiotic System: V2416 Sgr (PN M 3-18)

V2416 Sgr is an S-type symbiotic system comprised of a hot primary and an M5-M6 class companion (Belczyński et al. 2000). Strong [OIII] emission lines led to the classification of V2416 Sgr as a PN; however, Luna & Costa (2005) determined the electron density of the [OIII] emission is  $N_e \sim 6.06 \times 10^7 \text{ cm}^{-3}$ , much too high to be due to a diffuse nebula and likely to arise from shocks in a colliding binary wind scenario or photoionization of the M companion's dense envelope.

V2416 Sgr was targeted on 2000-03-22 (Revolution 52, ObsID 0099760201) by XMM with the intention to calibrate the Optical Monitor grisms, hence the faint X-

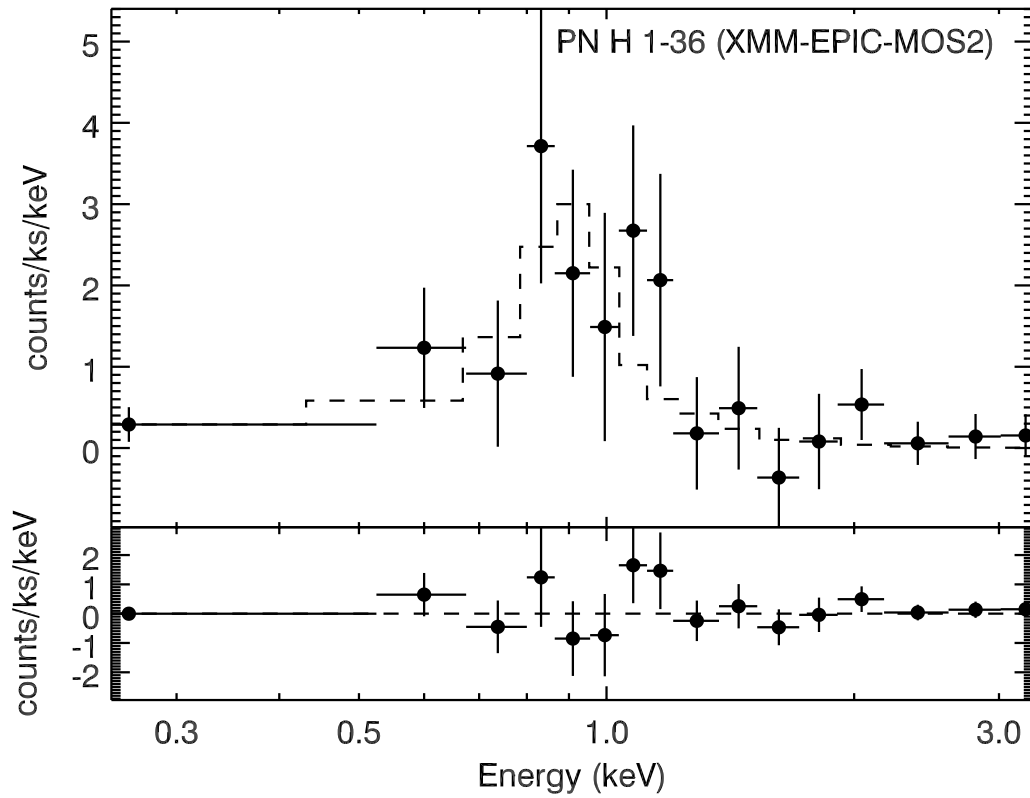


Figure 7.6 The X-ray spectrum detected from the serendipitous XMM observation of the symbiotic system H 1-36. The best-fit thermal bremsstrahlung model with intervening absorption is over plotted (dashed line) onto the X-ray spectrum extracted from the position of H 1-36 on the EPIC MOS2 detector. The range of the best-fit parameters agree with the predictions made by Angeloni et al. (2007).

ray detection of V2416 Sgr on the EPIC detectors has yet to be reported or examined. The observation was obtained in full-frame imaging mode with the medium filter. After filtering for high background periods and applying the standard energy and event grade filters, the resulting exposure times are 36, 49, and 49 ks on the pn, MOS1, and MOS2 detectors, respectively. The X-ray emission in the range of 0.3

to 3.0 keV and the smooth X-ray contours overlaid upon a 2MASS J band image centered on V2416 Sgr are depicted in Figures 7.7-7.8. The contours are created by smoothing the X-ray emission with a Gaussian filter with a FWHM of  $\sim 6''$ . In Figure 7.7, the effect of the nearby chip gap in the EPIC-pn observation can be seen below the emission from V2416 Sgr.

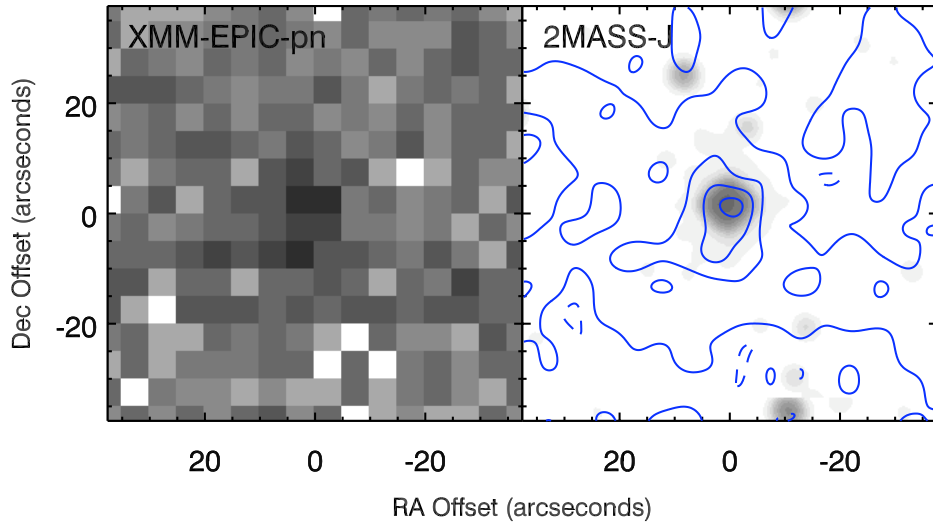


Figure 7.7 The X-ray emission detected from the serendipitous XMM pn observation of the symbiotic system V2416 Sgr. Left: the X-ray emission from the EPIC pn detector filtered from 0.3 to 3.0 keV. Right: the contours of the X-ray emission smoothed by a Gaussian filter with a FWHM of  $\sim 6''$  overlaid upon the 2MASS J band image.

The X-ray spectra extracted from the position of V2416 Sgr on the three EPIC detectors are shown in Figure 7.9. The EPIC spectra are simultaneously fit in XSPEC with an optically-thin thermal plasma model (*mekal*) with intervening absorption (*wabs*). The best-fit model is plotted as a dashed line in Figure 7.9. The best-

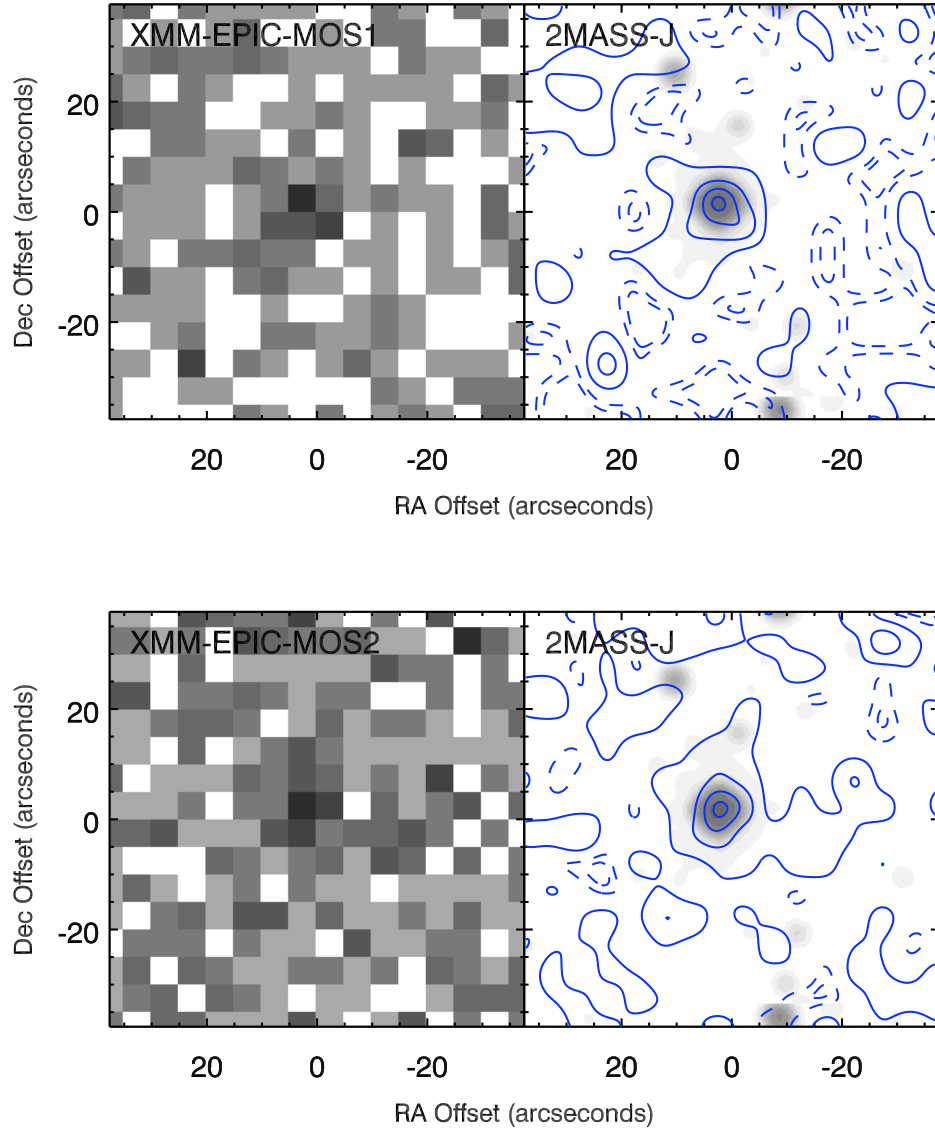


Figure 7.8 The X-ray emission detected from the serendipitous XMM MOS1 and MOS2 observations of the symbiotic system V2416 Sgr. Left: the X-ray emission from the EPIC MOS1 (top) and MOS2 (bottom) detectors filtered from 0.3 to 3.0 keV. Right: the contours of the respective X-ray emission smoothed by a Gaussian filter with a FWHM of  $\sim 6''$  overlaid upon the 2MASS J band image.



fit temperature is  $7.6 \times 10^6$  K with a 90% confidence range of  $1.8 - 10 \times 10^6$  K and the best-fit column density is  $9.0 \times 10^{21} \text{ cm}^{-2}$  with a 90% confidence range of  $5.9 - 15 \times 10^{21} \text{ cm}^{-2}$ , which agrees with the color excess determined by Luna & Costa (2005),  $E(B - V) = 1.69$  mag, from a spectroscopic survey of symbiotic systems. The best-fit model gives an observed flux in the energy range of 0.3 to 3.0 keV of  $3.7 \times 10^{-15} \text{ ergs cm}^{-2} \text{ s}^{-1}$ , an unabsorbed flux of  $3.3 \times 10^{-14} \text{ ergs cm}^{-2} \text{ s}^{-1}$ , and an X-ray luminosity of  $2.1 \times 10^{31} (D/(2.3 \text{ kpc}))^2 \text{ ergs s}^{-1}$ , for the distance of 2.3 kpc reported by Allen (1980).

### 7.3 Non-Detections

Many of the serendipitous observations do not detect X-ray emission from the PNe. For a 10 ks XMM observation, the minimum detectable flux in the 0.5 to 2.0 keV energy range is  $\sim 2 \times 10^{-15} \text{ erg cm}^{-2} \text{ s}^{-1}$  and  $\sim 5 \times 10^{-15} \text{ erg cm}^{-2} \text{ s}^{-1}$  for the EPIC pn and MOS detectors, respectively. However, in addition to the exposure time of the observation and the spectrum of the source, this minimum detectable flux also depends on the background level, which varies tremendously from observation to observation (due to nearby bright sources, space weather, and bright but unresolved background sources). Hence, the detection threshold must be quantified for the specific conditions of each observation.

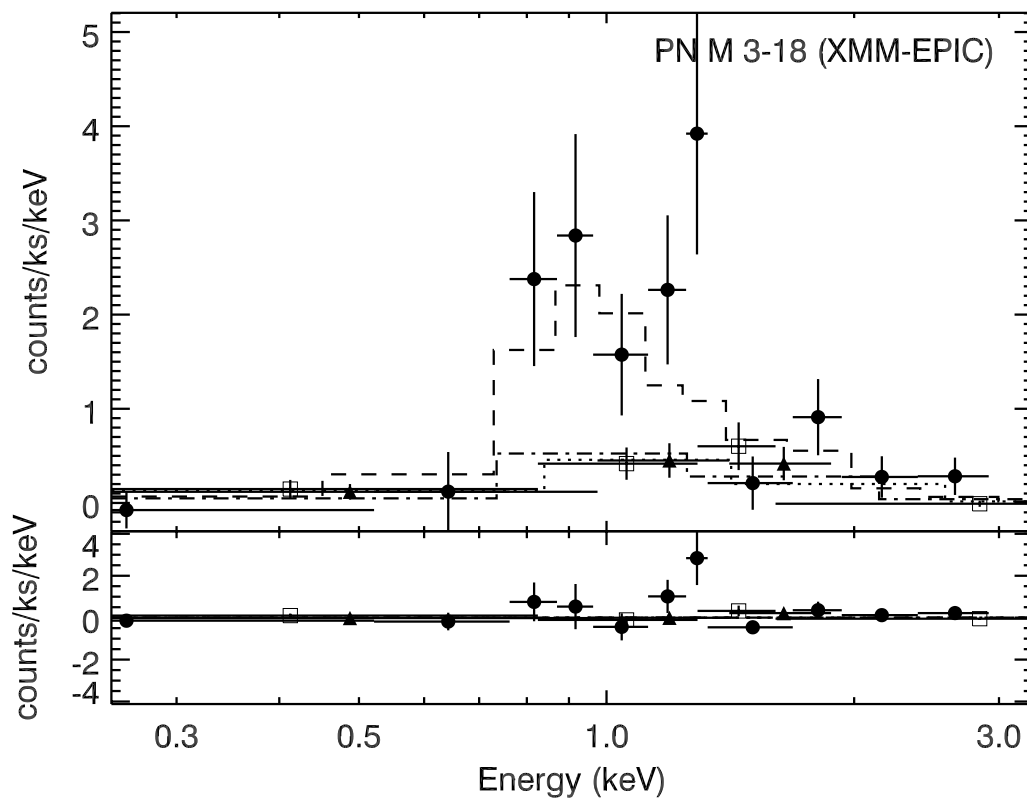


Figure 7.9 The X-ray spectra detected from the serendipitous XMM observation of the symbiotic system V2416 Sgr. The best-fit optically-thin thermal plasma model with intervening absorption is over plotted (dashed histogram) on the X-ray spectrum extracted from the position of V2416 Sgr on the three EPIC detectors (pn – filled circle, MOS1 – open squares, MOS2 – filled triangle).

### 7.3.1 Determining the $3\text{-}\sigma$ Count Rate

A detailed description of the method used to determine the detection threshold is given in Chapter 3 and summarized here. For each PN and ObsID pair, the data gathered from the background spectral extraction region is used to determine the

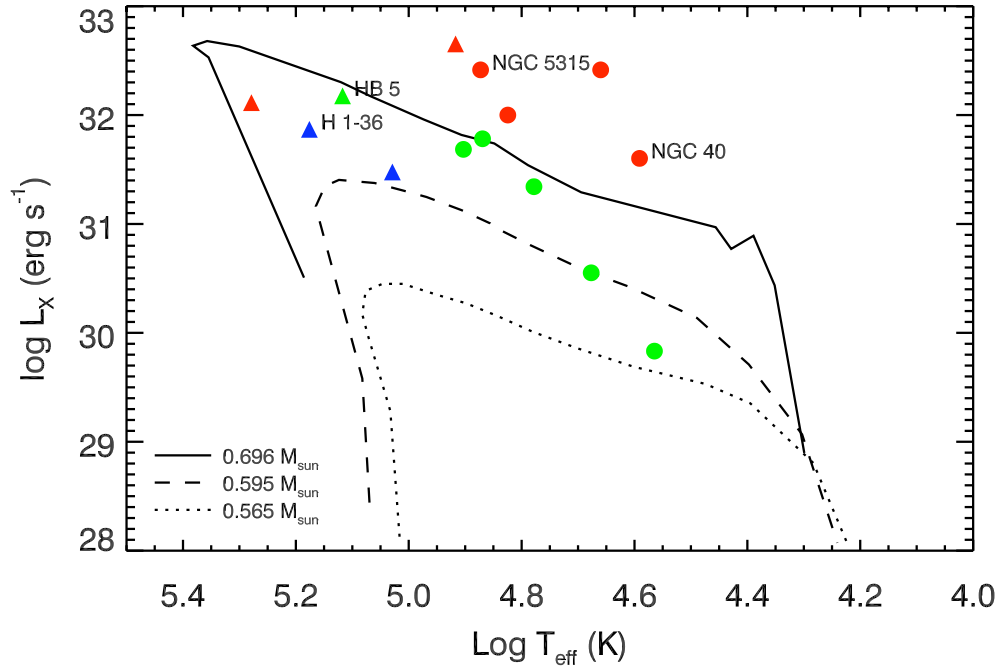


Figure 7.10 Model Predictions of Hot Bubble X-ray Luminosity. The model predictions from Steffen et al. (2008) of the evolution of the X-ray emission from colliding winds in a PNe with effective temperature of the central star. Over plotted are  $L_X$  values from detections of diffuse X-ray emission. The serendipitous sources from this survey are include along with the serendipitous CXO detection of NGC 5315 and the CXO detection of NGC 40, both reported in Chapter 4. The red symbols indicate objects with hydrogen-poor chemical compositions, the green symbols indicate hydrogen-rich chemical compositions, and the blue symbol indicate symbiotic systems.

background count rate in three energy bands (0.45-2.5 keV, 2.5-8.0 keV, and 0.45-8.0 keV; for this study, only the count rate in the 0.45-2.5 keV band is used), which is then normalized by the background area given in square-arcseconds. The normalized source count rates are determined via a similar process but using the source spectral

extraction region. The source spectral extraction region should be similar to the size of the nebula, but as Table A.4 shows, the XMMSSPNe sample is comprised of compact nebula ( $< 10''$ ), hence, the extraction regions are dominated by the FWHM of the detector, or circular regions with a radius equal to  $\sim 15''$ . We compare the normalized count rates in the source and background region to search for potential faint sources that escape visual detection. For undetected sources, the normalized background count rate is multiplied by the source extraction area (a circular region with a radius equal to  $\sim 15''$ ). From this count rate, the  $3\text{-}\sigma$  count rate ( $CR_{3\sigma}$ ) value is calculated. This upper limit count rate is used as input into the Portable, Interactive Multi-Mission Simulator, or PIMMS<sup>5</sup> to determine the upper limit flux of the PN, assuming an optically-thin thermal emission spectrum affected by intervening absorption.

### 7.3.2 Selection of Characteristic $T_X$ for Hot Bubbles and Coronae

To perform the PIMMS upper limit calculation, we must assume an emission model. Both the hot bubble and coronal emission emit as optically-thin, thermal plasmas, hence we assume a Raymond-Smith plasma model (*raymond*). By selecting a plasma temperature,  $T_X$ , we determine the model normalization required to produce the observed count rate ( $CR_{3\sigma}$ ). The observed hot bubble  $T_X$  (Table 2.1) and model calculations (Steffen et al. 2008) suggest the X-ray temperatures of hot bubbles fall

---

<sup>5</sup>PIMMS is available online at <http://heasarc.gsfc.nasa.gov/docs/software/tools/pimms.html>

between 1 – 3 MK. Hence, we adopt a characteristic hot bubble  $T_X \sim 2.5$  MK. The coronal emission detected from suspected spun-up companions is characteristically comprised of two components, a soft component at a few MK and a hotter component with  $T_X > 10$  MK (see Chapter 6). The presence of a 10 MK plasma provides the most compelling evidence for coronal emission (Soker & Kastner 2002), hence, we adopt a characteristic coronal  $T_X \sim 10$  MK. To bracket the potential range of upper limit  $L_X$ , also calculate the upper limits for a range of  $T_X$  from 1 to 15 MK.

### 7.3.3 Intervening Absorption of X-rays

X-ray emission is absorbed by intervening material in the interstellar medium. Values of intervening absorption column densities,  $N_H$ , are taken from the literature when available. When no literature value exists, a moderate value of  $5 \times 10^{21} \text{ cm}^2$  is assumed. We also perform calculations of the upper limit X-ray fluxes and luminosities for range of column densities from  $3 \times 10^{20}$  to  $3 \times 10^{22} \text{ cm}^{-2}$ .

### 7.3.4 Distances of the Sample PNe

Distances are perhaps the least constrained properties of PNe. The distance estimates provided in the Acker et al. (1994) catalog are listed in Table A.4 and used to calculate the upper limit X-ray luminosity from the upper limit flux of each PN. For objects at an unknown distance, an optimistic distance of 1 kpc is assumed.

### 7.3.5 Results of Upper Limit X-ray Properties Calculations

The results of the upper limit X-ray property calculations are presented in full in Appendix A. The best upper limit results using the characteristic temperatures are summarized in Table 7.1 for objects with distance estimates and in Table 7.2 for objects with unknown distance estimates.

## 7.4 Evolution of X-ray Emitting Hot Bubbles

The upper limit fluxes and luminosities provide helpful constraints on the X-ray properties of PNe, but the assumption of  $T_X$  limits their application as tests of models that predict the X-ray emission properties. In Chapter 2 the X-ray emission of targeted PNe were listed in Table 2.1 and plotted along with the 1-D hydrodynamical simulations performed by Steffen et al. (2008). These hydrodynamical simulations follow both the evolution of the X-ray emission produced by interacting stellar winds and the evolution of the central star. This holistic simulation method allows for the correlation of the X-ray emission properties of the PN with the central star properties and greatly improve the utility of the upper limit X-ray properties determined in this chapter provided that supplementary information regarding the central star can be found in the literature. Properties that may be correlated with the X-ray emission based on the simulations performed by Steffen et al. (2008) include the wind momentum, which requires a determination of the mass loss rate; the age of the nebula, which requires the determination of the expansion velocity, distance, and nebular size;

and the central star temperature. Only two of the objects in the serendipitous sample have mass loss rates or expansion velocity determinations, while many have effective temperature estimates.

### 7.4.1 Central Star Temperatures

Of the central star properties, the effective temperature is perhaps one of the most important and most debated properties. Direct measurements are difficult to obtain since the central stars of planetary nebulae (CSPNe) are often obscured and/or very faint compared to the nebular emission. Indirect methods use the properties of the nebular emission to infer the effective temperature of the CSPNe. With a measurement of the continuum emission due to the CSPNe and a spectroscopically nearby nebular emission line, the number of photons responsible for ionizing the nebular emission line can be determined. Assuming the star is responsible for these photons and emits like a blackbody at the wavelengths of interest, one can estimate the effective temperature with high accuracy. This is called the Zanstra method, named after its founder, and temperatures derived with this method are called Zanstra temperatures. CSPNe with Zanstra temperatures are catalogued by Phillips (2003) and by Tylenda et al. (1991) for Galactic bulge PNe.

Successful Zanstra temperature determinations require that the nebula be optically thick to the ionizing photons and that the central star is observable; not all PN meet these criteria. For CSPNe without Zanstra temperatures, the energy balance, or Stoy temperature, is used. Energy balance temperatures use a ratio of line fluxes

to determine the number of ionizing photons, then assuming the star is emitting as a blackbody, the effective temperature of the star is inferred. Preite-Martinez & Potasch (1983) expanded the Stoy method to optically-thin and -thick nebulae. Energy balance temperatures for a number of CSPNe are calculated in Preite-Martinez et al. (1989) and Preite-Martinez et al. (1991) and, where overlap exists, give reasonable agreement with Zanstra temperatures.

### 7.4.2 Constraining the Evolution of X-ray Emitting Hot Bubbles

The results of the XMMSSPNe sample are illustrated in Figures 7.10 and 7.11. The new serendipitous detections follow the trends observed from prior detections of hot diffuse X-ray emission. The PNe with hydrogen-poor, Wolf-Rayet central stars once again show higher X-ray luminosities, while the collimated sources of X-ray emission, which likely arise from leading shock fronts, occupy the high  $L_X$ - $T_{\text{eff}}$  region of Figures 7.10. Among the PNe with only upper limits on X-ray luminosities and with measured  $T_{\text{eff}}$  (Figure 7.11), half ( $\sim 8$ ) are ruled out as having high central star final masses ( $0.696 M_{\odot}$ ), and two or three are further ruled out as having moderate central star final masses ( $0.595 M_{\odot}$ ). The remaining upper limit X-ray luminosities on hot bubble emission ( $\sim 8$ ) are too large to place useful constraints on the central star masses. Collectively, however, Figure 7.11 indicates that the upper limit X-ray luminosities are consistent with heat conduction calculations.



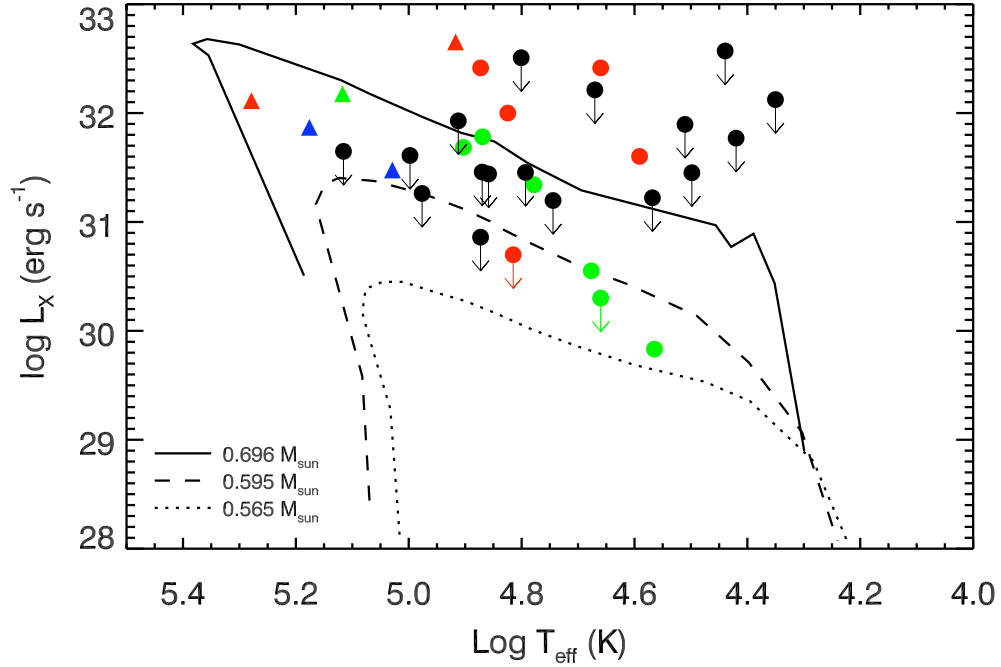


Figure 7.11 Model Predictions of Hot Bubble X-ray Luminosity with Upper Limits. The model predictions from Steffen et al. (2008) of the evolution of the X-ray emission from colliding winds in a PNe with effective temperature of the central star. Over plotted are  $L_X$  values from detections of diffuse X-ray emission and upper limit  $L_X$  values from undetected PNe. The red symbols indicate objects with hydrogen-poor chemical compositions, the green symbols indicate hydrogen-rich chemical compositions, and the blue symbol indicate symbiotic systems. Black symbols indicate unknown compositions.

## 7.5 Constraining the Existence of Spun-up Companions

As shown in Chapter 6, hard point-like X-ray emission from the nuclei of binary PNe likely arises from spun-up main sequence or giant late-type companions. To constrain

the existence of such companions we assumed hot ( $T_X \sim 10$  MK) coronal emission to calculate upper limits on X-ray fluxes from point-source nondetections. If we further assume that a spun-up companion is producing coronal X-ray emission at saturation levels,  $L_X/L_{\text{bol}} \sim 10^{-3}$  (e.g. Güdel & Nazé 2009), then we can determine the bolometric luminosity,  $L_{\text{bol}}$ —and, thus, the earliest spectral type—of the putative spun-up companion. Applying these considerations to the upper limit X-ray properties determined for undetected PNe produces the results shown in Figures 7.12 and 7.13. In these figures, we display the upper limits of the X-ray luminosities of the sample PNe along with the level of  $L_X$  expected from late-type, main sequence companions spun up to saturation levels (i.e.  $L_X/L_{\text{bol}} \sim 10^{-3}$ ) and late-type, giant companions with typical emission at  $L_X/L_{\text{bol}} \sim 10^{-4}$ , respectively. Also included are the X-ray properties of binary PNe LoTr 5 (spun-up giant), HFG 1, and DS 1 (main sequence late-type companions). Based on this analysis, the upper limit X-ray luminosities constrain any putative spun-up companions to later than G0. Upper limits with no distance estimates (square upper limits in Figures 7.12 and 7.13) cast doubt on the (arbitrary) assignment of a 1 kpc distance to PNe with unknown distances, since this group is systematically fainter in upper limit X-ray luminosities than PNe with known or estimated distances.

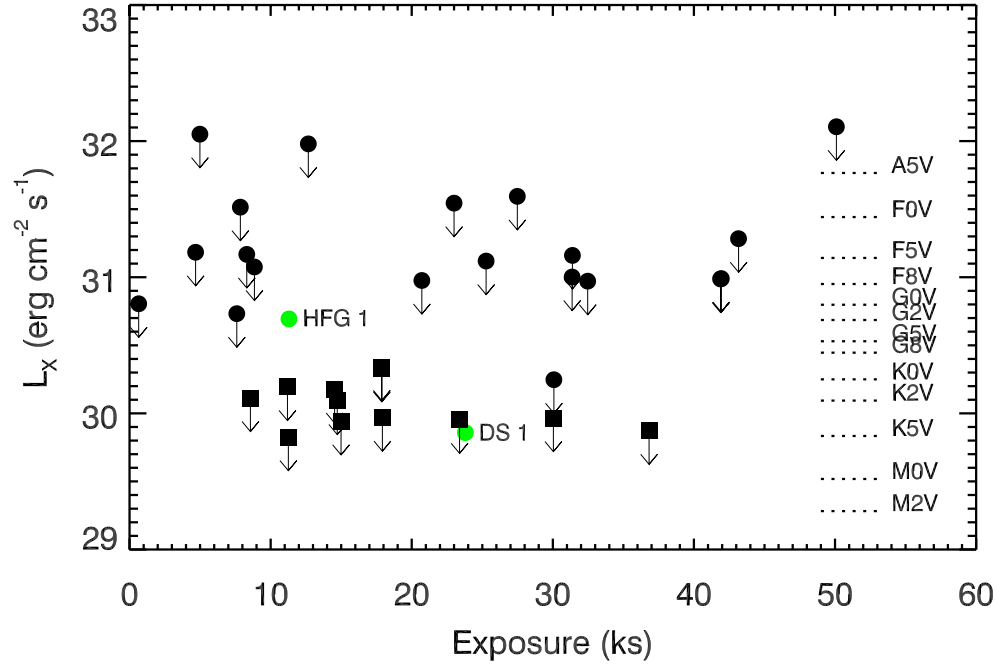


Figure 7.12 Upper Limits on Putative Spun-up Main Sequence Companions. Upper limit values of  $L_X$  determined for PNe with distance estimates are given by the filled circles (Table 7.1), while those without distance estimates are assumed to be at 1 kpc and given by the filled squares (Table 7.2). The X-ray parameters of binary PNe HFG 1 and DS 1 (Chapter 6) are included as representative of the X-ray emission from spun-up, late-type, main sequence companions. The spectral types for saturated companions ( $L_X/L_{\text{bol}} \sim 10^{-3}$ ) are included. This figure indicates that the 1 kpc distance assumed for many of the sample PNe is very likely overly optimistic.

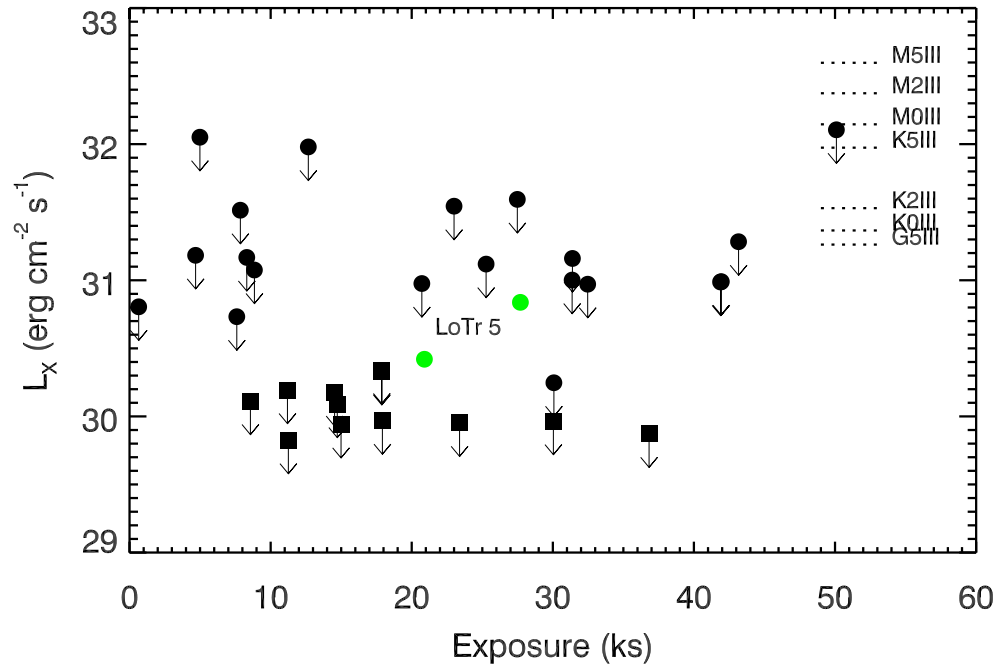


Figure 7.13 Upper Limits on Putative Spun-up Giant Companions. Similar to Figure 7.12, but assuming a spun-up giant companion ( $L_X/L_{\text{bol}} \sim 10^{-4}$ ). The X-ray parameters of binary PN LoTr 5 are included as representative of X-ray emission from a spun-up, late-type giant companion.

Table 7.1 XMMSSPNe Upper Limit Results for PNe with Distance Estimates

PN	D (kpc)	ObsID	$t_{\text{exp}}$ (ks)	CR <sub>src</sub> (n.c.r.)	CR <sub>bkg</sub> (n.c.r.)	$F_{X,\text{obs}}$ (c.g.s.)	$F_{X,\text{cool}}$ (c.g.s.)	$L_{X,\text{cool}}$ (c.g.s.)	$F_{X,\text{hot}}$ (c.g.s.)	$L_{X,\text{hot}}$ (c.g.s.)
PN H 1-13	1.6	0150220101	30.07	2.35E-07	2.54E-07	-14.760	-13.653	30.860	-14.266	30.247
PN H 1-43	13.2	0500540101	50.10	3.55E-06	3.62E-06	-14.857	-13.749	32.570	-14.214	32.105
PN H 1-54	4.4	0205800201	32.47	1.25E-06	2.54E-06	-14.874	-14.153	31.222	-14.404	30.971
PN H 2-37	3.6	0152420101	41.94	3.18E-06	3.11E-06	-14.851	-13.743	31.454	-14.208	30.990
PN H 4-1	13.1	0124710401	12.67	5.27E-06	5.81E-06	-14.502	-14.384	31.929	-14.333	31.980
Hen 2-102	3.5	0007422401	8.85	2.01E-06	1.65E-06	-14.660	-13.708	31.458	-14.091	31.075
PN K 1-16	0.4	0110950501	0.65	1.93E-04	1.73E-04	-13.083	-11.976	31.262	-12.432	30.805
PN K 3-57	4.0	0212481201	25.27	3.63E-07	3.36E-07	-14.662	-13.554	31.732	-14.167	31.119
PN K 3-92	6.8	0153752201	27.48	5.37E-07	3.90E-07	-14.660	-13.531	32.213	-14.150	31.594
PN M 1-28	2.8	0306700501	8.31	3.86E-06	4.13E-06	-14.438	-13.330	31.632	-13.795	31.168
PN M 1-29	2.4	0154750301	31.37	2.06E-06	2.07E-06	-14.325	-13.217	31.611	-13.826	31.001
PN M 1-37	4.2	0152420101	41.89	1.88E-06	1.72E-06	-14.980	-13.872	31.452	-14.337	30.987
PN M 2-19	4.0	0402280101	43.16	1.26E-06	1.25E-06	-14.494	-13.386	31.896	-13.999	31.283
PN M 2-45	2.0	0301880401	7.60	1.21E-06	1.91E-06	-14.586	-13.478	31.197	-13.943	30.733
PN M 3-17	9.1	0085581001	4.99	9.19E-07	1.25E-06	-14.596	-13.488	32.508	-13.945	32.051
PN M 3-19	4.9	0050940201	23.00	1.06E-06	9.74E-07	-14.410	-13.303	32.157	-13.916	31.544
PN M 3-28	2.7	0135741601	4.68	3.48E-06	2.77E-06	-14.400	-13.292	31.648	-13.757	31.183
PN M 3-44	2.9	0154750301	31.39	2.35E-06	2.04E-06	-14.329	-13.221	31.770	-13.830	31.160
PN M 3-46	4.3	0085581001	7.85	3.89E-07	4.95E-07	-14.335	-13.227	32.124	-13.836	31.515
PN M 3-55	2.7	0122700401	20.72	6.74E-06	4.72E-06	-14.608	-13.500	31.441	-13.965	30.976

Units: n.c.r. – normalized count rate (cnt s<sup>-1</sup> arcseconds<sup>-2</sup>), c.g.s – erg s<sup>-1</sup> cm<sup>-2</sup> ( $F_X$ ) and erg s<sup>-1</sup> ( $L_X$ ).Note:  $F_{X,\text{cool}}$  and  $L_{X,\text{cool}}$  assume  $T_X \sim 3 \times 10^6$  K,  $F_{X,\text{hot}}$  and  $L_{X,\text{hot}}$  assume  $T_X \sim 10^7$  K.

Table 7.2 XMMSSPNe Upper Limit Results for PNe with Unknown Distances

PN	D (kpc)	ObsID	$t_{\text{exp}}$ (ks)	CR <sub>src</sub> (n.c.r.)	CR <sub>bkg</sub> (n.c.r.)	$F_{X,\text{obs}}$ (c.g.s.)	$F_{X,\text{cool}}$ (c.g.s.)	$L_{X,\text{cool}}$ (c.g.s.)	$F_{X,\text{hot}}$ (c.g.s.)	$L_{X,\text{hot}}$ (c.g.s.)
PN Bl 3-10	–	0402280101	36.82	2.84E-06	2.76E-06	-14.849	-13.741	30.337	-14.206	29.872
PN Bl 3-13	–	0302570101	23.39	2.70E-06	2.54E-06	-14.769	-13.661	30.417	-14.125	29.953
PN H 1-58	–	0403110601	17.92	1.93E-06	2.10E-06	-14.752	-13.644	30.434	-14.109	29.969
PN M 3-47	–	0050940201	14.53	4.52E-06	4.40E-06	-14.546	-13.438	30.640	-13.903	30.175
PN PBOZ 10	–	0201200101	14.72	4.29E-06	3.03E-06	-14.630	-13.522	30.556	-13.987	30.091
PN SHW1 5	–	0203040101	14.99	1.90E-06	2.07E-06	-14.723	-13.734	30.344	-14.136	29.942
PN SUWT 2	–	0007422301	11.25	7.69E-07	6.81E-07	-14.896	-13.788	30.290	-14.252	29.826
Terz N 2022	–	0112971801	8.57	1.49E-06	1.95E-06	-14.608	-13.500	30.578	-13.965	30.113
PN Th 4-3	–	0306700501	11.19	5.46E-07	5.48E-07	-14.379	-13.271	30.807	-13.884	30.194
PN VBE 2	–	0204270101	17.88	2.02E-06	1.72E-06	-14.232	-13.124	30.954	-13.737	30.341
PN VBE 3	–	0204270101	17.88	2.68E-06	1.65E-06	-14.242	-13.134	30.944	-13.747	30.331
PN Vd 1-8	–	0083280401	30.04	4.58E-07	3.94E-07	-14.583	-13.475	30.603	-14.112	29.965

Units: n.c.r. – normalized count rate ( $\text{cnt s}^{-1} \text{ arcseconds}^{-2}$ ), c.g.s –  $\text{erg s}^{-1} \text{ cm}^{-2}$  ( $F_X$ ) and  $\text{erg s}^{-1}$  ( $L_X$ ).

Note:  $F_{X,\text{cool}}$  and  $L_{X,\text{cool}}$  assume  $T_X \sim 3 \times 10^6 \text{ K}$ ,  $F_{X,\text{hot}}$  and  $L_{X,\text{hot}}$  assume  $T_X \sim 10^7 \text{ K}$ .

# Chapter 8

## Summary and Conclusions

### 8.1 Unveiling Binarity

Hydrodynamical calculations which attempt to explain the vast range of PN morphologies assume dense equatorial structures exist around the central star (e.g., Frank et al. 1993). These structures collimate the fast wind of the central star, which allow the fast wind to shape the PN into the observed morphologies (see Chapters 1 and 5). One possible mechanism for the formation of this dense equatorial obstruction is a binary central star. Binary interactions may lead to preferential mass loss into the orbital plane (Mastrodemos & Morris 1998, 1999). The case for binarity's influence on the formation of PNe has become stronger in recent years (De Marco 2009, see Chapter 1, Section 1.4). Yet the known fraction of binary central stars in PNe is very low ( $\sim 17\%$ , Miszalski et al. 2009). The low detection rate of binarity in PNe is due

to the difficulty of detecting binarity in obscured nuclei of PNe and the bright emission from the dying star. I have presented a novel method to use X-ray observations of PNe to search for evidence of binarity in PNe (Chapter 6). I have argued that hard ( $T_X \sim 10^7$  K), point-like X-ray emission from the nuclei of PNe with known binary stars is consistent with the spun-up companion scenario. In this scenario, the companion of the dying star accretes angular momentum during a common envelope phase, leading to an increased rotation rate for the companion. This increased rotation rate raises the level of coronal activity on the companion, making such spun-up companions likely sources of hard X-ray emission. The hard X-ray emission in the three binary systems in the PNe LoTr 5, HFG 1, and DS 1 (Chapter 6, Section 6.4.5) are likely due to this very mechanism. I have calculated the upper limit X-ray properties of many undetected hard X-ray point sources in PNe and used these upper limits to place limits on the spectral type of a potentially spun-up companion (Chapter 7, Section 7.5). I find that roughly half of these non-detection upper limit calculations can place moderate constraints on potential F0-G0 spun-up companions. However, most of the upper limits on CSPNe with distance estimates available in the literature are too high to detect the spun-up companions in LoTr 5, HFG 1, and DS 1. The results described in Chapter 6 suggest that the hard X-ray point sources in NGC 6543 and NGC 2392 may be due to spun-up companions in these PNe. The binarity of these two PN central stars is suspected, but unknown.



## 8.2 Unveiling Wind Collisions

The theory of PNe formation (e.g. Kwok et al. 1978; Frank et al. 1993) predicts the presence of a hot gas, shocked by the collision of a fast, tenuous stellar wind with a slower, dense stellar wind. This “hot bubble” was not unambiguously observed until the high-resolution X-ray observations performed by the CXO. Preliminary results from early observations of PNe suggested that the hot bubble temperatures were too cool given the measured properties of the fast stellar winds emerging from the central stars. I have confirmed that this low temperature problem persists in all hot bubble detections of PNe (Chapters 3, 4, 5, and 7). The hot bubble evolutionary models calculated for several generic central star masses (Steffen et al. 2008) provide convincing evidence that the low temperature problem can be explained by heat conduction between the dense nebular material of the PN and the tenuous shocked gas in the hot bubble. Using these calculations, I have confirmed that many of the detected hot bubbles agree with this scenario (Chapters 3 and 7). I have calculated the upper limit X-ray properties of many undetected hot bubbles in PNe and used the central star parameters to further test the heat conduction models (Chapter 7, Section 7.4). I find that roughly half of these non-detection upper limit calculations are consistent with the calculations (Steffen et al. 2008) for lower mass central stars. While the other half do not provide adequate constraints on the existence of a hot bubble. I have identified a class of hot bubbles which do not follow the trends predicted by the calculations performed by Steffen et al. (2008) (Chapter 4). This class of hot bubbles belong to PNe with hydrogen-poor Wolf-Rayet central stars. Although these hot bubbles have well-regulated temperatures like their hydrogen-rich counterparts, they

have consistently brighter X-ray luminosities than predicted for the most massive central star calculations.

### 8.3 New Questions and Future Directions

Through this thesis I have offered new insights into the nature of PNe using X-ray observation. However, I have also raised new questions which suggest promising new avenues of research. For example, from the observed trends and developed methods, we can pose the following questions:

- Can the method developed for the binary PNe studied in this thesis be expanded to PNe with central stars of unknown multiplicity?
- Can the CSPNe X-ray parameters be combined with multi-wavelength limits on possible binary companions to determine the nature of the hard X-ray emission in PNe like NGC 6543 and NGC 2392?
- Why are the hot bubbles in PNe with hydrogen-poor, Wolf-Rayet central stars brighter than their hydrogen-rich counterparts?
- Does this suggest a difference of chemical composition of the hot gas, the conduction of heat in hydrogen-poor environments, or is it fundamental to the uncertain origin of Wolf-Rayet central stars?

Addressing these questions with future observing and modeling campaigns can increase the scientific yield from X-ray observations of PNe and expand the role of PNe

as astrophysical laboratories in the realm of binary interactions and fundamental physics in hydrogen-poor environments.



# Bibliography

2007, Asymmetrical Planetary Nebulae IV,

Acker, A., Gorny, S. K., & Cuisinier, F. 1996, A&A, 305, 944

Acker, A., Ochsenbein, F., Stenholm, B., Tylanda, R., Marcout, J., & Schohn, C.  
1994, VizieR Online Data Catalog, 5084, 0

Acker, A., Marcout, J., Ochsenbein, F., Stenholm, B., & Tylanda, R. 1992, Garching:  
European Southern Observatory, 1992,

Akashi, M., Soker, N., Behar, E., & Blondin, J. 2007, MNRAS, 375, 137

Akashi, M., Meiron, Y., & Soker, N. 2008, New Astronomy, 13, 563

Akashi, M., Soker, N., & Behar, E. 2006, MNRAS, 368, 1706

Allen, D. A. 1984, Proceedings of the Astronomical Society of Australia, 5, 369

Allen, D. A. 1983, MNRAS, 204, 113

Allen, D. A. 1980, MNRAS, 192, 521

Anders, E., & Grevesse, N. 1989, Geochim. Cosmochim. Acta, 53, 197

- Angeloni, R., Contini, M., Ciroi, S., & Rafanelli, P. 2007, *A&A*, 471, 825
- Apparao, K. M. V., & Tarafdar, S. P. 1989, *ApJ*, 344, 826
- Arnaud, K. A. 1996, *Astronomical Data Analysis Software and Systems V*, 101, 17
- Arnaud, K., Borkowski, K. J., & Harrington, J. P. 1996, *ApJ*, 462, L75
- Balick, B., & Frank, A. 2002, *ARA&A*, 40, 439
- Balick, B., & Hajian, A. R. 2004, *AJ*, 127, 2269
- Belczyński, K., Mikołajewska, J., Munari, U., Ivison, R. J., & Friedjung, M. 2000, *A&AS*, 146, 407
- Bernard-Salas, J., & Tielens, A. G. G. M. 2005, *A&A*, 431, 523
- Blackman, E. G., Frank, A., Markiel, J. A., Thomas, J. H., & Van Horn, H. M. 2001, *Nature*, 409, 485
- Blocker, T., & Schonberner, D. 1993, *Planetary Nebulae*, 155, 479
- Bohm, K. H., & Cassinelli, J. 1971, *A&A*, 12, 21
- Bond, H. E., Ciardullo, R., Fleming, T. A., & Grauer, A. D. 1989, *Planetary Nebulae*, 131, 310
- Bond, H. E. 2000, *Asymmetrical Planetary Nebulae II: From Origins to Microstructures*, 199, 115
- Bond, H. E., & Livio, M. 1990, *ApJ*, 355, 568

- Bopp, B. W., & Stencel, R. E. 1981, *ApJ*, 247, L131
- Boumis, P., Meaburn, J., Lloyd, M., & Akras, S. 2009, *MNRAS*, 396, 1186
- Bruch, A. 1992, *A&A*, 266, 237
- Cahn, J. H., Kaler, J. B., & Stanghellini, L. 1992, *A&AS*, 94, 399
- Cargill, P. J., & Klimchuk, J. A. 2006, *ApJ*, 643, 438
- Cassinelli, J. P., Cohen, D. H., Macfarlane, J. J., Sanders, W. T., & Welsh, B. Y. 1994, *ApJ*, 421, 705
- Cassinelli, J. P., Waldron, W. L., Sanders, W. T., Harnden, F. R., Jr., Rosner, R., & Vaiana, G. S. 1981, *ApJ*, 250, 677
- Chu, Y.-H., Gruendl, R. A., Guerrero, M. A., & Su, K. Y.-L. 2007, 15th European Workshop on White Dwarfs, 372, 337
- Chu, Y.-H., Gruendl, R. A., & Conway, G. M. 1998, *AJ*, 116, 1882
- Chu, Y.-H., Guerrero, M. A., Gruendl, R. A., & Webbink, R. F. 2004, *AJ*, 127, 477
- Chu, Y.-H., Guerrero, M. A., Gruendl, R. A., Williams, R. M., & Kaler, J. B. 2001, *ApJ*, 553, L69
- Churazov, E., Gilfanov, M., Forman, W., & Jones, C. 1996, *ApJ*, 471, 673
- Conway, G. M., & Chu, Y.-H. 1997, *Planetary Nebulae*, 180, 214
- Corradi, R. L. M., Sánchez-Blázquez, P., Mellema, G., Giammanco, C., & Schwarz, H. E. 2004, *A&A*, 417, 637

- Corradi, R. L. M., & Schwarz, H. E. 1993, *A&A*, 269, 462
- Cox, P., Huggins, P. J., Maillard, J.-P., Habart, E., Morisset, C., Bachiller, R., & Forveille, T. 2002, *A&A*, 384, 603
- Crowther, P. A., De Marco, O., & Barlow, M. J. 1998, *MNRAS*, 296, 367
- De Marco, O., & Barlow, M. J. 2001, *Ap&SS*, 275, 53
- de Marco, O. 2009, *PASP*, 121, 316
- De Marco, O., Hillwig, T. C., & Smith, A. J. 2008, *AJ*, 136, 323
- Dempsey, R. C., Linsky, J. L., Fleming, T. A., & Schmitt, J. H. M. M. 1993, *ApJS*, 86, 599
- Dempsey, R. C., Linsky, J. L., Schmitt, J. H. M. M., & Fleming, T. A. 1993, *ApJ*, 413, 333
- Drake, J. J., & Sarna, M. J. 2003, *ApJ*, 594, L55
- Drilling, J. S. 1985, *ApJ*, 294, L107
- Eggleton, P. P. 1983, *ApJ*, 268, 368
- Ehle, M., de la Calle, I., Daz Trigo, M., Gonzalez Riestra, R., Loiseau, N., Rodriguez, P. 2008, *XMM-Newton Users' Handbook*, Issue 2.6
- Exter, K. M., Pollacco, D. L., Maxted, P. F. L., Napiwotzki, R., & Bell, S. A. 2005, *MNRAS*, 359, 315



Feibelman, W. A., & Kaler, J. B. 1983, *ApJ*, 269, 592

Feibelman, W. A. 1994, *PASP*, 106, 756

Frank, A., Balick, B., Icke, V., & Mellema, G. 1993, *ApJ*, 404, L25

Frank, J., King, A., & Raine, D. J. 2002, *Accretion Power in Astrophysics*, by Juhan Frank and Andrew King and Derek Raine, pp. 398. ISBN 0521620538. Cambridge, UK: Cambridge University Press, February 2002.,

Frew, D., 2008, Ph.D. thesis, MacQuarie University

Fruscione, A., et al. 2006, *Proc. SPIE*, 6270,

Ghizzardi, S. 2002, XMM-Newton Calibration Documentation (XMM-SOC-CAL-TN-0029)

Górny, S. K., & Tyllenda, R. 2000, *A&A*, 362, 1008

Güdel, M. 2004, *A&A Rev.*, 12, 71

Güdel, M., & Nazé, Y. 2009, *A&A Rev.*, 17, 309

Girard, T., & Willson, L. A. 1987, *A&A*, 183, 247

Gondoin, P. 2007, *A&A*, 464, 1101

Gondoin, P. 2005, *A&A*, 444, 531

Gorny, S. K., & Stasińska, G. 1995, *A&A*, 303, 893

- Graham, M. F., Meaburn, J., López, J. A., Harman, D. J., & Holloway, A. J. 2004, MNRAS, 347, 1370
- Grauer, A. D., Bond, H. E., Ciardullo, R., & Fleming, T. A. 1987, BAAS, 19, 643
- Groth, H. G., Kudritzki, R. P., & Heber, U. 1985, A&A, 152, 107
- Gruendl, R. A., Guerrero, M. A., Chu, Y.-H., & Williams, R. M. 2006, ApJ, 653, 339
- Guerrero, M. A., Chu, Y.-H., Gruendl, R. A., & Meixner, M. 2005, A&A, 430, L69
- Guerrero, M. A., Gruendl, R. A., & Chu, Y.-H. 2002, A&A, 387, L1
- Guerrero, M. A., Chu, Y.-H., & Gruendl, R. A. 2000, ApJS, 129, 295
- Guerrero, M. A., Chu, Y.-H., Gruendl, R. A., Williams, R. M., & Kaler, J. B. 2001, ApJ, 553, L55
- Harpaz, A., & Soker, N. 1995, Asymmetrical Planetary Nebulae , 11,
- Harpaz, A., & Soker, N. 1995, Asymmetrical planetary nebulae : University of Haifa at Oranim conference. Annals of the Israel Physical Society, Vol. 11. Edited by Amos Harpaz and Noam Soker. Bristol; Philadelphia: Institute of Physics Pub.; Jerusalem: Israel Physical Society in association with the American Institute of Physics, New York, 1995.,
- Heckathorn, J. N., & Fesen, R. A. 1985, A&A, 143, 475
- Heckathorn, J. N., Fesen, R. A., & Gull, T. R. 1982, A&A, 114, 414
- Herwig, F. 2001, Ap&SS, 275, 15

- Hilditch, R. W., Harries, T. J., & Hill, G. 1996, MNRAS, 279, 1380
- Hjellming, M. S., & Taam, R. E. 1991, ApJ, 370, 709
- Iben, I., Jr., & Livio, M. 1993, PASP, 105, 1373
- Jasniewicz, G., Thevenin, F., Monier, R., & Skiff, B. A. 1996, A&A, 307, 200
- Jeffries, R. D., & Stevens, I. R. 1996, MNRAS, 279, 180
- Jordan, S., Wolff, B., Koester, D., & Napiwotzki, R. 1994, A&A, 290, 834
- Kaastra, J.S. 1992, An X-Ray Spectral Code for Optically Thin Plasmas (Internal SRON-Leiden Report, updated version 2.0)
- Kaler, J. B., Shaw, R. A., Feibelman, W. A., & Lutz, J. H. 1989, ApJS, 70, 213
- Kastner, J. H., Soker, N., & Rappaport, S. 2000, Asymmetrical Planetary Nebulae II: From Origins to Microstructures, 199,
- Kastner, J. H., Balick, B., Blackman, E. G., Frank, A., Soker, N., Vrtílek, S. D., & Li, J. 2003, ApJ, 591, L37
- Kastner, J. H., Li, J., Vrtilek, S. D., Gatley, I., Merrill, K. M., & Soker, N. 2002, ApJ, 581, 1225
- Kastner, J. H., Montez, R., Jr., Balick, B., & De Marco, O. 2008, ApJ, 672, 957
- Kastner, J. H., Soker, N., Vrtilek, S. D., & Dgani, R. 2000, ApJ, 545, L57
- Kastner, J. H., Vrtilek, S. D., & Soker, N. 2001, ApJ, 550, L189

- Kenny, H. T., & Taylor, A. R. 2005, *ApJ*, 619, 527
- Koesterke, L., Dreizler, S., & Rauch, T. 1998, *A&A*, 330, 1041
- Kreysing, H. C., Diesch, C., Zweigle, J., Staubert, R., Grewing, M., & Hasinger, G. 1992, *A&A*, 264, 623
- Kuczawska, E., & Mikolajewski, M. 1993, *Acta Astronomica*, 43, 445
- Kwok, S., Purton, C. R., & Fitzgerald, P. M. 1978, *ApJ*, 219, L125
- Kwok, S. 2000, *The origin and evolution of planetary nebulae / Sun Kwok*. Cambridge ; New York : Cambridge University Press, 2000. (Cambridge astrophysics series ; 33),
- Landolt, A. U., & Drilling, J. S. 1986, *AJ*, 91, 1372
- Leuenhagen, U., Hamann, W.-R., & Jeffery, C. S. 1996, *A&A*, 312, 167
- Li, J., Harrington, J. P., & Borkowski, K. J. 2002, *AJ*, 123, 2676
- Li, J., Kastner, J. H., Prigozhin, G. Y., & Schulz, N. S. 2003, *ApJ*, 590, 586
- Liedahl, D. A., Osterheld, A. L., & Goldstein, W. H. 1995, *ApJ*, 438, L115
- Longmore, A. J., & Tritton, S. B. 1980, *MNRAS*, 193, 521
- Luna, G. J. M., & Costa, R. D. D. 2005, *A&A*, 435, 1087
- Mürset, U., & Schmid, H. M. 1999, *A&AS*, 137, 473
- Malasan, H. L., Yamasaki, A., & Kondo, M. 1991, *AJ*, 101, 2131

- Marcolino, W. L. F., Hillier, D. J., de Araujo, F. X., & Pereira, C. B. 2007, *ApJ*, 654, 1068
- Marsh, M. C., et al. 1997, *MNRAS*, 286, 369
- Martin, J., Xilouris, K., & Soker, N. 2002, *A&A*, 391, 689
- Mastrodemos, N., & Morris, M. 1999, *ApJ*, 523, 357
- Mastrodemos, N., & Morris, M. 1998, *ApJ*, 497, 303
- Mathioudakis, M., Fruscione, A., Drake, J. J., McDonald, K., Bowyer, S., & Malina, R. F. 1995, *A&A*, 300, 775
- Meaburn, J., Lopez, J. A., Bryce, M., & Mellema, G. 1996, *A&A*, 307, 579
- Medina Tanco, G. A., & Steiner, J. E. 1995, *AJ*, 109, 1770
- Meixner, M., Kastner, J. H., Balick, B., & Soker, N. 2004, *Asymmetrical Planetary Nebulae III: Winds, Structure and the Thunderbird*, 313,
- Mendez, R. H., Kudritzki, R. P., Herrero, A., Husfeld, D., & Groth, H. G. 1988, *A&A*, 190, 113
- Mewe, R., Gronenschild, E. H. B. M., & van den Oord, G. H. J. 1985, *A&AS*, 62, 197
- Mewe, R., Lemen, J. R., & van den Oord, G. H. J. 1986, *A&AS*, 65, 511
- Miszalski, B., Acker, A., Parker, Q. A., & Moffat, A. F. J. 2009, *A&A*, 505, 249
- Modigliani, A., Patriarchi, P., & Perinotto, M. 1993, *ApJ*, 415, 258

- Montez, R., Jr., Kastner, J. H., De Marco, O., & Soker, N. 2005, *ApJ*, 635, 381
- Morrison, R., & McCammon, D. 1983, *ApJ*, 270, 119
- Motch, C., Werner, K., & Pakull, M. W. 1993, *A&A*, 268, 561
- Muerset, U., Jordan, S., & Walder, R. 1995, *A&A*, 297, L87
- Muerset, U., Wolff, B., & Jordan, S. 1997, *A&A*, 319, 201
- Mukai, K. 1993, *Legacy*, vol. 3, p.21-31, 3, 21
- Mullan, D. J., Mathioudakis, M., Bloomfield, D. S., & Christian, D. J. 2006, *ApJS*, 164, 173
- Ness, J.-U., Güdel, M., Schmitt, J. H. M. M., Audard, M., & Telleschi, A. 2004, *A&A*, 427, 667
- Nordhaus, J., Blackman, E. G., & Frank, A. 2007, *MNRAS*, 376, 599
- O'Dwyer, I. J., Chu, Y.-H., Gruendl, R. A., Guerrero, M. A., & Webbink, R. F. 2003, *AJ*, 125, 2239
- Owocki, S. P., Castor, J. I., & Rybicki, G. B. 1988, *ApJ*, 335, 914
- Paczynski, B. 1976, *Structure and Evolution of Close Binary Systems*, 73, 75
- Pallavicini, R., Golub, L., Rosner, R., Vaiana, G. S., Ayres, T., & Linsky, J. L. 1981, *ApJ*, 248, 279
- Pauldrach, A., Puls, J., Kudritzki, R. P., Mendez, R. H., & Heap, S. R. 1988, *A&A*, 207, 123

- Peimbert, M., Peimbert, A., Ruiz, M. T., & Esteban, C. 2004, *ApJS*, 150, 431
- Peña, M., Stasińska, G., & Medina, S. 2001, *A&A*, 367, 983
- Pearson, K. J., Horne, K., & Skidmore, W. 2004, *IAU Colloq. 190: Magnetic Cateclysmic Variables*, 315, 279
- Pearson, K. J., Horne, K., & Skidmore, W. 2005, *ApJ*, 619, 999
- Pereira, C. B., Landaberry, S. J. C., & Junqueira, S. 1998, *A&A*, 333, 658
- Perinotto, M., Cerruti-Sola, M., & Lamers, H. J. G. L. M. 1989, *ApJ*, 337, 382
- Phillips, J. P. 2003, *MNRAS*, 344, 501
- Pismis, P., Manteiga, M., & Mampaso Recio, A. 2000, *Asymmetrical Planetary Nebulae II: From Origins to Microstructures*, 199, 397
- Pizzolato, N., Maggio, A., Micela, G., Sciortino, S., & Ventura, P. 2003, *A&A*, 397, 147
- Pottasch, S. R., & Surendiranath, R. 2007, *A&A*, 462, 179
- Pottasch, S. R., Beintema, D. A., Bernard Salas, J., Koornneef, J., & Feibelman, W. A. 2002, *A&A*, 393, 285
- Pottasch, S. R., Wesselius, P. R., Wu, C.-C., & van Duinen, R. J. 1977, *A&A*, 54, 435
- Preibisch, T., & Feigelson, E. D. 2005, *ApJS*, 160, 390

- Preite-Martinez, A., Acker, A., Koeppen, J., & Stenholm, B. 1991, *A&AS*, 88, 121
- Preite-Martinez, A., Acker, A., Koeppen, J., & Stenholm, B. 1989, *A&AS*, 81, 309
- Preite-Martinez, A., & Pottasch, S. R. 1983, *A&A*, 126, 31
- Press, W. H., Teukolsky, S. A., Vetterling, W. T., & Flannery, B. P. 1992, Cambridge: University Press, —c1992, 2nd ed.,
- Quireza, C., Rocha-Pinto, H. J., & Maciel, W. J. 2007, *A&A*, 475, 217
- Raymond, J. C. 2009, *A&A*, 500, 311
- Rice, M., Schwarz, H., & Monteiro, H. 2004, *Bulletin of the American Astronomical Society*, 36, 1572
- Ricker, P. M., & Taam, R. E. 2008, *ApJ*, 672, L41
- Rosner, R., Tucker, W. H., & Vaiana, G. S. 1978, *ApJ*, 220, 643
- Sahai, R., Kastner, J. H., Frank, A., Morris, M., & Blackman, E. G. 2003, *ApJ*, 599, L87
- Sanz-Forcada, J., Brickhouse, N. S., & Dupree, A. K. 2003, *ApJS*, 145, 147
- Sarna, M. J., Dhillon, V. S., Marsh, T. R., & Marks, P. B. 1995, *MNRAS*, 272, L41
- Schonberner, D., & Drilling, J. S. 1984, *ApJ*, 278, 702
- Schreiber, M. R., Gänsicke, B. T. 2003, *A&A*, 406, 305
- Serber, A. V. 1990, *Soviet Ast.*, 34, 291



- Shimanskii, V. V., Borisov, N. V., Sakhibullin, N. A., & Surkov, A. E. 2004, *Astronomy Reports*, 48, 563
- Snowden, S. L. 2002, arXiv:astro-ph/0203311
- Soker, N. 2004, *A&A*, 414, 943
- Soker, N. 2006, *ApJ*, 640, 966
- Soker, N. 2004, *New Astronomy*, 9, 399
- Soker, N., & Kastner, J. H. 2003, *ApJ*, 583, 368
- Soker, N., & Kastner, J. H. 2002, *ApJ*, 570, 245
- Stassun, K. G., Ardila, D. R., Barsony, M., Basri, G., & Mathieu, R. D. 2004, *AJ*, 127, 3537
- Steffen, M., Schönberner, D., & Warmuth, A. 2008, *A&A*, 489, 173
- Strassmeier, K. G., Hubl, B., & Rice, J. B. 1997, *A&A*, 322, 511
- Stute, M., & Sahai, R. 2006, *ApJ*, 651, 882
- Swings, P. 1940, *ApJ*, 92, 289
- Tarafdar, S. P., & Apparao, K. M. V. 1988, *ApJ*, 327, 342
- Thevenin, F., & Jasiewicz, G. 1997, *A&A*, 320, 913
- Thomas, J. H., Markiel, J. A., & van Horn, H. M. 1995, *ApJ*, 453, 403
- Tout, C. A., & Pringle, J. E. 1992, *MNRAS*, 256, 269

- Tylenda, R., Stasińska, G., Acker, A., & Stenholm, B. 1991, *A&A*, 246, 221
- Uttley, P., & McHardy, I. M. 2001, *MNRAS*, 323, L26
- Volk, K., & Kwok, S. 1985, *A&A*, 153, 79
- Walder, R. 1998, *Ap&SS*, 260, 243
- Walter, F. M., & Bowyer, S. 1981, *ApJ*, 245, 671
- Watson, M. G., et al. 2001, *A&A*, 365, L51
- Watson, M. G., et al. 2009, *A&A*, 493, 339
- Weisskopf, M. C., Wu, K., Trimble, V., O'Dell, S. L., Elsner, R. F., Zavlin, V. E., & Kouveliotou, C. 2007, *ApJ*, 657, 1026
- Whitelock, P. A. 1987, *PASP*, 99, 573
- Willson, L. A., Wallerstein, G., Brugel, E. W., & Stencel, R. E. 1984, *A&A*, 133, 154
- Yu, Y. S., Nordon, R., Kastner, J. H., Houck, J., Behar, E., & Soker, N. 2009, *ApJ*, 690, 440
- Zhekov, S. A., & Perinotto, M. 1998, *A&A*, 334, 239
- Zhekov, S. A., & Perinotto, M. 1996, *A&A*, 309, 648

# Appendix A

## Tables and Data for the XMM Serendipitous Survey of PNe

### A.1 Survey Sample Tables and Data

Table A.1: XMM Serendipitously Observed PNe: Observations

No.	Name	ObsID	$t_{exp}$ (ks) [pn,MOS1,MOS2]	Offset (')	Q
1	PN BL 3-10	0206590201	19.0, 20.7, 20.7	12.7	
		0085581801	5.2, 7.6, 7.6	14.9	F
		0402280101	42.2, 43.8, 43.8	12.6	
		0206590101	15.2, 13.2, 13.2	11.9	
		0085581501	5.1, 6.8, 6.8	14.9	F
2	PN BL 3-13	0302570101	27.2, 31.2, 31.2	11.5	
		0203040201	33.5, 31.2, 31.2	11.4	

(continued on next page)

Table A.1 (continued from previous page)

No.	Name	ObsID	$t_{exp}$ (ks) [pn,MOS1,MOS2]	Offset (')	Q
3	PN H 1-13	0150220101	19.9, 30.5, 30.5	10.7	
4	PN H 1-43	0032940101	15.5, 18.3, 18.3	6.1	
		0203750101	41.7, 45.7, 45.7	4.3	
5	PN H 1-54	0157960101	9.4, 16.7, 16.7	11.6	
		0205800201	36.7, 38.4, 38.4	12.4	
6	PN H 1-58	0403110601	20.4, 22.0, 22.0	7.4	
7	PN H 2-37	0152420101	48.0, 49.7, 49.7	7.5	
8	PN H 4-1	0124710501	25.2, 26.0, 26.0	8.9	G
		0124710401	20.0, 19.0, 19.2	9.7	
9	PN HATR 8	0301881001	14.4, 16.0, 14.8	12.4	F
		0301880101	4.1, 5.0, 5.0	14.6	F
10	PN HB 5	0152920101	50.3, 52.0, 52.0	7.3	
11	HEN 2-81	0103260901	4.9, 6.6, 6.6	9.3	T
12	HEN 2-96	0140350101	42.0, 40.7, 40.7	10.3	G
13	HEN 2-102	0007422401	10.0, 12.3, 12.3	3.5	
14	HEN 2-207	0200680201	24.7, 26.7, 26.7	14.5	F
15	PN K 1-16	0110950501	4.9, 5.0, 5.0	2.3	T
16	PN K 3-57	0212481201	24.7, 25.5, 25.6	11.1	
17	PN K 3-92	0153752001	31.3, 33.0, 33.0	14.3	F
		0153751801	20.6, 22.3, 22.3	13.0	F
		0004010101	7.8, 7.7, 7.7	14.9	F
		0004010201	22.2, 22.1, 22.1	14.9	F
		0153752101	19.5, 17.0, 17.0	14.5	F
		0153752201	27.0, 28.7, 28.7	9.1	
		0153751701	20.6, 20.4, 20.4	11.1	
18	PN LOTR 5	0012850201	24.1, 26.4, 26.4	6.3	

(continued on next page)

Table A.1 (continued from previous page)

No.	Name	ObsID	$t_{exp}$ (ks) [pn,MOS1,MOS2]	Offset (')	Q
19	PN M 1-28	0306700501	10.1, 11.6, 11.6	7.9	
20	PN M 1-29	0154750301	33.7, 35.0, 35.2	13.7	
		0202790101	18.1, 21.4, 21.7	11.9	
21	PN M 1-37	0152420101	48.0, 49.7, 49.7	14.3	
22	PN M 1-43	0152835401	7.0, 8.7, 8.7	6.7	
		0152835501	7.1, 8.7, 8.7	13.7	
23	PN M 2-19	0206590201	19.0, 20.7, 20.7	12.6	
		0206590101	15.2, 13.2, 13.2	13.9	
		0402280101	42.2, 43.8, 43.8	12.6	
24	PN M 2-20	0206590101	15.2, 13.2, 13.2	13.52	F
		0206590201	19.0, 20.7, 20.7	14.0	F
25	PN M 2-21	0050940201	20.0, 24.0, 24.0	13.6	F
26	PN M 2-34	0304220401	12.9, 13.1, 13.1	10.5	
27	PN M 2-45	0301880401	8.5, 10.2, 10.2	6.3	
28	PN M 3-17	0085580201	7.1, 9.1, 9.1	14.3	
		0085581001	5.3, 7.9, 7.9	14.3	
		0085581101	5.0, 6.7, 6.7	12.4	
29	PN M 3-19	0050940201	20.0, 24.0, 24.0	12.4	
30	PN M 3-28	0135741601	5.5, 7.8, 7.8	7.3	T
31	PN M 3-44	0202790101	18.1, 21.4, 21.7	14.2	F
		0154750301	33.7, 35.0, 35.2	13.2	
32	PN M 3-46	0085581101	5.0, 6.7, 6.7	12.2	
		0085580201	7.1, 9.1, 9.1	10.6	
		0085581001	5.3, 7.9, 7.9	10.6	
33	PN M 3-47	0050940201	20.0, 24.0, 24.0	7.7	
34	PN M 3-55	0122700401	29.6, 28.9, 28.9	9.2	

(continued on next page)

Table A.1 (continued from previous page)

No.	Name	ObsID	$t_{exp}$ (ks) [pn,MOS1,MOS2]	Offset (')	Q
35	NGC 6543	0112310401	4.7, 5.8, 5.9	9.0	
		0112310801	5.8, 7.5, 7.5	8.8	
36	PN PBOZ 10	0201200101	16.1, 17.6, 17.6	8.9	
37	PN PE 1-11	0203040501	24.7, 28.7, 28.7	13.9	F
38	PN SHWI 5	0203040101	17.5, 21.5, 21.5	11.3	
		0050940101	20.0, 24.0, 24.0	9.4	
39	PN SUWT 2	0007422301	12.7, 15.0, 15.0	13.2	
		0007421401	10.0, 12.3, 12.3	12.0	
40	Terz N 2022	0112971801	9.9, 14.6, 14.6	11.6	
41	PN TH 4-3	0306700501	10.1, 11.6, 11.6	12.3	
42	Terz N 41	0112410101	9.6, 12.2, 12.2	14.8	F
43	PN VBE 2	0400890101	57.1, 54.4, 54.5	7.5	
		0204270101	46.1, 49.0, 49.0	7.25	
44	PN VBE 3	0204270101	46.1, 49.0, 49.0	9.1	
45	PN VD 1-8	0083280201	32.0, 32.0, 32.6	7.8	
		0083280101	24.7, 25.2, 26.1	7.8	
		0083280401	30.5, 30.4, 31.0	7.8	
		0083280301	19.8, 19.8, 20.4	7.8	
46	WRAY 16-128	0152131201	3.5, 9.7, 9.7	5.5	
		0152130101	1.6, 3.4, 3.4	5.9	
47	WRAY 16-146	0204010101	22.7, 18.4, 18.3	14.6	F
48	WRAY 16-158	0103261001	5.0, 5.7, 5.7	13.4	T
49	WRAY 17-107	0152420101	48.0, 49.7, 49.7	14.4	F

Quality column (Q) notes: X – target is not covered by the observation (CCD chip is switched off or in subarray mode), F – target is outside the FOV, G – target falls in a chip gap, and T – exposure time is too short for useful scientific products.

Table A.2: Serendipitously Observed Symbiotic Systems

No.	Name	ObsID	$t_{exp}$ (ks) [pn,MOS1,MOS2]	Offset (')	Q
1	PN H 1-36	0139560101	44.9, 45.6, 45.1	4.4	
		0405510701	–, –, –	6.0	X
2	PN M 3-18	0099760201	48.0, 50.0, 50.0	0.2	

Quality column (Q) notes: X – target is not covered by the observation (CCD chip is switched off or in subarray mode), F – target is outside the FOV, G – target falls in a chip gap, and T – exposure time is too short for useful scientific products.

Table A.3: Removed Objects and Observations

Name	Type	ObsID	$\theta$ (')	Name	Type	ObsID	$\theta$ (')
19W96	HII	0302884101	14.7	ESO 209-13	PN?	0401790301	15.0
		0302883201	9.0	PN PM 1-135	PN?	0502080101	9.2
		0302882501	9.0	PN RPZM 3	PN?	0203470501	7.9
		0302882701	14.4			0093670201	6.0
		0112970501	11.3	PN RPZM 39	PN?	0152920101	12.9
		0302883901	9.5	PN RPZM 48	PN?	0400340101	13.2
		0504940101	9.5	PN SHWI 2	PN?	0050940101	13.8
PN CN 1-1	?	0401670301	1.1			0203040101	14.2
PN H 2-12	SNR	0084100101	2.4	PN SHWI 4	PN?	0203040101	14.4
WHBE 1	HII	0400910301	10.5			0050940101	13.0
PN AL 2-N	PN?	0510010401	9.9	PN ST 2-128	PN?	0304220401	3.6
PN BL 3-14	PN?	0307110101	7.4	TDC 2	PN?	0136030101	14.4
WRAY 17-73	PN?	0204250101	11.1	WRAY 16-203	PN?	0146310201	2.8
		0208010101	6.				



Table A.4: XMM Serendipitously Observed PNe: Basic Data

Name	$R_{nebula}$ (")	$D$ (kpc)	$D_{statistical}$ (kpc)	$\log N_H(\text{cm}^{-2})$	$T_{\text{eff}}$ (kK)
PN BL 3-10	4.50	—	—	—	121.9 (PM91)
PN BL 3-13	2.60	—	—	—	20.0 (Ty91)
PN H 1-13	4.80	—	0.80,2.49	—	74.6 (PM89)
PN H 1-43	1.00	—	13.20	—	27.5 (Ph03)
PN H 1-54	2.40	—	3.00,4.90,5.46	21.4836 (C92)	37.0 (Ph03)
PN H 1-58	3.15	—	—	—	47.5 (Ph03)
PN H 2-37	2.10	—	2.00,5.26	—	62.1 (PM89)
PN H 4-1	1.35	—	9.90,11.87,12.70,17.80	20.6543 (C92)	81.7 (Ph03)
PN HATR 8	6.00	—	—	—	—
PN HB 5	7.50	2.00,2.00	0.69,0.84,1.20,1.24	21.8492 (C92)	107.0 (Ph03)
HEN 2-81	3.20	—	0.90,3.43	—	124.0 (PM89)
HEN 2-96	2.00	—	0.90,3.91	—	56.4 (PM91)
HEN 2-102	4.50	—	2.60,3.51,3.89,4.00	21.6243 (C92)	74.1 (PM91)
HEN 2-207	17.50	—	—	—	130.4 (PM91)
PN K 1-16	57.00	0.38	1.00,1.30,2.50	0.0000 (C92)	94.7 (Ph03)
PN K 3-57	3.00	—	4.02	—	—
PN K 3-92	6.10	—	6.81	21.7118 (C92)	46.8 (Ph03)
PN LOTR 5	262.50	0.40	6.29	0.0000 (C92)	—
PN M 1-28	7.40	—	2.29,2.40,2.89,3.50	—	—
PN M 1-29	3.80	—	0.70,2.03,2.80,3.07	—	99.5 (PM89)
PN M 1-37	—	—	4.20	—	31.5 (Ph03)
PN M 1-43	2.60	—	0.70,3.15	—	23.0 (Ph03)
PN M 2-19	4.10	—	1.00,3.17,3.66,8.18	—	32.4 (Ty91)
PN M 2-20	3.30	—	—	—	37.2 (Ty91)
PN M 2-21	3.60	—	6.14	21.2911 (C92)	65.5 (Ph03)

(continued on next page)

Table A.4 – continued from previous page

Name	$R_{nebula}$ (")	$D$ (kpc)	$D_{statistical}$ (kpc)	$\log N_H$ (cm $^{-2}$ )	$T_{eff}$ (kK)
PN M 2-34	4.20	–	2.00,3.17,3.78	–	146.1 (PM89)
PN M 2-45	3.20	–	1.40,1.63,2.42,2.50	–	55.5 (PM89)
PN M 3-17	2.50	–	9.10	–	63.2 (Ph03)
PN M 3-19	2.85	–	2.20,4.60,5.05,7.80	–	–
PN M 3-28	4.50	–	0.90,2.27,2.80,4.86	–	130.5 (PM89)
PN M 3-44	2.20	–	1.00,2.80,3.51,4.11	–	26.3 (PM89)
PN M 3-46	2.10	–	2.60,6.05	–	22.4 (Ty91)
PN M 3-47	–	–	–	–	–
PN M 3-55	3.60	–	1.40,3.13,3.56	–	72.2 (PM89)
NGC 6543	9.75	0.89	0.55,0.64,0.65,0.70	20.6543 (C92)	63.0 (Ph03)
PN PBOZ 10	–	–	–	–	–
PN PE 1-11	4.40	–	2.30,3.89,6.43	–	151.5 (PM89)
PN SHWI 5	2.00	–	–	21.6358 (C92)	119.2 (PM89)
PN SUWT 2	32.50	–	–	–	–
Terz N 2022	6.00	–	–	–	–
PN TH 4-3	–	–	–	–	–
Terz N 41	5.80	–	–	–	–
PN VBE 2	–	–	–	–	–
PN VBE 3	6.00	–	–	–	–
PN VD 1-8	–	–	–	–	100.5 (PM89)
WRAY 16-128	9.00	–	–	–	–
WRAY 16-146	–	–	–	–	–
WRAY 16-158	–	–	–	–	–
WRAY 17-107	6.00	–	–	–	–

Extinction references: C92 – Cahn et al. (1992). Effective temperature references: Ty91 – Tyllenda et al. (1991), Ph03 – Phillips (2003), PM89 – Preite-Martinez et al. (1989), and PM91 – Preite-Martinez et al. (1991).

## A.2 Non-Detections

Tables and plots of the basic information, images, and the results of calculations of the upper limit X-ray flux and luminosity of undetected PNe in the serendipitous survey presented in Chapter 7 are presented in this section of the Appendix.

## PN B1 3-10 , ObsID 0206590101

Table A.5 Summary of the Analysis for the XMM EPIC observation (ObsID 0206590101) of PN B1 3-10.

Basic Data			
Parameter	Value	Notes	
RA (J2000)	268.835571		
DEC (J2000)	-29.960036	Offset (')	11.83
$R_{\text{nebula}}$ (")	4.5	from literature (A94)	
$D$ (kpc)	1.0	unknown, assumed value	
$\log N_H$ (cm <sup>-2</sup> )	21.6990	unknown, assumed value	
$T_{\text{eff}}$ (kK)	121.90	HeI or HeII Zanstra (Ph03)	
Date Obs:	2004-04-06	XMM Filter:	Medium

Calculations			
Parameter	EMOS1	EMOS2	EPN
$t_{\text{exp}}$ (ks)	7.5	8.6	–
$\text{CR}_{\text{src}}$ (cnt s <sup>-1</sup> )	7.962E-06	6.488E-06	–
$\text{CR}_{\text{bkg}}$ (cnt s <sup>-1</sup> )	7.483E-06	7.151E-06	–

Hot Bubble Upper Limits ( $T_X \sim 3 \times 10^6$ K)			
Parameter	EMOS1	EMOS2	EPN
$F_X$ (erg cm <sup>-2</sup> s <sup>-1</sup> )	-12.6160	-12.6550	–
$L_X$ (erg s <sup>-1</sup> )	31.4619	31.4229	–

Spun-up Companion Upper Limits ( $T_X \sim 10^7$ K)			
Parameter	EMOS1	EMOS2	EPN
$F_X$ (erg cm <sup>-2</sup> s <sup>-1</sup> )	-13.2291	-13.2680	–
$L_X$ (erg s <sup>-1</sup> )	30.8488	30.8099	–
$L_*$ ( $L_{\text{sun}}$ )	1.8363	1.6788	–
$M_{\text{bol}}$ (mag)	4.0801	4.1775	–
Spectral Type	F8-G0V	F8-G0V	–

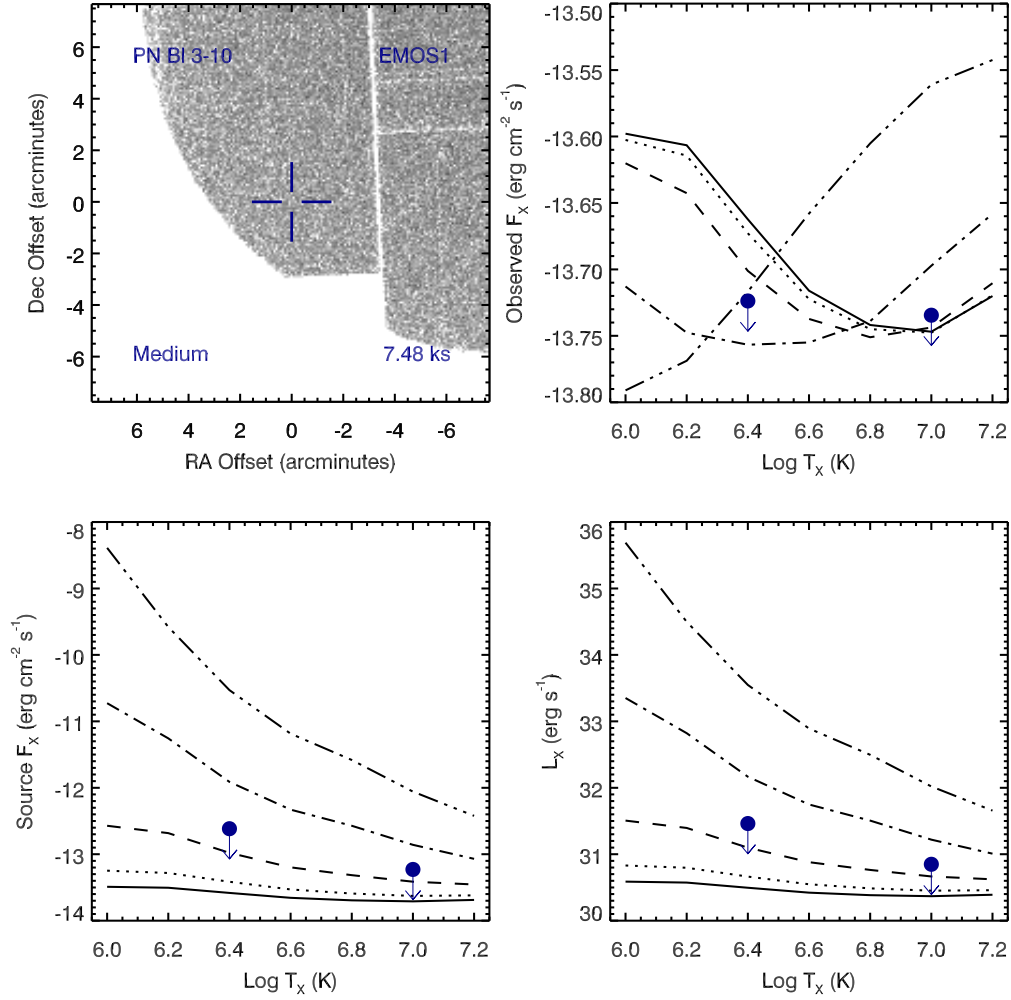


Figure A.1 Serendipitous XMM EMOS1 observation (ObsID 0206590101) of PN BI 3-10. Clock-wise from top-left: broad band (0.3 to 8.0 keV) image at the PN position, upper limits of the observed flux, X-ray luminosity, and source X-ray flux. The upper limits calculations are based on the upper limit count rates, a thermal plasma model at a range temperatures, and a range of intervening absorption values:  $N_H(10^{22} \text{ cm}^{-2}) = 0.03$  (solid), 0.1 (dotted), 0.3 (dashed), 1 (dot-dashed), and 3 (dot-dot-dashed). The hot bubble and spun-up companion upper limits are depicted as the filled circles with downward pointing arrows at  $\log T_x$  of 6.4 and 7.0, respectively.

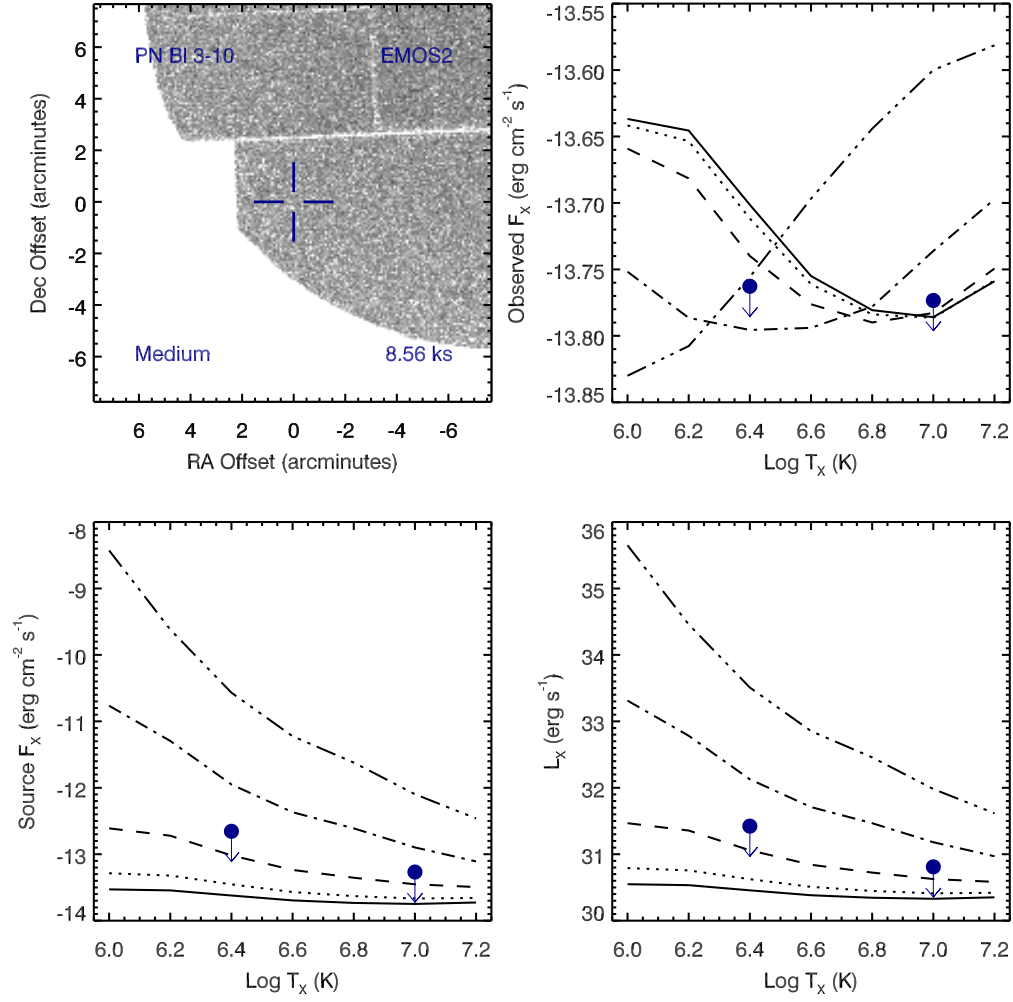


Figure A.2 Serendipitous XMM EMOS2 observation (ObsID 0206590101) of PN Bl 3-10 ; panels as in Figure A.1.

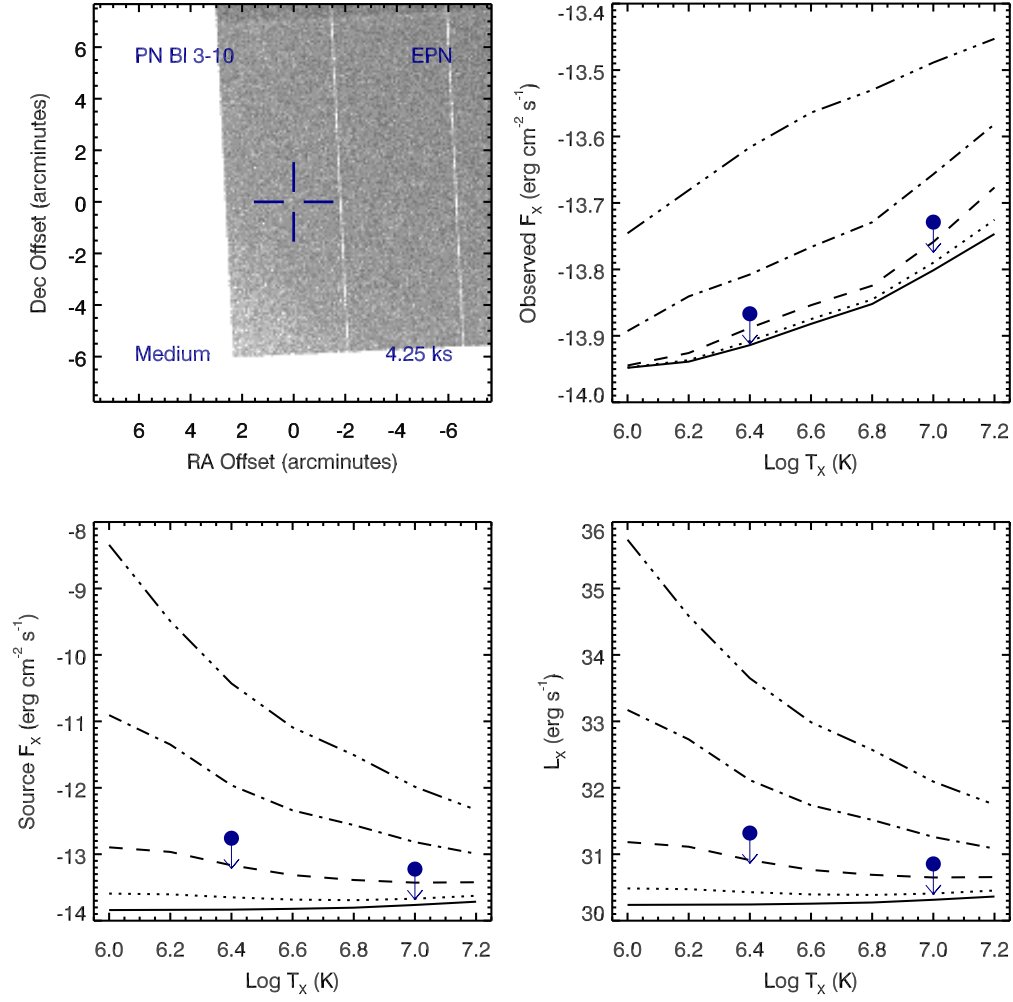


Figure A.3 Serendipitous XMM EPN observation (ObsID 0206590101) of PN Bl 3-10 ; panels as in Figure A.1.

## PN B1 3-10 , ObsID 0206590201

Table A.6 Summary of the Analysis for the XMM EPIC observation (ObsID 0206590201) of PN B1 3-10.

Basic Data			
Parameter	Value	Notes	
RA (J2000)	268.835571		
DEC (J2000)	-29.960036	Offset (')	11.83
$R_{\text{nebula}}$ (")	4.5	from literature (A94)	
$D$ (kpc)	1.0	unknown, assumed value	
$\log N_H$ (cm <sup>-2</sup> )	21.6990	unknown, assumed value	
$T_{\text{eff}}$ (kK)	121.90	HeI or HeII Zanstra (Ph03)	
Date Obs:	2004-09-05	XMM Filter:	Medium

Calculations			
Parameter	EMOS1	EMOS2	EPN
$t_{\text{exp}}$ (ks)	20.3	20.4	–
$\text{CR}_{\text{src}}$ (cnt s <sup>-1</sup> )	8.271E-07	7.004E-07	–
$\text{CR}_{\text{bkg}}$ (cnt s <sup>-1</sup> )	7.600E-07	8.976E-07	–

Hot Bubble Upper Limits ( $T_X \sim 3 \times 10^6$ K)			
Parameter	EMOS1	EMOS2	EPN
$F_X$ (erg cm <sup>-2</sup> s <sup>-1</sup> )	-13.3296	-13.2939	–
$L_X$ (erg s <sup>-1</sup> )	30.7483	30.7840	–

Spun-up Companion Upper Limits ( $T_X \sim 10^7$ K)			
Parameter	EMOS1	EMOS2	EPN
$F_X$ (erg cm <sup>-2</sup> s <sup>-1</sup> )	-13.9427	-13.9069	–
$L_X$ (erg s <sup>-1</sup> )	30.1352	30.1710	–
$L_*$ ( $L_{\text{sun}}$ )	0.3551	0.3856	–
$M_{\text{bol}}$ (mag)	5.8642	5.7748	–
Spectral Type	K0-K2V	K0-K2V	–



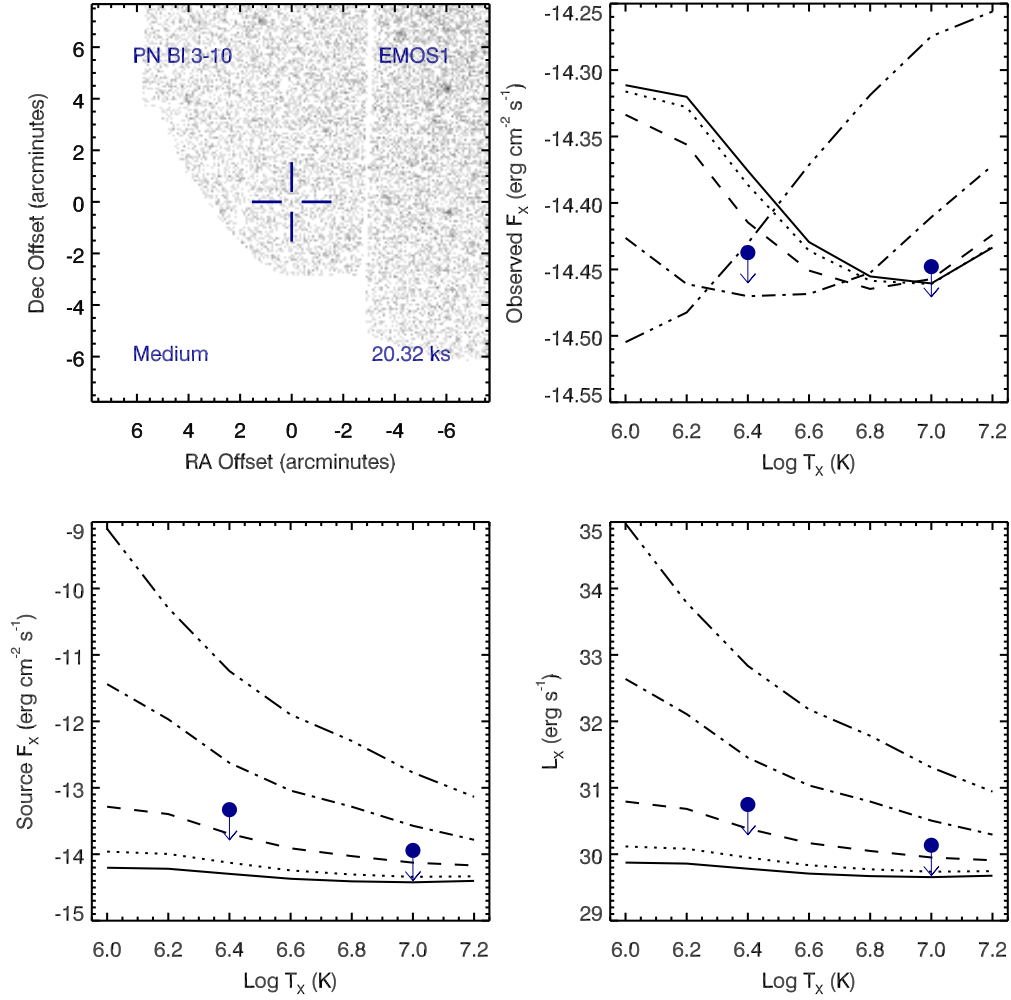


Figure A.4 Serendipitous XMM EMOS1 observation (ObsID 0206590201) of PN BI 3-10. Clock-wise from top-left: broad band (0.3 to 8.0 keV) image at the PN position, upper limits of the observed flux, X-ray luminosity, and source X-ray flux. The upper limits calculations are based on the upper limit count rates, a thermal plasma model at a range temperatures, and a range of intervening absorption values:  $N_H(10^{22} \text{ cm}^{-2}) = 0.03$  (solid), 0.1 (dotted), 0.3 (dashed), 1 (dot-dashed), and 3 (dot-dot-dashed). The hot bubble and spun-up companion upper limits are depicted as the filled circles with downward pointing arrows at  $\log T_x$  of 6.4 and 7.0, respectively.

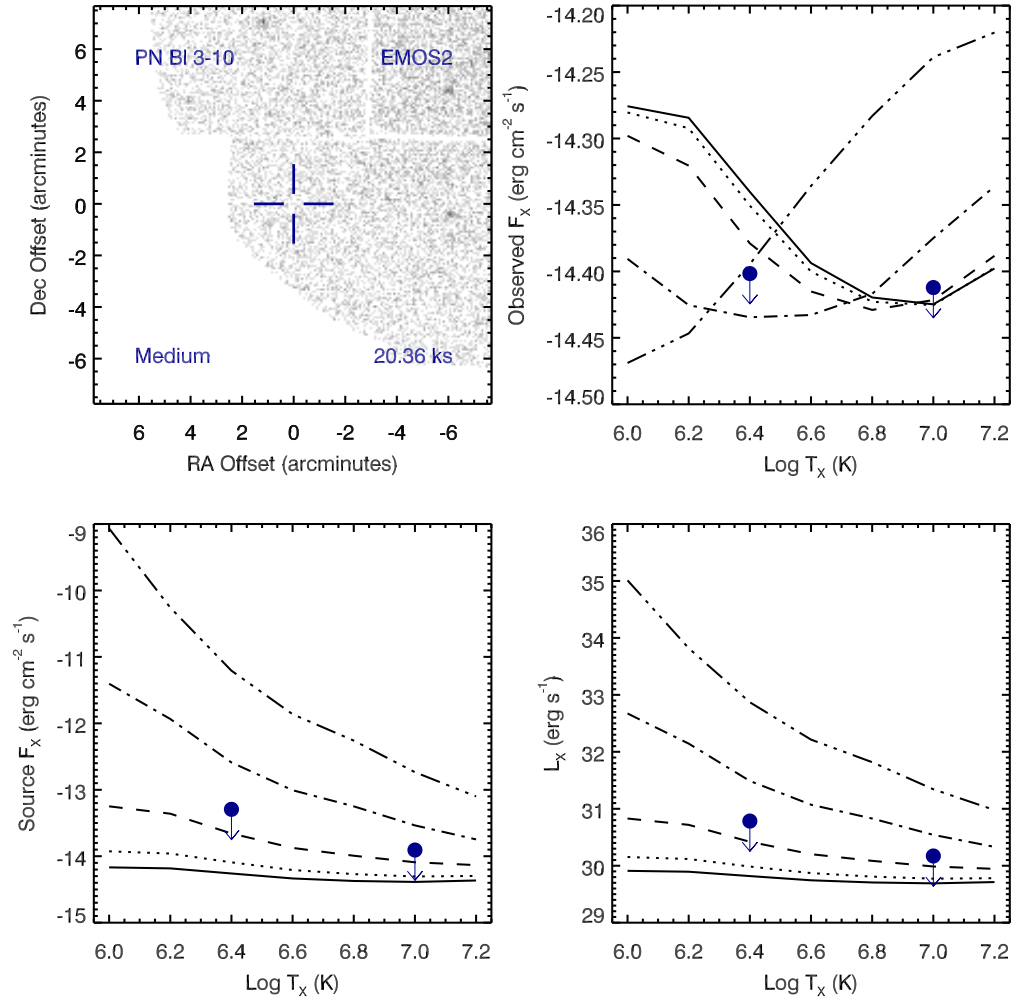


Figure A.5 Serendipitous XMM EMOS2 observation (ObsID 0206590201) of PN BI 3-10 ; panels as in Figure A.4.

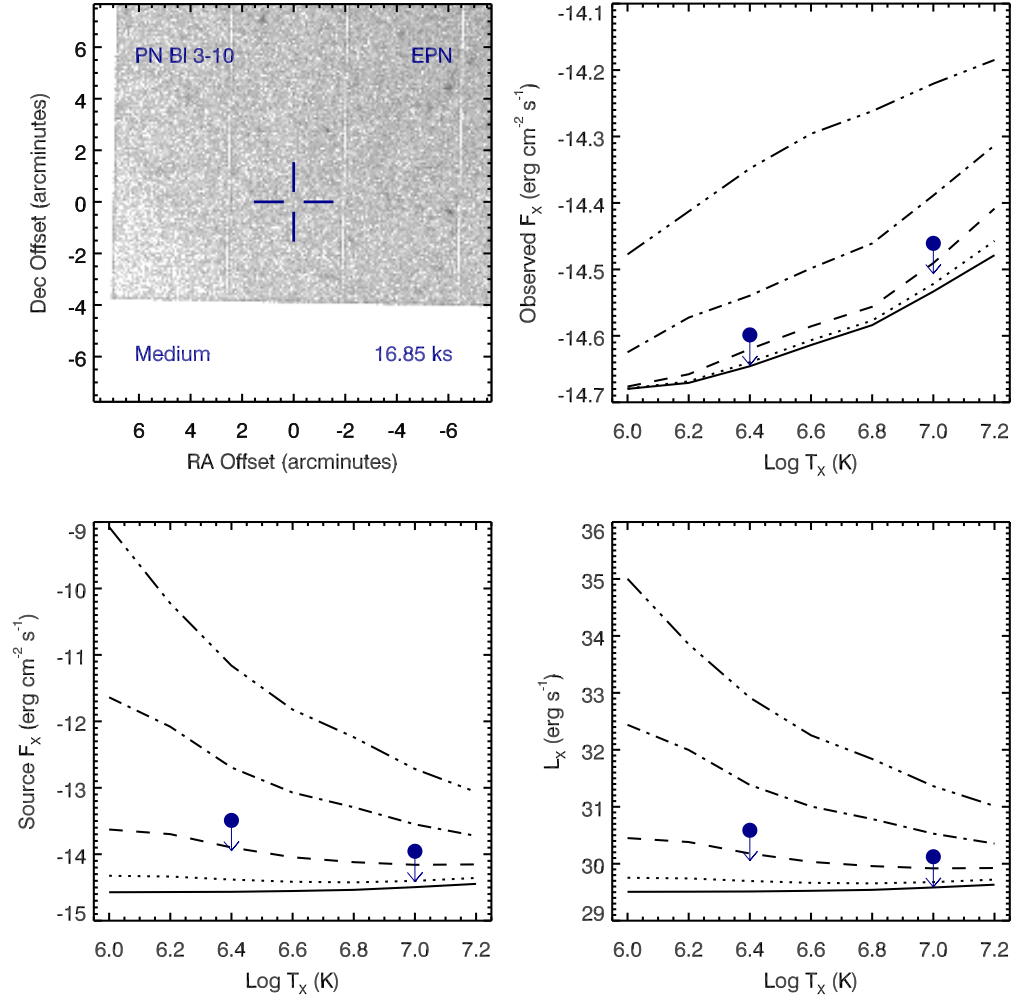


Figure A.6 Serendipitous XMM EPN observation (ObsID 0206590201) of PN Bl 3-10 ; panels as in Figure A.4.

## PN B1 3-10 , ObsID 0402280101

Table A.7 Summary of the Analysis for the XMM EPIC observation (ObsID 0402280101) of PN B1 3-10.

Basic Data			
Parameter	Value	Notes	
RA (J2000)	268.835571		
DEC (J2000)	-29.960036	Offset (')	11.83
$R_{\text{nebula}}$ (")	4.5	from literature (A94)	
$D$ (kpc)	1.0	unknown, assumed value	
$\log N_H$ (cm <sup>-2</sup> )	21.6990	unknown, assumed value	
$T_{\text{eff}}$ (kK)	121.90	HeI or HeII Zanstra (Ph03)	
Date Obs:	2006-09-10	XMM Filter:	Medium

Calculations			
Parameter	EMOS1	EMOS2	EPN
$t_{\text{exp}}$ (ks)	43.2	43.2	–
$\text{CR}_{\text{src}}$ (cnt s <sup>-1</sup> )	7.788E-07	7.429E-07	–
$\text{CR}_{\text{bkg}}$ (cnt s <sup>-1</sup> )	7.047E-07	8.489E-07	–

Hot Bubble Upper Limits ( $T_X \sim 3 \times 10^6$ K)			
Parameter	EMOS1	EMOS2	EPN
$F_X$ (erg cm <sup>-2</sup> s <sup>-1</sup> )	-13.5096	-13.4693	–
$L_X$ (erg s <sup>-1</sup> )	30.5683	30.6086	–

Spun-up Companion Upper Limits ( $T_X \sim 10^7$ K)			
Parameter	EMOS1	EMOS2	EPN
$F_X$ (erg cm <sup>-2</sup> s <sup>-1</sup> )	-14.1226	-14.0823	–
$L_X$ (erg s <sup>-1</sup> )	29.9553	29.9956	–
$L_*$ ( $L_{\text{sun}}$ )	0.2347	0.2574	–
$M_{\text{bol}}$ (mag)	6.3139	6.2133	–
Spectral Type	K2-K5V	K2-K5V	–

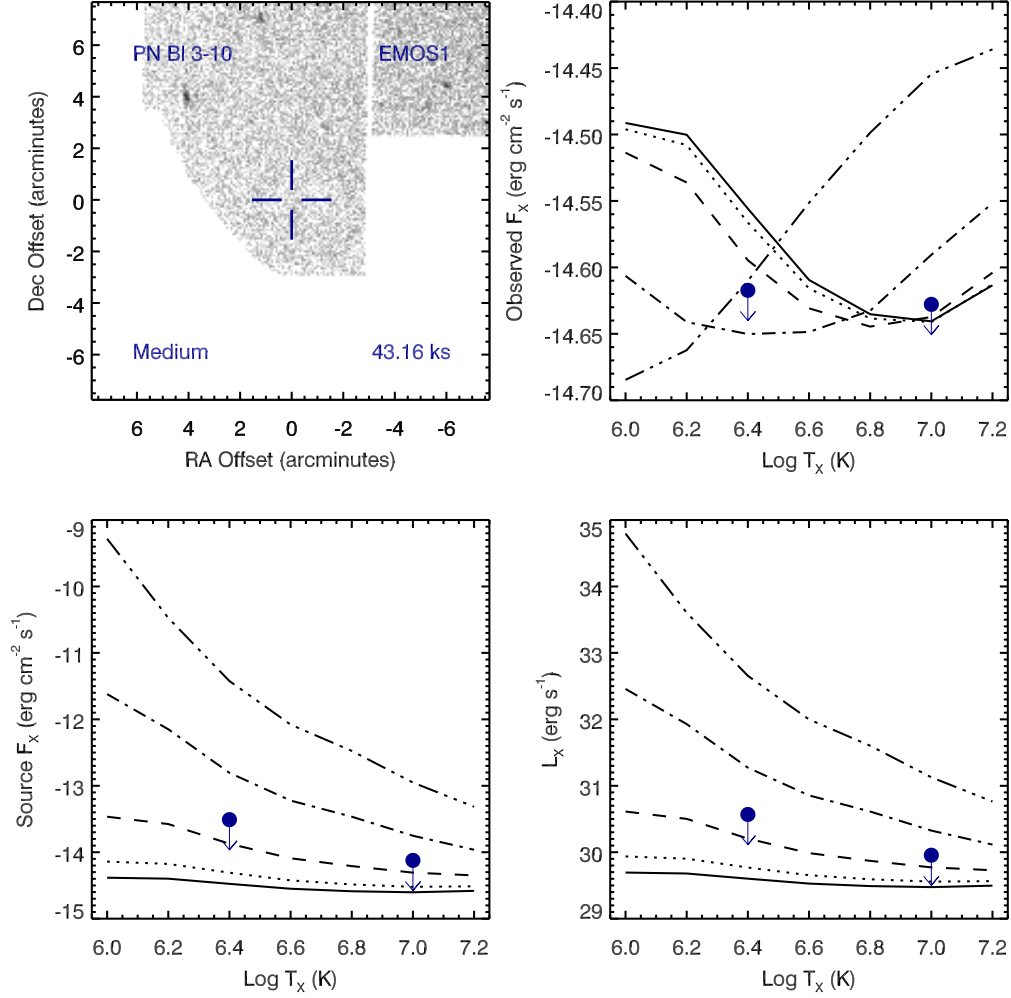


Figure A.7 Serendipitous XMM EMOS1 observation (ObsID 0402280101) of PN BI 3-10. Clock-wise from top-left: broad band (0.3 to 8.0 keV) image at the PN position, upper limits of the observed flux, X-ray luminosity, and source X-ray flux. The upper limits calculations are based on the upper limit count rates, a thermal plasma model at a range temperatures, and a range of intervening absorption values:  $N_H(10^{22} \text{ cm}^{-2}) = 0.03$  (solid), 0.1 (dotted), 0.3 (dashed), 1 (dot-dashed), and 3 (dot-dot-dashed). The hot bubble and spun-up companion upper limits are depicted as the filled circles with downward pointing arrows at  $\log T_X$  of 6.4 and 7.0, respectively.

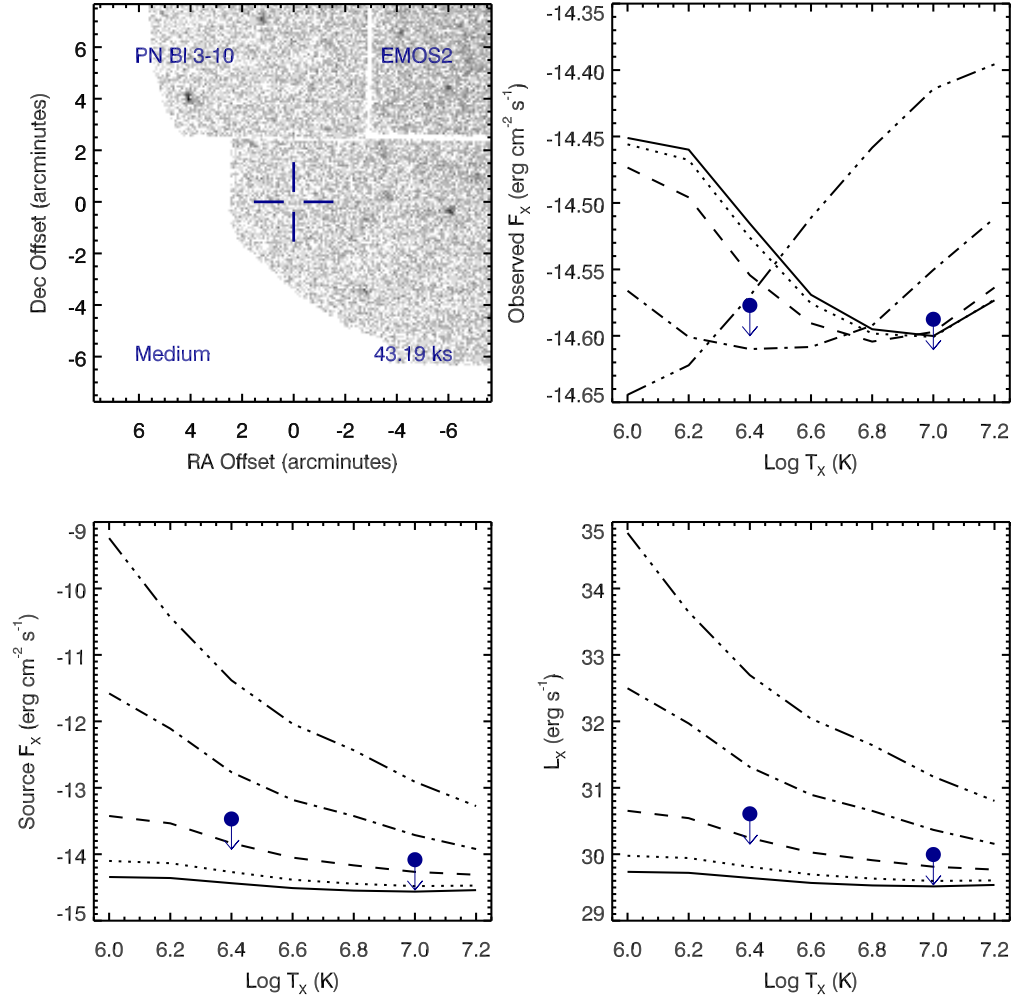


Figure A.8 Serendipitous XMM EMOS2 observation (ObsID 0402280101) of PN BI 3-10 ; panels as in Figure A.7.

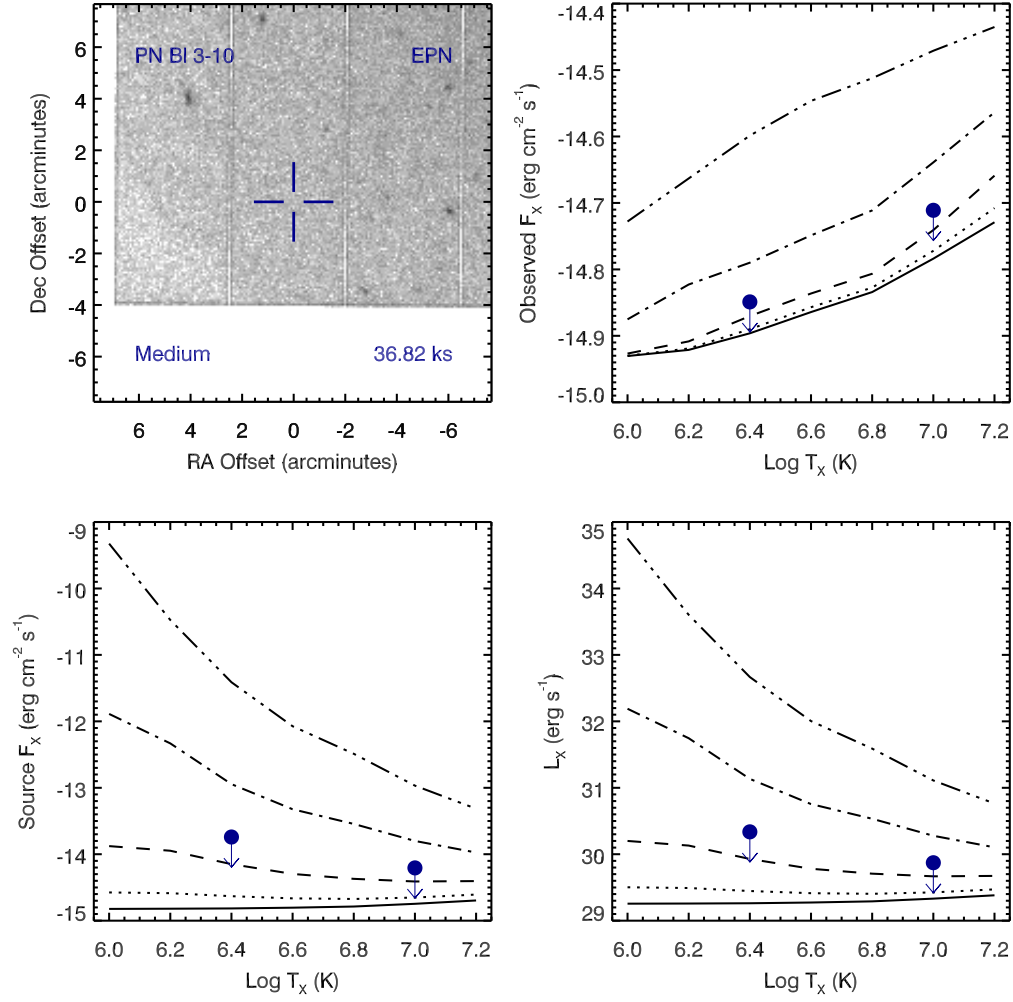


Figure A.9 Serendipitous XMM EPN observation (ObsID 0402280101) of PN Bl 3-10 ; panels as in Figure A.7.

## PN B1 3-13 , ObsID 0203040201

Table A.8 Summary of the Analysis for the XMM EPIC observation (ObsID 0203040201) of PN B1 3-13.

Basic Data			
Parameter	Value	Notes	
RA (J2000)	269.011496		
DEC (J2000)	-29.187836	Offset (')	11.49
$R_{\text{nebula}}$ (")	2.6	from literature (A94)	
$D$ (kpc)	1.0	unknown, assumed value	
$\log N_H$ ( $\text{cm}^{-2}$ )	21.6990	unknown, assumed value	
$T_{\text{eff}}$ (kK)	20.00	HeI or HeII Zanstra (Ph03)	
Date Obs:	2004-02-28	XMM Filter:	Medium

Calculations			
Parameter	EMOS1	EMOS2	EPN
$t_{\text{exp}}$ (ks)	–	23.2	–
$\text{CR}_{\text{src}}$ ( $\text{cnt s}^{-1}$ )	–	2.629E-06	–
$\text{CR}_{\text{bkg}}$ ( $\text{cnt s}^{-1}$ )	–	2.946E-06	–

Hot Bubble Upper Limits ( $T_X \sim 3 \times 10^6$ K)			
Parameter	EMOS1	EMOS2	EPN
$F_X$ ( $\text{erg cm}^{-2} \text{ s}^{-1}$ )	–	-13.0646	–
$L_X$ ( $\text{erg s}^{-1}$ )	–	31.0133	–

Spun-up Companion Upper Limits ( $T_X \sim 10^7$ K)			
Parameter	EMOS1	EMOS2	EPN
$F_X$ ( $\text{erg cm}^{-2} \text{ s}^{-1}$ )	–	-13.6776	–
$L_X$ ( $\text{erg s}^{-1}$ )	–	30.4003	–
$L_*$ ( $L_{\text{sun}}$ )	–	0.6538	–
$M_{\text{bol}}$ (mag)	–	5.2014	–
Spectral Type	–	G8-K0V	–



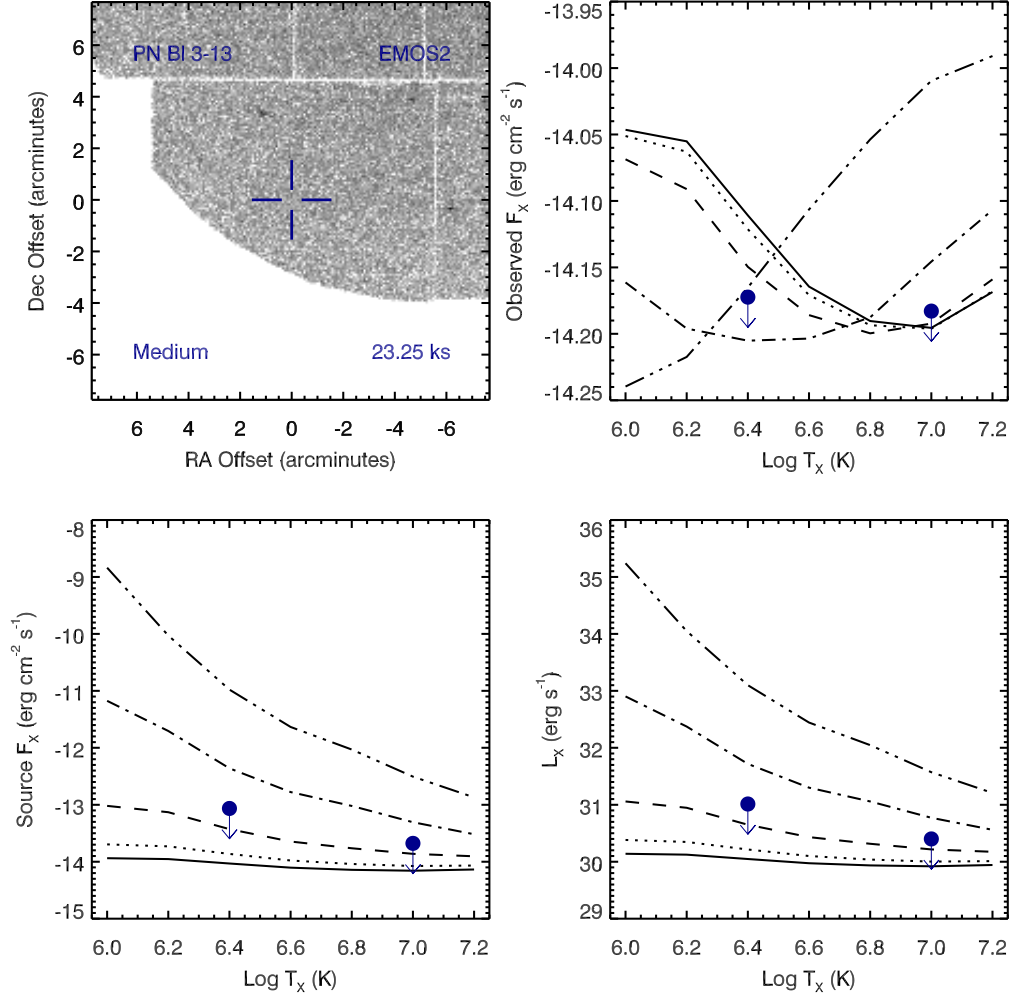


Figure A.10 Serendipitous XMM EMOS2 observation (ObsID 0203040201) of PN Bl 3-13. Clock-wise from top-left: broad band (0.3 to 8.0 keV) image at the PN position, upper limits of the observed flux, X-ray luminosity, and source X-ray flux. The upper limits calculations are based on the upper limit count rates, a thermal plasma model at a range temperatures, and a range of intervening absorption values:  $N_H(10^{22} \text{ cm}^{-2}) = 0.03$  (solid), 0.1 (dotted), 0.3 (dashed), 1 (dot-dashed), and 3 (dot-dot-dashed). The hot bubble and spun-up companion upper limits are depicted as the filled circles with downward pointing arrows at  $\log T_X$  of 6.4 and 7.0, respectively.

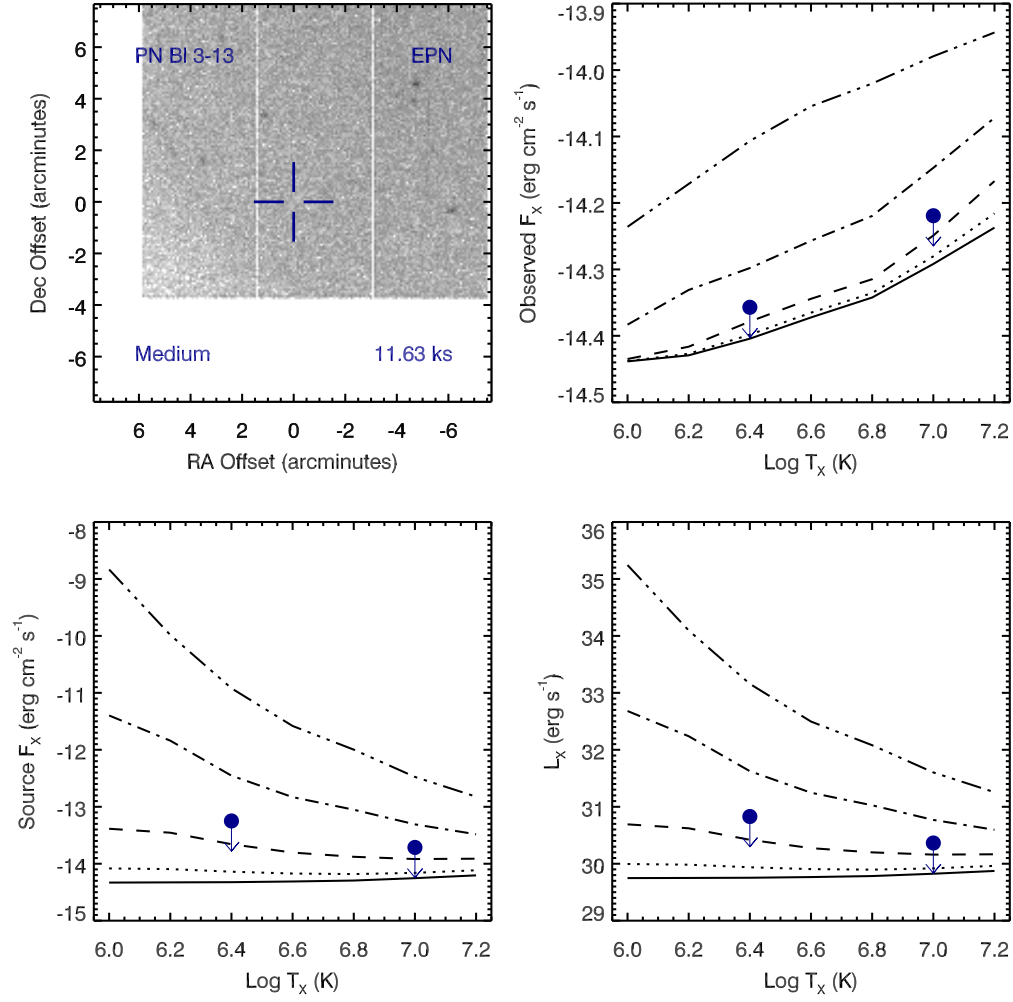


Figure A.11 Serendipitous XMM EPN observation (ObsID 0203040201) of PN Bl 3-13 ; panels as in Figure A.10.

## PN B1 3-13 , ObsID 0302570101

Table A.9 Summary of the Analysis for the XMM EPIC observation (ObsID 0302570101) of PN B1 3-13.

Basic Data			
Parameter	Value	Notes	
RA (J2000)	269.011496		
DEC (J2000)	-29.187836	Offset (')	11.49
$R_{\text{nebula}}$ (")	2.6	from literature (A94)	
$D$ (kpc)	1.0	unknown, assumed value	
$\log N_H$ (cm $^{-2}$ )	21.6990	unknown, assumed value	
$T_{\text{eff}}$ (kK)	20.00	HeI or HeII Zanstra (Ph03)	
Date Obs:	2005-10-04	XMM Filter:	Medium

Calculations			
Parameter	EMOS1	EMOS2	EPN
$t_{\text{exp}}$ (ks)	30.8	30.8	–
$\text{CR}_{\text{src}}$ (cnt s $^{-1}$ )	8.941E-07	1.059E-06	–
$\text{CR}_{\text{bkg}}$ (cnt s $^{-1}$ )	6.416E-07	8.232E-07	–

Hot Bubble Upper Limits ( $T_X \sim 3 \times 10^6$ K)			
Parameter	EMOS1	EMOS2	EPN
$F_X$ (erg cm $^{-2}$ s $^{-1}$ )	-13.4564	-13.4025	–
$L_X$ (erg s $^{-1}$ )	30.6215	30.6754	–

Spun-up Companion Upper Limits ( $T_X \sim 10^7$ K)			
Parameter	EMOS1	EMOS2	EPN
$F_X$ (erg cm $^{-2}$ s $^{-1}$ )	-14.0694	-14.0155	–
$L_X$ (erg s $^{-1}$ )	30.0085	30.0624	–
$L_*$ ( $L_{\text{sun}}$ )	0.2652	0.3003	–
$M_{\text{bol}}$ (mag)	6.1810	6.0463	–
Spectral Type	K2-K5V	K2-K5V	–

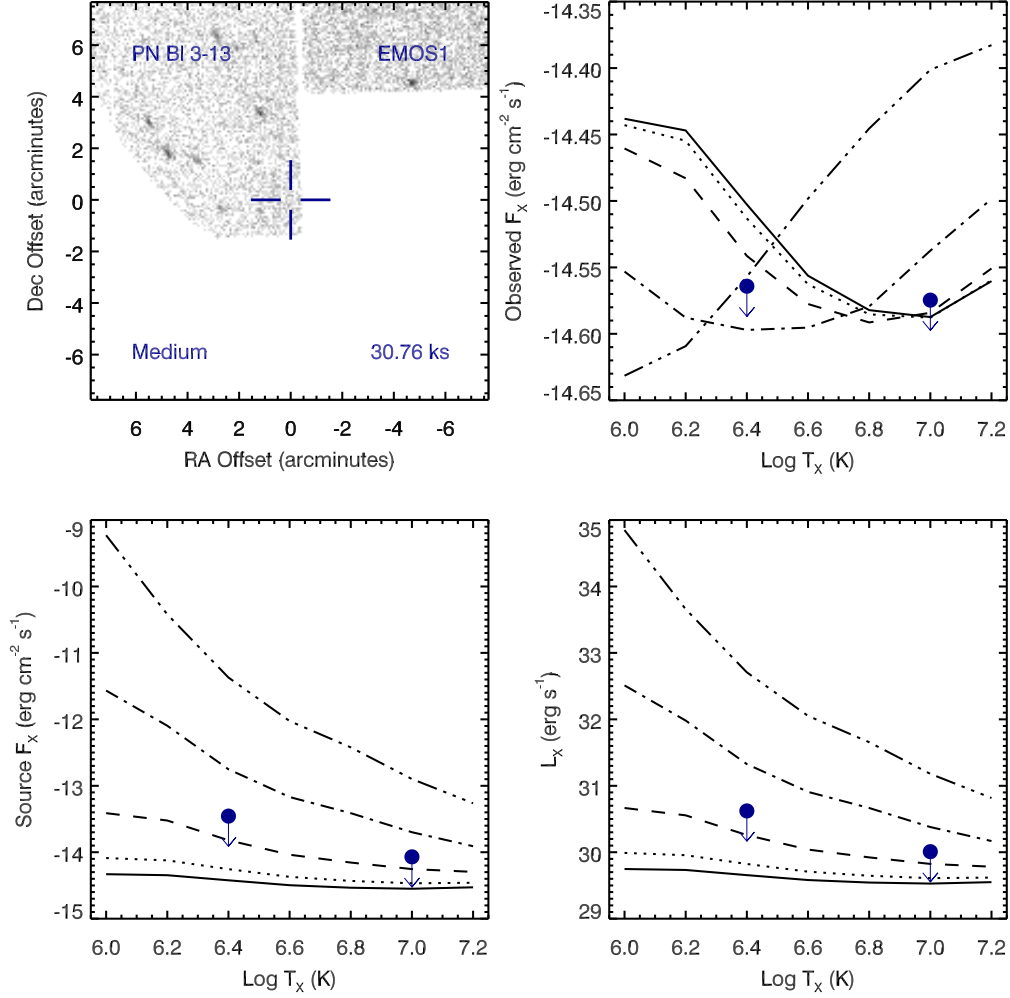


Figure A.12 Serendipitous XMM EMOS1 observation (ObsID 0302570101) of PN BI 3-13. Clock-wise from top-left: broad band (0.3 to 8.0 keV) image at the PN position, upper limits of the observed flux, X-ray luminosity, and source X-ray flux. The upper limits calculations are based on the upper limit count rates, a thermal plasma model at a range temperatures, and a range of intervening absorption values:  $N_H(10^{22} \text{ cm}^{-2}) = 0.03$  (solid), 0.1 (dotted), 0.3 (dashed), 1 (dot-dashed), and 3 (dot-dot-dashed). The hot bubble and spun-up companion upper limits are depicted as the filled circles with downward pointing arrows at  $\log T_x$  of 6.4 and 7.0, respectively.

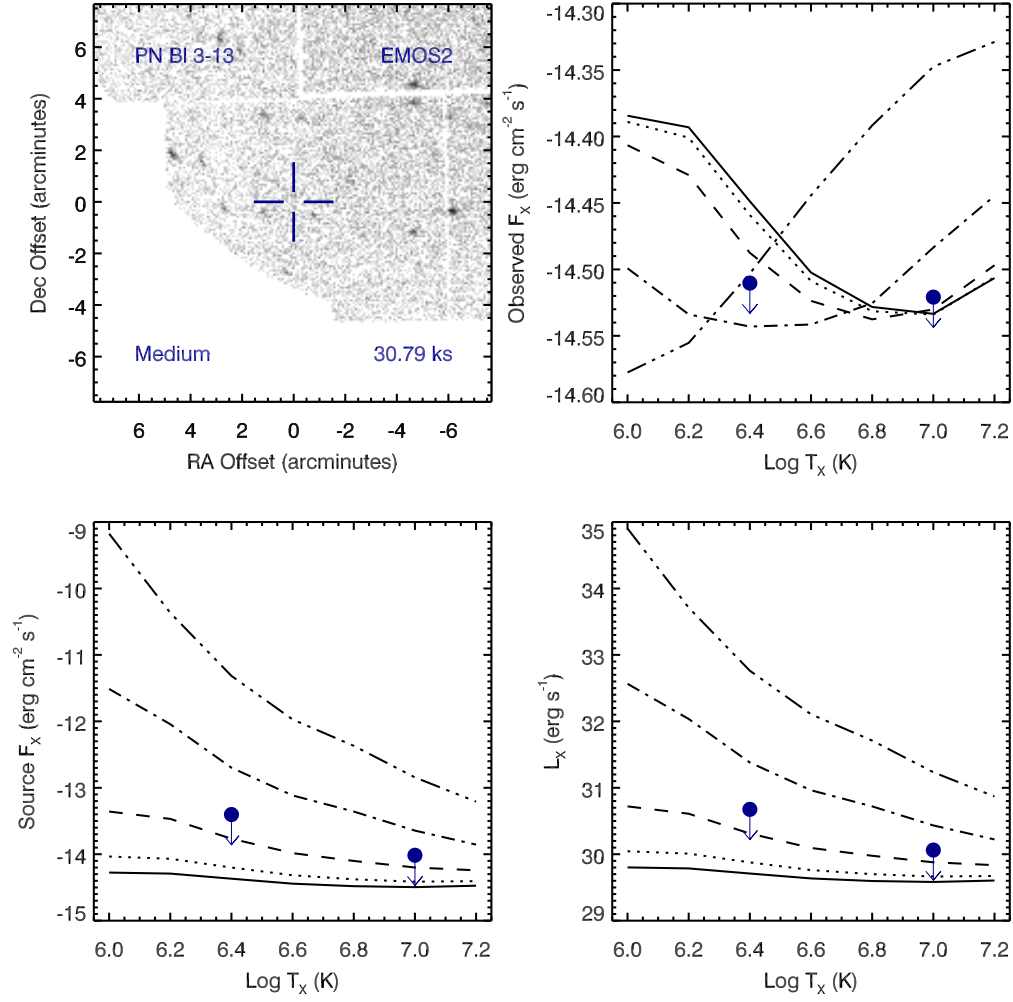


Figure A.13 Serendipitous XMM EMOS2 observation (ObsID 0302570101) of PN BI 3-13 ; panels as in Figure A.12.

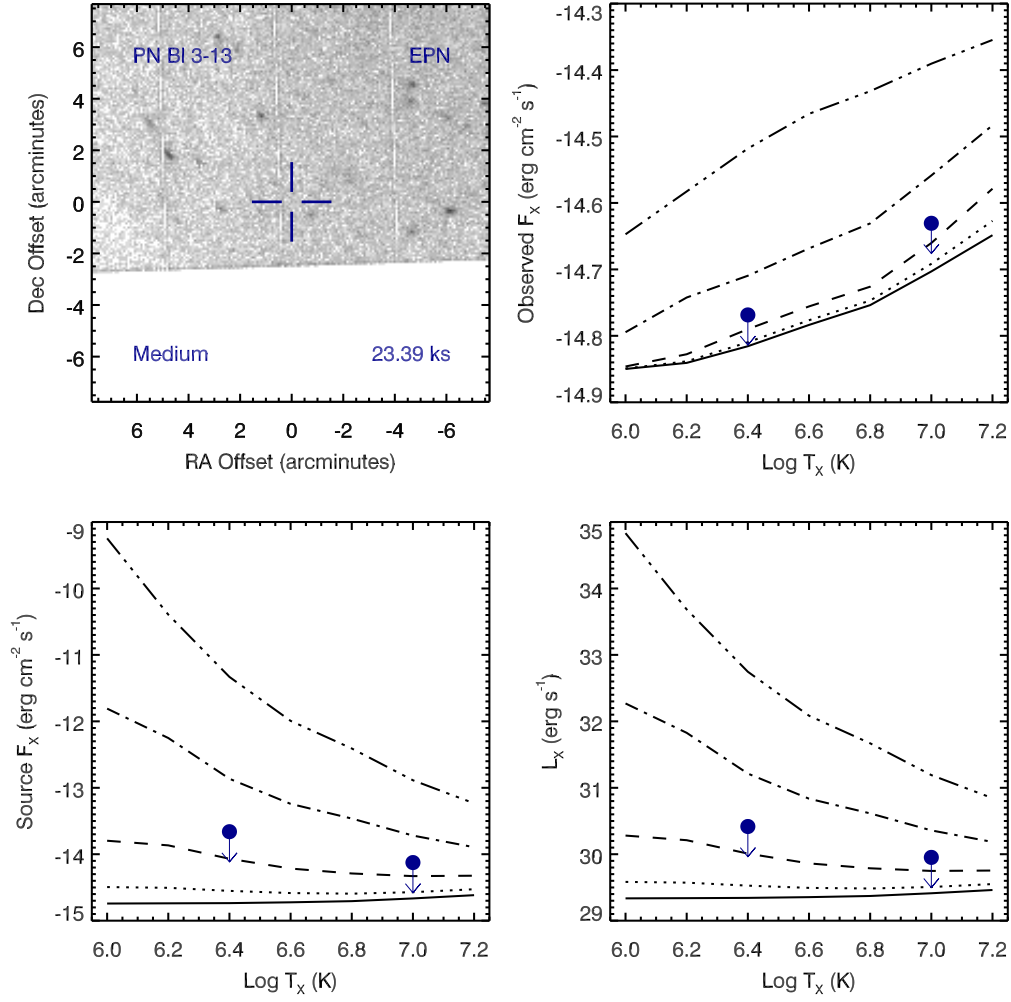


Figure A.14 Serendipitous XMM EPN observation (ObsID 0302570101) of PN Bl 3-13 ; panels as in Figure A.12.

## PN H 1-13 , ObsID 0150220101

Table A.10 Summary of the Analysis for the XMM EPIC observation (ObsID 0150220101) of PN H 1-13.

Basic Data			
Parameter	Value	Notes	
RA (J2000)	262.114737		
DEC (J2000)	-35.125453	Offset (')	9.73
$R_{\text{nebula}}$ (")	4.8	from literature (A94)	
$D$ (kpc)	1.65	from statistical methods (A94)	
$\log N_H$ ( $\text{cm}^{-2}$ )	21.6990	unknown, assumed value	
$T_{\text{eff}}$ (kK)	74.60	HeI or HeII Zanstra (Ph03)	
Date Obs:	2002-10-03	XMM Filter:	Medium

Calculations			
Parameter	EMOS1	EMOS2	EPN
$t_{\text{exp}}$ (ks)	30.1	30.1	–
$\text{CR}_{\text{src}}$ ( $\text{cnt s}^{-1}$ )	3.758E-07	2.352E-07	–
$\text{CR}_{\text{bkg}}$ ( $\text{cnt s}^{-1}$ )	2.833E-07	2.540E-07	–

Hot Bubble Upper Limits ( $T_X \sim 3 \times 10^6$ K)			
Parameter	EMOS1	EMOS2	EPN
$F_X$ ( $\text{erg cm}^{-2} \text{s}^{-1}$ )	-13.6293	-13.6527	–
$L_X$ ( $\text{erg s}^{-1}$ )	30.8836	30.8602	–

Spun-up Companion Upper Limits ( $T_X \sim 10^7$ K)			
Parameter	EMOS1	EMOS2	EPN
$F_X$ ( $\text{erg cm}^{-2} \text{s}^{-1}$ )	-14.2423	-14.2657	–
$L_X$ ( $\text{erg s}^{-1}$ )	30.2706	30.2472	–
$L_*$ ( $L_{\text{sun}}$ )	0.4849	0.4595	–
$M_{\text{bol}}$ (mag)	5.5258	5.5842	–
Spectral Type	G8-K0V	G8-K0V	–

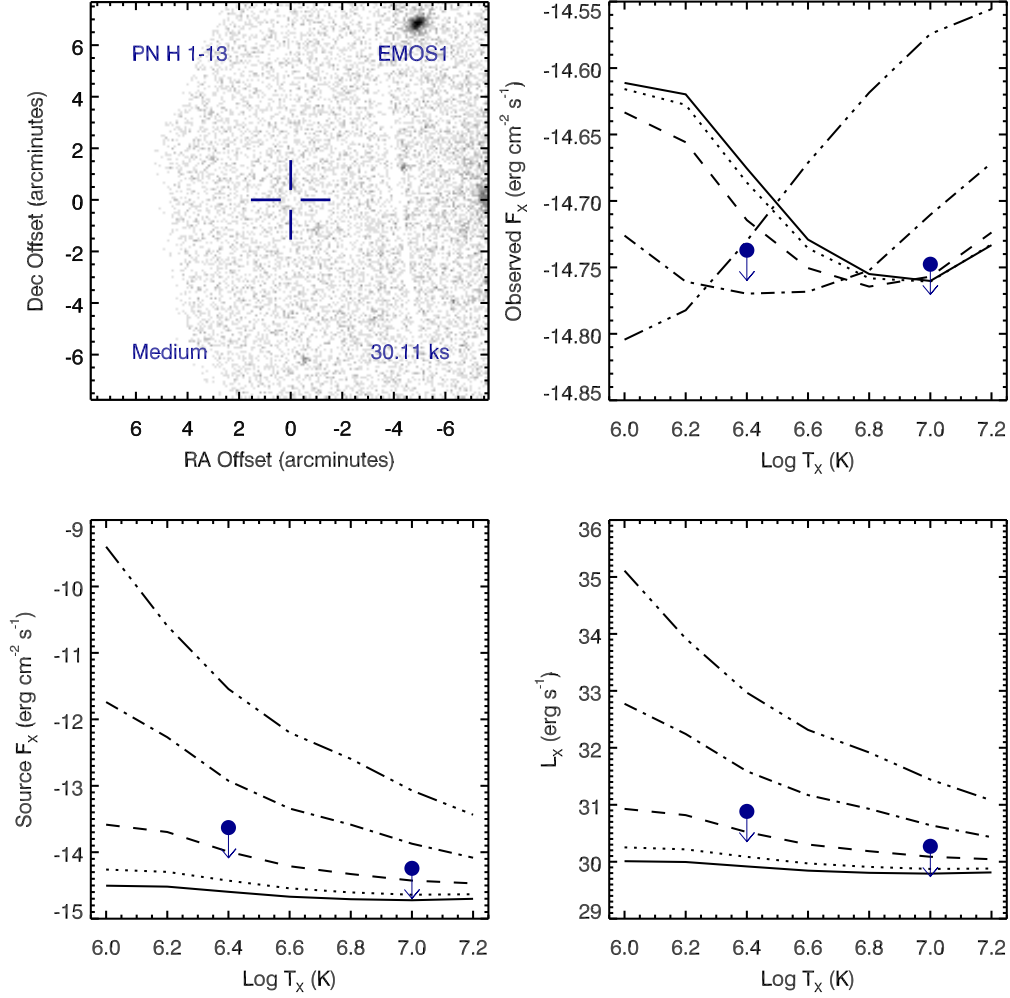


Figure A.15 Serendipitous XMM EMOS1 observation (ObsID 0150220101) of PN H 1-13. Clock-wise from top-left: broad band (0.3 to 8.0 keV) image at the PN position, upper limits of the observed flux, X-ray luminosity, and source X-ray flux. The upper limits calculations are based on the upper limit count rates, a thermal plasma model at a range temperatures, and a range of intervening absorption values:  $N_H(10^{22} \text{ cm}^{-2}) = 0.03$  (solid), 0.1 (dotted), 0.3 (dashed), 1 (dot-dashed), and 3 (dot-dot-dashed). The hot bubble and spun-up companion upper limits are depicted as the filled circles with downward pointing arrows at  $\log T_X$  of 6.4 and 7.0, respectively.



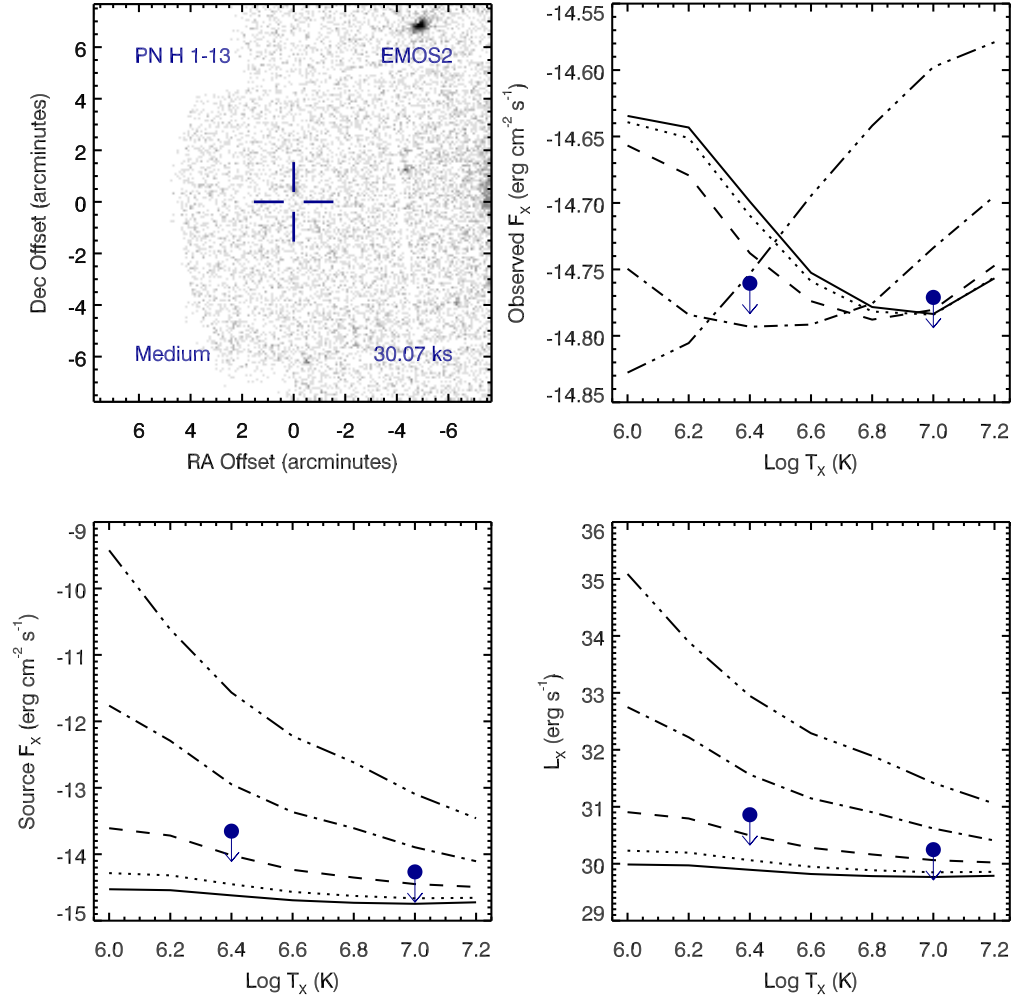


Figure A.16 Serendipitous XMM EMOS2 observation (ObsID 0150220101) of PN H 1-13 ; panels as in Figure A.15.

# PN H 1-43 , ObsID 0203750101

Table A.11 Summary of the Analysis for the XMM EPIC observation (ObsID 0203750101) of PN H 1-43.

Basic Data			
Parameter	Value	Notes	
RA (J2000)	269.560170		
DEC (J2000)	-33.793750	Offset (')	5.37
$R_{\text{nebula}}$ (")	1.0	from literature (A94)	
$D$ (kpc)	13.20	from statistical methods (A94)	
$\log N_H$ (cm <sup>-2</sup> )	21.6990	unknown, assumed value	
$T_{\text{eff}}$ (kK)	27.50	HeI or HeII Zanstra (Ph03)	
Date Obs:	2004-09-18	XMM Filter:	Medium

Calculations			
Parameter	EMOS1	EMOS2	EPN
$t_{\text{exp}}$ (ks)	45.1	45.2	–
$\text{CR}_{\text{src}}$ (cnt s <sup>-1</sup> )	5.871E-07	9.362E-07	–
$\text{CR}_{\text{bkg}}$ (cnt s <sup>-1</sup> )	7.083E-07	7.363E-07	–

Hot Bubble Upper Limits ( $T_X \sim 3 \times 10^6$ K)			
Parameter	EMOS1	EMOS2	EPN
$F_X$ (erg cm <sup>-2</sup> s <sup>-1</sup> )	-13.5180	-13.5099	–
$L_X$ (erg s <sup>-1</sup> )	32.8011	32.8092	–

Spun-up Companion Upper Limits ( $T_X \sim 10^7$ K)			
Parameter	EMOS1	EMOS2	EPN
$F_X$ (erg cm <sup>-2</sup> s <sup>-1</sup> )	-14.1311	-14.1229	–
$L_X$ (erg s <sup>-1</sup> )	32.1880	32.1962	–
$L_*$ ( $L_{\text{sun}}$ )	40.0959	40.8603	–
$M_{\text{bol}}$ (mag)	0.7323	0.7117	–
Spectral Type	A0-A2V	A0-A2V	–

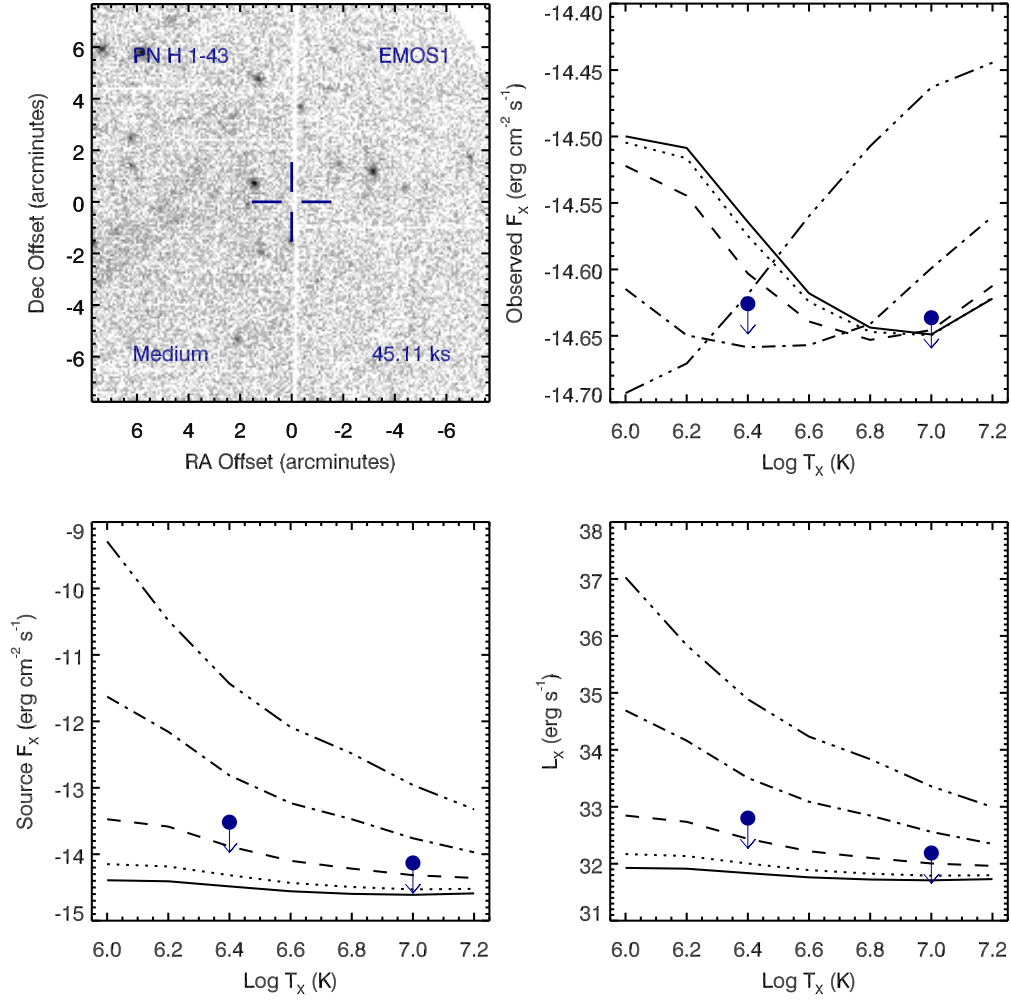


Figure A.17 Serendipitous XMM EMOS1 observation (ObsID 0203750101) of PN H 1-43. Clock-wise from top-left: broad band (0.3 to 8.0 keV) image at the PN position, upper limits of the observed flux, X-ray luminosity, and source X-ray flux. The upper limits calculations are based on the upper limit count rates, a thermal plasma model at a range temperatures, and a range of intervening absorption values:  $N_H(10^{22} \text{ cm}^{-2}) = 0.03$  (solid), 0.1 (dotted), 0.3 (dashed), 1 (dot-dashed), and 3 (dot-dot-dashed). The hot bubble and spun-up companion upper limits are depicted as the filled circles with downward pointing arrows at  $\log T_x$  of 6.4 and 7.0, respectively.

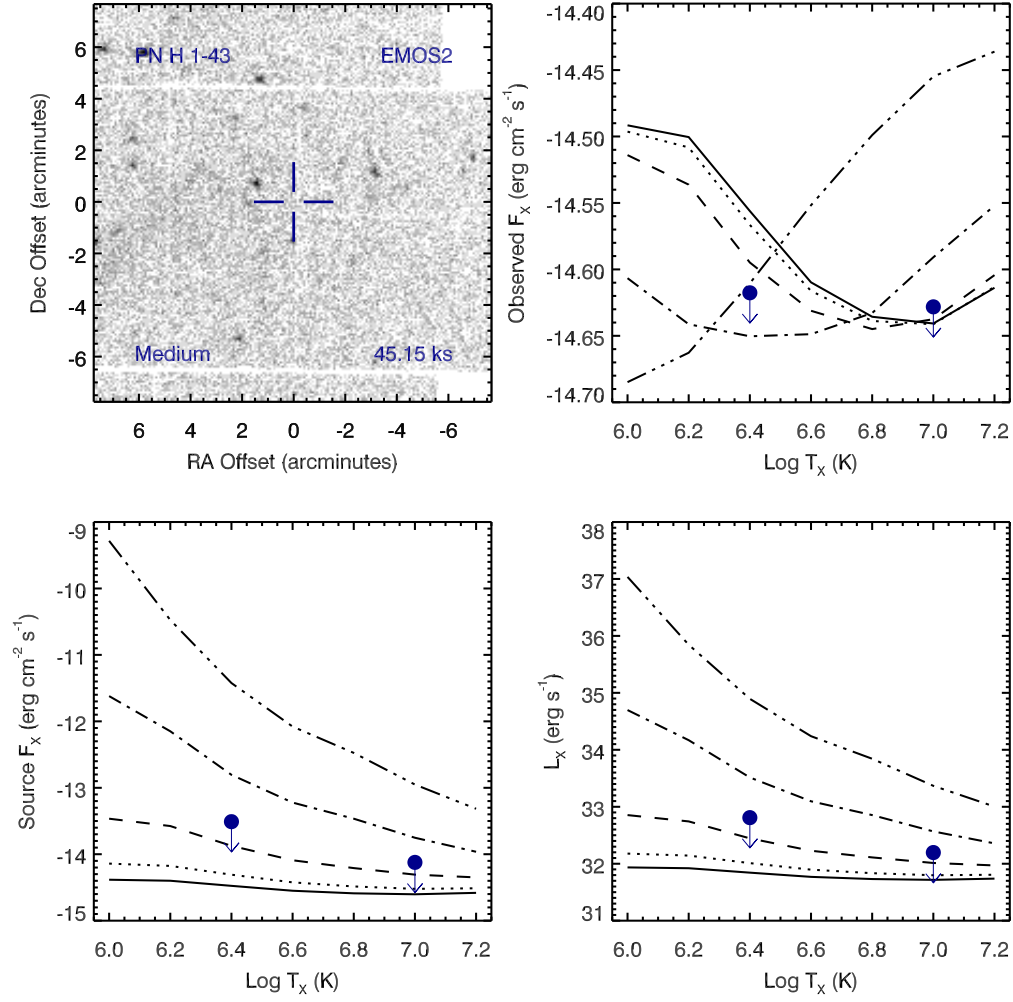


Figure A.18 Serendipitous XMM EMOS2 observation (ObsID 0203750101) of PN H 1-43 ; panels as in Figure A.17.

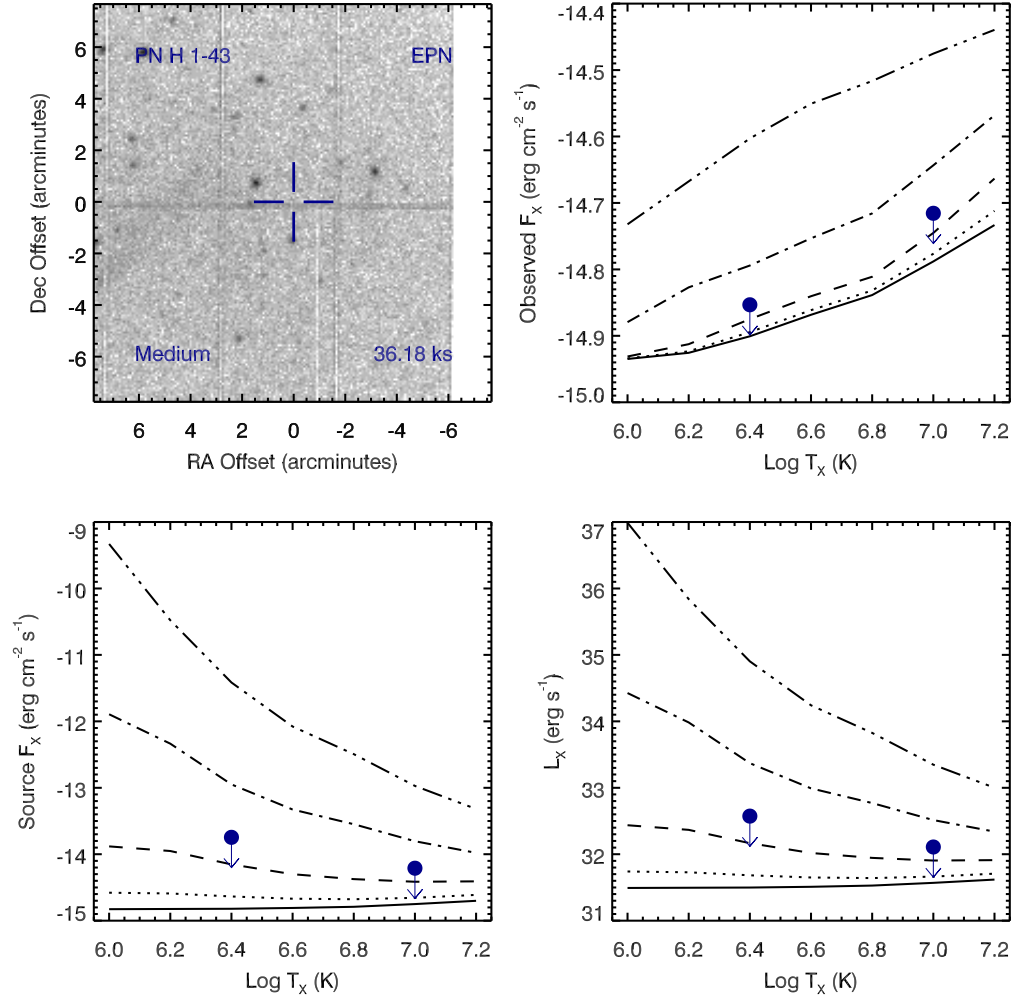


Figure A.19 Serendipitous XMM EPN observation (ObsID 0203750101) of PN H 1-43 ; panels as in Figure A.17.

# PN H 1-43 , ObsID 0500540101

Table A.12 Summary of the Analysis for the XMM EPIC observation (ObsID 0500540101) of PN H 1-43.

Basic Data			
Parameter	Value	Notes	
RA (J2000)	269.560170		
DEC (J2000)	-33.793750	Offset (')	5.37
$R_{\text{nebula}}$ (")	1.0	from literature (A94)	
$D$ (kpc)	13.20	from statistical methods (A94)	
$\log N_H$ (cm <sup>-2</sup> )	21.6990	unknown, assumed value	
$T_{\text{eff}}$ (kK)	27.50	HeI or HeII Zanstra (Ph03)	
Date Obs:	2008-03-15	XMM Filter:	Medium

Calculations			
Parameter	EMOS1	EMOS2	EPN
$t_{\text{exp}}$ (ks)	—	—	—
$\text{CR}_{\text{src}}$ (cnt s <sup>-1</sup> )	—	—	—
$\text{CR}_{\text{bkg}}$ (cnt s <sup>-1</sup> )	—	—	—

Hot Bubble Upper Limits ( $T_X \sim 3 \times 10^6$ K)			
Parameter	EMOS1	EMOS2	EPN
$F_X$ (erg cm <sup>-2</sup> s <sup>-1</sup> )	—	—	—
$L_X$ (erg s <sup>-1</sup> )	—	—	—

Spun-up Companion Upper Limits ( $T_X \sim 10^7$ K)			
Parameter	EMOS1	EMOS2	EPN
$F_X$ (erg cm <sup>-2</sup> s <sup>-1</sup> )	—	—	—
$L_X$ (erg s <sup>-1</sup> )	—	—	—
$L_*$ ( $L_{\text{sun}}$ )	—	—	—
$M_{\text{bol}}$ (mag)	—	—	—
Spectral Type	—	—	—

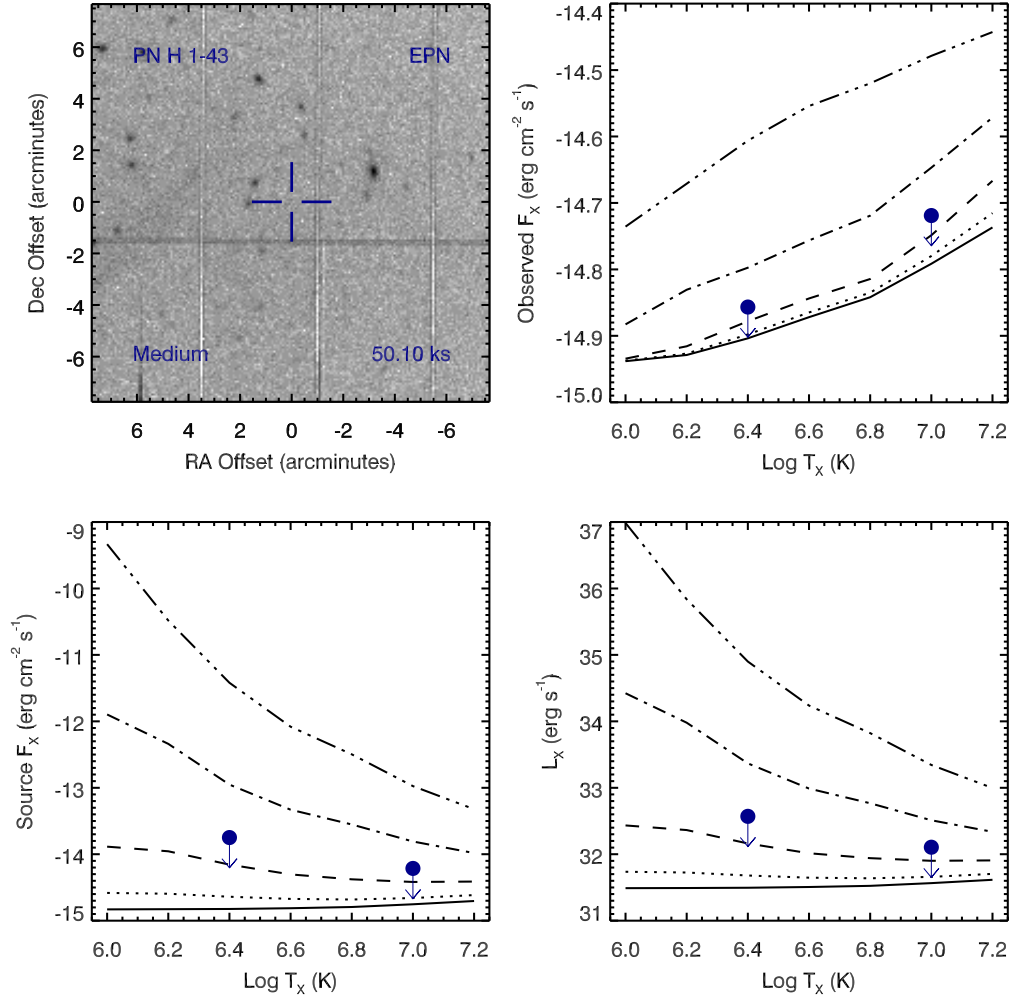


Figure A.20 Serendipitous XMM EPN observation (ObsID 0500540101) of PN H 1-43. Clock-wise from top-left: broad band (0.3 to 8.0 keV) image at the PN position, upper limits of the observed flux, X-ray luminosity, and source X-ray flux. The upper limits calculations are based on the upper limit count rates, a thermal plasma model at a range temperatures, and a range of intervening absorption values:  $N_H(10^{22} \text{ cm}^{-2}) = 0.03$  (solid), 0.1 (dotted), 0.3 (dashed), 1 (dot-dashed), and 3 (dot-dot-dashed). The hot bubble and spun-up companion upper limits are depicted as the filled circles with downward pointing arrows at  $\log T_X$  of 6.4 and 7.0, respectively.

# PN H 1-43 , ObsID 0032940101

Table A.13 Summary of the Analysis for the XMM EPIC observation (ObsID 0032940101) of PN H 1-43.

Basic Data			
Parameter	Value	Notes	
RA (J2000)	269.560170		
DEC (J2000)	-33.793750	Offset (')	5.36
$R_{\text{nebula}}$ (")	1.0	from literature (A94)	
$D$ (kpc)	13.20	from statistical methods (A94)	
$\log N_H$ ( $\text{cm}^{-2}$ )	21.6990	unknown, assumed value	
$T_{\text{eff}}$ (kK)	27.50	HeI or HeII Zanstra (Ph03)	
Date Obs:	2001-03-08	XMM Filter:	Medium

Calculations			
Parameter	EMOS1	EMOS2	EPN
$t_{\text{exp}}$ (ks)	—	—	—
$\text{CR}_{\text{src}}$ ( $\text{cnt s}^{-1}$ )	—	—	—
$\text{CR}_{\text{bkg}}$ ( $\text{cnt s}^{-1}$ )	—	—	—

Hot Bubble Upper Limits ( $T_X \sim 3 \times 10^6$ K)			
Parameter	EMOS1	EMOS2	EPN
$F_X$ ( $\text{erg cm}^{-2} \text{s}^{-1}$ )	—	—	—
$L_X$ ( $\text{erg s}^{-1}$ )	—	—	—

Spun-up Companion Upper Limits ( $T_X \sim 10^7$ K)			
Parameter	EMOS1	EMOS2	EPN
$F_X$ ( $\text{erg cm}^{-2} \text{s}^{-1}$ )	—	—	—
$L_X$ ( $\text{erg s}^{-1}$ )	—	—	—
$L_*$ ( $L_{\text{sun}}$ )	—	—	—
$M_{\text{bol}}$ (mag)	—	—	—
Spectral Type	—	—	—



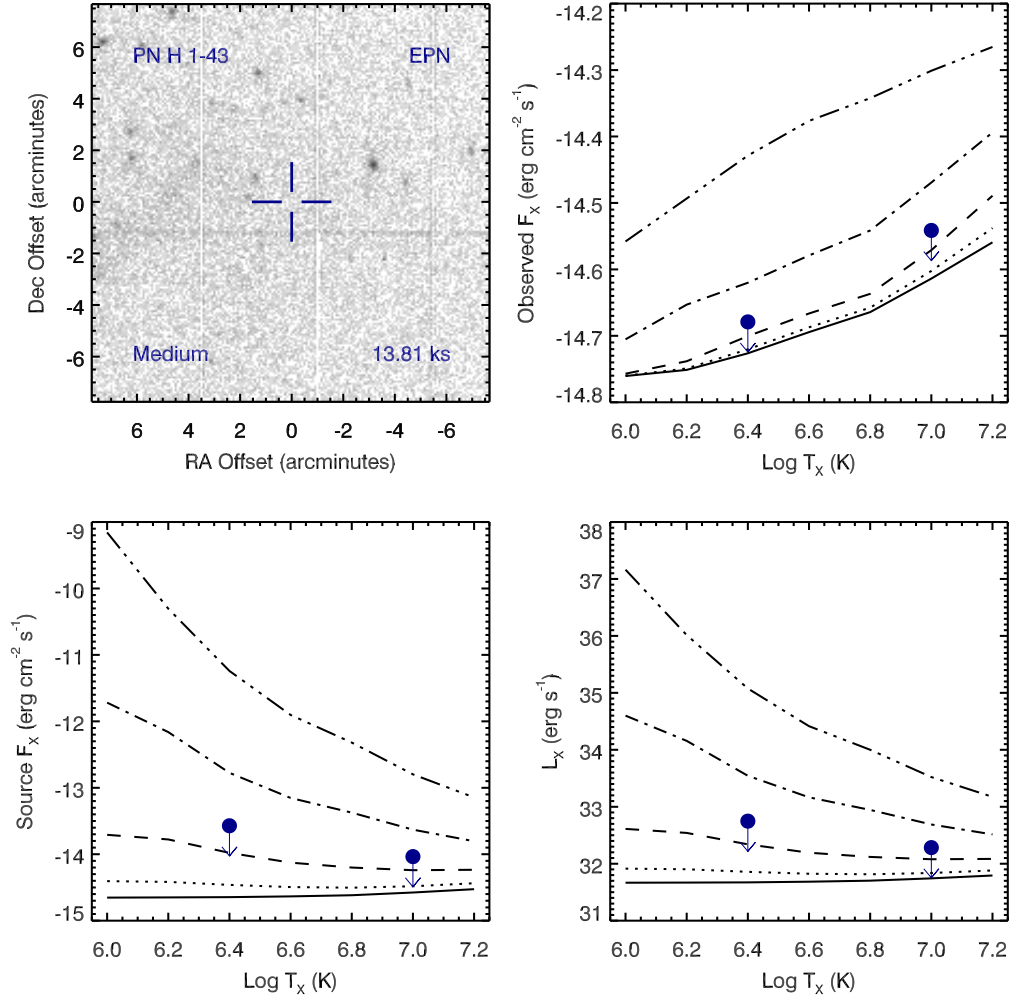


Figure A.21 Serendipitous XMM EPN observation (ObsID 0032940101) of PN H 1-43. Clock-wise from top-left: broad band (0.3 to 8.0 keV) image at the PN position, upper limits of the observed flux, X-ray luminosity, and source X-ray flux. The upper limits calculations are based on the upper limit count rates, a thermal plasma model at a range temperatures, and a range of intervening absorption values:  $N_H(10^{22} \text{ cm}^{-2}) = 0.03$  (solid), 0.1 (dotted), 0.3 (dashed), 1 (dot-dashed), and 3 (dot-dot-dashed). The hot bubble and spun-up companion upper limits are depicted as the filled circles with downward pointing arrows at  $\log T_X$  of 6.4 and 7.0, respectively.

## PN H 1-54 , ObsID 0157960101

Table A.14 Summary of the Analysis for the XMM EPIC observation (ObsID 0157960101) of PN H 1-54.

Basic Data			
Parameter	Value	Notes	
RA (J2000)	271.780163		
DEC (J2000)	-29.218431	Offset (')	11.50
$R_{\text{nebula}}$ (")	2.4	from literature (A94)	
$D$ (kpc)	4.45	from statistical methods (A94)	
$\log N_H$ (cm <sup>-2</sup> )	21.4836	optical extinction (C92)	
$T_{\text{eff}}$ (kK)	37.00	HeI or HeII Zanstra (Ph03)	
Date Obs:	2003-03-22	XMM Filter:	Thick

Calculations			
Parameter	EMOS1	EMOS2	EPN
$t_{\text{exp}}$ (ks)	16.5	16.5	–
$\text{CR}_{\text{src}}$ (cnt s <sup>-1</sup> )	8.167E-07	8.596E-07	–
$\text{CR}_{\text{bkg}}$ (cnt s <sup>-1</sup> )	6.189E-07	8.225E-07	–

Hot Bubble Upper Limits ( $T_X \sim 3 \times 10^6$ K)			
Parameter	EMOS1	EMOS2	EPN
$F_X$ (erg cm <sup>-2</sup> s <sup>-1</sup> )	-13.6029	-13.5412	–
$L_X$ (erg s <sup>-1</sup> )	31.7717	31.8334	–

Spun-up Companion Upper Limits ( $T_X \sim 10^7$ K)			
Parameter	EMOS1	EMOS2	EPN
$F_X$ (erg cm <sup>-2</sup> s <sup>-1</sup> )	-14.0639	-14.0021	–
$L_X$ (erg s <sup>-1</sup> )	31.3107	31.3725	–
$L_*$ ( $L_{\text{sun}}$ )	5.3192	6.1320	–
$M_{\text{bol}}$ (mag)	2.9254	2.7710	–
Spectral Type	F0-F2V	F0-F2V	–

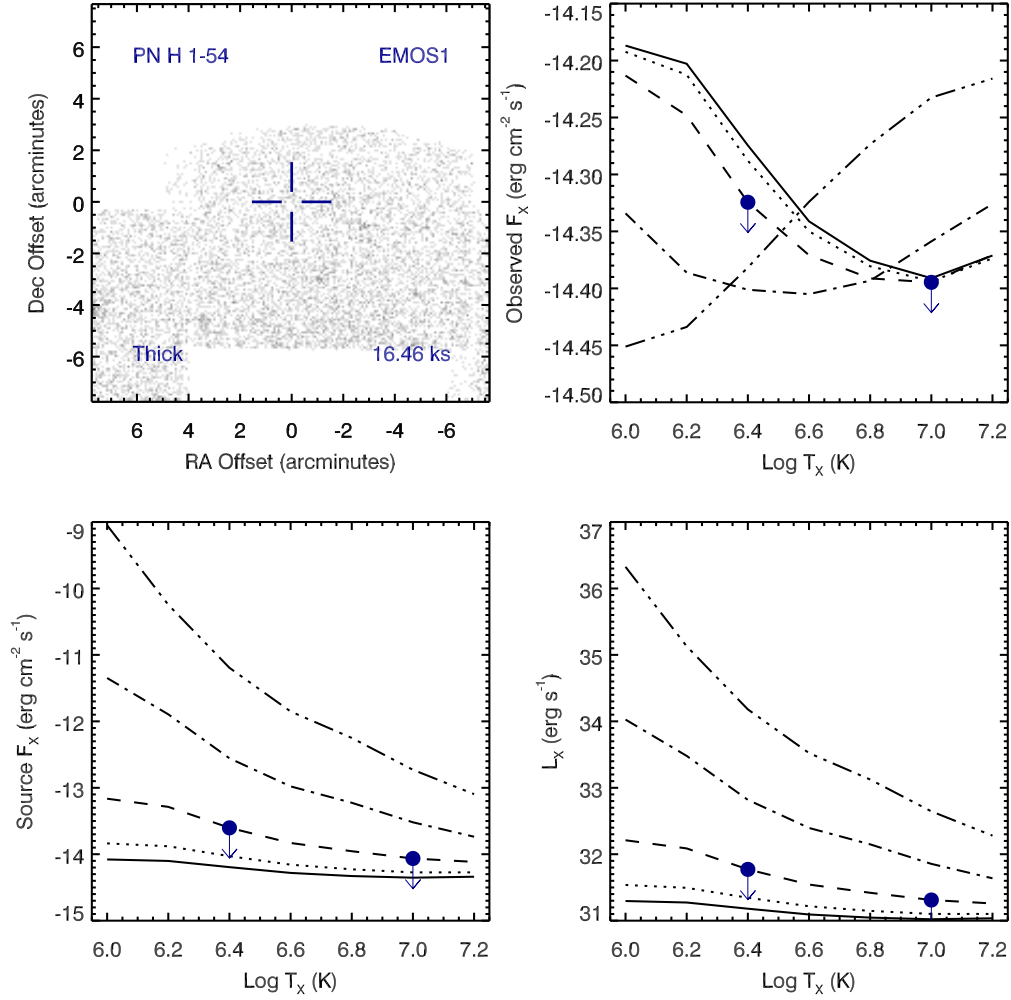


Figure A.22 Serendipitous XMM EMOS1 observation (ObsID 0157960101) of PN H 1-54. Clock-wise from top-left: broad band (0.3 to 8.0 keV) image at the PN position, upper limits of the observed flux, X-ray luminosity, and source X-ray flux. The upper limits calculations are based on the upper limit count rates, a thermal plasma model at a range temperatures, and a range of intervening absorption values:  $N_H(10^{22} \text{ cm}^{-2}) = 0.03$  (solid), 0.1 (dotted), 0.3 (dashed), 1 (dot-dashed), and 3 (dot-dot-dashed). The hot bubble and spun-up companion upper limits are depicted as the filled circles with downward pointing arrows at  $\log T_x$  of 6.4 and 7.0, respectively.

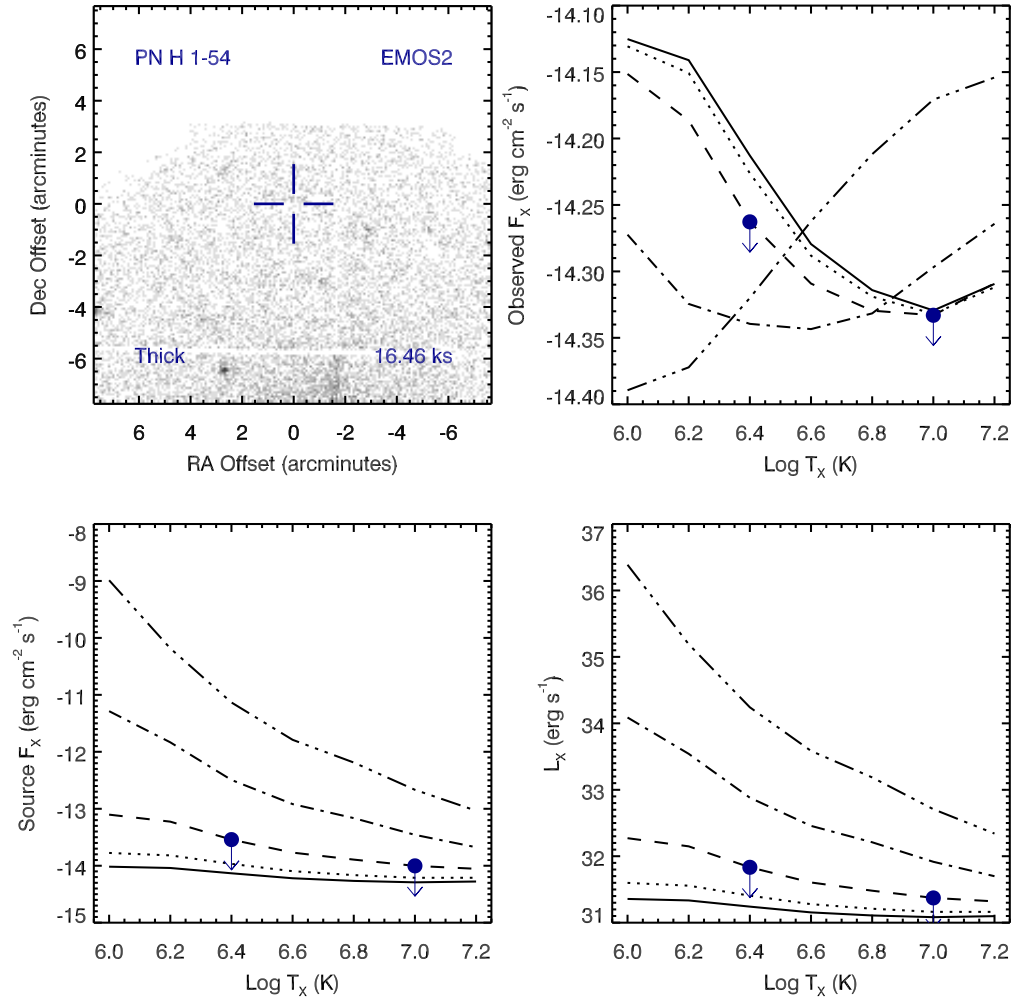


Figure A.23 Serendipitous XMM EMOS2 observation (ObsID 0157960101) of PN H 1-54 ; panels as in Figure A.22.

## PN H 1-54 , ObsID 0205800201

Table A.15 Summary of the Analysis for the XMM EPIC observation (ObsID 0205800201) of PN H 1-54.

Basic Data			
Parameter	Value	Notes	
RA (J2000)	271.780163		
DEC (J2000)	-29.218431	Offset (')	11.51
$R_{\text{nebula}}$ (")	2.4	from literature (A94)	
$D$ (kpc)	4.45	from statistical methods (A94)	
$\log N_H$ (cm <sup>-2</sup> )	21.4836	optical extinction (C92)	
$T_{\text{eff}}$ (kK)	37.00	HeI or HeII Zanstra (Ph03)	
Date Obs:	2004-09-08	XMM Filter:	Thin1

Calculations			
Parameter	EMOS1	EMOS2	EPN
$t_{\text{exp}}$ (ks)	36.7	36.9	–
$\text{CR}_{\text{src}}$ (cnt s <sup>-1</sup> )	9.990E-07	8.292E-07	–
$\text{CR}_{\text{bkg}}$ (cnt s <sup>-1</sup> )	8.254E-07	8.125E-07	–

Hot Bubble Upper Limits ( $T_X \sim 3 \times 10^6$ K)			
Parameter	EMOS1	EMOS2	EPN
$F_X$ (erg cm <sup>-2</sup> s <sup>-1</sup> )	-13.8167	-13.8210	–
$L_X$ (erg s <sup>-1</sup> )	31.5579	31.5536	–

Spun-up Companion Upper Limits ( $T_X \sim 10^7$ K)			
Parameter	EMOS1	EMOS2	EPN
$F_X$ (erg cm <sup>-2</sup> s <sup>-1</sup> )	-14.2443	-14.2486	–
$L_X$ (erg s <sup>-1</sup> )	31.1304	31.1261	–
$L_*$ ( $L_{\text{sun}}$ )	3.5112	3.4767	–
$M_{\text{bol}}$ (mag)	3.3764	3.3871	–
Spectral Type	F5-F2V	F5-F2V	–

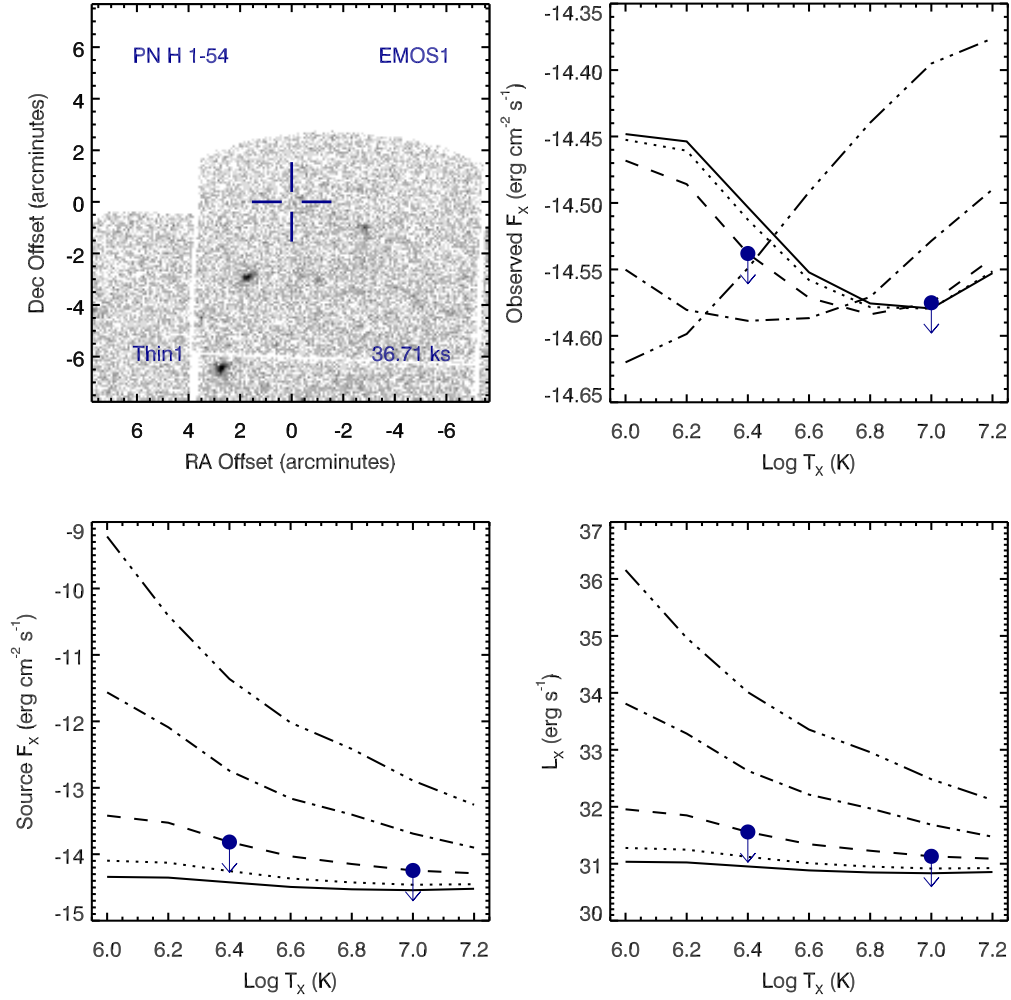


Figure A.24 Serendipitous XMM EMOS1 observation (ObsID 0205800201) of PN H 1-54. Clock-wise from top-left: broad band (0.3 to 8.0 keV) image at the PN position, upper limits of the observed flux, X-ray luminosity, and source X-ray flux. The upper limits calculations are based on the upper limit count rates, a thermal plasma model at a range temperatures, and a range of intervening absorption values:  $N_H(10^{22} \text{ cm}^{-2}) = 0.03$  (solid), 0.1 (dotted), 0.3 (dashed), 1 (dot-dashed), and 3 (dot-dot-dashed). The hot bubble and spun-up companion upper limits are depicted as the filled circles with downward pointing arrows at  $\log T_x$  of 6.4 and 7.0, respectively.

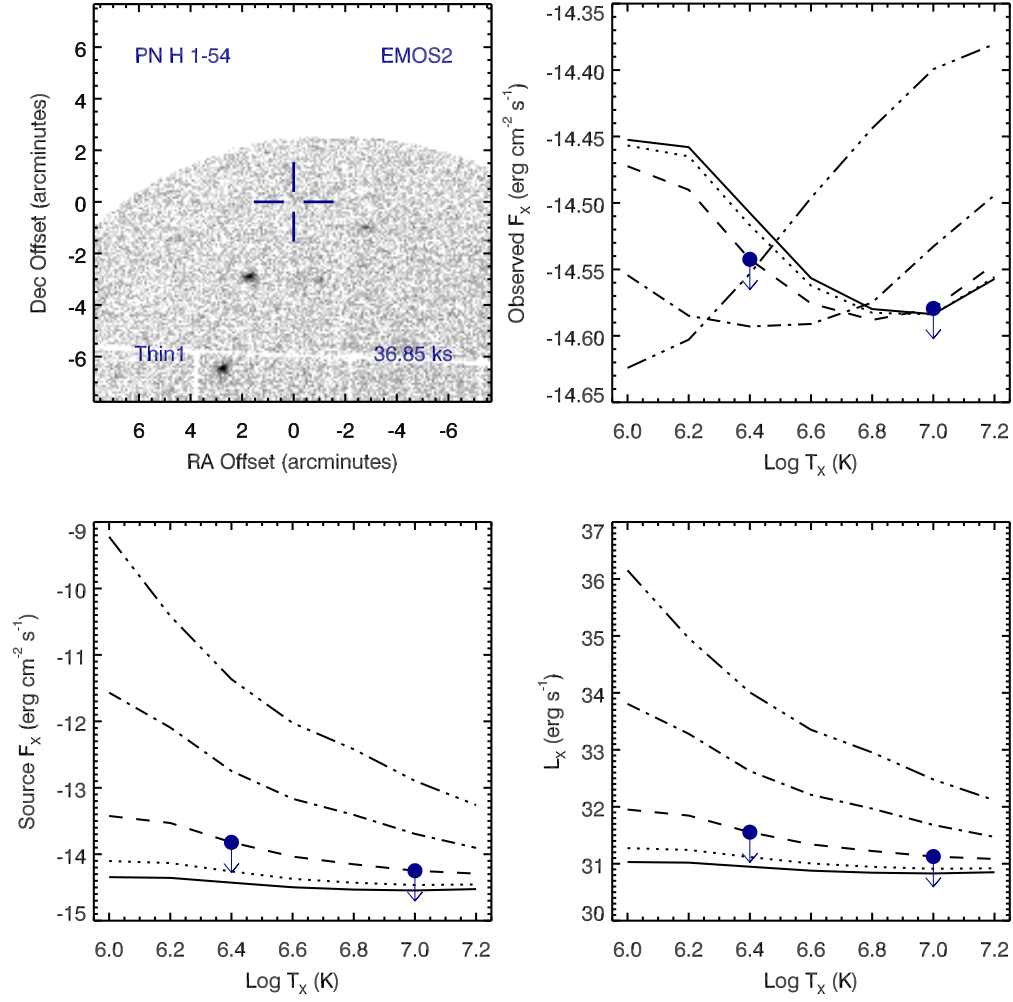


Figure A.25 Serendipitous XMM EMOS2 observation (ObsID 0205800201) of PN H 1-54 ; panels as in Figure A.24.

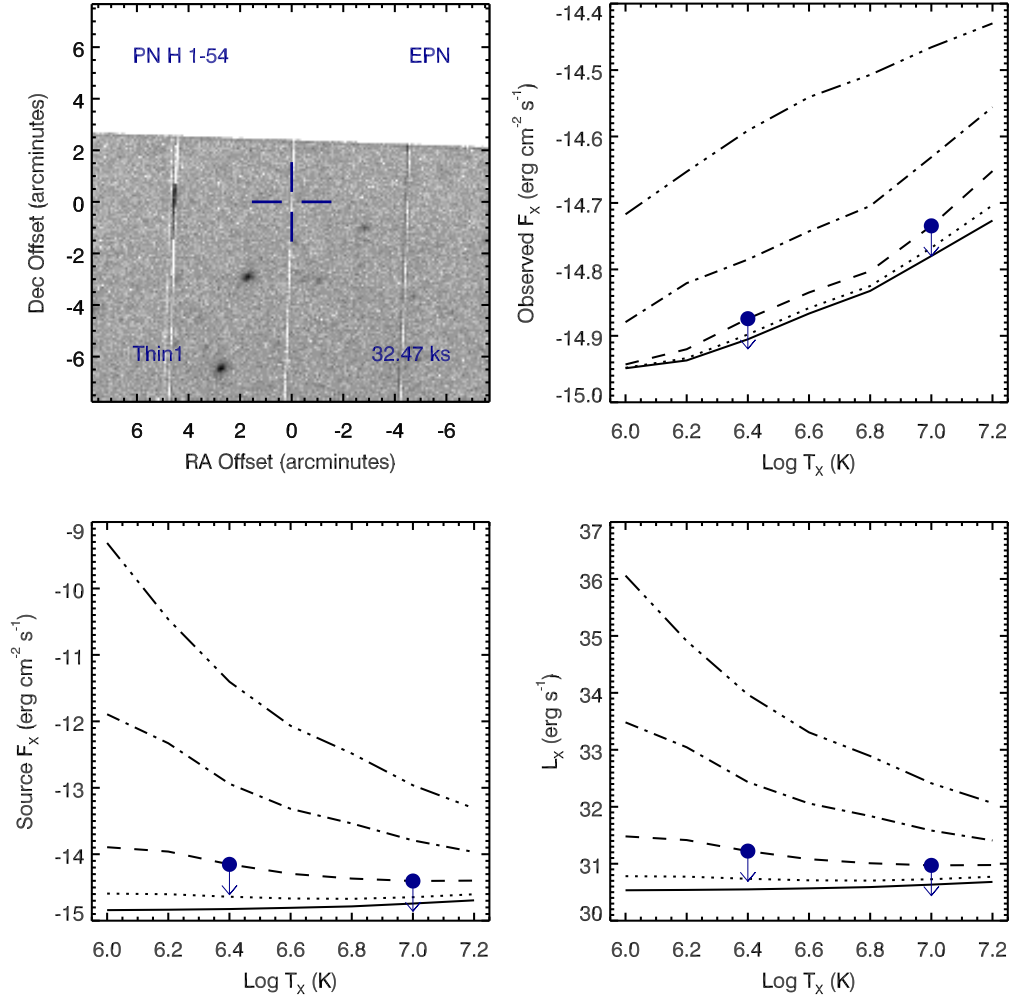


Figure A.26 Serendipitous XMM EPN observation (ObsID 0205800201) of PN H 1-54 ; panels as in Figure A.24.



## PN H 1-58 , ObsID 0403110601

Table A.16 Summary of the Analysis for the XMM EPIC observation (ObsID 0403110601) of PN H 1-58.

Basic Data			
Parameter	Value	Notes	
RA (J2000)	272.307646		
DEC (J2000)	-26.041328	Offset (')	8.01
$R_{\text{nebula}}$ (")	3.2	from literature (A94)	
$D$ (kpc)	1.0	unknown, assumed value	
$\log N_H$ (cm <sup>-2</sup> )	21.6990	unknown, assumed value	
$T_{\text{eff}}$ (kK)	47.50	HeI or HeII Zanstra (Ph03)	
Date Obs:	2006-10-06	XMM Filter:	Medium

Calculations			
Parameter	EMOS1	EMOS2	EPN
$t_{\text{exp}}$ (ks)	–	21.7	–
$\text{CR}_{\text{src}}$ (cnt s <sup>-1</sup> )	–	5.864E-07	–
$\text{CR}_{\text{bkg}}$ (cnt s <sup>-1</sup> )	–	5.701E-07	–

Hot Bubble Upper Limits ( $T_X \sim 3 \times 10^6$ K)			
Parameter	EMOS1	EMOS2	EPN
$F_X$ (erg cm <sup>-2</sup> s <sup>-1</sup> )	–	-13.4064	–
$L_X$ (erg s <sup>-1</sup> )	–	30.6715	–

Spun-up Companion Upper Limits ( $T_X \sim 10^7$ K)			
Parameter	EMOS1	EMOS2	EPN
$F_X$ (erg cm <sup>-2</sup> s <sup>-1</sup> )	–	-14.0194	–
$L_X$ (erg s <sup>-1</sup> )	–	30.0585	–
$L_*$ ( $L_{\text{sun}}$ )	–	0.2976	–
$M_{\text{bol}}$ (mag)	–	6.0560	–
Spectral Type	–	K2-K5V	–

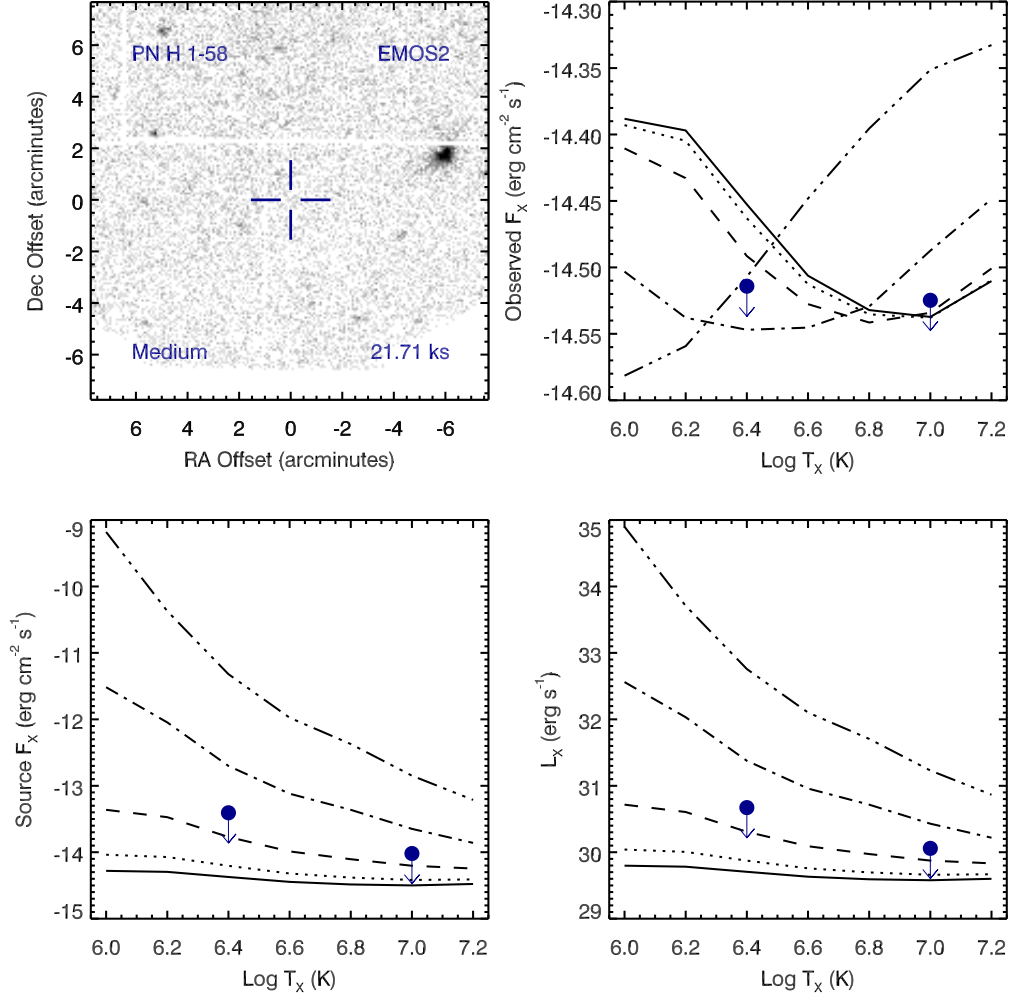


Figure A.27 Serendipitous XMM EMOS2 observation (ObsID 0403110601) of PN H 1-58. Clock-wise from top-left: broad band (0.3 to 8.0 keV) image at the PN position, upper limits of the observed flux, X-ray luminosity, and source X-ray flux. The upper limits calculations are based on the upper limit count rates, a thermal plasma model at a range temperatures, and a range of intervening absorption values:  $N_H(10^{22} \text{ cm}^{-2}) = 0.03$  (solid), 0.1 (dotted), 0.3 (dashed), 1 (dot-dashed), and 3 (dot-dot-dashed). The hot bubble and spun-up companion upper limits are depicted as the filled circles with downward pointing arrows at  $\log T_X$  of 6.4 and 7.0, respectively.

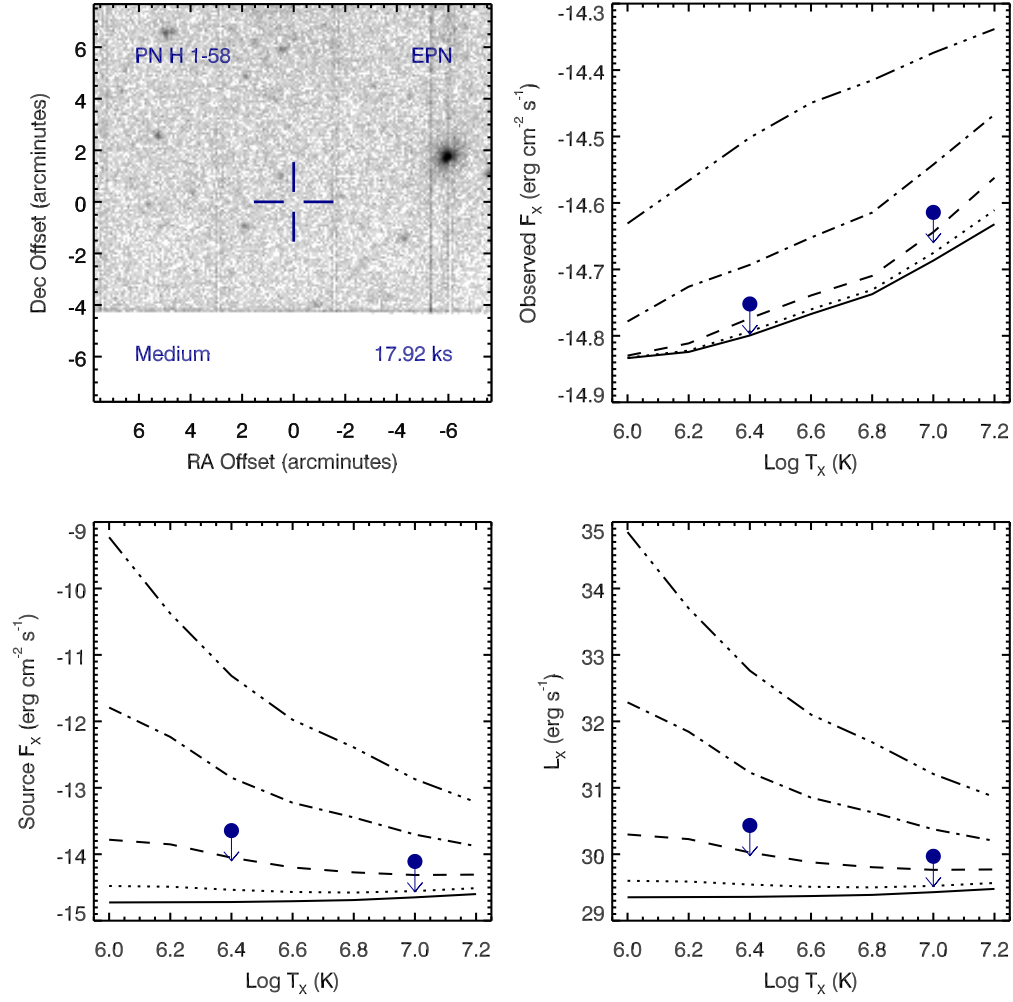


Figure A.28 Serendipitous XMM EPN observation (ObsID 0403110601) of PN H 1-58 ; panels as in Figure A.27.

## PN H 2-37 , ObsID 0152420101

Table A.17 Summary of the Analysis for the XMM EPIC observation (ObsID 0152420101) of PN H 2-37.

Basic Data			
Parameter	Value	Notes	
RA (J2000)	271.120308		
DEC (J2000)	-28.626264	Offset (')	8.50
$R_{\text{nebula}}$ (")	2.1	from literature (A94)	
$D$ (kpc)	3.63	from statistical methods (A94)	
$\log N_H$ (cm <sup>-2</sup> )	21.6990	unknown, assumed value	
$T_{\text{eff}}$ (kK)	62.10	HeI or HeII Zanstra (Ph03)	
Date Obs:	2002-09-21	XMM Filter:	Medium

Calculations			
Parameter	EMOS1	EMOS2	EPN
$t_{\text{exp}}$ (ks)	49.0	49.1	–
$\text{CR}_{\text{src}}$ (cnt s <sup>-1</sup> )	6.335E-07	9.237E-07	–
$\text{CR}_{\text{bkg}}$ (cnt s <sup>-1</sup> )	8.390E-07	8.913E-07	–

Hot Bubble Upper Limits ( $T_X \sim 3 \times 10^6$ K)			
Parameter	EMOS1	EMOS2	EPN
$F_X$ (erg cm <sup>-2</sup> s <sup>-1</sup> )	-13.4995	-13.4865	–
$L_X$ (erg s <sup>-1</sup> )	31.6982	31.7112	–

Spun-up Companion Upper Limits ( $T_X \sim 10^7$ K)			
Parameter	EMOS1	EMOS2	EPN
$F_X$ (erg cm <sup>-2</sup> s <sup>-1</sup> )	-14.1124	-14.0995	–
$L_X$ (erg s <sup>-1</sup> )	31.0853	31.0983	–
$L_*$ ( $L_{\text{sun}}$ )	3.1651	3.2611	–
$M_{\text{bol}}$ (mag)	3.4890	3.4566	–
Spectral Type	F5-F2V	F5-F2V	–

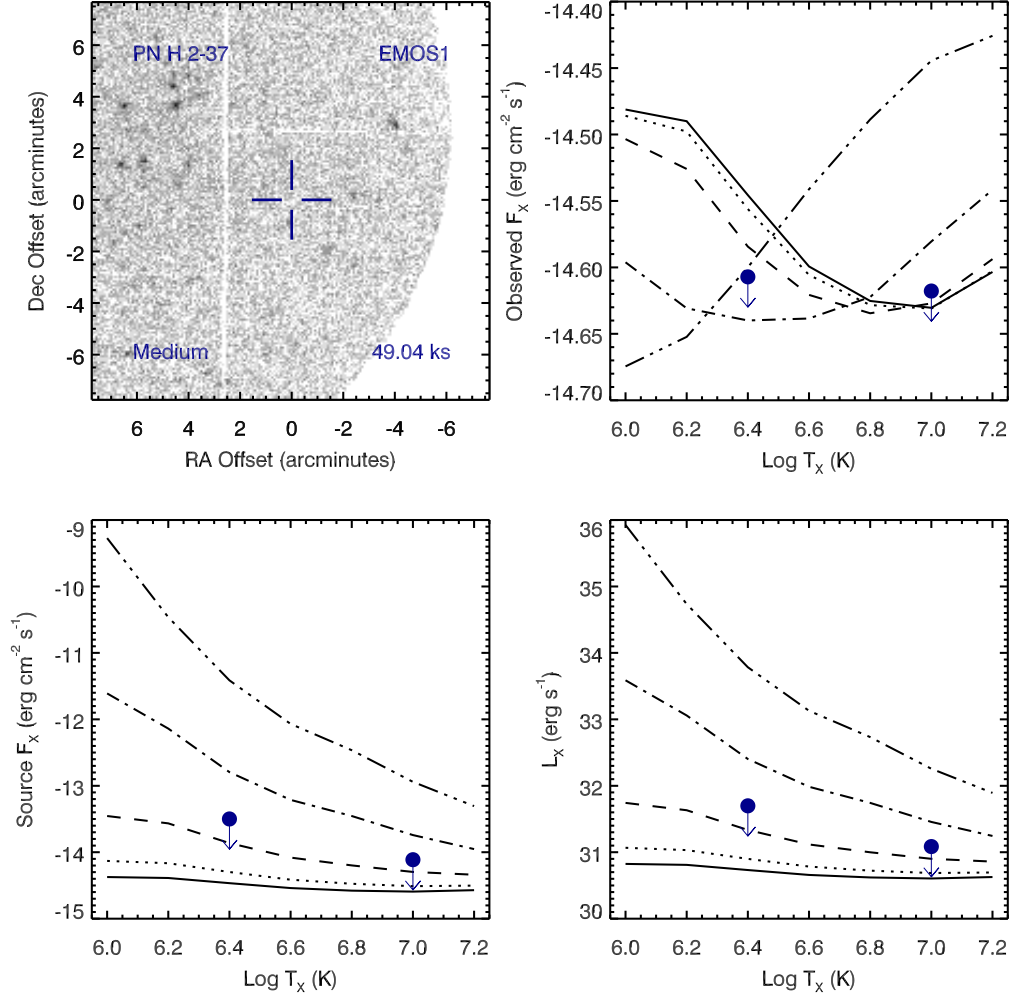


Figure A.29 Serendipitous XMM EMOS1 observation (ObsID 0152420101) of PN H 2-37. Clock-wise from top-left: broad band (0.3 to 8.0 keV) image at the PN position, upper limits of the observed flux, X-ray luminosity, and source X-ray flux. The upper limits calculations are based on the upper limit count rates, a thermal plasma model at a range temperatures, and a range of intervening absorption values:  $N_H(10^{22} \text{ cm}^{-2}) = 0.03$  (solid), 0.1 (dotted), 0.3 (dashed), 1 (dot-dashed), and 3 (dot-dot-dashed). The hot bubble and spun-up companion upper limits are depicted as the filled circles with downward pointing arrows at log  $T_x$  of 6.4 and 7.0, respectively.

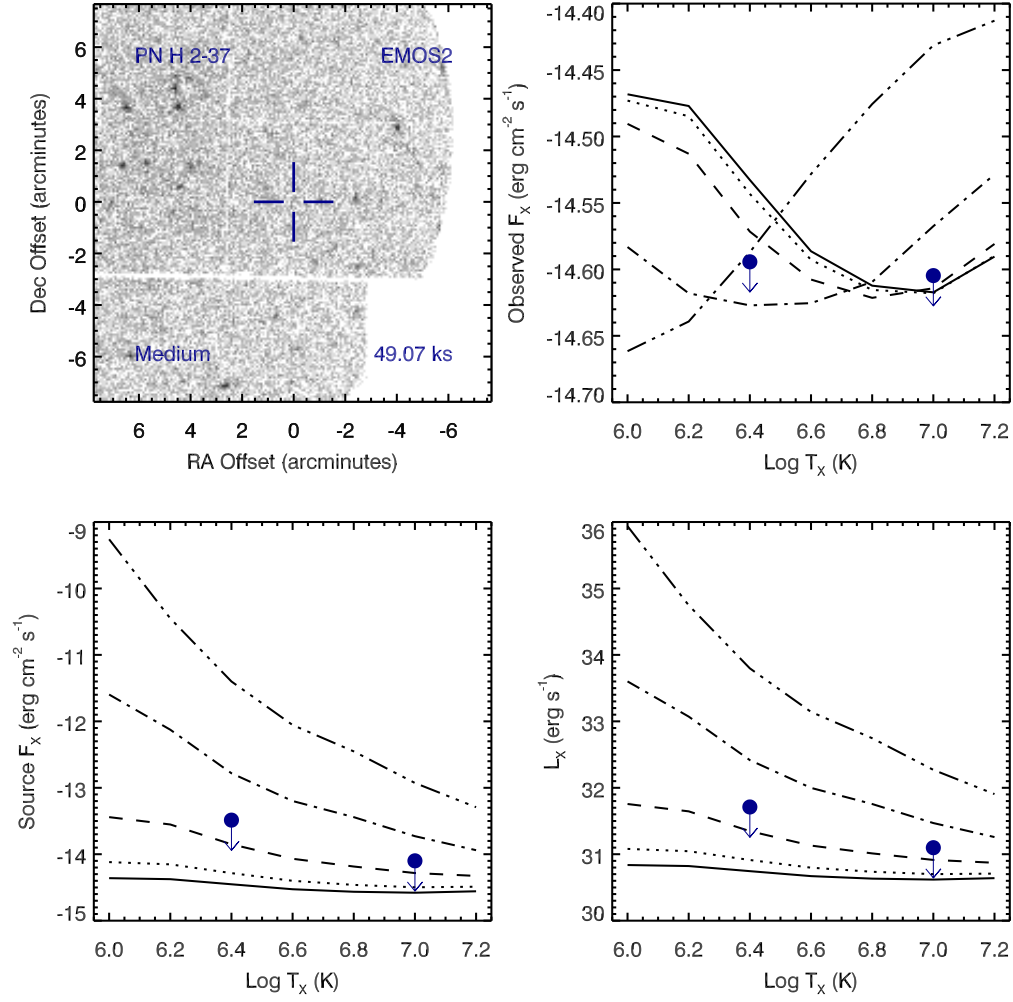


Figure A.30 Serendipitous XMM EMOS2 observation (ObsID 0152420101) of PN H 2-37 ; panels as in Figure A.29.

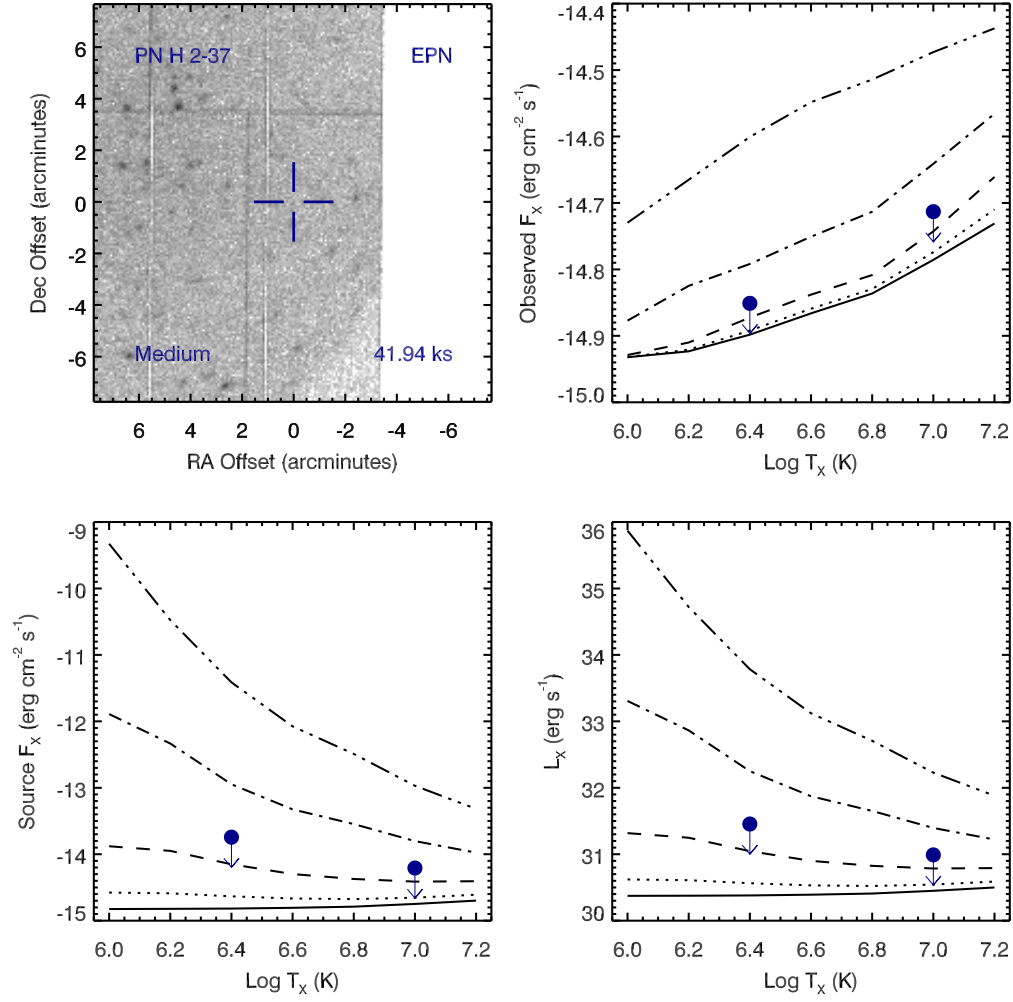


Figure A.31 Serendipitous XMM EPN observation (ObsID 0152420101) of PN H 2-37 ; panels as in Figure A.29.

# PN H 4-1 , ObsID 0124710401

Table A.18 Summary of the Analysis for the XMM EPIC observation (ObsID 0124710401) of PN H 4-1.

Basic Data			
Parameter	Value	Notes	
RA (J2000)	194.865710		
DEC (J2000)	27.636250	Offset (')	10.61
$R_{\text{nebula}}$ (")	1.4	from literature (A94)	
$D$ (kpc)	13.10	from statistical methods (A94)	
$\log N_H$ (cm <sup>-2</sup> )	20.6543	optical extinction (C92)	
$T_{\text{eff}}$ (kK)	81.70	HeI or HeII Zanstra (Ph03)	
Date Obs:	2000-06-23	XMM Filter:	Medium

Calculations			
Parameter	EMOS1	EMOS2	EPN
$t_{\text{exp}}$ (ks)	14.8	14.8	–
$\text{CR}_{\text{src}}$ (cnt s <sup>-1</sup> )	1.544E-06	2.104E-06	–
$\text{CR}_{\text{bkg}}$ (cnt s <sup>-1</sup> )	1.709E-06	1.916E-06	–

Hot Bubble Upper Limits ( $T_X \sim 3 \times 10^6$ K)			
Parameter	EMOS1	EMOS2	EPN
$F_X$ (erg cm <sup>-2</sup> s <sup>-1</sup> )	-14.0160	-13.9901	–
$L_X$ (erg s <sup>-1</sup> )	32.2964	32.3223	–

Spun-up Companion Upper Limits ( $T_X \sim 10^7$ K)			
Parameter	EMOS1	EMOS2	EPN
$F_X$ (erg cm <sup>-2</sup> s <sup>-1</sup> )	-14.1612	-14.1351	–
$L_X$ (erg s <sup>-1</sup> )	32.1513	32.1773	–
$L_*$ ( $L_{\text{sun}}$ )	36.8473	39.1224	–
$M_{\text{bol}}$ (mag)	0.8240	0.7589	–
Spectral Type	A0-A2V	A0-A2V	–



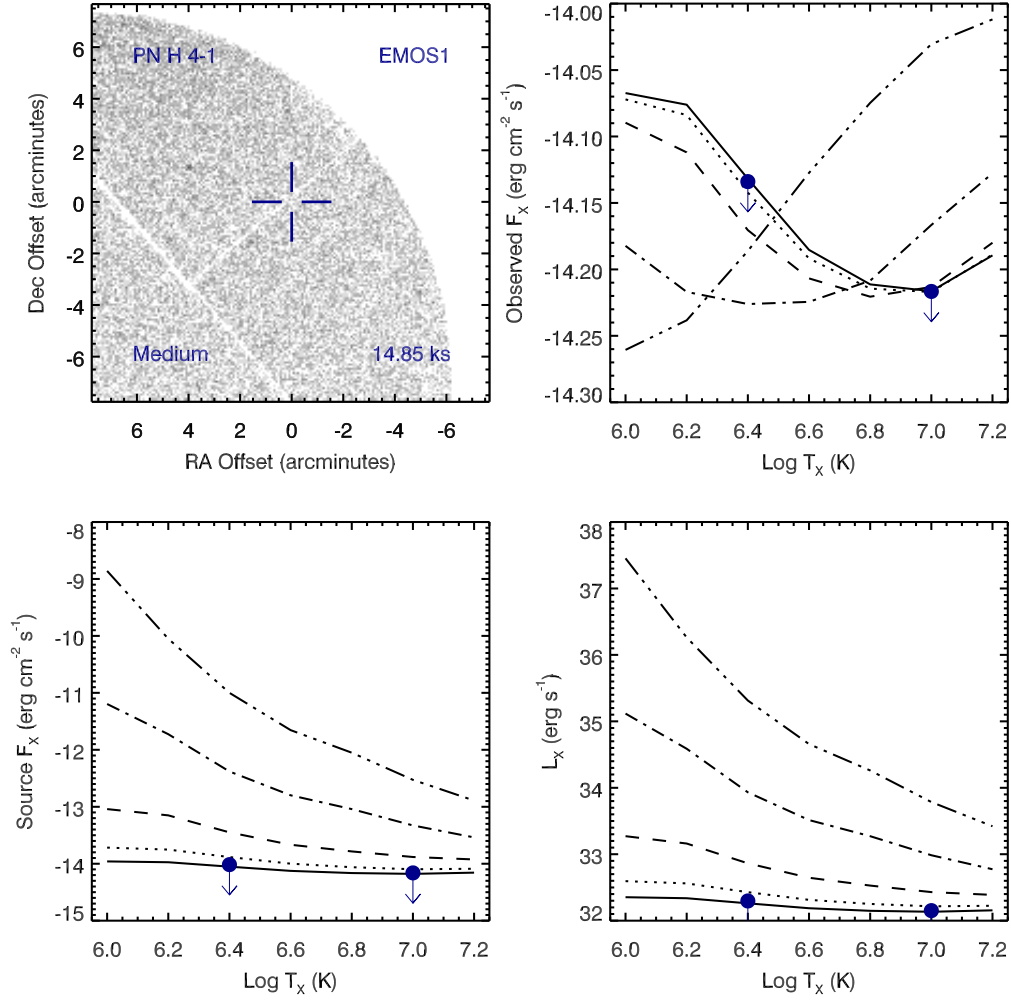


Figure A.32 Serendipitous XMM EMOS1 observation (ObsID 0124710401) of PN H 4-1. Clock-wise from top-left: broad band (0.3 to 8.0 keV) image at the PN position, upper limits of the observed flux, X-ray luminosity, and source X-ray flux. The upper limits calculations are based on the upper limit count rates, a thermal plasma model at a range temperatures, and a range of intervening absorption values:  $N_H(10^{22} \text{ cm}^{-2}) = 0.03$  (solid), 0.1 (dotted), 0.3 (dashed), 1 (dot-dashed), and 3 (dot-dot-dashed). The hot bubble and spun-up companion upper limits are depicted as the filled circles with downward pointing arrows at  $\log T_x$  of 6.4 and 7.0, respectively.

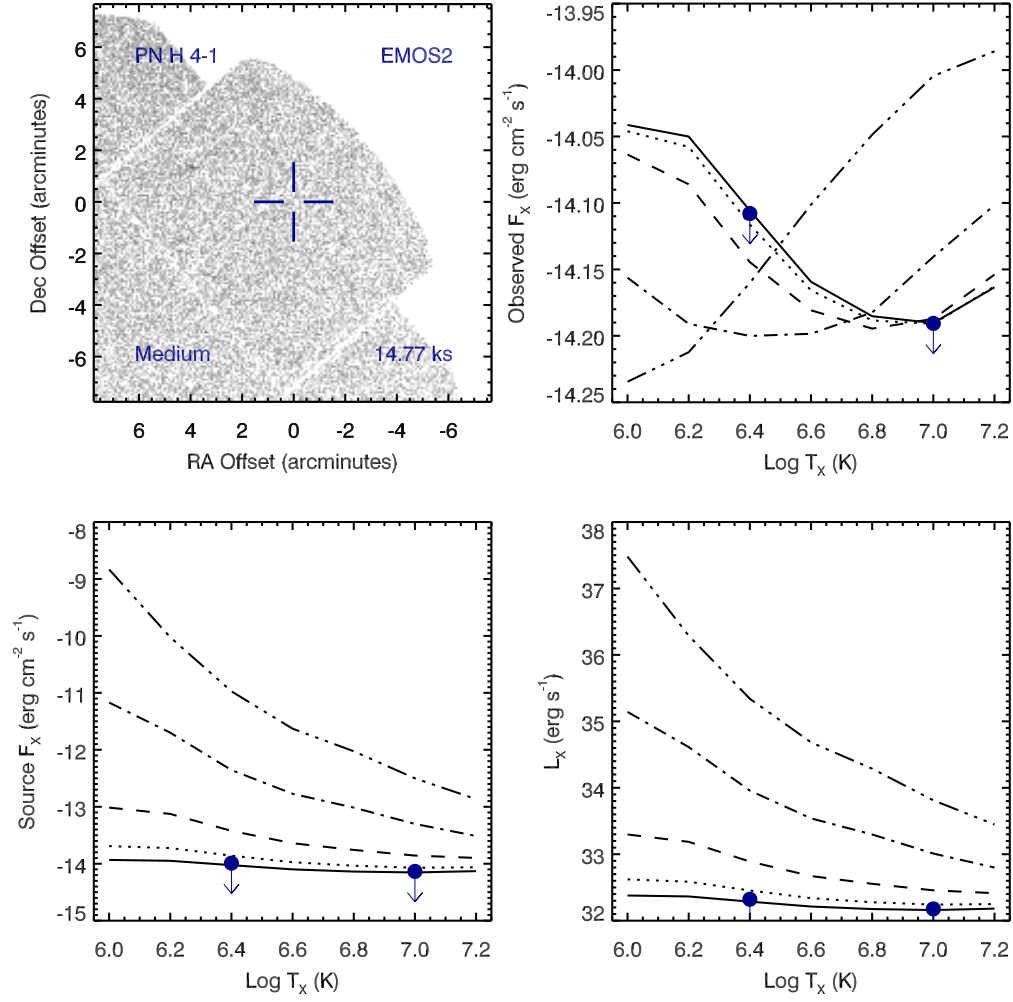


Figure A.33 Serendipitous XMM EMOS2 observation (ObsID 0124710401) of PN H 4-1 ; panels as in Figure A.32.

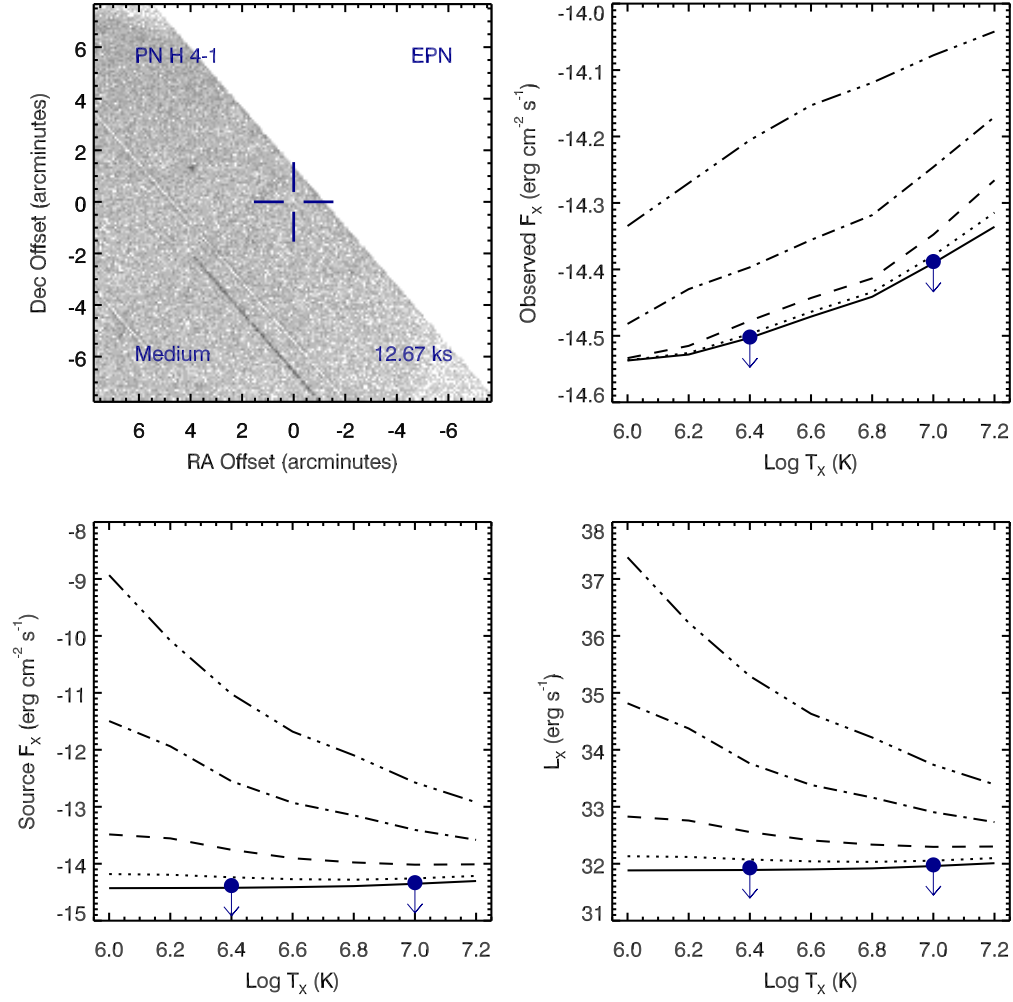


Figure A.34 Serendipitous XMM EPN observation (ObsID 0124710401) of PN H 4-1 ; panels as in Figure A.32.

## Hen 2-102 , ObsID 0007422401

Table A.19 Summary of the Analysis for the XMM EPIC observation (ObsID 0007422401) of Hen 2-102.

Basic Data			
Parameter	Value	Notes	
RA (J2000)	209.557775		
DEC (J2000)	-58.908828	Offset (')	4.11
$R_{\text{nebula}}$ (")	4.5	from literature (A94)	
$D$ (kpc)	3.50	from statistical methods (A94)	
$\log N_H$ ( $\text{cm}^{-2}$ )	21.6243	optical extinction (C92)	
$T_{\text{eff}}$ (kK)	74.10	HeI or HeII Zanstra (Ph03)	
Date Obs:	2002-02-20	XMM Filter:	Medium

Calculations			
Parameter	EMOS1	EMOS2	EPN
$t_{\text{exp}}$ (ks)	12.0	12.1	–
$\text{CR}_{\text{src}}$ ( $\text{cnt s}^{-1}$ )	5.921E-07	5.053E-07	–
$\text{CR}_{\text{bkg}}$ ( $\text{cnt s}^{-1}$ )	4.602E-07	5.849E-07	–

Hot Bubble Upper Limits ( $T_X \sim 3 \times 10^6$ K)			
Parameter	EMOS1	EMOS2	EPN
$F_X$ ( $\text{erg cm}^{-2} \text{s}^{-1}$ )	-13.4719	-13.4207	–
$L_X$ ( $\text{erg s}^{-1}$ )	31.6942	31.7454	–

Spun-up Companion Upper Limits ( $T_X \sim 10^7$ K)			
Parameter	EMOS1	EMOS2	EPN
$F_X$ ( $\text{erg cm}^{-2} \text{s}^{-1}$ )	-14.0129	-13.9618	–
$L_X$ ( $\text{erg s}^{-1}$ )	31.1532	31.2043	–
$L_*$ ( $L_{\text{sun}}$ )	3.7007	4.1627	–
$M_{\text{bol}}$ (mag)	3.3193	3.1916	–
Spectral Type	F0-F2V	F0-F2V	–

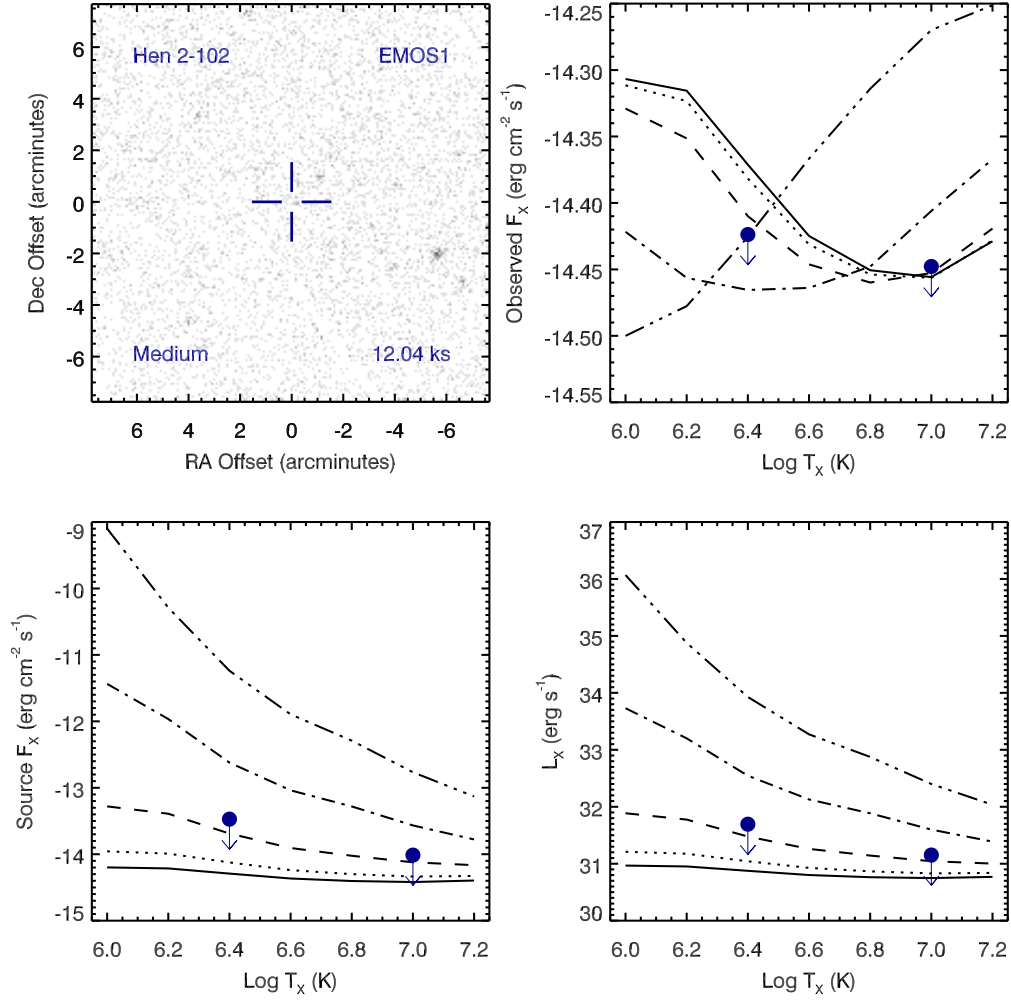


Figure A.35 Serendipitous XMM EMOS1 observation (ObsID 0007422401) of Hen 2-102. Clock-wise from top-left: broad band (0.3 to 8.0 keV) image at the PN position, upper limits of the observed flux, X-ray luminosity, and source X-ray flux. The upper limits calculations are based on the upper limit count rates, a thermal plasma model at a range temperatures, and a range of intervening absorption values:  $N_H(10^{22} \text{ cm}^{-2}) = 0.03$  (solid), 0.1 (dotted), 0.3 (dashed), 1 (dot-dashed), and 3 (dot-dot-dashed). The hot bubble and spun-up companion upper limits are depicted as the filled circles with downward pointing arrows at  $\log T_X$  of 6.4 and 7.0, respectively.

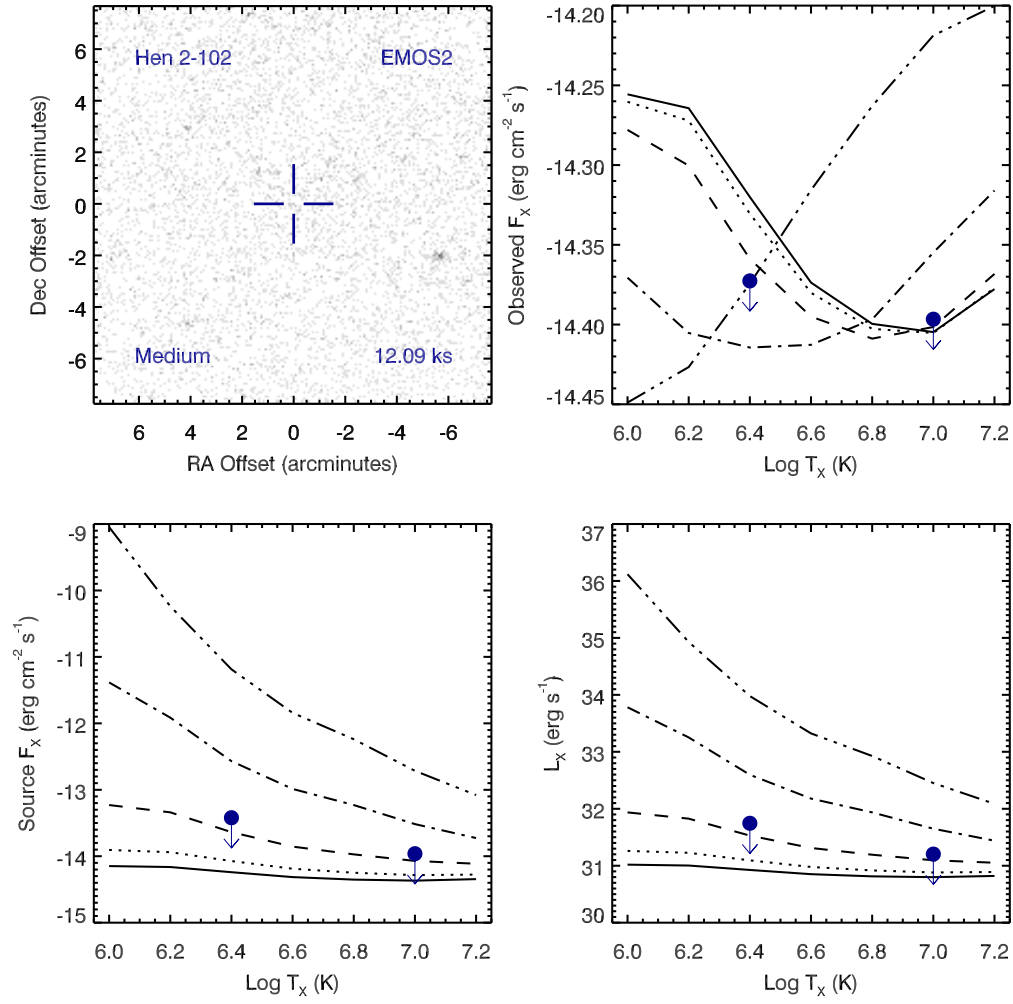


Figure A.36 Serendipitous XMM EMOS2 observation (ObsID 0007422401) of Hen 2-102 ; panels as in Figure A.35.

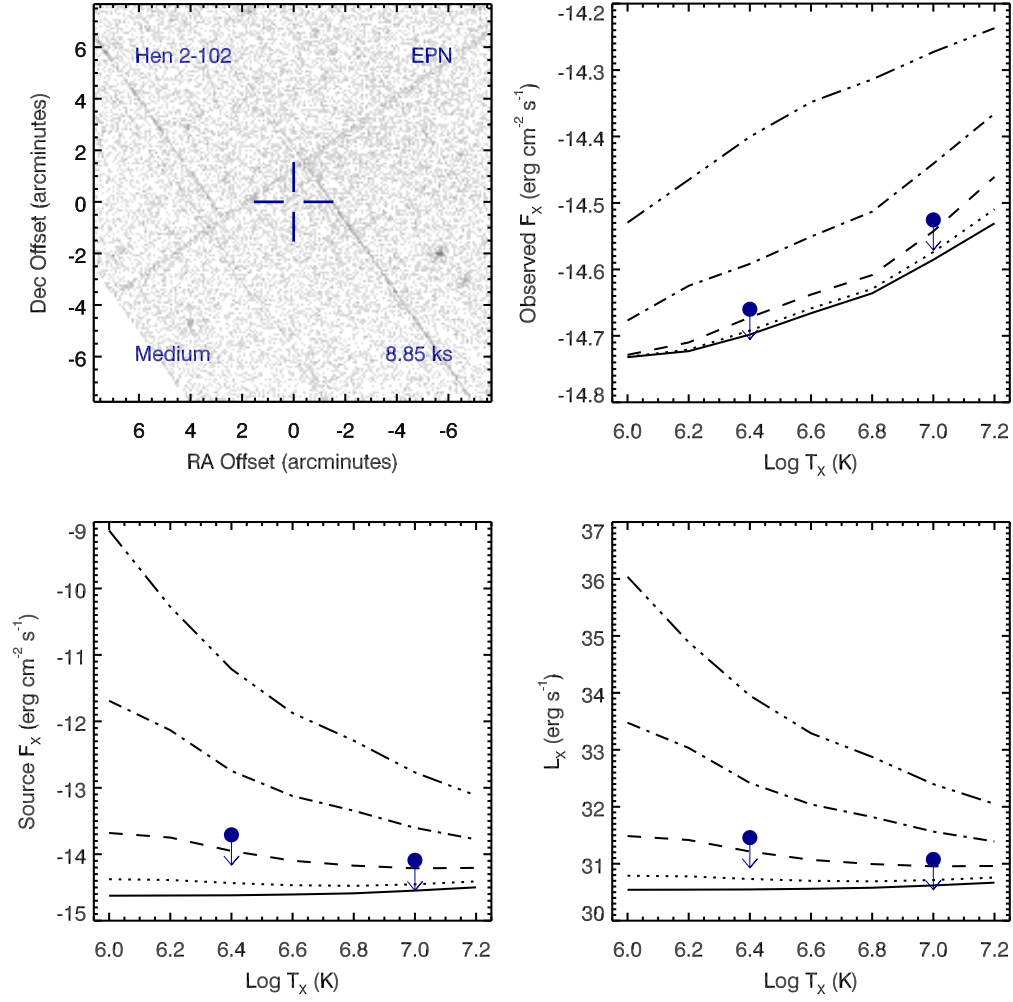


Figure A.37 Serendipitous XMM EPN observation (ObsID 0007422401) of Hen 2-102 ; panels as in Figure A.35.

# PN K 1-16 , ObsID 0110950501

Table A.20 Summary of the Analysis for the XMM EPIC observation (ObsID 0110950501) of PN K 1-16.

Basic Data			
Parameter	Value	Notes	
RA (J2000)	275.467546		
DEC (J2000)	64.365086	Offset (')	1.40
$R_{\text{nebula}}$ (")	57.0	from literature (A94)	
$D$ (kpc)	0.38	from literature (A94)	
$\log N_H$ (cm <sup>-2</sup> )	0.0000	optical extinction (C92)	
$T_{\text{eff}}$ (kK)	94.70	HeI or HeII Zanstra (Ph03)	
Date Obs:	2002-10-16	XMM Filter:	Thin1

Calculations			
Parameter	EMOS1	EMOS2	EPN
$t_{\text{exp}}$ (ks)	–	–	–
$\text{CR}_{\text{src}}$ (cnt s <sup>-1</sup> )	–	–	–
$\text{CR}_{\text{bkg}}$ (cnt s <sup>-1</sup> )	–	–	–

Hot Bubble Upper Limits ( $T_X \sim 3 \times 10^6$ K)			
Parameter	EMOS1	EMOS2	EPN
$F_X$ (erg cm <sup>-2</sup> s <sup>-1</sup> )	–	–	–
$L_X$ (erg s <sup>-1</sup> )	–	–	–

Spun-up Companion Upper Limits ( $T_X \sim 10^7$ K)			
Parameter	EMOS1	EMOS2	EPN
$F_X$ (erg cm <sup>-2</sup> s <sup>-1</sup> )	–	–	–
$L_X$ (erg s <sup>-1</sup> )	–	–	–
$L_*$ ( $L_{\text{sun}}$ )	–	–	–
$M_{\text{bol}}$ (mag)	–	–	–
Spectral Type	–	–	–



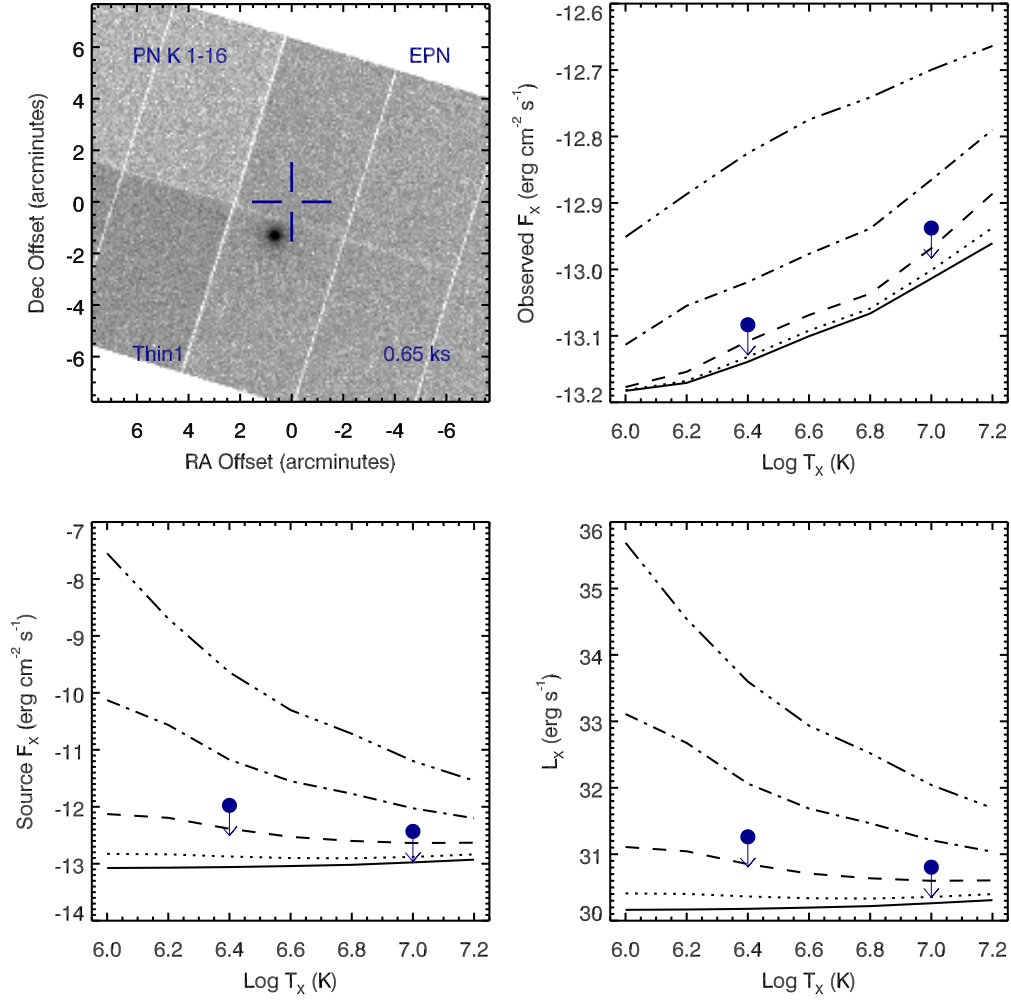


Figure A.38 Serendipitous XMM EPN observation (ObsID 0110950501) of PN K 1-16. Clock-wise from top-left: broad band (0.3 to 8.0 keV) image at the PN position, upper limits of the observed flux, X-ray luminosity, and source X-ray flux. The upper limits calculations are based on the upper limit count rates, a thermal plasma model at a range temperatures, and a range of intervening absorption values:  $N_H(10^{22} \text{ cm}^{-2}) = 0.03$  (solid), 0.1 (dotted), 0.3 (dashed), 1 (dot-dashed), and 3 (dot-dot-dashed). The hot bubble and spun-up companion upper limits are depicted as the filled circles with downward pointing arrows at  $\log T_X$  of 6.4 and 7.0, respectively.

# PN K 3-57 , ObsID 0212481201

Table A.21 Summary of the Analysis for the XMM EPIC observation (ObsID 0212481201) of PN K 3-57.

Basic Data			
Parameter	Value	Notes	
RA (J2000)	303.198663		
DEC (J2000)	34.342367	Offset (')	12.05
$R_{\text{nebula}}$ (")	3.0	from literature (A94)	
$D$ (kpc)	4.02	from statistical methods (A94)	
$\log N_H$ ( $\text{cm}^{-2}$ )	21.6990	unknown, assumed value	
$T_{\text{eff}}$ (kK)	–		
Date Obs:	2005-10-12	XMM Filter:	Medium

Calculations			
Parameter	EMOS1	EMOS2	EPN
$t_{\text{exp}}$ (ks)	25.3	25.3	–
$\text{CR}_{\text{src}}$ ( $\text{cnt s}^{-1}$ )	4.636E-07	3.627E-07	–
$\text{CR}_{\text{bkg}}$ ( $\text{cnt s}^{-1}$ )	3.873E-07	3.359E-07	–

Hot Bubble Upper Limits ( $T_X \sim 3 \times 10^6$ K)			
Parameter	EMOS1	EMOS2	EPN
$F_X$ ( $\text{erg cm}^{-2} \text{s}^{-1}$ )	-13.5233	-13.5542	–
$L_X$ ( $\text{erg s}^{-1}$ )	31.7630	31.7321	–

Spun-up Companion Upper Limits ( $T_X \sim 10^7$ K)			
Parameter	EMOS1	EMOS2	EPN
$F_X$ ( $\text{erg cm}^{-2} \text{s}^{-1}$ )	-14.1363	-14.1673	–
$L_X$ ( $\text{erg s}^{-1}$ )	31.1501	31.1191	–
$L_*$ ( $L_{\text{sun}}$ )	3.6746	3.4211	–
$M_{\text{bol}}$ (mag)	3.3270	3.4046	–
Spectral Type	F0-F2V	F5-F2V	–

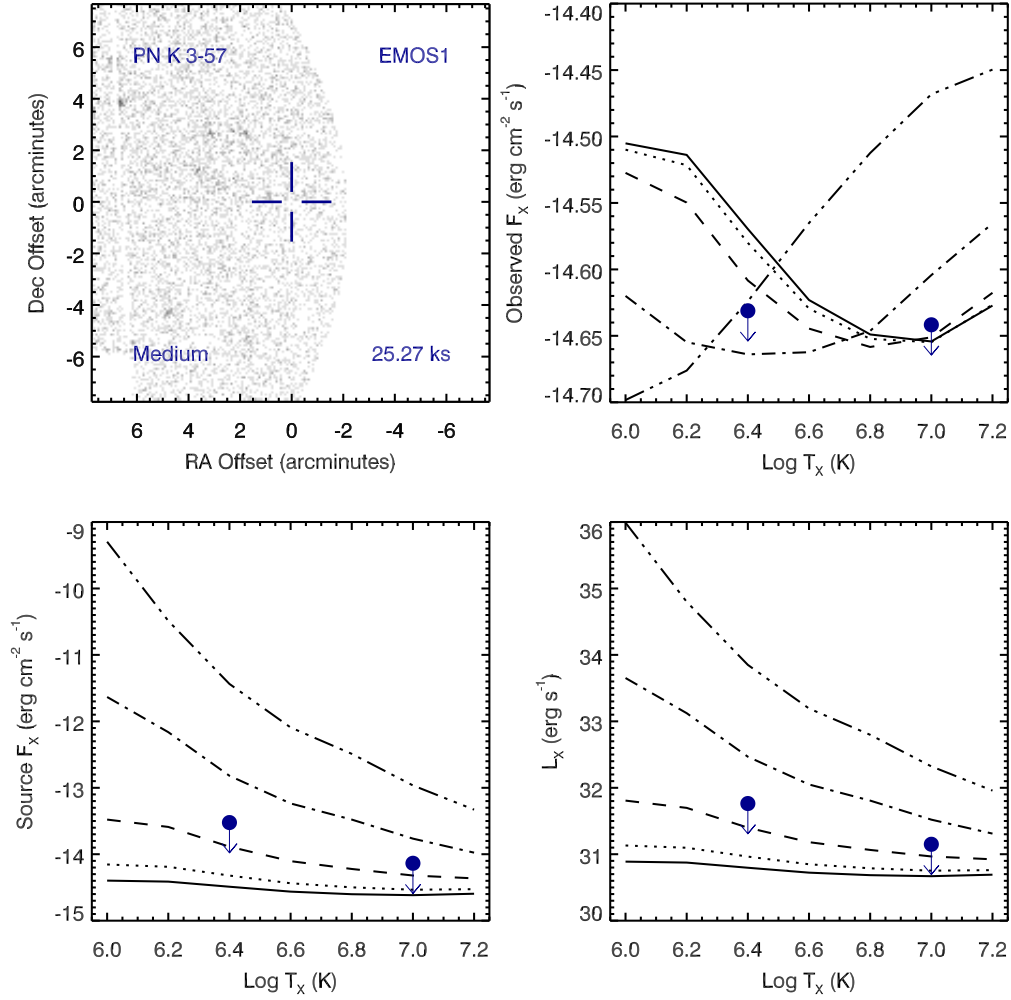


Figure A.39 Serendipitous XMM EMOS1 observation (ObsID 0212481201) of PN K 3-57. Clock-wise from top-left: broad band (0.3 to 8.0 keV) image at the PN position, upper limits of the observed flux, X-ray luminosity, and source X-ray flux. The upper limits calculations are based on the upper limit count rates, a thermal plasma model at a range temperatures, and a range of intervening absorption values:  $N_H(10^{22} \text{ cm}^{-2}) = 0.03$  (solid), 0.1 (dotted), 0.3 (dashed), 1 (dot-dashed), and 3 (dot-dot-dashed). The hot bubble and spun-up companion upper limits are depicted as the filled circles with downward pointing arrows at  $\log T_X$  of 6.4 and 7.0, respectively.

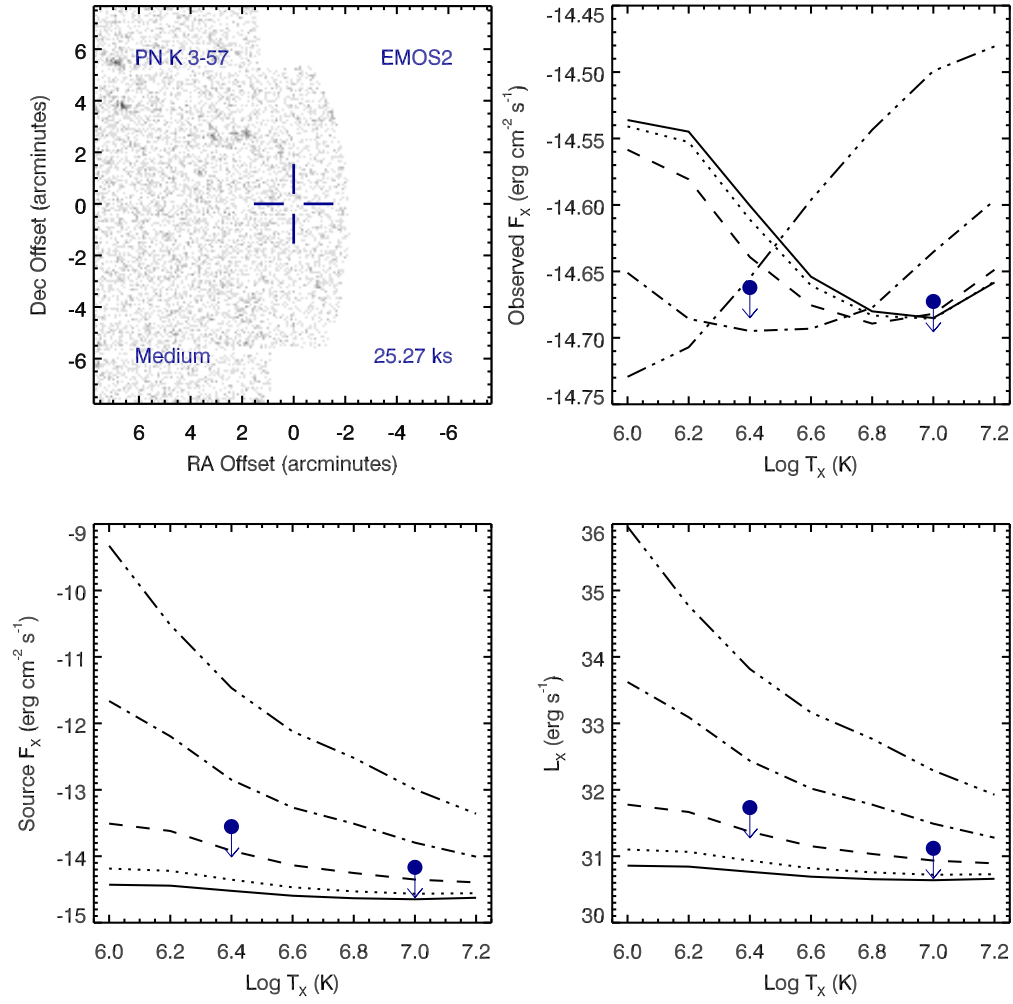


Figure A.40 Serendipitous XMM EMOS2 observation (ObsID 0212481201) of PN K 3-57 ; panels as in Figure A.39.

# PN K 3-92 , ObsID 0153752201

Table A.22 Summary of the Analysis for the XMM EPIC observation (ObsID 0153752201) of PN K 3-92.

Basic Data			
Parameter	Value	Notes	
RA (J2000)	30.921546		
DEC (J2000)	64.960522	Offset (')	9.21
$R_{\text{nebula}}$ (")	6.1	from literature (A94)	
$D$ (kpc)	6.81	from statistical methods (A94)	
$\log N_H$ ( $\text{cm}^{-2}$ )	21.7118	optical extinction (C92)	
$T_{\text{eff}}$ (kK)	46.80	HeI or HeII Zanstra (Ph03)	
Date Obs:	2002-09-11	XMM Filter:	Thin1

Calculations			
Parameter	EMOS1	EMOS2	EPN
$t_{\text{exp}}$ (ks)	27.5	27.5	–
$\text{CR}_{\text{src}}$ ( $\text{cnt s}^{-1}$ )	5.374E-07	6.117E-07	–
$\text{CR}_{\text{bkg}}$ ( $\text{cnt s}^{-1}$ )	3.903E-07	5.106E-07	–

Hot Bubble Upper Limits ( $T_X \sim 3 \times 10^6$ K)			
Parameter	EMOS1	EMOS2	EPN
$F_X$ ( $\text{erg cm}^{-2} \text{ s}^{-1}$ )	-13.5312	-13.4728	–
$L_X$ ( $\text{erg s}^{-1}$ )	32.2130	32.2714	–

Spun-up Companion Upper Limits ( $T_X \sim 10^7$ K)			
Parameter	EMOS1	EMOS2	EPN
$F_X$ ( $\text{erg cm}^{-2} \text{ s}^{-1}$ )	-14.1499	-14.0915	–
$L_X$ ( $\text{erg s}^{-1}$ )	31.5943	31.6527	–
$L_*$ ( $L_{\text{sun}}$ )	10.2189	11.6895	–
$M_{\text{bol}}$ (mag)	2.2165	2.0705	–
Spectral Type	A5-F0V	A5-F0V	–

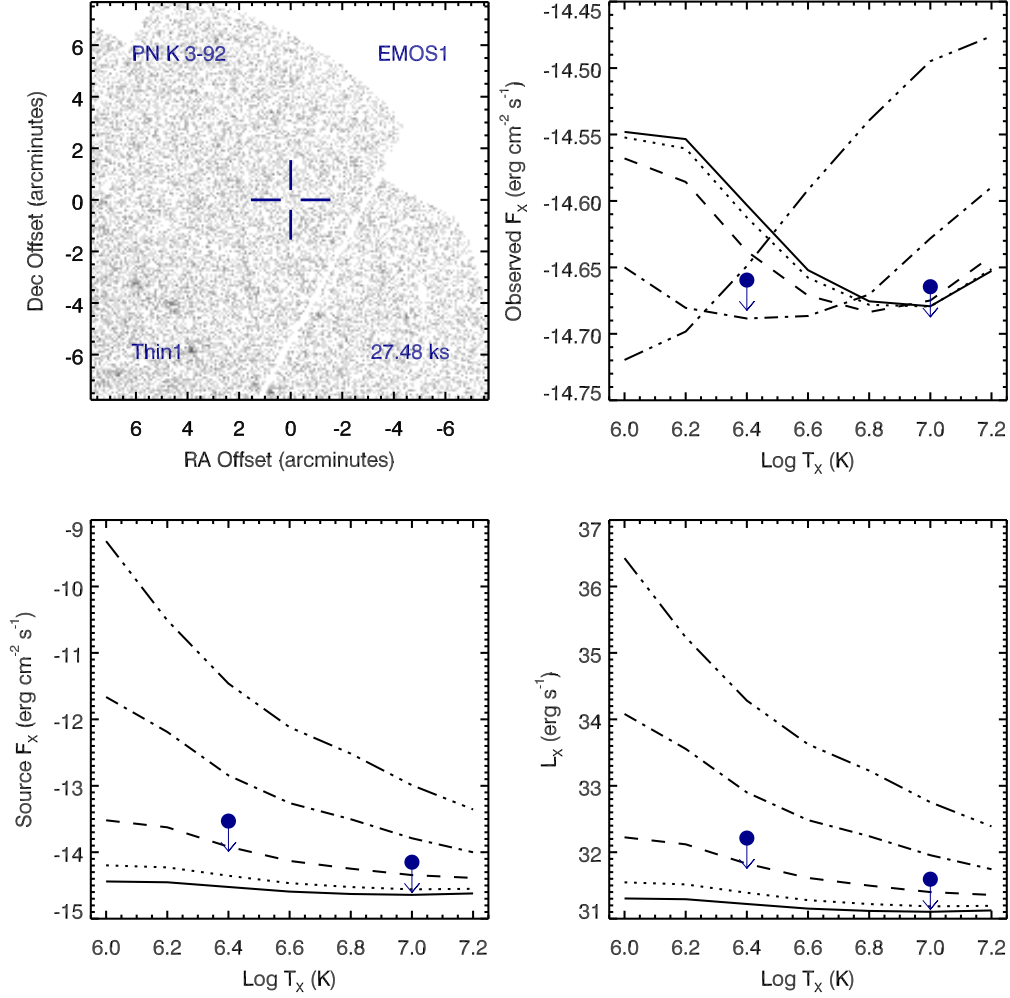


Figure A.41 Serendipitous XMM EMOS1 observation (ObsID 0153752201) of PN K 3-92. Clock-wise from top-left: broad band (0.3 to 8.0 keV) image at the PN position, upper limits of the observed flux, X-ray luminosity, and source X-ray flux. The upper limits calculations are based on the upper limit count rates, a thermal plasma model at a range temperatures, and a range of intervening absorption values:  $N_H(10^{22} \text{ cm}^{-2}) = 0.03$  (solid), 0.1 (dotted), 0.3 (dashed), 1 (dot-dashed), and 3 (dot-dot-dashed). The hot bubble and spun-up companion upper limits are depicted as the filled circles with downward pointing arrows at  $\log T_x$  of 6.4 and 7.0, respectively.

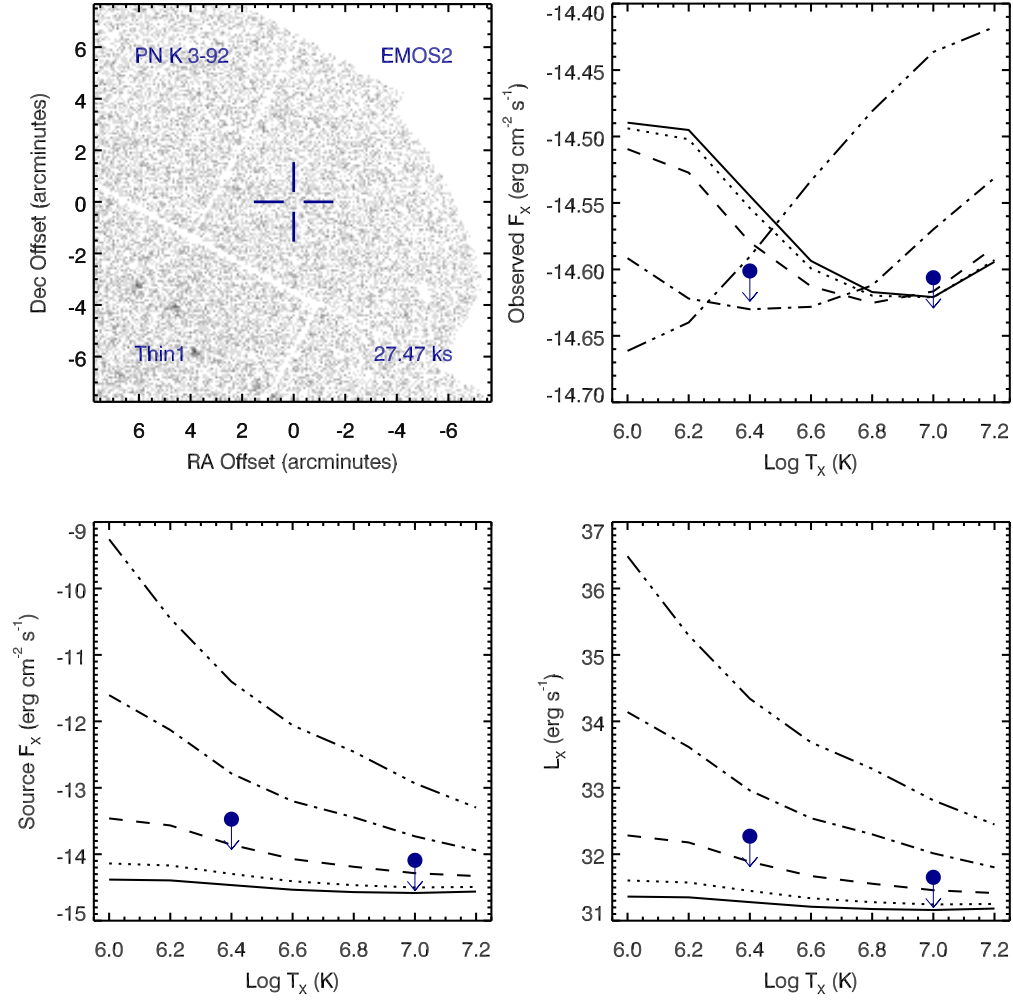


Figure A.42 Serendipitous XMM EMOS2 observation (ObsID 0153752201) of PN K 3-92 ; panels as in Figure A.41.

## PN K 3-92 , ObsID 0153751701

Table A.23 Summary of the Analysis for the XMM EPIC observation (ObsID 0153751701) of PN K 3-92.

Basic Data			
Parameter	Value	Notes	
RA (J2000)	30.921546		
DEC (J2000)	64.960522	Offset (')	11.19
$R_{\text{nebula}}$ (")	6.1	from literature (A94)	
$D$ (kpc)	6.81	from statistical methods (A94)	
$\log N_H$ ( $\text{cm}^{-2}$ )	21.7118	optical extinction (C92)	
$T_{\text{eff}}$ (kK)	46.80	HeI or HeII Zanstra (Ph03)	
Date Obs:	2002-09-13	XMM Filter:	Thin1

Calculations			
Parameter	EMOS1	EMOS2	EPN
$t_{\text{exp}}$ (ks)	1.0	1.0	–
$\text{CR}_{\text{src}}$ ( $\text{cnt s}^{-1}$ )	2.616E-06	4.967E-06	–
$\text{CR}_{\text{bkg}}$ ( $\text{cnt s}^{-1}$ )	3.149E-06	3.909E-06	–

Hot Bubble Upper Limits ( $T_X \sim 3 \times 10^6$ K)			
Parameter	EMOS1	EMOS2	EPN
$F_X$ ( $\text{erg cm}^{-2} \text{ s}^{-1}$ )	-12.3524	-12.3168	–
$L_X$ ( $\text{erg s}^{-1}$ )	33.3918	33.4274	–

Spun-up Companion Upper Limits ( $T_X \sim 10^7$ K)			
Parameter	EMOS1	EMOS2	EPN
$F_X$ ( $\text{erg cm}^{-2} \text{ s}^{-1}$ )	-12.9710	-12.9355	–
$L_X$ ( $\text{erg s}^{-1}$ )	32.7732	32.8087	–
$L_*$ ( $L_{\text{sun}}$ )	154.2715	167.4041	–
$M_{\text{bol}}$ (mag)	-0.7307	-0.8194	–
Spectral Type	B8-A0V	B8-A0V	–



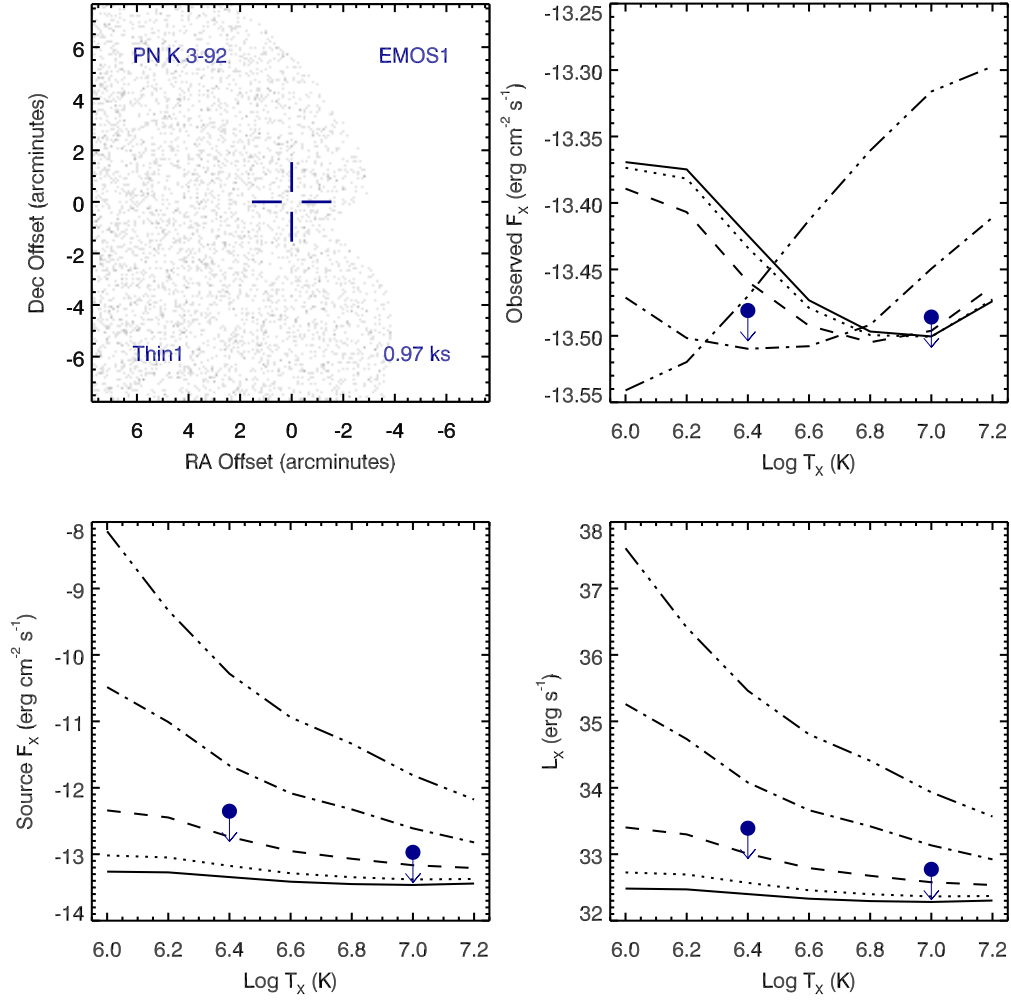


Figure A.43 Serendipitous XMM EMOS1 observation (ObsID 0153751701) of PN K 3-92. Clock-wise from top-left: broad band (0.3 to 8.0 keV) image at the PN position, upper limits of the observed flux, X-ray luminosity, and source X-ray flux. The upper limits calculations are based on the upper limit count rates, a thermal plasma model at a range temperatures, and a range of intervening absorption values:  $N_H(10^{22} \text{ cm}^{-2}) = 0.03$  (solid), 0.1 (dotted), 0.3 (dashed), 1 (dot-dashed), and 3 (dot-dot-dashed). The hot bubble and spun-up companion upper limits are depicted as the filled circles with downward pointing arrows at log  $T_x$  of 6.4 and 7.0, respectively.

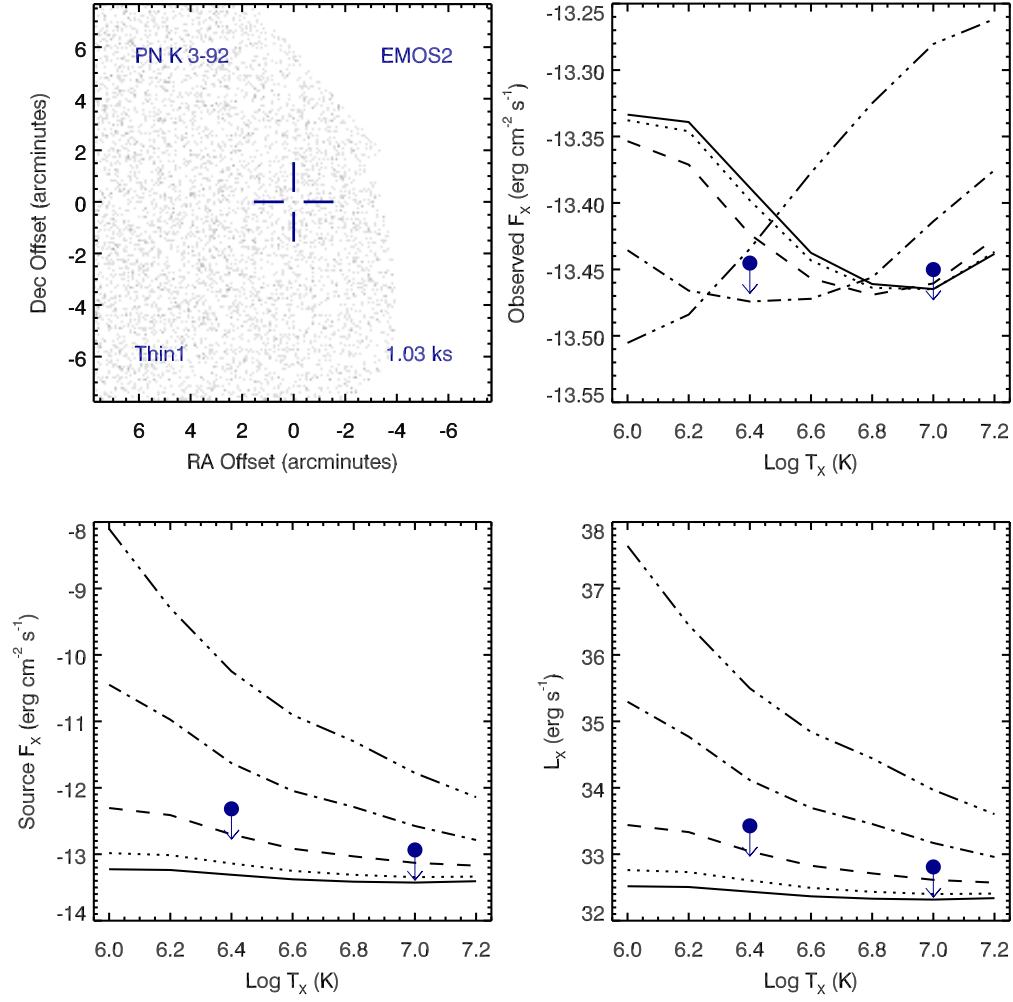


Figure A.44 Serendipitous XMM EMOS2 observation (ObsID 0153751701) of PN K 3-92 ; panels as in Figure A.43.

# PN K 3-92 , ObsID 0153751701u

Table A.24 Summary of the Analysis for the XMM EPIC observation (ObsID 0153751701u) of PN K 3-92.

Basic Data			
Parameter	Value	Notes	
RA (J2000)	30.921546		
DEC (J2000)	64.960522	Offset (')	11.19
$R_{\text{nebula}}$ (")	6.1	from literature (A94)	
$D$ (kpc)	6.81	from statistical methods (A94)	
$\log N_H$ ( $\text{cm}^{-2}$ )	21.7118	optical extinction (C92)	
$T_{\text{eff}}$ (kK)	46.80	HeI or HeII Zanstra (Ph03)	
Date Obs:	2002-09-13	XMM Filter:	Thin1

Calculations			
Parameter	EMOS1	EMOS2	EPN
$t_{\text{exp}}$ (ks)	17.1	17.1	–
$\text{CR}_{\text{src}}$ ( $\text{cnt s}^{-1}$ )	9.829E-07	8.927E-07	–
$\text{CR}_{\text{bkg}}$ ( $\text{cnt s}^{-1}$ )	6.964E-07	9.161E-07	–

Hot Bubble Upper Limits ( $T_X \sim 3 \times 10^6$ K)			
Parameter	EMOS1	EMOS2	EPN
$F_X$ ( $\text{erg cm}^{-2} \text{ s}^{-1}$ )	-13.3024	-13.2431	–
$L_X$ ( $\text{erg s}^{-1}$ )	32.4418	32.5011	–

Spun-up Companion Upper Limits ( $T_X \sim 10^7$ K)			
Parameter	EMOS1	EMOS2	EPN
$F_X$ ( $\text{erg cm}^{-2} \text{ s}^{-1}$ )	-13.9212	-13.8617	–
$L_X$ ( $\text{erg s}^{-1}$ )	31.8230	31.8825	–
$L_*$ ( $L_{\text{sun}}$ )	17.3033	19.8432	–
$M_{\text{bol}}$ (mag)	1.6447	1.4960	–
Spectral Type	A2-A5V	A2-A5V	–

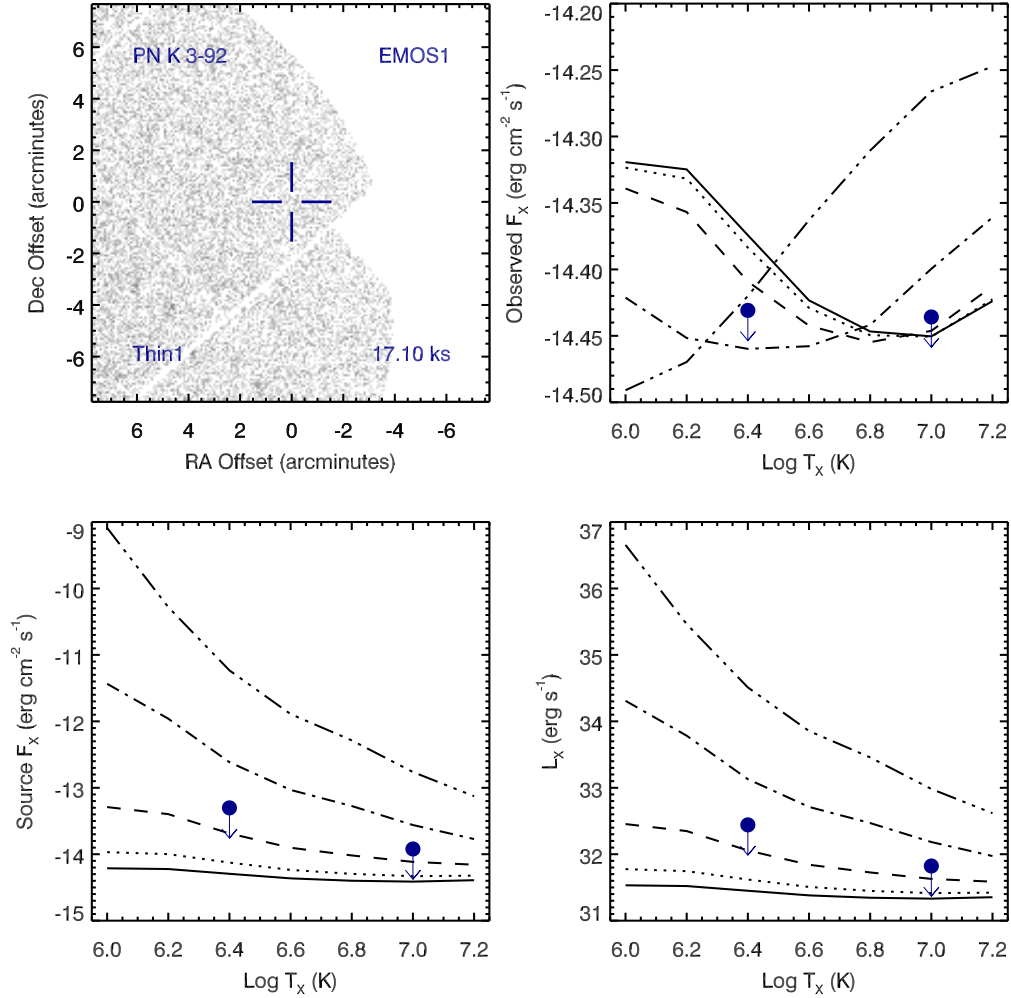


Figure A.45 Serendipitous XMM EMOS1 observation (ObsID 0153751701u) of PN K 3-92. Clock-wise from top-left: broad band (0.3 to 8.0 keV) image at the PN position, upper limits of the observed flux, X-ray luminosity, and source X-ray flux. The upper limits calculations are based on the upper limit count rates, a thermal plasma model at a range temperatures, and a range of intervening absorption values:  $N_H(10^{22} \text{ cm}^{-2}) = 0.03$  (solid), 0.1 (dotted), 0.3 (dashed), 1 (dot-dashed), and 3 (dot-dot-dashed). The hot bubble and spun-up companion upper limits are depicted as the filled circles with downward pointing arrows at  $\log T_X$  of 6.4 and 7.0, respectively.

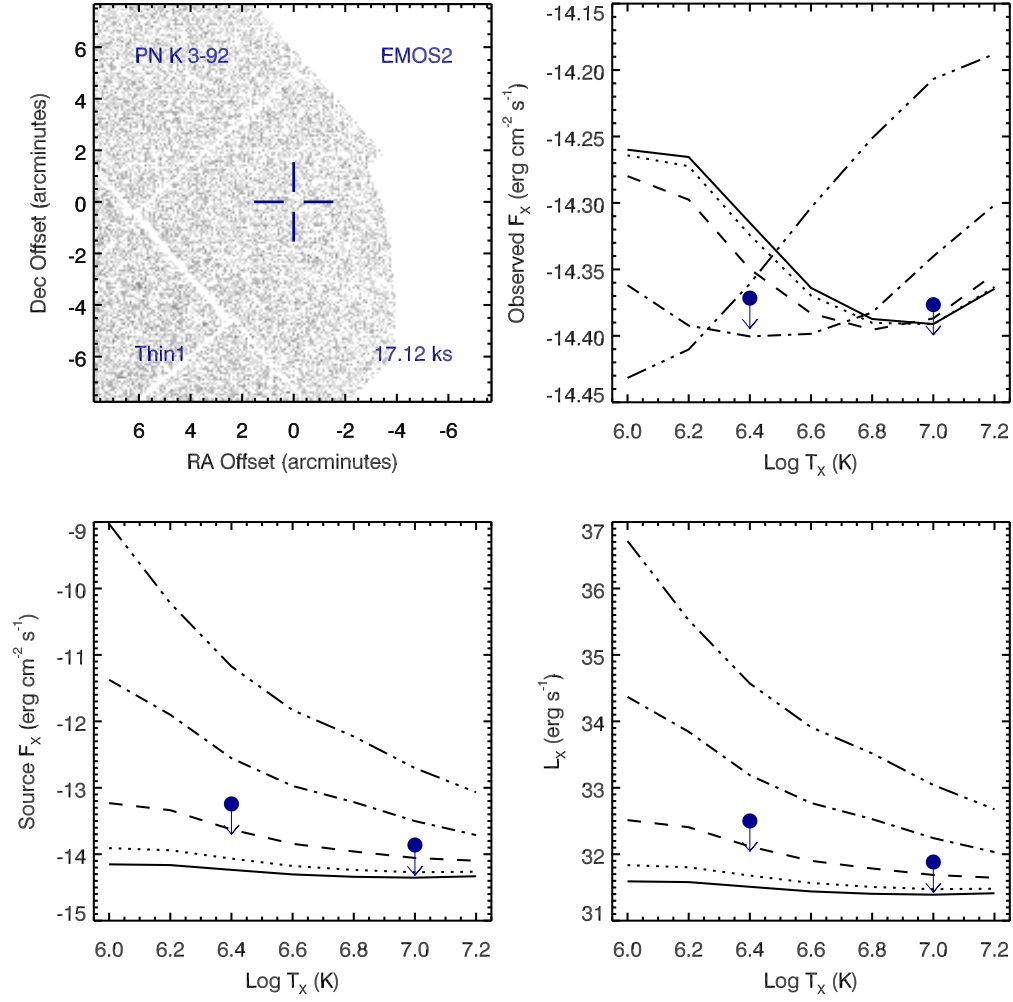


Figure A.46 Serendipitous XMM EMOS2 observation (ObsID 0153751701u) of PN K 3-92 ; panels as in Figure A.45.

## PN M 1-28 , ObsID 0306700501

Table A.25 Summary of the Analysis for the XMM EPIC observation (ObsID 0306700501) of PN M 1-28.

Basic Data			
Parameter	Value	Notes	
RA (J2000)	266.911700		
DEC (J2000)	-22.107200	Offset (')	8.03
$R_{\text{nebula}}$ (")	7.4	from literature (A94)	
$D$ (kpc)	2.77	from statistical methods (A94)	
$\log N_H$ ( $\text{cm}^{-2}$ )	21.6990	unknown, assumed value	
$T_{\text{eff}}$ (kK)	–		
Date Obs:	2006-03-01	XMM Filter:	Medium

Calculations			
Parameter	EMOS1	EMOS2	EPN
$t_{\text{exp}}$ (ks)	–	11.2	–
$\text{CR}_{\text{src}}$ ( $\text{cnt s}^{-1}$ )	–	7.721E-07	–
$\text{CR}_{\text{bkg}}$ ( $\text{cnt s}^{-1}$ )	–	8.620E-07	–

Hot Bubble Upper Limits ( $T_X \sim 3 \times 10^6$ K)			
Parameter	EMOS1	EMOS2	EPN
$F_X$ ( $\text{erg cm}^{-2} \text{s}^{-1}$ )	–	-13.1731	–
$L_X$ ( $\text{erg s}^{-1}$ )	–	31.7897	–

Spun-up Companion Upper Limits ( $T_X \sim 10^7$ K)			
Parameter	EMOS1	EMOS2	EPN
$F_X$ ( $\text{erg cm}^{-2} \text{s}^{-1}$ )	–	-13.7862	–
$L_X$ ( $\text{erg s}^{-1}$ )	–	31.1767	–
$L_*$ ( $L_{\text{sun}}$ )	–	3.9062	–
$M_{\text{bol}}$ (mag)	–	3.2606	–
Spectral Type	–	F0-F2V	–

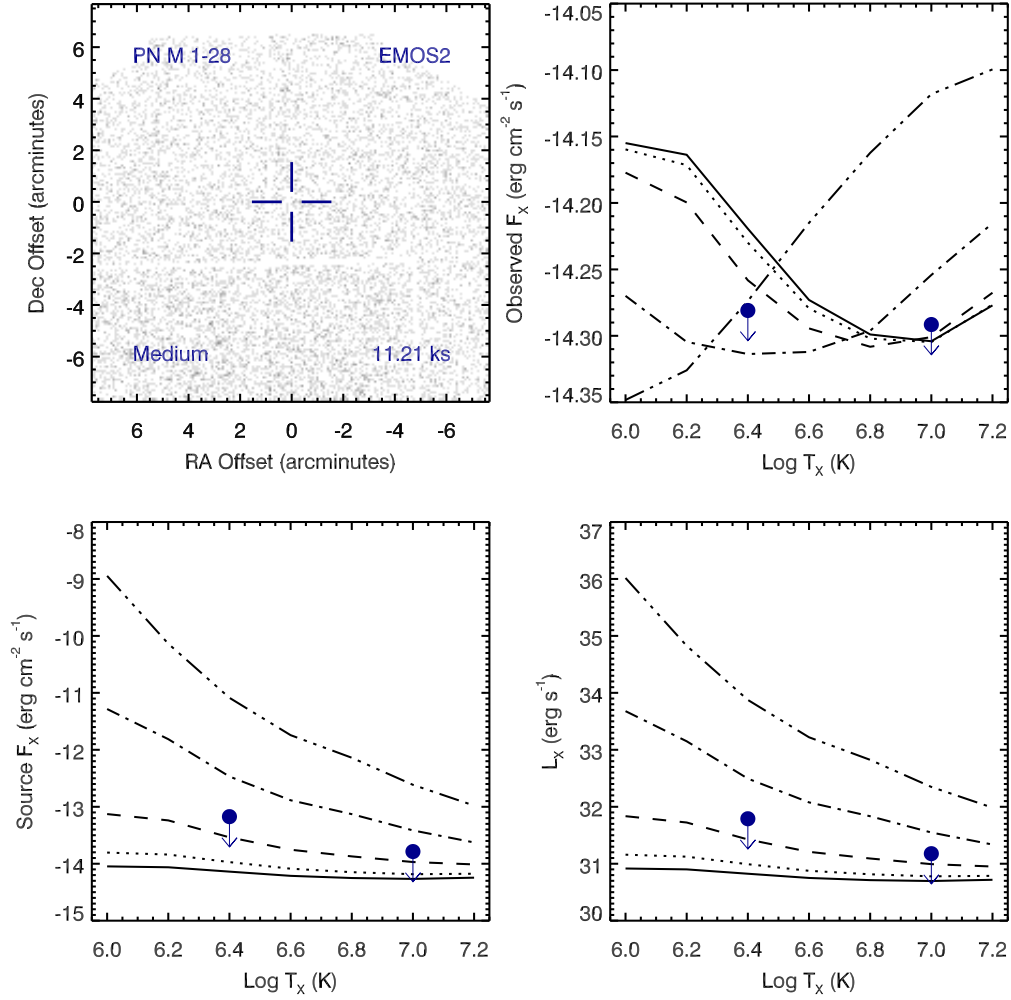


Figure A.47 Serendipitous XMM EMOS2 observation (ObsID 0306700501) of PN M 1-28. Clock-wise from top-left: broad band (0.3 to 8.0 keV) image at the PN position, upper limits of the observed flux, X-ray luminosity, and source X-ray flux. The upper limits calculations are based on the upper limit count rates, a thermal plasma model at a range temperatures, and a range of intervening absorption values:  $N_H(10^{22} \text{ cm}^{-2}) = 0.03$  (solid), 0.1 (dotted), 0.3 (dashed), 1 (dot-dashed), and 3 (dot-dot-dashed). The hot bubble and spun-up companion upper limits are depicted as the filled circles with downward pointing arrows at  $\log T_X$  of 6.4 and 7.0, respectively.

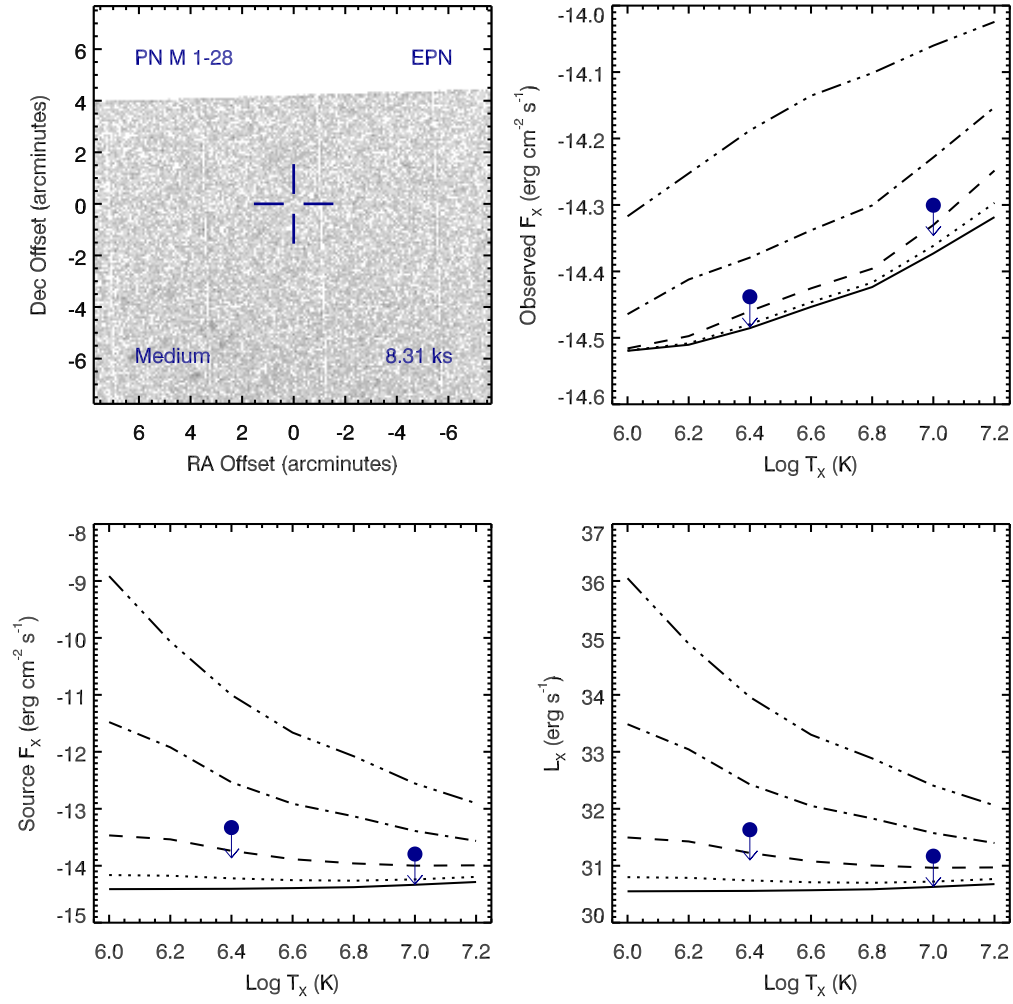


Figure A.48 Serendipitous XMM EPN observation (ObsID 0306700501) of PN M 1-28 ; panels as in Figure A.47.



## PN M 1-29 , ObsID 0202790101

Table A.26 Summary of the Analysis for the XMM EPIC observation (ObsID 0202790101) of PN M 1-29.

Basic Data			
Parameter	Value	Notes	
RA (J2000)	267.575012		
DEC (J2000)	-30.581917	Offset (')	12.74
$R_{\text{nebula}}$ (")	3.8	from literature (A94)	
$D$ (kpc)	2.37	from statistical methods (A94)	
$\log N_H$ ( $\text{cm}^{-2}$ )	21.6990	unknown, assumed value	
$T_{\text{eff}}$ (kK)	99.50	HeI or HeII Zanstra (Ph03)	
Date Obs:	2004-09-15	XMM Filter:	Thin1

Calculations			
Parameter	EMOS1	EMOS2	EPN
$t_{\text{exp}}$ (ks)	13.8	14.3	–
$\text{CR}_{\text{src}}$ ( $\text{cnt s}^{-1}$ )	2.147E-06	2.597E-06	–
$\text{CR}_{\text{bkg}}$ ( $\text{cnt s}^{-1}$ )	2.528E-06	2.116E-06	–

Hot Bubble Upper Limits ( $T_X \sim 3 \times 10^6$ K)			
Parameter	EMOS1	EMOS2	EPN
$F_X$ ( $\text{erg cm}^{-2} \text{s}^{-1}$ )	-12.9948	-13.0312	–
$L_X$ ( $\text{erg s}^{-1}$ )	31.8326	31.7962	–

Spun-up Companion Upper Limits ( $T_X \sim 10^7$ K)			
Parameter	EMOS1	EMOS2	EPN
$F_X$ ( $\text{erg cm}^{-2} \text{s}^{-1}$ )	-13.6040	-13.6442	–
$L_X$ ( $\text{erg s}^{-1}$ )	31.2234	31.1832	–
$L_*$ ( $L_{\text{sun}}$ )	4.3505	3.9659	–
$M_{\text{bol}}$ (mag)	3.1437	3.2441	–
Spectral Type	F0-F2V	F0-F2V	–

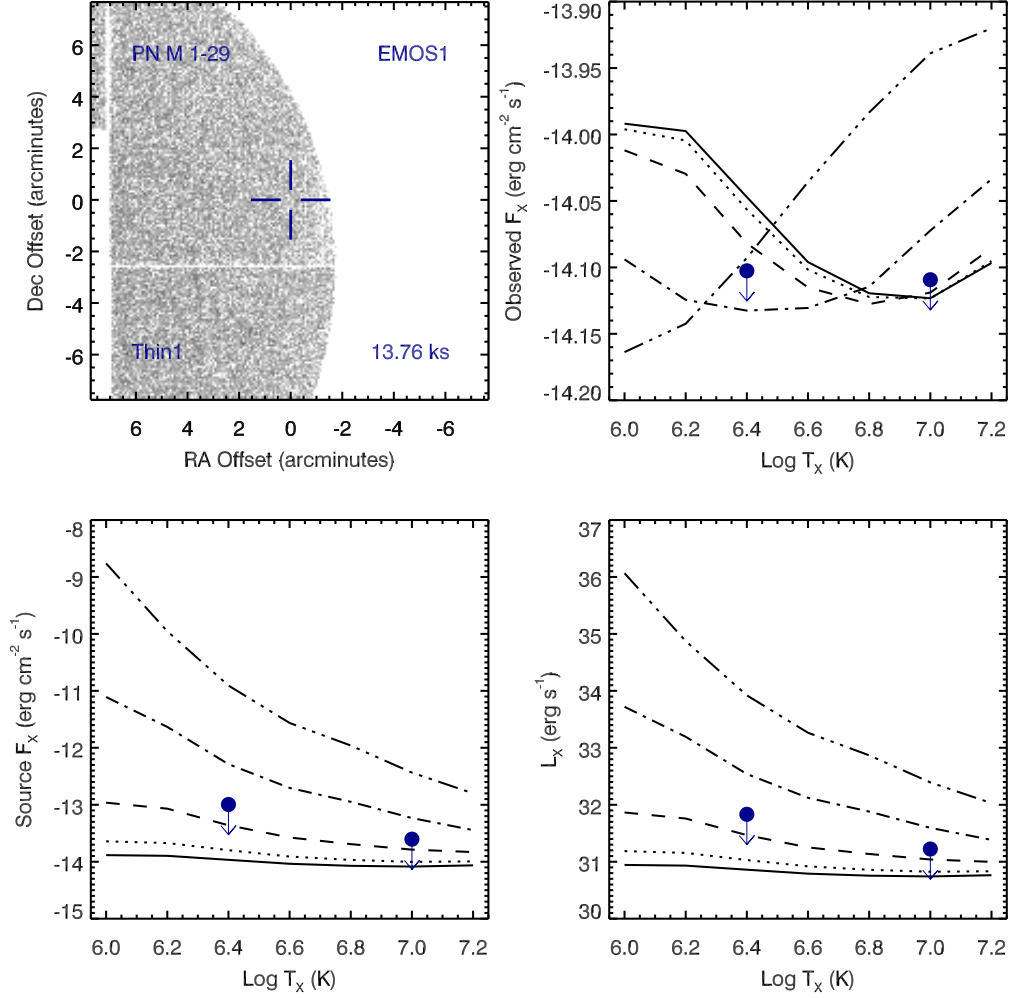


Figure A.49 Serendipitous XMM EMOS1 observation (ObsID 0202790101) of PN M 1-29. Clock-wise from top-left: broad band (0.3 to 8.0 keV) image at the PN position, upper limits of the observed flux, X-ray luminosity, and source X-ray flux. The upper limits calculations are based on the upper limit count rates, a thermal plasma model at a range temperatures, and a range of intervening absorption values:  $N_H(10^{22} \text{ cm}^{-2}) = 0.03$  (solid), 0.1 (dotted), 0.3 (dashed), 1 (dot-dashed), and 3 (dot-dot-dashed). The hot bubble and spun-up companion upper limits are depicted as the filled circles with downward pointing arrows at  $\log T_x$  of 6.4 and 7.0, respectively.

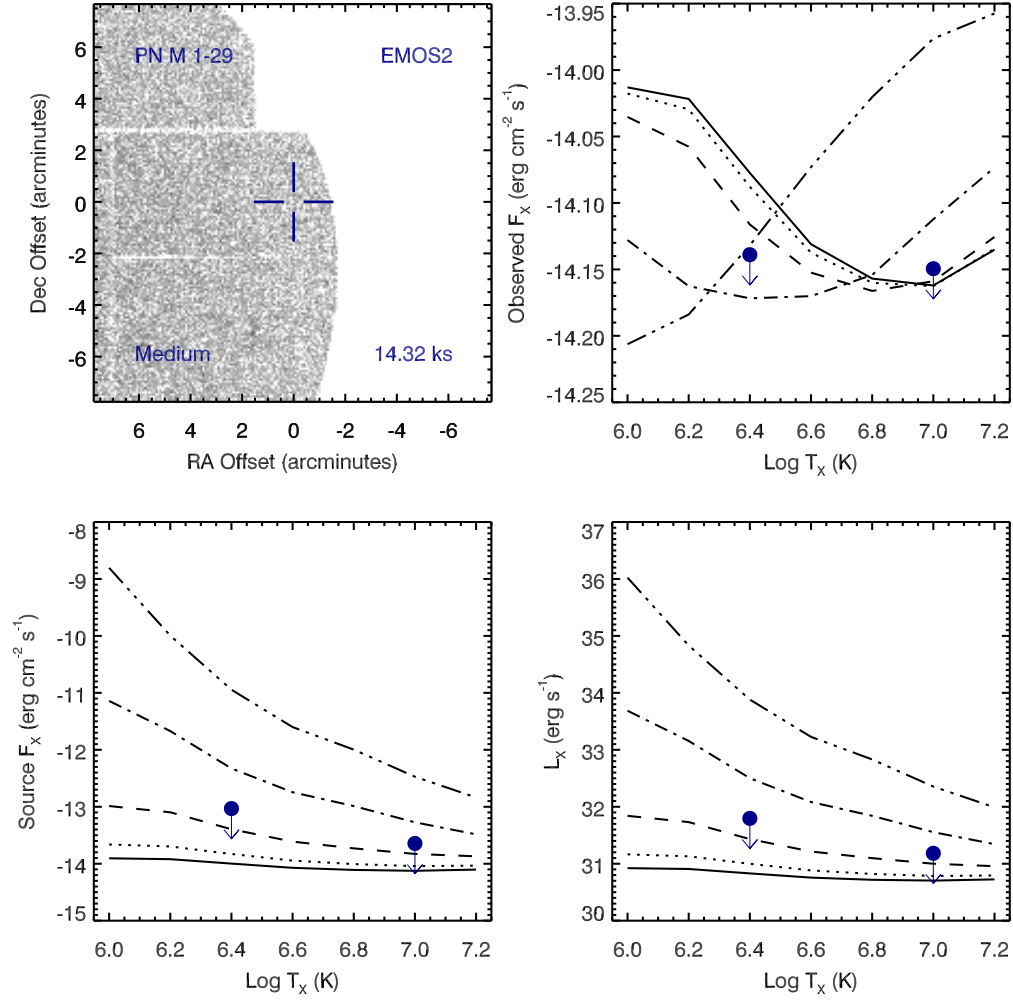


Figure A.50 Serendipitous XMM EMOS2 observation (ObsID 0202790101) of PN M 1-29 ; panels as in Figure A.49.

# PN M 1-29 , ObsID 0154750301

Table A.27 Summary of the Analysis for the XMM EPIC observation (ObsID 0154750301) of PN M 1-29.

Basic Data			
Parameter	Value	Notes	
RA (J2000)	267.575012		
DEC (J2000)	-30.581917	Offset (')	12.74
$R_{\text{nebula}}$ (")	3.8	from literature (A94)	
$D$ (kpc)	2.37	from statistical methods (A94)	
$\log N_H$ ( $\text{cm}^{-2}$ )	21.6990	unknown, assumed value	
$T_{\text{eff}}$ (kK)	99.50	HeI or HeII Zanstra (Ph03)	
Date Obs:	2002-04-07	XMM Filter:	Thin1

Calculations			
Parameter	EMOS1	EMOS2	EPN
$t_{\text{exp}}$ (ks)	31.4	30.0	–
$\text{CR}_{\text{src}}$ ( $\text{cnt s}^{-1}$ )	2.062E-06	2.461E-06	–
$\text{CR}_{\text{bkg}}$ ( $\text{cnt s}^{-1}$ )	2.075E-06	2.232E-06	–

Hot Bubble Upper Limits ( $T_X \sim 3 \times 10^6$ K)			
Parameter	EMOS1	EMOS2	EPN
$F_X$ ( $\text{erg cm}^{-2} \text{s}^{-1}$ )	-13.2168	-13.1912	–
$L_X$ ( $\text{erg s}^{-1}$ )	31.6106	31.6362	–

Spun-up Companion Upper Limits ( $T_X \sim 10^7$ K)			
Parameter	EMOS1	EMOS2	EPN
$F_X$ ( $\text{erg cm}^{-2} \text{s}^{-1}$ )	-13.8259	-13.8005	–
$L_X$ ( $\text{erg s}^{-1}$ )	31.0015	31.0269	–
$L_*$ ( $L_{\text{sun}}$ )	2.6096	2.7669	–
$M_{\text{bol}}$ (mag)	3.6986	3.6350	–
Spectral Type	F5-F8V	F5-F8V	–

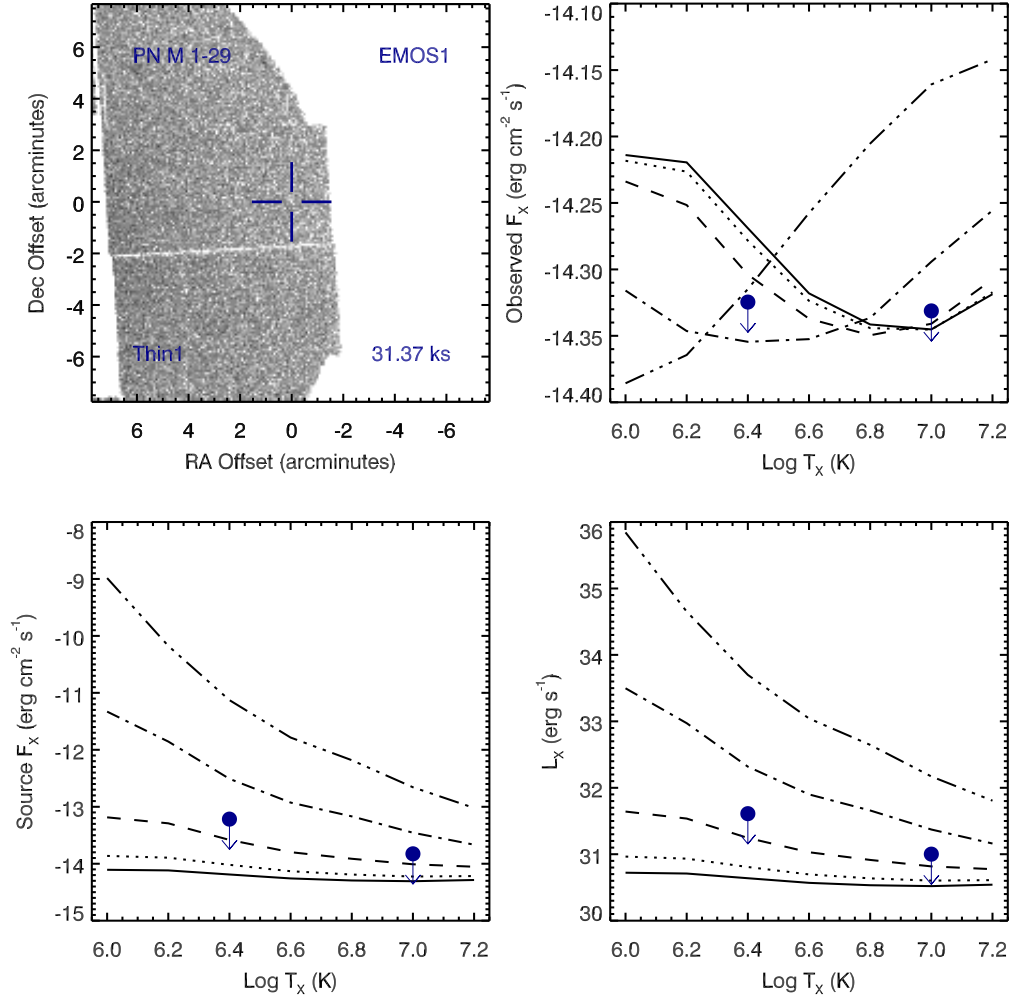


Figure A.51 Serendipitous XMM EMOS1 observation (ObsID 0154750301) of PN M 1-29. Clock-wise from top-left: broad band (0.3 to 8.0 keV) image at the PN position, upper limits of the observed flux, X-ray luminosity, and source X-ray flux. The upper limits calculations are based on the upper limit count rates, a thermal plasma model at a range temperatures, and a range of intervening absorption values:  $N_H(10^{22} \text{ cm}^{-2}) = 0.03$  (solid), 0.1 (dotted), 0.3 (dashed), 1 (dot-dashed), and 3 (dot-dot-dashed). The hot bubble and spun-up companion upper limits are depicted as the filled circles with downward pointing arrows at  $\log T_x$  of 6.4 and 7.0, respectively.

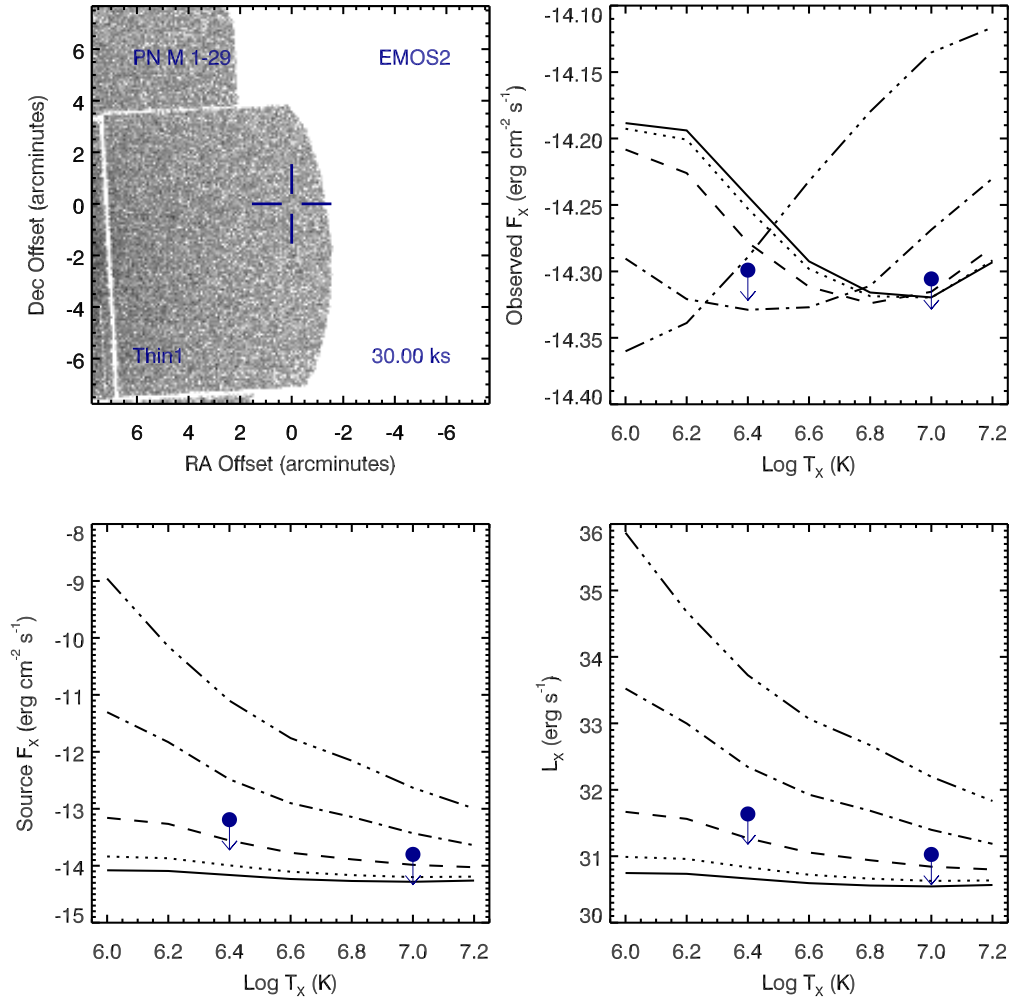


Figure A.52 Serendipitous XMM EMOS2 observation (ObsID 0154750301) of PN M 1-29 ; panels as in Figure A.51.

## PN M 1-37 , ObsID 0152420101

Table A.28 Summary of the Analysis for the XMM EPIC observation (ObsID 0152420101) of PN M 1-37.

Basic Data			
Parameter	Value	Notes	
RA (J2000)	271.357540		
DEC (J2000)	-28.367860	Offset (')	13.41
$R_{\text{nebula}}$ (")	—		
$D$ (kpc)	4.20	from statistical methods (A94)	
$\log N_H$ (cm <sup>-2</sup> )	21.6990	unknown, assumed value	
$T_{\text{eff}}$ (kK)	31.50	HeI or HeII Zanstra (Ph03)	
Date Obs:	2002-09-21	XMM Filter:	Medium

Calculations			
Parameter	EMOS1	EMOS2	EPN
$t_{\text{exp}}$ (ks)	49.0	49.1	—
$\text{CR}_{\text{src}}$ (cnt s <sup>-1</sup> )	5.712E-07	6.435E-07	—
$\text{CR}_{\text{bkg}}$ (cnt s <sup>-1</sup> )	4.231E-07	3.868E-07	—

Hot Bubble Upper Limits ( $T_X \sim 3 \times 10^6$ K)			
Parameter	EMOS1	EMOS2	EPN
$F_X$ (erg cm <sup>-2</sup> s <sup>-1</sup> )	-13.6482	-13.6678	—
$L_X$ (erg s <sup>-1</sup> )	31.6762	31.6566	—

Spun-up Companion Upper Limits ( $T_X \sim 10^7$ K)			
Parameter	EMOS1	EMOS2	EPN
$F_X$ (erg cm <sup>-2</sup> s <sup>-1</sup> )	-14.2611	-14.2808	—
$L_X$ (erg s <sup>-1</sup> )	31.0633	31.0437	—
$L_*$ ( $L_{\text{sun}}$ )	3.0087	2.8758	—
$M_{\text{bol}}$ (mag)	3.5441	3.5931	—
Spectral Type	F5-F8V	F5-F8V	—

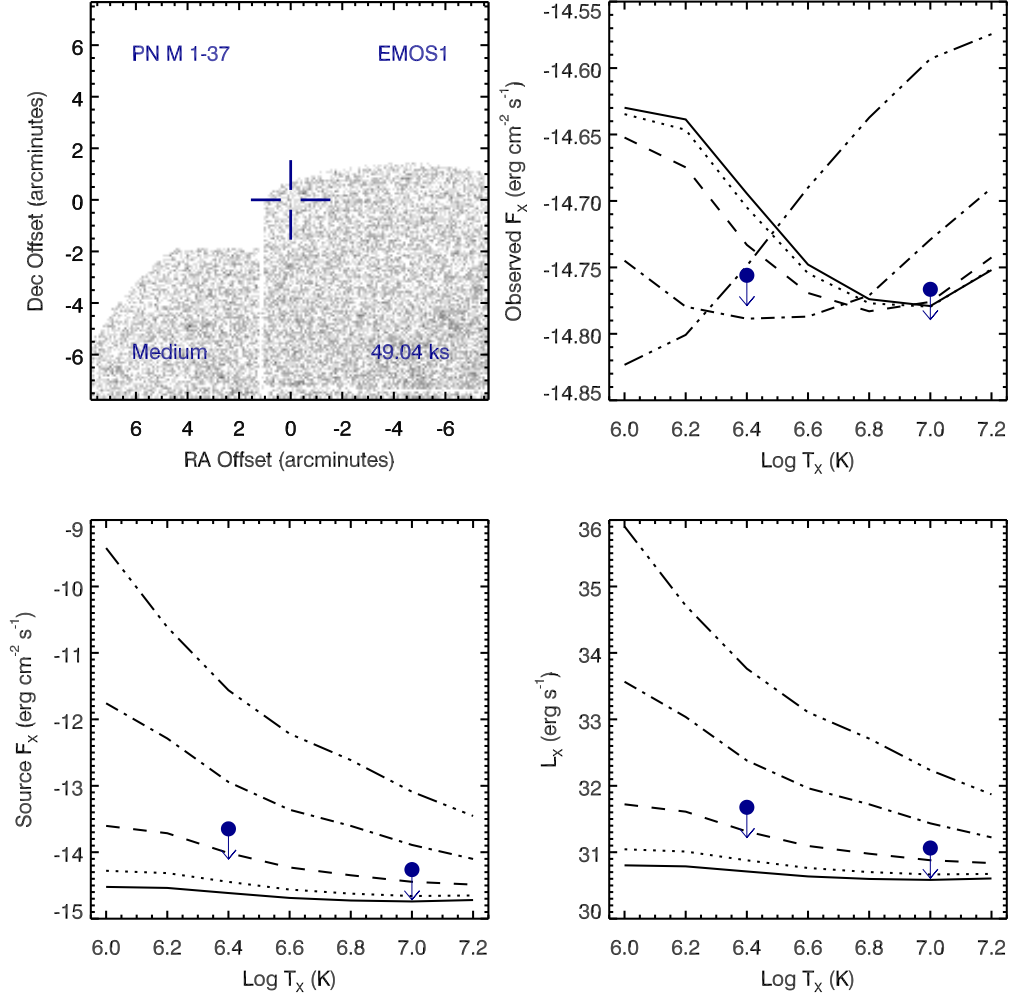


Figure A.53 Serendipitous XMM EMOS1 observation (ObsID 0152420101) of PN M 1-37. Clock-wise from top-left: broad band (0.3 to 8.0 keV) image at the PN position, upper limits of the observed flux, X-ray luminosity, and source X-ray flux. The upper limits calculations are based on the upper limit count rates, a thermal plasma model at a range temperatures, and a range of intervening absorption values:  $N_H(10^{22} \text{ cm}^{-2}) = 0.03$  (solid), 0.1 (dotted), 0.3 (dashed), 1 (dot-dashed), and 3 (dot-dot-dashed). The hot bubble and spun-up companion upper limits are depicted as the filled circles with downward pointing arrows at  $\log T_x$  of 6.4 and 7.0, respectively.



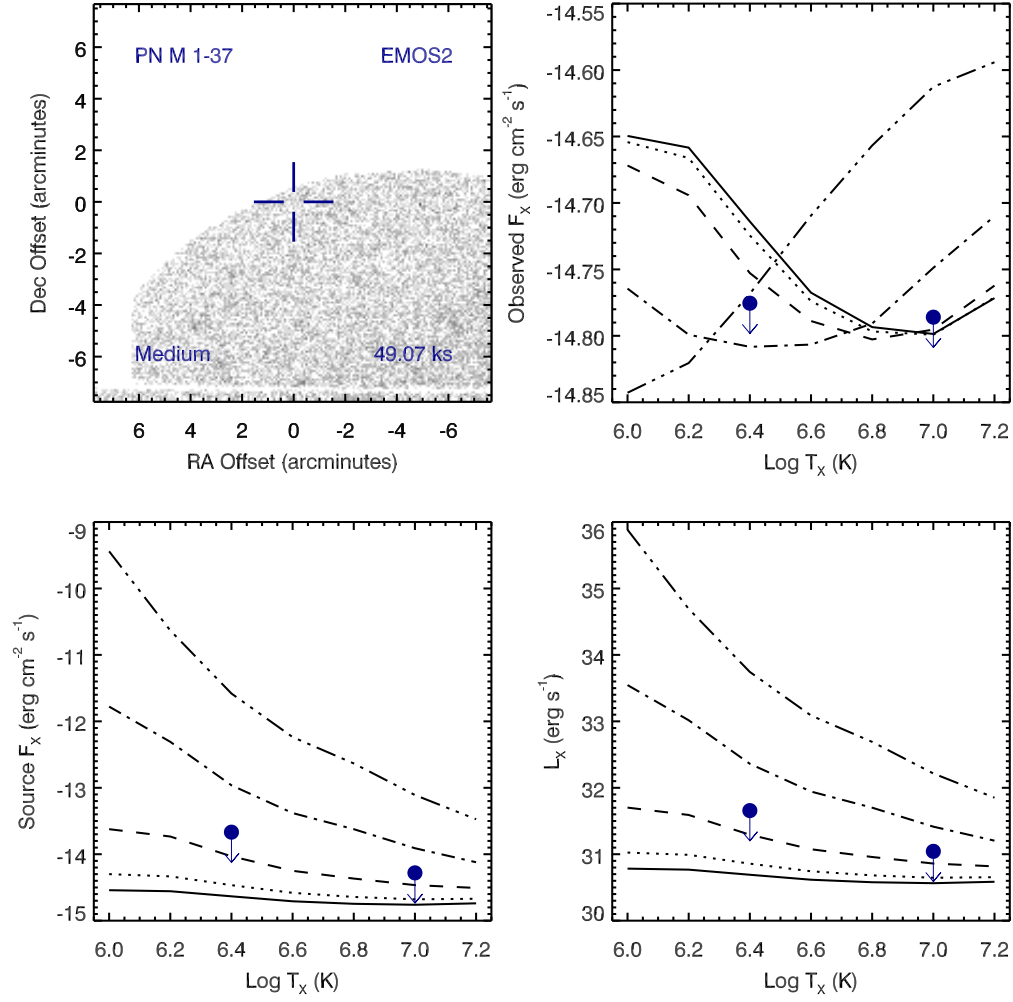


Figure A.54 Serendipitous XMM EMOS2 observation (ObsID 0152420101) of PN M 1-37 ; panels as in Figure A.53.

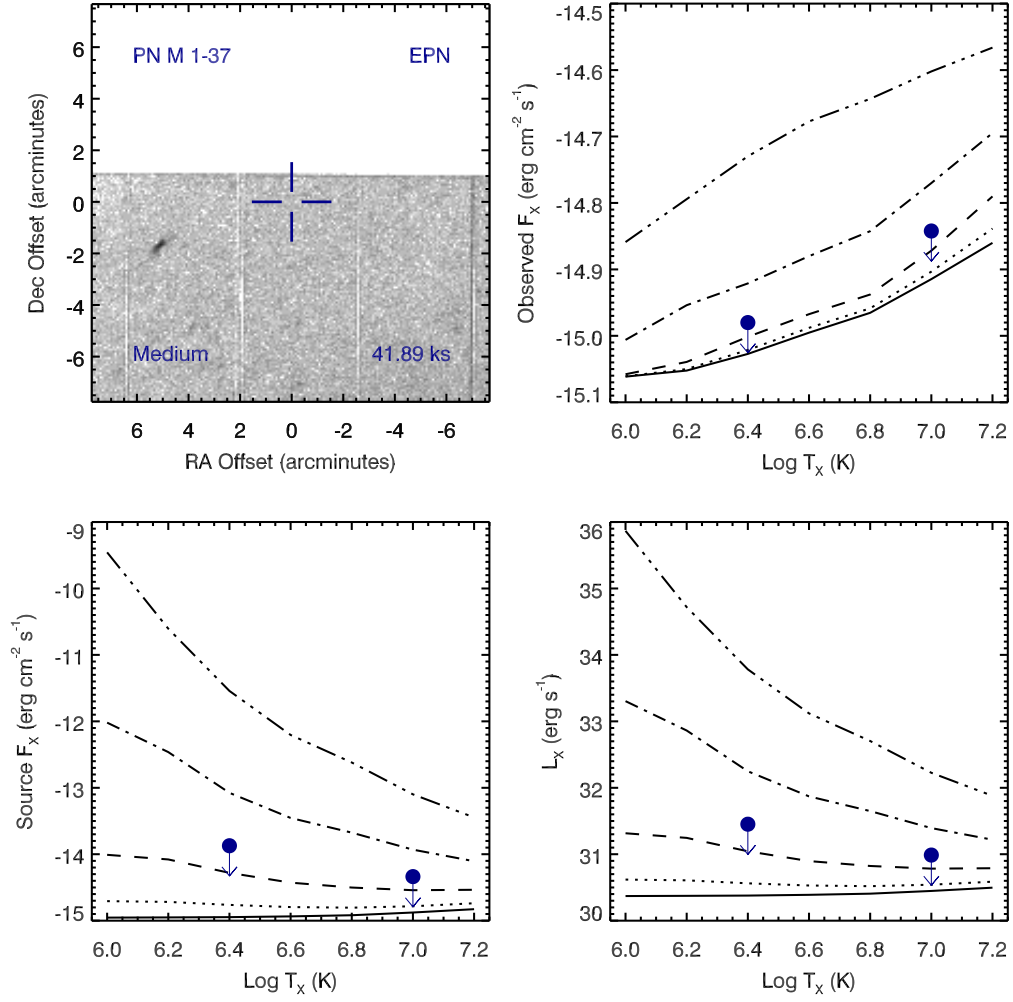


Figure A.55 Serendipitous XMM EPN observation (ObsID 0152420101) of PN M 1-37 ; panels as in Figure A.53.

## PN M 2-19 , ObsID 0206590201

Table A.29 Summary of the Analysis for the XMM EPIC observation (ObsID 0206590201) of PN M 2-19.

Basic Data			
Parameter	Value	Notes	
RA (J2000)	268.440079		
DEC (J2000)	-29.729539	Offset (')	13.29
$R_{\text{nebula}}$ (")	4.1	from literature (A94)	
$D$ (kpc)	4.00	from statistical methods (A94)	
$\log N_H$ (cm <sup>-2</sup> )	21.6990	unknown, assumed value	
$T_{\text{eff}}$ (kK)	32.40	HeI or HeII Zanstra (Ph03)	
Date Obs:	2004-09-05	XMM Filter:	Medium

Calculations			
Parameter	EMOS1	EMOS2	EPN
$t_{\text{exp}}$ (ks)	20.4	–	–
$\text{CR}_{\text{src}}$ (cnt s <sup>-1</sup> )	1.201E-06	–	–
$\text{CR}_{\text{bkg}}$ (cnt s <sup>-1</sup> )	1.233E-06	–	–

Hot Bubble Upper Limits ( $T_X \sim 3 \times 10^6$ K)			
Parameter	EMOS1	EMOS2	EPN
$F_X$ (erg cm <sup>-2</sup> s <sup>-1</sup> )	-13.2249	–	–
$L_X$ (erg s <sup>-1</sup> )	32.0571	–	–

Spun-up Companion Upper Limits ( $T_X \sim 10^7$ K)			
Parameter	EMOS1	EMOS2	EPN
$F_X$ (erg cm <sup>-2</sup> s <sup>-1</sup> )	-13.8380	–	–
$L_X$ (erg s <sup>-1</sup> )	31.4440	–	–
$L_*$ ( $L_{\text{sun}}$ )	7.2294	–	–
$M_{\text{bol}}$ (mag)	2.5922	–	–
Spectral Type	A5-F0V	–	–

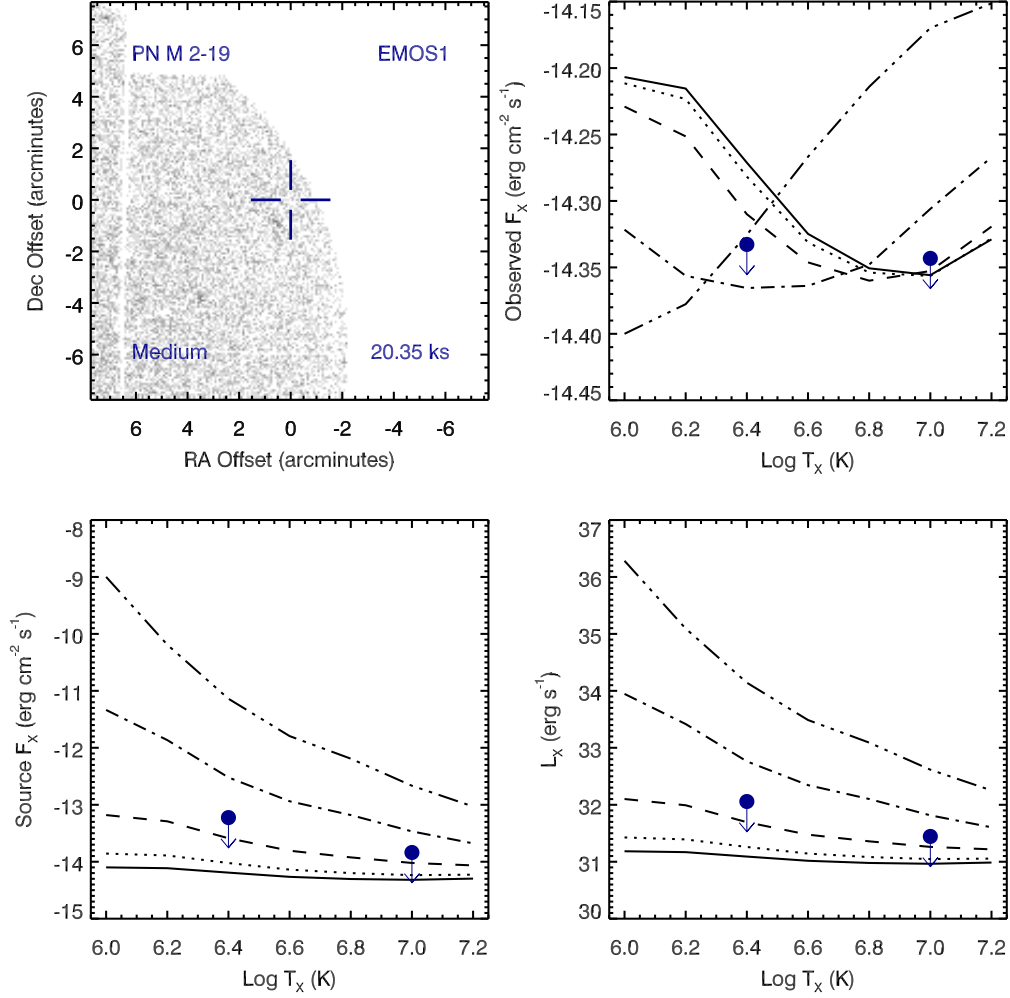


Figure A.56 Serendipitous XMM EMOS1 observation (ObsID 0206590201) of PN M 2-19. Clock-wise from top-left: broad band (0.3 to 8.0 keV) image at the PN position, upper limits of the observed flux, X-ray luminosity, and source X-ray flux. The upper limits calculations are based on the upper limit count rates, a thermal plasma model at a range temperatures, and a range of intervening absorption values:  $N_H(10^{22} \text{ cm}^{-2}) = 0.03$  (solid), 0.1 (dotted), 0.3 (dashed), 1 (dot-dashed), and 3 (dot-dot-dashed). The hot bubble and spun-up companion upper limits are depicted as the filled circles with downward pointing arrows at  $\log T_X$  of 6.4 and 7.0, respectively.

## PN M 2-19 , ObsID 0402280101

Table A.30 Summary of the Analysis for the XMM EPIC observation (ObsID 0402280101) of PN M 2-19.

Basic Data			
Parameter	Value	Notes	
RA (J2000)	268.440079		
DEC (J2000)	-29.729539	Offset (')	13.29
$R_{\text{nebula}}$ (")	4.1	from literature (A94)	
$D$ (kpc)	4.00	from statistical methods (A94)	
$\log N_H$ (cm <sup>-2</sup> )	21.6990	unknown, assumed value	
$T_{\text{eff}}$ (kK)	32.40	HeI or HeII Zanstra (Ph03)	
Date Obs:	2006-09-10	XMM Filter:	Medium

Calculations			
Parameter	EMOS1	EMOS2	EPN
$t_{\text{exp}}$ (ks)	43.2	–	–
$\text{CR}_{\text{src}}$ (cnt s <sup>-1</sup> )	1.263E-06	–	–
$\text{CR}_{\text{bkg}}$ (cnt s <sup>-1</sup> )	1.246E-06	–	–

Hot Bubble Upper Limits ( $T_X \sim 3 \times 10^6$ K)			
Parameter	EMOS1	EMOS2	EPN
$F_X$ (erg cm <sup>-2</sup> s <sup>-1</sup> )	-13.3859	–	–
$L_X$ (erg s <sup>-1</sup> )	31.8961	–	–

Spun-up Companion Upper Limits ( $T_X \sim 10^7$ K)			
Parameter	EMOS1	EMOS2	EPN
$F_X$ (erg cm <sup>-2</sup> s <sup>-1</sup> )	-13.9987	–	–
$L_X$ (erg s <sup>-1</sup> )	31.2833	–	–
$L_*$ ( $L_{\text{sun}}$ )	4.9939	–	–
$M_{\text{bol}}$ (mag)	2.9939	–	–
Spectral Type	F0-F2V	–	–

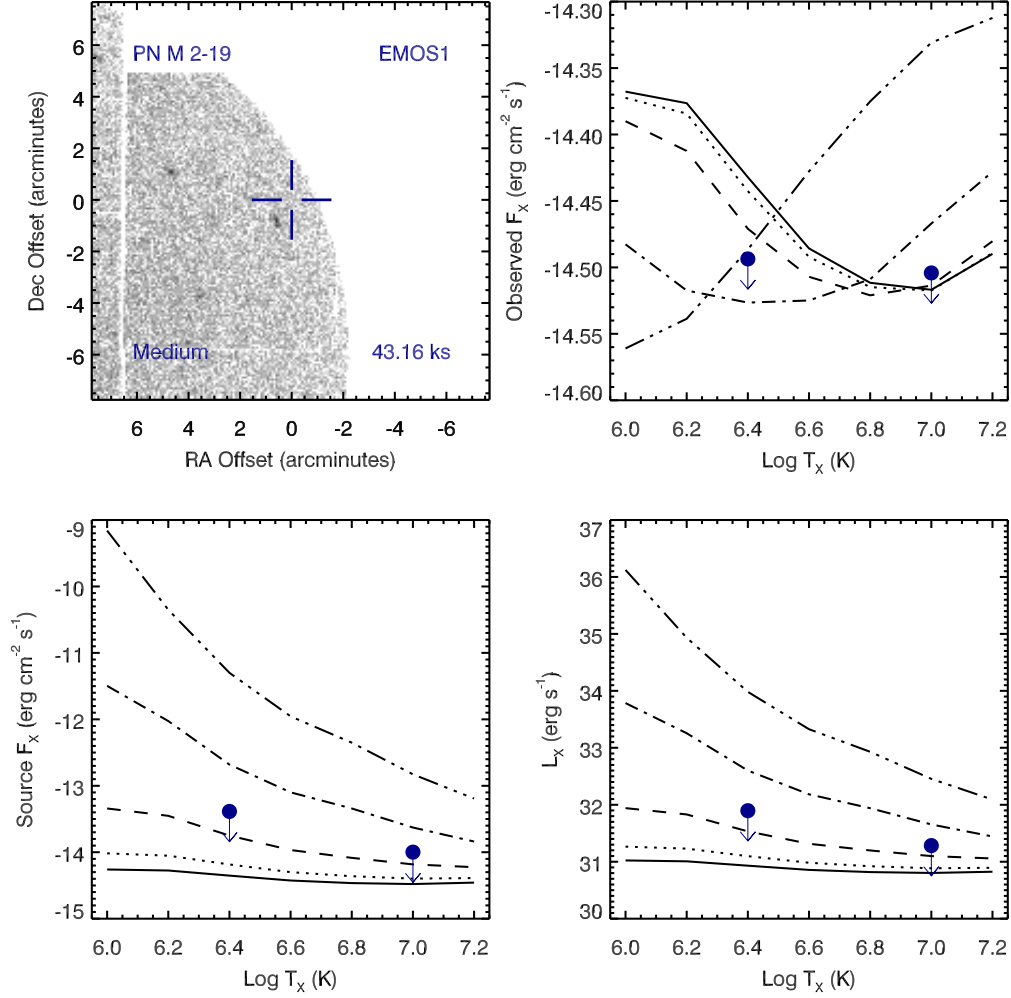


Figure A.57 Serendipitous XMM EMOS1 observation (ObsID 0402280101) of PN M 2-19. Clock-wise from top-left: broad band (0.3 to 8.0 keV) image at the PN position, upper limits of the observed flux, X-ray luminosity, and source X-ray flux. The upper limits calculations are based on the upper limit count rates, a thermal plasma model at a range temperatures, and a range of intervening absorption values:  $N_H(10^{22} \text{ cm}^{-2}) = 0.03$  (solid), 0.1 (dotted), 0.3 (dashed), 1 (dot-dashed), and 3 (dot-dot-dashed). The hot bubble and spun-up companion upper limits are depicted as the filled circles with downward pointing arrows at  $\log T_x$  of 6.4 and 7.0, respectively.

## PN M 2-19 , ObsID 0206590101

Table A.31 Summary of the Analysis for the XMM EPIC observation (ObsID 0206590101) of PN M 2-19.

Basic Data			
Parameter	Value	Notes	
RA (J2000)	268.440079		
DEC (J2000)	-29.729539	Offset (')	13.29
$R_{\text{nebula}}$ (")	4.1	from literature (A94)	
$D$ (kpc)	4.00	from statistical methods (A94)	
$\log N_H$ (cm <sup>-2</sup> )	21.6990	unknown, assumed value	
$T_{\text{eff}}$ (kK)	32.40	HeI or HeII Zanstra (Ph03)	
Date Obs:	2004-04-06	XMM Filter:	Medium

Calculations			
Parameter	EMOS1	EMOS2	EPN
$t_{\text{exp}}$ (ks)	7.5	8.5	–
$\text{CR}_{\text{src}}$ (cnt s <sup>-1</sup> )	7.022E-06	6.740E-06	–
$\text{CR}_{\text{bkg}}$ (cnt s <sup>-1</sup> )	6.460E-06	6.830E-06	–

Hot Bubble Upper Limits ( $T_X \sim 3 \times 10^6$ K)			
Parameter	EMOS1	EMOS2	EPN
$F_X$ (erg cm <sup>-2</sup> s <sup>-1</sup> )	-12.6476	-12.6645	–
$L_X$ (erg s <sup>-1</sup> )	32.6344	32.6175	–

Spun-up Companion Upper Limits ( $T_X \sim 10^7$ K)			
Parameter	EMOS1	EMOS2	EPN
$F_X$ (erg cm <sup>-2</sup> s <sup>-1</sup> )	-13.2606	-13.2775	–
$L_X$ (erg s <sup>-1</sup> )	32.0214	32.0045	–
$L_*$ ( $L_{\text{sun}}$ )	27.3244	26.2788	–
$M_{\text{bol}}$ (mag)	1.1486	1.1910	–
Spectral Type	A2-A5V	A2-A5V	–

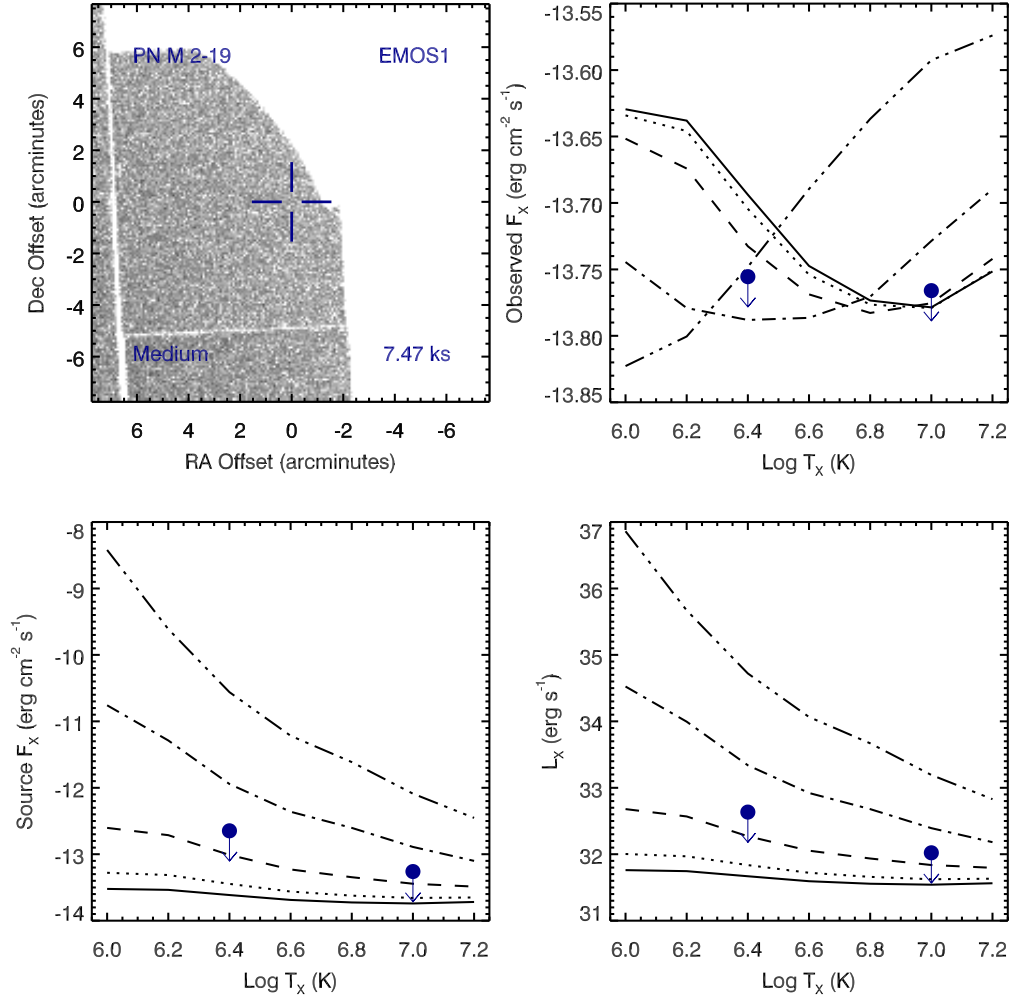


Figure A.58 Serendipitous XMM EMOS1 observation (ObsID 0206590101) of PN M 2-19. Clock-wise from top-left: broad band (0.3 to 8.0 keV) image at the PN position, upper limits of the observed flux, X-ray luminosity, and source X-ray flux. The upper limits calculations are based on the upper limit count rates, a thermal plasma model at a range temperatures, and a range of intervening absorption values:  $N_H(10^{22} \text{ cm}^{-2}) = 0.03$  (solid), 0.1 (dotted), 0.3 (dashed), 1 (dot-dashed), and 3 (dot-dot-dashed). The hot bubble and spun-up companion upper limits are depicted as the filled circles with downward pointing arrows at  $\log T_x$  of 6.4 and 7.0, respectively.



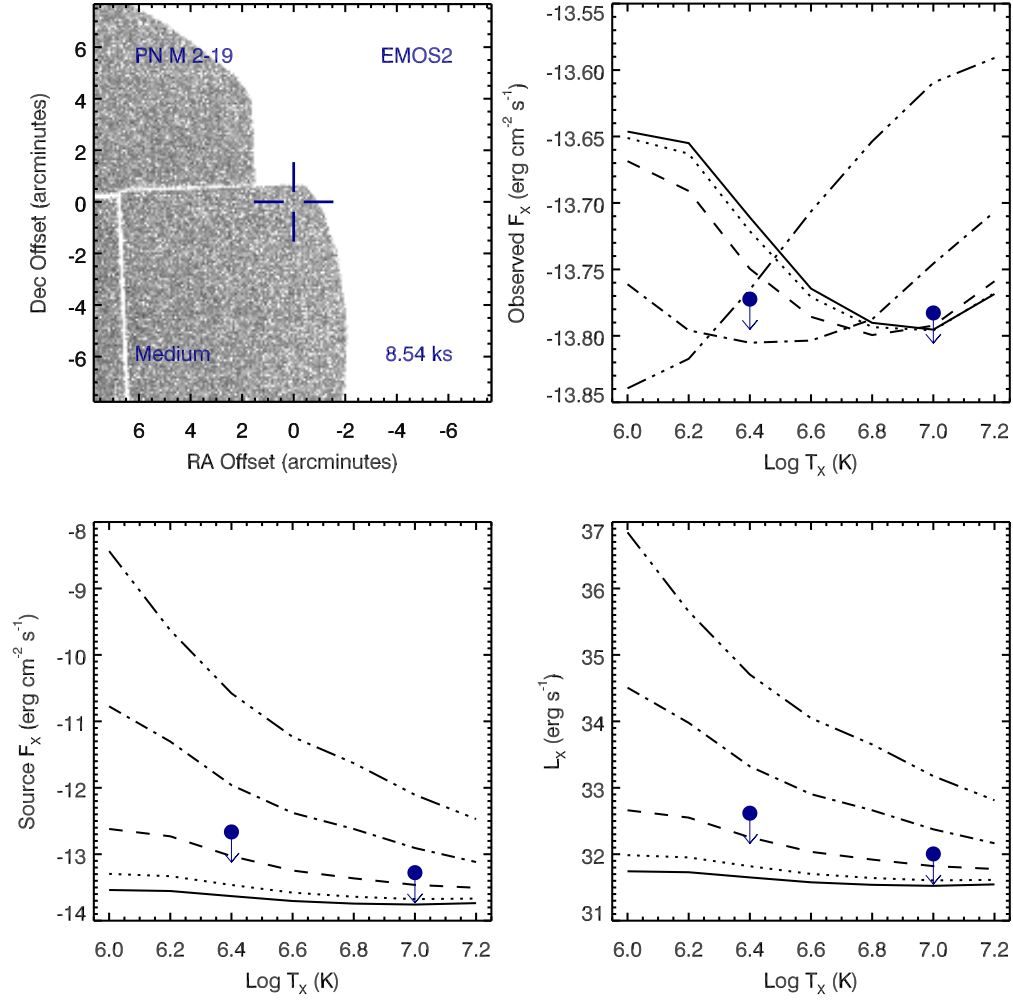


Figure A.59 Serendipitous XMM EMOS2 observation (ObsID 0206590101) of PN M 2-19 ; panels as in Figure A.64.

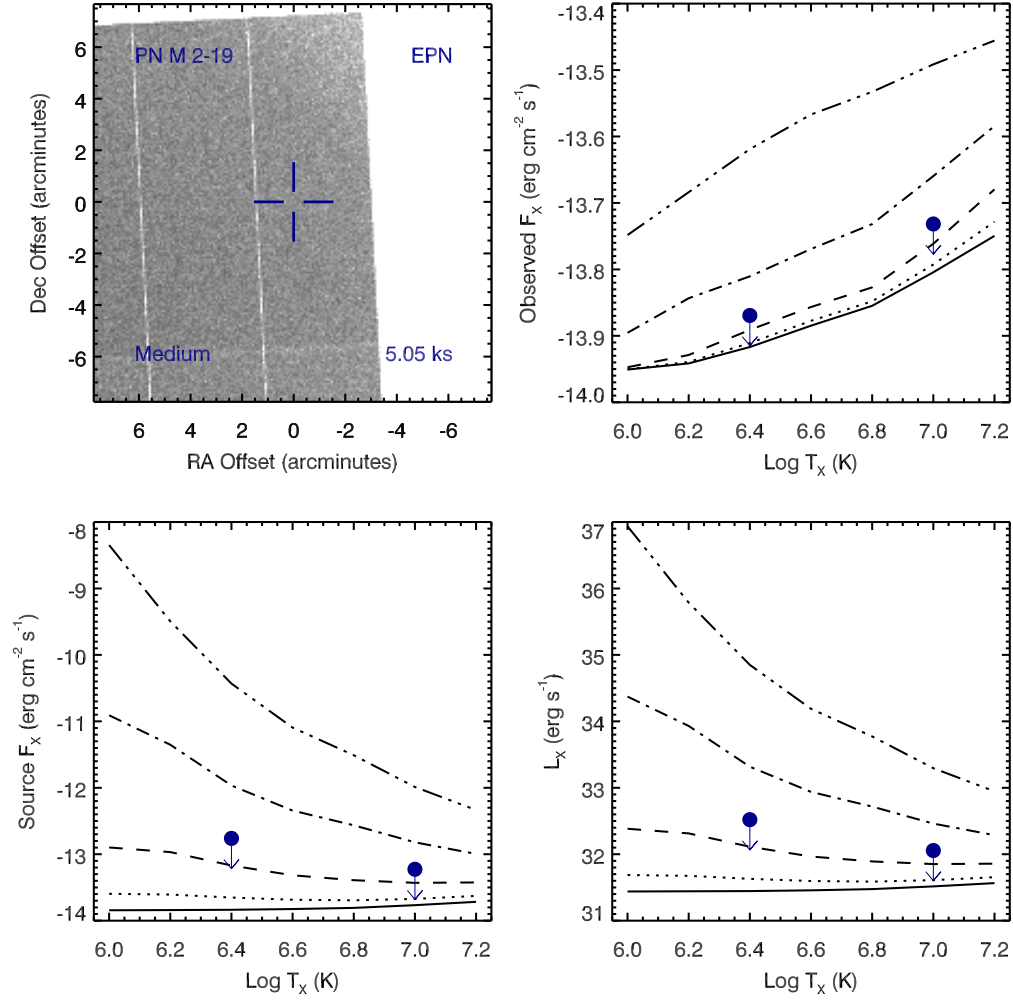


Figure A.60 Serendipitous XMM EPN observation (ObsID 0206590101) of PN M 2-19 ; panels as in Figure A.64.

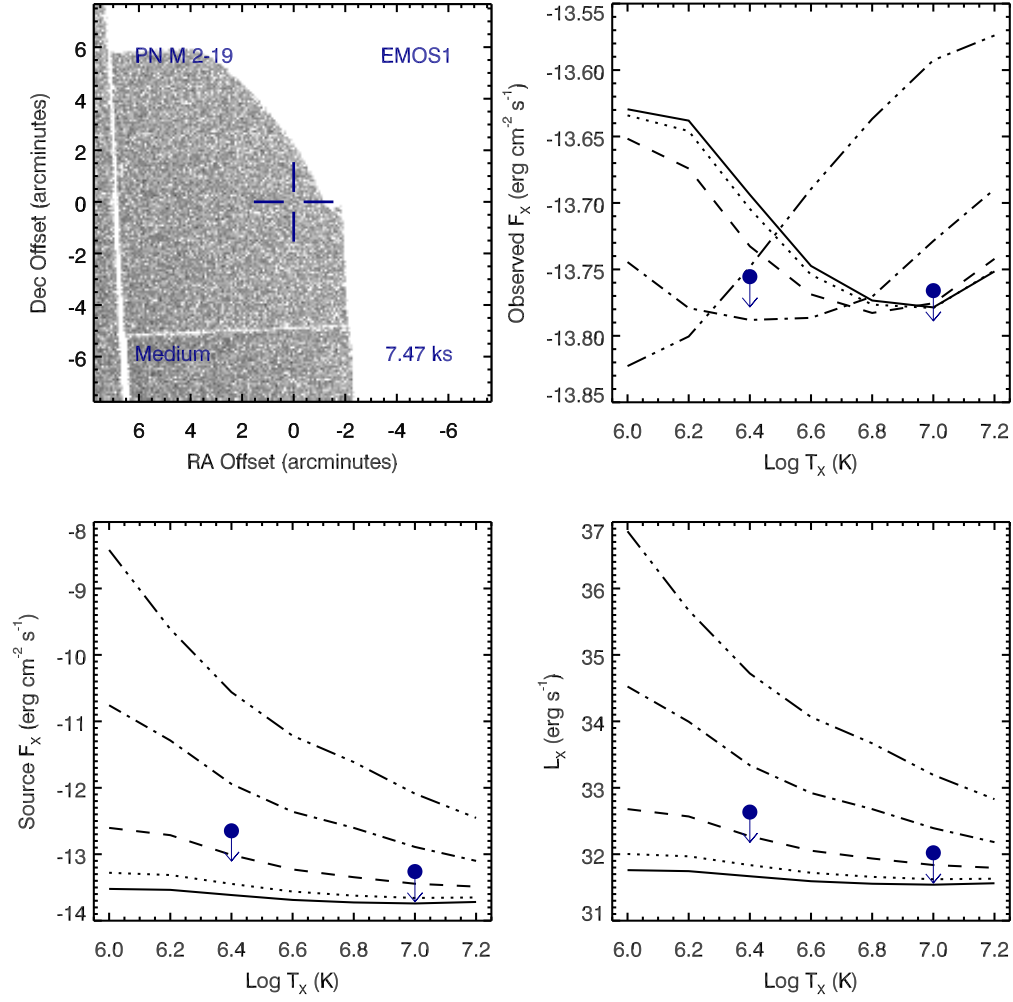


Figure A.61 Serendipitous XMM EMOS1 observation (ObsID 0206590101) of PN M 2-19 ; panels as in Figure A.64.

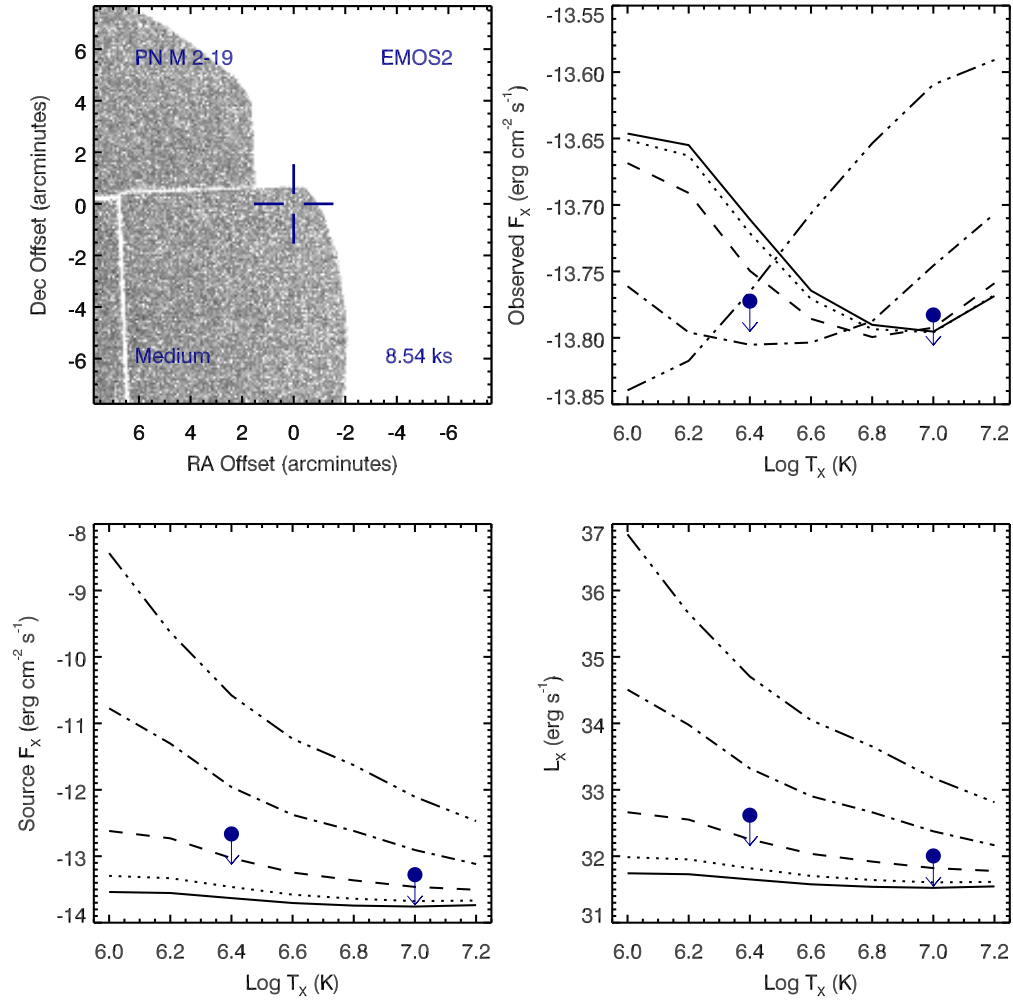


Figure A.62 Serendipitous XMM EMOS2 observation (ObsID 0206590101) of PN M 2-19 ; panels as in Figure A.64.

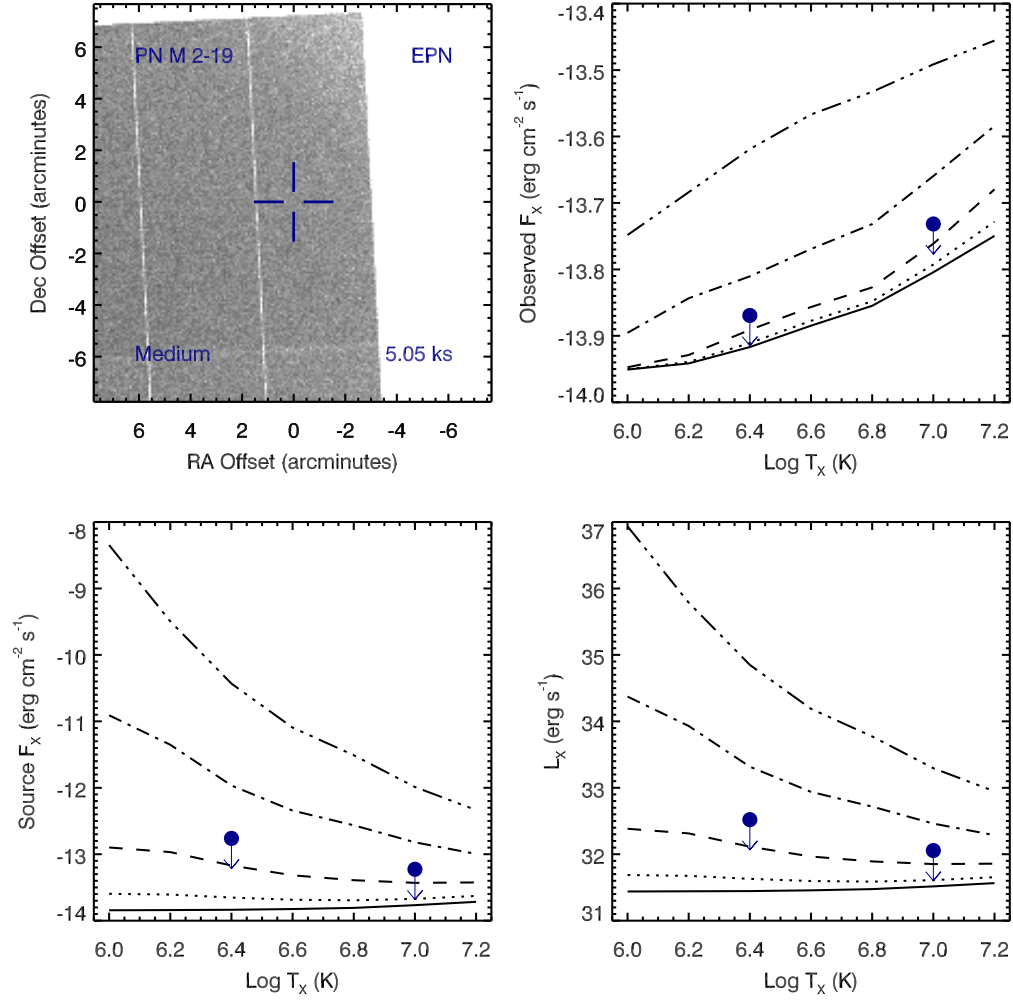


Figure A.63 Serendipitous XMM EPN observation (ObsID 0206590101) of PN M 2-19 ; panels as in Figure A.64.

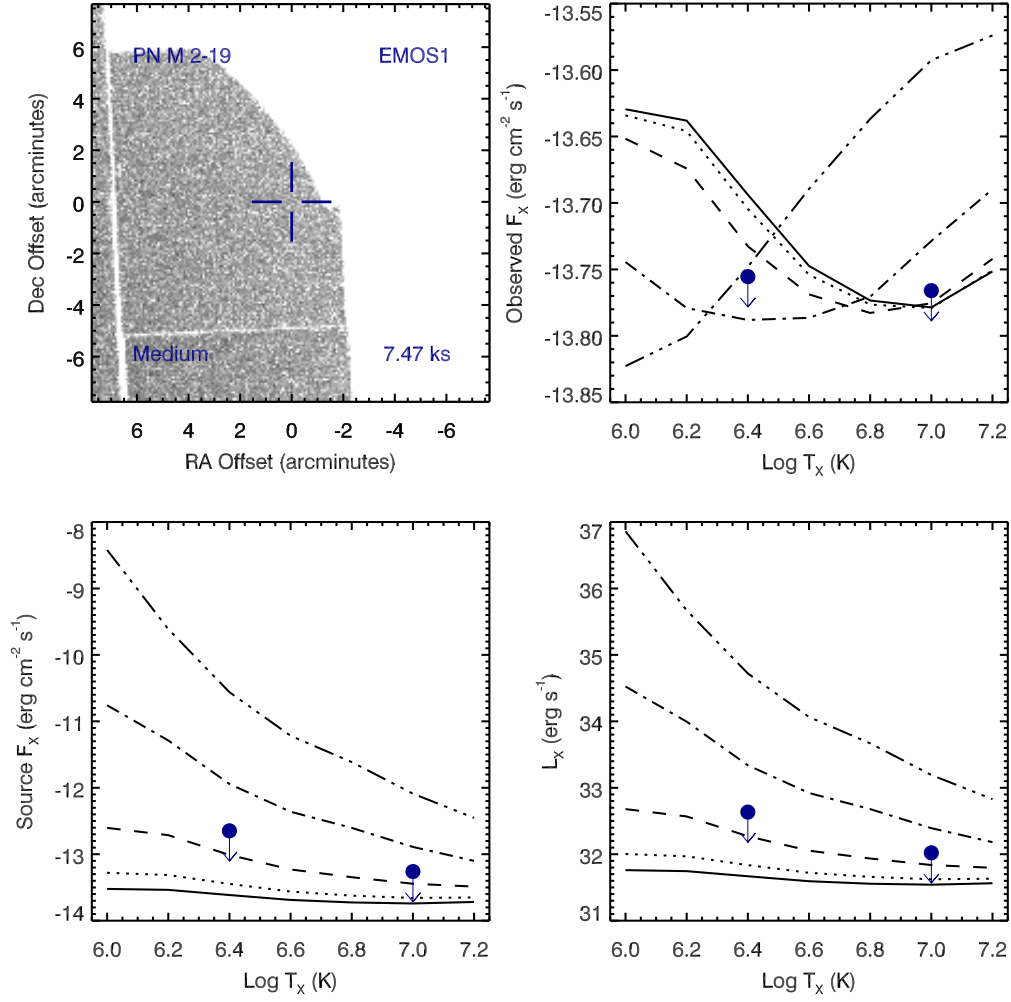


Figure A.64 Serendipitous XMM EMOS1 observation (ObsID 0206590101) of PN M 2-19 ; panels as in Figure A.64.

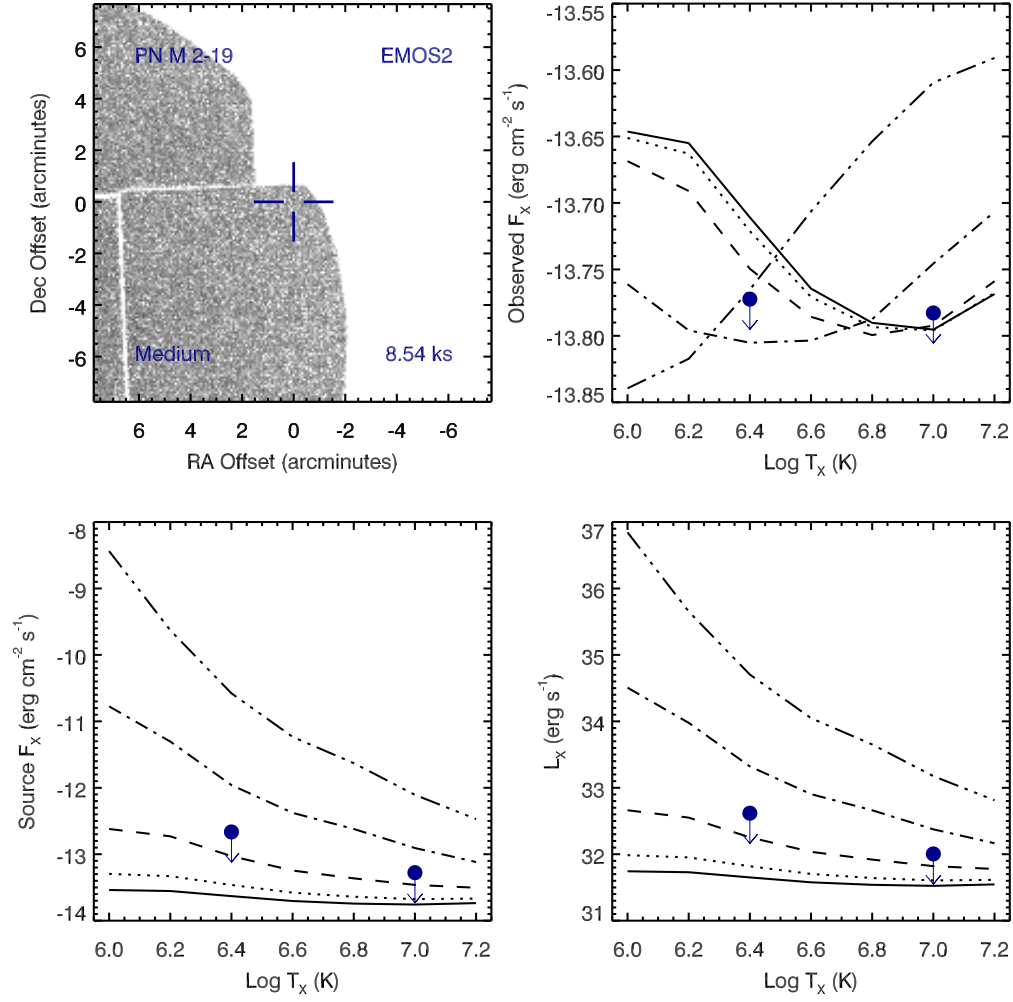


Figure A.65 Serendipitous XMM EMOS2 observation (ObsID 0206590101) of PN M 2-19 ; panels as in Figure A.64.

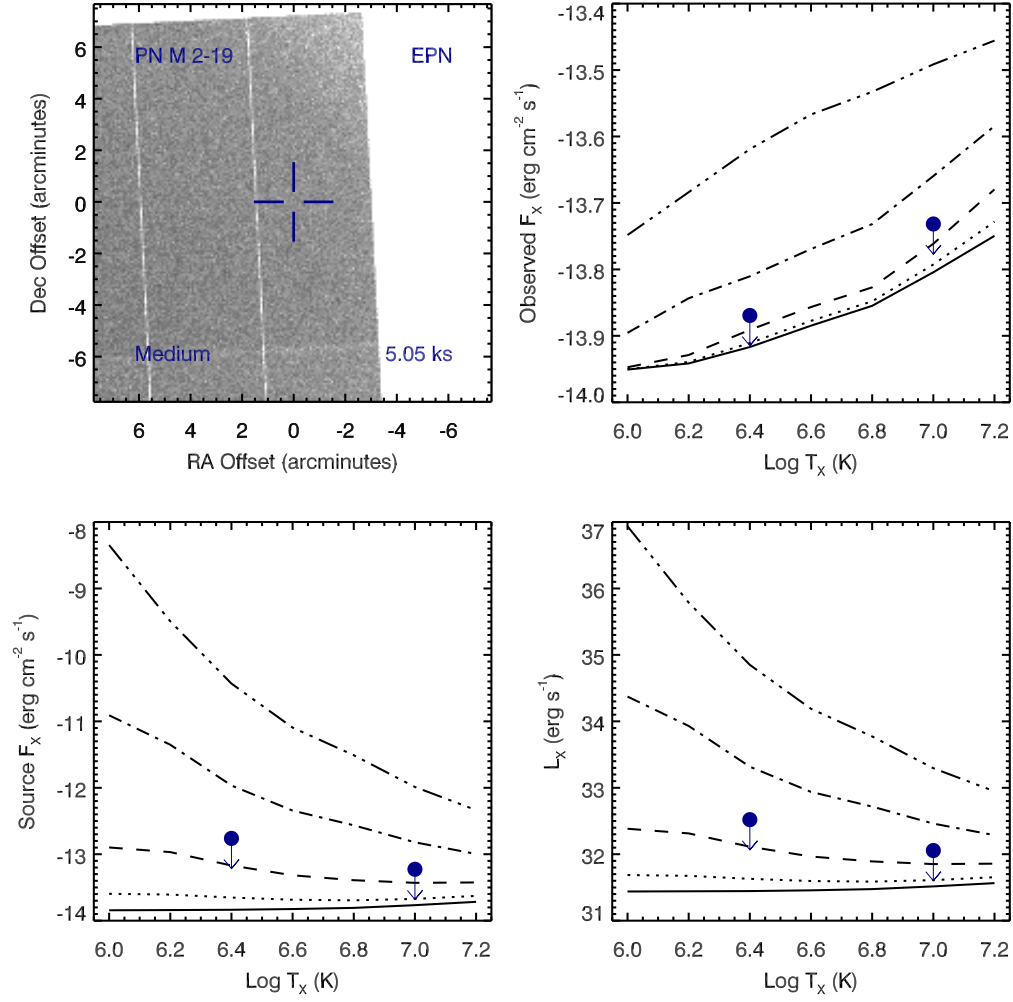


Figure A.66 Serendipitous XMM EPN observation (ObsID 0206590101) of PN M 2-19 ; panels as in Figure A.64.



# PN M 2-45 , ObsID 0301880401

Table A.32 Summary of the Analysis for the XMM EPIC observation (ObsID 0301880401) of PN M 2-45.

Basic Data			
Parameter	Value	Notes	
RA (J2000)	279.841170		
DEC (J2000)	-4.330830	Offset (')	7.30
$R_{\text{nebula}}$ (")	3.2	from literature (A94)	
$D$ (kpc)	1.99	from statistical methods (A94)	
$\log N_H$ ( $\text{cm}^{-2}$ )	21.6990	unknown, assumed value	
$T_{\text{eff}}$ (kK)	55.50	HeI or HeII Zanstra (Ph03)	
Date Obs:	2005-10-04	XMM Filter:	Medium

Calculations			
Parameter	EMOS1	EMOS2	EPN
$t_{\text{exp}}$ (ks)	10.1	10.1	–
$\text{CR}_{\text{src}}$ ( $\text{cnt s}^{-1}$ )	5.067E-07	4.052E-07	–
$\text{CR}_{\text{bkg}}$ ( $\text{cnt s}^{-1}$ )	4.574E-07	3.635E-07	–

Hot Bubble Upper Limits ( $T_X \sim 3 \times 10^6$ K)			
Parameter	EMOS1	EMOS2	EPN
$F_X$ ( $\text{erg cm}^{-2} \text{s}^{-1}$ )	-13.2870	-13.3370	–
$L_X$ ( $\text{erg s}^{-1}$ )	31.3886	31.3387	–

Spun-up Companion Upper Limits ( $T_X \sim 10^7$ K)			
Parameter	EMOS1	EMOS2	EPN
$F_X$ ( $\text{erg cm}^{-2} \text{s}^{-1}$ )	-13.9000	-13.9500	–
$L_X$ ( $\text{erg s}^{-1}$ )	30.7756	30.7256	–
$L_*$ ( $L_{\text{sun}}$ )	1.5515	1.3827	–
$M_{\text{bol}}$ (mag)	4.2631	4.3882	–
Spectral Type	G0-G2V	G0-G2V	–

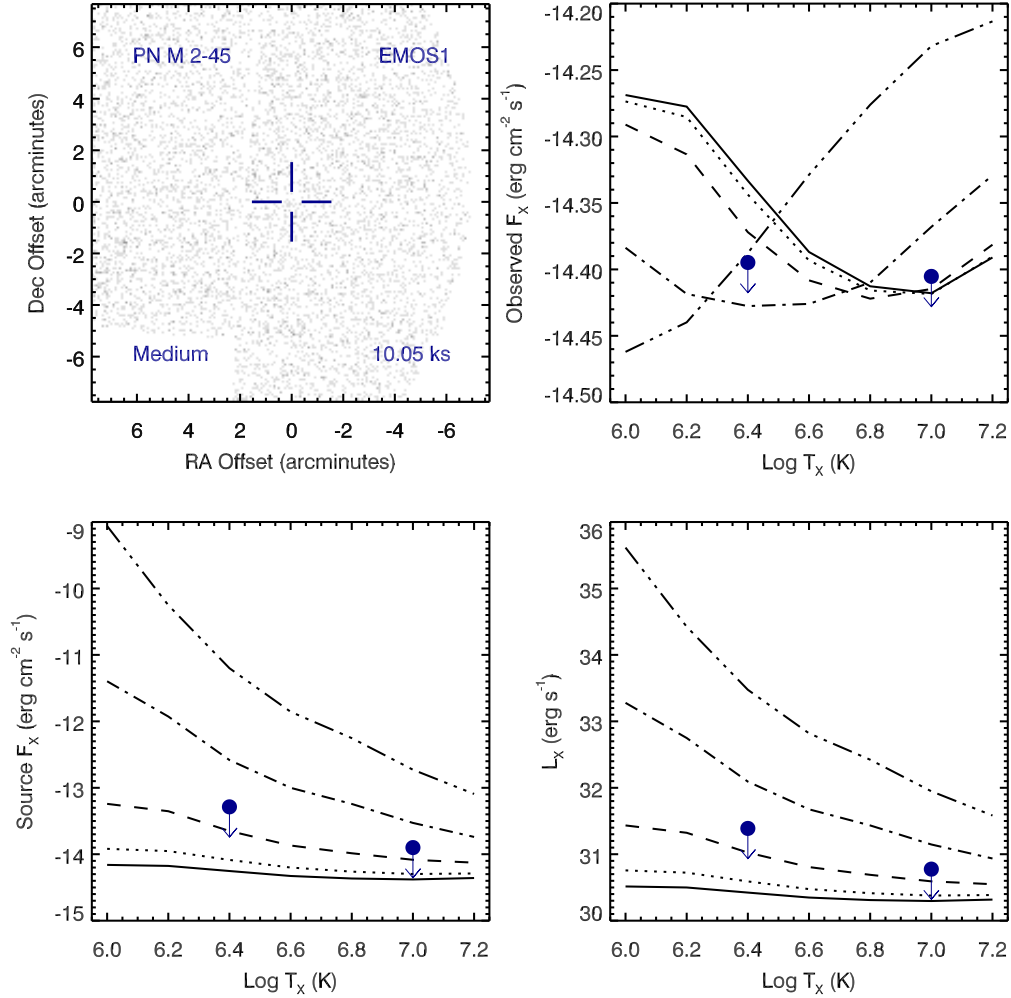


Figure A.67 Serendipitous XMM EMOS1 observation (ObsID 0301880401) of PN M 2-45. Clock-wise from top-left: broad band (0.3 to 8.0 keV) image at the PN position, upper limits of the observed flux, X-ray luminosity, and source X-ray flux. The upper limits calculations are based on the upper limit count rates, a thermal plasma model at a range temperatures, and a range of intervening absorption values:  $N_H(10^{22} \text{ cm}^{-2}) = 0.03$  (solid), 0.1 (dotted), 0.3 (dashed), 1 (dot-dashed), and 3 (dot-dot-dashed). The hot bubble and spun-up companion upper limits are depicted as the filled circles with downward pointing arrows at  $\log T_x$  of 6.4 and 7.0, respectively.

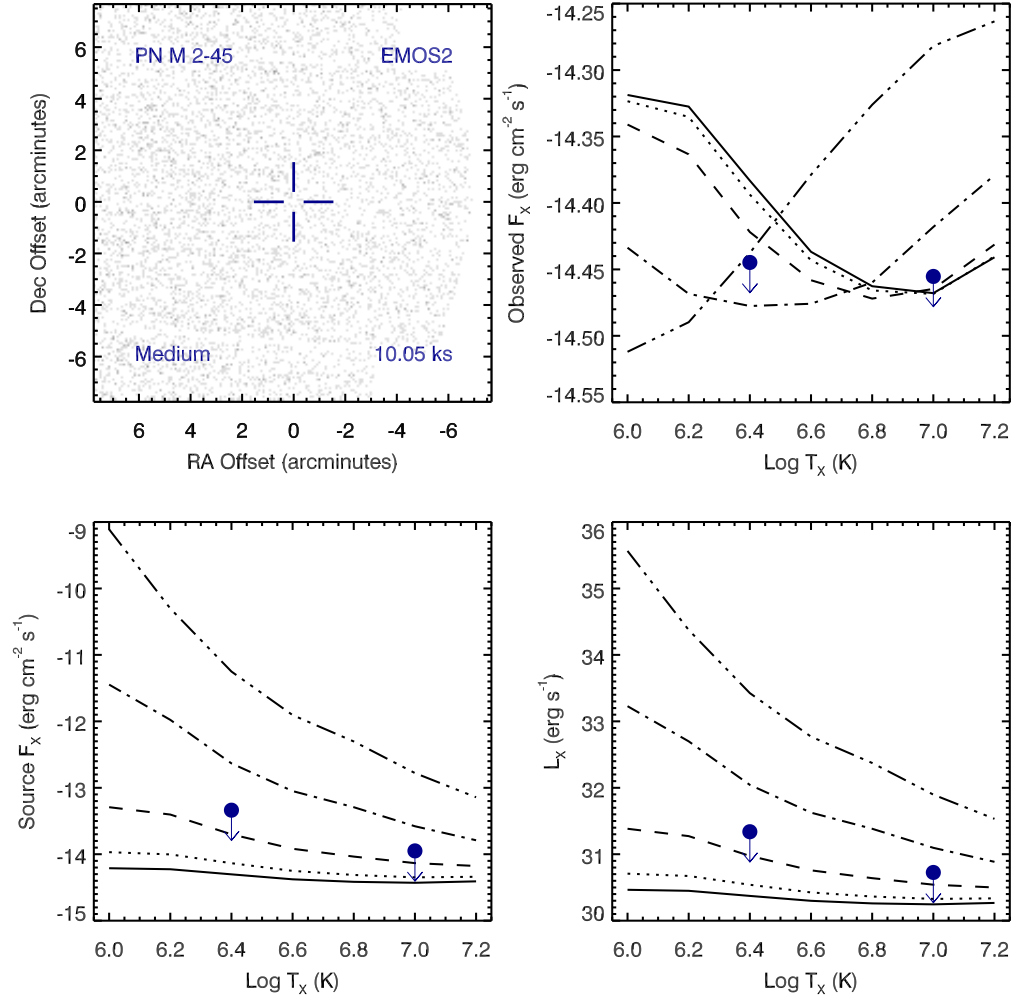


Figure A.68 Serendipitous XMM EMOS2 observation (ObsID 0301880401) of PN M 2-45 ; panels as in Figure A.67.

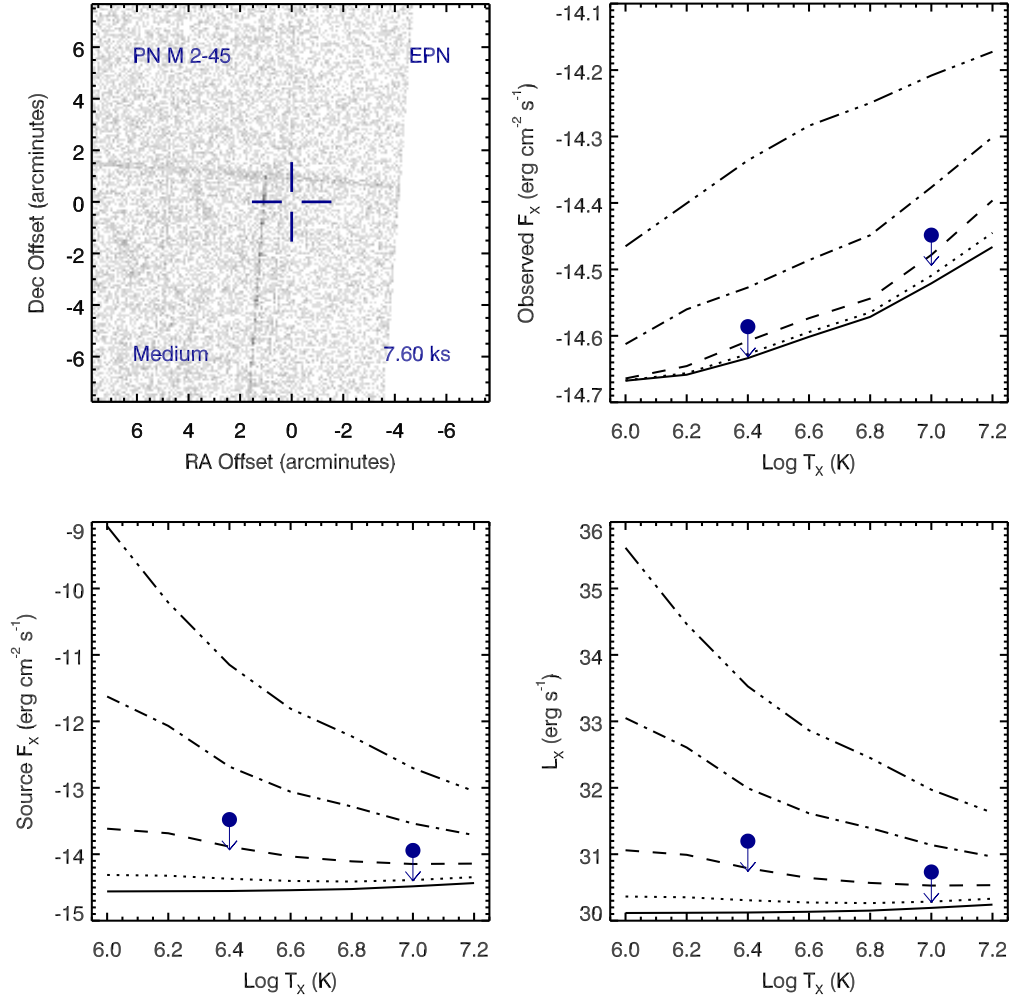


Figure A.69 Serendipitous XMM EPN observation (ObsID 0301880401) of PN M 2-45 ; panels as in Figure A.67.

## PN M 3-17 , ObsID 0085581101

Table A.33 Summary of the Analysis for the XMM EPIC observation (ObsID 0085581101) of PN M 3-17.

Basic Data			
Parameter	Value	Notes	
RA (J2000)	269.106833		
DEC (J2000)	-31.071339	Offset (')	13.25
$R_{\text{nebula}}$ (")	2.5	from literature (A94)	
$D$ (kpc)	9.10	from statistical methods (A94)	
$\log N_H$ ( $\text{cm}^{-2}$ )	21.6990	unknown, assumed value	
$T_{\text{eff}}$ (kK)	63.20	HeI or HeII Zanstra (Ph03)	
Date Obs:	2001-03-24	XMM Filter:	Thin1

Calculations			
Parameter	EMOS1	EMOS2	EPN
$t_{\text{exp}}$ (ks)	6.6	6.6	–
$\text{CR}_{\text{src}}$ ( $\text{cnt s}^{-1}$ )	9.225E-07	6.917E-07	–
$\text{CR}_{\text{bkg}}$ ( $\text{cnt s}^{-1}$ )	4.805E-07	7.649E-07	–

Hot Bubble Upper Limits ( $T_X \sim 3 \times 10^6$ K)			
Parameter	EMOS1	EMOS2	EPN
$F_X$ ( $\text{erg cm}^{-2} \text{s}^{-1}$ )	-13.1967	-13.0959	–
$L_X$ ( $\text{erg s}^{-1}$ )	32.7992	32.9001	–

Spun-up Companion Upper Limits ( $T_X \sim 10^7$ K)			
Parameter	EMOS1	EMOS2	EPN
$F_X$ ( $\text{erg cm}^{-2} \text{s}^{-1}$ )	-13.8058	-13.7051	–
$L_X$ ( $\text{erg s}^{-1}$ )	32.1902	32.2909	–
$L_*$ ( $L_{\text{sun}}$ )	40.3028	50.8165	–
$M_{\text{bol}}$ (mag)	0.7267	0.4750	–
Spectral Type	A0-A2V	A0-A2V	–

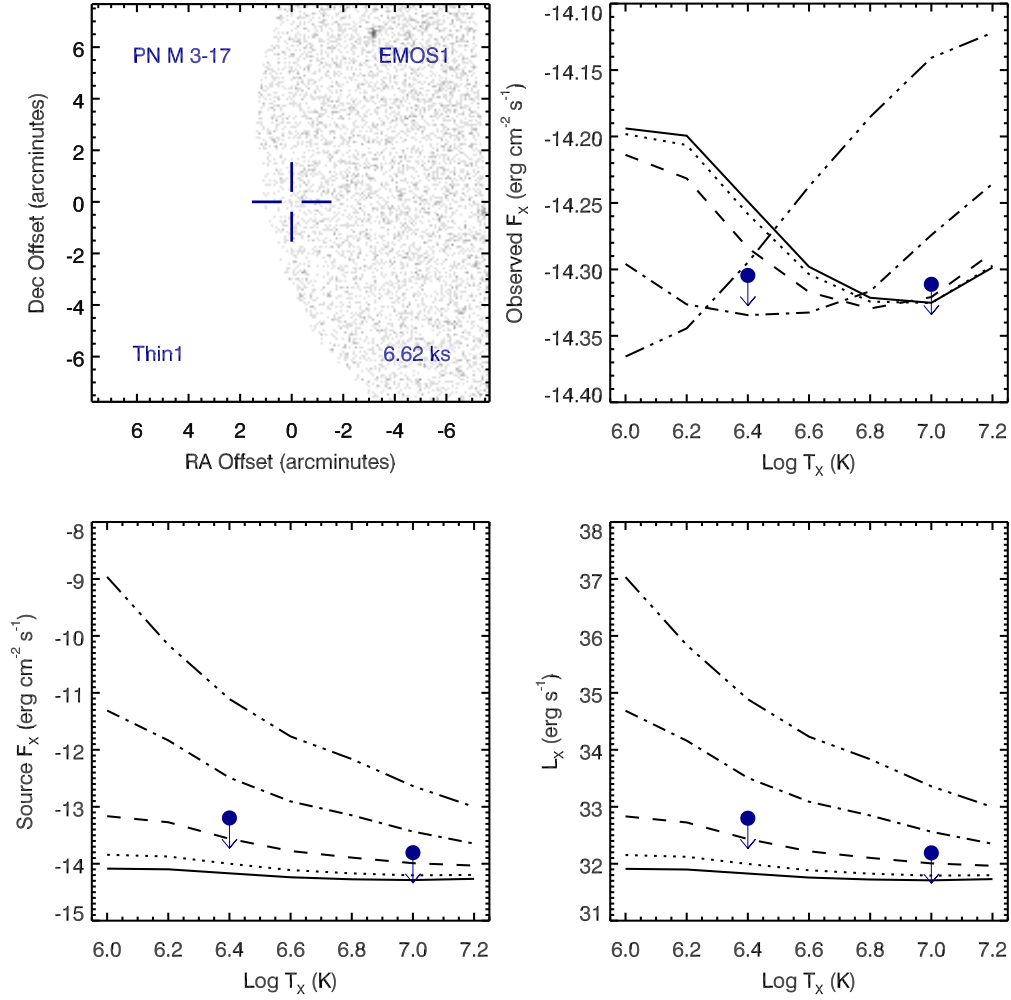


Figure A.70 Serendipitous XMM EMOS1 observation (ObsID 0085581101) of PN M 3-17. Clock-wise from top-left: broad band (0.3 to 8.0 keV) image at the PN position, upper limits of the observed flux, X-ray luminosity, and source X-ray flux. The upper limits calculations are based on the upper limit count rates, a thermal plasma model at a range temperatures, and a range of intervening absorption values:  $N_H(10^{22} \text{ cm}^{-2}) = 0.03$  (solid), 0.1 (dotted), 0.3 (dashed), 1 (dot-dashed), and 3 (dot-dot-dashed). The hot bubble and spun-up companion upper limits are depicted as the filled circles with downward pointing arrows at  $\log T_x$  of 6.4 and 7.0, respectively.

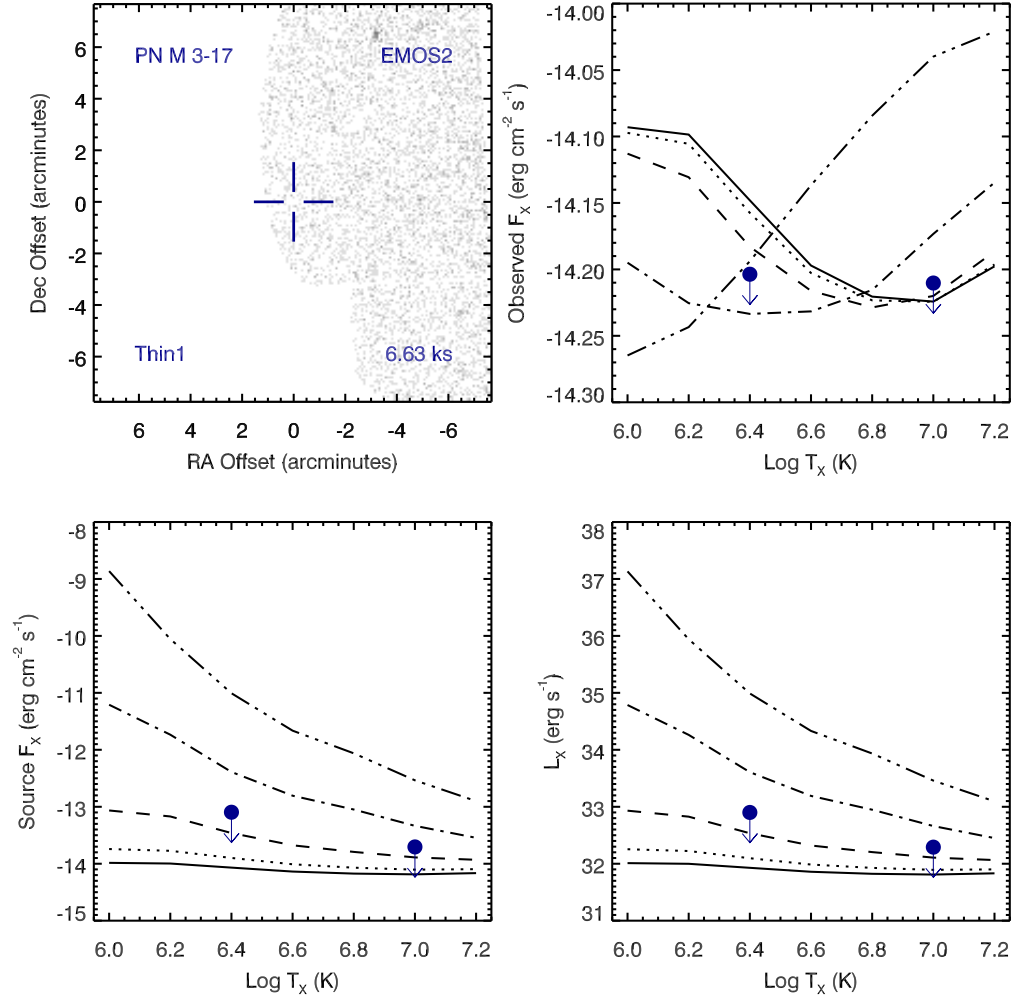


Figure A.71 Serendipitous XMM EMOS2 observation (ObsID 0085581101) of PN M 3-17 ; panels as in Figure A.70.

## PN M 3-17 , ObsID 0085581001

Table A.34 Summary of the Analysis for the XMM EPIC observation (ObsID 0085581001) of PN M 3-17.

Basic Data			
Parameter	Value	Notes	
RA (J2000)	269.106833		
DEC (J2000)	-31.071339	Offset (')	13.25
$R_{\text{nebula}}$ (")	2.5	from literature (A94)	
$D$ (kpc)	9.10	from statistical methods (A94)	
$\log N_H$ ( $\text{cm}^{-2}$ )	21.6990	unknown, assumed value	
$T_{\text{eff}}$ (kK)	63.20	HeI or HeII Zanstra (Ph03)	
Date Obs:	2001-09-07	XMM Filter:	Thin1

Calculations			
Parameter	EMOS1	EMOS2	EPN
$t_{\text{exp}}$ (ks)	7.8	7.9	–
$\text{CR}_{\text{src}}$ ( $\text{cnt s}^{-1}$ )	4.546E-07	3.893E-07	–
$\text{CR}_{\text{bkg}}$ ( $\text{cnt s}^{-1}$ )	2.706E-07	4.505E-07	–

Hot Bubble Upper Limits ( $T_X \sim 3 \times 10^6$ K)			
Parameter	EMOS1	EMOS2	EPN
$F_X$ ( $\text{erg cm}^{-2} \text{s}^{-1}$ )	-13.3580	-13.2476	–
$L_X$ ( $\text{erg s}^{-1}$ )	32.6380	32.7484	–

Spun-up Companion Upper Limits ( $T_X \sim 10^7$ K)			
Parameter	EMOS1	EMOS2	EPN
$F_X$ ( $\text{erg cm}^{-2} \text{s}^{-1}$ )	-13.9670	-13.8567	–
$L_X$ ( $\text{erg s}^{-1}$ )	32.0290	32.1393	–
$L_*$ ( $L_{\text{sun}}$ )	27.8047	35.8446	–
$M_{\text{bol}}$ (mag)	1.1297	0.8539	–
Spectral Type	A2-A5V	A0-A2V	–



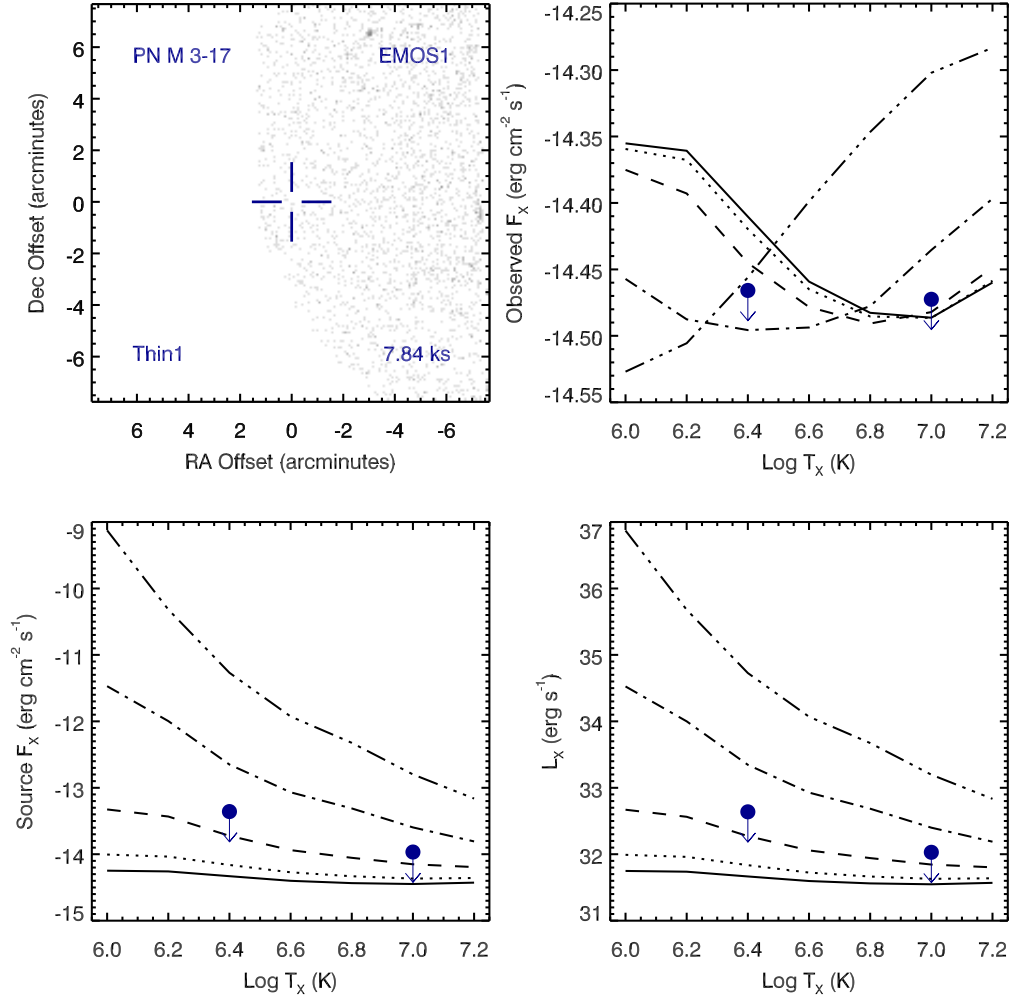


Figure A.72 Serendipitous XMM EMOS1 observation (ObsID 0085581001) of PN M 3-17. Clock-wise from top-left: broad band (0.3 to 8.0 keV) image at the PN position, upper limits of the observed flux, X-ray luminosity, and source X-ray flux. The upper limits calculations are based on the upper limit count rates, a thermal plasma model at a range temperatures, and a range of intervening absorption values:  $N_H(10^{22} \text{ cm}^{-2}) = 0.03$  (solid), 0.1 (dotted), 0.3 (dashed), 1 (dot-dashed), and 3 (dot-dot-dashed). The hot bubble and spun-up companion upper limits are depicted as the filled circles with downward pointing arrows at log  $T_x$  of 6.4 and 7.0, respectively.

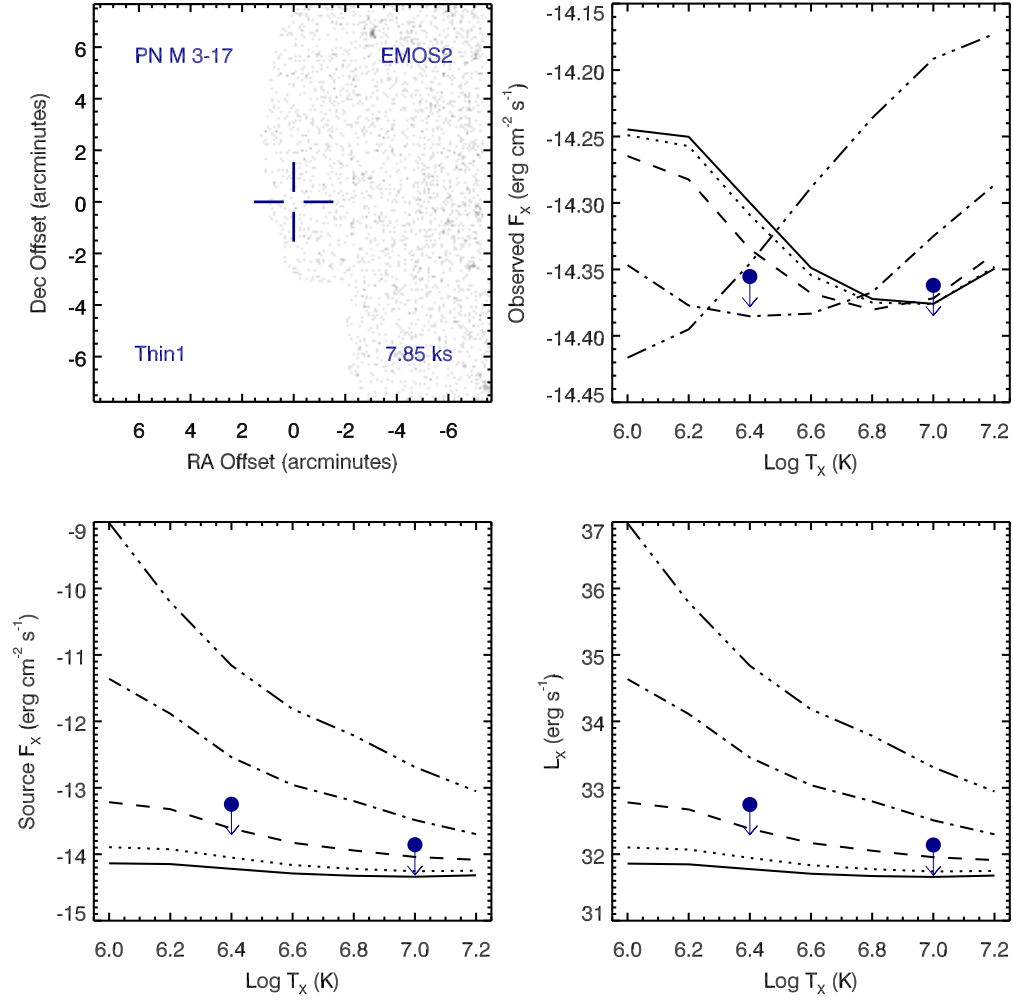


Figure A.73 Serendipitous XMM EMOS2 observation (ObsID 0085581001) of PN M 3-17 ; panels as in Figure A.72.

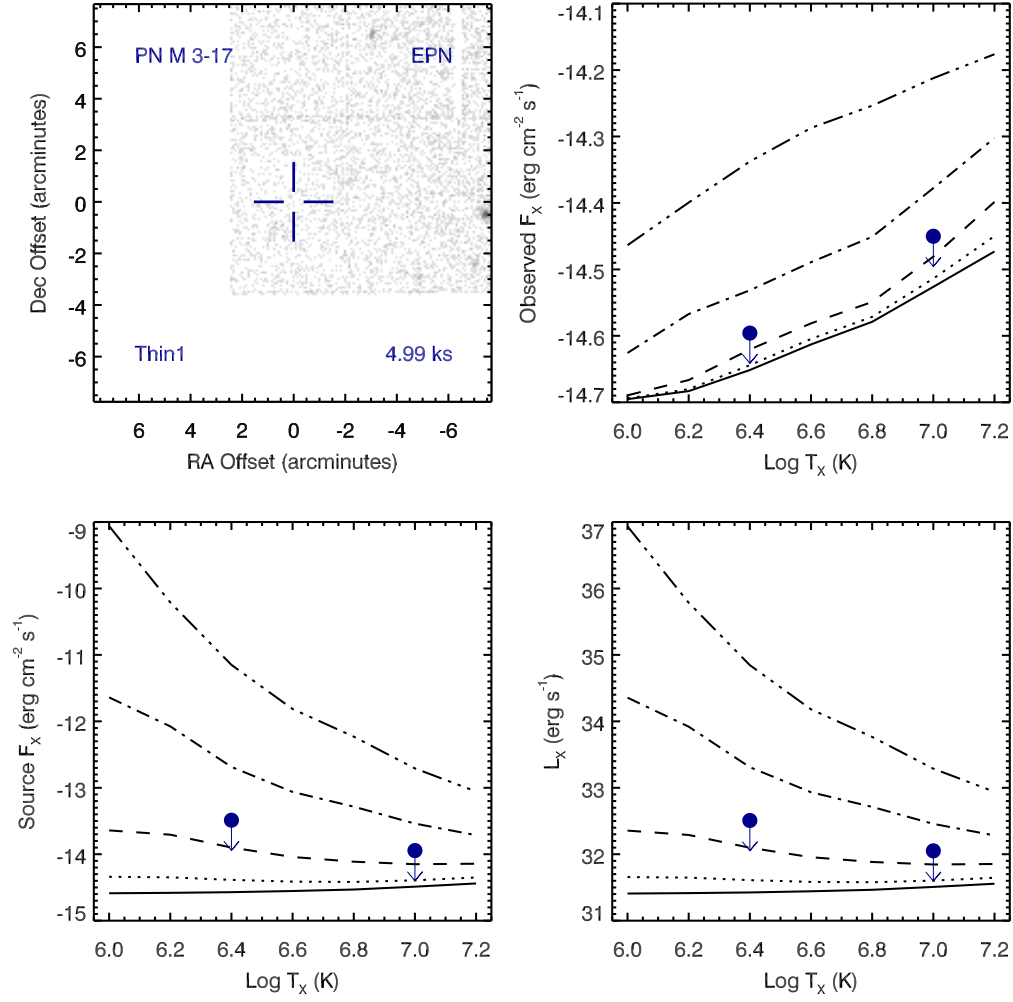


Figure A.74 Serendipitous XMM EPN observation (ObsID 0085581001) of PN M 3-17 ; panels as in Figure A.72.

# PN M 3-17 , ObsID 0085580201

Table A.35 Summary of the Analysis for the XMM EPIC observation (ObsID 0085580201) of PN M 3-17.

Basic Data			
Parameter	Value	Notes	
RA (J2000)	269.106833		
DEC (J2000)	-31.071339	Offset (')	13.25
$R_{\text{nebula}}$ (")	2.5	from literature (A94)	
$D$ (kpc)	9.10	from statistical methods (A94)	
$\log N_H$ (cm <sup>-2</sup> )	21.6990	unknown, assumed value	
$T_{\text{eff}}$ (kK)	63.20	HeI or HeII Zanstra (Ph03)	
Date Obs:	2000-10-11	XMM Filter:	Thin1

Calculations			
Parameter	EMOS1	EMOS2	EPN
$t_{\text{exp}}$ (ks)	9.0	9.1	–
$\text{CR}_{\text{src}}$ (cnt s <sup>-1</sup> )	2.252E-07	6.745E-07	–
$\text{CR}_{\text{bkg}}$ (cnt s <sup>-1</sup> )	4.821E-07	6.376E-07	–

Hot Bubble Upper Limits ( $T_X \sim 3 \times 10^6$ K)			
Parameter	EMOS1	EMOS2	EPN
$F_X$ (erg cm <sup>-2</sup> s <sup>-1</sup> )	-13.2637	-13.2034	–
$L_X$ (erg s <sup>-1</sup> )	32.7323	32.7926	–

Spun-up Companion Upper Limits ( $T_X \sim 10^7$ K)			
Parameter	EMOS1	EMOS2	EPN
$F_X$ (erg cm <sup>-2</sup> s <sup>-1</sup> )	-13.8729	-13.8125	–
$L_X$ (erg s <sup>-1</sup> )	32.1231	32.1835	–
$L_*$ ( $L_{\text{sun}}$ )	34.5306	39.6845	–
$M_{\text{bol}}$ (mag)	0.8945	0.7434	–
Spectral Type	A0-A2V	A0-A2V	–

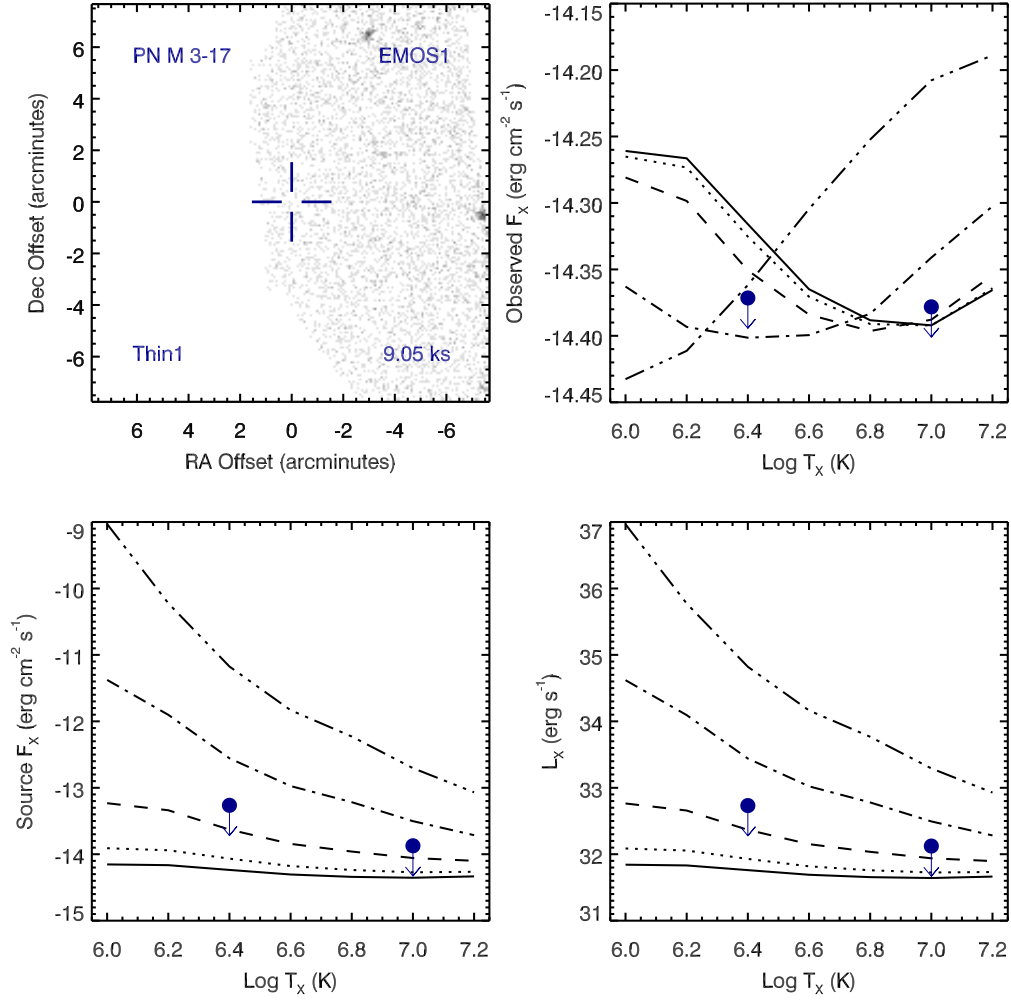


Figure A.75 Serendipitous XMM EMOS1 observation (ObsID 0085580201) of PN M 3-17. Clock-wise from top-left: broad band (0.3 to 8.0 keV) image at the PN position, upper limits of the observed flux, X-ray luminosity, and source X-ray flux. The upper limits calculations are based on the upper limit count rates, a thermal plasma model at a range temperatures, and a range of intervening absorption values:  $N_H(10^{22} \text{ cm}^{-2}) = 0.03$  (solid), 0.1 (dotted), 0.3 (dashed), 1 (dot-dashed), and 3 (dot-dot-dashed). The hot bubble and spun-up companion upper limits are depicted as the filled circles with downward pointing arrows at  $\log T_x$  of 6.4 and 7.0, respectively.

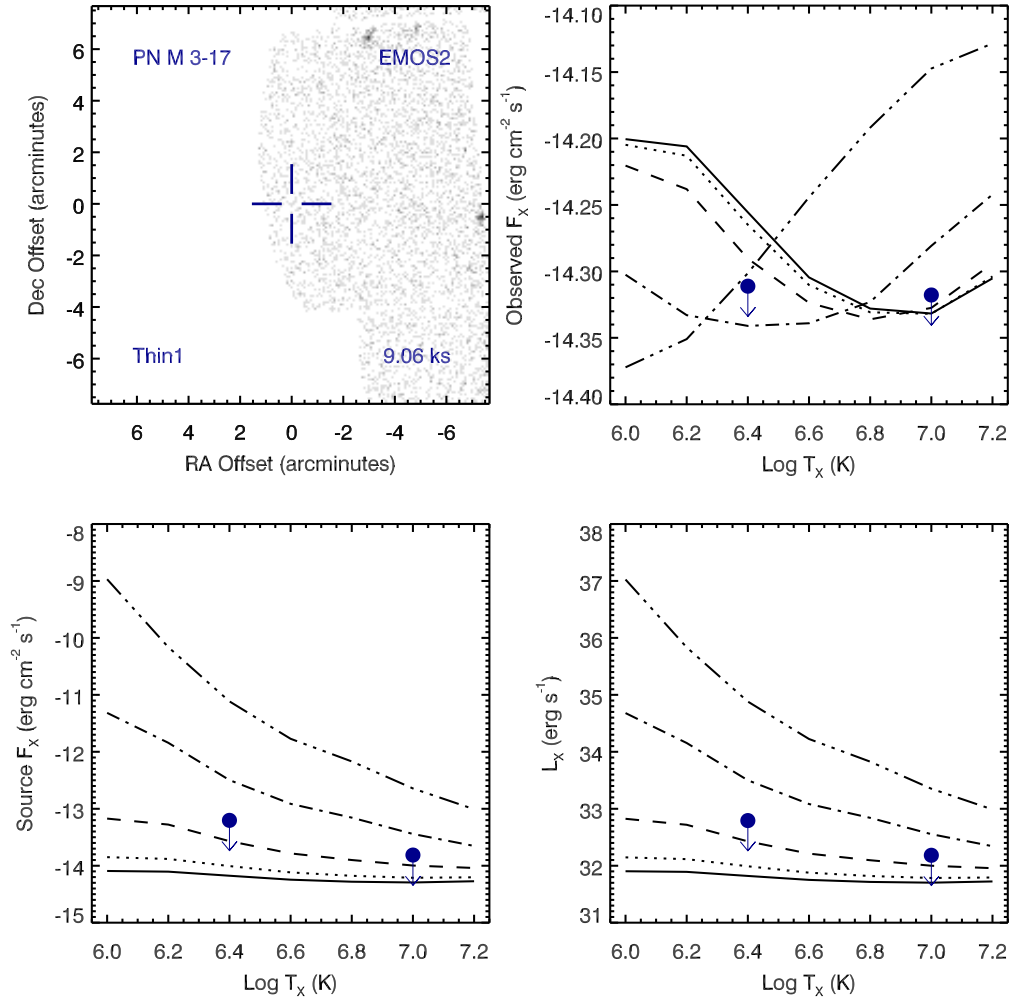


Figure A.76 Serendipitous XMM EMOS2 observation (ObsID 0085580201) of PN M 3-17 ; panels as in Figure A.75.

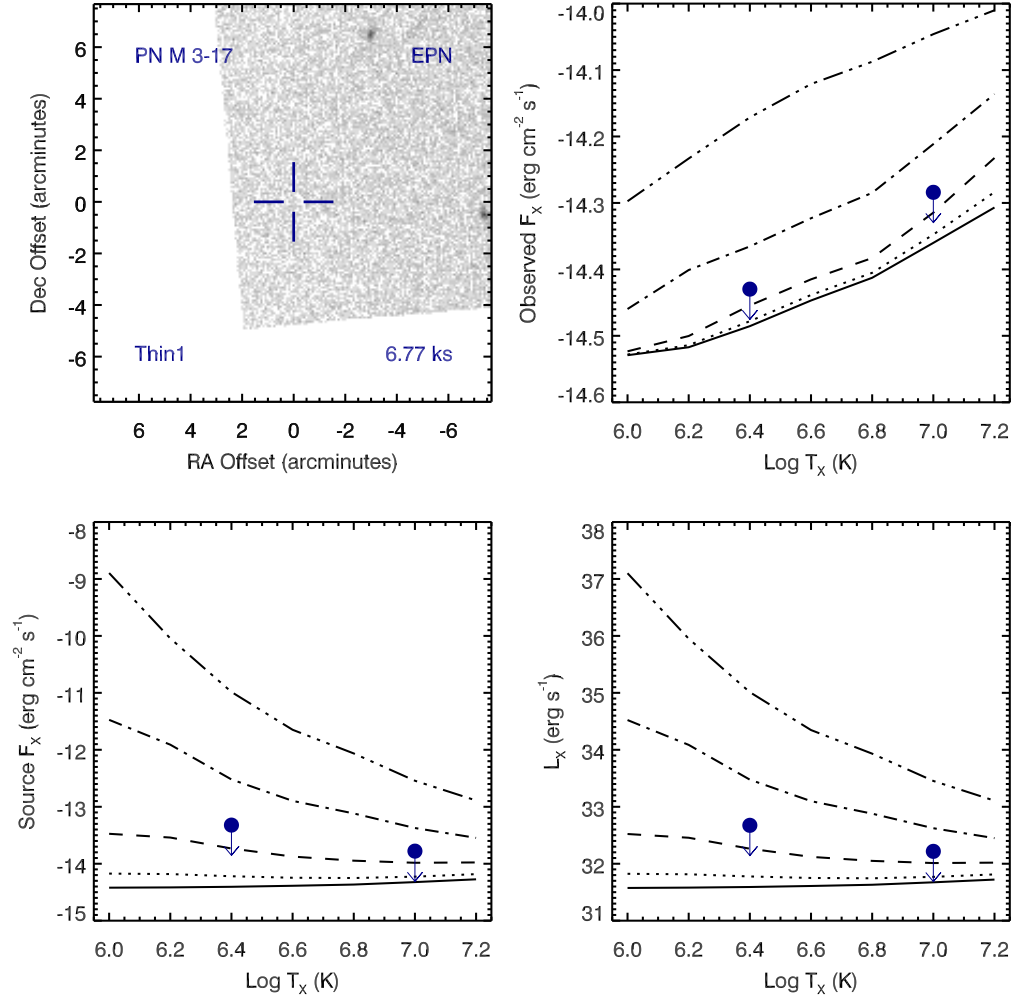


Figure A.77 Serendipitous XMM EPN observation (ObsID 0085580201) of PN M 3-17 ; panels as in Figure A.75.

## PN M 3-19 , ObsID 0050940201

Table A.36 Summary of the Analysis for the XMM EPIC observation (ObsID 0050940201) of PN M 3-19.

Basic Data			
Parameter	Value	Notes	
RA (J2000)	269.580571		
DEC (J2000)	-30.010922	Offset (')	12.98
$R_{\text{nebula}}$ (")	2.8	from literature (A94)	
$D$ (kpc)	4.91	from statistical methods (A94)	
$\log N_H$ ( $\text{cm}^{-2}$ )	21.6990	unknown, assumed value	
$T_{\text{eff}}$ (kK)	—		
Date Obs:	2002-03-12	XMM Filter:	Medium

Calculations			
Parameter	EMOS1	EMOS2	EPN
$t_{\text{exp}}$ (ks)	23.0	—	—
$\text{CR}_{\text{src}}$ ( $\text{cnt s}^{-1}$ )	1.063E-06	—	—
$\text{CR}_{\text{bkg}}$ ( $\text{cnt s}^{-1}$ )	9.739E-07	—	—

Hot Bubble Upper Limits ( $T_X \sim 3 \times 10^6$ K)			
Parameter	EMOS1	EMOS2	EPN
$F_X$ ( $\text{erg cm}^{-2} \text{s}^{-1}$ )	-13.3027	—	—
$L_X$ ( $\text{erg s}^{-1}$ )	32.1574	—	—

Spun-up Companion Upper Limits ( $T_X \sim 10^7$ K)			
Parameter	EMOS1	EMOS2	EPN
$F_X$ ( $\text{erg cm}^{-2} \text{s}^{-1}$ )	-13.9158	—	—
$L_X$ ( $\text{erg s}^{-1}$ )	31.5443	—	—
$L_*$ ( $L_{\text{sun}}$ )	9.1075	—	—
$M_{\text{bol}}$ (mag)	2.3415	—	—
Spectral Type	A5-F0V	—	—



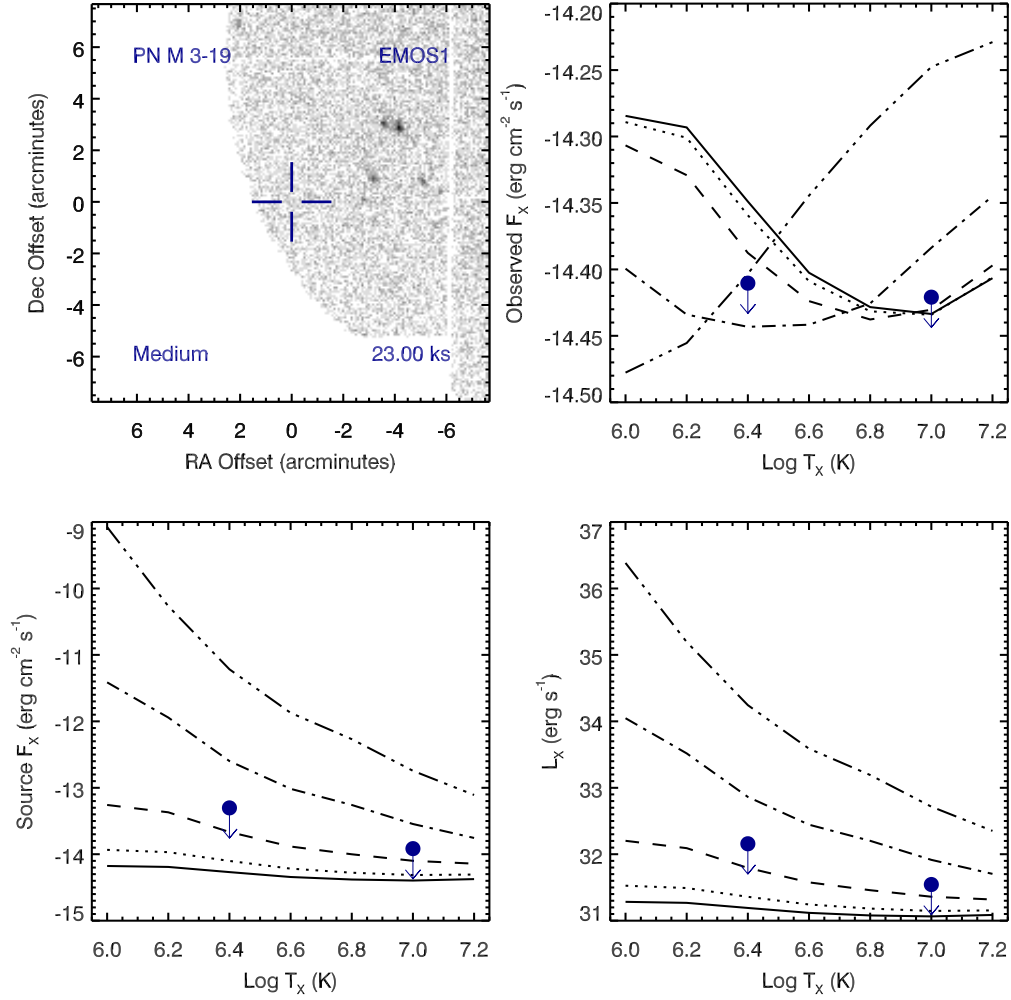


Figure A.78 Serendipitous XMM EMOS1 observation (ObsID 0050940201) of PN M 3-19. Clock-wise from top-left: broad band (0.3 to 8.0 keV) image at the PN position, upper limits of the observed flux, X-ray luminosity, and source X-ray flux. The upper limits calculations are based on the upper limit count rates, a thermal plasma model at a range temperatures, and a range of intervening absorption values:  $N_H(10^{22} \text{ cm}^{-2}) = 0.03$  (solid), 0.1 (dotted), 0.3 (dashed), 1 (dot-dashed), and 3 (dot-dot-dashed). The hot bubble and spun-up companion upper limits are depicted as the filled circles with downward pointing arrows at  $\log T_x$  of 6.4 and 7.0, respectively.

# PN M 3-28 , ObsID 0135741601

Table A.37 Summary of the Analysis for the XMM EPIC observation (ObsID 0135741601) of PN M 3-28.

Basic Data			
Parameter	Value	Notes	
RA (J2000)	278.172033		
DEC (J2000)	-10.097231	Offset (')	7.98
$R_{\text{nebula}}$ (")	4.5	from literature (A94)	
$D$ (kpc)	2.70	from statistical methods (A94)	
$\log N_H$ ( $\text{cm}^{-2}$ )	21.6990	unknown, assumed value	
$T_{\text{eff}}$ (kK)	130.50	HeI or HeII Zanstra (Ph03)	
Date Obs:	2002-03-15	XMM Filter:	Medium

Calculations			
Parameter	EMOS1	EMOS2	EPN
$t_{\text{exp}}$ (ks)	7.6	7.6	–
$\text{CR}_{\text{src}}$ ( $\text{cnt s}^{-1}$ )	8.054E-07	9.373E-07	–
$\text{CR}_{\text{bkg}}$ ( $\text{cnt s}^{-1}$ )	7.457E-07	6.044E-07	–

Hot Bubble Upper Limits ( $T_X \sim 3 \times 10^6$ K)			
Parameter	EMOS1	EMOS2	EPN
$F_X$ ( $\text{erg cm}^{-2} \text{s}^{-1}$ )	-13.1198	-13.1660	–
$L_X$ ( $\text{erg s}^{-1}$ )	31.8208	31.7746	–

Spun-up Companion Upper Limits ( $T_X \sim 10^7$ K)			
Parameter	EMOS1	EMOS2	EPN
$F_X$ ( $\text{erg cm}^{-2} \text{s}^{-1}$ )	-13.7328	-13.7791	–
$L_X$ ( $\text{erg s}^{-1}$ )	31.2078	31.1615	–
$L_*$ ( $L_{\text{sun}}$ )	4.1968	3.7726	–
$M_{\text{bol}}$ (mag)	3.1827	3.2984	–
Spectral Type	F0-F2V	F0-F2V	–

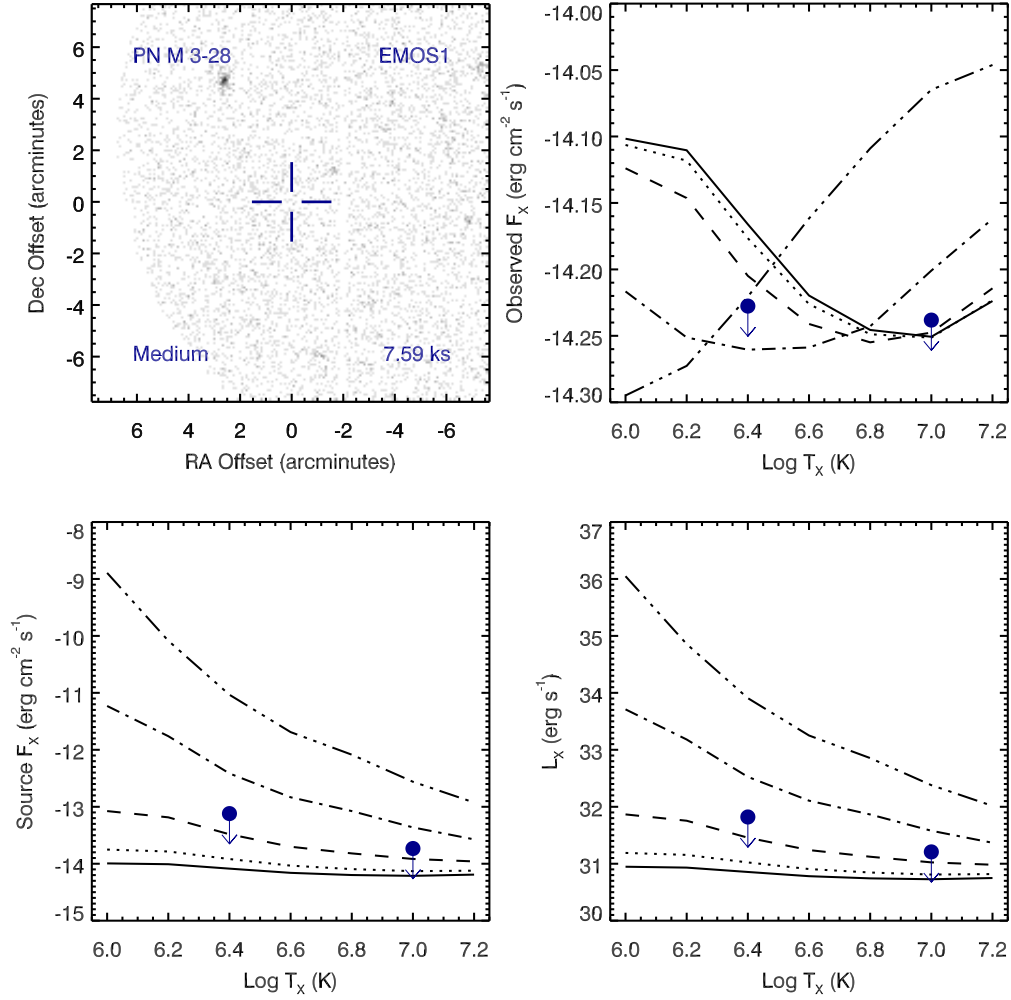


Figure A.79 Serendipitous XMM EMOS1 observation (ObsID 0135741601) of PN M 3-28. Clock-wise from top-left: broad band (0.3 to 8.0 keV) image at the PN position, upper limits of the observed flux, X-ray luminosity, and source X-ray flux. The upper limits calculations are based on the upper limit count rates, a thermal plasma model at a range temperatures, and a range of intervening absorption values:  $N_H(10^{22} \text{ cm}^{-2}) = 0.03$  (solid), 0.1 (dotted), 0.3 (dashed), 1 (dot-dashed), and 3 (dot-dot-dashed). The hot bubble and spun-up companion upper limits are depicted as the filled circles with downward pointing arrows at  $\log T_x$  of 6.4 and 7.0, respectively.

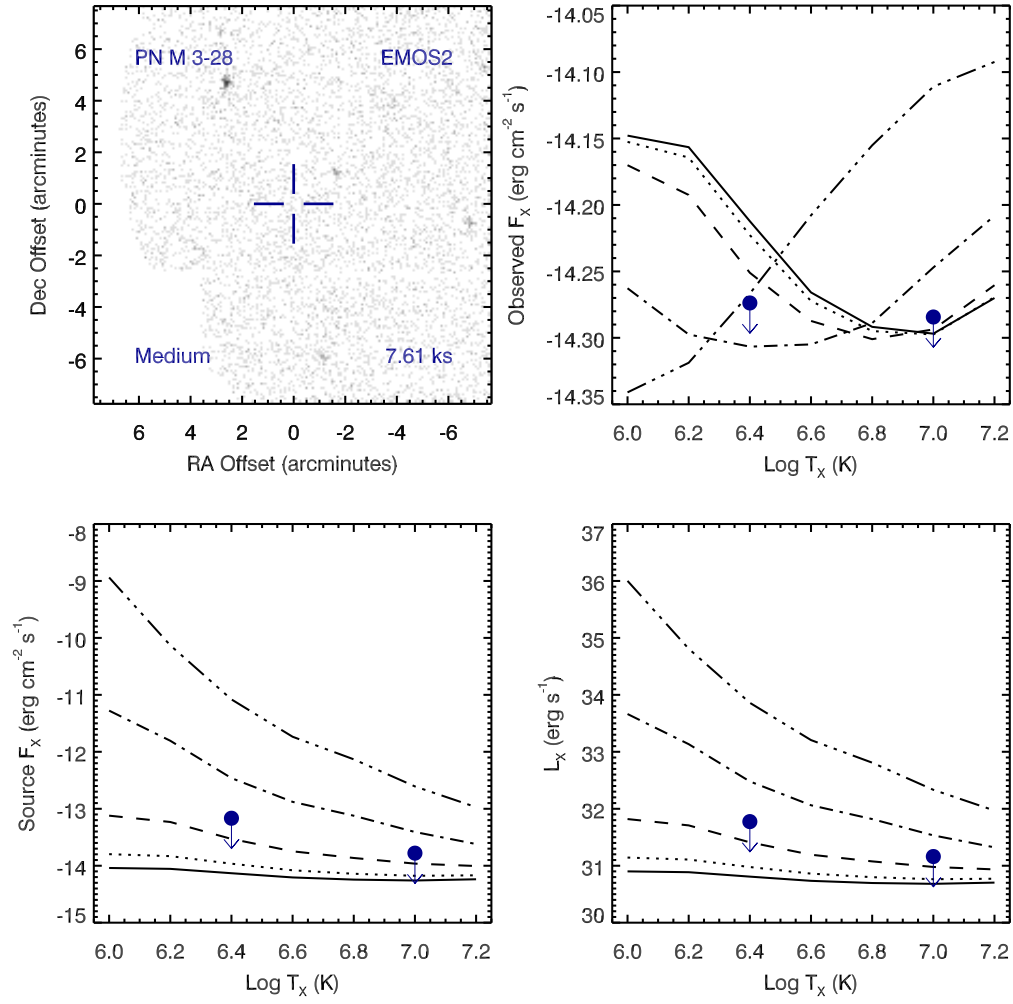


Figure A.80 Serendipitous XMM EMOS2 observation (ObsID 0135741601) of PN M 3-28 ; panels as in Figure A.79.

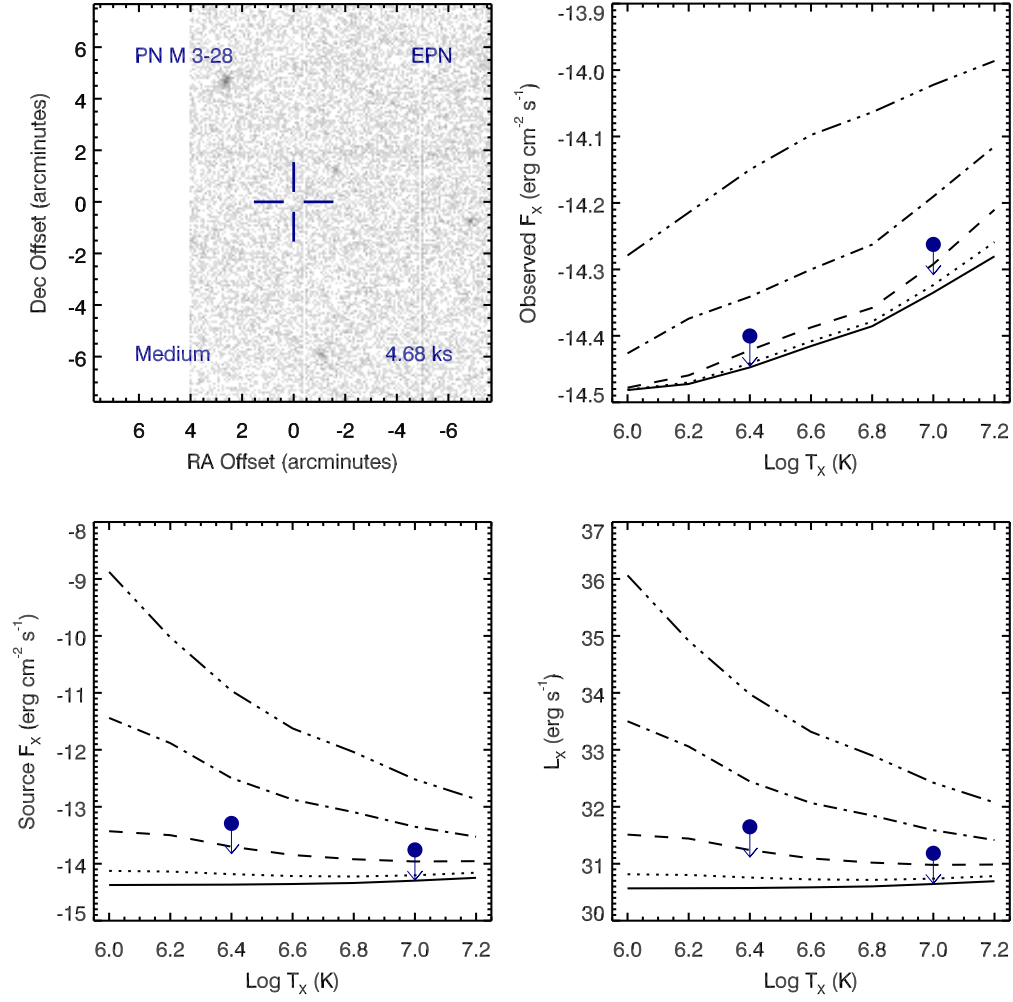


Figure A.81 Serendipitous XMM EPN observation (ObsID 0135741601) of PN M 3-28 ; panels as in Figure A.79.

# PN M 3-28 , ObsID 0135744401

Table A.38 Summary of the Analysis for the XMM EPIC observation (ObsID 0135744401) of PN M 3-28.

Basic Data			
Parameter	Value	Notes	
RA (J2000)	278.172033		
DEC (J2000)	-10.097231	Offset (')	7.98
$R_{\text{nebula}}$ (")	4.5	from literature (A94)	
$D$ (kpc)	2.70	from statistical methods (A94)	
$\log N_H$ ( $\text{cm}^{-2}$ )	21.6990	unknown, assumed value	
$T_{\text{eff}}$ (kK)	130.50	HeI or HeII Zanstra (Ph03)	
Date Obs:	2002-03-15	XMM Filter:	CalClosed

Calculations			
Parameter	EMOS1	EMOS2	EPN
$t_{\text{exp}}$ (ks)	4.4	4.4	–
$\text{CR}_{\text{src}}$ ( $\text{cnt s}^{-1}$ )	1.176E-05	2.757E-05	–
$\text{CR}_{\text{bkg}}$ ( $\text{cnt s}^{-1}$ )	9.925E-06	2.697E-05	–

Hot Bubble Upper Limits ( $T_X \sim 3 \times 10^6$ K)			
Parameter	EMOS1	EMOS2	EPN
$F_X$ ( $\text{erg cm}^{-2} \text{s}^{-1}$ )	-12.3585	-12.1412	–
$L_X$ ( $\text{erg s}^{-1}$ )	32.5821	32.7994	–

Spun-up Companion Upper Limits ( $T_X \sim 10^7$ K)			
Parameter	EMOS1	EMOS2	EPN
$F_X$ ( $\text{erg cm}^{-2} \text{s}^{-1}$ )	-12.9957	-12.7783	–
$L_X$ ( $\text{erg s}^{-1}$ )	31.9450	32.1623	–
$L_*$ ( $L_{\text{sun}}$ )	22.9121	37.7937	–
$M_{\text{bol}}$ (mag)	1.3398	0.7965	–
Spectral Type	A2-A5V	A0-A2V	–

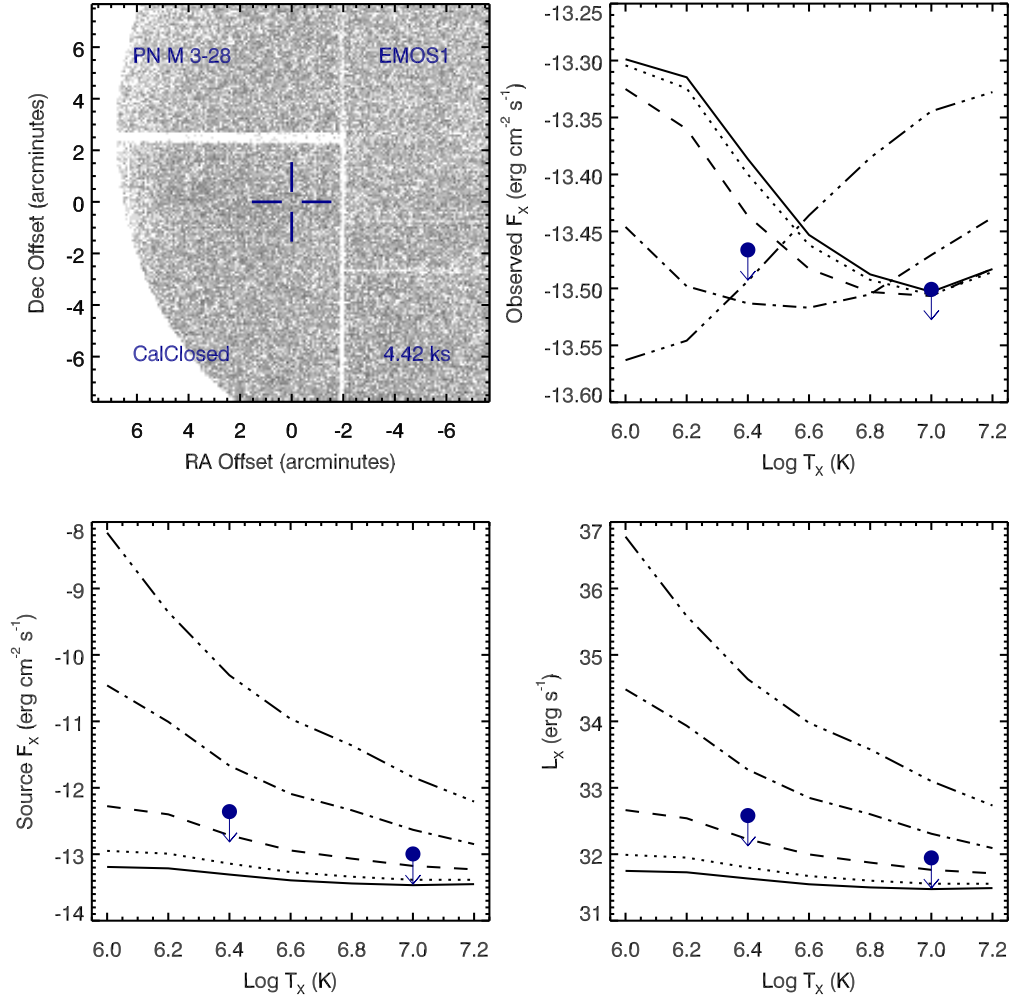


Figure A.82 Serendipitous XMM EMOS1 observation (ObsID 0135744401) of PN M 3-28. Clock-wise from top-left: broad band (0.3 to 8.0 keV) image at the PN position, upper limits of the observed flux, X-ray luminosity, and source X-ray flux. The upper limits calculations are based on the upper limit count rates, a thermal plasma model at a range temperatures, and a range of intervening absorption values:  $N_H(10^{22} \text{ cm}^{-2}) = 0.03$  (solid), 0.1 (dotted), 0.3 (dashed), 1 (dot-dashed), and 3 (dot-dot-dashed). The hot bubble and spun-up companion upper limits are depicted as the filled circles with downward pointing arrows at  $\log T_x$  of 6.4 and 7.0, respectively.

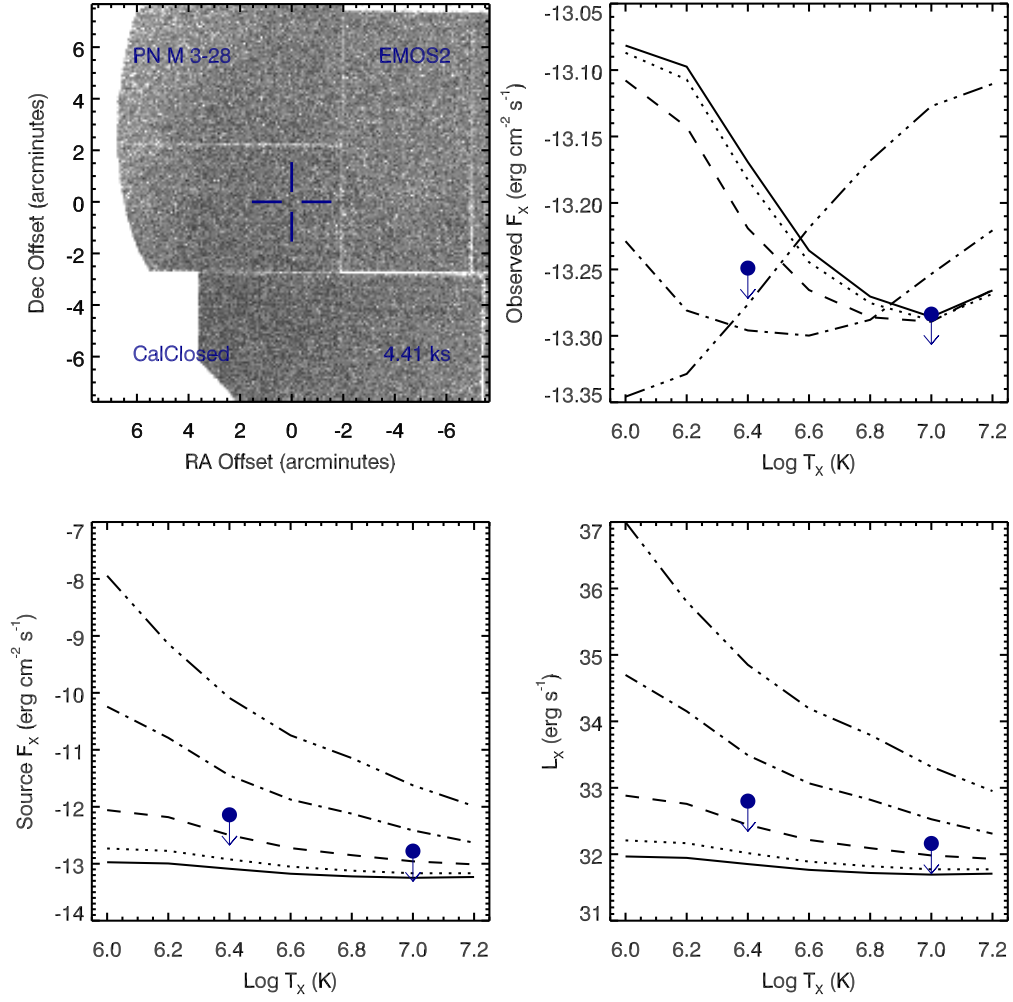


Figure A.83 Serendipitous XMM EMOS2 observation (ObsID 0135744401) of PN M 3-28 ; panels as in Figure A.82.



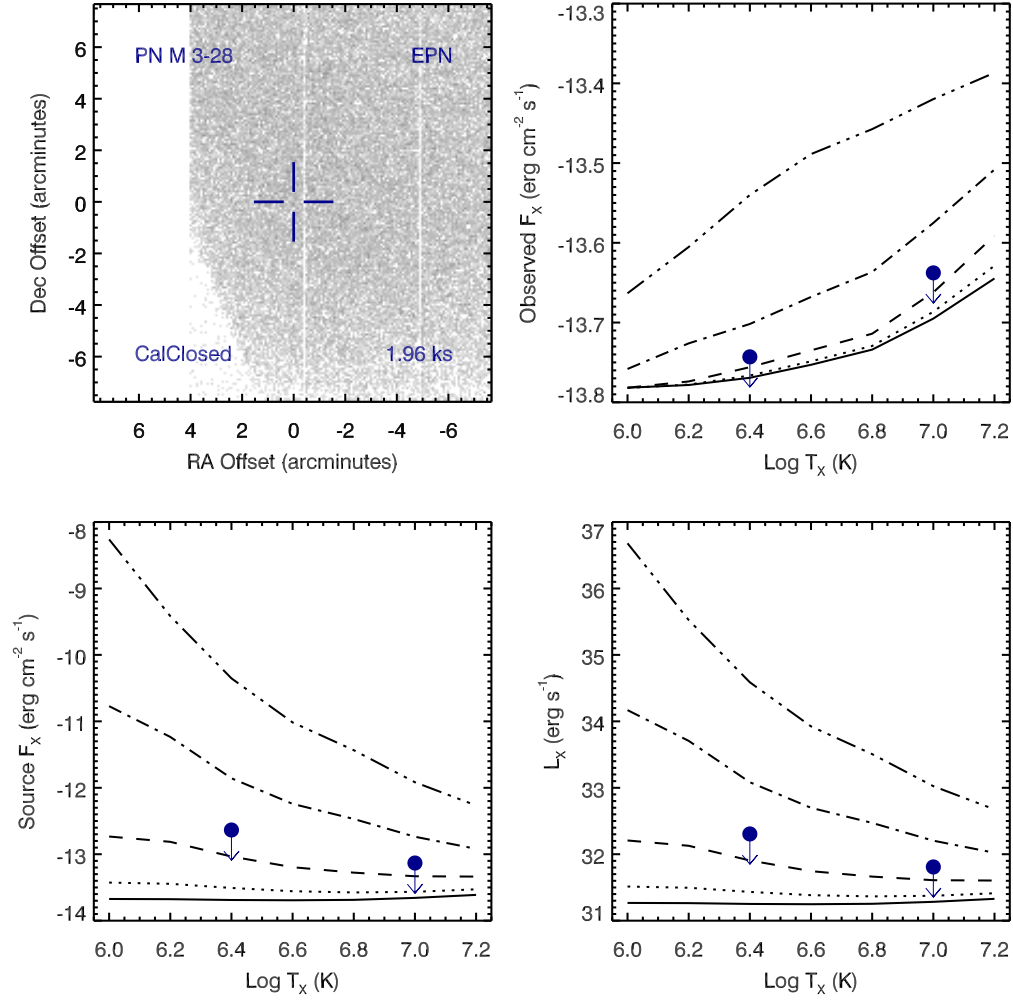


Figure A.84 Serendipitous XMM EPN observation (ObsID 0135744401) of PN M 3-28 ; panels as in Figure A.82.

## PN M 3-44 , ObsID 0154750301

Table A.39 Summary of the Analysis for the XMM EPIC observation (ObsID 0154750301) of PN M 3-44.

Basic Data			
Parameter	Value	Notes	
RA (J2000)	267.828725		
DEC (J2000)	-30.398053	Offset (')	13.63
$R_{\text{nebula}}$ (")	2.2	from literature (A94)	
$D$ (kpc)	2.86	from statistical methods (A94)	
$\log N_H$ ( $\text{cm}^{-2}$ )	21.6990	unknown, assumed value	
$T_{\text{eff}}$ (kK)	26.30	HeI or HeII Zanstra (Ph03)	
Date Obs:	2002-04-07	XMM Filter:	Thin1

Calculations			
Parameter	EMOS1	EMOS2	EPN
$t_{\text{exp}}$ (ks)	31.4	30.0	–
$\text{CR}_{\text{src}}$ ( $\text{cnt s}^{-1}$ )	2.353E-06	2.242E-06	–
$\text{CR}_{\text{bkg}}$ ( $\text{cnt s}^{-1}$ )	2.036E-06	2.328E-06	–

Hot Bubble Upper Limits ( $T_X \sim 3 \times 10^6$ K)			
Parameter	EMOS1	EMOS2	EPN
$F_X$ ( $\text{erg cm}^{-2} \text{s}^{-1}$ )	-13.2211	-13.1820	–
$L_X$ ( $\text{erg s}^{-1}$ )	31.7696	31.8087	–

Spun-up Companion Upper Limits ( $T_X \sim 10^7$ K)			
Parameter	EMOS1	EMOS2	EPN
$F_X$ ( $\text{erg cm}^{-2} \text{s}^{-1}$ )	-13.8303	-13.7910	–
$L_X$ ( $\text{erg s}^{-1}$ )	31.1603	31.1996	–
$L_*$ ( $L_{\text{sun}}$ )	3.7620	4.1184	–
$M_{\text{bol}}$ (mag)	3.3014	3.2032	–
Spectral Type	F0-F2V	F0-F2V	–

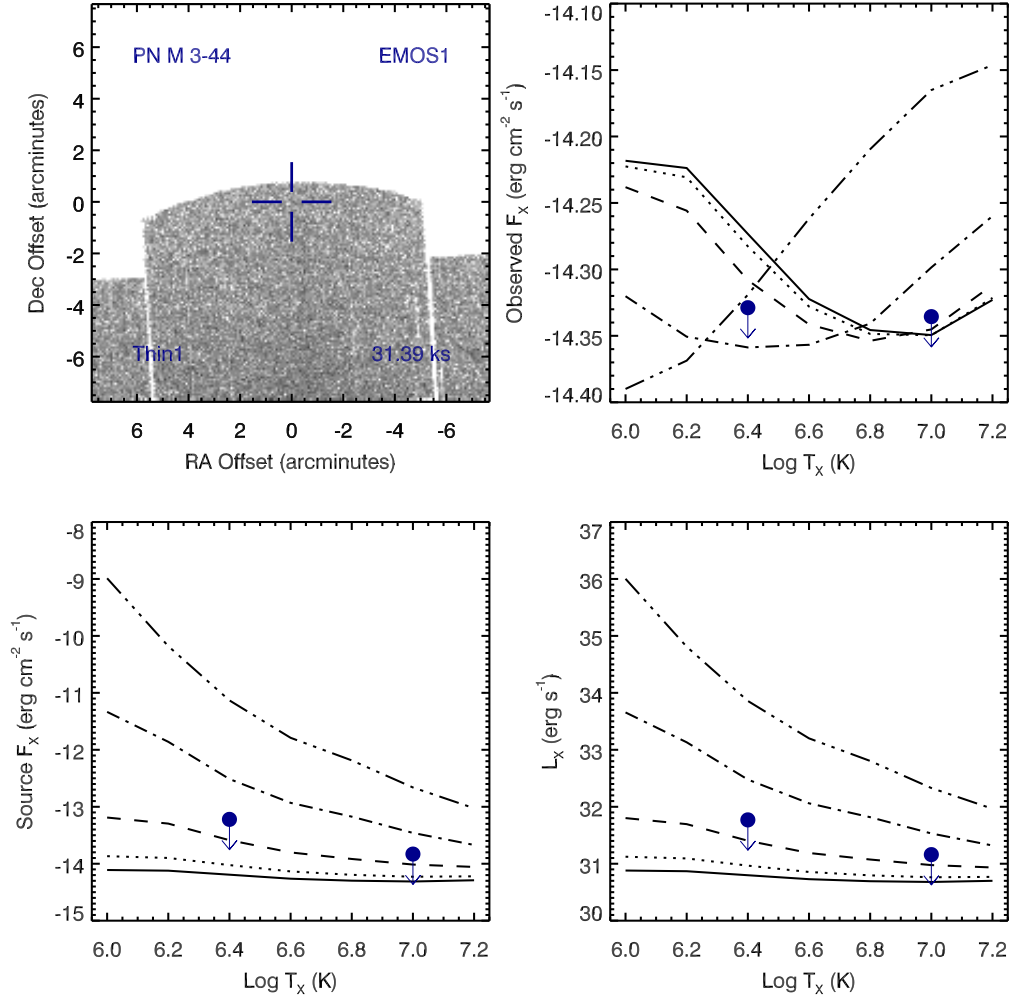


Figure A.85 Serendipitous XMM EMOS1 observation (ObsID 0154750301) of PN M 3-44. Clock-wise from top-left: broad band (0.3 to 8.0 keV) image at the PN position, upper limits of the observed flux, X-ray luminosity, and source X-ray flux. The upper limits calculations are based on the upper limit count rates, a thermal plasma model at a range of temperatures, and a range of intervening absorption values:  $N_H(10^{22} \text{ cm}^{-2}) = 0.03$  (solid), 0.1 (dotted), 0.3 (dashed), 1 (dot-dashed), and 3 (dot-dot-dashed). The hot bubble and spun-up companion upper limits are depicted as the filled circles with downward pointing arrows at  $\log T_x$  of 6.4 and 7.0, respectively.

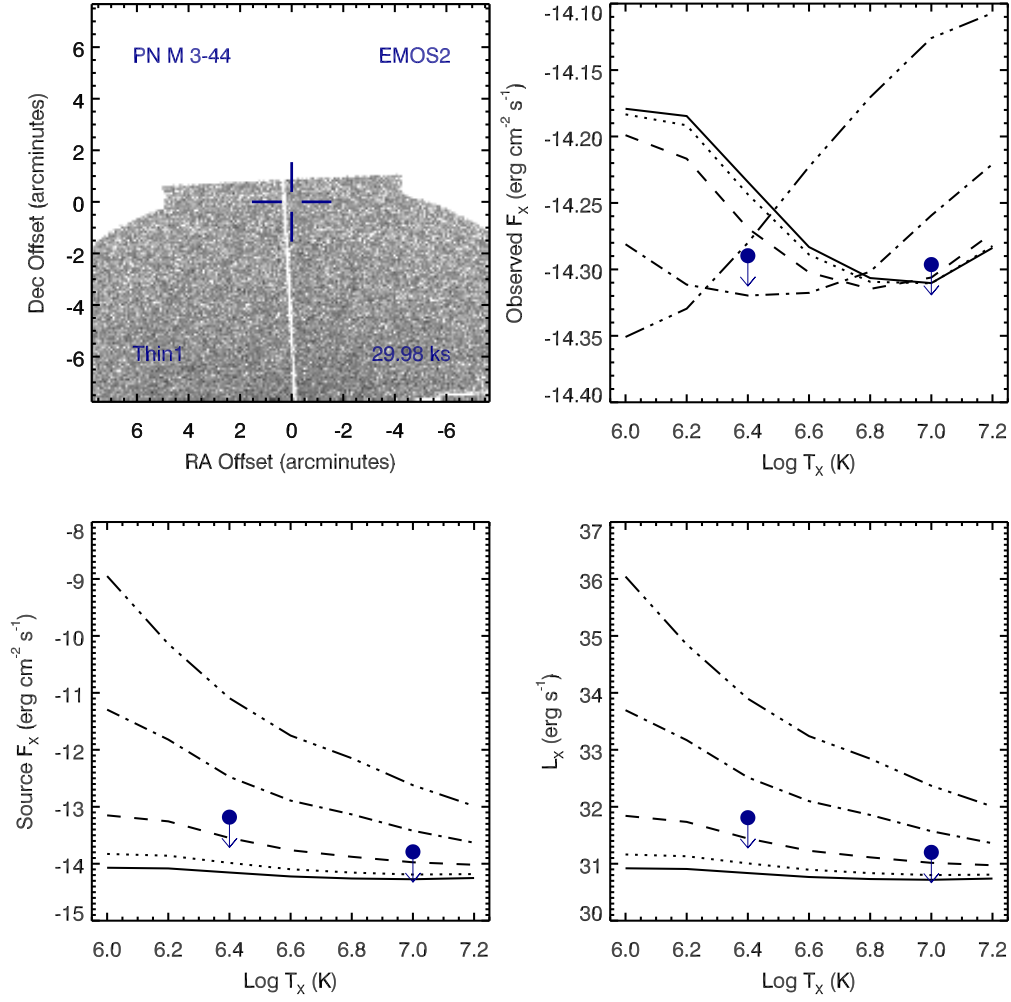


Figure A.86 Serendipitous XMM EMOS2 observation (ObsID 0154750301) of PN M 3-44 ; panels as in Figure A.85.

# PN M 3-46 , ObsID 0085580201

Table A.40 Summary of the Analysis for the XMM EPIC observation (ObsID 0085580201) of PN M 3-46.

Basic Data			
Parameter	Value	Notes	
RA (J2000)	268.774150		
DEC (J2000)	-31.204453	Offset (')	11.35
$R_{\text{nebula}}$ (")	2.1	from literature (A94)	
$D$ (kpc)	4.33	from statistical methods (A94)	
$\log N_H$ (cm <sup>-2</sup> )	21.6990	unknown, assumed value	
$T_{\text{eff}}$ (kK)	22.40	HeI or HeII Zanstra (Ph03)	
Date Obs:	2000-10-11	XMM Filter:	Thin1

Calculations			
Parameter	EMOS1	EMOS2	EPN
$t_{\text{exp}}$ (ks)	9.1	9.1	–
$\text{CR}_{\text{src}}$ (cnt s <sup>-1</sup> )	7.870E-07	1.068E-06	–
$\text{CR}_{\text{bkg}}$ (cnt s <sup>-1</sup> )	6.897E-07	8.850E-07	–

Hot Bubble Upper Limits ( $T_X \sim 3 \times 10^6$ K)			
Parameter	EMOS1	EMOS2	EPN
$F_X$ (erg cm <sup>-2</sup> s <sup>-1</sup> )	-13.1862	-13.1321	–
$L_X$ (erg s <sup>-1</sup> )	32.1647	32.2188	–

Spun-up Companion Upper Limits ( $T_X \sim 10^7$ K)			
Parameter	EMOS1	EMOS2	EPN
$F_X$ (erg cm <sup>-2</sup> s <sup>-1</sup> )	-13.7953	-13.7411	–
$L_X$ (erg s <sup>-1</sup> )	31.5555	31.6098	–
$L_*$ ( $L_{\text{sun}}$ )	9.3466	10.5893	–
$M_{\text{bol}}$ (mag)	2.3134	2.1778	–
Spectral Type	A5-F0V	A5-F0V	–

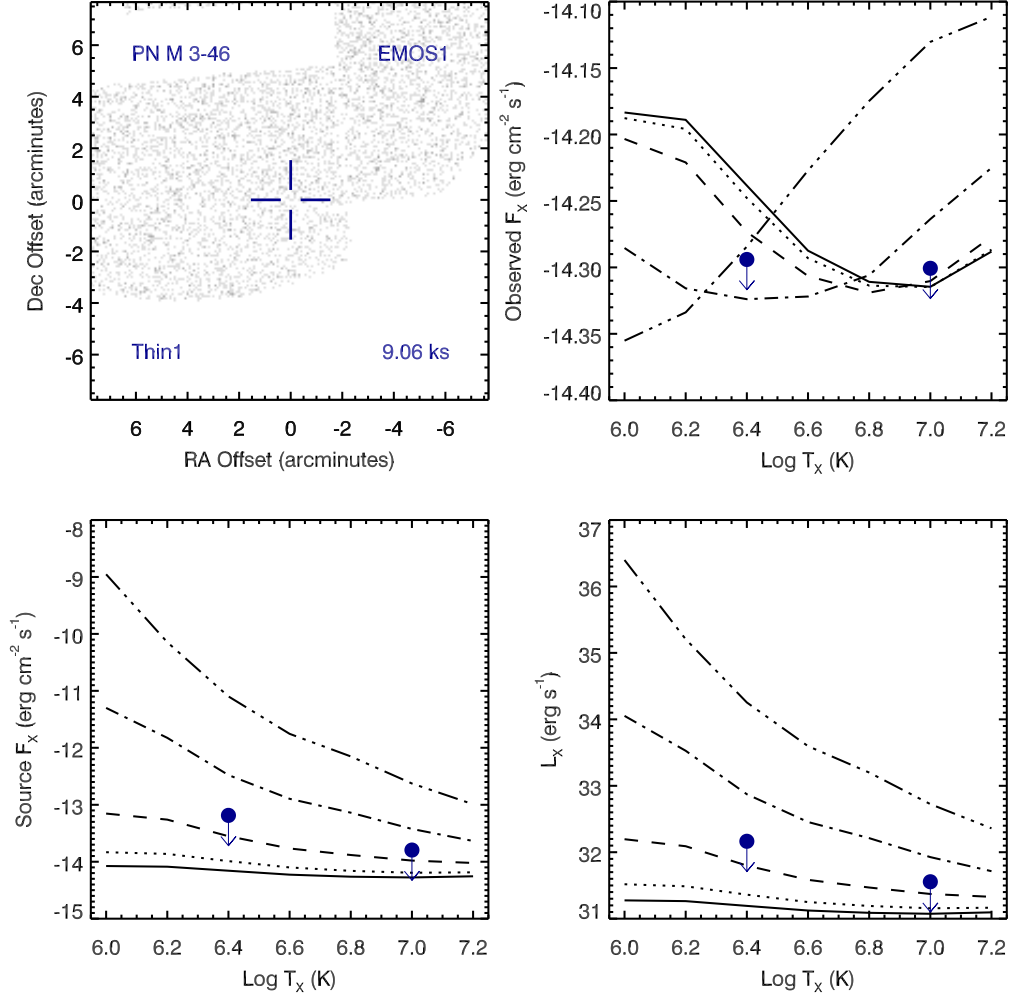


Figure A.87 Serendipitous XMM EMOS1 observation (ObsID 0085580201) of PN M 3-46. Clock-wise from top-left: broad band (0.3 to 8.0 keV) image at the PN position, upper limits of the observed flux, X-ray luminosity, and source X-ray flux. The upper limits calculations are based on the upper limit count rates, a thermal plasma model at a range of temperatures, and a range of intervening absorption values:  $N_H(10^{22} \text{ cm}^{-2}) = 0.03$  (solid), 0.1 (dotted), 0.3 (dashed), 1 (dot-dashed), and 3 (dot-dot-dashed). The hot bubble and spun-up companion upper limits are depicted as the filled circles with downward pointing arrows at  $\text{Log } T_x$  of 6.4 and 7.0, respectively.

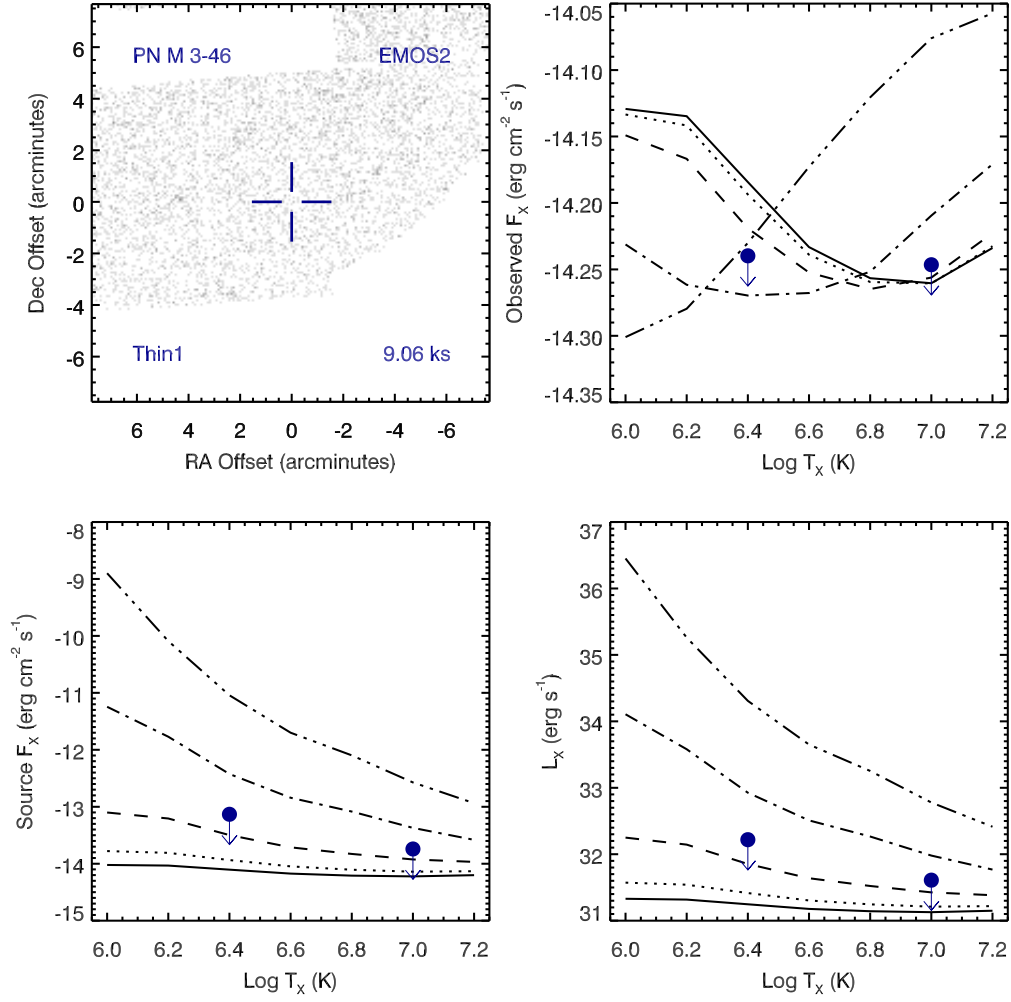


Figure A.88 Serendipitous XMM EMOS2 observation (ObsID 0085580201) of PN M 3-46 ; panels as in Figure A.87.

# PN M 3-46 , ObsID 0085581001

Table A.41 Summary of the Analysis for the XMM EPIC observation (ObsID 0085581001) of PN M 3-46.

Basic Data			
Parameter	Value	Notes	
RA (J2000)	268.774150		
DEC (J2000)	-31.204453	Offset (')	11.35
$R_{\text{nebula}}$ (")	2.1	from literature (A94)	
$D$ (kpc)	4.33	from statistical methods (A94)	
$\log N_H$ ( $\text{cm}^{-2}$ )	21.6990	unknown, assumed value	
$T_{\text{eff}}$ (kK)	22.40	HeI or HeII Zanstra (Ph03)	
Date Obs:	2001-09-07	XMM Filter:	Thin1

Calculations			
Parameter	EMOS1	EMOS2	EPN
$t_{\text{exp}}$ (ks)	7.9	7.8	–
$\text{CR}_{\text{src}}$ ( $\text{cnt s}^{-1}$ )	3.892E-07	4.543E-07	–
$\text{CR}_{\text{bkg}}$ ( $\text{cnt s}^{-1}$ )	4.955E-07	5.258E-07	–

Hot Bubble Upper Limits ( $T_X \sim 3 \times 10^6$ K)			
Parameter	EMOS1	EMOS2	EPN
$F_X$ ( $\text{erg cm}^{-2} \text{s}^{-1}$ )	-13.2269	-13.2140	–
$L_X$ ( $\text{erg s}^{-1}$ )	32.1239	32.1369	–

Spun-up Companion Upper Limits ( $T_X \sim 10^7$ K)			
Parameter	EMOS1	EMOS2	EPN
$F_X$ ( $\text{erg cm}^{-2} \text{s}^{-1}$ )	-13.8362	-13.8230	–
$L_X$ ( $\text{erg s}^{-1}$ )	31.5146	31.5278	–
$L_*$ ( $L_{\text{sun}}$ )	8.5064	8.7690	–
$M_{\text{bol}}$ (mag)	2.4156	2.3826	–
Spectral Type	A5-F0V	A5-F0V	–



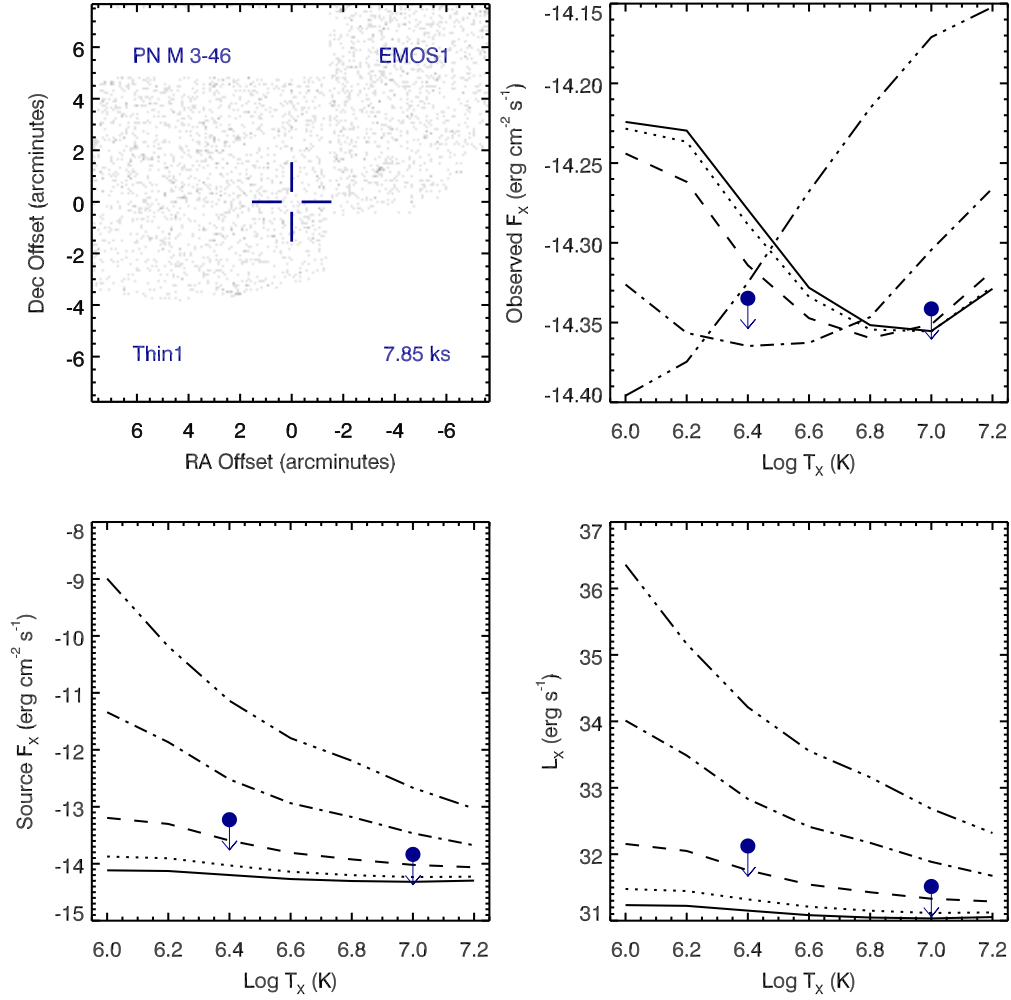


Figure A.89 Serendipitous XMM EMOS1 observation (ObsID 0085581001) of PN M 3-46. Clock-wise from top-left: broad band (0.3 to 8.0 keV) image at the PN position, upper limits of the observed flux, X-ray luminosity, and source X-ray flux. The upper limits calculations are based on the upper limit count rates, a thermal plasma model at a range temperatures, and a range of intervening absorption values:  $N_H(10^{22} \text{ cm}^{-2}) = 0.03$  (solid), 0.1 (dotted), 0.3 (dashed), 1 (dot-dashed), and 3 (dot-dot-dashed). The hot bubble and spun-up companion upper limits are depicted as the filled circles with downward pointing arrows at  $\log T_X$  of 6.4 and 7.0, respectively.

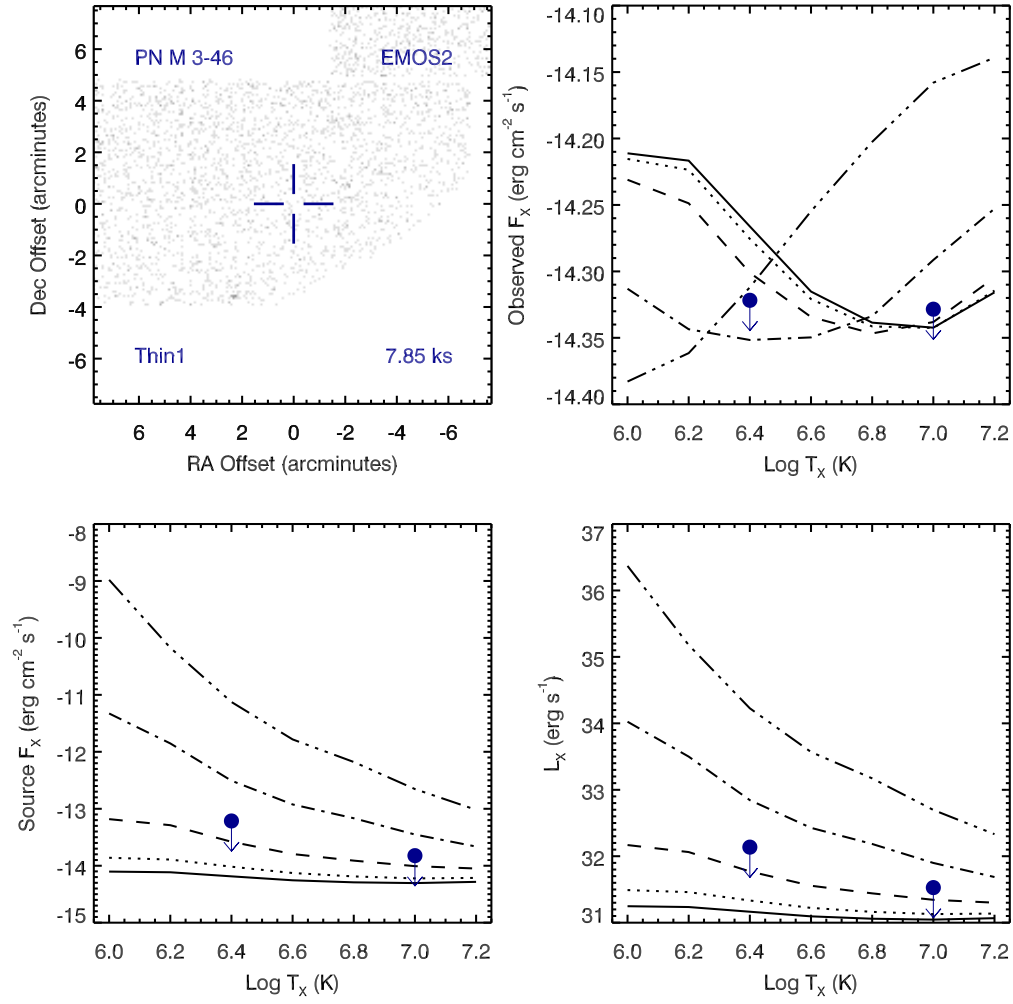


Figure A.90 Serendipitous XMM EMOS2 observation (ObsID 0085581001) of PN M 3-46 ; panels as in Figure A.89.

## PN M 3-46 , ObsID 0085581101

Table A.42 Summary of the Analysis for the XMM EPIC observation (ObsID 0085581101) of PN M 3-46.

Basic Data			
Parameter	Value	Notes	
RA (J2000)	268.774150		
DEC (J2000)	-31.204453	Offset (')	11.35
$R_{\text{nebula}}$ (")	2.1	from literature (A94)	
$D$ (kpc)	4.33	from statistical methods (A94)	
$\log N_H$ ( $\text{cm}^{-2}$ )	21.6990	unknown, assumed value	
$T_{\text{eff}}$ (kK)	22.40	HeI or HeII Zanstra (Ph03)	
Date Obs:	2001-03-24	XMM Filter:	Thin1

Calculations			
Parameter	EMOS1	EMOS2	EPN
$t_{\text{exp}}$ (ks)	6.6	6.6	–
$\text{CR}_{\text{src}}$ ( $\text{cnt s}^{-1}$ )	8.447E-07	5.375E-07	–
$\text{CR}_{\text{bkg}}$ ( $\text{cnt s}^{-1}$ )	7.465E-07	8.354E-07	–

Hot Bubble Upper Limits ( $T_X \sim 3 \times 10^6$ K)			
Parameter	EMOS1	EMOS2	EPN
$F_X$ ( $\text{erg cm}^{-2} \text{s}^{-1}$ )	-13.1013	-13.0769	–
$L_X$ ( $\text{erg s}^{-1}$ )	32.2496	32.2740	–

Spun-up Companion Upper Limits ( $T_X \sim 10^7$ K)			
Parameter	EMOS1	EMOS2	EPN
$F_X$ ( $\text{erg cm}^{-2} \text{s}^{-1}$ )	-13.7104	-13.6861	–
$L_X$ ( $\text{erg s}^{-1}$ )	31.6405	31.6648	–
$L_*$ ( $L_{\text{sun}}$ )	11.3653	12.0187	–
$M_{\text{bol}}$ (mag)	2.1010	2.0404	–
Spectral Type	A5-F0V	A5-F0V	–

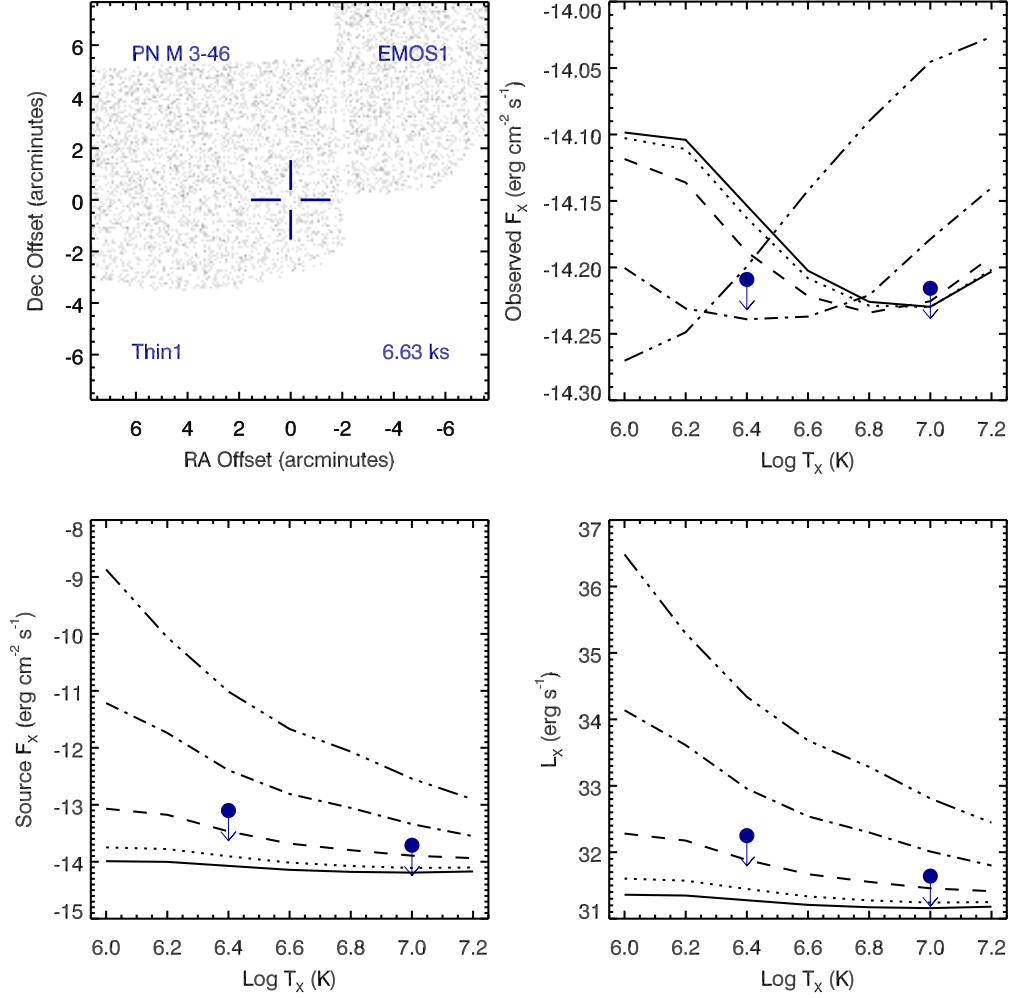


Figure A.91 Serendipitous XMM EMOS1 observation (ObsID 0085581101) of PN M 3-46. Clock-wise from top-left: broad band (0.3 to 8.0 keV) image at the PN position, upper limits of the observed flux, X-ray luminosity, and source X-ray flux. The upper limits calculations are based on the upper limit count rates, a thermal plasma model at a range temperatures, and a range of intervening absorption values:  $N_H(10^{22} \text{ cm}^{-2}) = 0.03$  (solid), 0.1 (dotted), 0.3 (dashed), 1 (dot-dashed), and 3 (dot-dot-dashed). The hot bubble and spun-up companion upper limits are depicted as the filled circles with downward pointing arrows at log  $T_x$  of 6.4 and 7.0, respectively.

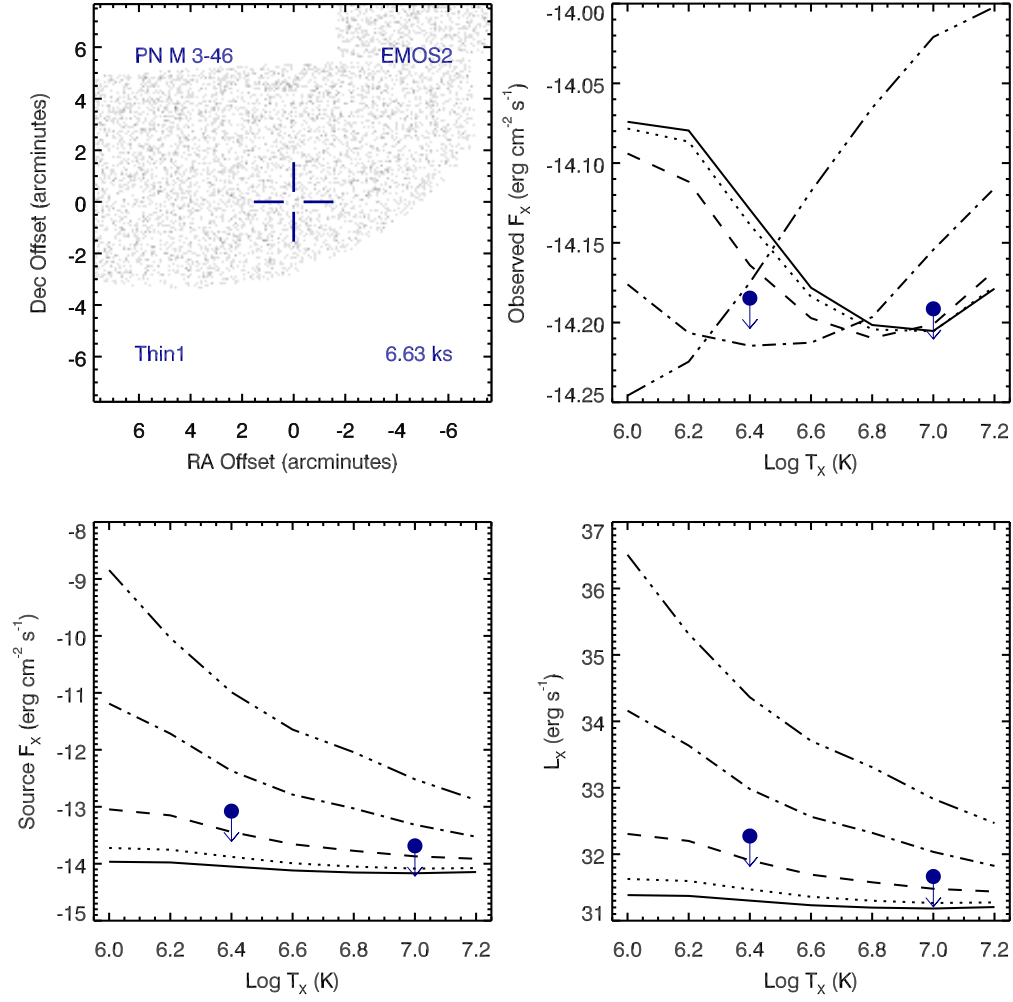


Figure A.92 Serendipitous XMM EMOS2 observation (ObsID 0085581101) of PN M 3-46 ; panels as in Figure A.91.

# PN M 3-47 , ObsID 0050940201

Table A.43 Summary of the Analysis for the XMM EPIC observation (ObsID 0050940201) of PN M 3-47.

Basic Data			
Parameter	Value	Notes	
RA (J2000)	269.430696		
DEC (J2000)	-30.041642	Offset (')	8.25
$R_{\text{nebula}}$ (")	–		
$D$ (kpc)	1.0	unknown, assumed value	
$\log N_H$ (cm <sup>-2</sup> )	21.6990	unknown, assumed value	
$T_{\text{eff}}$ (kK)	–		
Date Obs:	2002-03-12	XMM Filter:	Medium

Calculations			
Parameter	EMOS1	EMOS2	EPN
$t_{\text{exp}}$ (ks)	23.0	23.2	–
$\text{CR}_{\text{src}}$ (cnt s <sup>-1</sup> )	1.172E-06	1.055E-06	–
$\text{CR}_{\text{bkg}}$ (cnt s <sup>-1</sup> )	1.132E-06	1.074E-06	–

Hot Bubble Upper Limits ( $T_X \sim 3 \times 10^6$ K)			
Parameter	EMOS1	EMOS2	EPN
$F_X$ (erg cm <sup>-2</sup> s <sup>-1</sup> )	-13.2703	-13.2831	–
$L_X$ (erg s <sup>-1</sup> )	30.8076	30.7948	–

Spun-up Companion Upper Limits ( $T_X \sim 10^7$ K)			
Parameter	EMOS1	EMOS2	EPN
$F_X$ (erg cm <sup>-2</sup> s <sup>-1</sup> )	-13.8834	-13.8962	–
$L_X$ (erg s <sup>-1</sup> )	30.1945	30.1817	–
$L_*$ ( $L_{\text{sun}}$ )	0.4070	0.3952	–
$M_{\text{bol}}$ (mag)	5.7159	5.7480	–
Spectral Type	K0-K2V	K0-K2V	–

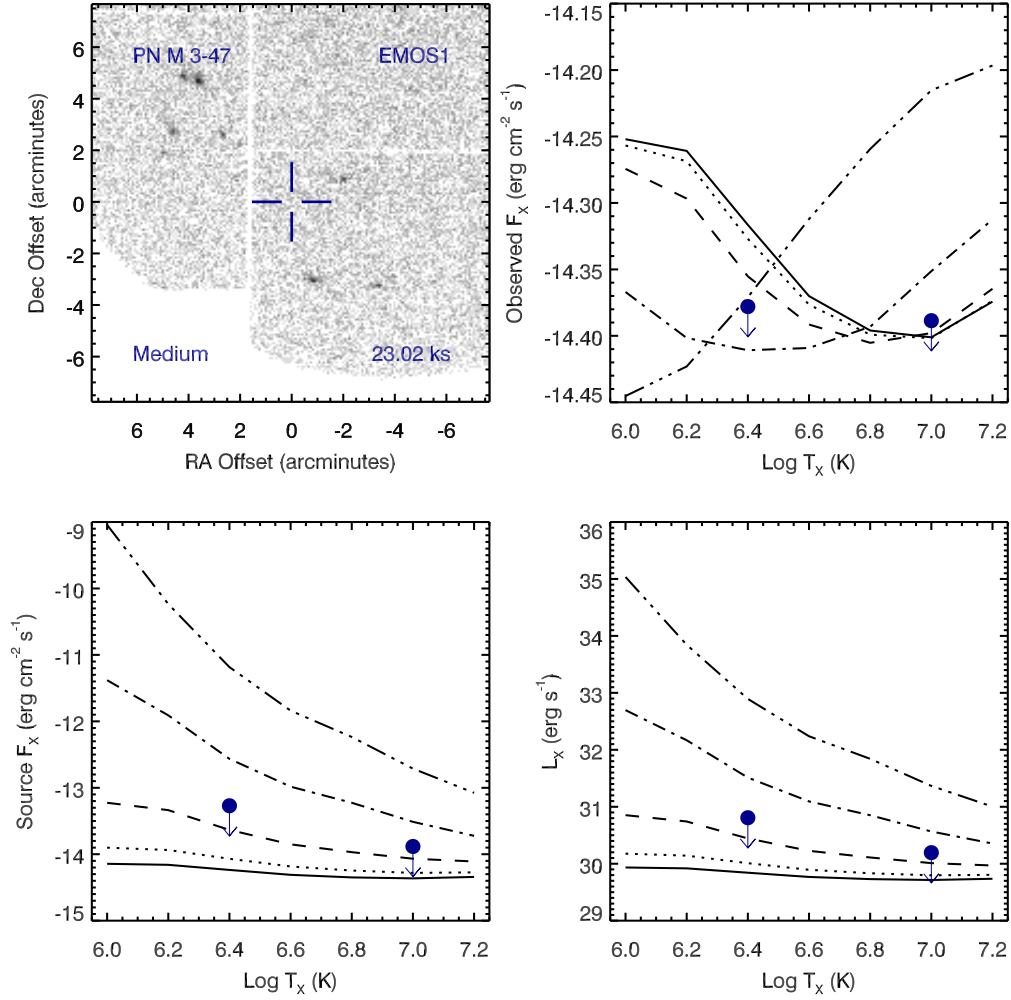


Figure A.93 Serendipitous XMM EMOS1 observation (ObsID 0050940201) of PN M 3-47. Clock-wise from top-left: broad band (0.3 to 8.0 keV) image at the PN position, upper limits of the observed flux, X-ray luminosity, and source X-ray flux. The upper limits calculations are based on the upper limit count rates, a thermal plasma model at a range temperatures, and a range of intervening absorption values:  $N_H(10^{22} \text{ cm}^{-2}) = 0.03$  (solid), 0.1 (dotted), 0.3 (dashed), 1 (dot-dashed), and 3 (dot-dot-dashed). The hot bubble and spun-up companion upper limits are depicted as the filled circles with downward pointing arrows at  $\log T_x$  of 6.4 and 7.0, respectively.

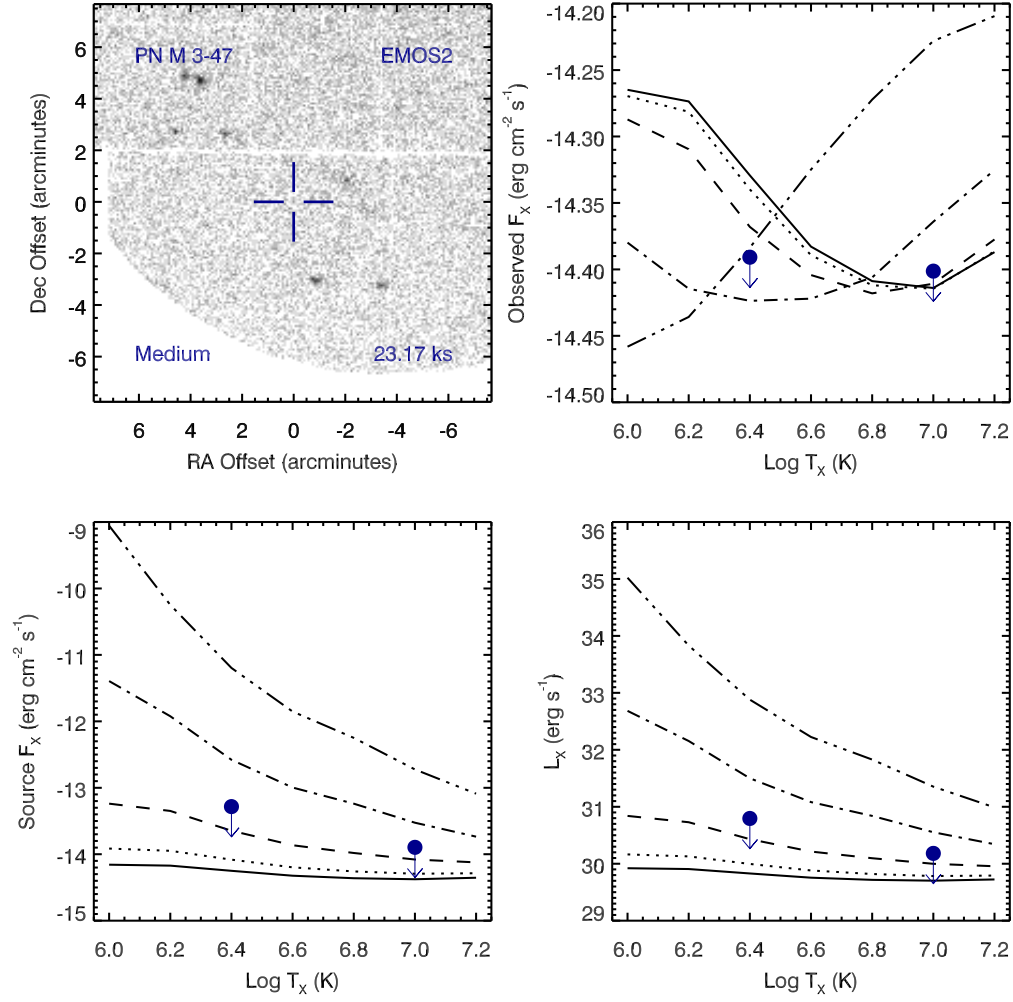


Figure A.94 Serendipitous XMM EMOS2 observation (ObsID 0050940201) of PN M 3-47 ; panels as in Figure A.93.



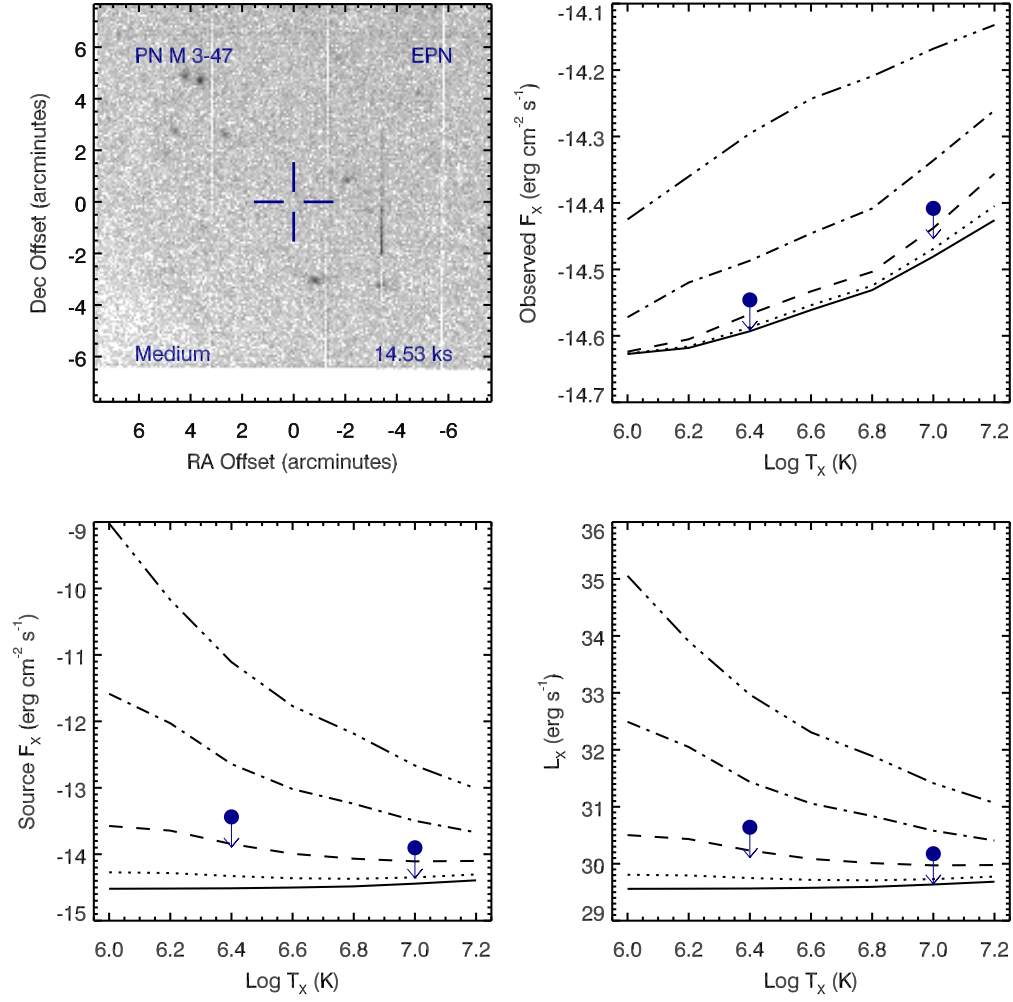


Figure A.95 Serendipitous XMM EPN observation (ObsID 0050940201) of PN M 3-47 ; panels as in Figure A.93.

# PN M 3-55 , ObsID 0122700401

Table A.44 Summary of the Analysis for the XMM EPIC observation (ObsID 0122700401) of PN M 3-55.

Basic Data			
Parameter	Value	Notes	
RA (J2000)	278.311554		
DEC (J2000)	-10.255403	Offset (')	9.14
$R_{\text{nebula}}$ (")	3.6	from literature (A94)	
$D$ (kpc)	2.70	from statistical methods (A94)	
$\log N_H$ ( $\text{cm}^{-2}$ )	21.6990	unknown, assumed value	
$T_{\text{eff}}$ (kK)	72.20	HeI or HeII Zanstra (Ph03)	
Date Obs:	2000-04-15	XMM Filter:	Medium

Calculations			
Parameter	EMOS1	EMOS2	EPN
$t_{\text{exp}}$ (ks)	25.5	25.6	–
$\text{CR}_{\text{src}}$ ( $\text{cnt s}^{-1}$ )	1.178E-06	2.052E-06	–
$\text{CR}_{\text{bkg}}$ ( $\text{cnt s}^{-1}$ )	1.239E-06	1.545E-06	–

Hot Bubble Upper Limits ( $T_X \sim 3 \times 10^6$ K)			
Parameter	EMOS1	EMOS2	EPN
$F_X$ ( $\text{erg cm}^{-2} \text{s}^{-1}$ )	-13.2729	-13.2253	–
$L_X$ ( $\text{erg s}^{-1}$ )	31.6677	31.7153	–

Spun-up Companion Upper Limits ( $T_X \sim 10^7$ K)			
Parameter	EMOS1	EMOS2	EPN
$F_X$ ( $\text{erg cm}^{-2} \text{s}^{-1}$ )	-13.8861	-13.8383	–
$L_X$ ( $\text{erg s}^{-1}$ )	31.0546	31.1023	–
$L_*$ ( $L_{\text{sun}}$ )	2.9491	3.2916	–
$M_{\text{bol}}$ (mag)	3.5658	3.4465	–
Spectral Type	F5-F8V	F5-F2V	–

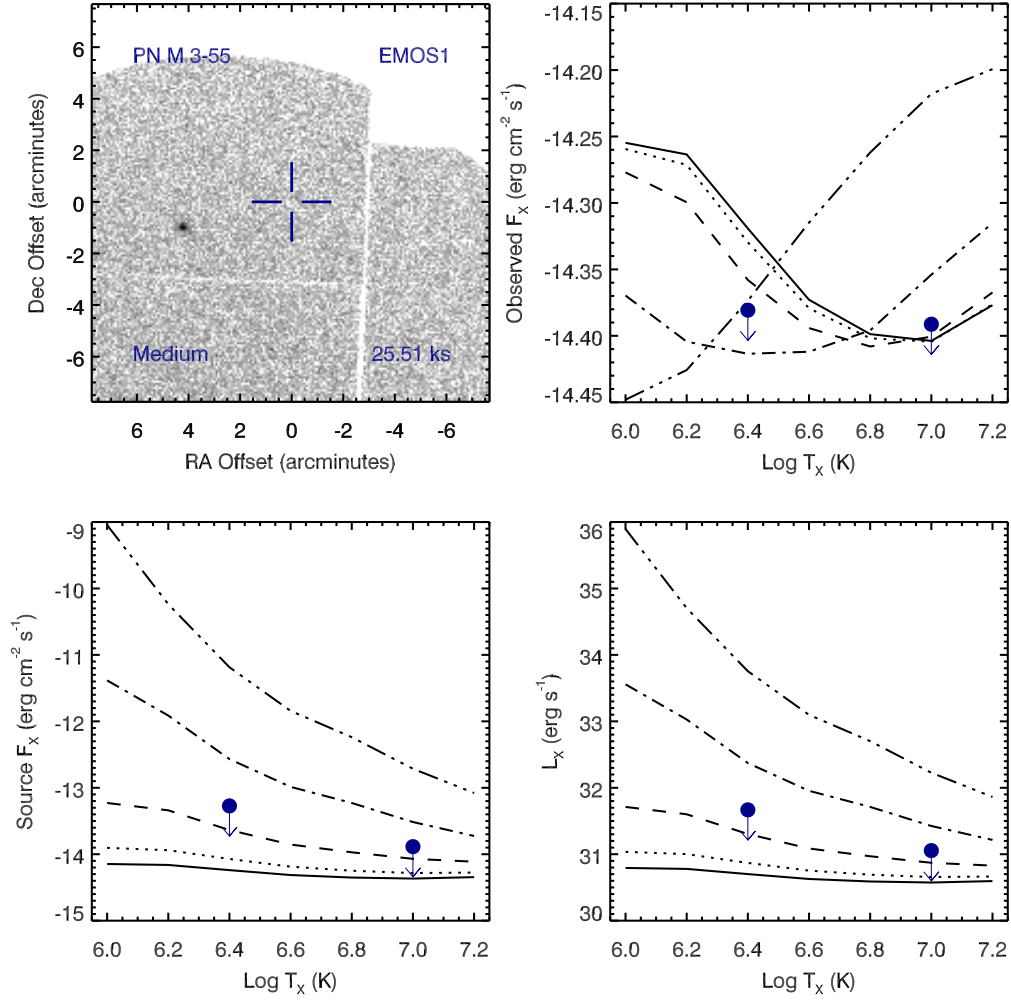


Figure A.96 Serendipitous XMM EMOS1 observation (ObsID 0122700401) of PN M 3-55. Clock-wise from top-left: broad band (0.3 to 8.0 keV) image at the PN position, upper limits of the observed flux, X-ray luminosity, and source X-ray flux. The upper limits calculations are based on the upper limit count rates, a thermal plasma model at a range temperatures, and a range of intervening absorption values:  $N_H(10^{22} \text{ cm}^{-2}) = 0.03$  (solid), 0.1 (dotted), 0.3 (dashed), 1 (dot-dashed), and 3 (dot-dot-dashed). The hot bubble and spun-up companion upper limits are depicted as the filled circles with downward pointing arrows at  $\log T_x$  of 6.4 and 7.0, respectively.

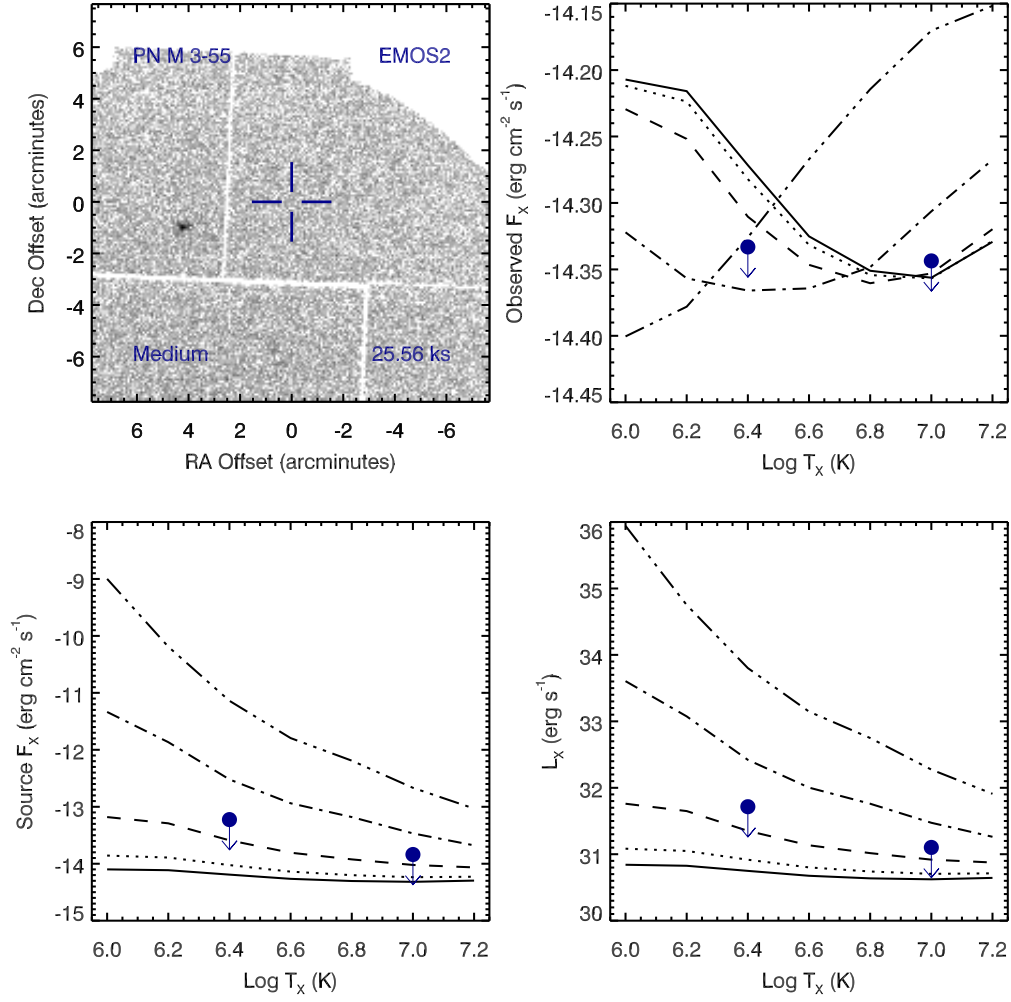


Figure A.97 Serendipitous XMM EMOS2 observation (ObsID 0122700401) of PN M 3-55 ; panels as in Figure A.96.

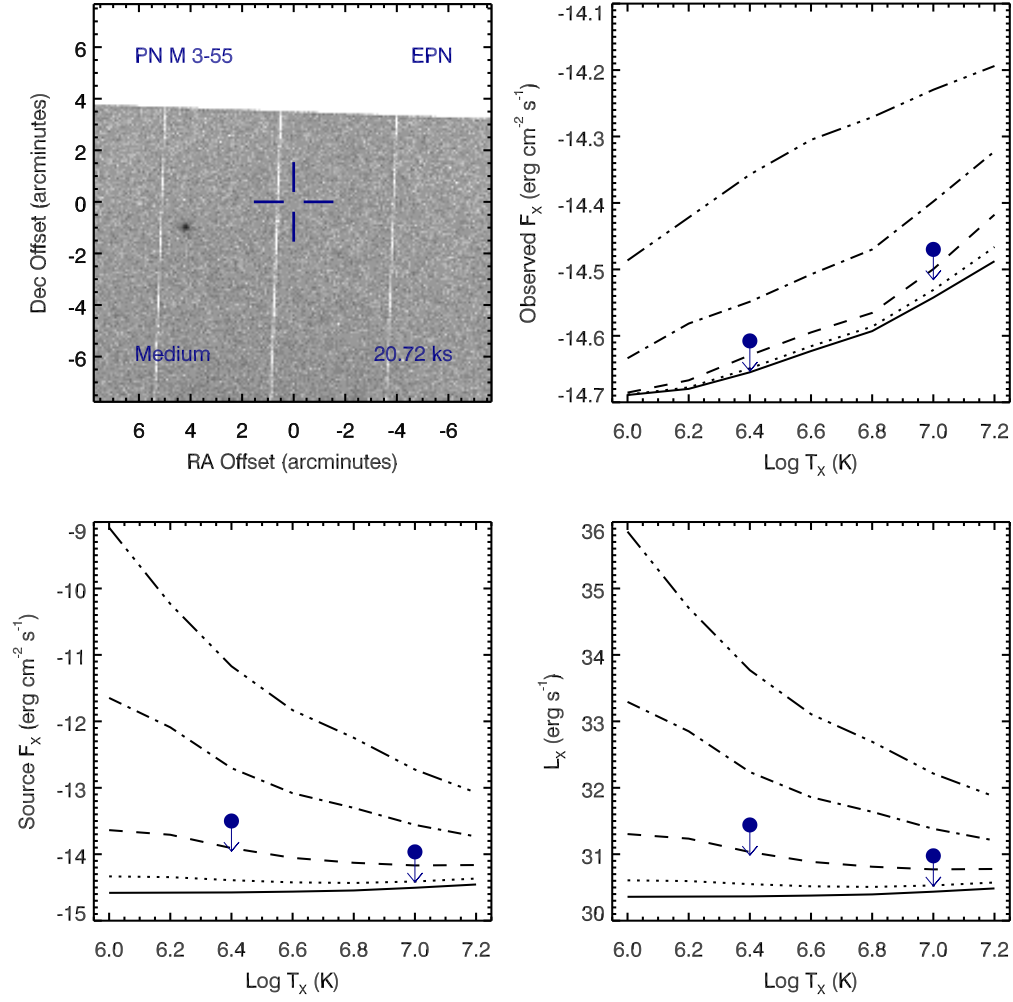


Figure A.98 Serendipitous XMM EPN observation (ObsID 0122700401) of PN M 3-55 ; panels as in Figure A.96.

# PN PBOZ 10 , ObsID 0201200101

Table A.45 Summary of the Analysis for the XMM EPIC observation (ObsID 0201200101) of PN PBOZ 10.

Basic Data			
Parameter	Value	Notes	
RA (J2000)	266.124620		
DEC (J2000)	-27.344670	Offset (')	7.78
$R_{\text{nebula}}$ (")	–		
$D$ (kpc)	1.0	unknown, assumed value	
$\log N_H$ (cm <sup>-2</sup> )	21.6990	unknown, assumed value	
$T_{\text{eff}}$ (kK)	–		
Date Obs:	2004-02-26	XMM Filter:	Medium

Calculations			
Parameter	EMOS1	EMOS2	EPN
$t_{\text{exp}}$ (ks)	17.1	17.2	–
$\text{CR}_{\text{src}}$ (cnt s <sup>-1</sup> )	9.206E-07	1.009E-06	–
$\text{CR}_{\text{bkg}}$ (cnt s <sup>-1</sup> )	8.662E-07	6.389E-07	–

Hot Bubble Upper Limits ( $T_X \sim 3 \times 10^6$ K)			
Parameter	EMOS1	EMOS2	EPN
$F_X$ (erg cm <sup>-2</sup> s <sup>-1</sup> )	-13.2644	-13.3306	–
$L_X$ (erg s <sup>-1</sup> )	30.8135	30.7473	–

Spun-up Companion Upper Limits ( $T_X \sim 10^7$ K)			
Parameter	EMOS1	EMOS2	EPN
$F_X$ (erg cm <sup>-2</sup> s <sup>-1</sup> )	-13.8775	-13.9435	–
$L_X$ (erg s <sup>-1</sup> )	30.2005	30.1344	–
$L_*$ ( $L_{\text{sun}}$ )	0.4126	0.3544	–
$M_{\text{bol}}$ (mag)	5.7011	5.8662	–
Spectral Type	K0-K2V	K0-K2V	–

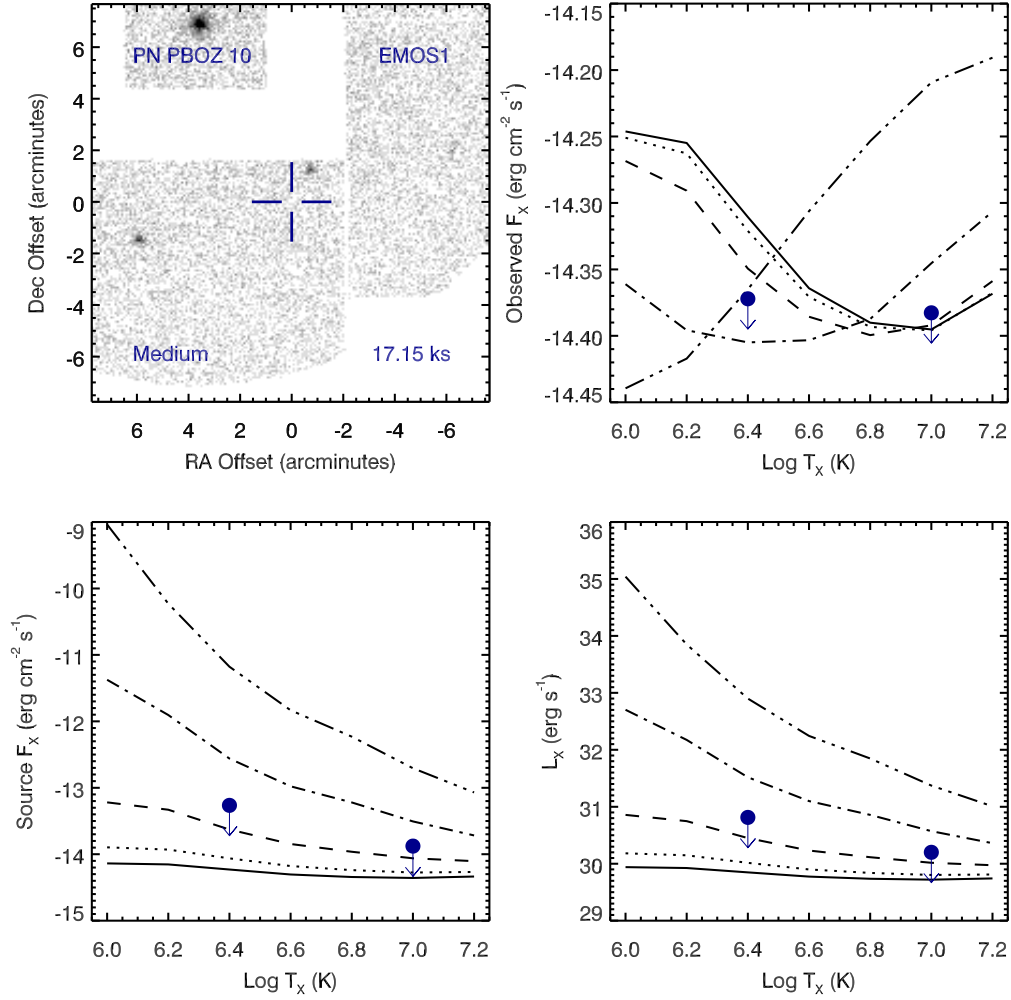


Figure A.99 Serendipitous XMM EMOS1 observation (ObsID 0201200101) of PN PBOZ 10. Clock-wise from top-left: broad band (0.3 to 8.0 keV) image at the PN position, upper limits of the observed flux, X-ray luminosity, and source X-ray flux. The upper limits calculations are based on the upper limit count rates, a thermal plasma model at a range temperatures, and a range of intervening absorption values:  $N_H(10^{22} \text{ cm}^{-2}) = 0.03$  (solid), 0.1 (dotted), 0.3 (dashed), 1 (dot-dashed), and 3 (dot-dot-dashed). The hot bubble and spun-up companion upper limits are depicted as the filled circles with downward pointing arrows at  $\log T_x$  of 6.4 and 7.0, respectively.

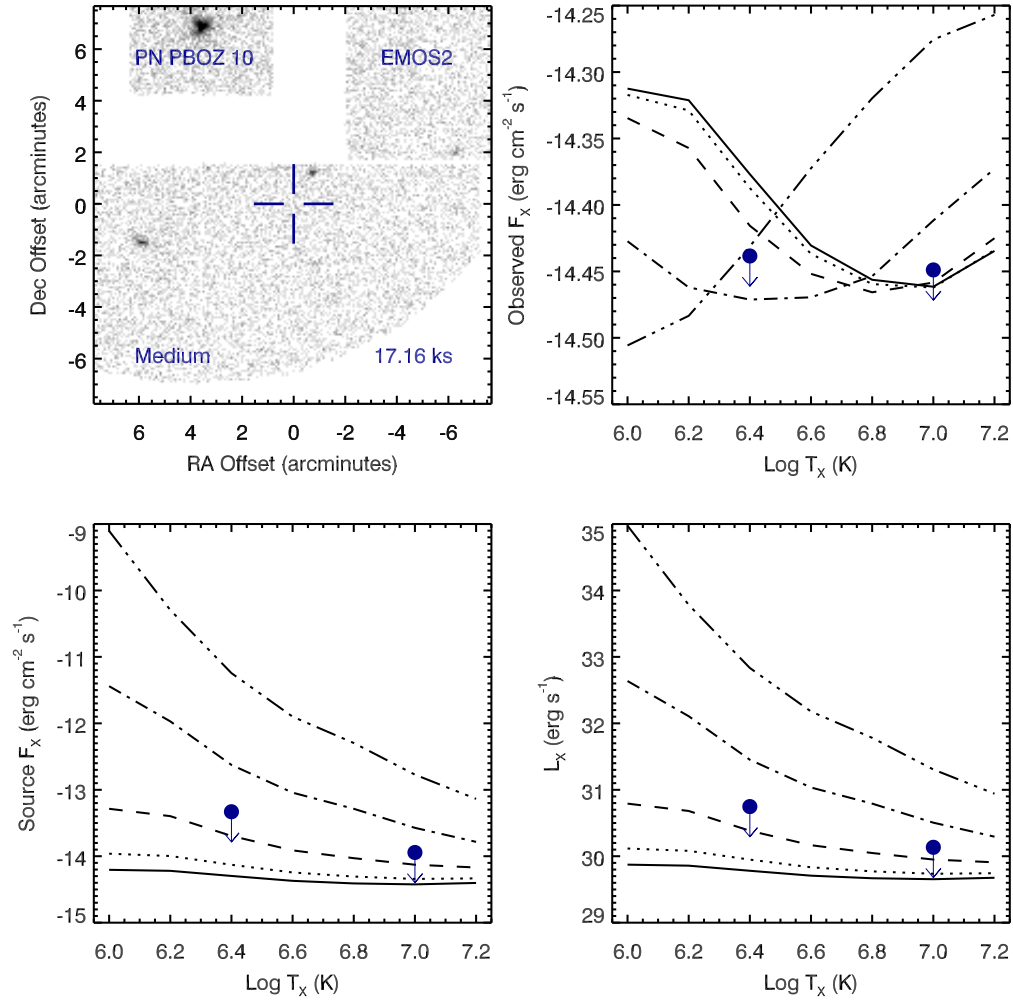


Figure A.100 Serendipitous XMM EMOS2 observation (ObsID 0201200101) of PN PBOZ 10 ; panels as in Figure A.99.



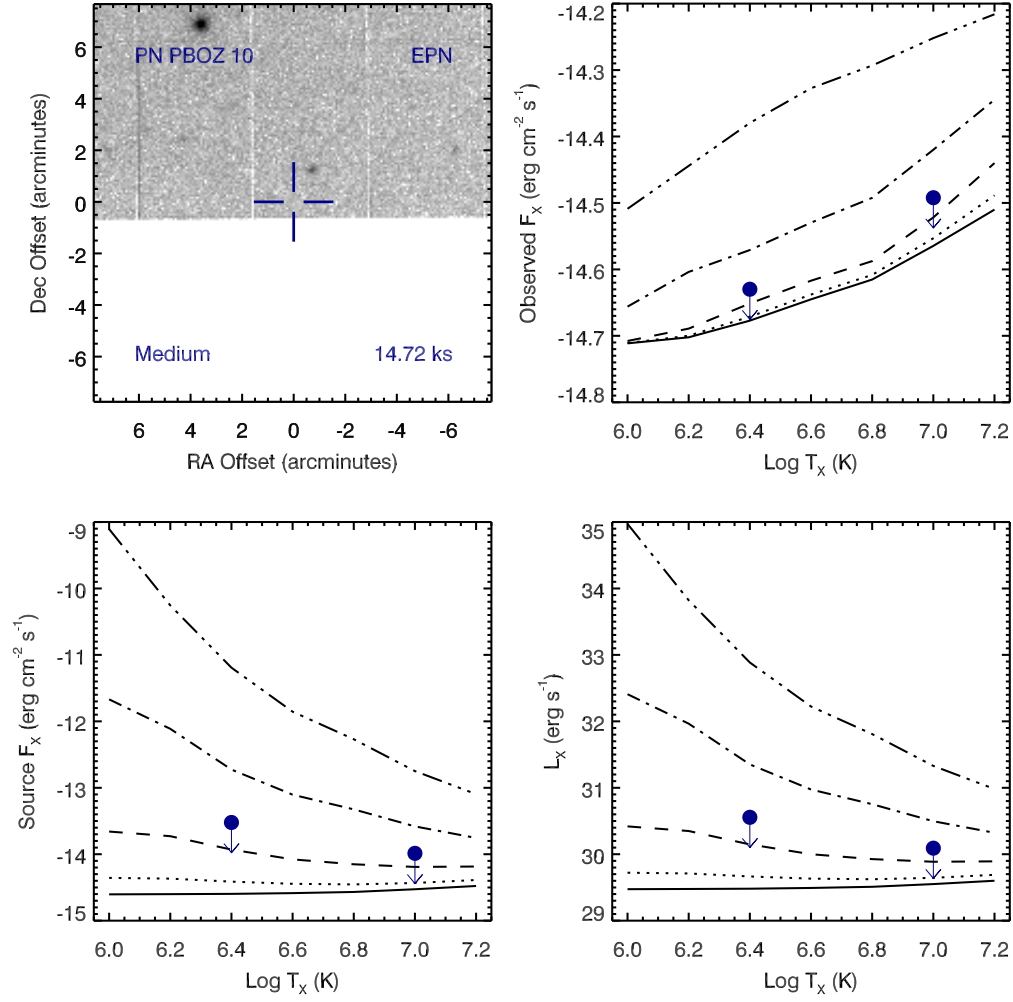


Figure A.101 Serendipitous XMM EPN observation (ObsID 0201200101) of PN PBOZ 10 ; panels as in Figure A.99.

# PN SHWI 5 , ObsID 0050940101

Table A.46 Summary of the Analysis for the XMM EPIC observation (ObsID 0050940101) of PN SHWI 5.

Basic Data			
Parameter	Value	Notes	
RA (J2000)	270.973583		
DEC (J2000)	-29.856081	Offset (')	10.29
$R_{\text{nebula}}$ (")	2.0	from literature (A94)	
$D$ (kpc)	1.0	unknown, assumed value	
$\log N_H$ (cm <sup>-2</sup> )	21.6358	optical extinction (C92)	
$T_{\text{eff}}$ (kK)	119.20	HeI or HeII Zanstra (Ph03)	
Date Obs:	2002-03-11	XMM Filter:	Medium

Calculations			
Parameter	EMOS1	EMOS2	EPN
$t_{\text{exp}}$ (ks)	23.0	23.1	–
$\text{CR}_{\text{src}}$ (cnt s <sup>-1</sup> )	1.107E-06	1.500E-06	–
$\text{CR}_{\text{bkg}}$ (cnt s <sup>-1</sup> )	9.278E-07	1.088E-06	–

Hot Bubble Upper Limits ( $T_X \sim 3 \times 10^6$ K)			
Parameter	EMOS1	EMOS2	EPN
$F_X$ (erg cm <sup>-2</sup> s <sup>-1</sup> )	-13.4249	-13.3912	–
$L_X$ (erg s <sup>-1</sup> )	30.6530	30.6868	–

Spun-up Companion Upper Limits ( $T_X \sim 10^7$ K)			
Parameter	EMOS1	EMOS2	EPN
$F_X$ (erg cm <sup>-2</sup> s <sup>-1</sup> )	-13.9834	-13.9496	–
$L_X$ (erg s <sup>-1</sup> )	30.0945	30.1283	–
$L_*$ ( $L_{\text{sun}}$ )	0.3233	0.3495	–
$M_{\text{bol}}$ (mag)	5.9659	5.8815	–
Spectral Type	K0-K2V	K0-K2V	–

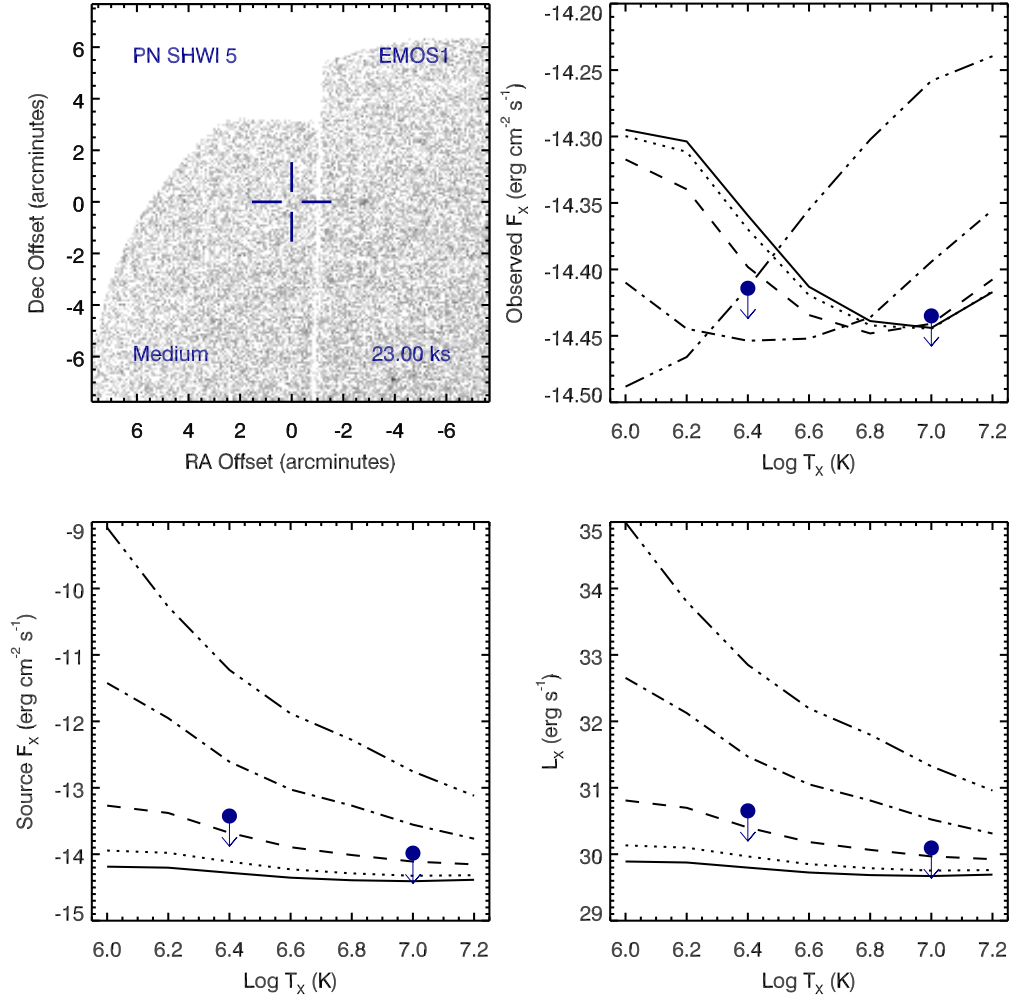


Figure A.102 Serendipitous XMM EMOS1 observation (ObsID 0050940101) of PN SHWI 5. Clock-wise from top-left: broad band (0.3 to 8.0 keV) image at the PN position, upper limits of the observed flux, X-ray luminosity, and source X-ray flux. The upper limits calculations are based on the upper limit count rates, a thermal plasma model at a range temperatures, and a range of intervening absorption values:  $N_H(10^{22} \text{ cm}^{-2}) = 0.03$  (solid), 0.1 (dotted), 0.3 (dashed), 1 (dot-dashed), and 3 (dot-dot-dashed). The hot bubble and spun-up companion upper limits are depicted as the filled circles with downward pointing arrows at  $\log T_x$  of 6.4 and 7.0, respectively.

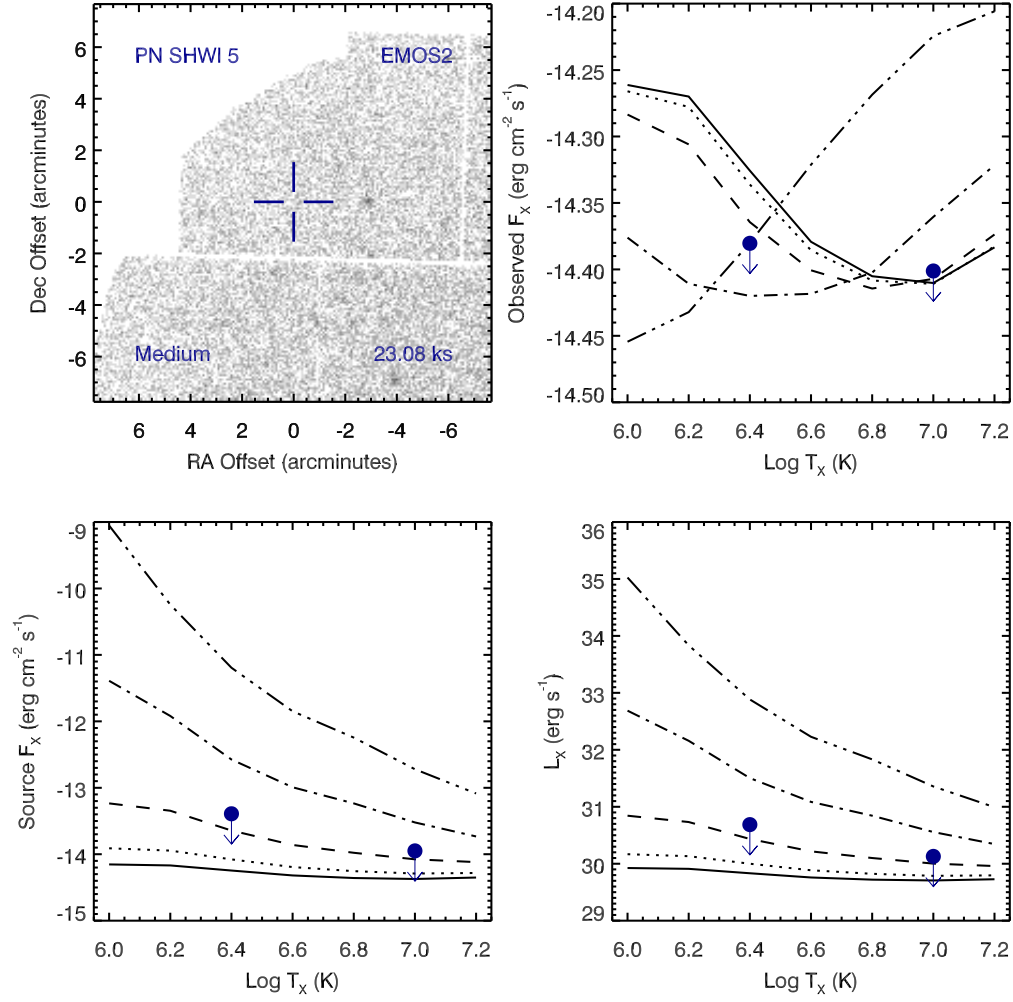


Figure A.103 Serendipitous XMM EMOS2 observation (ObsID 0050940101) of PN SHWI 5 ; panels as in Figure A.102.

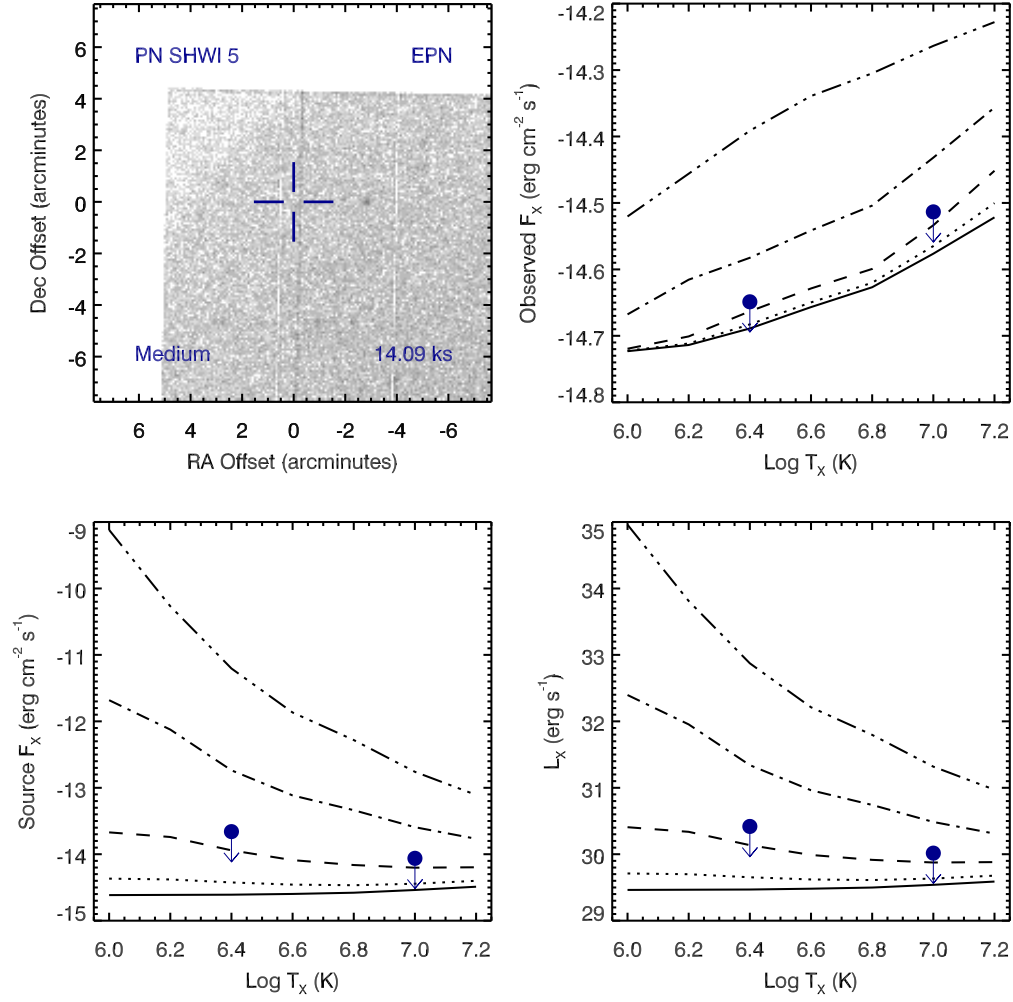


Figure A.104 Serendipitous XMM EPN observation (ObsID 0050940101) of PN SHWI 5 ; panels as in Figure A.102.

# PN SHWI 5 , ObsID 0203040101

Table A.47 Summary of the Analysis for the XMM EPIC observation (ObsID 0203040101) of PN SHWI 5.

Basic Data			
Parameter	Value	Notes	
RA (J2000)	270.973583		
DEC (J2000)	-29.856081	Offset (')	10.30
$R_{\text{nebula}}$ (")	2.0	from literature (A94)	
$D$ (kpc)	1.0	unknown, assumed value	
$\log N_H$ (cm <sup>-2</sup> )	21.6358	optical extinction (C92)	
$T_{\text{eff}}$ (kK)	119.20	HeI or HeII Zanstra (Ph03)	
Date Obs:	2004-09-30	XMM Filter:	Medium

Calculations			
Parameter	EMOS1	EMOS2	EPN
$t_{\text{exp}}$ (ks)	21.1	21.2	–
$\text{CR}_{\text{src}}$ (cnt s <sup>-1</sup> )	8.925E-07	8.187E-07	–
$\text{CR}_{\text{bkg}}$ (cnt s <sup>-1</sup> )	6.995E-07	5.598E-07	–

Hot Bubble Upper Limits ( $T_X \sim 3 \times 10^6$ K)			
Parameter	EMOS1	EMOS2	EPN
$F_X$ (erg cm <sup>-2</sup> s <sup>-1</sup> )	-13.4678	-13.5164	–
$L_X$ (erg s <sup>-1</sup> )	30.6102	30.5615	–

Spun-up Companion Upper Limits ( $T_X \sim 10^7$ K)			
Parameter	EMOS1	EMOS2	EPN
$F_X$ (erg cm <sup>-2</sup> s <sup>-1</sup> )	-14.0261	-14.0748	–
$L_X$ (erg s <sup>-1</sup> )	30.0518	30.0031	–
$L_*$ ( $L_{\text{sun}}$ )	0.2930	0.2620	–
$M_{\text{bol}}$ (mag)	6.0727	6.1944	–
Spectral Type	K2-K5V	K2-K5V	–

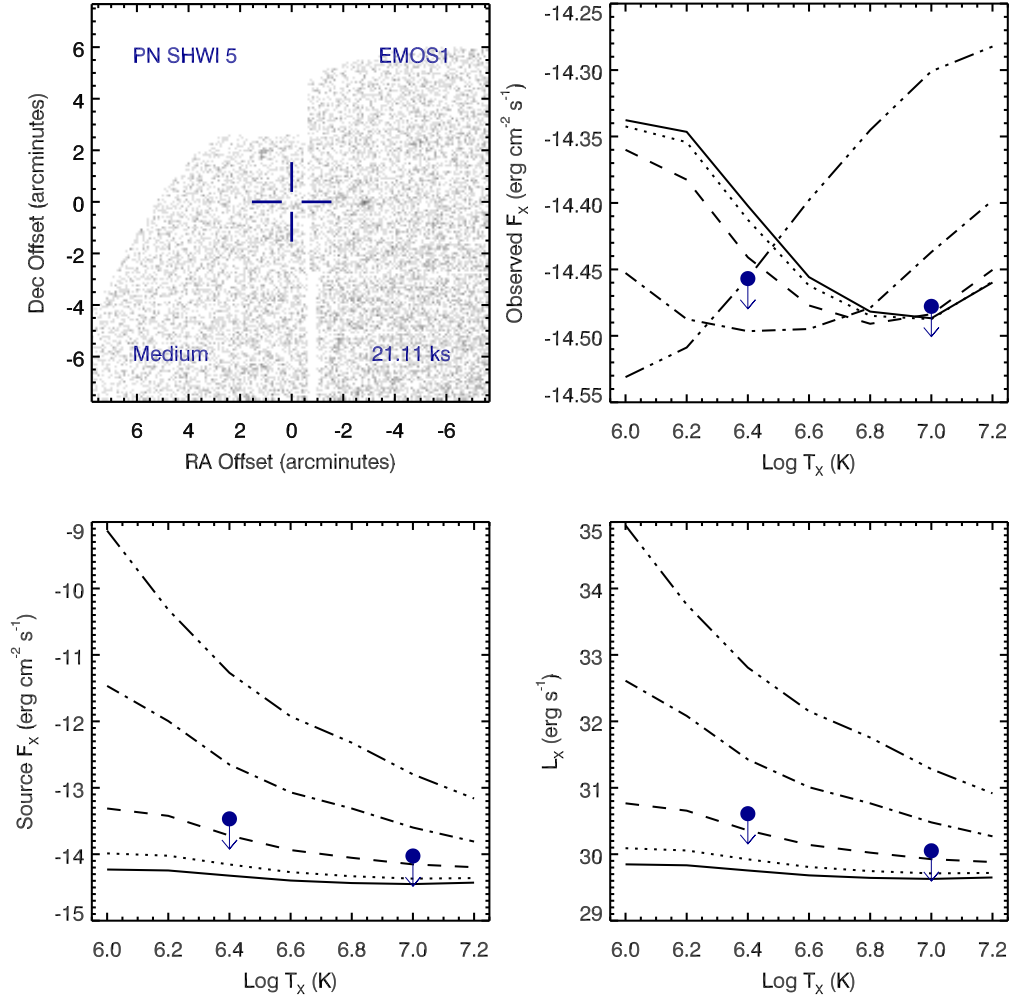


Figure A.105 Serendipitous XMM EMOS1 observation (ObsID 0203040101) of PN SHWI 5. Clock-wise from top-left: broad band (0.3 to 8.0 keV) image at the PN position, upper limits of the observed flux, X-ray luminosity, and source X-ray flux. The upper limits calculations are based on the upper limit count rates, a thermal plasma model at a range temperatures, and a range of intervening absorption values:  $N_H(10^{22} \text{ cm}^{-2}) = 0.03$  (solid), 0.1 (dotted), 0.3 (dashed), 1 (dot-dashed), and 3 (dot-dot-dashed). The hot bubble and spun-up companion upper limits are depicted as the filled circles with downward pointing arrows at  $\log T_x$  of 6.4 and 7.0, respectively.

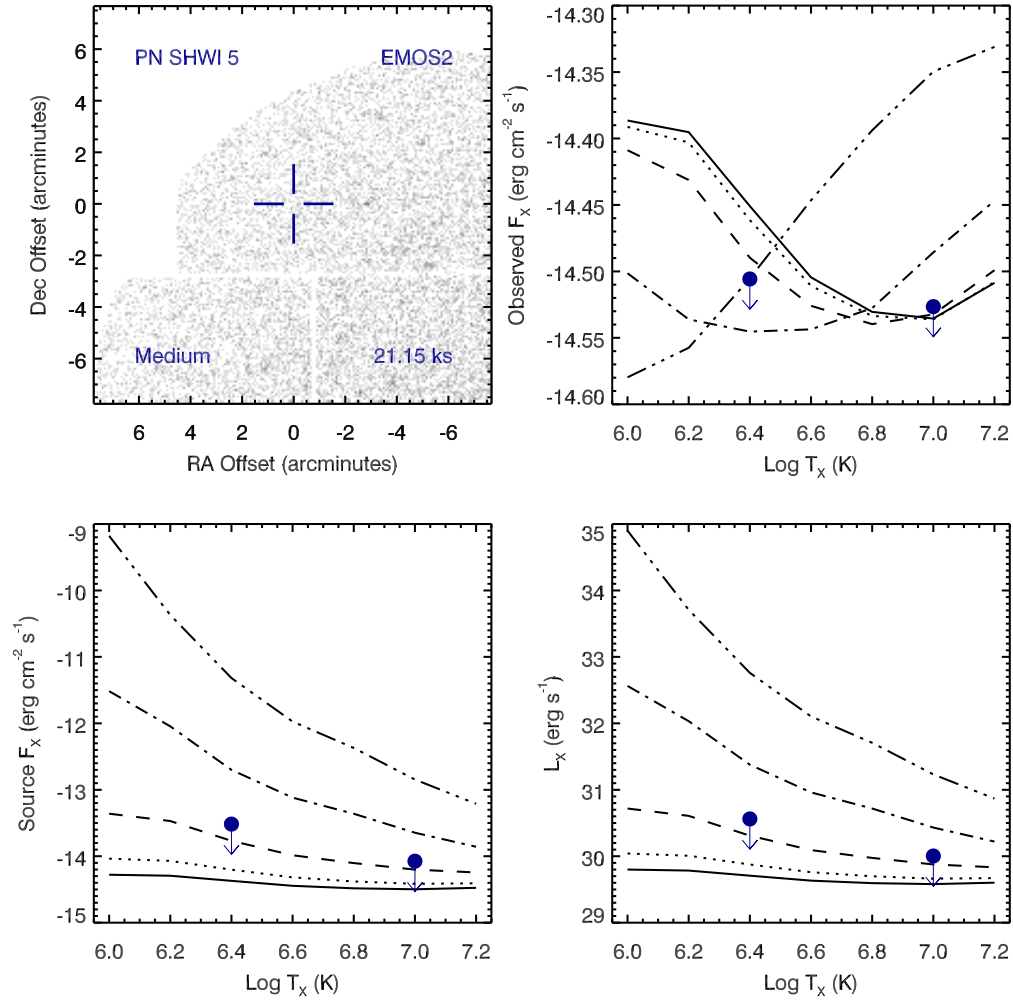


Figure A.106 Serendipitous XMM EMOS2 observation (ObsID 0203040101) of PN SHWI 5 ; panels as in Figure A.105.



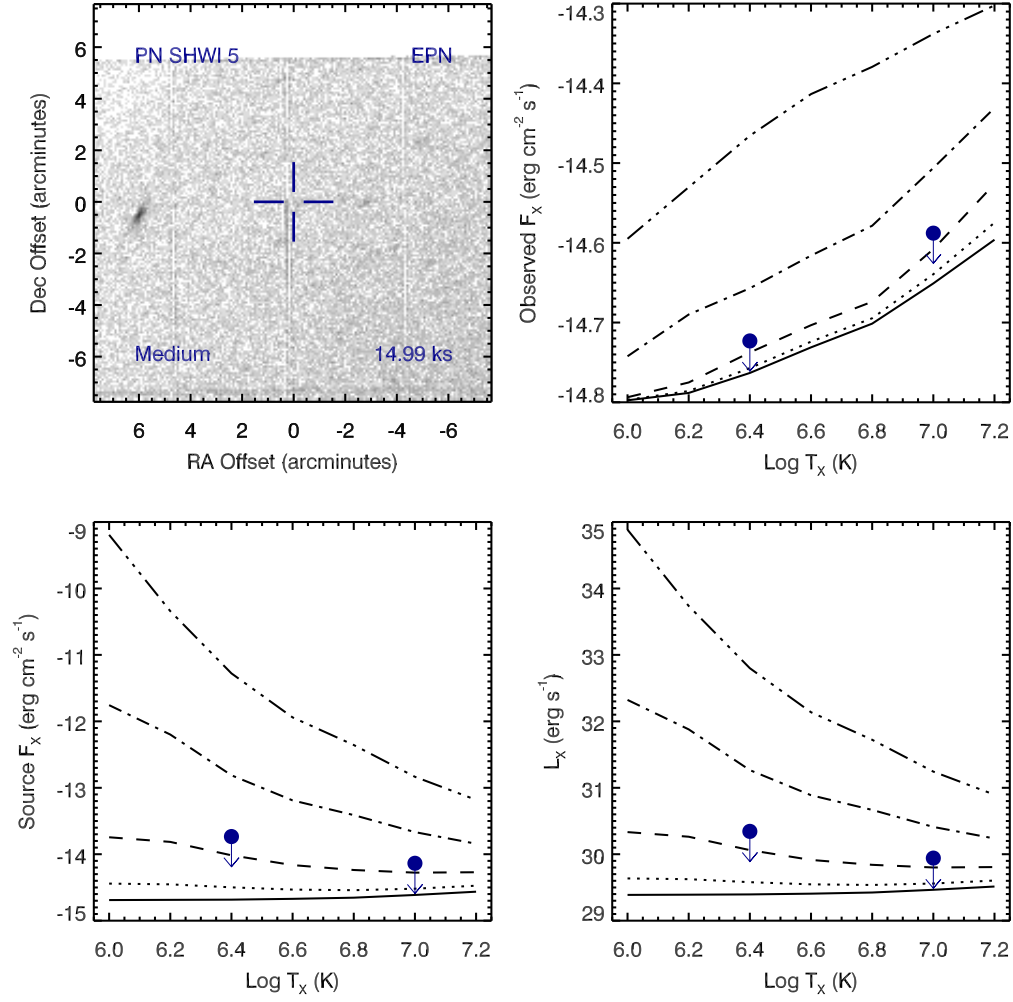


Figure A.107 Serendipitous XMM EPN observation (ObsID 0203040101) of PN SHW 5 ; panels as in Figure A.105.

## PN SUWT 2 , ObsID 0007421401

Table A.48 Summary of the Analysis for the XMM EPIC observation (ObsID 0007421401) of PN SUWT 2.

Basic Data			
Parameter	Value	Notes	
RA (J2000)	208.930120		
DEC (J2000)	-59.377750	Offset (')	12.82
$R_{\text{nebula}}$ (")	33.0	from literature (A94)	
$D$ (kpc)	1.0	unknown, assumed value	
$\log N_H$ (cm <sup>-2</sup> )	21.6990	unknown, assumed value	
$T_{\text{eff}}$ (kK)	–		
Date Obs:	2002-02-19	XMM Filter:	Medium

Calculations			
Parameter	EMOS1	EMOS2	EPN
$t_{\text{exp}}$ (ks)	12.1	12.2	–
$\text{CR}_{\text{src}}$ (cnt s <sup>-1</sup> )	1.678E-07	3.772E-07	–
$\text{CR}_{\text{bkg}}$ (cnt s <sup>-1</sup> )	2.525E-07	3.590E-07	–

Hot Bubble Upper Limits ( $T_X \sim 3 \times 10^6$ K)			
Parameter	EMOS1	EMOS2	EPN
$F_X$ (erg cm <sup>-2</sup> s <sup>-1</sup> )	-13.4571	-13.3808	–
$L_X$ (erg s <sup>-1</sup> )	30.6209	30.6971	–

Spun-up Companion Upper Limits ( $T_X \sim 10^7$ K)			
Parameter	EMOS1	EMOS2	EPN
$F_X$ (erg cm <sup>-2</sup> s <sup>-1</sup> )	-14.0700	-13.9940	–
$L_X$ (erg s <sup>-1</sup> )	30.0079	30.0840	–
$L_*$ ( $L_{\text{sun}}$ )	0.2648	0.3155	–
$M_{\text{bol}}$ (mag)	6.1825	5.9924	–
Spectral Type	K2-K5V	K2-K5V	–

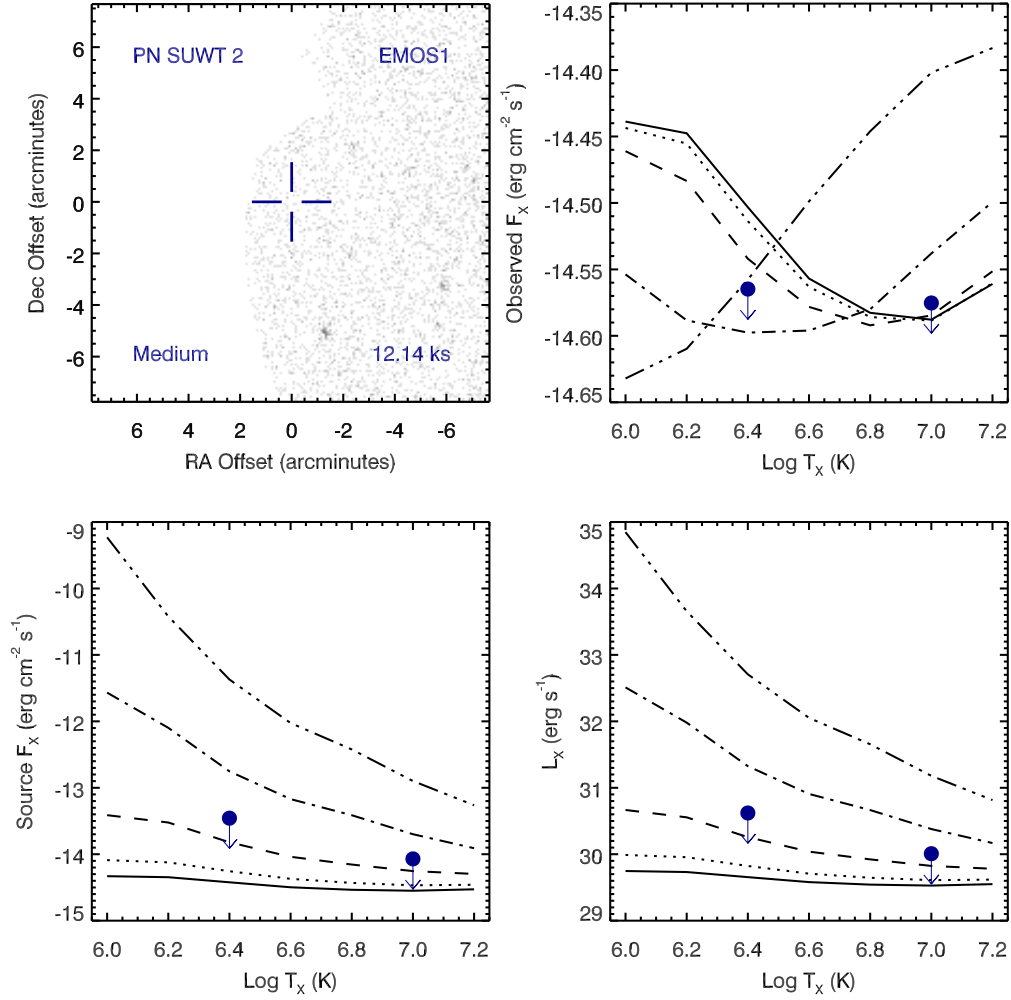


Figure A.108 Serendipitous XMM EMOS1 observation (ObsID 0007421401) of PN SUWT 2. Clock-wise from top-left: broad band (0.3 to 8.0 keV) image at the PN position, upper limits of the observed flux, X-ray luminosity, and source X-ray flux. The upper limits calculations are based on the upper limit count rates, a thermal plasma model at a range temperatures, and a range of intervening absorption values:  $N_H(10^{22} \text{ cm}^{-2}) = 0.03$  (solid), 0.1 (dotted), 0.3 (dashed), 1 (dot-dashed), and 3 (dot-dot-dashed). The hot bubble and spun-up companion upper limits are depicted as the filled circles with downward pointing arrows at  $\log T_x$  of 6.4 and 7.0, respectively.

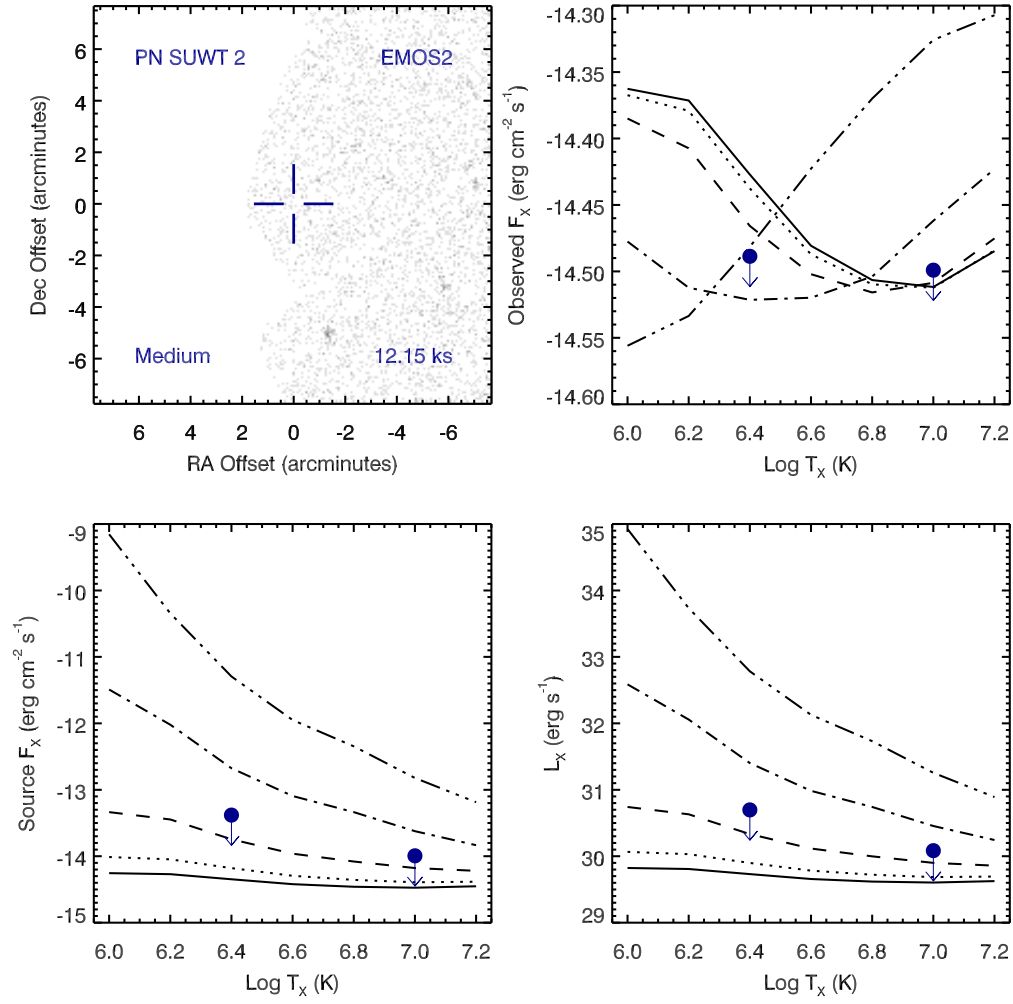


Figure A.109 Serendipitous XMM EMOS2 observation (ObsID 0007421401) of PN SUWT 2 ; panels as in Figure A.108.

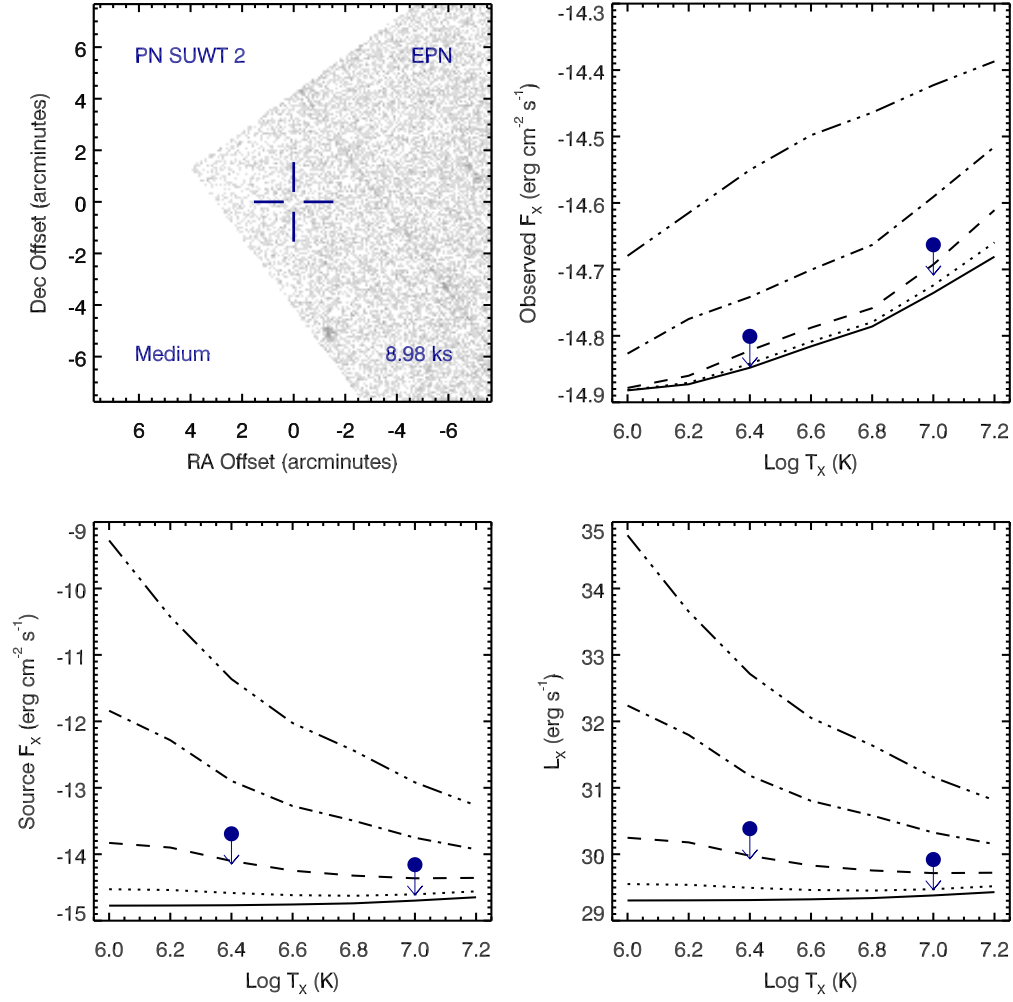


Figure A.110 Serendipitous XMM EPN observation (ObsID 0007421401) of PN SUWT 2 ; panels as in Figure A.108.

## PN SUWT 2 , ObsID 0007422301

Table A.49 Summary of the Analysis for the XMM EPIC observation (ObsID 0007422301) of PN SUWT 2.

Basic Data			
Parameter	Value	Notes	
RA (J2000)	208.930120		
DEC (J2000)	-59.377750	Offset (')	12.32
$R_{\text{nebula}}$ (")	33.0	from literature (A94)	
$D$ (kpc)	1.0	unknown, assumed value	
$\log N_H$ (cm <sup>-2</sup> )	21.6990	unknown, assumed value	
$T_{\text{eff}}$ (kK)	–		
Date Obs:	2001-02-08	XMM Filter:	Medium

Calculations			
Parameter	EMOS1	EMOS2	EPN
$t_{\text{exp}}$ (ks)	14.9	14.9	–
$\text{CR}_{\text{src}}$ (cnt s <sup>-1</sup> )	2.391E-07	2.390E-07	–
$\text{CR}_{\text{bkg}}$ (cnt s <sup>-1</sup> )	2.214E-07	2.055E-07	–

Hot Bubble Upper Limits ( $T_X \sim 3 \times 10^6$ K)			
Parameter	EMOS1	EMOS2	EPN
$F_X$ (erg cm <sup>-2</sup> s <sup>-1</sup> )	-13.5302	-13.5465	–
$L_X$ (erg s <sup>-1</sup> )	30.5477	30.5314	–

Spun-up Companion Upper Limits ( $T_X \sim 10^7$ K)			
Parameter	EMOS1	EMOS2	EPN
$F_X$ (erg cm <sup>-2</sup> s <sup>-1</sup> )	-14.1432	-14.1595	–
$L_X$ (erg s <sup>-1</sup> )	29.9347	29.9184	–
$L_*$ ( $L_{\text{sun}}$ )	0.2238	0.2155	–
$M_{\text{bol}}$ (mag)	6.3655	6.4063	–
Spectral Type	K2-K5V	K2-K5V	–

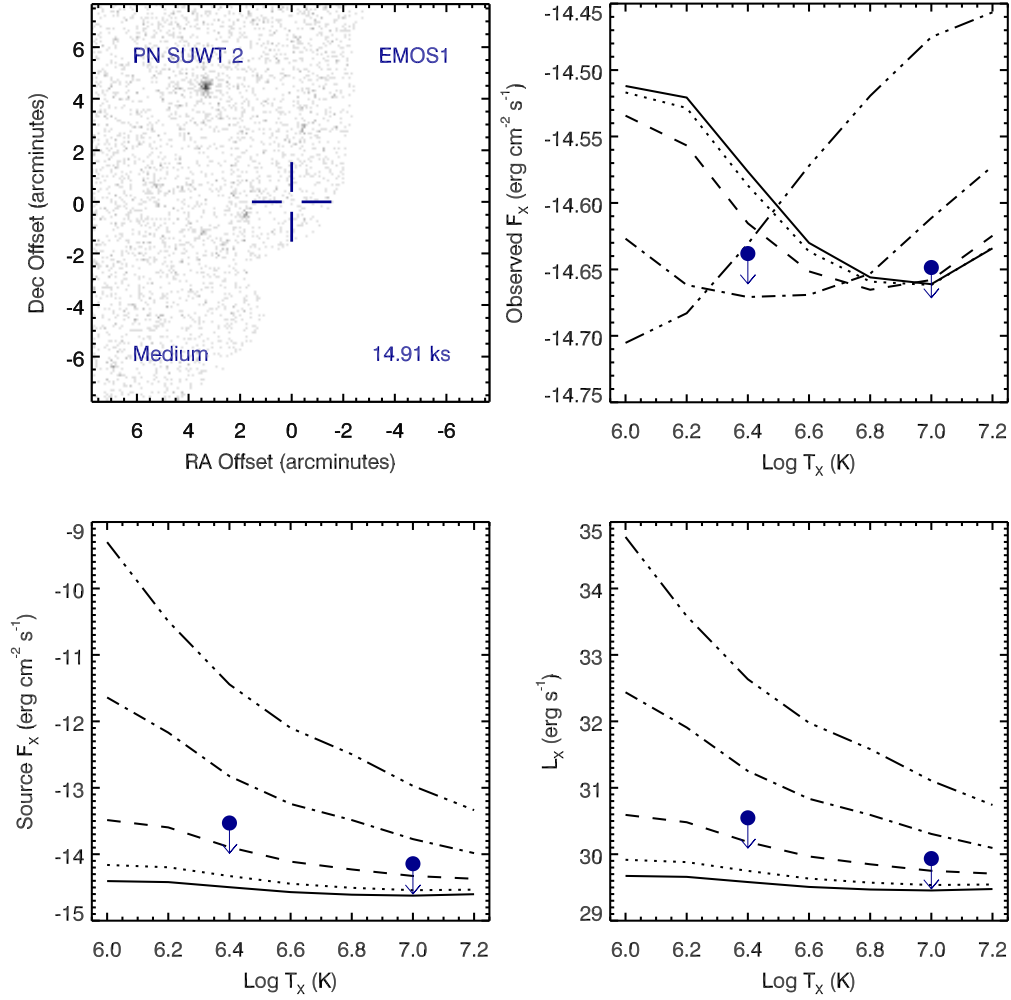


Figure A.111 Serendipitous XMM EMOS1 observation (ObsID 0007422301) of PN SUWT 2. Clock-wise from top-left: broad band (0.3 to 8.0 keV) image at the PN position, upper limits of the observed flux, X-ray luminosity, and source X-ray flux. The upper limits calculations are based on the upper limit count rates, a thermal plasma model at a range temperatures, and a range of intervening absorption values:  $N_H(10^{22} \text{ cm}^{-2}) = 0.03$  (solid), 0.1 (dotted), 0.3 (dashed), 1 (dot-dashed), and 3 (dot-dot-dashed). The hot bubble and spun-up companion upper limits are depicted as the filled circles with downward pointing arrows at  $\log T_x$  of 6.4 and 7.0, respectively.

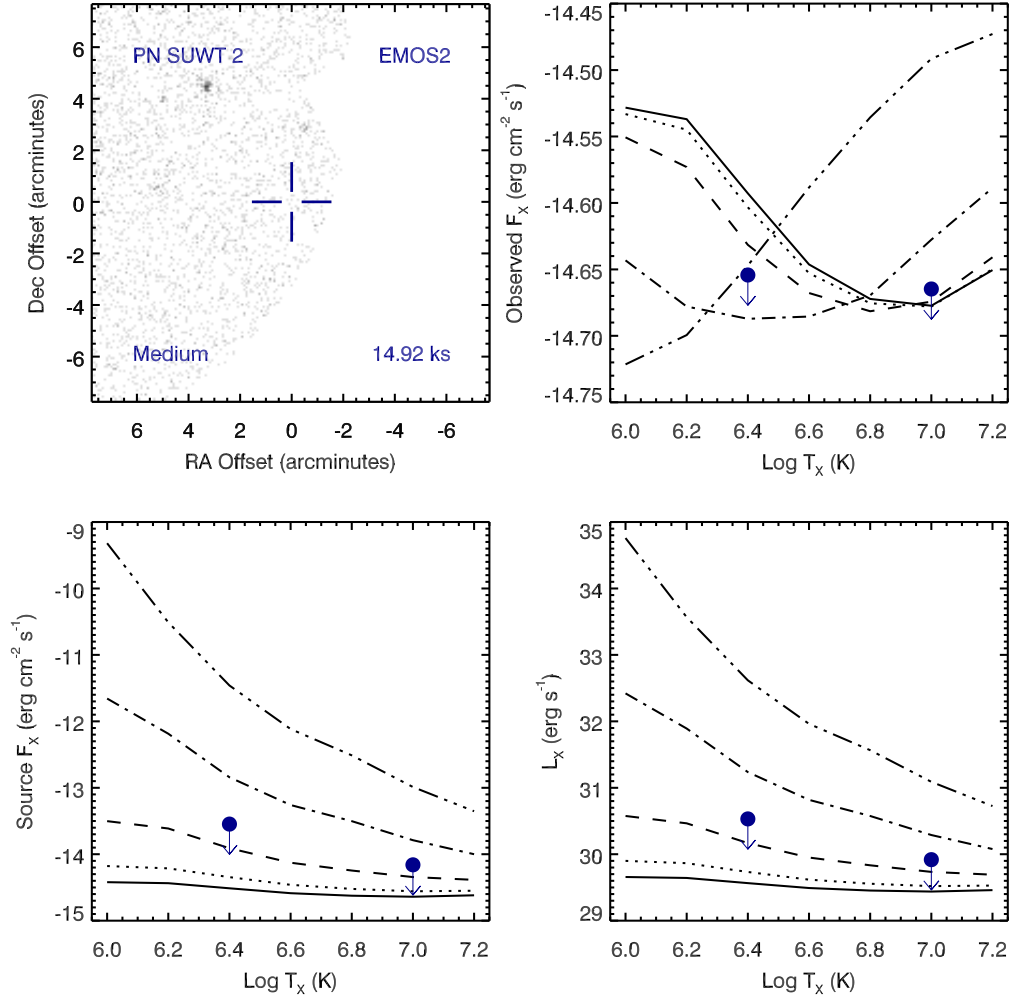


Figure A.112 Serendipitous XMM EMOS2 observation (ObsID 0007422301) of PN SUWT 2 ; panels as in Figure A.111.



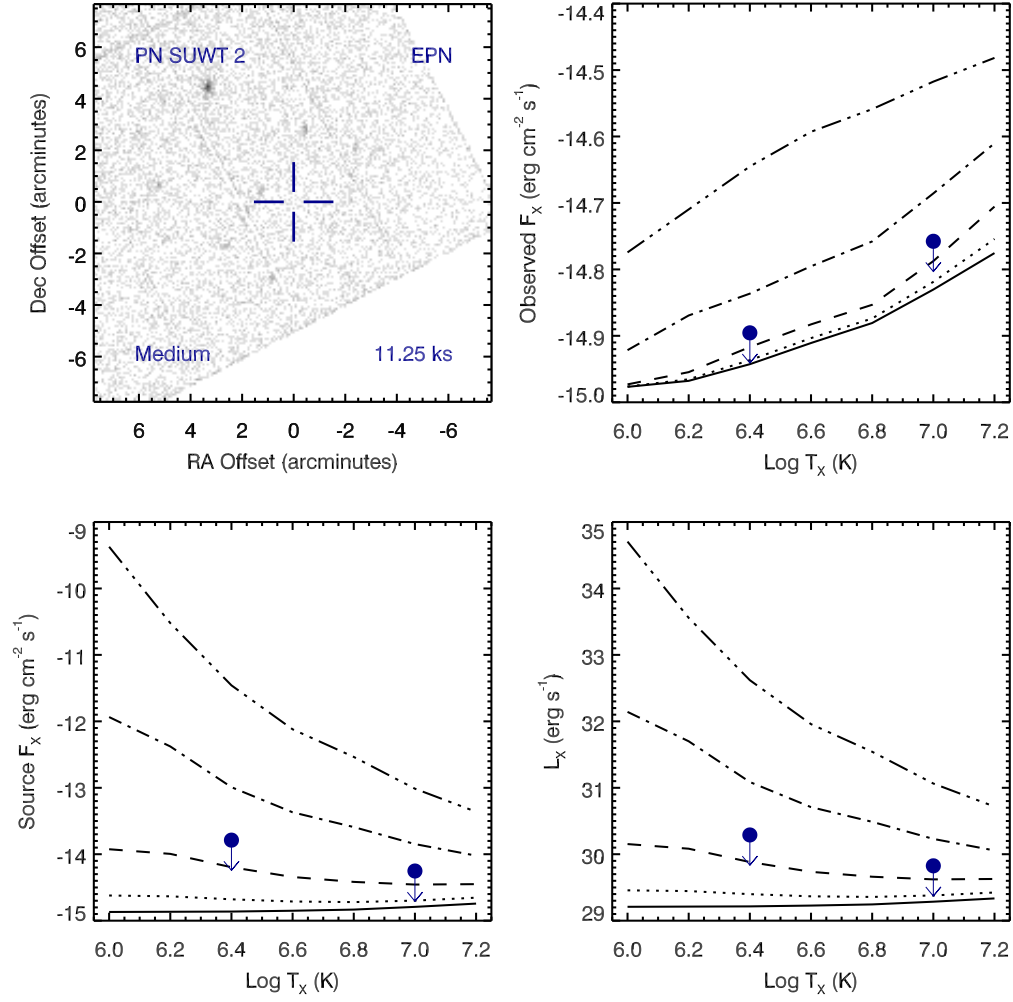


Figure A.113 Serendipitous XMM EPN observation (ObsID 0007422301) of PN SUWT 2 ; panels as in Figure A.111.

## Terz N 2022, ObsID 0112971801

Table A.50 Summary of the Analysis for the XMM EPIC observation (ObsID 0112971801) of Terz N 2022.

Basic Data			
Parameter	Value	Notes	
RA (J2000)	265.677229		
DEC (J2000)	-29.859706	Offset (')	10.45
$R_{\text{nebula}}$ (")	6.0	from literature (A94)	
$D$ (kpc)	1.0	unknown, assumed value	
$\log N_H$ (cm <sup>-2</sup> )	21.6990	unknown, assumed value	
$T_{\text{eff}}$ (kK)	–		
Date Obs:	2001-04-01	XMM Filter:	Medium

Calculations			
Parameter	EMOS1	EMOS2	EPN
$t_{\text{exp}}$ (ks)	11.5	11.6	–
$\text{CR}_{\text{src}}$ (cnt s <sup>-1</sup> )	8.836E-07	9.233E-07	–
$\text{CR}_{\text{bkg}}$ (cnt s <sup>-1</sup> )	5.081E-07	3.517E-07	–

Hot Bubble Upper Limits ( $T_X \sim 3 \times 10^6$ K)			
Parameter	EMOS1	EMOS2	EPN
$F_X$ (erg cm <sup>-2</sup> s <sup>-1</sup> )	-13.2940	-13.3749	–
$L_X$ (erg s <sup>-1</sup> )	30.7839	30.7030	–

Spun-up Companion Upper Limits ( $T_X \sim 10^7$ K)			
Parameter	EMOS1	EMOS2	EPN
$F_X$ (erg cm <sup>-2</sup> s <sup>-1</sup> )	-13.9069	-13.9880	–
$L_X$ (erg s <sup>-1</sup> )	30.1710	30.0899	–
$L_*$ ( $L_{\text{sun}}$ )	0.3856	0.3199	–
$M_{\text{bol}}$ (mag)	5.7748	5.9775	–
Spectral Type	K0-K2V	K0-K2V	–

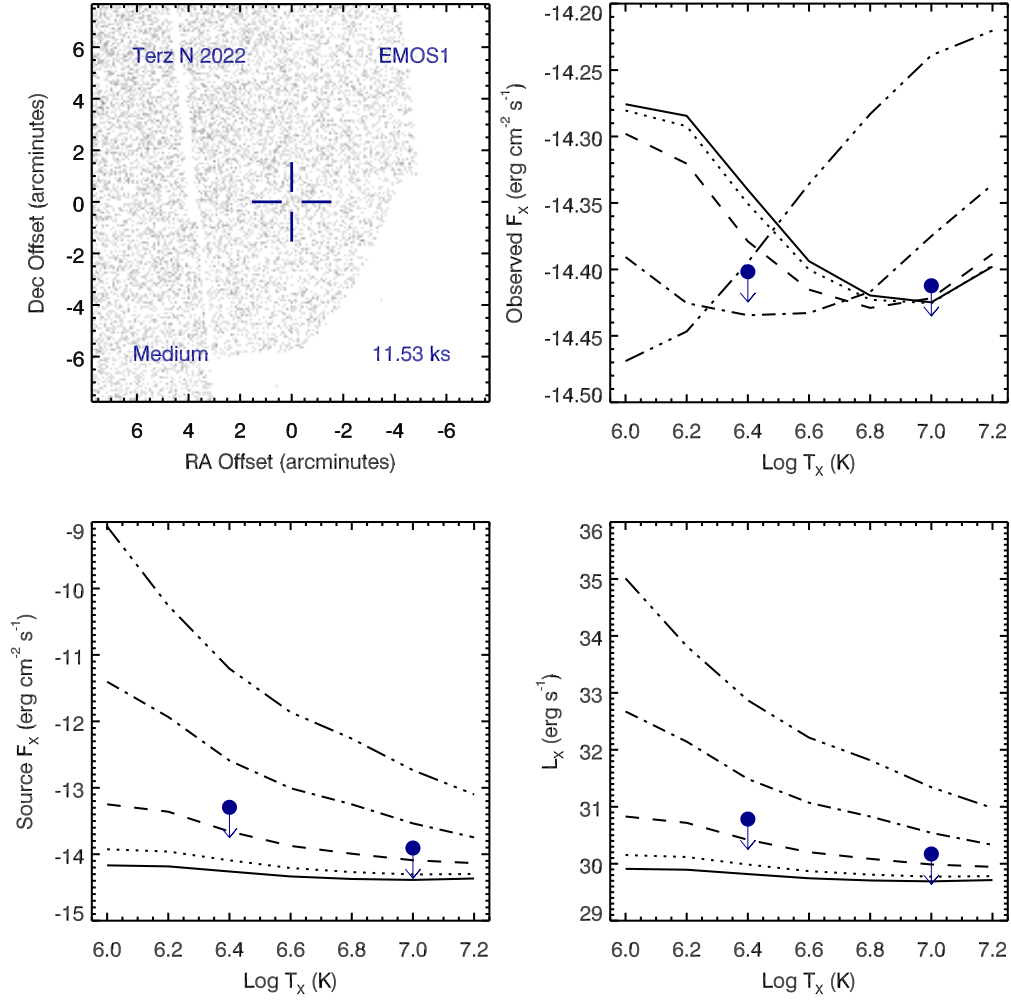


Figure A.114 Serendipitous XMM EMOS1 observation (ObsID 0112971801) of Terz N 2022. Clock-wise from top-left: broad band (0.3 to 8.0 keV) image at the PN position, upper limits of the observed flux, X-ray luminosity, and source X-ray flux. The upper limits calculations are based on the upper limit count rates, a thermal plasma model at a range temperatures, and a range of intervening absorption values:  $N_H(10^{22} \text{ cm}^{-2}) = 0.03$  (solid), 0.1 (dotted), 0.3 (dashed), 1 (dot-dashed), and 3 (dot-dot-dashed). The hot bubble and spun-up companion upper limits are depicted as the filled circles with downward pointing arrows at  $\log T_x$  of 6.4 and 7.0, respectively.

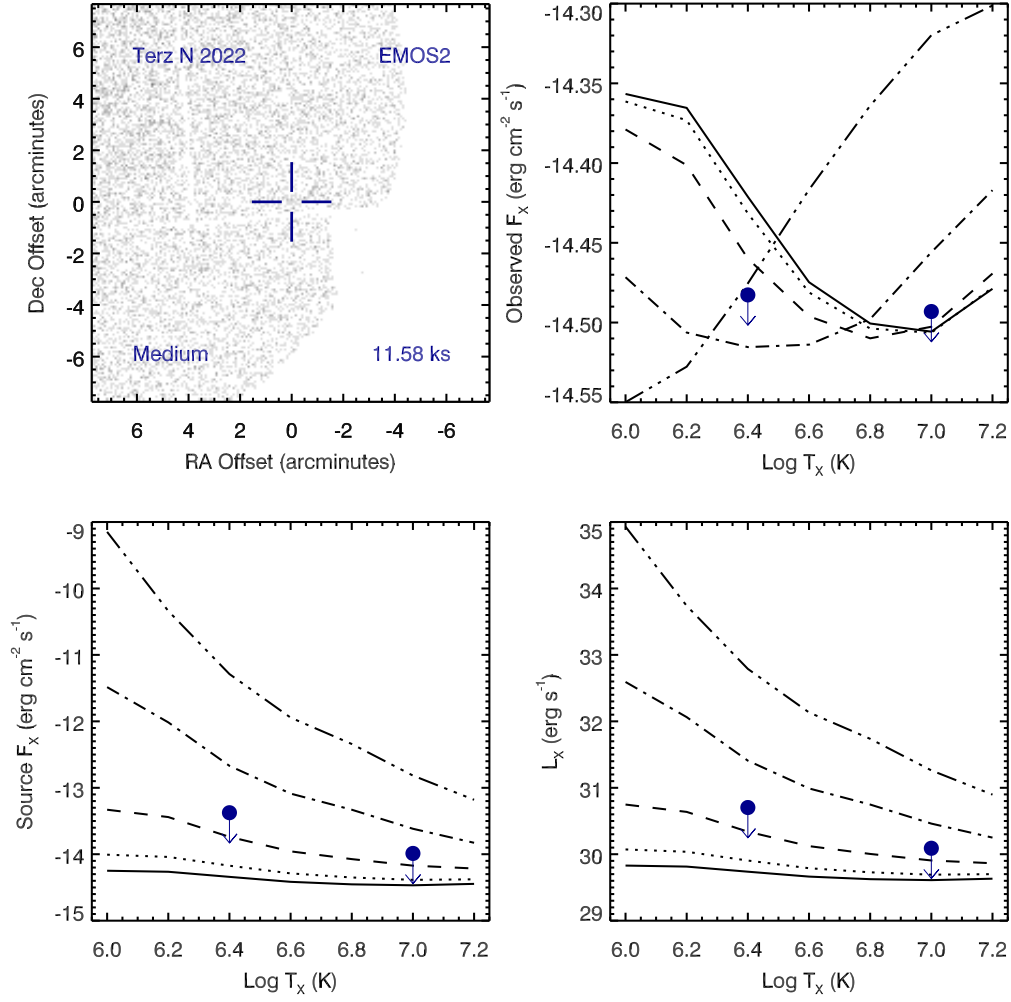


Figure A.115 Serendipitous XMM EMOS2 observation (ObsID 0112971801) of Terz N 2022; panels as in Figure A.114.

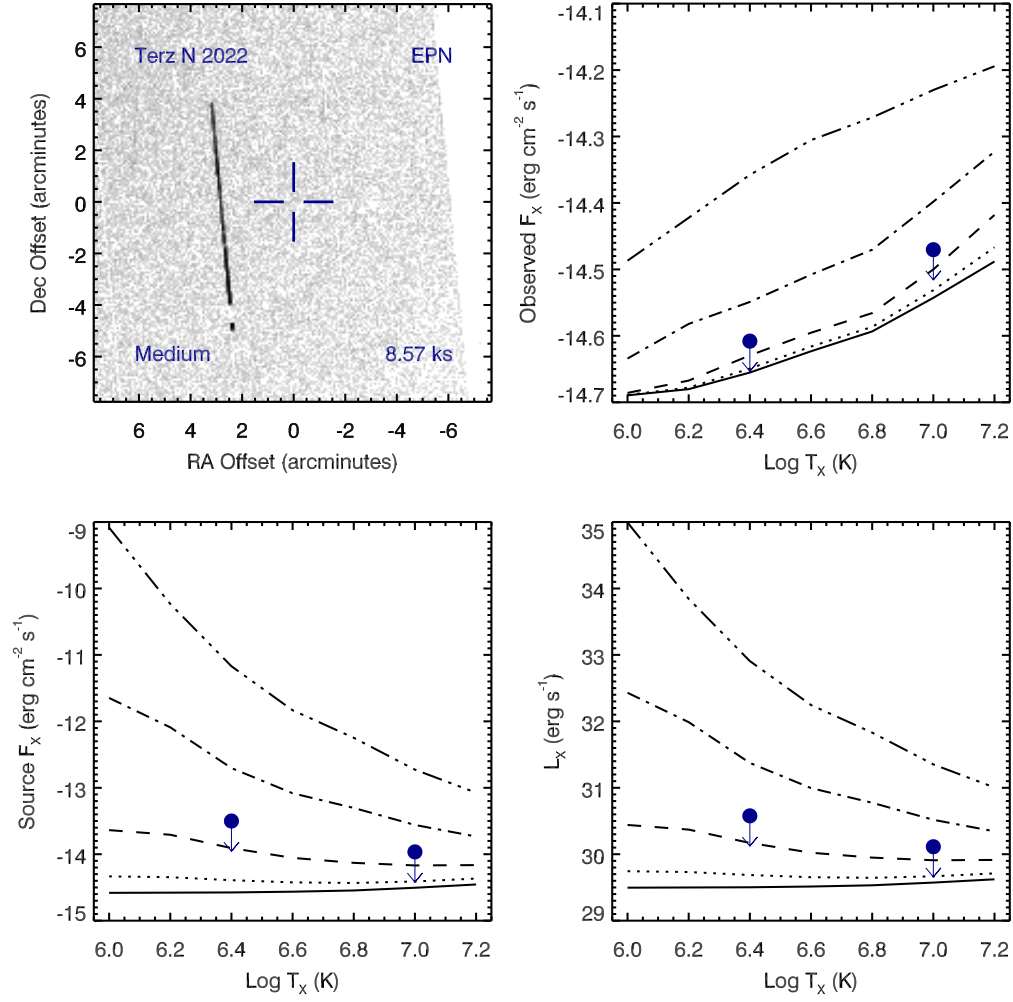


Figure A.116 Serendipitous XMM EPN observation (ObsID 0112971801) of Terz N 2022; panels as in Figure A.114.

## Terz N 2022, ObsID 0112970901

Table A.51 Summary of the Analysis for the XMM EPIC observation (ObsID 0112970901) of Terz N 2022.

Basic Data			
Parameter	Value	Notes	
RA (J2000)	265.677229		
DEC (J2000)	-29.859706	Offset (')	10.45
$R_{\text{nebula}}$ (")	6.0	from literature (A94)	
$D$ (kpc)	1.0	unknown, assumed value	
$\log N_H$ (cm <sup>-2</sup> )	21.6990	unknown, assumed value	
$T_{\text{eff}}$ (kK)	–		
Date Obs:	2000-09-15	XMM Filter:	Medium

Calculations			
Parameter	EMOS1	EMOS2	EPN
$t_{\text{exp}}$ (ks)	–	–	–
$\text{CR}_{\text{src}}$ (cnt s <sup>-1</sup> )	–	–	–
$\text{CR}_{\text{bkg}}$ (cnt s <sup>-1</sup> )	–	–	–

Hot Bubble Upper Limits ( $T_X \sim 3 \times 10^6$ K)			
Parameter	EMOS1	EMOS2	EPN
$F_X$ (erg cm <sup>-2</sup> s <sup>-1</sup> )	–	–	–
$L_X$ (erg s <sup>-1</sup> )	–	–	–

Spun-up Companion Upper Limits ( $T_X \sim 10^7$ K)			
Parameter	EMOS1	EMOS2	EPN
$F_X$ (erg cm <sup>-2</sup> s <sup>-1</sup> )	–	–	–
$L_X$ (erg s <sup>-1</sup> )	–	–	–
$L_*$ ( $L_{\text{sun}}$ )	–	–	–
$M_{\text{bol}}$ (mag)	–	–	–
Spectral Type	–	–	–

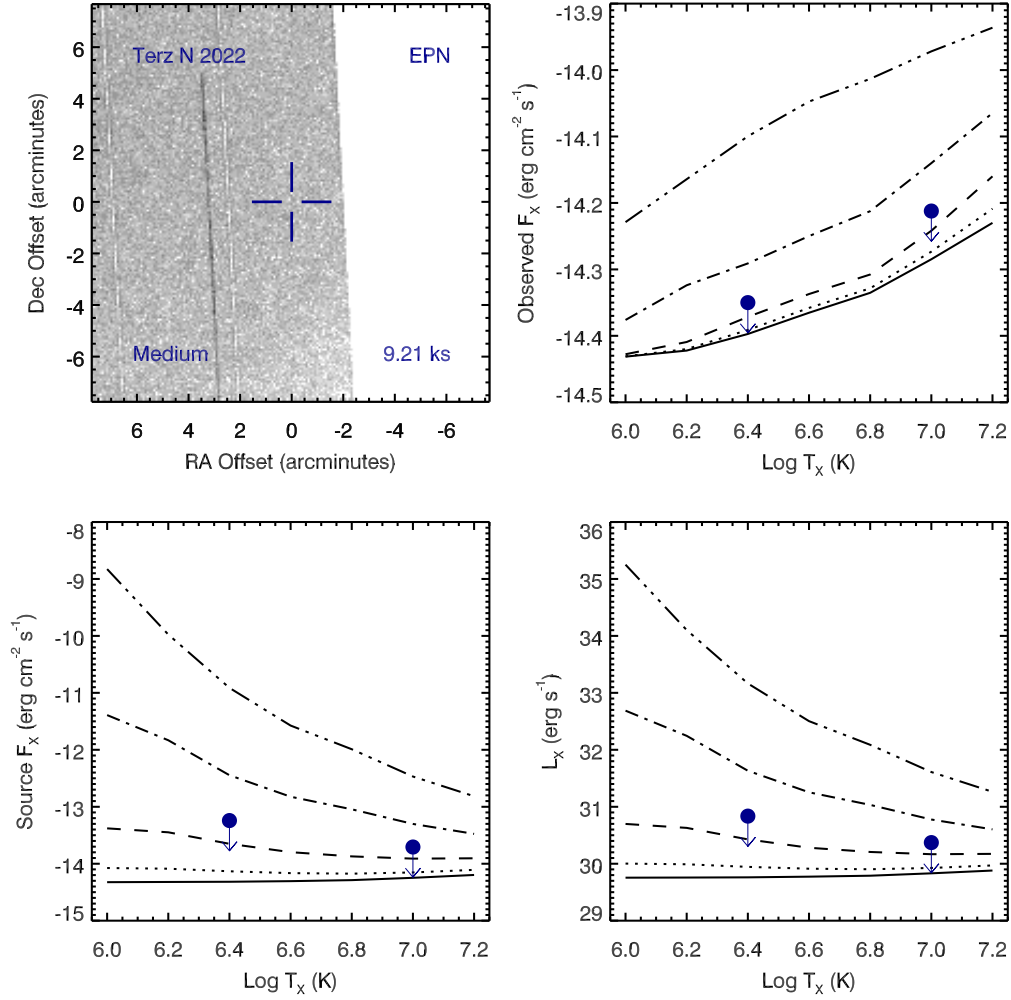


Figure A.117 Serendipitous XMM EPN observation (ObsID 0112970901) of Terz N 2022. Clock-wise from top-left: broad band (0.3 to 8.0 keV) image at the PN position, upper limits of the observed flux, X-ray luminosity, and source X-ray flux. The upper limits calculations are based on the upper limit count rates, a thermal plasma model at a range temperatures, and a range of intervening absorption values:  $N_H(10^{22} \text{ cm}^{-2}) = 0.03$  (solid), 0.1 (dotted), 0.3 (dashed), 1 (dot-dashed), and 3 (dot-dot-dashed). The hot bubble and spun-up companion upper limits are depicted as the filled circles with downward pointing arrows at  $\log T_X$  of 6.4 and 7.0, respectively.

## PN Th 4-3 , ObsID 0306700501

Table A.52 Summary of the Analysis for the XMM EPIC observation (ObsID 0306700501) of PN Th 4-3.

Basic Data			
Parameter	Value	Notes	
RA (J2000)	267.155792		
DEC (J2000)	-22.280219	Offset (')	13.26
$R_{\text{nebula}}$ (")	–		
$D$ (kpc)	1.0	unknown, assumed value	
$\log N_H$ (cm <sup>-2</sup> )	21.6990	unknown, assumed value	
$T_{\text{eff}}$ (kK)	–		
Date Obs:	2006-03-01	XMM Filter:	Medium

Calculations			
Parameter	EMOS1	EMOS2	EPN
$t_{\text{exp}}$ (ks)	11.2	11.2	–
$\text{CR}_{\text{src}}$ (cnt s <sup>-1</sup> )	5.460E-07	7.276E-07	–
$\text{CR}_{\text{bkg}}$ (cnt s <sup>-1</sup> )	5.477E-07	6.210E-07	–

Hot Bubble Upper Limits ( $T_X \sim 3 \times 10^6$ K)			
Parameter	EMOS1	EMOS2	EPN
$F_X$ (erg cm <sup>-2</sup> s <sup>-1</sup> )	-13.2712	-13.2441	–
$L_X$ (erg s <sup>-1</sup> )	30.8067	30.8338	–

Spun-up Companion Upper Limits ( $T_X \sim 10^7$ K)			
Parameter	EMOS1	EMOS2	EPN
$F_X$ (erg cm <sup>-2</sup> s <sup>-1</sup> )	-13.8844	-13.8570	–
$L_X$ (erg s <sup>-1</sup> )	30.1935	30.2209	–
$L_*$ ( $L_{\text{sun}}$ )	0.4061	0.4325	–
$M_{\text{bol}}$ (mag)	5.7184	5.6499	–
Spectral Type	K0-K2V	K0-K2V	–



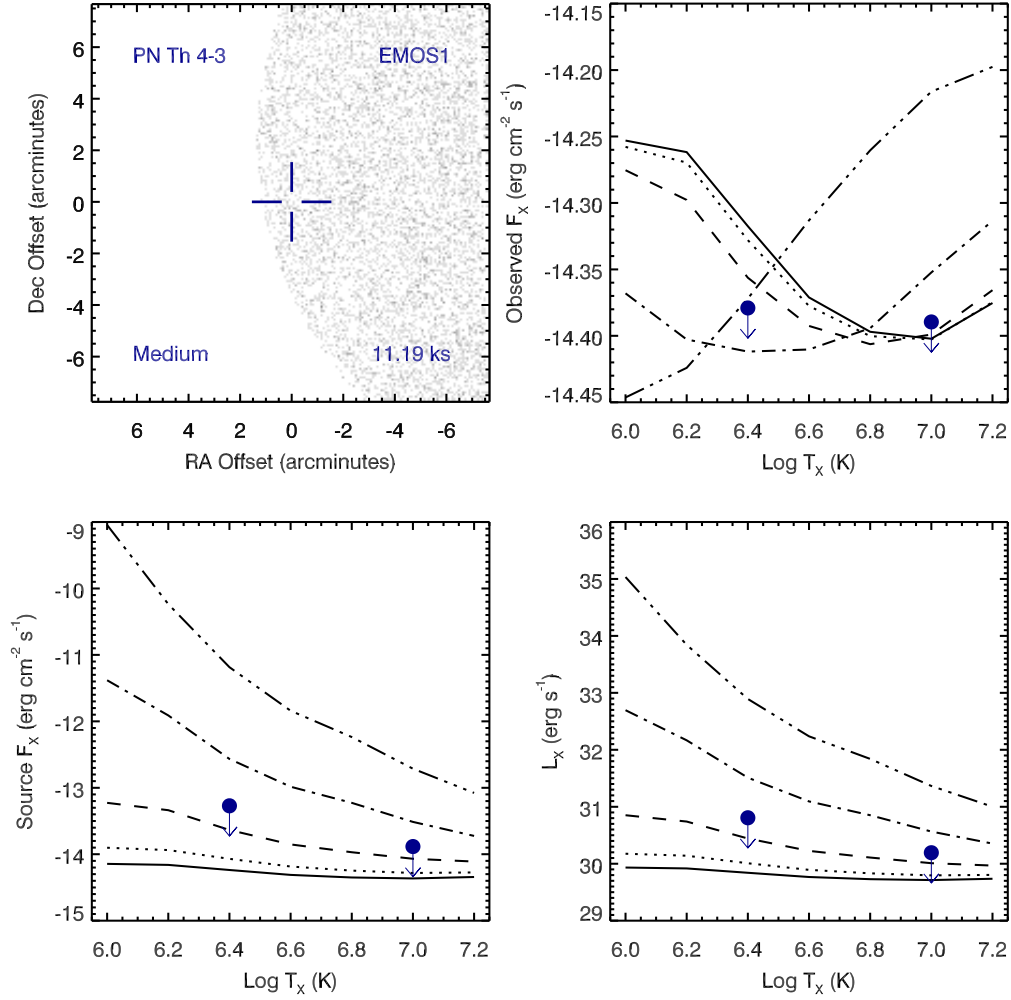


Figure A.118 Serendipitous XMM EMOS1 observation (ObsID 0306700501) of PN Th 4-3. Clock-wise from top-left: broad band (0.3 to 8.0 keV) image at the PN position, upper limits of the observed flux, X-ray luminosity, and source X-ray flux. The upper limits calculations are based on the upper limit count rates, a thermal plasma model at a range temperatures, and a range of intervening absorption values:  $N_H(10^{22} \text{ cm}^{-2}) = 0.03$  (solid), 0.1 (dotted), 0.3 (dashed), 1 (dot-dashed), and 3 (dot-dot-dashed). The hot bubble and spun-up companion upper limits are depicted as the filled circles with downward pointing arrows at log  $T_x$  of 6.4 and 7.0, respectively.

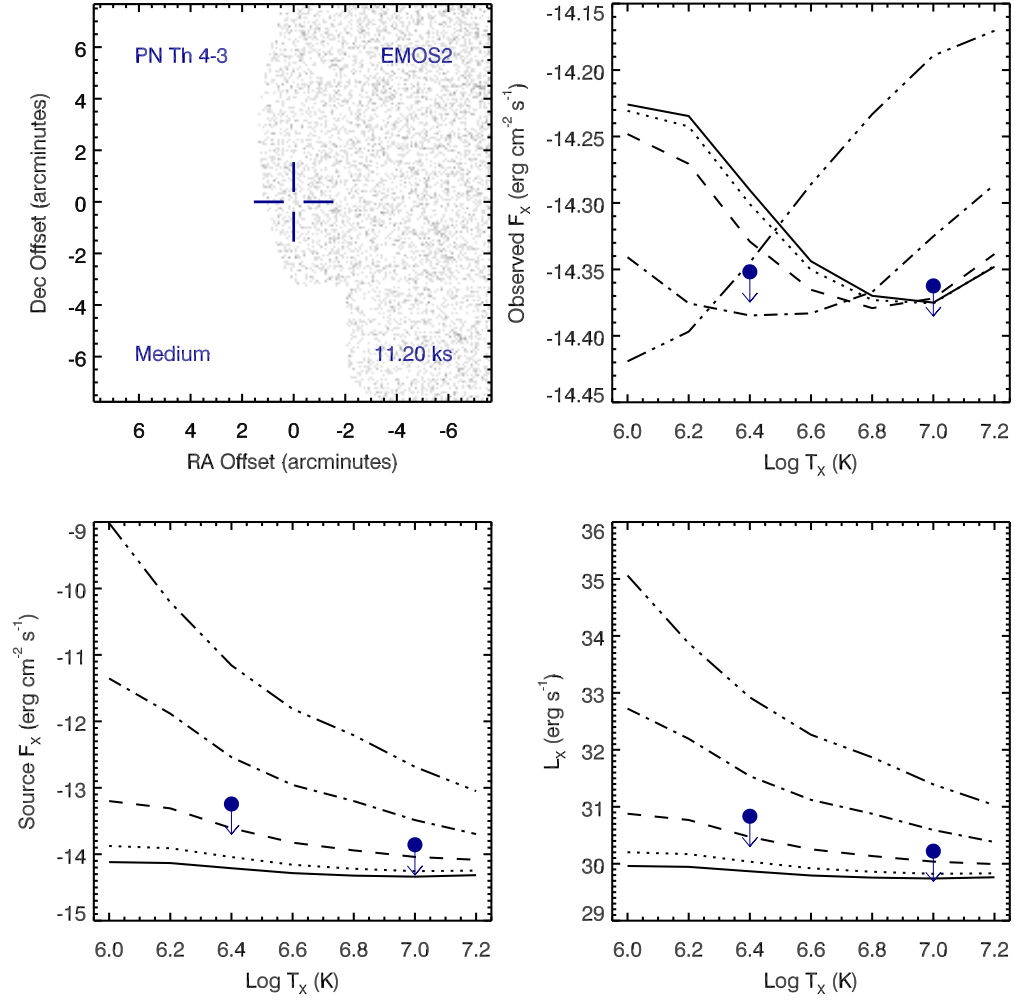


Figure A.119 Serendipitous XMM EMOS2 observation (ObsID 0306700501) of PN Th 4-3 ; panels as in Figure A.118.

## PN VBE 2 , ObsID 0204270101

Table A.53 Summary of the Analysis for the XMM EPIC observation (ObsID 0204270101) of PN VBE 2.

Basic Data			
Parameter	Value	Notes	
RA (J2000)	237.828420		
DEC (J2000)	-56.356060	Offset (')	8.40
$R_{\text{nebula}}$ (")	–		
$D$ (kpc)	1.0	unknown, assumed value	
$\log N_H$ (cm <sup>-2</sup> )	21.6990	unknown, assumed value	
$T_{\text{eff}}$ (kK)	–		
Date Obs:	2004-08-11	XMM Filter:	Medium

Calculations			
Parameter	EMOS1	EMOS2	EPN
$t_{\text{exp}}$ (ks)	17.2	17.9	–
$\text{CR}_{\text{src}}$ (cnt s <sup>-1</sup> )	2.309E-06	2.023E-06	–
$\text{CR}_{\text{bkg}}$ (cnt s <sup>-1</sup> )	2.199E-06	1.721E-06	–

Hot Bubble Upper Limits ( $T_X \sim 3 \times 10^6$ K)			
Parameter	EMOS1	EMOS2	EPN
$F_X$ (erg cm <sup>-2</sup> s <sup>-1</sup> )	-13.0627	-13.1242	–
$L_X$ (erg s <sup>-1</sup> )	31.0152	30.9537	–

Spun-up Companion Upper Limits ( $T_X \sim 10^7$ K)			
Parameter	EMOS1	EMOS2	EPN
$F_X$ (erg cm <sup>-2</sup> s <sup>-1</sup> )	-13.6757	-13.7373	–
$L_X$ (erg s <sup>-1</sup> )	30.4022	30.3406	–
$L_*$ ( $L_{\text{sun}}$ )	0.6566	0.5698	–
$M_{\text{bol}}$ (mag)	5.1968	5.3507	–
Spectral Type	G8-K0V	G8-K0V	–

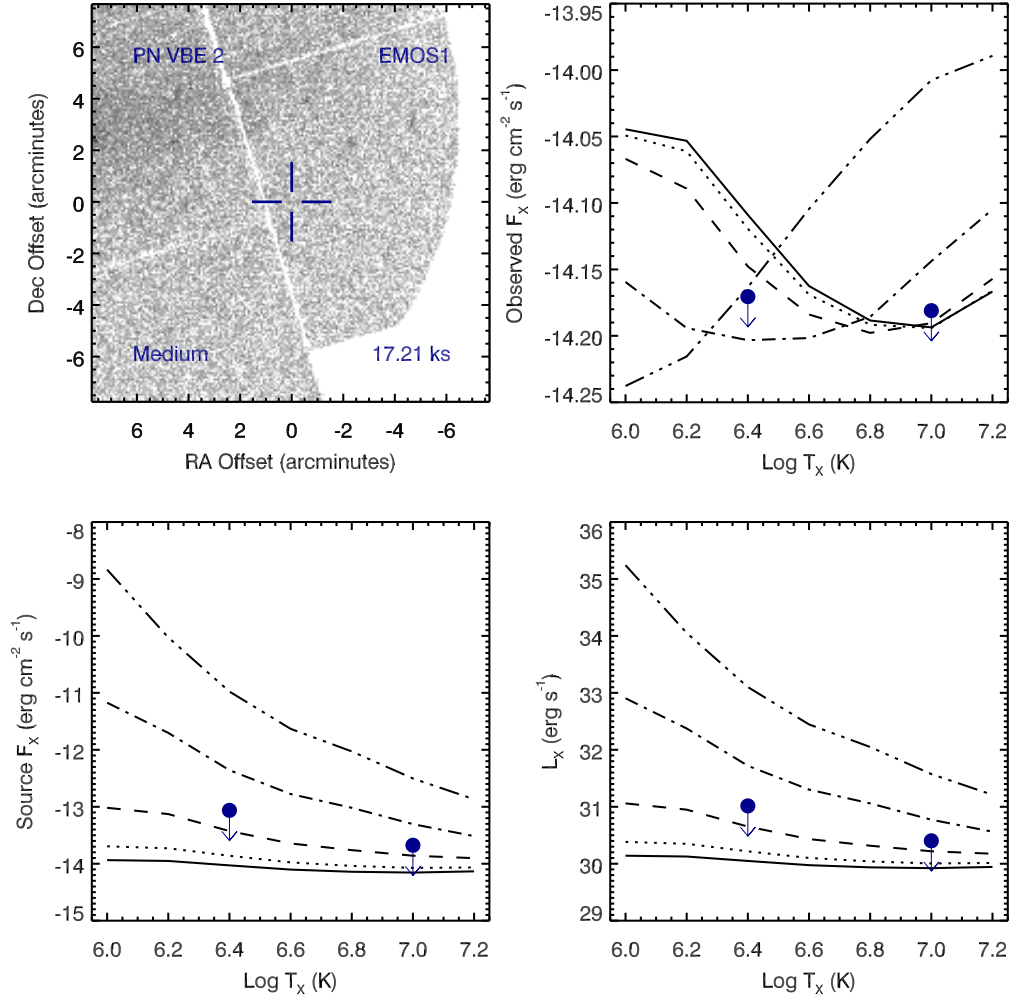


Figure A.120 Serendipitous XMM EMOS1 observation (ObsID 0204270101) of PN VBE 2. Clock-wise from top-left: broad band (0.3 to 8.0 keV) image at the PN position, upper limits of the observed flux, X-ray luminosity, and source X-ray flux. The upper limits calculations are based on the upper limit count rates, a thermal plasma model at a range temperatures, and a range of intervening absorption values:  $N_H(10^{22} \text{ cm}^{-2}) = 0.03$  (solid), 0.1 (dotted), 0.3 (dashed), 1 (dot-dashed), and 3 (dot-dot-dashed). The hot bubble and spun-up companion upper limits are depicted as the filled circles with downward pointing arrows at  $\log T_x$  of 6.4 and 7.0, respectively.

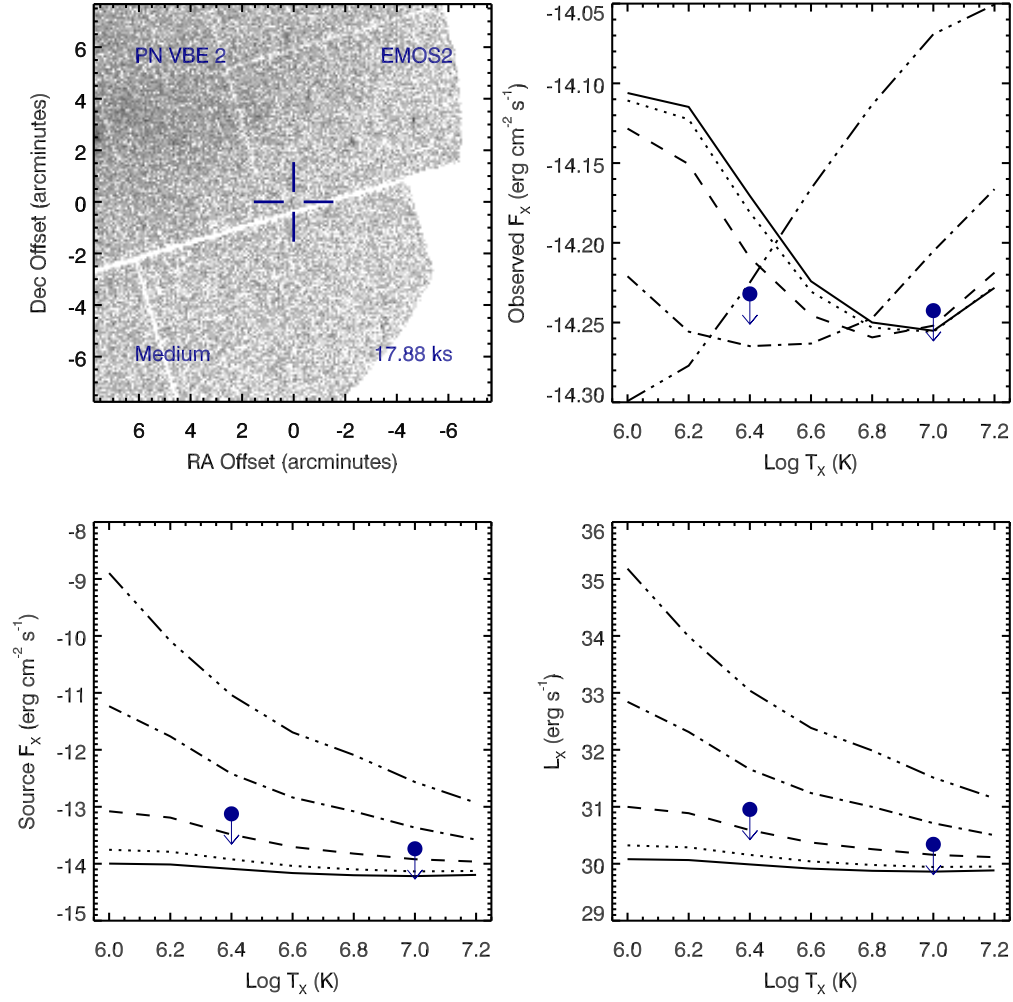


Figure A.121 Serendipitous XMM EMOS2 observation (ObsID 0204270101) of PN VBE 2 ; panels as in Figure A.120.

## PN VBE 3 , ObsID 0204270101

Table A.54 Summary of the Analysis for the XMM EPIC observation (ObsID 0204270101) of PN VBE 3.

Basic Data			
Parameter	Value	Notes	
RA (J2000)	238.246704		
DEC (J2000)	-56.407553	Offset (')	8.75
$R_{\text{nebula}}$ (")	6.0	from literature (A94)	
$D$ (kpc)	1.0	unknown, assumed value	
$\log N_H$ (cm <sup>-2</sup> )	21.6990	unknown, assumed value	
$T_{\text{eff}}$ (kK)	–		
Date Obs:	2004-08-11	XMM Filter:	Medium

Calculations			
Parameter	EMOS1	EMOS2	EPN
$t_{\text{exp}}$ (ks)	17.2	17.9	–
$\text{CR}_{\text{src}}$ (cnt s <sup>-1</sup> )	2.219E-06	2.678E-06	–
$\text{CR}_{\text{bkg}}$ (cnt s <sup>-1</sup> )	2.138E-06	1.647E-06	–

Hot Bubble Upper Limits ( $T_X \sim 3 \times 10^6$ K)			
Parameter	EMOS1	EMOS2	EPN
$F_X$ (erg cm <sup>-2</sup> s <sup>-1</sup> )	-13.0691	-13.1338	–
$L_X$ (erg s <sup>-1</sup> )	31.0089	30.9441	–

Spun-up Companion Upper Limits ( $T_X \sim 10^7$ K)			
Parameter	EMOS1	EMOS2	EPN
$F_X$ (erg cm <sup>-2</sup> s <sup>-1</sup> )	-13.6821	-13.7469	–
$L_X$ (erg s <sup>-1</sup> )	30.3958	30.3310	–
$L_*$ ( $L_{\text{sun}}$ )	0.6470	0.5573	–
$M_{\text{bol}}$ (mag)	5.2128	5.3747	–
Spectral Type	G8-K0V	G8-K0V	–

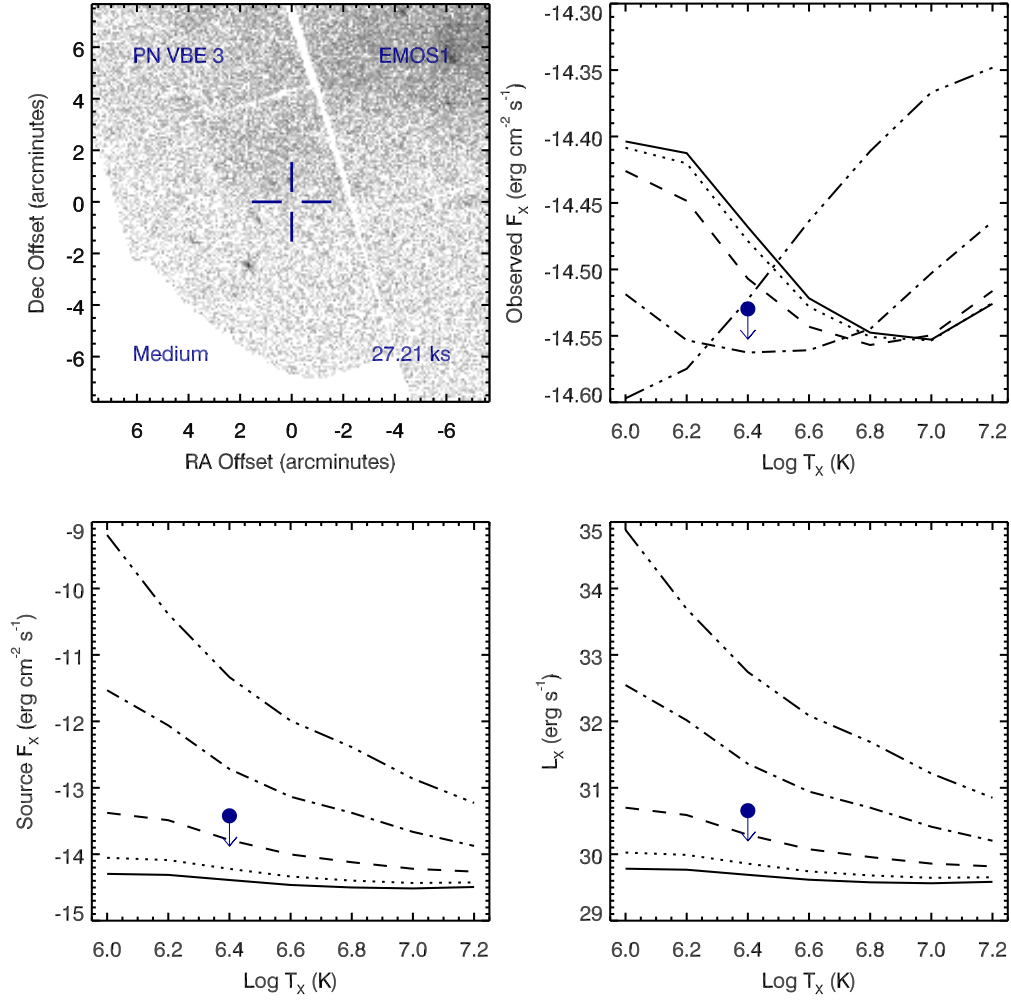


Figure A.122 Serendipitous XMM EMOS1 observation (ObsID 0204270101) of PN VBE 3. Clock-wise from top-left: broad band (0.3 to 8.0 keV) image at the PN position, upper limits of the observed flux, X-ray luminosity, and source X-ray flux. The upper limits calculations are based on the upper limit count rates, a thermal plasma model at a range temperatures, and a range of intervening absorption values:  $N_H(10^{22} \text{ cm}^{-2}) = 0.03$  (solid), 0.1 (dotted), 0.3 (dashed), 1 (dot-dashed), and 3 (dot-dot-dashed). The hot bubble and spun-up companion upper limits are depicted as the filled circles with downward pointing arrows at  $\log T_X$  of 6.4 and 7.0, respectively.

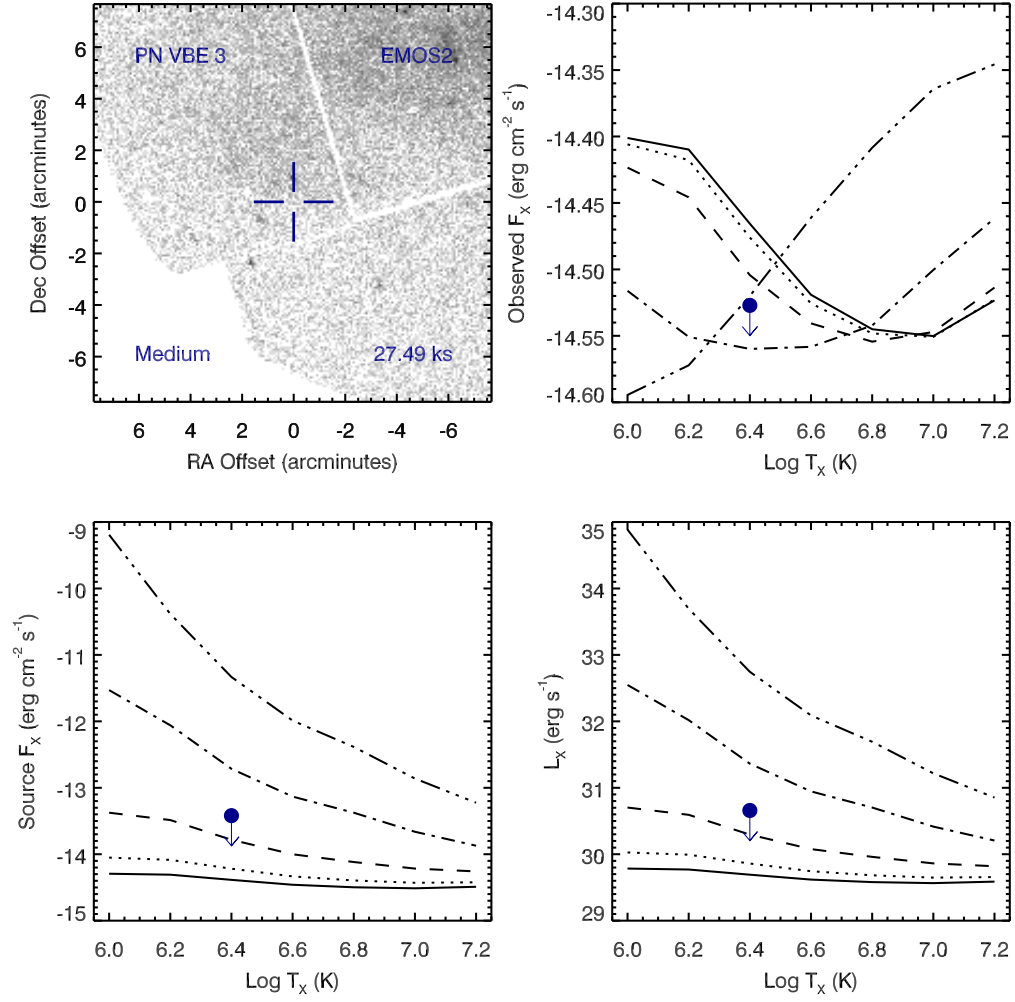


Figure A.123 Serendipitous XMM EMOS2 observation (ObsID 0204270101) of PN VBE 3 ; panels as in Figure A.122.



## PN Vd 1-8 , ObsID 0083280101

Table A.55 Summary of the Analysis for the XMM EPIC observation (ObsID 0083280101) of PN Vd 1-8.

Basic Data			
Parameter	Value	Notes	
RA (J2000)	256.140830		
DEC (J2000)	-37.887580	Offset (')	7.75
$R_{\text{nebula}}$ (")	—		
$D$ (kpc)	1.0	unknown, assumed value	
$\log N_H$ (cm <sup>-2</sup> )	21.6990	unknown, assumed value	
$T_{\text{eff}}$ (kK)	100.50	HeI or HeII Zanstra (Ph03)	
Date Obs:	2001-02-17	XMM Filter:	Thick

Calculations			
Parameter	EMOS1	EMOS2	EPN
$t_{\text{exp}}$ (ks)	24.5	25.7	—
$\text{CR}_{\text{src}}$ (cnt s <sup>-1</sup> )	5.814E-07	5.954E-07	—
$\text{CR}_{\text{bkg}}$ (cnt s <sup>-1</sup> )	5.239E-07	5.099E-07	—

Hot Bubble Upper Limits ( $T_X \sim 3 \times 10^6$ K)			
Parameter	EMOS1	EMOS2	EPN
$F_X$ (erg cm <sup>-2</sup> s <sup>-1</sup> )	-13.3694	-13.3851	—
$L_X$ (erg s <sup>-1</sup> )	30.7085	30.6928	—

Spun-up Companion Upper Limits ( $T_X \sim 10^7$ K)			
Parameter	EMOS1	EMOS2	EPN
$F_X$ (erg cm <sup>-2</sup> s <sup>-1</sup> )	-14.0065	-14.0222	—
$L_X$ (erg s <sup>-1</sup> )	30.0714	30.0557	—
$L_*$ ( $L_{\text{sun}}$ )	0.3065	0.2957	—
$M_{\text{bol}}$ (mag)	6.0238	6.0630	—
Spectral Type	K2-K5V	K2-K5V	—

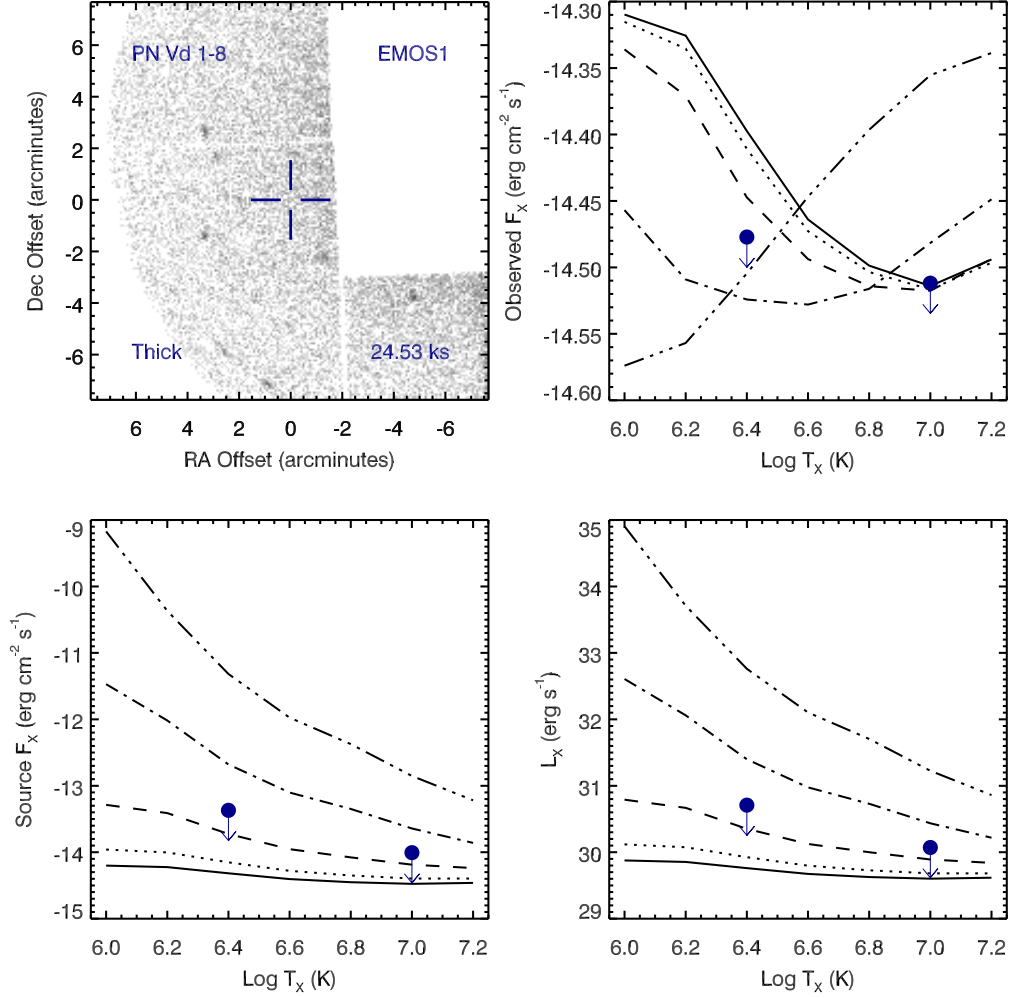


Figure A.124 Serendipitous XMM EMOS1 observation (ObsID 0083280101) of PN Vd 1-8. Clock-wise from top-left: broad band (0.3 to 8.0 keV) image at the PN position, upper limits of the observed flux, X-ray luminosity, and source X-ray flux. The upper limits calculations are based on the upper limit count rates, a thermal plasma model at a range temperatures, and a range of intervening absorption values:  $N_H(10^{22} \text{ cm}^{-2}) = 0.03$  (solid), 0.1 (dotted), 0.3 (dashed), 1 (dot-dashed), and 3 (dot-dot-dashed). The hot bubble and spun-up companion upper limits are depicted as the filled circles with downward pointing arrows at  $\log T_x$  of 6.4 and 7.0, respectively.

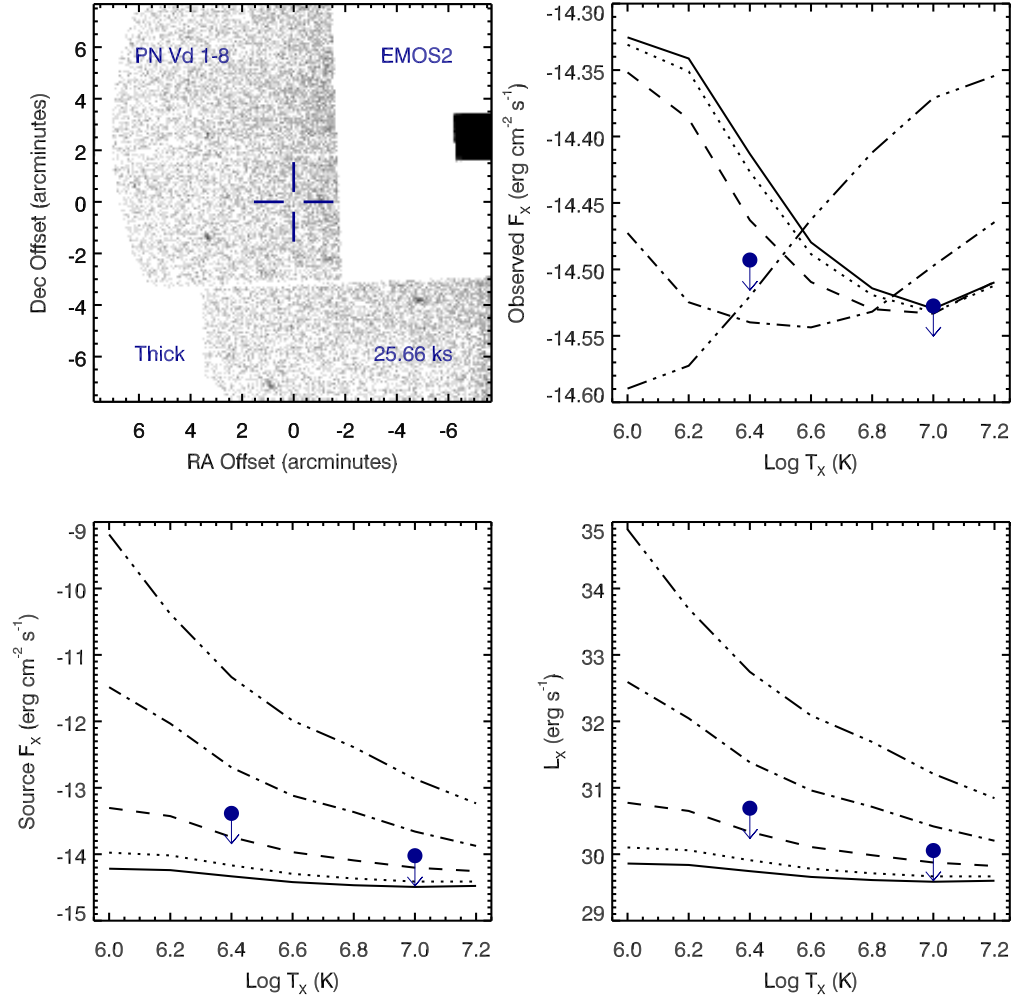


Figure A.125 Serendipitous XMM EMOS2 observation (ObsID 0083280101) of PN Vd 1-8 ; panels as in Figure A.124.

## PN Vd 1-8 , ObsID 0083280201

Table A.56 Summary of the Analysis for the XMM EPIC observation (ObsID 0083280201) of PN Vd 1-8.

Basic Data			
Parameter	Value	Notes	
RA (J2000)	256.140830		
DEC (J2000)	-37.887580	Offset (')	7.75
$R_{\text{nebula}}$ (")	—		
$D$ (kpc)	1.0	unknown, assumed value	
$\log N_H$ (cm <sup>-2</sup> )	21.6990	unknown, assumed value	
$T_{\text{eff}}$ (kK)	100.50	HeI or HeII Zanstra (Ph03)	
Date Obs:	2001-02-18	XMM Filter:	Thick

Calculations			
Parameter	EMOS1	EMOS2	EPN
$t_{\text{exp}}$ (ks)	31.6	32.3	—
$\text{CR}_{\text{src}}$ (cnt s <sup>-1</sup> )	6.930E-07	4.105E-07	—
$\text{CR}_{\text{bkg}}$ (cnt s <sup>-1</sup> )	7.163E-07	6.981E-07	—

Hot Bubble Upper Limits ( $T_X \sim 3 \times 10^6$ K)			
Parameter	EMOS1	EMOS2	EPN
$F_X$ (erg cm <sup>-2</sup> s <sup>-1</sup> )	-13.3565	-13.3665	—
$L_X$ (erg s <sup>-1</sup> )	30.7214	30.7114	—

Spun-up Companion Upper Limits ( $T_X \sim 10^7$ K)			
Parameter	EMOS1	EMOS2	EPN
$F_X$ (erg cm <sup>-2</sup> s <sup>-1</sup> )	-13.9935	-14.0037	—
$L_X$ (erg s <sup>-1</sup> )	30.0844	30.0742	—
$L_*$ ( $L_{\text{sun}}$ )	0.3159	0.3086	—
$M_{\text{bol}}$ (mag)	5.9913	6.0166	—
Spectral Type	K2-K5V	K2-K5V	—

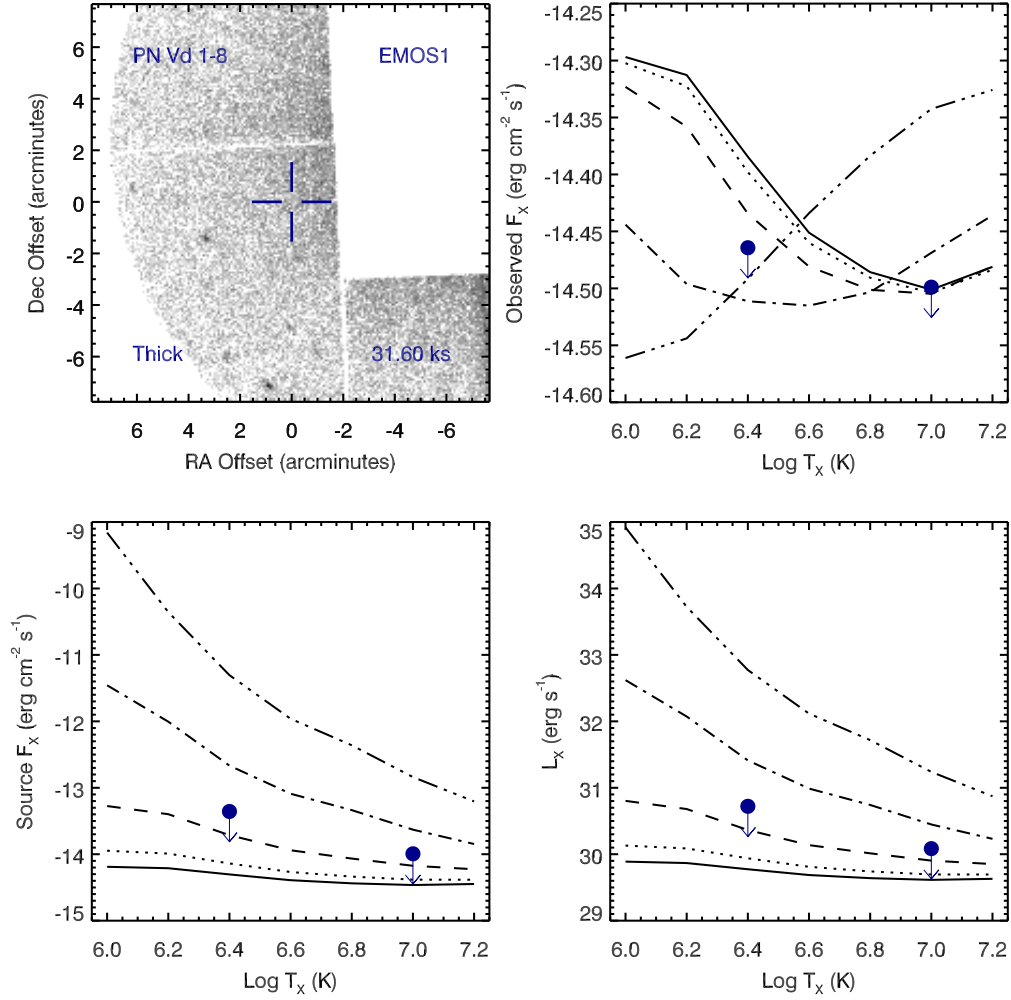


Figure A.126 Serendipitous XMM EMOS1 observation (ObsID 0083280201) of PN Vd 1-8. Clock-wise from top-left: broad band (0.3 to 8.0 keV) image at the PN position, upper limits of the observed flux, X-ray luminosity, and source X-ray flux. The upper limits calculations are based on the upper limit count rates, a thermal plasma model at a range temperatures, and a range of intervening absorption values:  $N_H(10^{22} \text{ cm}^{-2}) = 0.03$  (solid),  $0.1$  (dotted),  $0.3$  (dashed),  $1$  (dot-dashed), and  $3$  (dot-dot-dashed). The hot bubble and spun-up companion upper limits are depicted as the filled circles with downward pointing arrows at  $\log T_x$  of 6.4 and 7.0, respectively.

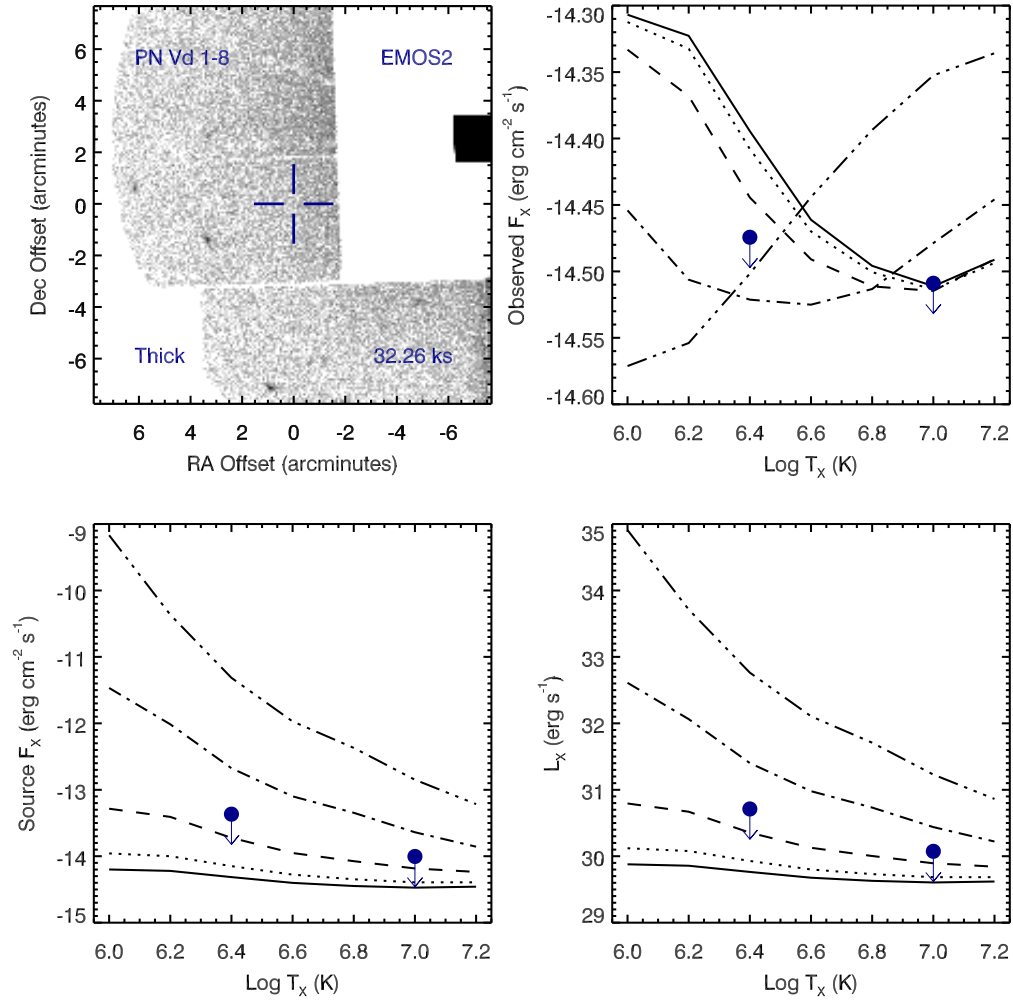


Figure A.127 Serendipitous XMM EMOS2 observation (ObsID 0083280201) of PN Vd 1-8 ; panels as in Figure A.126.

## PN Vd 1-8 , ObsID 0083280301

Table A.57 Summary of the Analysis for the XMM EPIC observation (ObsID 0083280301) of PN Vd 1-8.

Basic Data			
Parameter	Value	Notes	
RA (J2000)	256.140830		
DEC (J2000)	-37.887580	Offset (')	7.75
$R_{\text{nebula}}$ (")	—		
$D$ (kpc)	1.0	unknown, assumed value	
$\log N_H$ ( $\text{cm}^{-2}$ )	21.6990	unknown, assumed value	
$T_{\text{eff}}$ (kK)	100.50	HeI or HeII Zanstra (Ph03)	
Date Obs:	2001-02-19	XMM Filter:	Thick

Calculations			
Parameter	EMOS1	EMOS2	EPN
$t_{\text{exp}}$ (ks)	19.4	20.1	—
$\text{CR}_{\text{src}}$ ( $\text{cnt s}^{-1}$ )	3.670E-07	5.333E-07	—
$\text{CR}_{\text{bkg}}$ ( $\text{cnt s}^{-1}$ )	4.672E-07	4.174E-07	—

Hot Bubble Upper Limits ( $T_X \sim 3 \times 10^6$ K)			
Parameter	EMOS1	EMOS2	EPN
$F_X$ ( $\text{erg cm}^{-2} \text{ s}^{-1}$ )	-13.3437	-13.3750	—
$L_X$ ( $\text{erg s}^{-1}$ )	30.7342	30.7029	—

Spun-up Companion Upper Limits ( $T_X \sim 10^7$ K)			
Parameter	EMOS1	EMOS2	EPN
$F_X$ ( $\text{erg cm}^{-2} \text{ s}^{-1}$ )	-13.9809	-14.0122	—
$L_X$ ( $\text{erg s}^{-1}$ )	30.0970	30.0658	—
$L_*$ ( $L_{\text{sun}}$ )	0.3252	0.3026	—
$M_{\text{bol}}$ (mag)	5.9597	6.0378	—
Spectral Type	K0-K2V	K2-K5V	—

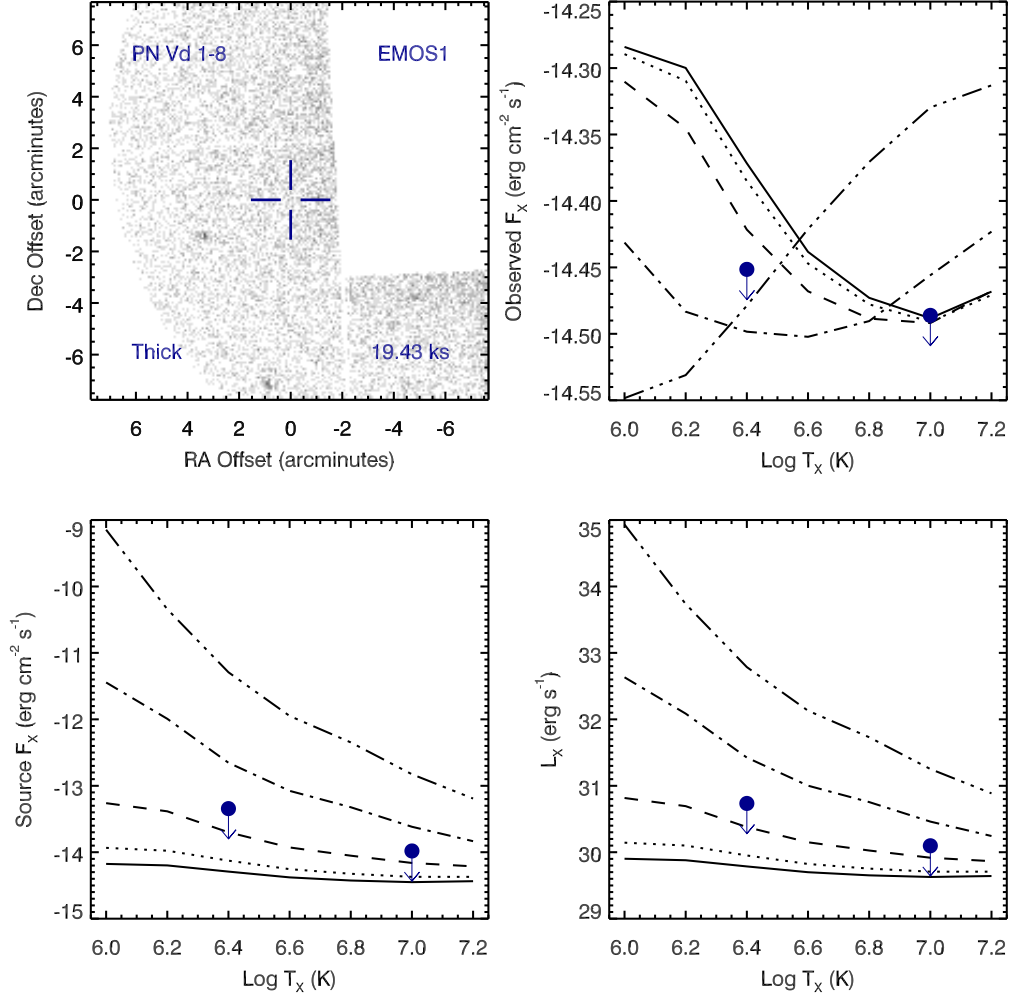


Figure A.128 Serendipitous XMM EMOS1 observation (ObsID 0083280301) of PN Vd 1-8. Clock-wise from top-left: broad band (0.3 to 8.0 keV) image at the PN position, upper limits of the observed flux, X-ray luminosity, and source X-ray flux. The upper limits calculations are based on the upper limit count rates, a thermal plasma model at a range temperatures, and a range of intervening absorption values:  $N_H(10^{22} \text{ cm}^{-2}) = 0.03$  (solid), 0.1 (dotted), 0.3 (dashed), 1 (dot-dashed), and 3 (dot-dot-dashed). The hot bubble and spun-up companion upper limits are depicted as the filled circles with downward pointing arrows at  $\log T_x$  of 6.4 and 7.0, respectively.



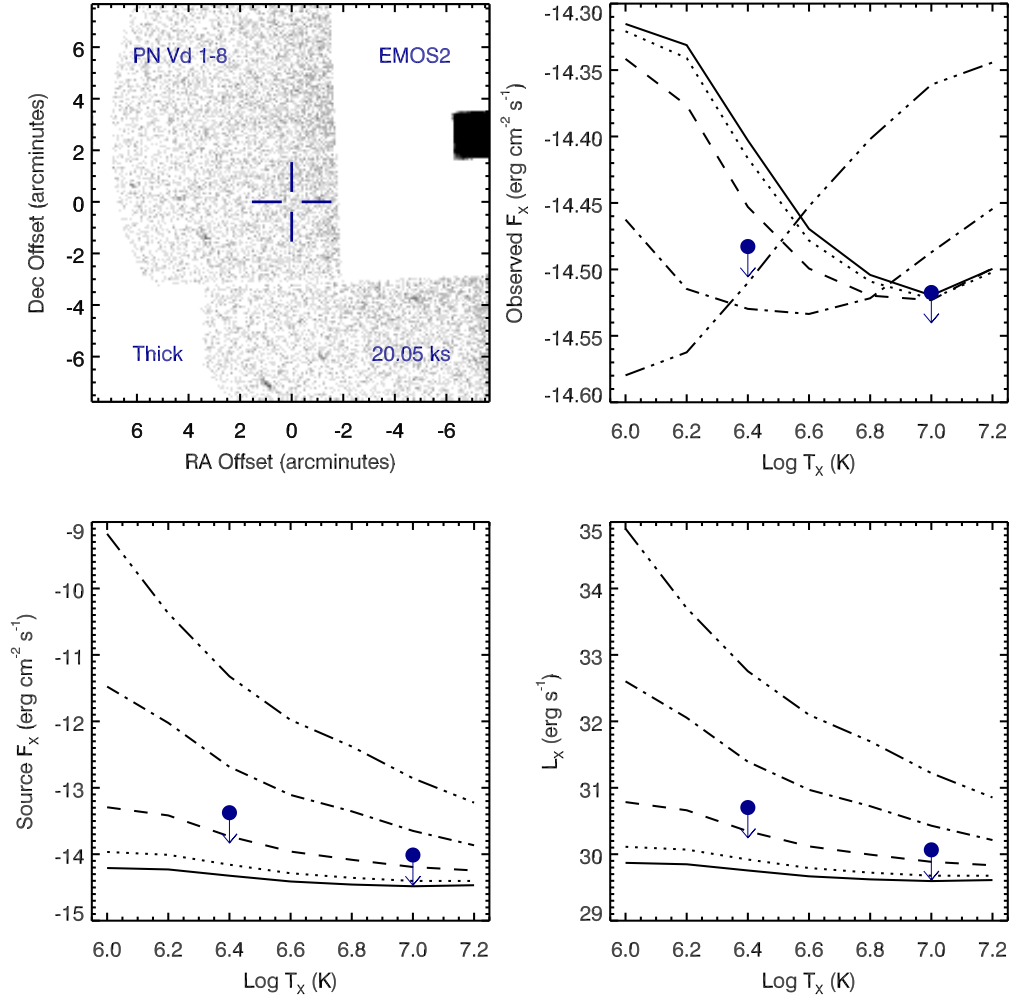


Figure A.129 Serendipitous XMM EMOS2 observation (ObsID 0083280301) of PN Vd 1-8 ; panels as in Figure A.128.

# PN Vd 1-8 , ObsID 0083280401

Table A.58 Summary of the Analysis for the XMM EPIC observation (ObsID 0083280401) of PN Vd 1-8.

Basic Data			
Parameter	Value	Notes	
RA (J2000)	256.140830		
DEC (J2000)	-37.887580	Offset (')	7.75
$R_{\text{nebula}}$ (")	—		
$D$ (kpc)	1.0	unknown, assumed value	
$\log N_H$ (cm <sup>-2</sup> )	21.6990	unknown, assumed value	
$T_{\text{eff}}$ (kK)	100.50	HeI or HeII Zanstra (Ph03)	
Date Obs:	2001-02-20	XMM Filter:	Thick

Calculations			
Parameter	EMOS1	EMOS2	EPN
$t_{\text{exp}}$ (ks)	30.0	30.7	—
$\text{CR}_{\text{src}}$ (cnt s <sup>-1</sup> )	4.578E-07	4.646E-07	—
$\text{CR}_{\text{bkg}}$ (cnt s <sup>-1</sup> )	3.940E-07	4.978E-07	—

Hot Bubble Upper Limits ( $T_X \sim 3 \times 10^6$ K)			
Parameter	EMOS1	EMOS2	EPN
$F_X$ (erg cm <sup>-2</sup> s <sup>-1</sup> )	-13.4753	-13.4291	—
$L_X$ (erg s <sup>-1</sup> )	30.6026	30.6488	—

Spun-up Companion Upper Limits ( $T_X \sim 10^7$ K)			
Parameter	EMOS1	EMOS2	EPN
$F_X$ (erg cm <sup>-2</sup> s <sup>-1</sup> )	-14.1124	-14.0663	—
$L_X$ (erg s <sup>-1</sup> )	29.9655	30.0116	—
$L_*$ ( $L_{\text{sun}}$ )	0.2402	0.2671	—
$M_{\text{bol}}$ (mag)	6.2886	6.1732	—
Spectral Type	K2-K5V	K2-K5V	—

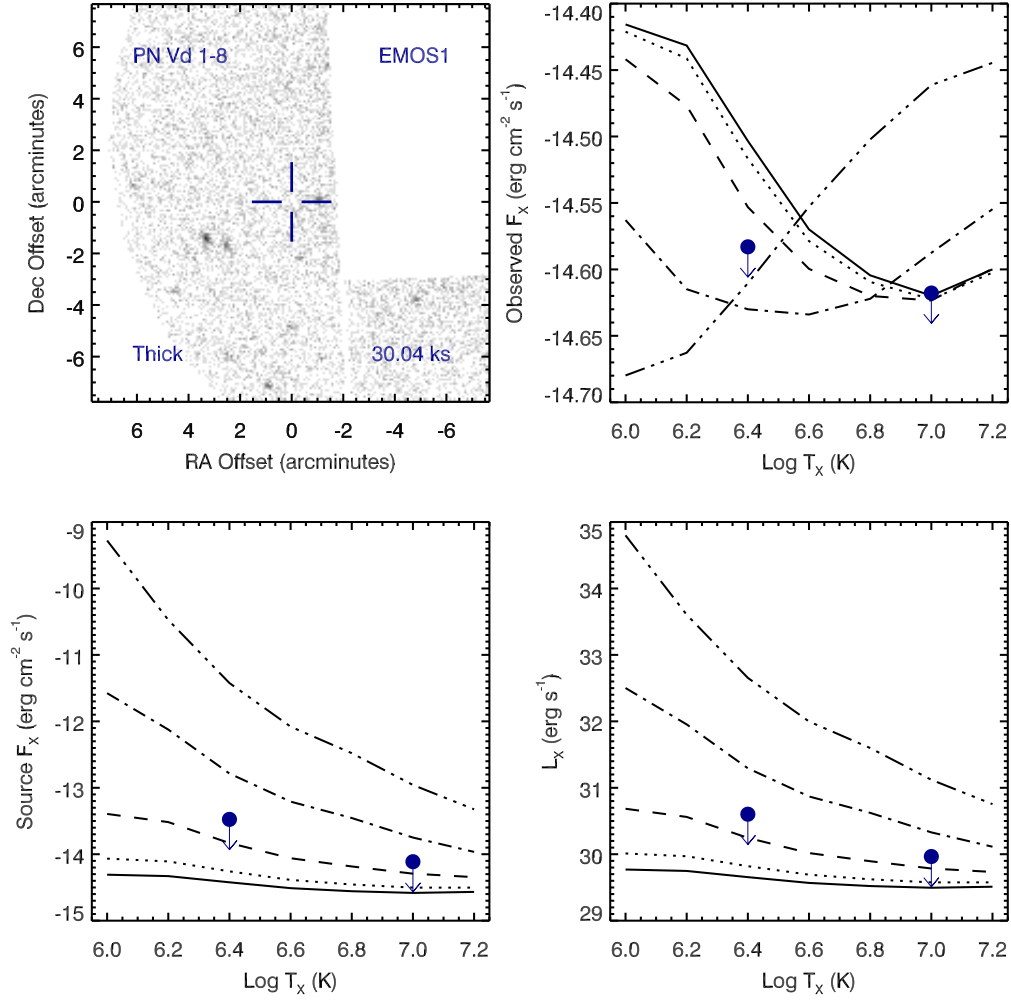


Figure A.130 Serendipitous XMM EMOS1 observation (ObsID 0083280401) of PN Vd 1-8. Clock-wise from top-left: broad band (0.3 to 8.0 keV) image at the PN position, upper limits of the observed flux, X-ray luminosity, and source X-ray flux. The upper limits calculations are based on the upper limit count rates, a thermal plasma model at a range temperatures, and a range of intervening absorption values:  $N_H(10^{22} \text{ cm}^{-2}) = 0.03$  (solid), 0.1 (dotted), 0.3 (dashed), 1 (dot-dashed), and 3 (dot-dot-dashed). The hot bubble and spun-up companion upper limits are depicted as the filled circles with downward pointing arrows at  $\log T_X$  of 6.4 and 7.0, respectively.

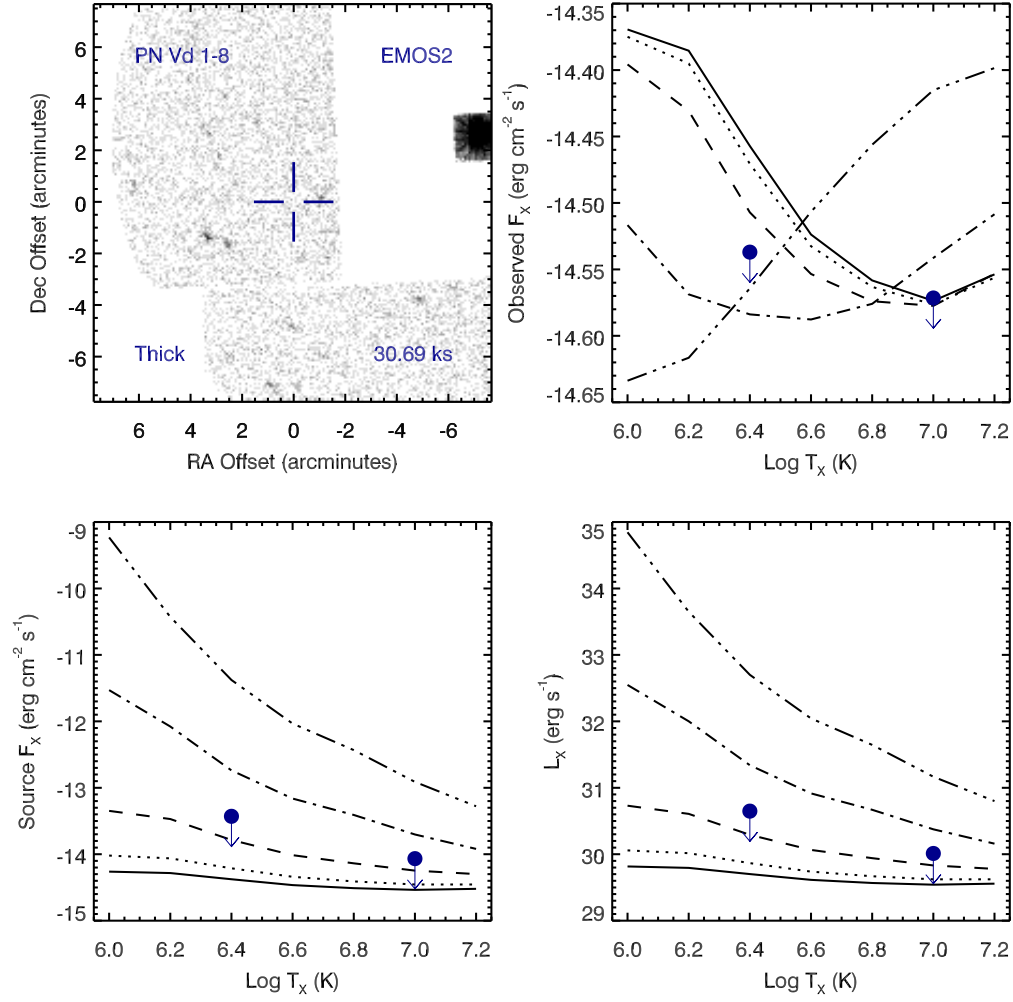


Figure A.131 Serendipitous XMM EMOS2 observation (ObsID 0083280401) of PN Vd 1-8 ; panels as in Figure A.130.